

DEVELOPMENT AND APPLICATION OF THE SURFACE LASER INDUCED  
FLUORESCENCE TECHNIQUE

Except where reference is made to the work of others, the work described in this dissertation is my own or was done in collaboration with my advisory committee.

This dissertation does not include proprietary or classified information.

---

Gregory W. Donath

Certificate of Approval:

---

Robert P. Chambers  
Professor  
Chemical Engineering

---

Steve R. Duke, Chair  
Associate Professor  
Chemical Engineering

---

Clifford Lange  
Associate Professor  
Civil and Environmental Engineering

---

Yoon Y. Lee  
Professor  
Chemical Engineering

---

George T. Flowers  
Dean  
Graduate School

DEVELOPMENT AND APPLICATION OF THE SURFACE LASER INDUCED  
FLUORESCENCE TECHNIQUE

Gregory Wayne Donath

A Dissertation

Submitted to

the Graduate Faculty of

Auburn University

in Partial Fulfillment of the

Requirements for the

Degree of

Doctor of Philosophy

Auburn, Alabama  
December 19<sup>th</sup>, 2008

DEVELOPMENT AND APPLICATION OF THE SURFACE LASER INDUCED  
FLUORESCENCE TECHNIQUE

Gregory Wayne Donath

Permission is granted to Auburn University to make copies of this dissertation at its discretion upon request of individuals or institutions at their expense. The author reserves all publication rights.

---

Signature of Author

---

Date of Graduation

DEVELOPMENT AND APPLICATION OF THE SURFACE LASER INDUCED  
FLUORESCENCE TECHNIQUE

Gregory W. Donath

Doctor of Philosophy, December 19<sup>th</sup> 2008  
(B.S., Michigan State University, 1998)

430 Typed Pages

Directed By Steve Duke

The mechanisms that control the mass transfer of gases across the air-water interface are not well understood. Current models for air and water gas transfer have limited effectiveness because they are based on large scale bulk conditions and empirical estimates, yet the mechanisms that control the transfer are small scale. The Surface Laser Induced Fluorescence (SLIF) technique was developed and it provided measurement of small scale variation in mass transfer across the surface of the liquid. The SLIF technique was applied to study the relationship between atmospheric humidity and oxygen mass transfer across the air-water interface.

The Surface Laser Induced Fluorescence technique is based on the premise that variation of surface-imaged fluorescence intensity of a dissolved fluorescent probe corresponds to variation in the oxygen concentration below the surface because the oxygen acts as a quencher of the probe. A tank system was developed to create a known

difference in the concentration gradient within the same SLIF image to demonstrate that the SLIF system detects variation in fluorescence related solely to variations in oxygen concentration. Image processing procedures were developed to remove uneven incident radiation. The SLIF system demonstrated large fluorescence intensity differences between water saturated with dissolved oxygen and water with low levels of dissolved oxygen.

The SLIF technique was applied to study oxygen mass transfer across flat air-water interfaces. The SLIF images were transformed into mapped estimates of the relative mass transfer rates and boundary layer thicknesses with high spatial resolution. The Surface Laser Induced Fluorescence technique identified mass transfer variations related to Rayleigh-Bénard downwelling within flat air-water interface images and maps.

The effect of relative humidity on mass transfer across flat air-water interfaces was examined using the SLIF technique. It was shown that the relative humidity had an effect upon the presence, size, speed, and relative thickness of Rayleigh-Bénard downwelling zones under flat air-water interfaces. It is theorized that Rayleigh-Bénard circulations affect the mass transfer of gases across the interface by convective transport of oxygen rich liquid to downwelling zones from the surrounding liquid just below the air-water interface. The transport of oxygen rich liquid from this near-surface zone reduces the resistance to mass transfer across the interface for renewed areas but increases the mass transfer resistance across the downwelling zones.

## ACKNOWLEDGEMENTS

I should first like to thank my advisor, Dr. Steve R. Duke whose grace and patience have allowed me to succeed in this endeavor. I would like to thank Dr. Yoon Lee, Dr. Robert Chambers, and Dr. Clifford Lange for their assistance with my defense. I would also like to thank the research group for their combined assistance over the years.

On a personal note, I would also like to thank my grandfather, Rolland Briggs Bates, whose foresight, wisdom, and generosity allowed me to reach this goal. I would like to thank my mother, Patricia for her unwavering support throughout my life. Finally, I wish to thank the various friends I have made at Auburn through the years. Their presence in my life has been quite rewarding.

The bibliography was prepared in the style of The Journal of Fluid Mechanics.

Microsoft Word, Microsoft Excel, Microsoft Photoshop, Microsoft Visio, Techplot and Matlab were used to prepare this manuscript.

## TABLE OF CONTENTS

LIST OF TABLES.....	xiv
LIST OF FIGURES.....	xvi
1. INTRODUCTION.....	1
2. BACKGROUND.....	7
2.1. Mass transfer of sparingly soluble gases.....	7
2.2. Gas transfer models.....	12
2.3. Overview of studies on air-water mass transfer.....	17
2.3.1. Overview of mass transfer studies.....	17
2.3.2 Overview of mass transfer studies using microscopic techniques.....	20
2.4. Dynamics of flat interfaces.....	23
2.4.1. Rayleigh- Bénard thermal instabilities.....	24
2.4.2. Pearson- Bénard thermal instability.....	26
2.4.3. Evaporative effect on instability.....	28
2.4.4. Thermal instability in water.....	31
2.5 Estimating the evaporation rate of water.....	33
Chapter 2 figures.....	34

3. SURFACE LASER INDUCED FLUORESCENCE THEORY.....	41
3.1. PBA quenching techniques and principles.....	41
3.1.1. Pyrene butyric acid.....	41
3.1.2. Collisional quenching.....	43
3.2. Relationship between CCD and surface.....	46
3.3. PBA SLIF.....	50
3.3.1. Raw fluorescence intensity for an oxygen-PBA system.....	50
3.3.2. Dimensionless oxygen concentration.....	50
3.3.4. Fully quenched conditions.....	51
3.3.5. Background subtraction.....	53
3.3.6. Mass transfer.....	54
3.4. Normalization.....	58
Chapter 3 figures.....	60
4. RESEARCH METHODS.....	65
4.1. Apparatus.....	65
4.1.1. UV laser system.....	65
4.1.2. Wave tank system.....	67
4.1.3. Imaging system.....	69
4.1.4. System connections.....	70
4.2. Auxiliary equipment.....	71
4.3. PBA solutions.....	71
4.4. Evaporation measurements.....	72
4.5. SLIF operational procedure.....	73
4.5.1. Alignment of laser and image system.....	73

4.5.2. Imaging of a quenched surface.....	75
4.5.3. Imaging of an unquenched surface.....	75
4.5.4. Dark current image generation.....	76
4.6. SLIF validation experiment.....	77
4.6.1. Equipment.....	78
4.6.2. Procedure.....	78
4.7. Experiment under controlled humidity.....	79
4.7.1. Equipment.....	79
4.7.2. Procedure.....	80
Chapter 4 figures.....	82
5. IMAGE PROCESSING.....	89
5.1 Overview image processing.....	90
5.1.1. Dark current removal.....	91
5.1.2. Scratch correction.....	92
5.1.3. Cropping.....	92
5.1.4. Normalization.....	93
5.1.5. Average quenched fluorescence array generation.....	94
5.1.6. Primary background correction.....	95
5.1.7. Secondary background correction.....	98
5.1.8. Relative boundary layer calculation.....	101
5.1.9. Relative mass transfer calculation.....	102
5.2. SLIF verification image processing.....	103
5.2.1. Dark current removal.....	104
5.2.2. Image cell cropping.....	104
5.2.3. Normalization of image cells.....	104

5.2.4	Creation of average quenched fluorescence arrays.....	105
5.2.5	Fluorescence correction.....	105
5.3	Data analysis.....	106
5.3.1	Locating the points of interest.....	106
5.3.2	Locating the shoulders of the downwelling zone.....	108
5.3.3	Calculating the dimensionless mass transfer coefficient for downwelling.....	109
5.3.4	Calculating the half max width.....	109
	Chapter 5 figures.....	111
6. RESULTS AND DISCUSSION:		
	SURFACE LASER INDUCED FLUORESCENCE VERIFICATION STUDY...	122
6.1	SLIF verification study results.....	122
6.1.1	Verification experiment images, 7mm tank.....	124
6.1.2	Verification experiment images, 50 mm tank.....	126
6.1.3	Image cell intensity measurements and analysis.....	130
6.2	Discussion of SLIF verification.....	135
6.2.2	Discussion of image cell data.....	135
6.2.3	Comparison of quenched/unquenched and quenched/quenched image cell sets.....	138
6.2.4	SLIF improvements.....	143
6.3	SLIF verification study conclusions.....	145
	Chapter 6 figures.....	148
7. RESULTS AND DISCUSSION: SLIF DEVELOPMENT STUDY.....		
7.1	SLIF results for development study.....	160

7.1.1. Data used for SLIF development.....	161
7.1.2. Examples of SLIF data.....	164
7.1.3. Adjustment of the SLIF excitation beam.....	168
7.1.4. Data acquired after SLIF excitation beam adjustments.....	170
7.1.5. Refinement of SLIF image processing.....	171
7.2 Image feature analysis.....	174
7.2.1. Analysis of undefined features.....	175
7.2.2. Development of image analysis programs.....	178
7.3 Evaluation of SLIF technique.....	182
7.3.1. Evaluation of qualitative analysis.....	182
7.3.2. Benefits of alterations to the SLIF system.....	185
7.3.3. Evaluation of image processing.....	187
Chapter 7 Figures.....	189

## 8. RESULTS AND DISCUSSION:

THE EFFECT OF ATMOSPHERIC HUMIDITY ON MASS TRANSFER.....	204
8.1. Evaluation of SLIF development data.....	205
8.2. Study of mass transfer and atmospheric humidity.....	211
8.2.1 Example SLIF data from evaporation and oxygen mass transfer experiments.....	215
8.2.2. Results SLIF study of atmospheric humidity and oxygen mass transfer	215
8.3. Discussion of evaporation induced thermal circulations.....	220
8.3.1. Atmospheric humidity and thermal circulation.....	221
8.3.2. Rayleigh-Bénard effects on oxygen mass transfer.....	224
Chapter 8 figures.....	228

9. CONCLUSIONS.....	246
REFERENCES.....	249
APPENDICES.....	258
A. SUPPLIMENTS TO RESEARCH METHODS.....	258
B. GENERATED MATLAB FUNCTIONS.....	264
C. SELECTED DIMENSIONLESS MASS TRANSFER PLOTS.....	294
D. IMAGE LABEL ROSETTA.....	403

## LIST OF TABLES

Table 2.1. Critical Rayleigh Numbers (Koschmeider, 1993).....	24
Table 2.2. Comparison of Marangoni and Rayleigh Critical Values over a range of Biot numbers (Neild, 1964).....	26
Table 4.1. UV24 Laser Properties.....	66
Table 6.1. List of two tank experiments using 7 mm wave tank.....	124
Table 6.2. List of verification study experiments using 50 mm deep wave tank.....	127
Table 6.3. Selected quenched/quenched image cell pairs from image set Ttest9.....	130
Table 6.4. Selected quenched/quenched image cell pairs from image set Ttest7.....	130
Table 6.5. Selected quenched/quenched image cell pairs from image set 1002M.....	133
Table 6.6. Selected unquenched/quenched image cell pairs from image set 1002N...	133
Table 7.1. Unquenched SLIF images for flat surfaces.....	163
Table 7.2. SLIF images for humidity experiments.....	171
Table 7.3. List of conditions in which dark streaks were located within data images..	175
Table 7.4. Stability values for a 10-mm deep open tank of water.....	180
Table 8.1. Applicable constants for water near 25 °C.....	207
Table 8.2. Stability values for a 10-mm deep open tank of water.....	208
Table 8.3. Data sets for humidity experiments.....	211
Table 8.4. Reduced Rayleigh numbers for a 10-mm deep open tank of water.....	214
Table 8.5. List of example images for data sets listed in table 8.2.....	214

Table 8.6. Frequency and start times for humidity study data sets.....	216
Table 8.7. Width measurements for data sets of the evaporation and oxygen mass transfer study.....	217
Table 8.8. Comparison of downwelling movement speed to relative humidity.....	218
Table 8.9. Dimensionless mass transfer coefficient values for SLIF data.....	220

## LIST OF FIGURES

Figure 2.1. Two film theory of mass transfer, illustrating the mass transfer of species A across an interface.....	33
Figure 2.2. Illustration of a circulation cell including mass transfer of species A (Golovin, 1991).....	33
Figure 2.3. Variation in mass transfer rates across the air-water interface showing the surface regimes (Liss and Merlivat, 1986).....	33
Figure 2.4. Constant Heat Flux System ( Jähne, 1995).....	34
Figure 2.5. Heat tracer data of surface renewal events (Shimpf, 1993).....	34
Figure 2.6. Hydrogen chloride mass transfer detection by Fluorecine (Münsterer and Jähne, 1998).....	35
Figure 2.7. Bénard cells (Koschmeider, 1993).....	35
Figure 2.8. Density and surface tension gradients under an adverse temperature gradient.....	36
Figure 2.9. Rayleigh neutral stability curve (Koschmeider, 1993).....	37
Figure 2.10. Pearson-Bénard neutral stability curves (Pearson, 1956).....	38
Figure 2.11. Critical Marangoni Number versus Surface Biot Number (Neild 1964)..	38
Figure 2.12. Comparison of normalized Marangoni number versus normalized Rayleigh number (Neild, 1964).....	39
Figure 2.13. Illustration of evaporative cell, (a) side view, (b) oblique view (Zhang and Chao, 1999).....	39
Figure 2.14. Downwelling zones in water (Berg et. al. 1966b).....	40

Figure 3.1. Absorbance spectra of PBA (Wolff, 1991).....	60
Figure 3.2. Response of PBA to UV excitation.....	60
Figure 3.3. Fluorescence spectra of PBA (Wolff, 1991).....	61
Figure 3.4. Front-face excitation beam geometry (Sharma and Schulman, 1999).....	61
Figure 3.5. PBA excitation in the SLIF system.....	62
Figure 3.6. Relationship between the CCD array and the image.....	62
Figure 3.7. Volume cell diagram.....	62
Figure 3.8. Absorption of excitation radiation.....	63
Figure 3.9. Diagram of tangential boundary layer (developed from Woodrow 2001).....	63
Figure 3.10. Diagram of effective boundary layer.....	64
Figure 4.1. Diagram of SLIF system.....	82
Figure 4.2. Image of SLIF system showing relation of wave tank, camera and laser optics.....	82
Figure 4.3. Image of SLIF system showing relation of wave tank, copy stand and UV24 laser.....	83
Figure 4.4. Optics cage with beam expander and neutral density filter.....	83
Figure 4.5. Targeting mirror assembly.....	84
Figure 4.6. Wave tank and deoxygenating tank (Woodrow 2001).....	84
Figure 4.7. Wave generator (Woodrow 2001).....	85
Figure 4.8. Focusing image using millimeter ruler.....	85
Figure 4.9. Diagram of relationship of inner tank, outer tank, and imaging location.	85
Figure 4.10. Image cell locations in terms of inner tank wall.....	86

Figure 4.11. Image of SLIF Uni-strut optics bench with the constant humidity enclosure attached.....	86
Figure 4.12. An image of the inside of the constant humidity enclosure showing the location of the camera lens opening and the supporting ring stand.....	87
Figure 4.13. An image of the CCD camera head showing the location of the protective shield and the cooling fins of the camera head.....	88
Figure 4.14. An image of the constant humidity enclosure access flap (a) closed (b) open.....	88
Figure 5.1. Image processing steps for standard SLIF, part 1.....	111
Figure 5.2. Image processing steps for standard SLIF, part 2.....	112
Figure 5.3. Image processing steps for standard SLIF, part 3.....	113
Figure 5.4. Contour plot of raw fluorescence intensity values for image D42AB_34; temperature 21 °C, pressure 30.33 inHg, humidity 42%, width 17.2 mm.....	114
Figure 5.5. Cropped raw fluorescence image of R63E_92; temperature 21.5 °C, pressure 29.71 inHg, humidity 63%, width 31.75 mm.....	114
Figure 5.6. Normalized fluorescence array for image R63E_92.....	115
Figure 5.7. Contour map of the intensity distribution function for image set D21A; temperature 25 °C, pressure 30.30 inHg, humidity 21%, width 17.2 mm.....	115
Figure 5.8. Contour plot of the normalized corrected fluorescence array for image R63E_92.....	116
Figure 5.9. Example cross sections of a correction array and quenched image showing alignment problems before secondary background correction. Taken from image D42AB_32 at y=100, x=(0 to 150).....	116
Figure 5.10. Secondary correction array for the image R63E_92.....	117
Figure 5.11. Contour plot of normalized corrected fluorescence values for the image R63E_92.....	117
Figure 5.12. Map of the normalized boundary layer thickness for image R63E_92...	118

Figure 5.13. Grayscale plot of the dimensionless mass transfer coefficient values for image R63E_92.....	118
Figure 5.14. SLIF verification study image processing diagram.....	119
Figure 5.15. Image indicating location of image cells in regards to tank features.....	120
Figure 5.16. Cross-section of dimensionless mass transfer coefficient data for image R63E_92 at x= 200.....	120
Figure 5.17. Ideal cross-section of dimensionless mass transfer coefficient data.....	121
Figure 6.1. General layout of the two tank images; TTEST8_1; outer tank, oxygen saturated, depth 5 mm; inner tanks oxygen saturated, depth 4.5 mm.....	148
Figure 6.2. Intensity image of Ttest9_9 with cell cropping locations indicated on the image by reducing the intensity for all excluded points; outer tank, oxygen saturated, depth 5 mm; inner tank, oxygen saturated, depth 4.5 mm.....	149
Figure 6.3. Intensity image of TTEST 9_9 without shading.....	149
Figure 6.4. Intensity image of TTEST 9_1; outer tank, oxygen saturated, depth 5 mm; inner tank, oxygen saturated, depth 4.5 mm.....	150
Figure 6.5. Intensity image of Ttest9_29 outer tank, oxygen saturated, depth 5 mm; inner tank, oxygen saturated, depth 4.5 mm.....	150
Figure 6.6. Intensity image of Ttest9_15; outer tank, oxygen saturated, depth 5 mm; inner tank, oxygen saturated, depth 4.5 mm.....	151
Figure 6.7 Intensity Image of Ttest7_2; outer tank, oxygen depleted, depth 5 mm; inner tank, oxygen saturated, depth 4.5 mm.....	151
Figure 6.8. Intensity image of Ttest7_3; outer tank, oxygen depleted, depth 5 mm; inner tank, oxygen saturated, depth 4.5 mm.....	152
Figure 6.9. Intensity image of Ttest7_4; outer tank, oxygen depleted, depth 5 mm; inner tank, oxygen unsaturated, depth 4.5 mm.....	152

Figure 6.10. Intensity image of Ttest7_5; outer tank, oxygen depleted, depth 5 mm; inner tank, oxygen saturated, depth 4.5 mm.....	153
Figure 6.11. Intensity image of Ttest7_12; outer tank, oxygen depleted, depth 5 mm; inner tank, oxygen saturated, depth 4.5 mm.....	153
Figure 6.12. Intensity image of 1002M_5 with cell cropping locations indicated on the image by reducing the intensity for all excluded points; outer tank, oxygen saturated, depth 35 mm; inner tank, oxygen saturated, depth 35 mm.....	154
Figure 6.13. Intensity image of 1002M_30; outer tank, oxygen saturated, depth 35 mm; inner tank, oxygen saturated, depth 35 mm.....	154
Figure 6.14. Intensity image of 1002M_36; outer tank, oxygen saturated, depth 35 mm; inner tank, oxygen saturated, depth 35 mm.....	155
Figure 6.15. Intensity image of 1002M_41; outer tank, oxygen saturated, depth 35 mm; inner tank, oxygen saturated, depth 35 mm.....	155
Figure 6.16. Intensity image of 1002N_1; outer tank, oxygen depleted, depth 35 mm; inner tank, oxygen saturated, depth 35 mm.....	156
Figure 6.17. Intensity image of 1002N_4; outer tank, oxygen depleted, depth 35 mm; inner tank, oxygen saturated, depth 35 mm.....	156
Figure 6.18. Intensity image of 1002N_7; outer tank, oxygen depleted, depth 35 mm; inner tank , oxygen saturated, depth 35 mm.....	157
Figure 6.19. Intensity image of 1002N_10; outer tank, oxygen depleted, depth 35 mm; inner tank, oxygen saturated, depth 35 mm.....	157
Figure 6.20. Intensity image of 1002N_30; outer tank, oxygen depleted, depth 35 mm; inner tank, oxygen saturated, depth 35 mm.....	158
Figure 6.21. Plot of mean corrected fluorescence values, 7 mm deep two tank system.....	158
Figure 6.22. Plot of mean corrected fluorescence values, 50 mm deep two tank system.....	159
Figure 7.1. Diagram of an example image.....	189

Figure 7.2. Intensity image D21AA_60; temperature 25 °C; pressure 30.33inHg, humidity 21%, width 17.2 mm.....	190
Figure 7.3. False color contour plot of raw fluorescence values for image D21AA_60.....	190
Figure 7.4. Intensity image of D21AB_60; temperature 25 °C, pressure 30.36inHg, humidity 21%, width 17.2 mm.....	191
Figure 7.5. False color contour plot of raw fluorescence values for image D21AB_60.....	191
Figure 7.6. Intensity image D32AA_79; temperature 23 °C, pressure 30.27inHg, humidity 32%, width 17.2 mm.....	192
Figure 7.7. False color contour plot of raw fluorescence values for image D32AA_89; temperature 23 °C, pressure 30.27inHg, humidity 32%, width 17.2 mm.....	192
Figure 7.8. Intensity image of D32AC_45, (a); 48, (b); 52, (c); and 56, (d); temperature 23 °C, pressure 30.27 inHg, humidity 32%, width 17.2 mm.....	193
Figure 7.9. Intensity image of D46BA_16, width 17.2 mm and D46BA_25, width 26.4 mm; temperature 22 °C, pressure 29.83inHg, humidity 46%.....	194
Figure 7.10. Profile view of fluorescence before beam adjustments.....	195
Figure 7.11. Profile view of fluorescence after laser beam was broadened.....	195
Figure 7.12. Profile view of fluorescence after addition of neutral density filters.....	195
Figure 7.13. Intensity image after laser beam expansion and correction, D36BA_10; temperature 22°C, pressure 30.39 inHg, humidity 36%, width 17.2 mm.....	196
Figure 7.14. (a) Intensity image of D42AB_34; (b) Contour plot of relative boundary layer thickness, D42AB_34; temperature 21 °C, pressure 30.33inHg, humidity 42%, width 17.4 mm. These figures compare the appearance in intensity of a dark streak versus the corresponding boundary layer thickness of the same dark streak. D42AB_34 has not undergone secondary background correction in the contour plot of relative boundary layer thickness.....	196

Figure 7.15. Contour plot of dimensionless mass transfer coefficient values for image D42AB_34 using image processing developed from SLIF theory.....	197
Figure 7.16. Raw fluorescence image showing poor illumination, R63E_92; temperature 21.5 °C, pressure 29.72inHg, humidity 63%, width 31.75 mm.....	197
Figure 7.17. Cropped raw fluorescence image of R63E_92.....	198
Figure 7.18. Cross-sectional plot of relative mass transfer values for image D42AB_64 at x=180; temperature 21 °C, pressure 30.33inHg, humidity 42%, width 17.4 mm.....	198
Figure 7.19. Secondary background correction array values for image R63E_92.....	199
Figure 7.20. Comparison of R63E_92 fluorescence intensity before (a) and after (b) secondary background correction.....	199
Figure 7.21. Contour plot of dimensionless mass transfer coefficient values for the image R27E_23; temperature 22 °C, pressure 29.96inHg, humidity 27%, width 31.75 mm.....	200
Figure 7.22. Contour plot of dimensionless mass transfer coefficient values for the image R46A_31; temperature 21 °C, pressure 29.70inHg, humidity 46%, width 31.75 mm.....	200
Figure 7.23. Grayscale plot of dimensionless mass transfer coefficient values for the image R58N_86; temperature 22 °C, pressure 29.71inHg, humidity 58%, width 31.75 mm.....	201
Figure 7.24. Composite intensity images of dark streaks reforming over time, (taken from data set R63).....	202
Figure 7.25. Illustration of cell formation and destruction from image set R27.....	202
Figure 7.26. Contour plot of normalized fluorescence values for R63E_92 before secondary correction.....	203
Figure 7.27. Contour plot of normalized corrected fluorescence values for the image R63E_92 after secondary correction.....	203

Figure 8.1.	Intensity images from data set R63; temperature 21.5 °C, pressure 29.71 inHg, humidity 63%, size 31.75 mm. The series of images show dark streaks combining over time.....	228
Figure 8.2.	Dimensionless mass transfer coefficient plots from data set R27; temperature 22.5 °C, pressure 39.72 inHg, humidity 27%, size 31.75 mm. The images illustrate cell formation and destruction from image set R27.....	229
Figure 8.3.	Grayscale plot of dimensionless mass transfer coefficient values for the image R27D_23; temperature 22.5 °C, pressure 39.72 inHg, humidity 27%, size 31.75 mm.....	229
Figure 8.4.	Grayscale plot of dimensionless mass transfer coefficient values for the image R46A_31; temperature 21.0 °C, pressure 29.97 inHg, humidity 46%, size 31.75 mm.....	230
Figure 8.5.	Grayscale plot of dimensionless mass transfer coefficient values for the image R58C_86; Temperature 22.0 °C, pressure 29.71 inHg, humidity 58%, size 31.75 mm.....	230
Figure 8.6.	Grayscale plot of dimensionless mass transfer coefficient values for the imageR63D_30; temperature 21.5 °C, pressure 29.71 inHg, humidity 63%, size 31.75 mm.....	231
Figure 8.7.	Grayscale plot of dimensionless mass transfer coefficient values for the image R91C_41; temperature 21.0 °C, pressure 29.71 inHg, humidity 91%, size 31.75 mm.....	231
Figure 8.8.	Grayscale plot of dimensionless mass transfer coefficient values for the imageR96A_96; temperature 22.0 °C, pressure 29.71 inHg, humidity 96%, size 31.75 mm.....	232
Figure 8.9.	Plot of downwelling frequency within all image sets for relative humidity from 27% to 96%. P indicates downwelling present while NP indicated downwelling not present.....	233
Figure 8.10.	Plot of overall downwelling frequency with to relative humidity. Imd is the number of images within the data set with downwelling; Imt is the total number of images in the data set.....	234

Figure 8.11. Plot of initial appearance time versus relative humidity for humidity levels of 27%, 58%, 63% and 96%.....	235
Figure 8.12. Idealized dimensionless mass transfer value cross section illustrating downwelling parameters.....	235
Figure 8.13. Cross-section of R045V_92 at $x=200$ ; Temperature 21.5 °C, pressure 29.71 inHg, humidity 63%, width 31.75mm.....	236
Figure 8.14. Average downwelling width versus humidity for humidity levels of 27%, 58%, 63% and 96%.....	236
Figure 8.15. Average downwelling width over time from start of experiment for humidity levels of 27%, 58%, 63% and 96%.....	237
Figure 8.16. Average downwelling width over time from initial appearance, post appearance time of downwelling for humidity levels of 27%, 58%, 63%, and 96%.....	237
Figure 8.17. Comparison of average dimensionless mass transfer value of the downwelling zone to the width of the downwelling zone for humidity levels of 27%, 58%, 63%, and 96%.....	238
Figure 8.18. Comparison of average rate of downwelling movement to the relative humidity for humidity levels 27%, 58%, 63% and 96%.....	239
Figure 8.19. Rate of downwelling movement over time for humidity levels of 27%, 58%, 63% and 96%.....	240
Figure 8.20. Dimensionless relative mass transfer coefficient values for downwelling areas over time for humidity levels of 27%, 58%, 63%, and 96%.....	241
Figure 8.21. Average dimensionless relative mass transfer coefficient values for downwelling areas over relative humidity from 27 to 96%.....	242
Figure 8.22. Dimensionless mass transfer coefficient plots from data set R63 at times of (a)R63B_22, 19 min, 24 sec, (b)R63B_24, 19 min, 35 sec, (c)R63B_25, 19 min, 47 sec; temperature 21.5 °C, pressure 29.71 inHg, humidity 63%, size 31.75 mm. The images illustrate the change of shape in a downwelling zone over time.....	242

Figure 8.23. Cross sectional plot of dimensionless mass transfer coefficient values at $y = 13.6$ mm for R63E_92. The cross section illustrates the value difference in dimensionless mass transfer coefficient values for downwelling zones (between 15 and 19 mm) and the surrounding liquid.....	243
Figure 8.24. Proposed model of Rayleigh-Bénard affected mass transport.....	244
Figure 8.25. Comparison of mass transfer coefficient to reduced Rayleigh number...	245

## 1. INTRODUCTION

Over the past several decades there has been an increasing emphasis on the reduction of chemical impurities from industrial and municipal chemical processes. As the need for even greater economic and material efficiency increases, the demand for developing and improving production techniques also increases. An improved understanding of the fundamental chemical and physical phenomenon will allow us to develop new chemical industrial processes such as reaction distillation and increase the efficiency of traditional processes such as aeration.

One area that has come under increasing scrutiny is the output of chemical impurities into the natural environment, the material being discharged from wastewater treatment of municipal and industrial effluents that affects the biological demands of the receiving water. An optimal balance needs to be established between the increasing economic costs of waste treatment and the environmental capacity to handle the discharge. The inter-phase mass transfer of solutes is a key phenomenon that affects both natural and industrial systems.

The mass transfer of gases such as oxygen, carbon dioxide, and nitrogen across the air-water interface has major impacts on everything from corrosion of process equipment to biological activity in lakes and streams. The forced transfer of these gases is an important part of many industrial chemical processes such as aeration and nitrification in wastewater treatment, and carbon dioxide removal in fermentation. In ultra pure

operations, the removal of carbon dioxide from water is needed to prevent corrosion. The balances of these sparingly soluble gases between the atmosphere and water bodies have major impacts on water and air quality. In aquatic environments, these gasses affect the rate that organisms can digest organic compounds. The amount of dissolved gas also affects the growth rate of aquatic plants and formation of noxious compounds. The global balance of carbon dioxide is believed to have an effect on the global environment through global warming.

The global warming theory has focused attention upon the global carbon dioxide balance. At the present time, thirty to forty percent of fossil fuel-produced carbon dioxide is estimated to be in the oceans (Donelan and Wanninkhoff, 2002). One wonders about the role of the world's surface waters in sequestering this carbon dioxide by mass transfer. Recent attempts to control the emissions of carbon dioxide, such as the Kyoto treaty, have made the efficient removal and sequestering of carbon dioxide important to industry.

Most of the current models for the mass transfer of gases, such as oxygen, across the air-water interface tend to have errors of up to 500%, with over 100% common (Moog and Jirka, 1998). The models for mass transfer of sparingly soluble gases across the air-water interface follow the general form

$$K_{1,2} = C_1 V^\alpha Sc^\beta H^\gamma (1 + C_2 F^\delta) u_*^\epsilon \quad (1.1)$$

where  $K_{1,2}$  is the mass transfer rate,  $V$  is the volumetric flow rate,  $Sc$  is the Schmidt number,  $H$  is the depth of the liquid,  $F$  is the Froude number, and  $u_*$  is the friction

velocity (Moog and Jirka, 1998). The parameters  $C_1$  and  $C_2$  and the exponents  $\alpha$ ,  $\beta$ ,  $\chi$ ,  $\delta$ , and  $\varepsilon$  are often determined from a limited set of experimental data, usually macro measurements of the dissolved gases present in the liquid.

In many situations, a small region just under the water surface, the aquatic concentration boundary layer, controls the mass transfer. Increasing our understanding of the behavior of the concentration boundary layer to shear stresses such as wind, surface movement caused by waves, and subsurface currents will allow for the construction of improved models for mass transfer of gases. One of the techniques utilized to investigate the behavior of the concentration boundary layer has come out of Laser Induced Fluorescence (LIF).

Laser Induced Fluorescence is an analytical chemistry technique that measures the concentration of a species based on the amount of fluorescence generated from a sample when excited by a laser. There are a variety of applications and designs of LIF in literature. One application, which is referred to as Planar Laser Induced Fluorescence (PLIF) in this thesis, uses a thin plane of laser light to generate concentration profiles. Surface Laser Induced Fluorescence (SLIF) is introduced in this work and applied to study gas transfer at the air-water interface.

Planar Laser Induced Fluorescence, PLIF, has been developed by several research groups to investigate the mass transfer of gases at the microscopic level. PLIF utilizes thin sheets of laser light to induce fluorescence in a cross section of liquid and high-resolution cameras to acquire images of those fluorescence cross sections. PLIF has allowed researchers to image the mass transfer boundary layer beneath the surface of a liquid. Since PLIF does not interfere with the fluid dynamics of the interface, it has

allowed researchers to calculate concentration gradients, measure the boundary layer thickness, and discover the presence of detached boundary layers in wind sheared wavy interfaces (Duke, 1996) and interfaces with mechanically generated waves (Woodrow and Duke, 2001). It has also shown that the mass transfer rates of gases across flat interfaces are larger than a simple diffusive model would suggest (Woodrow and Duke, 2001). PLIF has a limitation in not being able to acquire images of the concentration gradient across the fetch of the wave. The limitation of PLIF has hampered three-dimensional investigation of mass transfer across the air water interface.

We can investigate the behavior of mass transfer phenomena by generating and acquiring images of near surface fluorescence over the surface of the liquid. In place of generating a thin plane of fluorescence from the liquid, we can project a laser beam across the surface of the liquid and then acquire the resulting fluorescence using a CCD camera mounted directly above the air-water interface. We can demonstrate that the fluorescence generated by projecting a laser beam over the surface of the liquid would generate fluorescence values that could be related to the thickness of the mass transfer boundary layer.

The Surface Laser Induced Fluorescence was applied to the investigation into the spatial variation in mass transfer across the air water interface. The SLIF technique met the requirements for a usable fluorescence technique in investigating mass transfer differences across a surface. First, the SLIF apparatus generated a detectable difference in fluorescence between areas with thin oxygen boundary layers and thick oxygen boundary layers. Second, the SLIF technique was able to remove or ignore the variation in the distribution of the excitation energy. Third, the SLIF apparatus was able to acquire

clear focused images of the air-water interface and the near surface fluorescence. Fourth, we could relate the changes in near-surface fluorescence to the mass transfer coefficient between air and water. Fifth, we identified and removed the extraneous variations in near-surface fluorescence that did not relate to the boundary layer thickness. A properly designed SLIF technique enabled us to investigate the mass transfer affecting phenomena under flat air-water interface. The investigations of mass transfer across the air-water interface demonstrated the capabilities of the SLIF technique for the study of mass transfer across gas-liquid interfaces.

This thesis demonstrates the design and application of the SLIF system built at Auburn University. The underlying theory of the SLIF technique is detailed along with a study verifying the major principles of the SLIF theory in practice. The SLIF technique is applied to the study of oxygen mass transfer across a flat-air water interface. It has been theorized that thermally driven circulation, generated by evaporation at the interface, increases the mass transfer rate of oxygen into water (Woodrow 2001). The SLIF study of mass transfer across flat air-water interfaces will both demonstrate the ability of the SLIF system to measure relative mass transfer rates, and evaluate the changes to mass transfer with the presence of thermally driven circulation.

This work separates the process of detailing and verifying SLIF theory from the application of the SLIF to flat air-water interfaces. In Chapter 2, we review mass transfer at air-water interfaces, and thermal instabilities. In Chapter 3, we illustrate the theory relating SLIF images to relative mass transfer coefficients. Chapter 4 details the SLIF system constructed at Auburn University, and the SLIF system used for the verification study. Chapter 5 explains the image processing procedure for translating SLIF acquired

images into contour maps of relative mass transfer coefficients. In Chapter 6, the results of the SLIF verification study are presented. Chapter 7 presents the results of applying the SLIF technique to study flat air-water interfaces. Chapter 8 details the results of an investigation into the relationship between atmospheric humidity and the mass transfer of oxygen across a flat air-water interface. Chapter 9 presents the conclusions for the Surface Laser Induced Fluorescence technique and the relationship between atmospheric humidity and oxygen mass transfer.

## 2. BACKGROUND

### 2.1. Mass transfer of sparingly soluble gases

The mass transfer of a sparingly soluble gas between two immiscible fluids is driven by the overall chemical equilibrium of that species between the fluids. The mass transfer rate of the species between the fluids is controlled by the mass transport of the species within the fluids and the resistance to the species at the interface. The overall mass transport is both convective and diffusive (Jähne and Haußecker, 1998). Convective mass transport dominates where the movement of the fluid is greater than the diffusive transport of the species through the fluid, such as in a tank undergoing high agitation mixing. Diffusive mass transport dominates where the molecular mobility of the species is greater than the movement of the fluid, such as a stagnant fluid.

The relative ability of a species to be dispersed within a fluid by diffusive or convective mass transport is related to the Schmidt number. The Schmidt number is the ratio between the diffusion of momentum within the fluid and molecular diffusion of a given species within that fluid

$$Sc = \frac{\nu}{D_A} \quad (2.1)$$

where,  $Sc$  is the Schmidt number for the species A in the fluid,  $\nu$  is the kinematic viscosity of the fluid, and  $D_A$  is the molecular diffusion coefficient of species A in the

fluid. The kinematic viscosity represents the ability of a fluid to disperse momentum within a fluid.

For mass transfer across an interface, the two fluids can be divided into four layers (Donelan and Wanninkof, 2002) defined by the dominating form of mass transport. The convective layers are where convective mass transport dominates. At the interface, the diffusive layers are where diffusive mass transport dominates. The relative size of the diffusive layer is defined by the turbulence within the liquid and the Schmidt number. As the Schmidt number of a fluid increases, more of the mass transfer resistance for that fluid is within the diffusive layer (McKenna and McGillis, 2002). Under these conditions, the diffusive layer is referred to as the mass transfer boundary layer (Jähne and Haußecker, 1998).

The two-film model of Lewis and Whitman (1923) represents a gas-liquid system where the overall mass transfer across the interface is controlled by the diffusive mass transport across the boundary layers. The model is illustrated by Figure 2.1. The bulk concentration in each layer is denoted by  $[A]_{j,B}$  and the interface concentration  $[A]_{j,I}$  where B indicates the bulk concentration, I indicates the interface concentration, and  $j$  denotes the gas, 1 or liquid, 2 phase. The thickness of the mass transfer boundary layer is  $\delta_{x,y}$ . The mass transfer in each fluid is modeled by

$$N_A = k_l ([A]_{2,I} - [A]_{2,B}) \quad (2.2)$$

and

$$N_A = k_g ([A]_{1,I} - [A]_{1,B}) \quad (2.3)$$

where  $k_l$  is the mass transfer coefficient of the liquid,  $k_g$  is the mass transfer coefficient of the gas, and  $N_A$  is the mass flux of species A.

Henry's Law relates the interface concentrations of a species between gas and liquid

$$[A]_{1,I} = H[A]_{2,I} \quad (2.4)$$

where  $H$  is the Henry's Law constant. The interfacial mass flux of species A is represented by

$$N_A = K_{1,2}([A]_{2,I} - [A]_{2,B}) \quad (2.5)$$

where  $K_{1,2}$  is the overall mass transfer coefficient.

For systems where Henry's Law is applicable across the entire interface, the overall mass transfer can be stated as a relationship between the gas side mass transfer coefficient and the liquid side mass transfer coefficient. The model presented by Bird et al. (1960),

$$\frac{1}{K_{1,2}} = \frac{1}{k_l} + \frac{1}{k_g H} \quad (2.6)$$

is a sum of resistances. The components can be restated as the liquid side resistance and the gas side resistance,  $\mathfrak{R}_l$  and  $\mathfrak{R}_g$  respectively.

$$\mathfrak{R}_l = \frac{1}{k_l} \quad \mathfrak{R}_g = \frac{1}{k_g H} \quad (2.7, 2.8)$$

A ratio of the liquid side and gas side resistance compares the relative dominance of liquid mass transport or gas side mass transport in mass transfer,

$$\frac{\mathfrak{R}_g}{\mathfrak{R}_l} = \frac{k_l}{k_g H} \quad (2.9)$$

For resistance ratios less than one, the liquid side resistance dominates mass transfer. For resistance ratios greater than one, the gas side resistance dominates mass transfer. As the resistance ratio approaches unity, the resistances of both the liquid side and gas side are factors in the mass transfer across the interface. The solubility of the species has a large effect on which resistance is dominant.

In most situations, the major determinate of the dominating resistance is the Henry's Law constant (Thibodeaux, 1996). A highly water-soluble species, such as SO<sub>2</sub> has a small Henry's Law constant ( $H=0.833 \text{ atm/M}$ ). The resistance ratio for a small Henry's Law constant is much greater than one, with the gas side resistance dominating mass transfer. For species such as oxygen, that have a low solubility in water ( $H=769.2 \text{ atm/M}$ ), the liquid side resistance dominates, with the resistance ratio being much less than one.

The mass transfer of oxygen across the air water interface is controlled by the mass transport across the liquid side boundary layer. Oxygen has a high Schmidt number in water ( $Sc=450$ ), and a low solubility ( $H=769.2 \text{ atm/M}$ ) at 20° C. The high Schmidt number for oxygen in water indicates that rate of mass transport near the interface will be the limiting factor in the overall mass transfer rate. The relatively low solubility in water indicates that the liquid side resistance will dominate. The overall mass transfer coefficient can be approximated by the liquid mass transfer coefficient,

$$K_{1,2} \approx k_l \quad (2.10)$$

The variations in the overall mass transfer coefficient across the interface are from variations in the liquid side mass transport resistance. Further, since the mass transport resistance on the gas side is considered negligible, the interface concentration is assumed to be equivalent to the bulk gas concentration, or  $[A]_{1,B} \cong [A]_{1,I}$ . Substituting the bulk gas concentration for the interface concentration and the liquid mass transfer coefficient for the overall mass transfer coefficient into equation 2.5 generates

$$N_A = k_l ([A]_{2,I} - [A]_{2,B}) \quad (2.11)$$

for the flux of oxygen mass transfer between air and water.

## 2.2. Gas transfer models

Over the past decades, there has been interest in determining the overall mass transfer coefficient,  $K_{l,2}$ , for gases such as carbon dioxide and oxygen. The transfer of oxygen and other sparingly soluble gases from the atmosphere into bodies of water is important at both the global and local scale. Globally, oceans and fresh water bodies act as a carbon dioxide sink within the global carbon cycle. The rate that these bodies can absorb and release carbon dioxide is an important part of the global warming theory. At the same time, the health of fresh water and salt-water ecosystems depends on dissolved oxygen levels. Mass transfer rates affect how these systems will respond to flow upsets and new oxygen demands.

Empirical and theoretical models have been proposed over the years for mass transfer across the air-water interface. Empirical models have tended to work for limited situations, and tend to have high error rates. Theoretical models of gas transport across the air-water interface have been proposed, relating the observed mass transport rate to the proposed hydrodynamics of the system.

Most empirical models of mass transport for bodies of water in the environment follow the general relationship

$$k_l / u_*^y \propto Sc^n Re^j We^m \quad (2.12)$$

where  $u_*$  is the interfacial velocity,  $Sc$  is the Schmidt number,  $Re$  is the Reynolds number,  $We$  is the Weber number,  $n, j, m$ , and  $y$  are empirically found exponents (George, et al., 1995). Hanratty (1991) notes that for large interfacial stresses the mass transfer coefficient varies with the product of the friction velocity and the Schmidt number with

the superscripts  $y$  and  $n$  being  $-1/2$  in most cases. It has been noted that for dirty or flat interfaces the values for  $y$  and  $n$  are found to be  $-2/3$ . Moog and Jirka (1998) investigated several empirical models for oxygen transfer and found that model predictions vary from 100% to 500% from measured data. In most situations, the applicability of these models is limited.

An early theoretical model for mass transfer, proposed by Whitmann (1923), is the film diffusion model. This assumes that the mass transfer is completely diffusion controlled through a uniform viscous layer near the surface, denoted by thickness  $\bar{\delta}_c$ . The mass transfer coefficient is then modeled as

$$K_{1,2} = \frac{D_A}{\bar{\delta}_c} \quad (2.13)$$

However, most empirical studies have shown that the overall mass transfer coefficient  $K_{1,2}$  follows the relationship in equation 2.14, where  $n$  is less than one

$$K_{1,2} \propto (D_A)^n \quad (2.14)$$

A second theoretical model, known as the penetration theory, is based on the concept that the near surface boundary layer is penetrated by low concentration liquid from the bulk fluid. Higbie (1935) modeled this concept by creating discrete packets that were in contact with the gas for an average exposure time,  $t_e$ , then returned to the bulk liquid, as illustrated in Figure 2.2. The mass transfer coefficient is then expressed as

$$K_{1,2} = 2 \sqrt{\frac{D_A}{\pi t_c}} \quad (2.15)$$

Dankwerts (1951) proposed a modified form of Higbie's concept, known as the surface renewal theory. The average exposure time was replaced with a distribution of renewal times for each packet. The surface renewal theory is given as

$$K_{1,2} = \sqrt{D_A S^T} \quad (2.16)$$

where  $S^T$  is the fractional renewal rate.

Liss and Merlivat (1986) note that the presence of both breaking and non-breaking waves changes the overall mass transfer behavior. As shown in Figure 2.3, a change occurs in the behavior of mass transport rates (transfer velocities) with the onset of small capillary waves on the surface. The mass transfer rate is proportional to  $D_A^{-1/2}$  under small wave conditions and is proportional to  $D_A^{-2/3}$  under smooth conditions. The change is not attributed to an increase in surface area, but a systemic change caused by near surface turbulence.

As noted by Scriven (1968, 1969a), the connection between conditions such as wind speed and surface deformation to the mass transfer rate is dependent on the fluid dynamics near the surface. Fortescue and Pearson (1967) attempt to relate the penetration theory to a large eddy model, where convective eddies sweep liquid from the surface into the bulk. The Fortescue and Pearson model is

$$K_{1,2} = 1.46 \left( \frac{D_A v_p}{l_p} \right)^{1/2} \quad (2.17)$$

where  $v_p$  is the root-mean-square of the turbulent velocity fluctuations in the bulk and  $l_p$  is the characteristic length of the large eddies in the bulk.

Hanratty (1991) uses an eddy model with a distributed eddy size for the relationship

$$K_{1,2}/v_* = 0.71(\bar{\beta}_H^2)^{1/4} Sc^{-1/2} \quad (2.18)$$

where the characteristic value  $\beta_H$  is based on the wave distribution on the surface.

Govolin (1992) modeled the mass transfer under thermally driven circulation. He noted that for thin films under thermal circulation, the Sherwood number  $Sh_c$  could be related to the Marangoni number  $Ma$ , the Schmidt number  $Sc$ , and a characteristic value  $b$ . For chaotic cells the relationship is modeled by

$$Sh_c = b^2 Ma Sc^{-1/2} \quad (2.19)$$

while spatially ordered cells have the relationship given by

$$Sh_c = b^{4/3} Ma^{1/3} Sc^{1/6} \quad (2.20)$$

where

$$Sh_c = \frac{j_c L}{D_A \Delta[A]} \quad (2.21)$$

The Sherwood number is defined by  $j_c$  the interfacial mass flux and  $L$  is the depth of the diffusive boundary layer. These models are still dependent on an empirical designation of  $b$ , which is defined as the proportion of liquid returning to the surface that has a concentration equal to that of the bulk liquid.

The air-water mass transfer models presented have two common features: they attempt to relate the near surface fluid dynamics to mass transfer rates, and they model the fluid movement in terms of depth and fetch, or depth and span. Most of the models assume that near surface fluid movement is the controlling factor of liquid side mass

transfer. However, the mass transfer across the air-water interface varies three dimensionally. SLIF, with its ability to investigate boundary layer thickness across the surface of the air-water interface, will be a valuable tool in validating three dimensional mass transfer models, related to depth, fetch, and span.

## 2.3 Overview of studies on air-water mass transfer

### 2.3.1. Overview of mass transfer studies

A number of physical processes contribute to the gas transfer across the air-water interface at low wind speeds. These are connected to the presence of waves and subsurface turbulence (Macintyre et al., 2001). How the presence of waves on the surface, or how the turbulence beneath the air-water interface, increases mass transfer rates is not well understood.

Examples of studies of the relationship between waves and mass transfer across the air-water interface include the Daniil and Gulliver (1991) study relating wave height and frequency to mass transfer rates. Duke et al. (1995) investigated the relationship between wave slope and mass transfer rates. Broecker et al. (1978), Liss and Merlivat (1986), Alaei et al. (1995), and Panin et al. (2002) investigated the effect of wind shear on mass transfer rates.

There have also been studies of the mass transfer rate and turbulence beneath the liquid surface. Magnaudet et al. (1991) discusses that subsurface turbulence is an important part of defining the mass transfer rate across the air water interface. Rashidi et al. (1992) investigated the relationship between interfacial turbulence and mass transfer,

noting that the near surface turbulence was governed by the shear rate. The liquid turbulence was in the form of liquid regions that moved between the surface and bulk, affecting the mass transport rate across the air-water interface.

There are similar forms of turbulence created by an unstable density gradients (Rayleigh circulation) and surface tension gradients (Marangoni circulation) that affect the mass transfer rate (Adrian et al., 1986). Ruckenstein (1971), Dijkstra and Van de Vooren (1985), Govolin (1992) and Boyadjiev (2000) modeled the increase in mass transfer rates due to either Marangoni or Rayleigh circulation. Marangoni or Rayleigh circulation, described in section 2.4, has been shown to increase heat transfer rates (Bernaz et al., 2001). There has also been a large amount of work on the relationship between density driven circulation and mass transfer. Berg and Morig (1969) and Berg and Haselberger (1971) studied the mass transfer of a solute between two liquids under an induced temperature gradient. Boyadjiev and Halatchev (1998) investigated the effect of liquid heating, due to a reaction between solutes in the solvent, on the mass transfer rates of one of the solutes. Vázquez et al. (1996) investigated the absorption of carbon dioxide under an induced Marangoni effect. Okhotsimskii and Hozawa (1998) demonstrate the presence of induced circulation by evaporation and its effect on the mass transfer of carbon dioxide into various solvents.

The form and energetics of the near surface turbulence were found to be major components of air-water mass transfer. The forms of the mass transfer enhancing liquid movements appear similar between shear induced and instability induced turbulence. Rashidi et al. (1992) characterized the surface of the liquid undergoing shear as streaks with a characteristic distance between them. These streaks represented areas where the

surface liquid was bursting into the bulk liquid, while the spaces between them were where the bulk liquid approached the interface. This sounds very similar to the descriptions of thermally induced Rayleigh-Bénard circulation by Berg and Morig (1969) and Okhotsimskii and Hozawa (1998). Bernaz et al. (2001) pictured plumes of cold liquid returning into the bulk liquid and then breaking apart. A more careful inspection of the phenomena described for both shear induced and instability induced turbulence shows dissimilarity at the surface. The streaks of Rashidi et al. (1992) and Jähne (1995) tend to be parallel and merge in smooth transitions. The intersections of the downwelling zones of Berg et al. (1966a, 1966b) and Bernaz et al. (2001) are abrupt. Both Magnaudet et al. (1991) and Govolin (1992) compared the change in mass transfer rates to the change in parameters than can be related to the near surface turbulence, the friction velocity and the Marangoni number respectively. The model of Ruckenstein (1971) approximated the increase in mass transfer as a ratio between molecular diffusion and the velocity amplitude. These models demonstrated that the energetics of the turbulence, generally defined as the liquid velocity field and the rate of change of the turbulence structure, were important in how near surface-turbulence affects the mass transfer rate. The energetics of near surface turbulence created by wind shear as in Rashidi et al. (1992) was likely very different than the energetics imaged by Berg and Morig (1969). The overall fluid movement and the residence time of the turbulence structures were vastly different between the two cases.

Neither Berg and Morig (1969) or Rashidi et al. (1992) were directly measuring mass transfer. Spangenburg and Rowland (1961), Berg and Morig (1969), Berg et al. (1966a; 1966b), Okhotsimskii and Hozawa (1998), investigated Rayleigh-Bénard

circulation by visualizing the density gradient between the cold and warm fluid. Rashidi et al. (1992) acquired images of oxygen bubbles as turbulence tracers. Bernaz et al. (2001) imaged the temperature difference using a temperature sensitive fluorescence probe. Woodrow (2001) demonstrated both the presence of detached boundary layers under mechanical waves and the presence of thermally driven Rayleigh-Bénard circulation using Pyrene Butyric Acid (PBA) Planar Laser Induced Fluorescence to obtain normalized concentration gradients of oxygen under these surfaces. However, the turbulence under the air water interface is three dimensional as demonstrated by previous research, which showed variation in the turbulence structure over the surface (Rashidi et al., 1992; Jähne, 1995) and into the liquid (Berg and Morig, 1969; Bernaz et al., 2001).

The Surface Laser Induced Fluorescence technique allows for a three dimensional study of near-surface turbulence directly relating to mass transfer. PBA based SLIF will allow us to investigate the variation in mass transfer created by the near surface-turbulence across the interface. By combining SLIF and PLIF measurement of mass transfer, a basis for understanding the three dimensional subsurface fluorescence and how it affects the rate of mass transfer is possible.

### 2.3.2. Overview of mass transfer studies using microscopic techniques

Several studies utilize microscopic measurements of heat or chemical concentration to understand mass transfer. These techniques are designed to generate images of the near surface structure and how it affects mass transfer across the air water interface. Heat tracer studies allow researchers to map the variation in heat flux across a cooling surface both in the lab and in the field without having mechanical probes

interfere in the near interface fluid dynamics. Laser Induced Fluorescence (LIF) techniques allow researchers to study the chemical concentrations within a fluid in the laboratory without using oxygen probes beneath, or through, the air-water interface.

Jähne (1995) and Jähne and Haußecker (1998) utilized a heat tracer method to image the heat transfer at the liquid surface. The Constant Heat Flux (CHF) method utilizes the natural heat loss to the atmosphere by the ocean, known as *the cool skin of the ocean*, to generate a measure of the heat flux after heating a volume of water by IR radiation, Figure 2.4. Schimpf et al. (1999, 2000) demonstrated structures at a wavy interface that are stated to be surface renewal structures, Figure 2.5.

The heat transfer coefficient can be related to the mass transfer coefficient by the relationship

$$\frac{k_l}{k_{h2}} = \left( \frac{Sc_h}{Sc} \right)^n \quad (2.22)$$

where  $Sc_h$  is thermal Schmidt number,  $k_{h2}$  is the heat transfer coefficient, and  $n$  is a theoretical exponent, usually from  $-1/2$  to  $-2/3$ .

There are several studies using LIF to microscopically study the mass transport across the air-water interface. Münsterer (1996) uses a Planar Laser Induced Fluorescence (PLIF) technique, to measure the mass transfer of hydrogen chloride, HCl into water. Münsterer used a pH indicator probe (fluorescein) to detect the concentration profile of the chloride ion,  $Cl^-$  below the interface, Figure 2.6. Takehara and Etoh (2002) use a similar system studying the transport of carbon dioxide into water. Duke (1996) and Münsterer (1996) used a PLIF technique based on the molecular oxygen probe pyrene butyric acid, PBA. PBA is a fluorescent molecule that is collisionally quenched

by oxygen. The quenching of PBA fluorescence by oxygen allows for the relation between an image of induced fluorescence and the oxygen concentration below the surface. The resulting fluorescence images are processed into two-dimensional profiles of normalized oxygen concentration.

Münsterer (1996) generated concentration profiles for a circular, or infinite fetch wave tank. Duke (1996) generated concentration profiles for a linear, or finite fetch wave tank. The work of Woodrow and Duke (1999) used the PBA technique in a mechanical wave tank to eliminate wind shear as a factor in their results.

There have been limitations to the above systems in gaining mass transfer values over the air-water interface. The constant heat flux method allows for the investigation of heat transfer across the surface of a liquid, but care must be taken to avoid inducing instability due to the created inversed temperature gradient near the surface of the liquid. The surface variations can no be directly related to vertical profiles of heat transfer. PLIF methods are limited to cross sections of concentration, where only vertical profiles can be directly related to mass transfer coefficient values. The inability of PLIF to produce horizontal cross sections that can be related to mass transfer coefficient values was illustrated by Takehara and Etoh (2002) who could only compare the values of concentration at some depth across the surface. SLIF can investigate the variance of the mass transfer boundary layer thickness across the surface of the air-water interface that can be related to PLIF measurements since they use the same molecular probe.

## 2.4. Dynamics of flat interfaces

In 1901, Henry Bénard first systematically studied the dynamics of a thin liquid with an adverse temperature gradient (Koschmeider, 1993). He heated a flat, thin volume of whale oil from below using a steam chamber, allowing the liquid to be cooled by the air above. This condition is known as an adverse temperature gradient, where the contents of the lower layers of a liquid have higher temperatures than the upper layers. Upon heating the liquid, Bénard generated a pattern of hexagonal cells across the liquid surface (Koschmeider, 1993). Examples of such cells are shown in Figure 2.7. Bénard's experiments demonstrated a connection between liquid circulation cells and an adverse temperature gradient. It was later researchers who demonstrated mathematically and experimentally the driving forces behind the phenomenon.

There are two mechanisms for thermal instability under an adverse temperature gradient: density and capillary. The density driven instability is known as the Rayleigh-Bénard instability. Under an adverse temperature gradient the fluid becomes denser at the surface than the bulk fluid. The capillary driven instability is properly known as the Pearson-Bénard instability. The capillary instability is caused by the surface tension of the surface fluid being higher than in the bulk fluid. The unstable gradients are illustrated in Figure 2.8. In both cases, the potential energy of the system reduces if the bulk fluid replaces the surface fluid. When the system is disturbed, the liquid will begin to circulate between the bulk and the surface, reducing the overall potential energy of the system. Either the density or surface tension gradient can maintain the liquid's circulation if the

respective gradient is able to overcome the dissipative effects of heat and momentum transport in the fluid.

#### 2.4.1. Rayleigh-Bénard thermal instabilities

The thermal density, or Rayleigh- Bénard, circulation is generated by the density gradient that occurs under an adverse temperature gradient. Lord Rayleigh (1916) mathematically demonstrates the density instability in his model. The Rayleigh model assumes a finite fluid of depth  $\delta_R$  between two infinite plates with an imposed, linear temperature gradient  $\Delta T$ . Rayleigh simplifies the problem by using a Boussinesq approximation. Rayleigh's simplification assumes that the temperature effects on the buoyancy terms dominate. The relationship between buoyancy and temperature is modeled by the equation

$$\rho - \rho_0 = -\rho_0\alpha(T - T_0) \quad (2.23)$$

where  $\rho_0$  is the density at some temperature  $T_0$  and  $\alpha$  is the expansion coefficient of the liquid (Chandrasekhar, 1961; Getling, 1998). Rayleigh's solution to this model generates the following dimensionless quantity, known as the Rayleigh number,

$$Ra = \frac{\delta_R^3 \rho g \alpha \Delta T C_p}{\mu k^T} \quad (2.24)$$

where  $\delta_R$  is the depth of the circulation,  $\rho$  is the liquid density,  $g$  is the constant of gravity,  $\Delta T$  is the temperature gradient across  $\delta_R$ ,  $C_p$  is the heat capacity,  $\mu$  is the viscosity and  $k^T$  is the thermal conductivity. The Rayleigh number is the ratio of the forces inducing instability versus the dissipate forces within the liquid.

The classic solution to the Rayleigh model generates multiple solutions for the neutral condition with a given set of boundary conditions (Chandrasekhar, 1961). The neutral condition is where the dissipative forces of heat and momentum transport balance the instability created by the gradient in buoyancy. The stability curve is illustrated in Figure 2.9, with the neutral values falling on the stability curve. Liquid layers with Rayleigh number values above the neutral condition will be unstable, and maintain circulation after the system has been disturbed. For those systems that are below the line, the circulation will damp out after some length of time. The neutral condition is a function of the Rayleigh number, the non-dimensional characteristic wavelength  $a$ , and the boundary conditions. The minimum non-dimensional characteristic wavelength  $a_c$  is usually associated with the minimum circulation cell size.

Boundaries	The Critical Rayleigh Value, $Ra_c$	Characteristic wavelength $a_c$
Rigid-rigid	1707.8	2.016
Rigid-free	1100.7	2.342
Free-free	657.5	2.828

Table 2.1. Critical Rayleigh Numbers (Koschmeider, 1993)

The minimum neutral Rayleigh number is known as the critical Rayleigh number. The critical Rayleigh value  $Ra_c$  is dependent on the boundary conditions of the system, and independent of the fluid properties. The two definitions of the surface boundary conditions are a rigid boundary on which no slip occurs and a free boundary on which no tangential stresses act. In Figure 2.9 the critical values of wavelength and Rayleigh number for the free-free boundary conditions are illustrated. The three common critical values are given in Table 2.1.

The critical Raleigh value varies dramatically with the boundary definitions. The air-water system tends to be seen as being a Rigid-Free system with a critical Rayleigh value of 1100.7 (Koschmeider, 1993).

#### 2.4.2. Pearson- Bénard thermal instability

Rayleigh's solution does not address thin fluids that show stable circulation below the critical Rayleigh value, such as those obtained in Bénard's study. Pearson (1958) theorized that the circulation cells seen by Bénard were driven not by a density gradient, but by a surface tension gradient. This instability, labeled Pearson-Bénard, or more commonly Marangoni, is driven by the change in surface tension with temperature. As in Rayleigh's model, the temperature effect is isolated to only the surface tension, all other variances caused by the temperature gradient are considered too small to be significant. The equations utilized by Pearson is

$$\sigma = \sigma_0 + S\Delta T \quad (2.25)$$

$$S = \frac{\partial \sigma}{\partial T} \quad (2.26)$$

where  $\sigma$  is the surface tension,  $\sigma_0$  is the initial surface tension and  $S$  is the surface tension gradient. In most situations  $S$  is defined as a negative value. For traditional Pearson-Bénard circulation, the defined dimensionless number is the Marangoni number  $Ma$ ,

$$Ma = \frac{S\delta_s\Delta T}{\rho\nu\kappa} \quad (2.27)$$

$$\kappa = \frac{k^T}{\rho C_p} \quad (2.28)$$

$$Ma = \frac{S\delta_s \rho C_p \Delta T}{\mu \kappa^T} \quad (2.29)$$

where  $\kappa$  is the thermal diffusivity. The Marangoni number  $Ma$  is analogous to the Rayleigh number, where the capillary driving forces of the instability are compared to the dissipative effects of the system (Neild, 1965).

Pearson's model varies in other ways from the Rayleigh model. Pearson does not assume that an infinitely good conductor facilitates heat transfer out of the top surface. The Pearson model takes into account the heat transfer rate out of the liquid surface. It defines the Biot number,  $B_i$ , for the upper surface,

$$B_i = \frac{\Gamma d}{k^T} \quad (2.30)$$

$$\Gamma = \left( \frac{\partial Q_e}{\partial T} \right)_{T=T_{0, \text{surface}}} \quad (2.31)$$

where  $\Gamma$  is the rate of change in conduction in terms of temperature. As in the solution to the Rayleigh model, there exists a series of neutral values (Vidal and Acrivos, 1966, 1968). The neutral values of the Marangoni model, with an "insulating" bottom, are found by

$$Ma_N = \frac{8a[a \sinh(a) + B_i \cosh(a)] [a - \sinh(a) \cosh(a)]}{[a^3 \sinh(a) - a^2 \cosh(a) + 2a \sinh(a) - \sinh^2(a) \cosh(a)]} \quad (2.32)$$

where  $Ma_N$  is the neutral Marangoni number, and  $a$  is the non-dimensional characteristic wavelength. The neutral stability curves for different Biot numbers are shown in Figure 2.10. The critical Marangoni number,  $Ma_c$ , is defined as the minimum neutral value for a given set of boundary conditions. Unlike the Rayleigh model, the critical value varies

Biot Number Bi	Critical Marangoni Number Ma <sub>c</sub>	Critical Rayleigh Number Ra <sub>c</sub>
0	79.607	669.00
0.01	79.991	670.38
0.1	83.427	682.36
0.2	87.195	694.78
0.5	98.256	727.42
1	116.127	770.57
2	150.679	831.27
5	250.598	925.51
10	413.440	989.49
20	736.00	1036.30
50	1699.62	1072.19
100	3303.83	1085.902
1000	32170.1	1099.12
10 <sup>10</sup>	32.0730*10 <sup>10</sup>	1100.65

Table 2.2. Comparison of Marangoni and Rayleigh Critical Values over a range of Biot numbers (Neild, 1964).

with the surface Biot number, as shown in Figure 2.11. The typical critical Marangoni number for an open tank is 79.607 (Koschmeider, 1993).

Quoting Neild (1964): “some very heavy algebra” was used in the development of a thermal instability model combining the work of Rayleigh and Pearson. Neild looked at the variation of both critical values with the variation in the surface Biot number, shown in Table 2.2. As the surface Biot number increases from 0 to 1000, the critical Marangoni number increases by a factor of more than 400, while the critical Rayleigh number less than doubles. Neild created a joint stability curve shown in Figure 2.12. Koschmieder (1993) notes that one can say that for the normalized stability values,

$$\tilde{Ra} = Ra / Ra_c \quad (2.33)$$

$$\tilde{Ma} = Ma / Ma_c \quad (2.34)$$

that the neutral stability is where

$$\tilde{Ma} + \tilde{Ra} = 1. \quad (2.35)$$

The Dynamic Bond Number,  $Bo_d$ , is the comparison of surface tension and density gradients, determining which will dominate in a particular liquid layer.

$$Bo_d = Ra / Ma = \frac{\beta \rho g h^2}{S} \quad (2.36)$$

The Dynamic Bond number is the Reynolds number divided the Marangoni number. Above a Bond number of unity, buoyancy effects will dominate, below, surface tension effects should dominate (Schatz and Neitzel, 2001).

#### 2.4.3. Evaporative effect on instability

Evaporation of a liquid layer has been found to be a source for the development of Bénard circulation. Spangenburg and Rowland (1961) showed that even without an imposed temperature gradient, water circulated between the surface and bulk liquid. The evaporation of a liquid induces two separate effects. The first is an induced adverse temperature gradient generated by evaporative cooling. The second effect is the removal of the liquid from the surface. Quinn and Saville (1976) propose that evaporation will counter the effect of thermal instability. Quinn and Saville theorize that it would generate a velocity component normal to the surface that will suppress any movement of fluid back into the bulk. Quinn and Saville's theory is counter to the observations of Block (1956) who notes the presence of circulation cells in the presence of an imposed, stable temperature gradient. Block saw cells appear when cooling of the bottom surface

of the liquid layer. Several researchers have cooled the upper surface of a fluid as the source of an induced adverse temperature gradient (Spangenburg and Rowland, 1961; Berg et al. 1966a; 1966b). The discrepancy between traditional thermal stability models and the observations of Block may have been caused by evaporation.

In some papers investigating evaporating surfaces, the evaporation was taken as the source of an induced temperature gradient (Spangenburg and Rowland, 1961; Berg et al. 1966a; 1966b; Woodrow, 2001) and was simply substituted into the traditional forms of the Marangoni and Rayleigh stability equations. Other researchers studied the removal of thermal energy as an underlying mechanism, both experimentally (Yang et al., 1997; Ha and Lai, 1998; Chai and Zhang, 1998; Torii and Yang, 2002) and numerically (Torii and Yang, 1999; Zhang and Chao, 1999). They demonstrate that in the presence of an evaporating liquid, even with an imposed stable temperature gradient, some fraction of the liquid has an adverse temperature gradient. Within these sub-layers, stable circulation cells can form as illustrated in Figure 2.13.

As in the conventional models, either density or surface tension drives the circulation cells. The definition of the dimensionless temperature, used by both Rayleigh (1916) and Pearson (1958), is given in equation 2.35 where the dimensionless temperature is defined by the imposed adverse temperature gradient. For a system with evaporation, the dimensionless temperature gradient was modified to include both an imposed temperature gradient  $\Delta T$  and the heat loss due to evaporation  $\dot{V}\Delta h_v \delta_s / \mu k^T$ . In the modified equations, an imposed temperature gradient and an evaporative effect are the driving forces for the generation and sustainability of Bénard circulation (Zheng and Worek, 1996)

$$\hat{T} = \frac{T}{\Delta T} \quad (2.37)$$

$$\hat{T} = \frac{T}{\Delta T + (\dot{V}\Delta h_v \delta_s / \mu k^T)} \quad (2.38)$$

This substitution leads to the modified Marangoni number,  $Ma^*$  and modified Reynolds numbers  $Ra^*$

$$Ma^* = \frac{S\Delta T \delta_s}{\mu k^T} + \frac{S\dot{V}\Delta h_v \delta_s^2}{\mu C_p (k^T)^2} \quad (2.39)$$

$$Ra^* = \frac{\beta \rho g \Delta T \delta_s^3}{\mu k^T} + \frac{\beta \rho g \dot{V} \Delta h_v \delta_s^4}{\mu C_p (k^T)^2} \quad (2.40)$$

where  $\dot{V}$  is the volumetric evaporation rate and  $\Delta h_v$  is the heat of vaporization. The first term of the equations is the traditional value, where the driving force is a temperature gradient  $\Delta T$  imposed by heating or cooling the liquid. The second term is the evaporative component, where the driving force is the energy removed by evaporation.

#### 2.4.4. Thermal instability in water

Most published research focuses either on the study of thermal capillary instabilities or thermal buoyancy instabilities (Emery and Lee, 1999). For many liquids, such as oils, alcohol, and water, it has been shown that for depths greater than 10 mm the buoyancy force dominates (Zhang et al., 2002). The critical depth of 10 mm is used to separate the study of thermal capillary effects in thin films from Rayleigh-Bénard studies.

Several studies over the past years have found little evidence of Marangoni circulation being present in thin water layers (Cammenga et al., 1983; Barnes and Hunter,

1981; Barnes et al., 1994; Ward and Stanga, 2001). The common explanation is that the surfaces are too dirty for circulation to form. Block (1954) and Anisimova et al. (2001) stated that they observed Marangoni driven circulation in water. Block provides little data on his work, only general observations. Anisimova utilized three different methods to visualize an evaporative surface in ultra clean water; the results show the early onset of thermo-capillary structures that are superceded by buoyancy driven effects.

The evaporation of deep layers of water demonstrates the development of Rayleigh-Bénard circulation (Navon and Fenn, 1971). When the only source of the circulation is evaporation, the surface shows the presence of down-welling, or cold streamers, from the surface (Spangenburg and Rowland, 1961, Theerthan and Arakeri, 1994). These tend not to form ordered cells, but multisided cells that alter shape over time, as illustrated in Figure 2.14. This structure differs from other liquids that tend to also show up-welling, or hot streamers, from the bulk liquid (Berg et al., 1966a; 1966b). Rising, hot streamers are not seen in water except when heating the bottom surface (Chu and Goldstein, 1973; Theerthan and Arakeri, 1994). Under conditions of very high Rayleigh number,  $Ra > 10^6$ , these hot streamers can become mushroom-like plumes rising from the bottom surface (Sparrow et al., 1964; Sparrow et al., 1970). For liquid layers that are both heated and cooled, hot streamers rising from the bottom surface and cold streamers from the bottom have been seen, meeting at an isothermal layer at the center of the fluid (Adrian et al., 1986)

## 2.5. Estimating the evaporation rate of water

For open tanks of water with no imposed temperature gradient, equation 2.40 becomes

$$Ra^* = \frac{\beta \rho g \dot{V} \Delta h_v \delta_s^4}{\mu C_p (k^T)^2} \quad (2.41)$$

where the heat removal by evaporation dominates.

There exist several models for estimating the evaporation rate of an open pool of liquid. Under some conditions of humidity and temperature, the model used by the U.S. Weather Bureau provides an estimate of a condensation rate (Finkel, 1982) while a statistical model by Ward and Fang (1999) will estimate an evaporation rate under identical conditions. As detailed by Ward and Stanga (2001) and Navon and Fenn (1971) the conditions at the air-water interface controlling evaporation are not well understood. The presence of other chemicals in the water may affect the evaporation rate (Fang and Ward, 1999; Bedeaux and Kjelstrup, 1999). The widely used Carrier model for evaporation from pools has undergone several revisions as more accurate data has been obtained. Jones et al. (1993) proposed the following model for evaporation from pools

$$\dot{W} = \frac{(68.3 + 32.0 \times V_{air})(P_w - P_a)}{\Delta h_v} \quad (2.42)$$

where  $\dot{W}$  is the mass evaporation rate,  $V_{air}$  the air velocity over the pool,  $P_w$  is the saturation vapor pressure at the water temperature, and  $P_a$  is the saturation vapor pressure at air dew point.

Chapter 2 figures

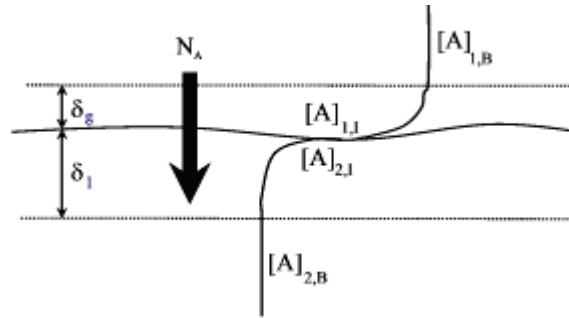


Figure 2.1. Two film theory of mass transfer, illustrating the mass transfer of species A across an interface.

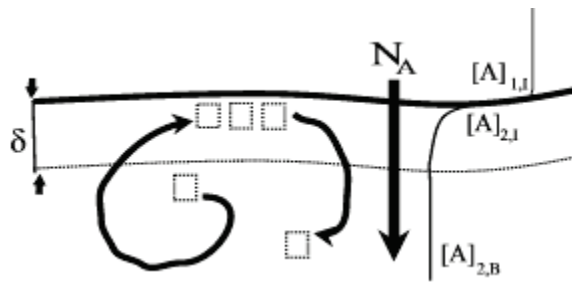


Figure 2.2. Illustration of a circulation cell including mass transfer of species A (Golovin, 1991).

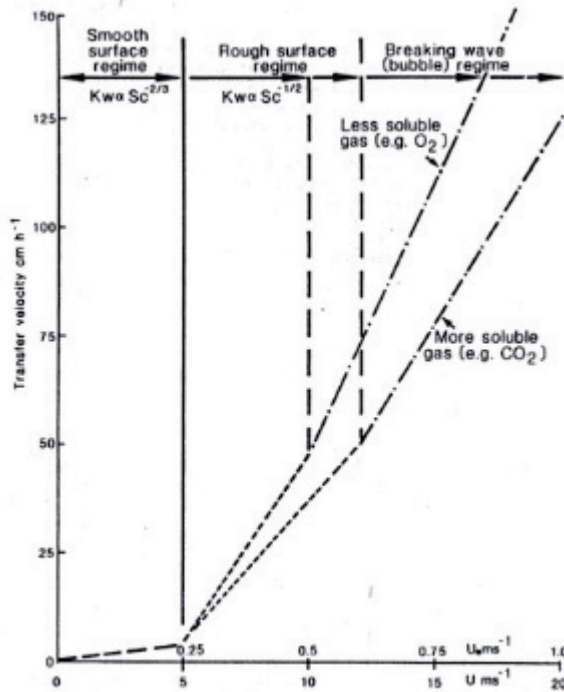


Figure 2.3. Variation in mass transfer rates across the air-water interface showing the surface regimes (Liss and Merlivat, 1986).

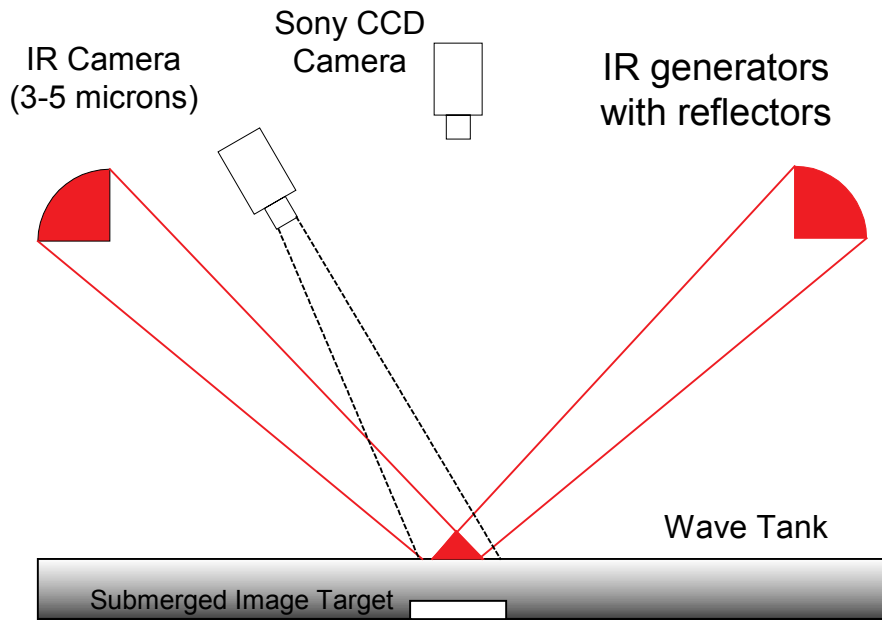


Figure 2.4. Constant Heat Flux System ( Jähne, 1995).

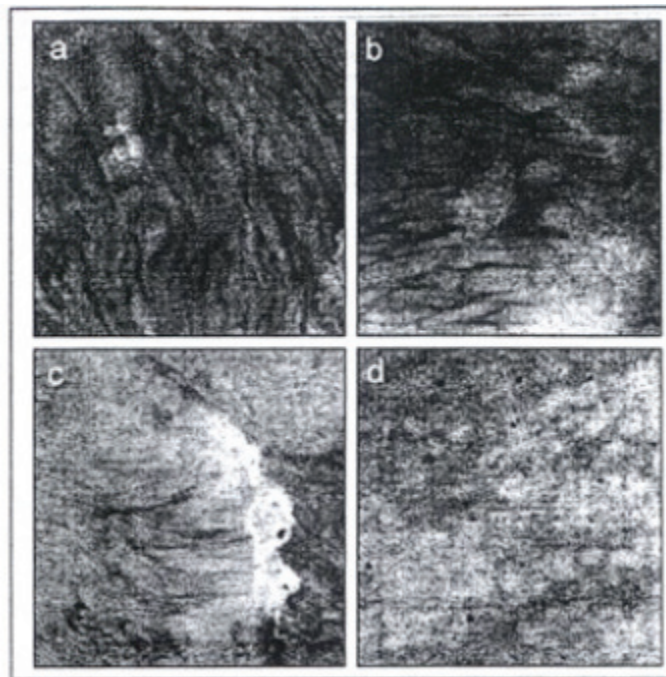


Figure 2.5. Heat tracer data of surface renewal events (Shimpf, 1993).

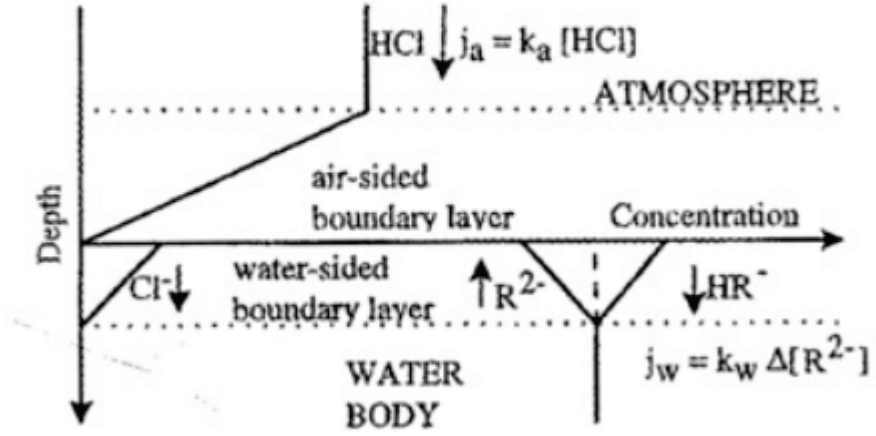


Figure 2.4. Hydrogen chloride mass transfer detection by Fluorecine (Münsterer and Jähne, 1998).

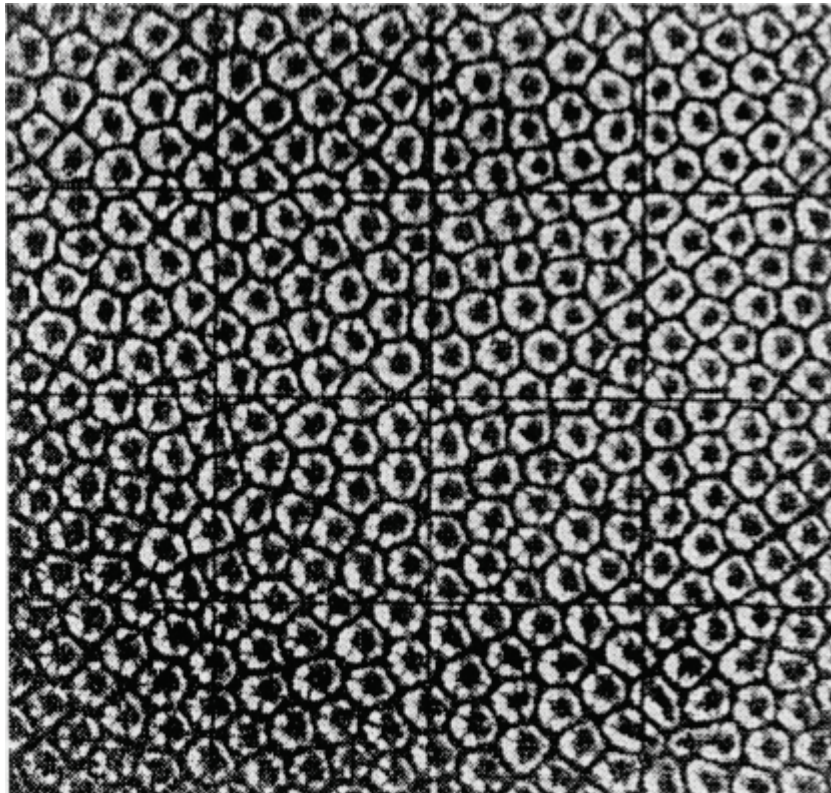


Figure 2.7. Bénard cells (Koschmeider, 1993)

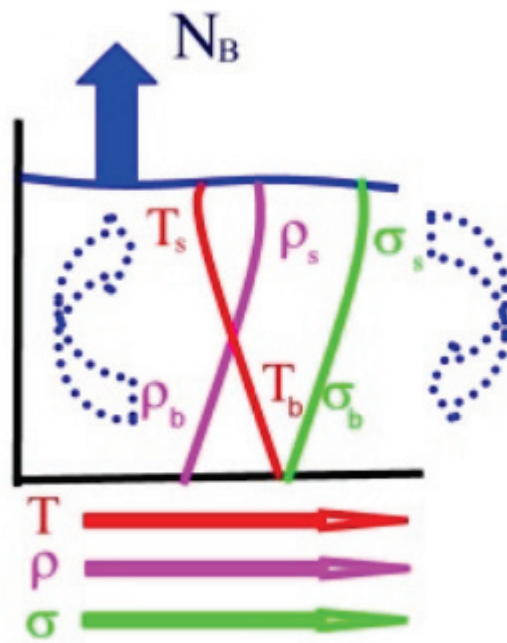


Figure 2.8. Density and surface tension gradients under an adverse temperature gradient.

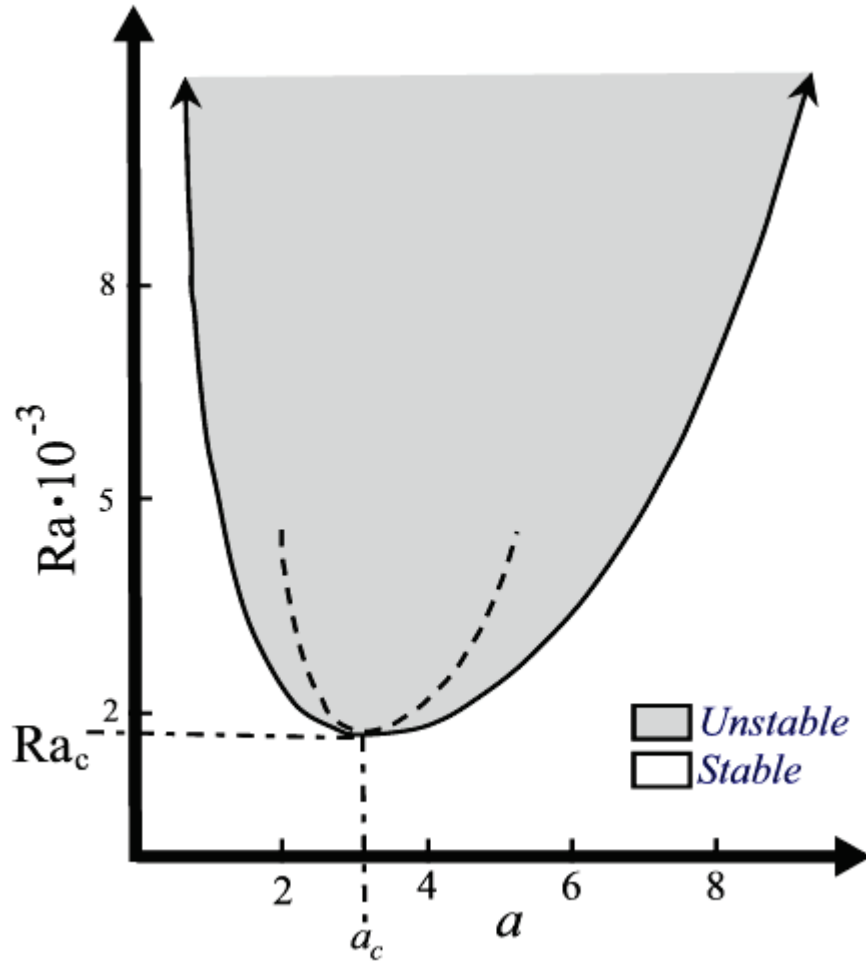


Figure 2.9. Rayleigh neutral stability curve (Koschmeider, 1993).

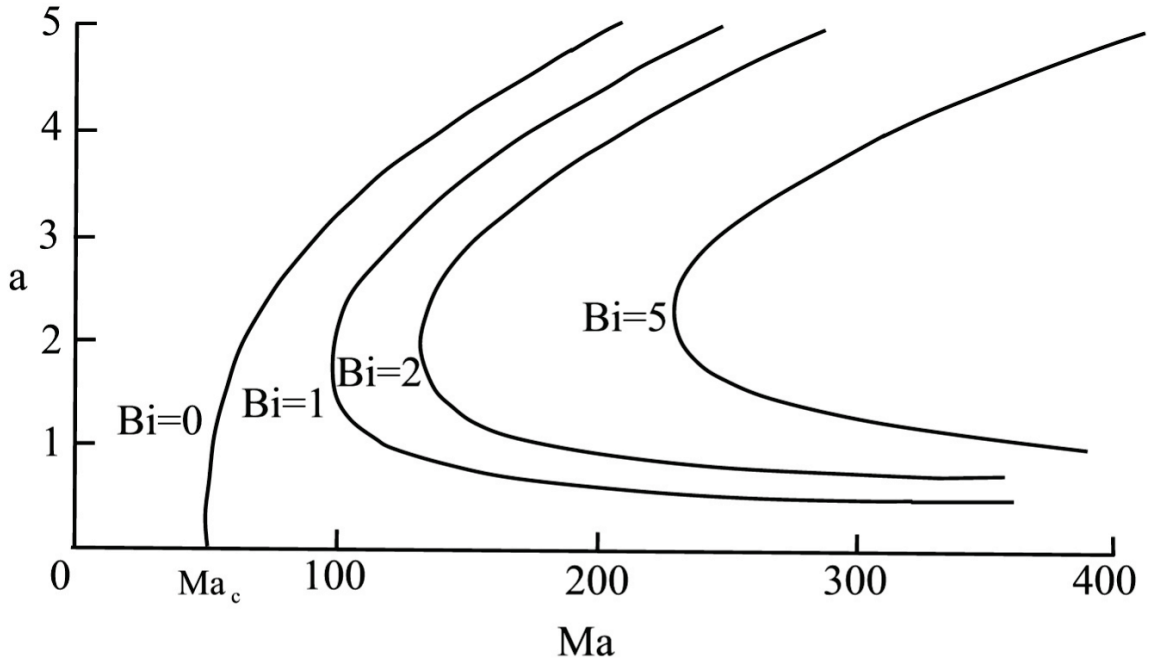


Figure 2.10. Pearson-Bénard neutral stability curves (Pearson, 1956).

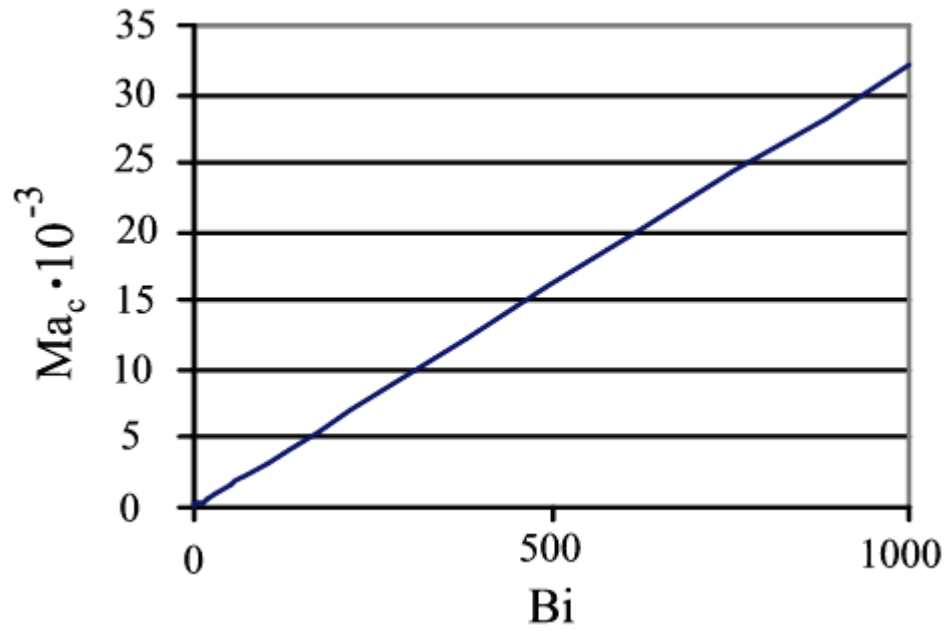


Figure 2.11. Critical Marangoni Number versus Surface Biot Number (Neild 1964).

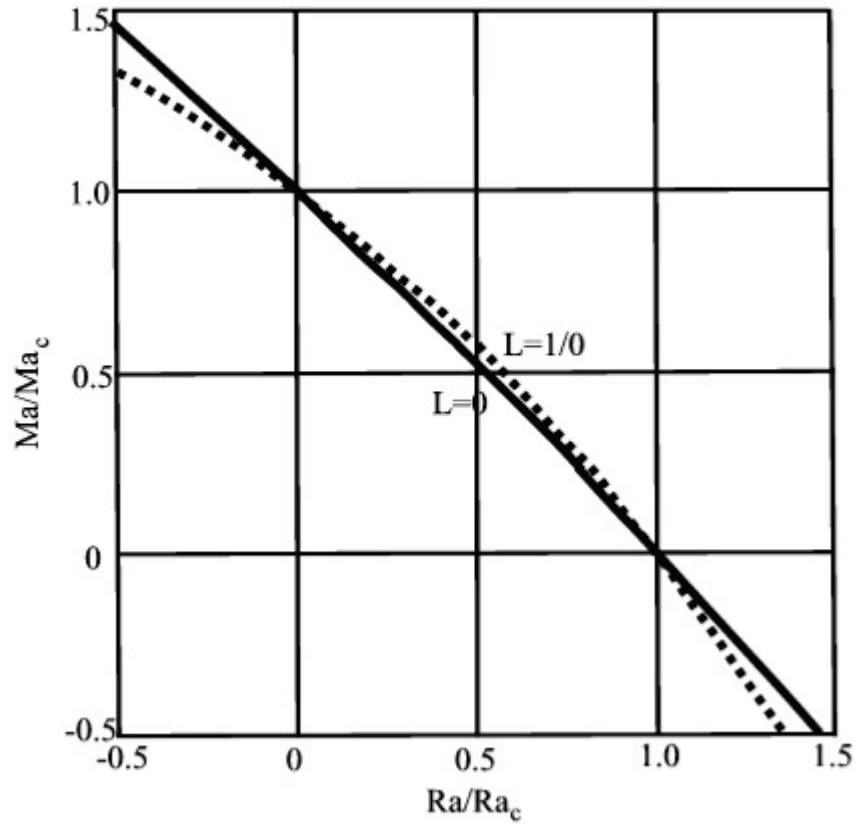


Figure 2.12. Comparison of normalized Marangoni number versus normalized Rayleigh number (Neild, 1964).

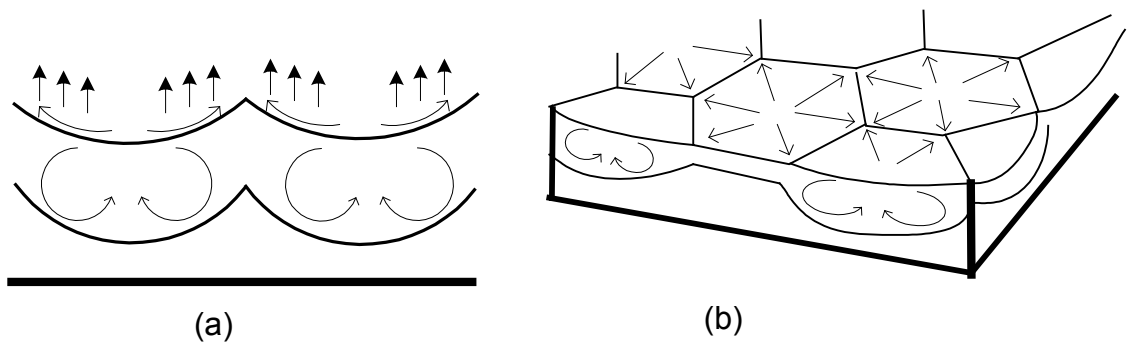


Figure 2.13. Illustration of evaporative cell, (a) side view, (b) oblique view (Zhang and Chao, 1999).

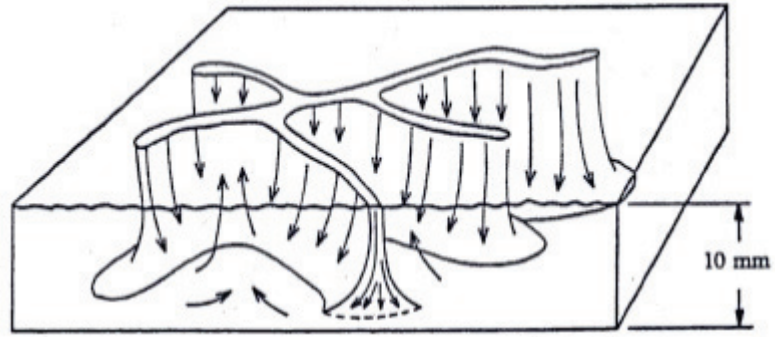


Figure 2.14. Downwelling zones in water (Berg et. al. 1966b).

### 3. SURFACE LASER INDUCED FLOURECENCE THEORY

#### 3.1. PBA quenching techniques and principles

Surface Laser Induced Fluorescence (SLIF) was developed to investigate the spatial variation of mass transfer across the air water interface. Surface Laser Induced Fluorescence is defined as a technique for investigating near surface concentration gradients by projecting a laser beam upon the liquid surface and acquiring high spatial resolution images of the induced subsurface fluorescence. SLIF coordinates with Planar Laser Induced Fluorescence (PLIF) methods. PLIF methods developed by Wolff, Liu and Hanratty (1991), Duke and Hanratty (1996), Münsterer (1996), Woodrow and Duke (2001), and Takehara and Etoh (2002) acquired images containing high resolution, vertical cross sections of the near surface concentration layer under air-water interfaces. The vertical cross-sections contain a thin slice of the overall behavior of the near surface boundary layer at any given time. The SLIF technique was developed to observe the behavior of the mass transfer boundary layer across the surface of the liquid rather than along one cross-section. The underlying theory of SLIF varies dramatically from PLIF systems that generate normalized concentration profiles at a given distance from the tank wall. SLIF generates relative values of boundary layer thickness for the entire imaged surface of the air-water interface.

There have been several Laser Induced Fluorescence (LIF) techniques developed that are similar to Surface Laser Induced Fluorescence. SLIF is comparable to front face excitation LIF that is utilized on turbid liquids and solids (Guibault, 1990). There were several examples of the use of LIF on solid surfaces to measure species concentration, most notably Hempstead (1993) who used a LIF technique to measure the concentration distribution of neodymium in a block of lithium niobate. Jähne (1991, 1998) imaged the mass transport of HCL across an air-water interface using an LIF technique using pH-controlled fluorescein. Takehara and Etoh (2002) visualized a horizontal cross section of the liquid side carbon dioxide boundary layer using fluorescein in a Planar LIF system. Hausbecker and Jähne (1998, 1999) imaged variation in heat transfer over an air-water interface using a projected heat spot similar to the laser beam spot of the SLIF technique.

The SLIF system described was designed to work with the Planar Laser Induced Fluorescence system of Woodrow (2001), which utilizes the oxygen quenching properties of Pyrene Butyric Acid (PBA). PBA has been shown to be a molecular indicator of oxygen. PBA has been used in several Planar Laser-Induced Fluorescence (PLIF) studies measuring dissolved oxygen concentration (Wolff & Hanratty, 1994; Munsterer, 1996; Duke, 1996; Woodrow, Donath, and Duke, 2001; Woodrow, 2001).

### 3.1.1. Pyrene butyric acid

Vaughan and Weber (1970) demonstrated that the fluorescence of PBA was quenched by the presence of oxygen. PBA absorbs light with wavelengths from 250 to 360 nm with a peak absorbance at approximately 340 nm. The UV absorbance spectra of PBA obtained by Wolff (1991) is shown in Figure 3.1. The excitation and energy release

pathways are illustrated in Figure 3.2. When PBA reaches an excited state it has two pathways to release the energy, either in the form of fluorescence or by transferring the energy to another molecule. The emission spectrum of fluorescence from PBA is shown in Figure 3.3. A PBA molecule can also release the energy via collisional quenching. In collisional quenching the excited fluorescent molecule, or probe, collides with an acceptable donor molecule, or quencher, and transfers the energy to the quenching molecule. The presence of quenching molecules in the water decreases the lifetime: the span of time that the fluorescent molecules produce fluorescence. The concentration of dissolved oxygen present in the liquid alters the lifetime of the fluorescence response  $\tau$  for PBA from 160 ns when no oxygen is present, to 65 ns in air-saturated water (Wolff 1991).

### 3.1.2. Collisional quenching

Collisional quenching is the process where an excited molecule transfers excess energy to another molecule via a molecular collision. The concentration of quencher will affect the time that fluorescent molecules will have to release energy via fluorescence. As the concentration of quencher molecules increases, the average time between a fluorescent molecule being excited and colliding with a quenching molecule decreases. As the average time between excitation and collision decreases, so does the overall lifetime of the fluorescence event  $\tau$ . The increase in quencher concentration also reduces the amount of excitation energy returned as fluorescence, which is measured as the quantum yield,  $\phi_i$ . The relationship between the lifetime  $\tau$  to the intrinsic lifetime  $\tau_0$  is given in terms of the quantum yield,  $\phi_i$  (Lakowicz, 1983).

$$\phi_i = \tau / \tau_o \quad (3.1)$$

The intrinsic lifetime is the lifetime of fluorescence under ideal conditions, where the value of the quantum yield is one. When the concentration of the fluorescent probe is constant, the quantum yield can be modeled by (Sharma and Schulman, 1999),

$$\phi_i = \phi_o \frac{1 - \gamma\xi}{1 + \gamma\kappa_{av}\tau_o[Q]_i} \quad (3.2)$$

where  $\phi_o$  is the quantum yield of the probe with no oxygen present,  $\gamma$  is the percent of probe-quencher complex that will disassociate,  $\kappa_{av}$  is a constant and  $[Q]_i$  is the quencher concentration at that point. The term  $\xi$  is the percentage of probe-quencher complexes that will fluoresce. Many types of collisional quenching, such as oxygen quenching of PBA, can be modeled by the Stern-Vollmer relationship (Longmuir and Knopp, 1976; Benson et al., 1980; Lakowiz, 1983; Turley and Offen, 1984),

$$\frac{F_{oi} - F_i}{F_i} = K_{sv}[Q]_i \quad (3.3)$$

where  $F_i$  is the fluorescence intensity at any given point,  $F_{oi}$  is the fluorescence with no quencher present, and  $K_{sv}$  is the constant for a given probe/quencher system. For systems that follow the Stern-Vollmer relationship, the percentage of probe-quencher complexes that fluoresce  $\xi$  approaches zero and the quantum yield ratio can be modeled as,

$$\frac{\phi_i}{\phi_o} = \frac{1}{1 + K_{sv}[Q]_i} \quad (3.4)$$

where  $K_{sv}$  is equivalent to  $\gamma\kappa_{av}\tau_o$  (Sharmen and Schulman, 1999). For a SLIF system using PBA,  $[Q]_i$  is the dissolved oxygen concentration and  $K_{sv}$ , the Stern-Vollmer constant, is approximately 176 L/g (Valeur, 2002).

### 3.2. SLIF measurement principles

Surface Laser Induced Fluorescence is designed to measure differences in mass transfer across the air-water interface from images of near surface fluorescence. An understanding of what the camera actually captures in terms of fluorescence and how that relates to quencher, or oxygen, concentration beneath the surface is needed. A modified form the Stern-Vollmer relation relates the raw surface fluorescence  $F$  to the quencher concentration,  $[Q]_i$ .

#### 3.2.1. Relationship between CCD and surface

At first glance Surface LIF appears to be similar to LIF techniques that use front-face excitation, as illustrated in Figure 3.4. The most notable similarity is the system geometry, with the excitation source and the detector on the same side of the sample. Figure 3.5 is a diagram of the SLIF relationship between the detector and the excitation energy. The use of a CCD camera as the detector of fluorescence allows for spatial resolution of the variance in quencher concentration.

For Surface LIF, the surface can be thought of as a grid of rectangles, corresponding to each element in the CCD array, shown in Figure 3.6. Each rectangle on the grid has the dimensions of  $m$  by  $n$ , which are defined by the image resolution. The numbers of rectangles along each side of the grid are  $M$  and  $N$  respectively. The

rectangle defines the surface area of a volume of depth  $d$ , illustrated in Figure 3.7. The depth of penetration  $d$  is determined by the penetration of the incident radiation  $I$  into the liquid.

Each volume cell, illustrated in Figure 3.7, corresponds to an element location  $(x,y)$  over the surface on the coordinate axis of  $\{x\}$  and  $\{y\}$ . Beneath the surface the volume cell can be divided into  $\omega$  depth levels, each labeled with the variable  $i$ . Each depth level will have a depth of  $z_i$  from the surface on the  $\{z\}$  axis and have values from 0 to  $d$ . The thickness of each level  $\Delta z$  is defined as

$$\Delta z = \frac{d}{\omega} \quad (3.5)$$

### 3.2.2. Surface fluorescence model

The fluorescence observed at location  $(x,y)$  has several components.  $F_{x,y}$  is the raw fluorescence intensity at the surface of the cell at location  $(x, y)$  imaged by the CCD array.  $F'_{i,x,y}$  is the fluorescence intensity generated by a volume  $m$  by  $n$  by  $\Delta z$  at depth  $z_i$ .  $F_{i,x,y}^*$  is the fluorescence intensity at the liquid surface for  $F'_{i,x,y}$  accounting for light absorbed by the liquid in the volume above. The observed raw fluorescence is the sum of all the fluorescence that is produced within that volume and can be defined as,

$$F_{x,y} = \sum_{i=0}^{\omega} F_{i,x,y}^* \quad (3.6)$$

The fluorescence generated within each small volume  $F'_{i,x,y}$  follows the law,

$$F'_{i,x,y} = \phi_i I_i A_i \quad (3.7)$$

where  $I_i$  is the excitation radiation at  $i$ ,  $A_i$  is the amount of that radiation absorbed at  $i$ , and  $\phi_i$  is the quantum yield for that depth level (Valeur, 2002). The raw component is related to the intermediate fluorescence and the effect of the absorbance by Lambert-Beer's decay

$$F_{i,x,y}^* = F'_{i,x,y} e^{-\varepsilon_2 [P] z_i} \quad (3.8)$$

where  $\varepsilon_2$  is the molar absorption coefficient of the fluorescence radiation by the fluorescence probe,  $[P]$  is the molecular concentration of the fluorescence probe in the liquid and  $z_i$  is the distance of the depth level  $i$  from the surface. Equations 3.6 to 3.8 can be combined to obtain:

$$F_{x,y} = \sum_{i=0}^{\omega} \phi_i I_i A_i e^{-\varepsilon_2 [P] z_i} \quad (3.9)$$

The absorption term  $A_i$  is a function of  $I(z)$  as is illustrated by Figure 3.8. Over the small distance  $\Delta z$  the excitation radiation is absorbed such that the PBA molecules are excited up to their active state as shown in Figure 3.2. From this excited state the PBA releases energy by collisional quenching with oxygen or by generating fluorescence as was previously discussed. The amount of radiation absorbed is determined by

$$A_i = 1 - \frac{I_{i+1}}{I_i} = \frac{\Delta I}{I_i} \quad (3.10)$$

From the theory of Lambert-Beers decay (Atkins, 1994), it is known that

$$\Delta I_i = I_i \varepsilon_1 [P] \Delta z \quad (3.11)$$

where  $\varepsilon_1$  is the molar absorption coefficient of the excitation radiation by the fluorescence probe. The excitation radiation that reaches  $i$  is the amount that has not

been absorbed before reaching that point. The Lambert-Beers Decay Law finds the amount of excitation radiation at  $i$  as

$$I_i = I_o e^{-\varepsilon_i [P] z_i} \quad (3.12)$$

A substitution of equations 3.6, 3.11, and 3.12 into 3.9 generates the SLIF raw fluorescence model

$$F_{x,y} = \sum_{i=0}^{\omega} \frac{I_o \phi_o \varepsilon_i [P] e^{-(\varepsilon_1 + \varepsilon_2) [P] z_i}}{1 + K_{sv} [Q]_i} \Delta z \quad (3.13)$$

This is the model of the measured fluorescence intensity at the surface location  $x$  and  $y$  for an SLIF system using Stern-Vollmer quenching.

### 3.3. PBA SLIF

#### 3.3.1. Raw fluorescence intensity for an oxygen-PBA system

Our SLIF method images the variation in quenching of PBA in a layer of water undergoing oxygen absorption. In this section we will develop a means of relating the raw fluorescence measured by the CCD to thickness of the oxygen concentration boundary layer. The quencher concentration  $[Q]$  is the dissolved oxygen concentration  $[Ox]$  for our system. The fluorescence probe is PBA. The molar concentration of PBA is  $[PBA]$ . For an Oxygen-PBA system, Equation 3.13 becomes

$$F_{x,y} = \sum_{i=0}^{\omega} \frac{I_o \phi_o \varepsilon_1 [PBA] e^{-(\varepsilon_1 + \varepsilon_2) [PBA] z_i}}{1 + K_{sv} [Ox](z)} \Delta z \quad (3.14)$$

#### 3.3.2. Dimensionless oxygen concentration

Consider the situation where the water is uniformly saturated with oxygen. Under these conditions, the fluorescence is fully quenched. The saturated oxygen concentration is defined by the term  $[Ox]'$ . Figure 3.9 shows the theoretical oxygen concentration profile of  $[Ox](z)$  based on Woodrow (2001) and the saturated oxygen concentration,  $[Ox]'$ . The relationship between the oxygen concentration at any given

depth and the saturated concentration is modeled by the dimensionless quencher concentration  $\psi(z)$

$$\psi(z) = \frac{[Ox](z)}{[Ox]'} \quad (3.15)$$

or

$$\psi(z) = \frac{[Ox]_i}{[Ox]'} \quad (3.16)$$

The dimensionless oxygen concentration relates the oxygen concentration to the saturated value under identical temperatures and pressures. Values for  $\psi(z)$  vary between zero and one, where one represents a fully saturated location and zero represents an area with no oxygen present. Equation 3.14 is rewritten in terms of the dimensionless quencher concentration to generate

$$F_{x,y} = \sum_{i=0}^{\omega} \frac{I_o \phi_o \varepsilon_1 [PBA] e^{-(\varepsilon_1 + \varepsilon_2)[PBA]z_i}}{1 + K_{sv} [Ox]' \psi(z_i)} \Delta z \quad (3.17)$$

where  $\psi(z_i)$  is the value of the dimensionless oxygen concentration at  $i$ .

### 3.3.3. Dimensionless excitation radiation distribution

Excitation radiation is emitted from the laser as a beam with a cross-sectional intensity distribution that is nominally gaussian. However, at the liquid surface the excitation radiation distribution is non-uniform and not gaussian. The change in the excitation radiation distribution is caused by the laser optics detailed in section 4.1.1. The distribution of the laser intensity at the surface can be approximated by the function  $I(x,y)$ . The excitation intensity distribution is defined as

$$I(x, y) = \bar{I}\Omega(x, y) \quad (3.18)$$

where is  $\bar{I}$  the average laser intensity over the surface, and  $\Omega(x,y)$  is the dimensionless excitation radiation distribution function of the laser over the surface. Substituting equation 3.18 for the surface incident radiation term in 3.17 generates

$$F_{x,y} = \sum_{i=0}^{\omega} \frac{\bar{I}\Omega(x, y)\phi_o \varepsilon_1 [PBA] e^{-(\varepsilon_1 + \varepsilon_2)[PBA]z_i}}{1 + K_{sv} [Ox]^i} \Delta z \quad (3.19)$$

### 3.3.4. Fully quenched conditions

At saturation, the fully quenched value of  $\psi(z)$  is one. Under fully quenched conditions, the quenched raw fluorescence  $F_{x,y}^q$  can be defined by

$$F_{x,y}^q = \bar{I}\Omega(x, y) \sum_{i=0}^{\omega} \frac{\phi_o \varepsilon [PBA] e^{-(\varepsilon_1 + \varepsilon_2)[PBA]z_i}}{1 + K_{sv} [Ox]^i} \Delta z \quad (3.20)$$

where  $F_{x,y}^q$  is the fully quenched value of  $F_{x,y}$ . Under fully quenched conditions, the mean value of the quenched raw fluorescence is

$$\bar{F}^q = \sum_{x=0}^N \sum_{y=0}^M \frac{F_{x,y}^q}{M * N} = \frac{1}{M * N} \sum_{x=0}^N \sum_{y=0}^M \bar{I}\Omega(x, y) \sum_{i=0}^{\omega} \frac{\phi_o \varepsilon [PBA] e^{-(\varepsilon_1 + \varepsilon_2)[PBA]z_i}}{1 + K_{sv} [Ox]^i} \Delta z \quad (3.21)$$

The term  $\bar{F}^q$  is the mean fully quenched value of fluorescence. The mean quenched value of fluorescence can be restated as

$$\bar{F}^q = \frac{\bar{I}}{M * N} \sum_{x=0}^N \sum_{y=0}^M \sum_{i=0}^{\infty} \frac{\phi_o \varepsilon_1 [PBA] e^{-(\varepsilon_1 + \varepsilon_2) [PBA] z_i}}{1 + K_{sv} [Ox]'} \Delta z \quad (3.22)$$

Under quenched conditions the dissolved oxygen concentration and the concentration of the PBA probe are uniform throughout the imaged volume. We can restate the average fully quenched fluorescence in the form

$$\bar{F}^q = \frac{\bar{I}}{M * N} \sum_{i=0}^{\infty} \frac{\phi_o \varepsilon_1 [PBA] e^{-(\varepsilon_1 + \varepsilon_2) [PBA] z_i}}{1 + K_{sv} [Ox]'} \Delta z \sum_{x=0}^N \sum_{y=0}^M 1 \quad (3.23)$$

or

$$\bar{F}^q = \bar{I} \sum_{i=0}^{\infty} \frac{\phi_o \varepsilon_1 [PBA] e^{-(\varepsilon_1 + \varepsilon_2) [PBA] z_i}}{1 + K_{sv} [Ox]'} \Delta z \quad (3.24)$$

### 3.3.5. Background subtraction

To generate comparable values for the boundary layer thickness within an image, the values of raw fluorescence intensity need to be scaled in terms of variance in the excitation radiation, which can be found from  $\Omega(x, y)$ . Background subtraction scales the raw fluorescence intensity values based on dimensionless excitation radiation distribution and sets the excitation radiation intensity  $I$  at all points to the average excitation radiation intensity  $\bar{I}$  (Russ, 2002). The fluorescence intensity values when the excitation radiation is subtracted are the corrected fluorescence values  $\langle F \rangle_{x,y}$ .

To generate the corrected fluorescence values, the excitation energy distribution function needs to be found experimentally. The correction array values  $\langle CA \rangle_{x,y}$  can be

calculated from the dimensionless excitation energy distribution  $\Omega(x, y)$ . The correction values are found by dividing the mean quenched fluorescence intensity by the raw quenched fluorescence intensity values (Weeks, 1996).

$$\langle CA \rangle_{x,y} = \frac{\bar{F}^q}{F_{x,y}^q} = \frac{1}{\Omega(x, y)} \quad (3.25)$$

The correction value for a given point is the inverse value of the dimensionless excitation distribution at that point. This can then be used to generate the corrected fluorescence, by using the correction value as illustrated

$$\langle F \rangle_{x,y} = F_{x,y} \langle CA \rangle_{x,y} = \sum_{i=0}^L \frac{\bar{I} \phi_o \varepsilon_1 [PBA] e^{-(\varepsilon_1 + \varepsilon_2) [PBA] z_i}}{1 + K_{sv} [Ox] \psi(z)} \Delta z \quad (3.26)$$

The next step is to generate an inverted value of the corrected fluorescence  $\theta_{x,y}$ .

This relates to the surface fluorescence by the relationship

$$\Theta_{x,y} = \frac{\langle F \rangle_{x,y}^q}{\langle F \rangle_{x,y}} = \frac{\sum \frac{C(z_i)}{1 + K_{sv} [Ox] \psi(z)} \Delta z}{\sum \frac{C(z_i)}{1 + K_{sv} [Ox] \psi(z)} \Delta z} \quad (3.27)$$

where

$$C(z_i) = \bar{I} \phi_o \varepsilon_1 [PBA] e^{-(\varepsilon_1 + \varepsilon_2) [PBA] z_i} \quad (3.28)$$

As  $\Delta z \rightarrow 0$  the summation can be restated as an integral in the form

$$\Theta_{x,y} = \frac{\langle F \rangle_{x,y}^q}{\langle F \rangle_{x,y}} = \frac{\int_0^d \frac{C(z)}{1 + K_{sv} [Ox] \psi(z)} dz}{\int_0^d \frac{C(z)}{1 + K_{sv} [Ox] \psi(z)} dz} \quad (3.29)$$

The equation can be rearranged, and simplified to

$$\Theta_{x,y} \int_0^d dz = \int_0^d \frac{1 + K_{sv}[Ox]'}{1 + K_{sv}[Ox]'} \psi(z) dz \quad (3.30)$$

The solution to the first integral and the simplification of the second generates

$$\Theta_{x,y} = \frac{1}{1 + K_{sv}[Ox]'} + \frac{K_{sv}[Ox]'}{1 + K_{sv}[Ox]'} \left( \frac{1}{d} \right) \int_0^d \psi(z) dz \quad (3.31)$$

The inverted corrected fluorescence  $\Theta_{x,y}$  for any point  $(x,y)$  is the integral of the dimensionless concentration multiplied by the inverse of the Stern-Vollmer gain and offset by the quenched quantum yield. The constants of the system are the Stern-Vollmer constant, the saturated oxygen concentration and the depth of penetration for the excitation radiation.

### 3.3.6. Mass transfer

Equation 2.13 can be restated as shown in equation 3.32.

$$\delta = D_A \left( \frac{1}{k} \right) \quad (3.32)$$

where  $\delta$  is the boundary layer thickness. The boundary layer thickness is proportional to the resistance to mass transfer  $\left( \frac{1}{k} \right)$ . Figure 3.9 illustrates the tangential boundary layer

$\delta^T$ . The tangential boundary layer is approximated by the equation

$$1 + \frac{d[Ox](z)}{dz} \Big|_{z=0} (\delta^T) = 0 \quad (3.33)$$

and

$$\delta^T = 1 / \left. -\frac{d[Ox](z)}{dz} \right|_{z=0} \quad (3.34)$$

where the inverse of slope of the oxygen concentration function at  $z = 0$  is the boundary layer thickness.

The effective boundary layer thickness is approximated by the equation

$$\delta^{eff} \left( [Ox]' - [Ox]_b \right) 0.5 = \int_0^D [Ox](z) dz - \int_0^D [Ox]_b dz \quad (3.35)$$

where  $[Ox]_b$  is the bulk oxygen concentration and  $D$  is the depth of the fluid. Equation 3.35 is graphically represented in Figure 3.10. The integral of the oxygen concentration function  $[Ox](z)$  from the interface to the bulk oxygen value is equivalent to a linear oxygen concentration gradient multiplied by the effective boundary layer thickness. Equation 3.35 can be restated in terms of the depth of penetration  $d$ ,

$$\delta^{eff} \left( [Ox]' - [Ox]_b \right) 0.5 = \int_0^d [Ox](z) dz + \int_d^D [Ox](z) dz - [Ox]_b D \quad (3.36)$$

The values of the oxygen concentration function for  $z$  greater than  $d$  can be taken to be fairly close to the bulk oxygen concentration.

$$\text{for } z > d \quad [Ox](z) \approx [Ox]_b \quad (3.37)$$

$$\delta^{eff} \left( [Ox]' - [Ox]_b \right) 0.5 = \int_0^d [Ox](z) dz + [Ox]_b D - [Ox]_b d - [Ox]_b D \quad (3.38)$$

$$\delta^{eff} \left( [Ox]' - [Ox]_b \right) 0.5 = \int_0^d [Ox](z) dz - [Ox]_b d \quad (3.39)$$

Equation 3.39 can be divided through by the saturated oxygen concentration  $[Ox]'$  to state it in terms of the dimensionless oxygen concentration.

$$\delta^{eff} (1 - \psi_b) 0.5 = \int_0^d \psi(z) dz - \psi_b d \quad (3.40)$$

The effective boundary layer thickness becomes

$$\delta^{eff} = \frac{\int_0^d \psi(z) dz - \psi_b d}{0.5(1 - \psi_b)} \quad (3.41)$$

Under the conditions of this study, detailed in Chapter 4, the bulk oxygen concentration is very close to zero

$$\psi_b \approx 0 \quad (3.42)$$

we can restate equation 3.41 without the dimensionless bulk oxygen concentration

$$\frac{\delta^{eff}}{2} = \int_0^d \psi(z) dz \quad (3.43)$$

Then rearranging equation 3.31 into

$$d \left( \Theta_{x,y} - \frac{1}{1 + K_{sv}[Ox]'} \right) \frac{1 + K_{sv}[Ox]'}{K_{sv}[Ox]'} = \int_0^d \psi(z) dz \quad (3.44)$$

and

$$\Theta_{x,y} \left( \frac{1 + K_{sv}[Ox]'}{K_{sv}[Ox]'} \right) d - \frac{d}{K_{sv}[Ox]'} = \int_0^d \psi(z) dz \quad (3.45)$$

Substituting in equation 3.43 allows the integral of the dimensionless quencher concentration to be defined in terms of  $\theta_{x,y}$

$$\delta_{x,y}^{eff} = 2 \left\{ \Theta_{x,y} \left( \frac{1 + K_{sv}[Ox]'}{K_{sv}[Ox]'} \right) d - \frac{d}{K_{sv}[Ox]'} \right\} \quad (3.46)$$

where the boundary layer thickness can be estimated from the inverted corrected fluorescence term, the depth of penetration  $d$ , and the saturated oxygen concentration  $[Ox]'$ . Equation 3.46 can be rearranged into the form

$$\delta_{x,y}/d = 2 \left\{ \Theta_{x,y} \left( \frac{1 + K_{xv}[Ox]'}{K_{sv}[Ox]'} \right) - \frac{1}{K_{sv}[Ox]'} \right\} \quad (3.47)$$

The specific mass transfer coefficient  $k_{x,y}$  at a given location can be estimated by

$$k_{x,y} = \frac{D_A}{\delta_{x,y}} \quad (3.48)$$

When  $\theta_{x,y}$  approaches the value of one, equation 3.47 becomes

$$\delta_{x,y}^q = 2d \quad (3.49)$$

where  $\delta_{x,y}^q$  is the quenched fluorescence boundary layer. The quenched fluorescence boundary layer is the maximum equivalent boundary layer determinable by the SLIF system, and is related to the depth of penetration. In practical terms, the assumption used in equation 3.42 comes apart long before the liquid reaches saturation, but equation 3.49 allows us to simplify equation 3.47 in terms of the maximum effective boundary layer thickness. The minimum measurable mass transfer coefficient can be defined at this point as  $k_{x,y}^d$

$$k_{x,y}^d = \frac{D_A}{\delta_{x,y}^q} = \frac{D_A}{2d} \quad (3.50)$$

The specific mass transfer coefficient can be restated as a dimensionless mass transfer coefficient,  $k'_{x,y}$

$$k'_{x,y} = \frac{k_{x,y}}{k_{x,y}^d} = \frac{D_A}{\delta_{x,y}} \frac{2d}{D_A} = \frac{2d}{\delta_{x,y}} = \frac{1}{\Theta_{x,y} \left( \frac{1 + K_{sv}[Ox]'}{K_{sv}[Ox]'} \right) - \frac{1}{K_{sv}[Ox]'}} \quad (3.51)$$

where  $k_{x,y}^d$  is the mass transfer coefficient when the relative corrected fluorescence is one. The relative mass transfer coefficient allows us to compare mass transfer coefficients across an imaged surface without defining the depth of penetration  $d$ .

### 3.4. Normalization

The SLIF apparatus at Auburn University has a large variance in the mean value of excitation radiation  $\bar{I}$  between each firing of the laser. To correct for this problem, each raw fluorescence image is normalized by its own two-dimensional mean. The normalization process can be considered analogous to scaling the mean value of excitation radiation  $\bar{I}$  to one. The normalization also scales the inverted flat field fluorescence  $\theta_{x,y}$  in terms of the mean measured boundary layer depth  $\bar{\delta}$ . The normalized boundary layer depth  $\delta_{x,y}/\bar{\delta}$  is a function of the normalized corrected fluorescence,

$$\frac{\delta_{x,y}}{\bar{\delta}} = 2 \frac{\langle F^q \rangle_{x,y} \bar{F}}{\langle F \rangle_{x,y} \bar{F}^q} \left( \frac{1 + K_{sv}[Ox]'}{K_{sv}[Ox]'} \right) - \frac{1}{K_{sv}[Ox]'} \quad (3.52)$$

where the term  $\bar{F}$  is the average raw fluorescence value,  $\langle F \rangle_{x,y}/\bar{F}$ , is the normalized corrected fluorescence, and the normalized quenched corrected fluorescence is

$\langle F^q \rangle_{x,y}/\bar{F}^q$ . The normalized terms can be rewritten to follow the form

$$\langle \hat{F}^q \rangle_{x,y} = \langle F^q \rangle_{x,y} / \bar{F}^q \quad (3.53)$$

and

$$\langle \hat{F} \rangle_{x,y} = \langle F \rangle_{x,y} / \bar{F} \quad (3.54)$$

where  $\langle \hat{F}^q \rangle_{x,y}$  is the normalized corrected quenched fluorescence and  $\langle \hat{F} \rangle_{x,y}$  is the normalized corrected fluorescence.

The normalized relative mass transfer coefficient  $\hat{k}'_{x,y}$  or the dimensionless mass transfer coefficient,  $k^*$  can be stated as

$$k^* = \hat{k}'_{x,y} = \frac{k'_{x,y}}{\bar{k}} = \frac{D_A}{\delta_{x,y}} \frac{\bar{\delta}}{D_A} = \frac{\bar{\delta}}{\delta_{x,y}} \quad (3.55)$$

where  $\bar{k}$  is the average mass transfer coefficient within the imaged area.

Chapter 3 figures

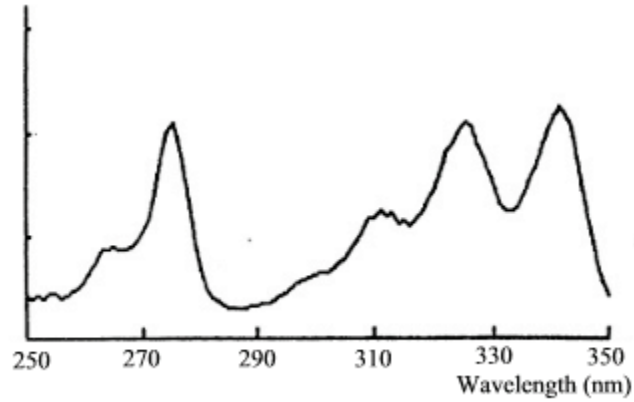


Figure 3.1. Absorbance spectra of PBA (Wolff, 1991).

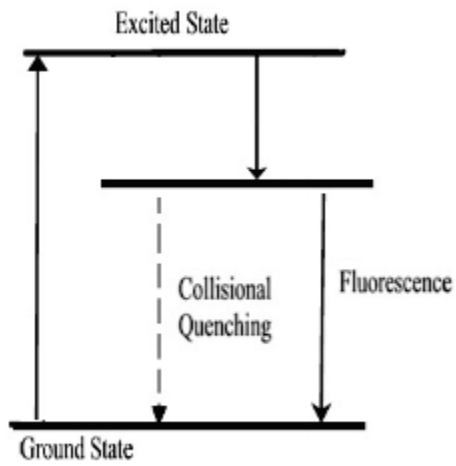


Figure 3.2. Response of PBA to UV excitation.

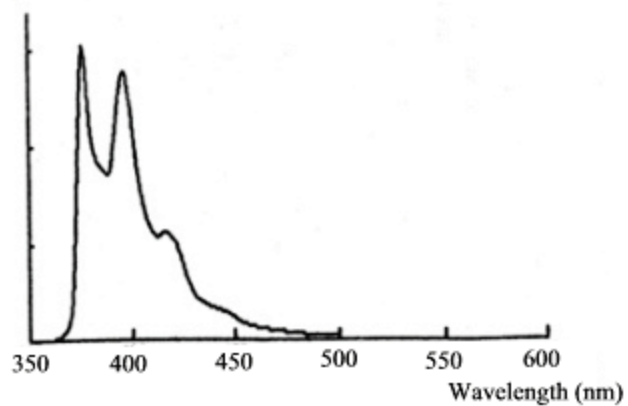


Figure 3.3. Fluorescence spectra of PBA (Wolff, 1991).

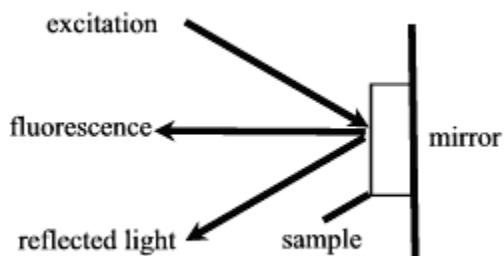


Figure 3.4. Front-face excitation beam geometry (Sharma and Schulman, 1999).

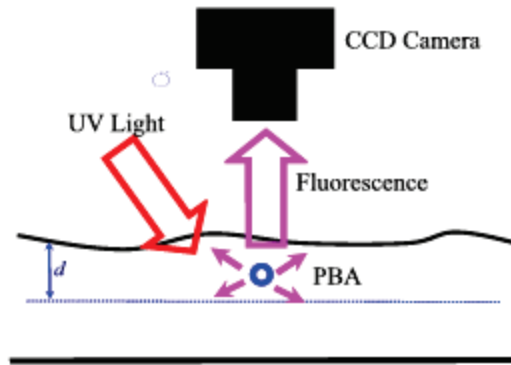


Figure 3.5. PBA excitation in the SLIF system.

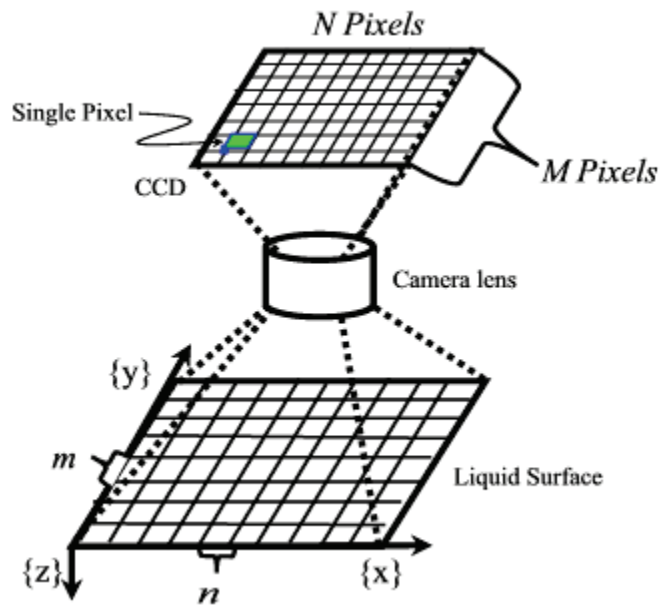


Figure 3.6. Relationship between the CCD array and the image.

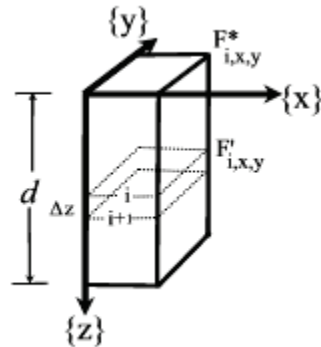


Figure 3.7. Volume cell diagram.

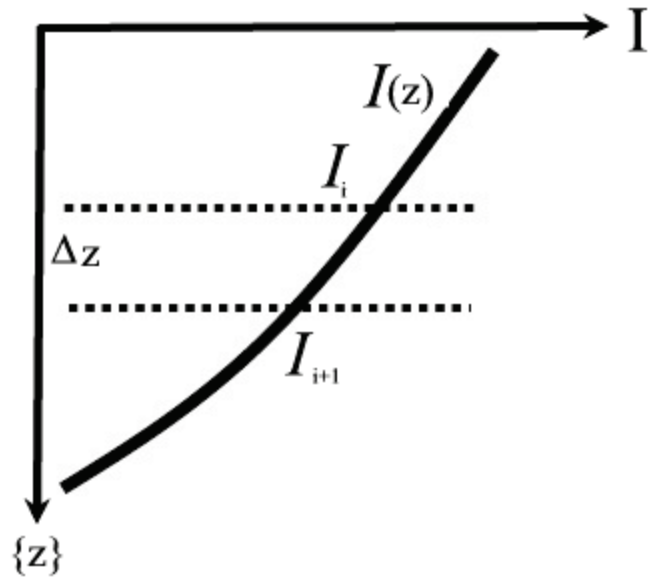


Figure 3.8. Absorption of excitation radiation.

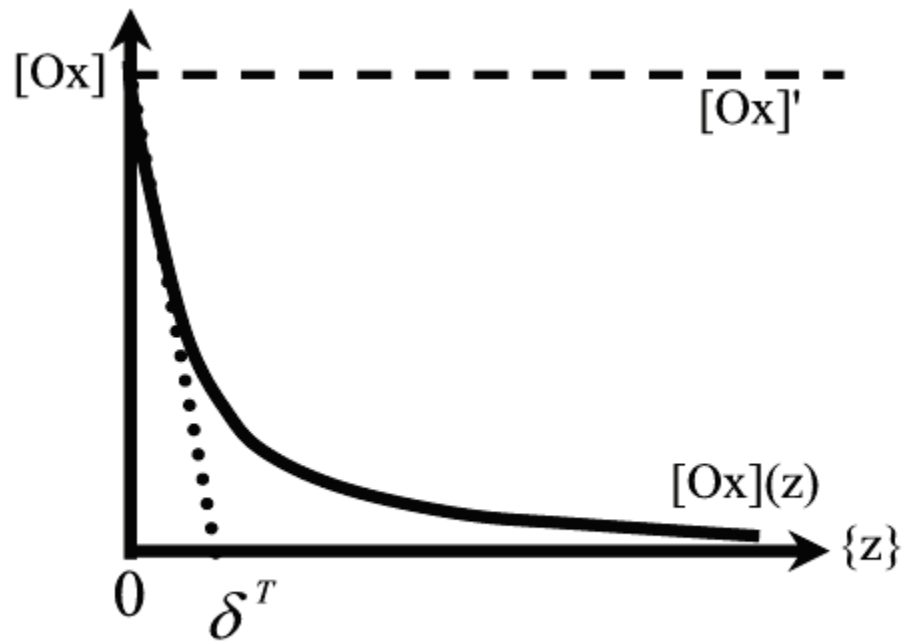


Figure 3.9. Diagram of tangential boundary layer (developed from Woodrow 2001).

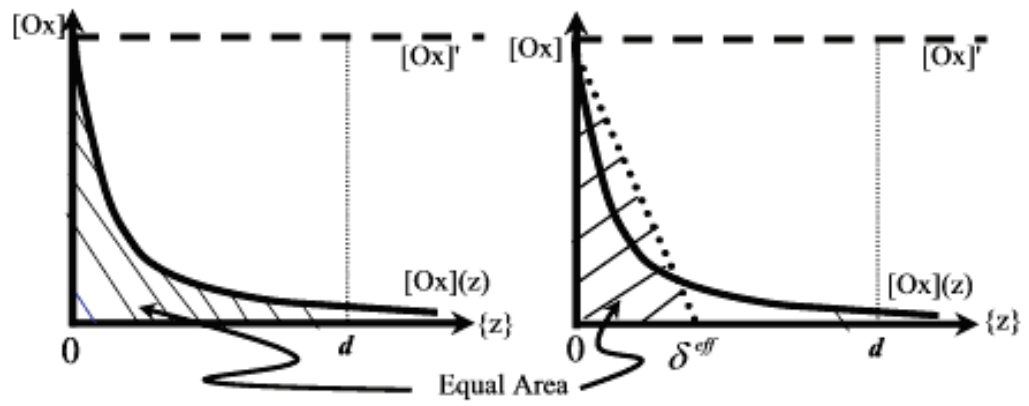


Figure 3.10. Diagram of effective boundary layer.

## 4. RESEARCH METHODS

### 4.1. Apparatus

The Surface Laser Induced Fluorescence apparatus is shown as a schematic diagram in Figure 4.1 and with images in Figures 4.2 and 4.3. The SLIF apparatus has three parts: the UV laser system, the wave tank system, and the imaging system. The components of the UV laser system are a nitrogen laser, a beam expander, and a targeting mirror. The UV laser system is the source of the excitation radiation  $I_0$ . The UV laser system produces and projects a beam of UV light on the surface of the wave tank. The wave tank system consists of a wave tank and a deoxygenation tank. The wave tank system is the one utilized by Woodrow (2001). The stripping tank lowers the dissolved oxygen concentration in the liquid before being transferred to the wave tank. The imaging system consists of a personal computer, a CCD camera and a camera lens. The CCD camera is the fluorescence detector for the system, spatially recording the intensity of the raw PBA fluorescence,  $F_{x,y}$ . The PC serves as the user interface for the camera controls and the data storage system.

#### 4.1.1. UV laser system

A UV24 nitrogen laser from Laser Photonics produces the excitation radiation. The laser generates a pulse of UV light at a wavelength of 337.5 nm, which is in the absorption range for PBA. The lasing cavity operates at 40 torr with a nitrogen

concentration above 90%. The sub-atmospheric pressure is maintained by an external vacuum pump from Bosh. The lasing cavity is fed industrial grade nitrogen gas at 20 psig from a cylinder. The laser emits a beam with a cross section of 6 mm by 32 mm in a short 10 ns pulse. The laser has three operating modes: *on*, *standby* and *fire*. The *on* mode powers the electronic components. There are interlocks must be closed for the laser to switch to *standby* mode. The interlocks are a warm-up timer for the thyatron and a pressure switch on the lasing chamber. The laser *standby* mode indicates that the thyatron, the high-energy electrical switch that generates a laser pulse, is operable. The laser is switched into *fire* mode by holding down the start button until the laser's capacitors are charged. The specifications of the UV24 are given in Table 4.1.

Item	Value	Unit
Pulse Energy, 20 Hz	9.0	mJ
Pulse Duration	10	Ns
Average Power, Max	330	mW
Repetition Rate, External	0-50	Hz
Beam Dimensions (Vert X Horiz)	6 x 32	Mm
Peak to Peak Stability	+/- 5	%
Time Delay from Trigger	0.6-1.0	μs

Table 4.1 UV24 Laser Properties

The ultraviolet laser beam is expanded to 30 mm by 50 mm using a beam expander mounted to an Uni-strut optics bench above the wave tank. The beam expander consists of two UV grade lenses, mounted in a 50mm optics cage (Thor Labs), pictured in Figure 4.4. The first lens is planar concave with a focal length of 50 mm and is of fused silica glass. The concave lens begins the expansion by bending the columnar laser beam into a spreading beam. The second lens is planar convex with a focal length of 150 mm and is of fused silica glass. The convex lens ends the beam expansion by bending the

light beam back to columnar form. The light penetration depth  $d$ , shown in Figure 3.7, is altered with a neutral density optical filter located in the last stage of the optics cage. The filter, comprised of two metallic UV density filters (Melles Griot), reduces the intensity of light between 200-400 nm by 75%. The optics cage has a blackout square mounted near the second lens. The blackout square absorbs the edges of the expanding UV light beam. The resulting circular 50mm beam is projected onto a targeting mirror.

The targeting mirror is a 100 mm square UV Aluminum front-coated mirror mounted to the optics bench, illustrated in Figure 4.5. The mirror mount consists of a large ball joint attached to a vertical rod with a slip joint. The rod is suspended from a horizontal translating stage mounted to the optics bench by two aluminum brackets. The ball joint allows the targeting mirror to be positioned to reflect light upon the surface of the liquid below. The translation stage positions the targeting mirror in the center of the laser beam. These components can be seen in Figure 4.2.

#### 4.1.2. Wave tank system

The wave tank system used in these studies is the same one used for the PLIF studies of Woodrow (2001). The system is illustrated in Figure 4.6. The wave tank is constructed of ½ inch Plexiglas and has dimensions of 4 ft by 1 ft by 4 inches. Plexiglas does not transmit UV light, and thus a fused silica window was installed for the PLIF work. This window is not needed for the SLIF imaging. The tank is fitted with a lid for a nitrogen blanket. The nitrogen blanket is generated during tank filling to maintain low oxygen concentration. The blanket nitrogen is fed through two holes on opposite ends of

the lid. The blanket nitrogen escapes through a hole cut in the center. The center hole also allows the camera lens to sit below the top of the tank.

The wave generator for this tank is an oscillating paddle system, shown in Figure 4.7. The paddle is constructed from an 11-1/2 inch long section of 1-1/2 inch PVC pipe that is attached to an 8 inch arm of Plexiglas. A variable speed DC motor controls the frequency and speed of the paddle. Mounting holes located on the paddle arm and on the motor flywheel control the amplitude of the paddle movement.

Dissolved oxygen is removed from the liquid in a separate deoxygenation tank. The deoxygenation tank is rectangular and has an approximate working volume of 10 liters. The deoxygenation tank measures 7 in by 7 in by 1 ft. The deoxygenation tank is mounted on a rolling cart and is raised approximately 5 feet off of the ground, allowing for the liquid to be gravity fed to the wave tank. The nitrogen gas is sparged through the fluid in the deoxygenation tank, displacing the dissolved oxygen. The nitrogen gas is supplied to the deoxygenation tank by 2 mm plastic tubing connected to a nitrogen gas cylinder. The sparger is constructed of 0.5 inch PVC pipe, and sits inside the tank, allowing it to be removed for cleaning. The sparger is in the form of a loop with a branch connecting to the gas supply tube above the tank top. The sparger emits nitrogen from a series of holes drilled along the loop. The top of the deoxygenation tank consists of 1/2 inch Plexiglass with two 1 inch diameter ports: one for the top of the sparging loop, and the other for a DO probe. The stripping tank is illustrated in Figure 4.6. The system has shown the ability to reduce oxygen levels from 9.0 mg/L to 0.5 mg/L for 3 L using nitrogen stripping for 15 minutes.

#### 4.1.3. Imaging system

A Charged Coupled Device (CCD) camera is used to image the emitted fluorescence field. The camera is a Photometrics Series 300 model. A CCD camera is a silicon based imaging device. The CCD camera has a 16 bit, 512 pixel by 512 pixel chip that is backside illuminated with an anti-reflective coating. The camera will capture an image in 512 by 512 pixels, each with 65,536 discrete intensity levels. The term backside illuminated refers to having a thinned head, allowing for an increase in both quantum efficiency and the detectable range of light. CCD cameras have a problem with dark current, or intensity measurements generated by heat. For low and very low light level applications, the camera head is maintained below ambient temperatures. The series 300 camera thermo-mechanically cools the camera chip to 248.15 °K (-25 °C) to reduce dark current.

The camera lens is a 50mm AF Nikkor lens manufactured by Nikon. A bayonet mount attaches the camera lens to a set of extension tubes. The lens to head distance is maintained by mounting the lens on a set of Vivitar extension tubes, which are interchanged depending on the resolution desired. A Hoya 52mm UV filter is mounted to the lens to reduce any reflected UV light being detected by the camera.

The camera head enclosure and camera lens are suspended over the tank using a Repro copy stand from Fierenze. The copy stand allows for the camera height to be adjusted using a cog and track system on the center post. The copy stand arm can be mounted at various lengths from the center post. An additional horizontal translation stage is mounted to the arm, allowing the camera to be positioned on three axes.

The controller for the Photometrics 300 camera is a unit that is separate from the camera head enclosure. It can be programmed using the connected PC with the appropriate PVCAM software, and utilize hardwired inputs and outputs for camera operation. A full description of the controller hardwired inputs and outputs are listed in Appendix A. The camera controller contains the A/D converter, sending each image to the PC.

A PC running PVCAM and V for Windows version 3.5 operates the camera. The images generated on the camera are sent to a camera card and are saved as 16-bit tiff images. V for Windows is a Pascal based program that allows for image translation, editing, and camera operation. PVCAM is the software that operates the camera controller and links with the V for Windows program (Photometrics 1997a; 1997b; 1996b). Although these programs allow for special sequences to be programmed for camera operation, the standard exposure function with an exposure time of 1 ms was used.

#### 4.1.4. System connections

The imaging system and UV laser system are synchronized through electronic connections. The laser external trigger is connected to the camera controller shutter status output (pin 3). The shutter status signal goes to high when the shutter opens, triggering the laser. Time delays between the shutter opening and the laser firing (0.2ms) and fluorescence of the PBA (165 ns max) was less than the minimum exposure time of the camera (1 ms). A shielded wire connects the laser external trigger with a BNC connection to a male nine pin connection at the camera controller.

## 4.2. Auxiliary equipment

For the investigation into oxygen mass transport several pieces of equipment not directly connected to the SLIF apparatus are needed. The image-processing portion of the experiments was done with Matlab 6.2 on SUN workstations or PCs running Windows XP. A Control Company desk weather station measures humidity, room temperature, and atmospheric pressure.

Bulk-liquid measurements of oxygen concentration are taken using a calibrated YSI 52 dissolved oxygen meter. The oxygen meter uses an YSI 5793 temperature and pressure compensated probe. The unit is calibrated in 100% humid air (See Appendix A). A zero point is found using an aqueous solution of excess sodium sulfite. The oxygen meter displays concentration in terms of mg/L and air saturation.

## 4.3. PBA solutions

Pyrene Buyteric Acid is the oxygen probe used in our experiments. The PBA concentration of the water being studied is  $4 \times 10^{-5}$  molar. This was determined by both Duke and Woodrow (unpublished) as the optimal concentration for their PLIF work. A stock solution of  $4 \times 10^{-3}$  molar PBA solution is diluted with distilled water. The stock solution is produced in 100 mL batches by heating a solution of 0.05 M NaOH to 45 C, then stirring the liquid while adding 0.1163 grams of PBA. The stock solution is stirred as it cools to ambient temperature. Since PBA is light sensitive, the stock solution is made in near-dark conditions and stored in darkness.

#### 4.4. Evaporation measurements

Evaporation rate data was be taken as models for evaporation rates were found to vary by over 100 percent, section 2.5. Two independent methods are used to measure the evaporation rate of water during the SLIF experiment. These measure the change in volume and the change in mass over a given period of time.

The displacement method measures the change in height in a large plastic tub over the time of the experiment. The tub measures approximately 3 feet by 4 feet and is 8 inches deep. The tank is filled with PBA dosed water to the approximate height of the liquid within the wave tank. The height is measured using a cathotometer at both the beginning of the experiment and the end of the experiment. The difference is used to estimate a volumetric evaporation rate.

The second method measures the change in mass of a sample solution over time. A metal pan of 10 inches by 12 inches is filled with 10 cm of water and placed on an electronic balance. The weight is recorded at the beginning of the experiment and the end. The results for both methods are compared for calculating the estimated evaporation rate  $\dot{V}$ .

## 4.5. SLIF operational procedure

### 4.5.1. Alignment of laser and image system

The laser beam and the imaging system must be aligned. The fluorescence response occurs beneath the liquid surface where the laser beam impacts. A change in the depth of the liquid will affect the location of the beam spot on the liquid surface. The alignment procedure sets the location of the laser beam spot on the liquid surface, overlays the imaging area on that location, and brings the near surface fluorescence into focus.

The wave tank is filled with a known volume of PBA solution. Both the camera and nitrogen laser start up procedures are initiated. The vacuum pump and laser are turned on. After fifteen minutes, the thyatron warm-up interlock closes, and the laser needs to be set into the firing mode. The laser nitrogen gas supply valve is opened. Nitrogen gas is supplied at 20 psig to ensure enough flow of nitrogen into the lasing cavity. The internal pressure of the lasing cavity is set to 40 torr using the vacuum regulator. With the pressure in the lasing cavity is within the operational limits, the laser can be switch into *standby* mode. After the laser switches to the *stand-by* mode, the Photometrics camera is turn on. The camera head is allowed to cool to  $-25\text{ }^{\circ}\text{C}$  before images are taken. The laser is switched into to the *fire* mode and set to use the internal trigger. The laser shutter is opened and the camera lens cap is removed.

The laser beam pulses are targeted onto a location on the liquid surface. The beam pulses are generated using the internal trigger of the laser. The beam spot location is moved by adjustment of the targeting mirror. A target is used to locate the beam on the

surface. The target is a metal 200 mm ruler suspended from an optics rail supported by the tank walls. The ruler is adjusted to lie, face up, just below the surface of the PBA solution. The location of the center of the beam is recorded. With the beam in the appropriate location, the targeting mirror is locked into position. The laser is switched into the *on* mode as the internal trigger is switched off and the nitrogen gas supply valve is closed.

The camera imaging area is positioned over the chosen liquid surface location, and the camera is then focused on the surface. The V for windows program is opened on the PC. The software links with camera controller, allowing the user to control the camera. The V for Windows function *focus* sets the camera to taking and displaying repetitive, unsaved images. Using the *focus* function, the camera's height is adjusted until the ruler is in focus. An image of the target is shown in Figure 4.8. The system works such that the height adjustment on the copy stand is used as a course adjustment to the focus. The focus ring on the Nikon lens acts as a fine adjustment. After focusing the liquid surface, final adjustment of the horizontal placement of the camera is made to locate it over the predetermined target location.

After adjusting and focusing the camera, the alignment between the imaging area and the laser beam spot is checked. The laser is again switched to the *fire* mode, but operating on the external trigger. Several images are taken with the ruler in place. Final adjustments of camera focus and alignment are made. The target is then removed from the tank.

#### 4.5.2. Imaging of a quenched surface

Quenched (fully saturated) images are obtained according to the following procedure. (It is assumed that this follows the alignment procedure in the progress of an experiment.) The laser is switched to *firing* mode. The imaging sequence is initiated on the computer. The camera CCD chip is cleared of existing charge as the camera shutter opens. As the shutter reaches the open position, the *shutter open* signal trips the laser external trigger. The laser generates a 10 ns burst of UV light that is projected onto the liquid surface, as detailed in section 4.1.1. The PBA responds as detailed in section 3.1.1. The camera images the resulting fluorescence. The shutter closes after being open for 1 ms. The fluorescence image is sent to the computer. The computer stores the image as a 16-bit tiff file and displays the image on the screen. The SLIF system is ready for another image to be taken.

The quenched image set size depends on the operating conditions and desired amount of data. The quenched image sets are saved before image processing is done. Data such as evaporation rate, temperature, humidity, and atmospheric pressure are recorded with the image set. A run number and file labeling system refers to the year, month, set letter of that month, and then the number from 0-99. For example, 0303f\_55 would refer to the 55<sup>th</sup> image of set f generated in the third month of 2003. Some images are not saved due to misfires or computer errors that generate blank or noise images.

#### 4.5.3. Imaging of an unquenched surface

After obtaining the quenched image set, the system is reset for unquenched images. The laser is returned to *standby* mode, and the shutter closed. The PBA solution is drained into a clean bucket and returned to the stripping tank. Nitrogen gas is sparged

through the water solution for 15 minutes at low pressure (< 5 psig). The wave tank lid is positioned on the tank. After ten minutes, the nitrogen lines for the nitrogen blanket are opened and nitrogen gas fills the wave tank.

After being stripped of oxygen, the water solution is gravity fed into the wave tank. Waves on the liquid surface are allowed to damp out. The nitrogen gas supply to the stripping and wave tanks is turned off. The top of the wave tank is removed. The laser is again started, and the laser shutter is opened. The unquenched images are acquired in the same method as the quenched image set.

#### 4.5.4. Dark current image generation

The Photometrics 300 series camera is designed to reduce *dark current* by cooling the camera head. This does not remove all of the dark current, the remaining must be removed by image processing. A series forty of dark frame images were captured with the UV filter replaced with a lens cap. A random set of fourteen images was selected and averaged. The fourteen dark current images were processed in the V for Windows program by adding the intensity values of each image into the corresponding pixel of an overall array. The resulting intensity values were divided through by the integer 14 and rounded to the nearest whole number. The resulting array was termed *DRC AVG* and saved as a 16-bit tiff image. As will be described in Chapter 5, Image Processing, *DRC AVG* is used to remove intensity due to dark current.

## 4.6. SLIF validation experiment

The SLIF validation experiment was designed to validate equation 3-26 between the corrected fluorescence  $\langle F \rangle_{x,y}$  and the dimensionless quencher concentration,  $\psi(z)$ . The experiment was designed such that the SLIF system would image two independent regions of liquid that differed in the oxygen concentration. A second, inner tank was installed to maintain two independent bodies of water, such that regions of both liquids could be seen within a single image.

### 4.6.1. Equipment

The first set of SLIF validation experiments used a shallow, commercial wave tank of 1000 by 1000 by 9 mm. The inner tank was a small plastic container adhered to the bottom of the outer tank with silicon putty. This design proved to have several flaws. The difference in liquid depths, 0.1 mm, combined with the thin liquid depth, 2 mm, led to an observed offset within the raw fluorescence data. A more detailed discussion can be found in section 6.1. The two tank system was replaced with the wave tank described in section 4.1.2 as the new outer tank.

The new inner tank was designed to remove the problems in observing  $F_{x,y}$  in the original two tank design. The outer tank allowed a much deeper liquid level. To remove any difference in the liquid depths, the inner tank was built upon a false bottom fitted to the outer wave tank. This also allowed the inner tank to be removable. As illustrated in Figure 4.9, the inner tank was installed at an angle, with the long wall parallel to the laser beam path. Aligning the beam and the wall reduced any shadow effects caused by the

inner tank wall. The inner tank was constructed of thin plastic mounted to the false bottom by chemical welding. After being secured, the inner tank was tested for leaks using dyed water. Several leaks were identified and sealed using silicon putty.

#### 4.6.2. Procedure

The validation experiment followed the same general procedure as the standard experiments with a few modifications. First, the camera was positioned by locating the wall in the center of the image, as shown in Figure 4.10. Second, the inner tank was filled with 760 mL of water solution that was aerated for 15 minutes in a small glass sparger using room air, to establish a saturated oxygen concentration. The outer tank was filled with 5 L of water solution that was nitrogen stripped. Both tanks were filled to an even depth of 30 mm. The first image set was taken almost immediately after the stripped water was added to the outer tank. The second set of images was taken several hours later when the outer tank had approached a saturated concentration.

The image sets were defined as either quenched/unquenched or quenched/quenched. Special attention was paid to the wall location to allow image cells to be selected to omit wall or near wall effects. Near wall effects tend to be caused by either the meniscus of the liquid or shadowing caused by the slight angle between the wall and the imaging system. Image cells were defined as 65 pixel by 65 pixel areas and used in the image processing and analysis (Figure 4.10). Image cells are further detailed in Chapter 5.

#### 4.7. Experiments under controlled humidity

Several experiments were conducted using the SLIF system to relate mass transport phenomenon at flat air-water interfaces to the evaporation rate of water from the surface. The evaporation rate from the surface of the liquid  $\dot{W}$ , is a function of the relative humidity of the air near the surface of the liquid. By placing the wave tank into a controlled humidity environment, the amount of water evaporating from the surface of the wave tank could be varied.

##### 4.7.1. Equipment

There were two changes to the SLIF equipment to conduct the controlled humidity experiments. First, the wave tank was placed into a humidity controlled enclosure. Second, a cool mist humidifier was placed inside the enclosure to help control the relative humidity inside of the enclosure.

The controlled humidity enclosure was constructed on the optics bench as illustrated in Figure 4.11. The controlled humidity enclosure was constructed of opaque, 1.5 mil plastic sheeting. The plastic sheeting was attached to the optics bench by two inch wide duct tape. The seams of the controlled humidity enclosure were sealed with two inch wide duct tape. The UV laser beam was admitted into the controlled humidity enclosure through the first stage of the beam expander, detailed in section 4.1.1. The enclosure was attached to the first stage of the beam expander and the opening within the first stage was fitted with one of the two neutral density filters. An opening for the camera lens was made in the enclosure and fitted around a ring stand (Figure 4.12), allowing the lens to capture the surface fluorescence unimpeded. A protective shield was added to the camera head to keep the plastic sheeting of the enclosure from coming into

contact with the hot portions of the CCD camera head (Figure 4.13). Two flaps with magnetic closures allowed access into the enclosure (Figure 4.14a,b). The magnetic closures consisted of one inch magnetic striping stapled down the seam of the opening. The magnetic closure allowed the seam to be easily sealed to maintain the proper level of humidity within the controlled humidity enclosure.

Humidity controlled experiments utilized a Holmes Cool Mist Humidifier (HM1851). The humidifier had a maximum liquid output of 15.1 liters per day. The humidifier released moist air into an area by passing air through a wetted, circular wick. The air was moved through the wick by a two speed fan located in the top of the unit. The wick soaked up water located in a pan at the bottom of the humidifier. The water in the humidifier pan was replenished from a water tank located above the pan. The humidifier could be run in three modes, controlled humidity, low humidity, or high humidity. The humidifier in controlled humidity mode had five preset relative humidity levels that the unit would maintain, 35 percent, 40 percent, 45 percent, 50 percent and 55 percent. The humidity modes of low humidity and high humidity only set the fan speed in continuous operation.

#### 4.7.2. Procedure

The controlled humidity experiments followed the same general procedure as detailed in section 4.5. However, before the experiment was started, the humidity in the humidity chamber was set. First the water level in the humidifier tank was checked. If the humidifier water level was low, the tank was removed and filled with distilled water. Next the humidifier was set to the appropriate mode. For those experiments conducted between 30 and 55 percent relative humidity, the controlled humidity mode was used.

For experiments above 55 percent relative humidity, the humidifier was set on high and the access flaps were partially opened to allow less humid air into the chamber. For the highest humidity level achieved, 96 percent, the chamber was almost completely sealed off from the room. The humidity in the chamber was monitored on the weather station, detailed in section 4.2, which was placed inside of the chamber just below the wave tank.

After achieving the desired level of humidity, the standard SLIF procedure was followed. Care was taken to minimize opening and closing of the humidity chamber for access.

Chapter 4 figures

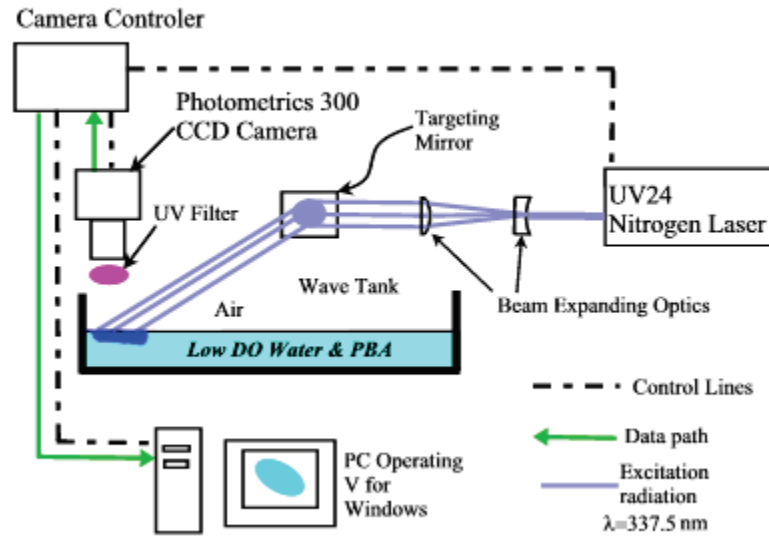


Figure 4.1. Diagram of SLIF system.

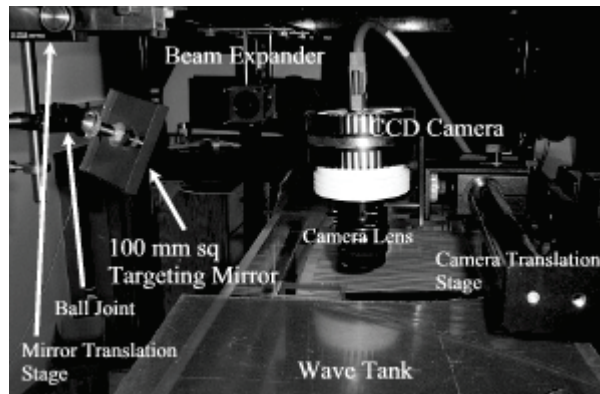


Figure 4.2. Image of SLIF system showing relation of wave tank, camera and laser optics.

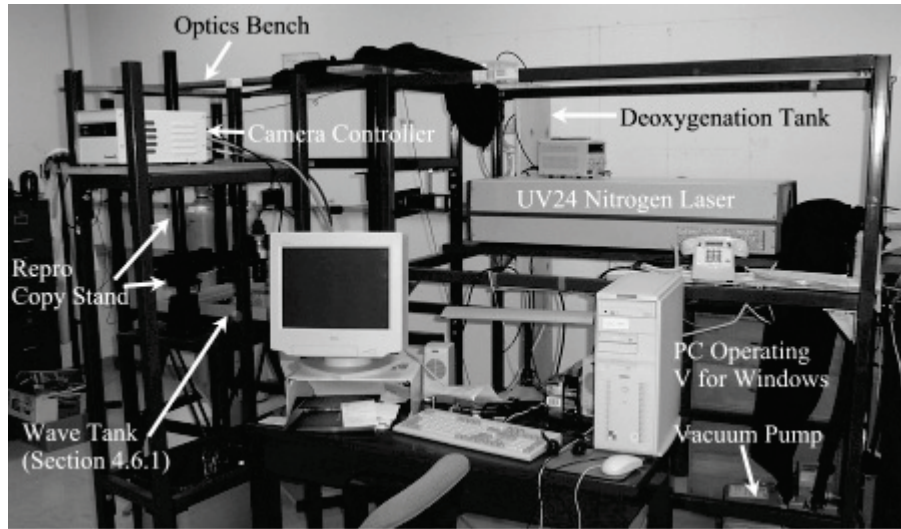


Figure 4.3. Image of SLIF system showing relation of wave tank, copy stand and UV24 laser.

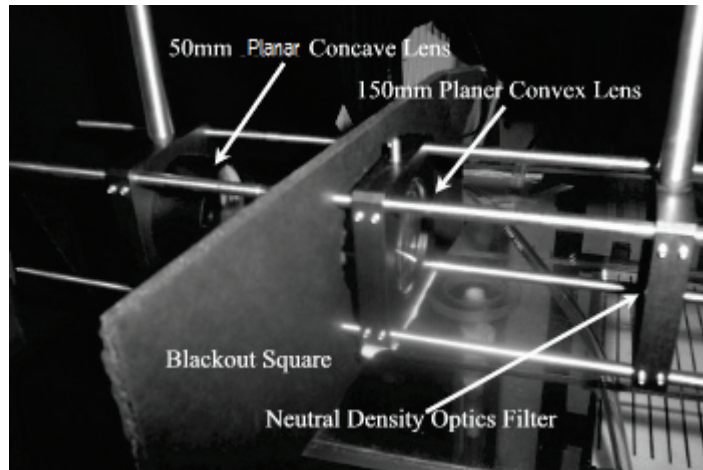


Figure 4.4. Optics cage with beam expander and neutral density filter.

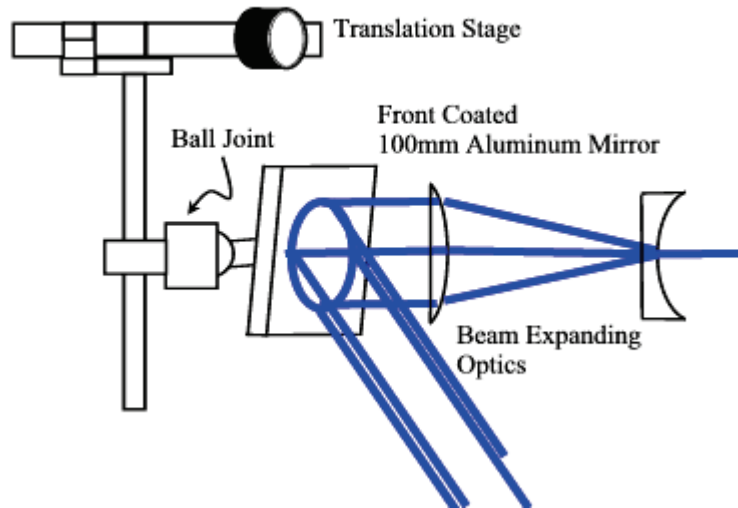


Figure 4.5. Targeting mirror assembly.

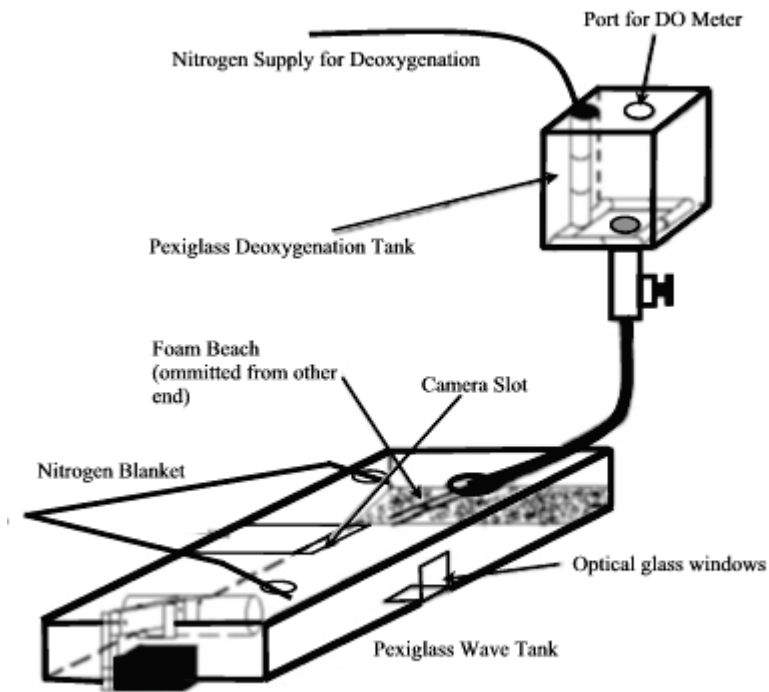


Figure 4.6. Wave tank and deoxygenating tank (Woodrow 2001).

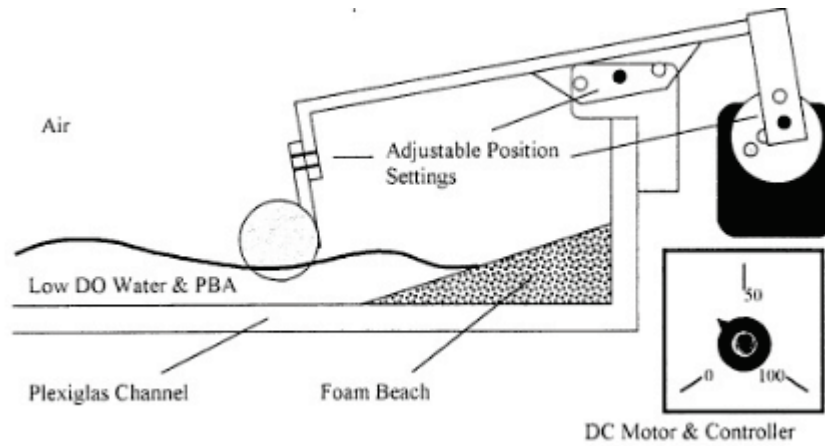


Figure 4.7. Wave generator (Woodrow 2001).

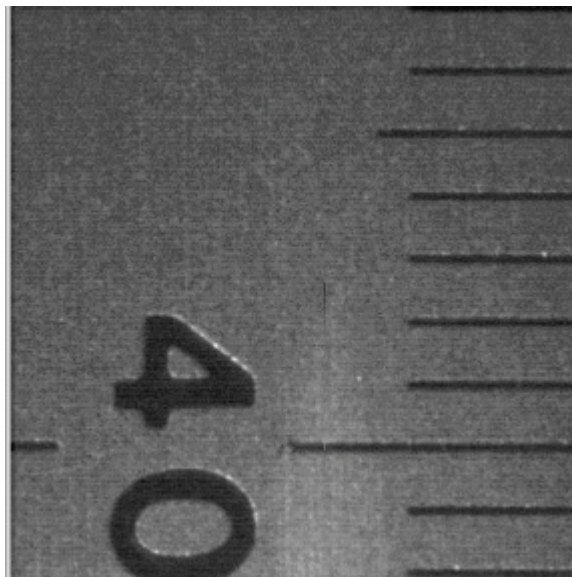


Figure 4.8. Focusing image using millimeter ruler.

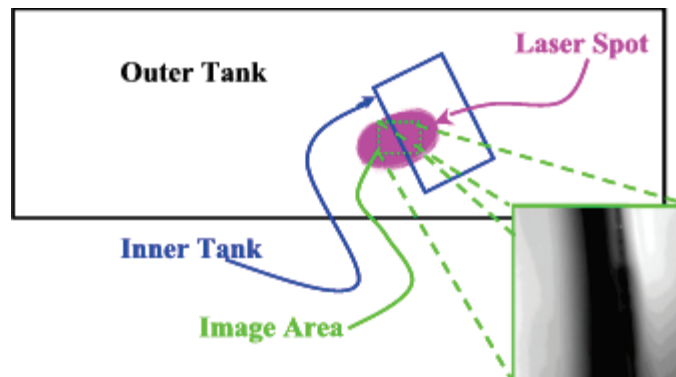


Figure 4.9. Diagram of relationship of inner tank, outer tank, and imaging location.

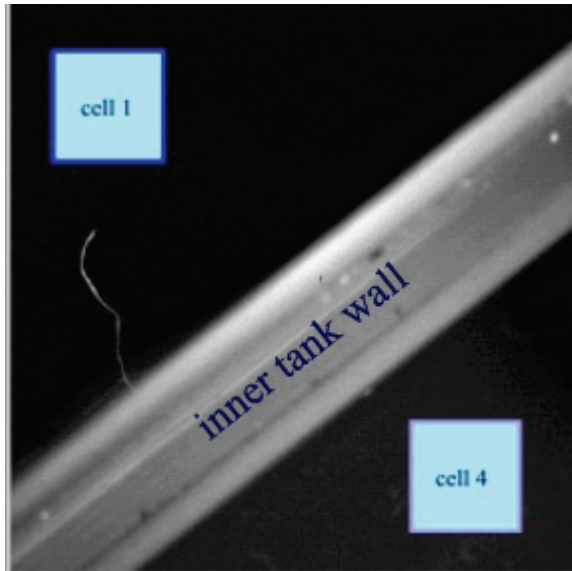


Figure 4.10. Image cell locations in terms of inner tank wall.



Figure 4.11. Image of SLIF Uni-strut optics bench with the constant humidity enclosure attached.

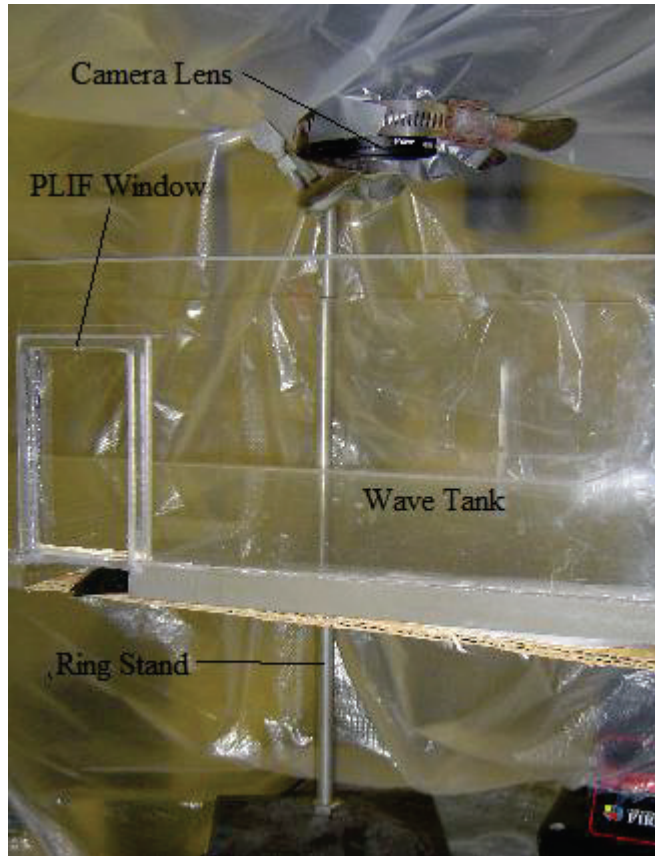


Figure 4.12. An image of the inside of the constant humidity enclosure showing the location of the camera lens opening and the supporting ring stand.

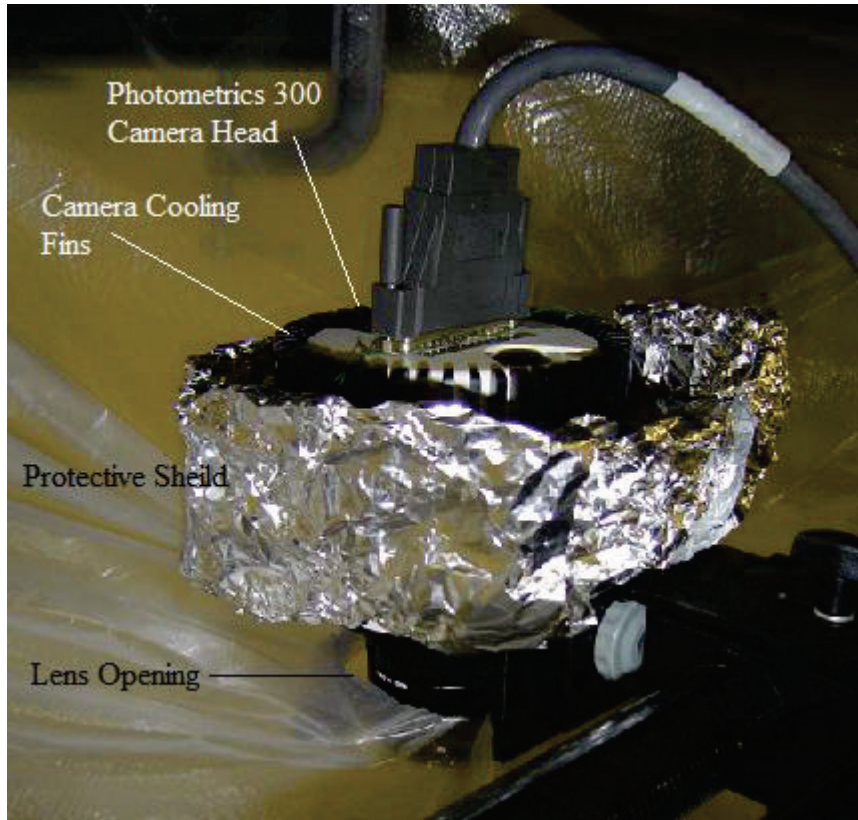


Figure 4.13. An image of the CCD camera head showing the location of the protective shield and the cooling fins of the camera head.



Figure 4.14. An image of the constant humidity enclosure access flap (a) closed (b) open.

## 5. IMAGE PROCESSING

Image processing and analysis procedures were developed for the SLIF technique. The image processing procedures generate a surface map of the normalized relative mass transfer coefficients from intensity images obtained by the CCD camera, as described in sections 4.5.2 and 4.5.3. The SLIF image processing procedure also utilized images taken of flat air-water interfaces at full oxygen saturation (quenched) for each experimental data set. The image processing procedure was modified for the SLIF verification study detailed in Chapter 6. The SLIF verification image processing procedure was specific to the SLIF verification experiments (section 4.6.2). The image analysis techniques were designed specifically for the SLIF study of humidity and oxygen mass transfer across air-water interfaces detailed in Chapter 8.

Intensity images were obtained at a 16-bit intensity resolution by the Photometrics V for Windows program. The intensity images were exported in TIFF format to a network drive for processing in Matlab 6.2 with the image processing toolbox. The image processing toolbox has several functions that are not available on standard copies of Matlab. The TIFF images are imported into Matlab using the function *imread*, and converted into arrays using the function *double*.

Matlab functions used in image processing are named in italics within the text. All original and modified functions used in image processing are detailed in Appendix B. The Matlab copyrighted functions, provided via Matlab, are not detailed in Appendix B.

## 5.1. Overview image processing

The image processing procedure is illustrated using a flowchart in Figures 5.1, 5.2 and 5.3. The objectives of the image processing procedure are to process intensity values  $P_{x,y}$  into raw fluorescence values  $F_{x,y}$  and to generate a map of the variance in dimensionless oxygen mass transfer coefficient  $k_{x,y}^*$  over the imaged surface. The image processing is divided into two stages. The first stage of image processing steps are designed to generate normalized values of surface fluorescence  $F_{x,y}$  and an array of the average quenched fluorescence values  $\bar{F}_{x,y}$ . The second stage of image processing steps are designed to translate these surface fluorescence values into a map of the dimensionless oxygen mass transfer coefficient.

The initial image processing steps are: the removal of dark current, normalization and the creation of an average quenched fluorescence array. The initial image processing steps are illustrated in Figure 5.1. As seen in the figure, the process involves three subsets of images. The first subset, subset A, is a selected set of fourteen quenched images that will be the basis of the fluorescence correction array. The intensity images of the fluorescence correction array are randomly selected from the quenched image set produced at the beginning of each data acquisition, as detailed in section 4.5.2. A quenched image set typically has forty to sixty images. Subset B is a second subset of selected quenched images from the same quenched image set as subset A. The independence of subset A and subset B is maintained by not having any common intensity images between them. The third subset, subset C, is the unquenched data set. The unquenched image set typically consists of thirty to ninety images.

The next set of image processing steps consists of correcting the fluorescence images in subsets B and C, calculating the relative boundary layer thickness across the surface for subset C, and creating a map of relative mass transfer values based on the relative boundary layer thickness. The second half of the image processing procedure is illustrated in Figures 5.2 and 5.3.

#### 5.1.1. Dark current removal

The SLIF system generates an intensity image with values  $P_{x,y}$  at each pixel as given in equation 5.1

$$P_{x,y} = F_{x,y} + DC_{x,y} \quad (5.1)$$

where  $DC_{x,y}$  is the intensity attributed to dark current at that location. Imaging processing converts the intensity image into a raw fluorescence image by removing the dark noise  $DC_{x,y}$  from the intensity values. The dark current is removed by subtracting the dark current correction array, DKCRAV, from the intensity image. The generation of the dark current correction array is detailed in section 4.5.4.

Figure 5.4 shows a contour plot of raw the fluorescence image D42AB\_34 detailed in section 7.2, produced by the function *contourf*. In this plot, the raw fluorescence values are divided into 20 different intensity levels that are illustrated by the color bar on the right side of the figure. The lowest level of raw fluorescence intensity is dark blue at values near 2,500. The highest level of raw fluorescence intensity is colored red for values above 6,000. The black points represent either a change in the level of raw fluorescence or noise outside of the range of the surrounding level.

### 5.1.2. Scratch correction

The CCD camera has a defect from  $(x=86, y=95)$  to  $(x=86, y=210)$ . The pixels of the scratch are replaced by the function *scratchcorrection2*. The function *scratchcorrection2* calculates the average of the horizontally adjoining pixels for each pixel of the scratch and uses it to replace the value of the affected pixel.

### 5.1.3. Cropping

The next step of the image processing procedure is to crop out areas of poor illumination. The cropping process removes triangular areas from both the upper right and lower left corners. These areas are set to a value of zero and are ignored in the following image processing procedures. The cropped areas are set to zero by multiplying the values of each image with the areas of the cropping array.

The cropping array is generated in a two step process from the quenched image series. In the first step, linear approximations for the desired cropping contour level  $l_e$  are calculated by the function *linefind4*. In the second step, the average slope and intercept values from *linefind4* are sent to the function *cropset* to generate the cropping array.

The function *linefind4* calculates two linear approximations for the contour lines for a given normalized level of mean intensity. In Figure 5.4 there are two poorly illuminated areas in the upper right, and lower left corners. The function *linefind* divides the image into an upper and lower sub image; to avoid having the contour points of the two distinct lines being merged together in the next step. The upper and lower sub images are sent to the Matlab function *contourc*, which returns an array of tagged locations at a given value. The tags are removed and the  $x$  and  $y$  locations of the points

are used in a linear regression to find the slope  $l_s$  and intercept  $l_i$ . The line parameters for each quenched image are averaged and forwarded to the next step.

The function *cropset* generates the cropping array. The function *cropset* takes an array of 512 pixels by 512 pixels with a value of one and applies equations 5.2 and 5.3 to each point  $x_n, y_n$

$$y_n > l_{s1}x_n + l_{i1} \quad (x_n, y_n) = 0 \quad (5.2)$$

$$y_n < l_{s2}x_n + l_{i2} \quad (x_n, y_n) = 0 \quad (5.3)$$

where  $l_{s1}$  and  $l_{s2}$  are the slopes of the first and second linear contour approximations, while  $l_{i1}$  and  $l_{i2}$  are the respective intercepts. An example of a cropped raw fluorescence image, R63E\_92 is shown in Figure 5.5.

#### 5.1.4. Normalization

The second step of the image processing procedure is to normalize each raw fluorescence image, as detailed in section 3.4. This corrects for the variation of the mean excitation radiation  $\bar{I}$  between each image. The normalization scales the raw fluorescence values in terms of the mean raw fluorescence value. The two-dimensional mean of the raw fluorescence values is found by the function *mean2b*. The function *mean2b* removes the cropped values of the array before calculating the two-dimensional mean. The raw fluorescence values are then divided by the two-dimensional mean to find the normalized raw fluorescence values.

A normalized array is illustrated by a contour map in Figure 5.6. This contour map is again of image R63E\_92.

### 5.1.5. Average quenched fluorescence array generation

The first intermediate step is the production of an average quenched fluorescence value array. The average quenched fluorescence value array is the estimate of the variation from ideal of the distribution of the excitation radiation, and the source of the intensity distribution function  $\Omega(x, y)$ . The normalized raw fluorescence values of subset A are averaged between images to generate an array of averaged normalized quenched fluorescence values,  $\hat{F}_{x,y}^{Aq}$

$$\hat{F}_{x,y}^{Aq} = \frac{1}{14} \sum_{l=1}^{14} \hat{F}_{x,y}^q(l) \quad (5.4)$$

where  $\hat{F}_{x,y}^q(l)$  is the normalized quenched normalized fluorescence value at location  $x, y$  for image number  $l$ . The excitation radiation intensity at any given point  $I_{x,y}$  varies across the surface. Under ideal conditions, the distribution of the excitation radiation intensity would be a Gaussian distribution from the center of the beam outwards. The excitation radiation intensity distribution produced by the Auburn University SLIF system is asymmetrical. The excitation radiation intensity distribution is formed by the use of an off-centered targeting mirror above the liquid surface, as detailed in section 4.1.1.

A contour map of an intensity distribution function is shown in Figure 5.7. The intensity distribution function is derived from the image set D21A. The intensity distribution function was determined from the distribution of the intensity  $P_{x,y}$  within the image. The intensity distribution in image set D21A is from the variance in the excitation radiation intensity  $I_{x,y}$ .

As detailed in section 3.3, the analysis of the SLIF data needs to be in terms of a uniform level of excitation radiation intensity  $I_{x,y}$ . The fluorescence intensity values under a uniform level of excitation radiation are corrected fluorescence values  $\langle F \rangle_{x,y}$ , or normalized corrected fluorescence values  $\langle \hat{F} \rangle_{x,y}$ .

#### 5.1.6. Primary background correction

The primary background correction part of the imaging processing procedure involves three steps: the scaling of the average quenched normalized fluorescence values, the creation of a correction array, and correcting the normalized raw fluorescence images into corrected fluorescence arrays. The first step is performed using a block processing methodology shown in the function *CFcorrect*. The second and third steps of background correction are performed within the function *t2filter*, detailed in Appendix B, and illustrated in Figure 5.2.

The average quenched normalized fluorescence array is scaled to match the distribution of the normalized fluorescence image. The effectiveness of the background subtraction varies depending on the difference between the standard deviation of the normalized fluorescence array and the normalized fluorescence image. The major source of deviation from the mean in both the average quenched normalized fluorescence array and the normalized fluorescence image is the laser intensity distribution  $\Omega(x,y)$ . Since the laser intensity distribution is not a function of the incident radiation level, the standard deviation of both the average quenched normalized fluorescence array and the normalized fluorescence image should be identical. However, if the measured average

fluorescence deviated from the actual fluorescence by some base noise level, such as un-subtracted dark current,  $C_i$  then an error would be propagated forward in terms of the laser intensity distribution. By scaling the average quenched normalized fluorescence array, or the correction array, by a ratio of two dimensional standard deviations, attenuates any base noise within the image. The two dimensional standard deviation for both the average quenched normalized fluorescence array, and the normalized fluorescence image are calculated by the function *std2b*, which ignores the cropped values in the calculation. The scaling is implemented by multiplying each point of the average quenched normalized fluorescence array by the ratio of the two dimensional standard deviation of the normalized fluorescence image over the two dimensional standard deviation of the average quenched normalized fluorescence array.

The function *t2filter* combines three image processing steps: filtering, correction array generation and the correction process. The function *t2filter* imports the arrays of average quenched normalized fluorescence values and a normalized raw fluorescence image, from subset C. The first operation the function *t2filter* is to filter out any negative or zero values from the array of average quenched fluorescence values. The function *t2filter* replaces zero or negative normalized quenched fluorescence values with the average of the adjacent values. The function *t2filter* imports the cropping array to ignore the cropped points of the image.

The second operation of the function *t2filter* is to generate the values of the fluorescence correction array. This is done within the image processing toolbox function *blkproc*. The function *blkproc* reforms the supplied array of averaged quenched raw fluorescence values  $\hat{F}_{x,y}^{Aq}$  into a linear string and exports each value and the mean value of

the averaged quenched values  $\hat{F}^q$  to the function *Inv3*. The function *Inv3* implements equation 3.25 for each location of  $x$  and  $y$ . The function *Inv3* divides the mean value of the normalized quenched fluorescence  $\hat{F}^q$  by the supplied averaged quenched fluorescence  $\hat{F}_{x,y}^{Aq}$  as detailed in Appendix B. This produces the correction array value  $\langle CA \rangle_{x,y}$  at the same location as the averaged quenched fluorescence supplied. The function *Inv3* returns the generated correction array value  $\langle CA \rangle_{x,y}$  to the calling function. *blkproc* reorganizes the linear string of correction array values into the correction array. The dimensions of the correction array are identical to the averaged quenched fluorescence array supplied to the function *blkproc*.

The third step of the function *t2filter* is the generation of the corrected fluorescence array. The function *t2filter* multiplies each value of the imported normalized raw fluorescence image  $\hat{F}_{x,y}$  by the corresponding value of the correction array  $\langle CA \rangle_{x,y}$  to generate the corresponding normalized corrected fluorescence value  $\langle \hat{F} \rangle_{x,y}$ , as detailed in equation 3.26. The resulting normalized corrected fluorescence array is exported to the next processing step.

A contour plot of the normalized corrected fluorescence array for image R63E\_92 is shown in Figure 5.8.

### 5.1.7. Secondary background correction

The primary background correction process removes the time invariant background distribution caused by the distribution of the excitation radiation. However, initial processing demonstrates that there appears to be a significant time variant background component,  $B(t)_{x,y}$  which needs to be removed to generate usable corrected fluorescence values  $\langle F_{x,y} \rangle$ .

The time variant background  $B(t)_{x,y}$  appears to be a compound rotation about the x and y axis. The cross sections of normalized fluorescence values versus the correction array values do not lie upon each other, as seen in Figure 5.9. However, the features of both cross sections do appear to correspond. For a rotation in three dimensions, the translation of the of the correction array values  $X_{CA}$  to the normalized fluorescence values  $X_{FA}$  can be represented as

$$X_{FA} = X_{CA}R \quad (5.5)$$

where  $R$  is the rotation matrix between the points  $X_{FA}$  and  $X_{CA}$ . These variables are defined in matrix form as

$$X_{FA} = \begin{bmatrix} x' - x_r \\ y' - y_r \\ F_{x,y} \end{bmatrix} F \quad X_{CA} = \begin{bmatrix} x - x_r \\ y - y_r \\ \langle CA \rangle_{x,y} \end{bmatrix} \quad R = R_x R_y \quad (5.6a,b,c)$$

where  $(x_r, y_r)$  is the center of rotation, the rotation around the x axis,  $R_x$ , and the rotation around the y axis,  $R_y$ , are defined from Jähne (1997)

$$R_x = \begin{bmatrix} 1 & 0 & 0 \\ 0 & \cos\theta_x & \sin\theta_x \\ 0 & -\sin\theta_x & \cos\theta_x \end{bmatrix} \quad R_y = \begin{bmatrix} \cos\theta_y & \sin\theta_y & 0 \\ -\sin\theta_y & \cos\theta_y & 0 \\ 0 & 0 & 1 \end{bmatrix} \quad (5.7a,b)$$

The angle of rotation around the x axis is defined as  $\theta_x$  and the angle of rotation around the y axis is defined as  $\theta_y$ .

There are three possible sources of a time variant rotation  $R$  in the Auburn SLIF system. Vibrations caused by either the vacuum pump, or from external sources could cause the targeting mirror to slightly vibrate and cause changes in the excitation surface distribution  $\Omega_{x,y}$ . Also it is possible, but unlikely, that the circulation cells caused by evaporation may effect the apparent surface distribution as it curves towards downwelling areas. The third possible cause is that vibrations caused by nearby construction are causing the camera head to vibrate slightly. This is the most likely cause as the CDD camera head is cantilevered out from the main post of the copy stand making it more susceptible to low frequency vibration.

To correct for the time variant background,  $B(t)_{x,y}$ , an estimate of the rotation matrix  $R$  is needed. In general, rotations are non-commutative, such that

$$R_x R_y \neq R_y R_x \quad (5.8)$$

except in situations where the cosine of the angle approaches one. This states that in general terms to calculate the rotation matrix  $R$ , the values and order of rotation are needed. However, if one angle of rotation is less than 1.15 degrees, with the cosine of the angle being greater than 0.999, the rotations can be treated as commutative (Jahne, 1997) such that

$$R = R_x R_y = R_y R_x = \begin{bmatrix} 1 - \sin \theta_x \sin \theta_y & \sin \theta_x + \sin \theta_y & 0 \\ -\sin \theta_x - \sin \theta_y & 1 - \sin \theta_x \sin \theta_y & 0 \\ 0 & 0 & 1 \end{bmatrix} \quad (5.9)$$

where we have simplified  $\cos \theta_x$  and  $\cos \theta_y$  to be approximately one.

The temporal varying background function,  $B(t)_{x,y}$  can be estimated for each given image by finding the estimated secondary background function for each image using a method described by Russ(2002). A number of points are selected for the analysis from across the image. An background estimate function,  $B_e(x, y)$  is then fitted to these data points by a least squares fitting method. A two-dimensional, second-order form of  $B_e(x, y)$  is

$$B_e(x, y) = a_0 + a_1x + a_2y + a_3xy + a_4x^2 + a_5y^2 \quad (5.10)$$

where  $a_0 \dots a_5$  are the fitting constants. For small, two-dimensional rotations, the temporal varying background function,  $B(t)_{x,y}$ , can be simplified to the form

$$B_e(t)_{x,y} = a_0 + a_1x + a_2y + a_3xy \quad (5.11)$$

The temporal varying background function,  $B(t)_{x,y}$  of each image is estimated using the function *B2find*. The function takes the normalized corrected fluorescence image and divides it into a series of twelve pixel by twelve pixel image cells; ignoring the six rows and columns along the edge. The function *B2find* then finds the maximum value within each image cell and records the location of this value in terms of  $x$  and  $y$ . The image cell maxima, and their locations, are recorded in an array of values for the next step. The function *B2find* then uses the Matlab function *lsqcurvefit* to fit the constants  $a_0 \dots a_3$  by finding the minimum squared remainder. The function is designed to fit a

single dimension polynomial, not a two dimensional polynomial, however it can be forced to fit a two dimensional polynomial (Redfern and Campbell, 1998). *B2find* exports the polynomial constants in a single dimension array.

The normalized corrected fluorescence image is corrected for the temporal varying background function,  $B(t)_{x,y}$  in the Matlab function *B2filter*. The function first generates a secondary correction array based on the temporal varying background function generated by *B2find*. A contour plot of the example secondary correction array for the image R63E\_92 is shown in Figure 5.10. For each location on the image, the function divides the normalized corrected fluorescence image by the value of the secondary correction array for that location. A contour plot of the normalized corrected fluorescence values for R63E\_92 is shown in Figure 5.11.

#### 5.1.8. Relative boundary layer calculation

A map of the relative mass transport boundary layer thickness  $\delta_{x,y}/\bar{\delta}$  can be generated from a normalized corrected fluorescence array, an average corrected quenched fluorescence value array, and the saturated oxygen concentration supplied to the function *boundarylayer*. The process within the function *boundarylayer* is illustrated by equations 3.27, 3.36, and 3.43. The production of a normalized corrected fluorescence array was detailed in section 5.1.5. The average corrected quenched fluorescence array is produced by a process similar to that of the average quenched fluorescence array (section 5.1.3).

The average corrected quenched fluorescence array is produced from the quenched image subset B. Each of the fourteen images of subset B are corrected in the

manner illustrated in section 5.1.5. These fourteen images are then averaged by the formula

$$\langle \hat{F}^q \rangle_{x,y}^A = \frac{1}{14} \sum_{l=1}^{14} \langle \hat{F}^q \rangle_{x,y} [l] \quad (5.12)$$

where  $\langle \hat{F}^q \rangle_{x,y}^A$  is the average corrected quenched fluorescence value at location [x, y] and

$\langle \hat{F}^q \rangle_{x,y}$  is the corrected quenched fluorescence value at the same location.

The function *boundarylayer* divides each value of the average corrected quenched fluorescence array by the corresponding value of the normalized corrected fluorescence array. The resulting intermediate value is multiplied by the saturated Stern-Vollmer response term and the saturated oxygen range is subtracted, equation 3.44. The resulting values are the relative boundary layer thickness  $\delta_{x,y} / \bar{\delta}$ .

A map of the normalized boundary layer thickness for image R63E\_92 is plotted in Figure 5.12 and discussed in section 8.1.

#### 5.1.9. Relative mass transfer calculation

The final step of the image processing procedure is to generate a map of the relative mass transfer coefficient across the liquid surface. The normalized relative mass transfer coefficient  $k^*$  is defined from equation 3.46 as

$$k^* = \frac{\bar{\delta}}{\delta_{x,y}} \quad (5.13)$$

The values of relative boundary layer thickness are inverted by using the function *blkproc* to call the function *Inv3*.

A map of the dimensionless mass transfer coefficient for image R63E\_92 is plotted in Figure 5.13 and detailed in section 8.1.

## 5.2. SLIF verification image processing

The SLIF verification study was designed to validate equation 3.26 between the corrected fluorescence,  $\langle F \rangle_{x,y}$  and the dimensionless quencher concentration,  $\psi(z)$ . The verification image processing procedure generates a pair of normalized corrected fluorescence image-cells with a large difference in boundary layer thickness under the same mean excitation radiation  $\bar{I}$ . The identical excitation radiation allows for the comparison of the corrected fluorescence between the two image-cells generated by the difference in corrected fluorescence to be related directly to the difference in boundary layer thickness. The SLIF image processing procedure for the verification process follows the most of the steps covered in section 5.1. The verification image processing procedure has several steps: removal of dark current, normalization, creation of correction arrays, generating corrected fluorescence array-cells. The verification image processing procedure is diagramed in Figure 5.14.

The SLIF verification study used both the apparatus and procedure described in section 4.6. A wall allowing for differing conditions on each side is found through the middle of the images acquired in the SLIF verification study. A change in the subsets is made such that subset A consists of fourteen quenched/quenched images, subset B consists of quenched/unquenched intensity images, and subset C consists of independent

quenched/quenched images. Each of these subsets have two 65 pixel by 65 pixel image-cells for each original intensity image as detailed in Chapter 4. Image-cell 1 is located over the outer tank, while Image-cell 4 is over the inner tank. The relative locations of Image-cell 1 and Image-cell 4 are shown in Figure 5.15. The image-cells from each image are maintained as an image-cell pair. The image-cells of each image pair are labeled with both their subset and their cell number, such as the image-cell  $A1$  or  $A4$ . Image-cell 1 is a quenched image-cell in subsets A and C, and unquenched in subset B. Image-cell 4 of each subset is the quenched image cell in all of the verification images.

Figure 5.16 illustrates the difference in intensity  $P_{x,y}$  between the quenched/quenched and unquenched/quenched verification images.

#### 5.2.1. Dark current removal

The first step of dark current removal from the intensity measurements is identical to section 5.1.1.

#### 5.2.2. Image-cell cropping

The second step is the cropping of the two 65 pixel by 65 pixel image-cells from the verification raw fluorescence images. The cell locations avoid any effects caused by the inter-tank wall or the laser spot edges.

#### 5.2.3. Normalization of image cells

The normalization procedure is similar to that discussed in section 5.1.4. Each image-cell pair is divided by the mean of Image-cell 4 of the pair. This normalizes both image cells relative to Image-cell 4.

#### 5.2.4. Creation of average quenched fluorescence arrays

The image processing to generate an average quenched fluorescence array one and an average quenched fluorescence array four is similar to the process described in section 5.1.5. In this case each set of 65 pixel by 65 pixel image-cells in subset A is treated as an individual group of images to generate two average quenched fluorescence arrays. For each group of image-cells the same methodology of producing the average quenched fluorescence array is identical to the one described in section 5.1.5.

#### 5.2.5. Fluorescence correction

The process of fluorescence correction in the verification study image processing procedure again uses the function *t2filter*. The image processing within *t2filter* is illustrated in section 5.1.6. Each image-cell of subsets B and C are processed using the average quenched fluorescence array corresponding to that image-cell. For example an image cell B4 or C4 would be corrected using the average quenched fluorescence array four to produce the corresponding corrected fluorescence array four. The image processing steps used for each image-cell is identical to the image processing steps discussed in section 5.1.6. The results are four image cells in two sets, unquenched/quenched and quenched/quenched. These results are discussed in Chapter 6.

### 5.3. Data analysis

A data analysis function *SlifRBanalysis* is applied to the dimensionless mass transfer data produced by the SLIF technique. The data analysis function *SlifRBanalysis* is designed to rigorously determine key features of Rayleigh-Bénard downwelling zones, described in chapter 8: the center of the downwelling points, the locations of the edges of the data points, the dimensionless mass transfer value for the downwelling zone, and the approximate width of the downwelling zone.

#### 5.3.1. Locating the points of interest

The first task of the data analysis function is to distinguish the ‘downwelling’ data points from the surrounding flat surface values. The identification process is handled by the function *dwlocate*. The selection process utilized by *dwlocate* focuses on three attributes of these downwelling zones found in the SLIF data: that downwelling zones appears as a minima within the SLIF data, that the downwelling zones are continuous, that the downwelling zones are linear. Figure 5.13, illustrates an example of a downwelling zone within the dimensionless mass transfer data. It appears as a dark line, or minima, compared to the surrounding liquid. By defining downwelling points using these attributes, rather than some threshold value, the downwelling detection program could reduce the number of false detections caused by poor illumination or noise.

The first step of the function *dwlocate* is to generate a map of the major minima points located within the image. Figure 5.17 presents a cross sectional plot of the SLIF data which shows that there are major minima within the data as well as minor minima generated by noise. To deal with this problem, the minima are identified by estimating

the second derivative values of the SLIF dimensionless mass transport function. This estimate is generated by using a 33 x 1 differential kernel for the first derivative and an 11x 1 kernel for the second derivative as described in Stotzer et al (2006). The large kernel size allows for the removal of high frequency noise. The second derivative attenuates narrow band signals, such as downwelling over low frequency noise (Butler and Hopkins, 1970). The use of the first and second derivatives to find valleys, or local minima, for spectral data has been utilized for years (Stauffer and Sakai, 1968; Butler and Hopkins, 1970; Shenk et al., 2001; Duckworth, 2004); typically in IR spectroscopy to assist in differentiating overlapping peaks and absorption data to differentiate overlapping absorption bands.

The second step of the function *dwlocate* is to identify the continuous linear minima within the data. The function *dwlocate* generates a logic map to indicate the special location of the major minima. The function *dwlocate* then applies a linear filter subroutine, *zline* to the logic map. The subroutine *zline* applies 92 unique 5x5 continuous line kernels to the data to detect minima points which may form a continuous line. This continuous line filter is an alteration of a standard edge detection routine as described by Jain (1989) and Weeks (1996). The kernel method described in Weeks (1996) applies a kernel to the values surrounding each point, with a kernel for each possible edge alignment. The maximum kernel value is then stored in an array with the highest values on the image being the edge. This standard kernel routine was altered by adding additional kernels that allowed for the detection of points located within a curve. The resulting map of linear points is then forwarded to the function *findcontpoints*. The subroutine *findcontpoints* calculates each 'line' value in terms of the number of

continuous points. The subroutine starts with a point on the linear points map and then identifies any contiguous points. The process continues with identifying any contiguous points to the first identified contiguous point, ignoring points already 'found'. This process of identifying contiguous points continues by the routine until all of the points that can form a continuous line with the first point have been identified. This 'line' is given a weight equal to the number of points within it by the function *linerank*. The function *dwlocate* then generates a new logic map with all of the points that are greater than a predetermined threshold, typically five.

### 5.3.2. Locating the shoulders of the downwelling zone

The next step of the image analysis process is identifying the approximate location of the shoulders of the downwelling feature. The shoulders of the downwelling feature are identified on an idealized cross-sectional plot is shown in Figure 5.18 with the symbol S. The approximate locations of downwelling shoulders in a real cross-sectional plot are shown in Figure 5.19. The function *SlifRBanalysis* calls the function *shoulderfind* to identify the shoulder locations for each linear data point identified by *dwlocate* and hands off the entire cross-sectional data of the image for that point and the cross sectional values of the first and second derivative calculated in the function *dwlocate*. The function *shoulderfind* begins at the center point of the downwelling zone calculated by *dwlocate* and begins to search for the local minima of the first derivative values calculated in *dwlocate*. The first derivative values of *dwlocate* approach minima at the inflection points, or shoulders, of the zero order function (Butler and Hopkins, 1970).

After the function *shoulderfind* identifies the approximate location of the shoulders, it then calculates the average of the five dimensionless mass transfer coefficient values near each shoulder location.

### 5.3.3. Calculating the dimensionless mass transfer coefficient for downwelling

The next step in the image analysis procedure is to calculate the approximate value of the downwelling. The function *SlifRBanalysis* averages the five dimensionless mass transfer coefficient values from the points adjacent to, and including, the downwelling location calculated by *dwlocate*. The difference between the average shoulder values at S and the downwelling values, at D in Figure 5.19 is used to calculate the half maximum value, H.

### 5.3.4. Calculating the half max width

The half max width of the downwelling zone is used as the measure of width of the downwelling. The half max width is found by locating the two points between the downwelling shoulders that have the closest dimensionless mass transfer coefficient values to half of the maximum difference between the central downwelling value and average shoulder value of the downwelling zone. The half max width is illustrated in Figures 5.18 and 5.20. The half max width is calculated by the function *halfmaxwidth*.

For each data image of the SLIF experiments, a file was generated that contained the values of dimensionless mass transfer coefficient, the width, the shoulder locations, and the shoulder dimensionless mass transfer coefficient values for each cross section of downwelling analyzed. An average value for the width and dimensionless mass transfer coefficient was calculated for the entire image.

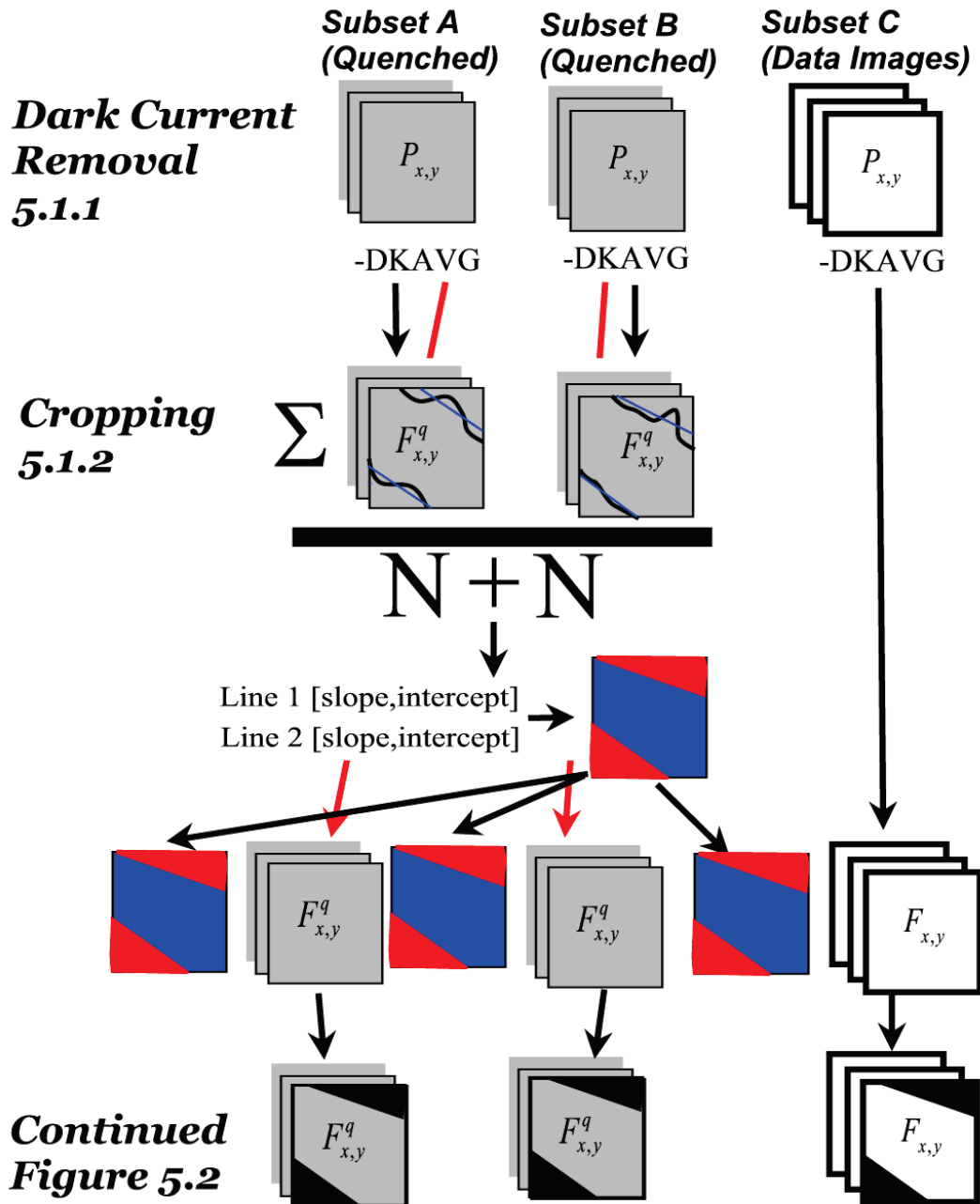


Figure 5.1. Image processing steps for standard SLIF, part 1.

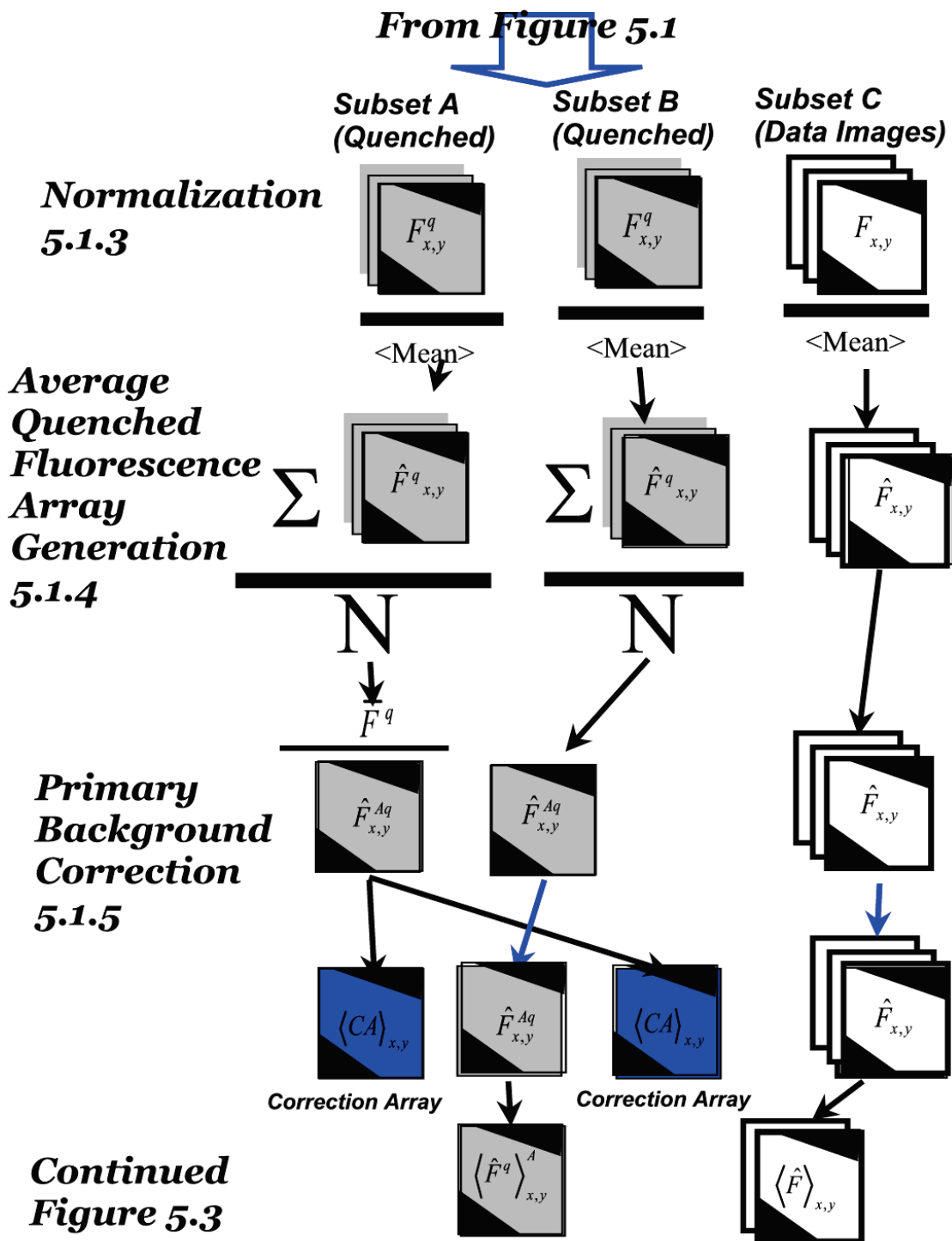


Figure 5.2. Image processing steps for standard SLIF, part 2.

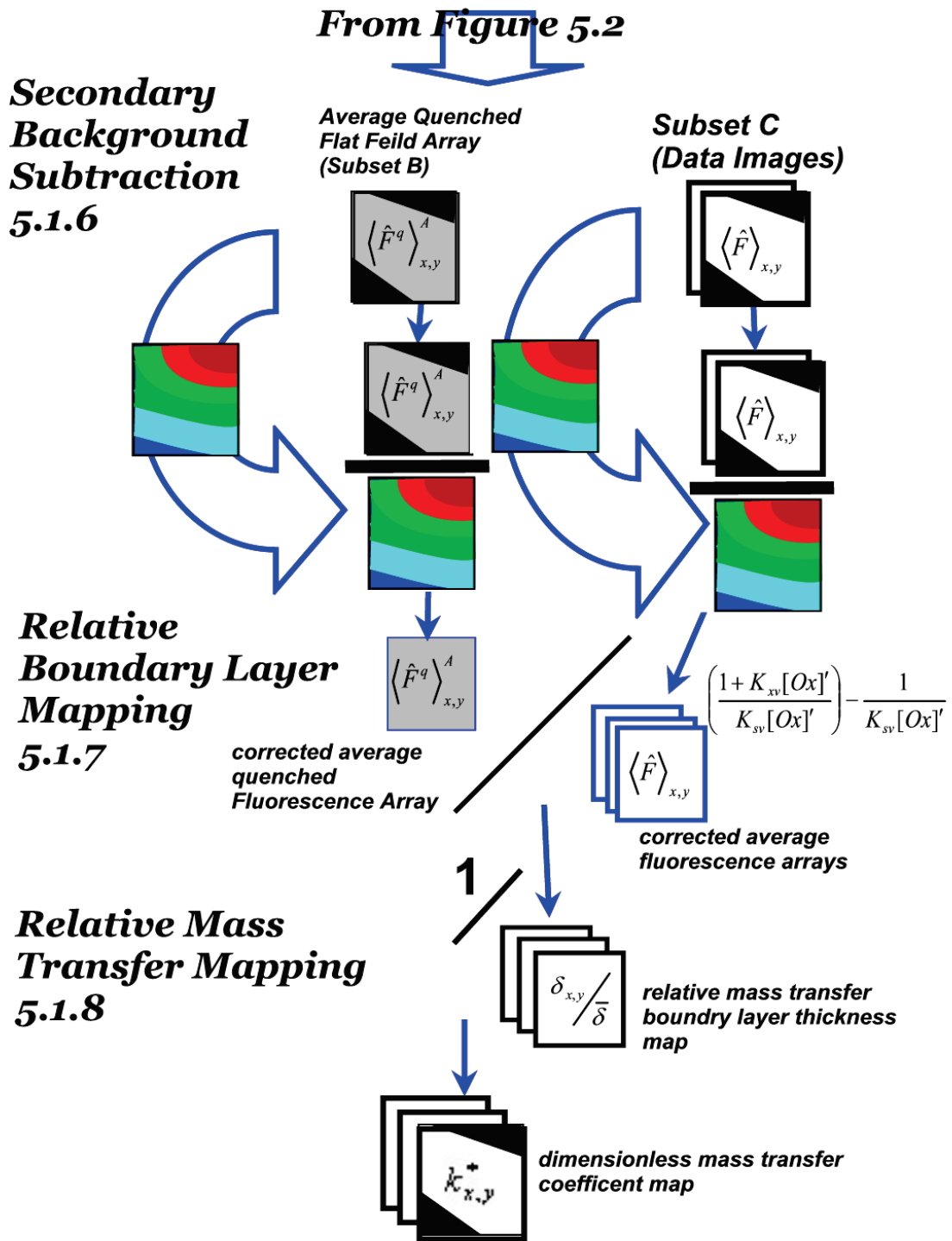


Figure 5.3. Image processing steps for standard SLIF, part 3.

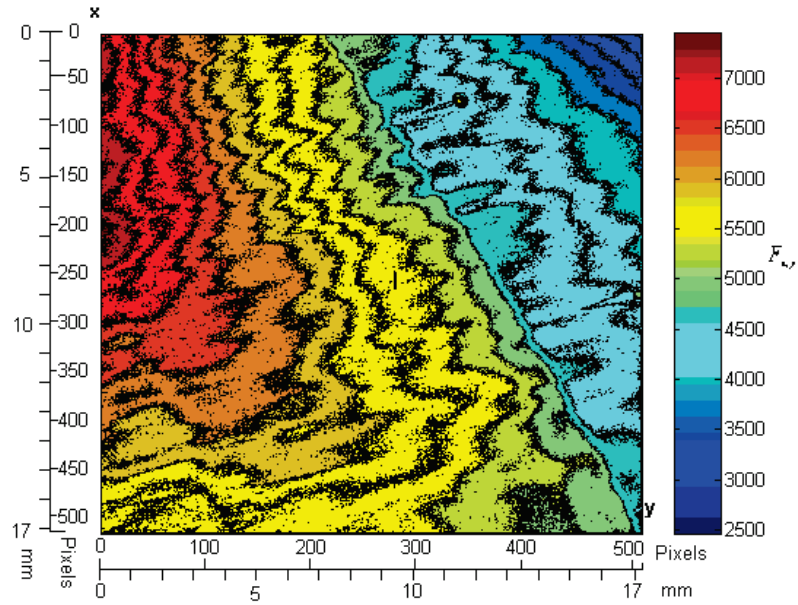


Figure 5.4. Contour plot of raw fluorescence intensity values for image D42AB\_34; temperature 21 °C, pressure 30.33 inHg, humidity 42%, width 17.2 mm.

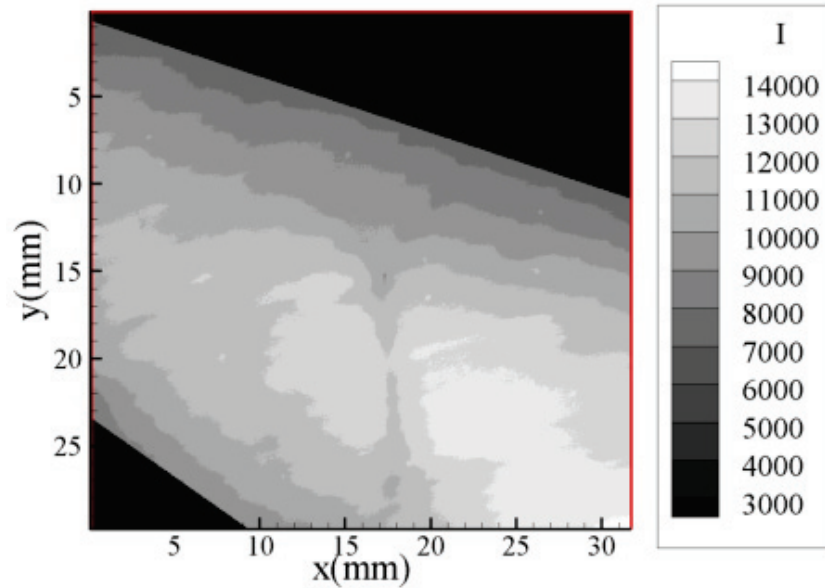


Figure 5.5 Cropped raw fluorescence image of R63E\_92; temperature 21.5 °C, pressure 29.71 inHg, humidity 63%, width 31.75 mm.

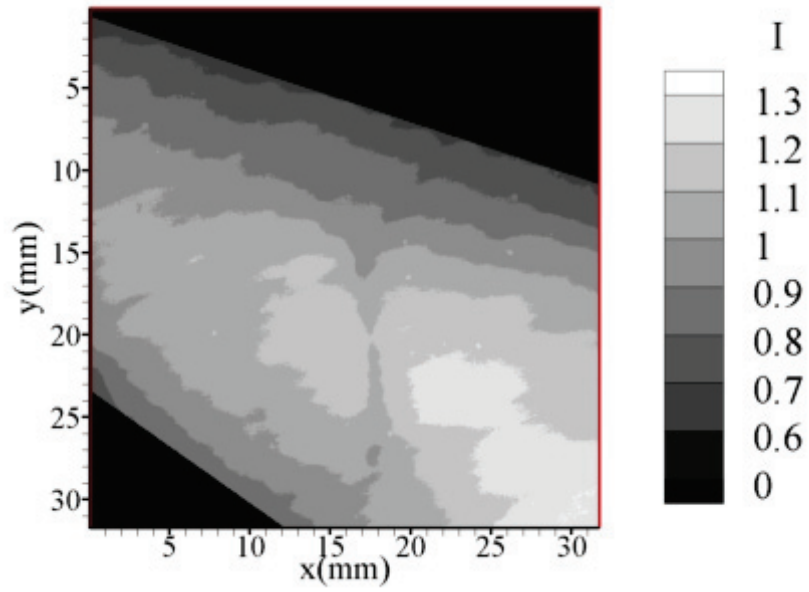


Figure 5.6 Normalized fluorescence array for image R63E\_92.

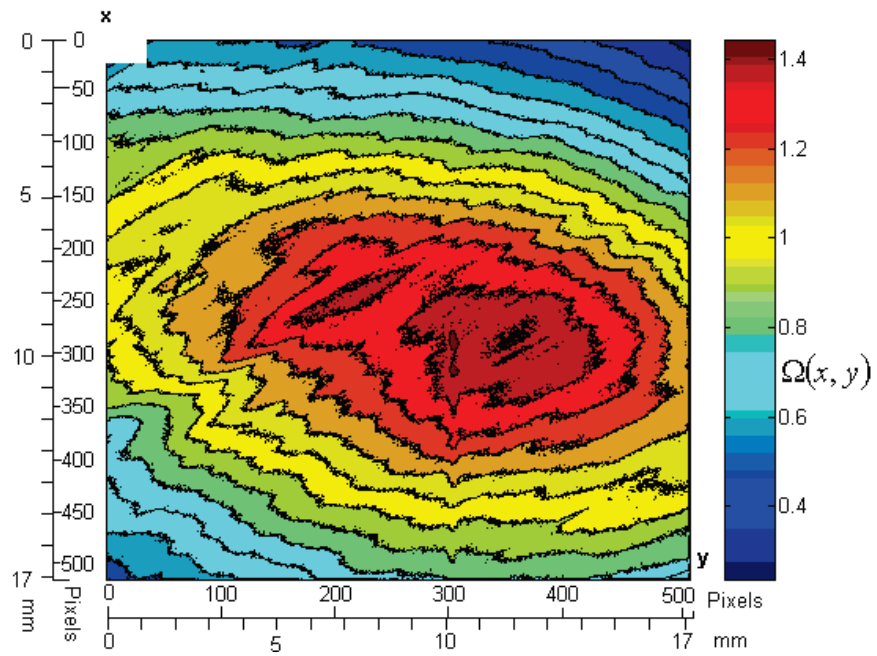


Figure 5.7. Contour map of the intensity distribution function for image set D21A; temperature 25 °C, pressure 30.30 inHg, humidity 21%, width 17.2 mm.

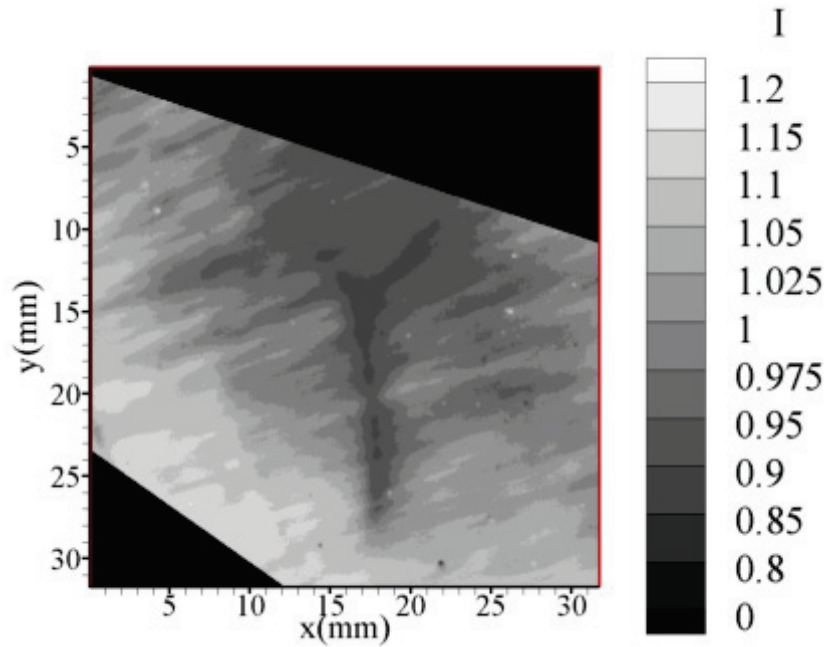


Figure 5.8. Contour plot of the normalized corrected fluorescence array for image R63E\_92.

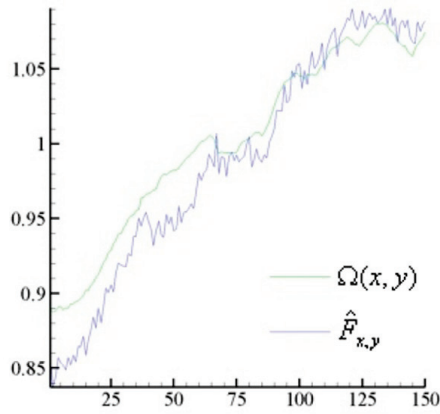


Figure 5.9. Example cross-sections of a correction array and quenched image showing alignment problems before secondary background correction. Taken from image D42AB\_32 at  $y=100$ ,  $x=(0 \text{ to } 150)$

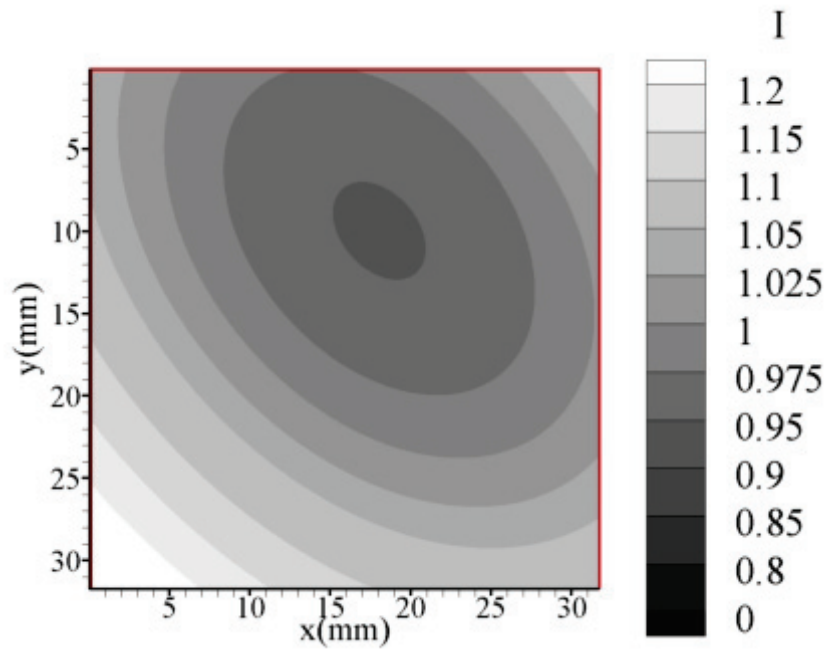


Figure 5.10. Secondary correction array for the image R63E\_92.

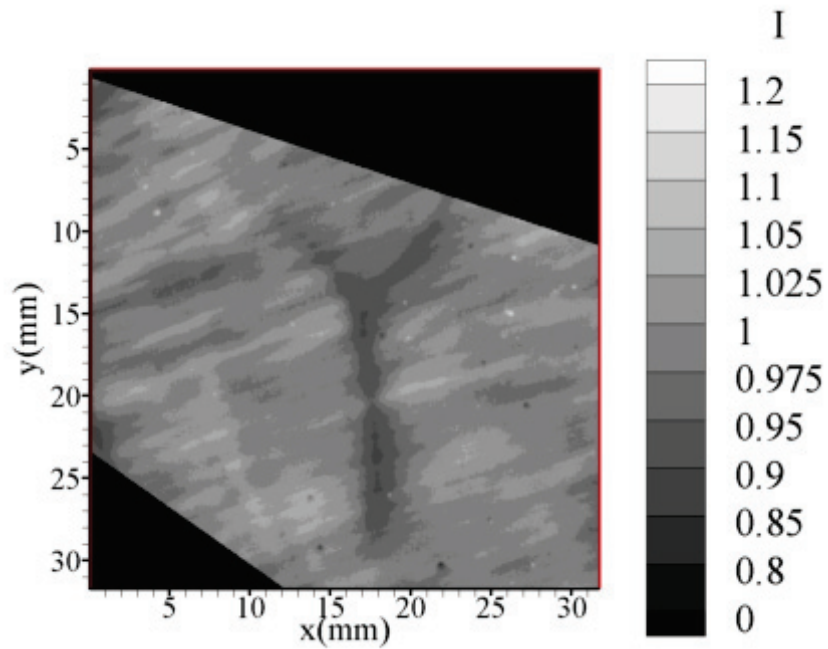


Figure 5.11. Contour plot of normalized corrected fluorescence values for the image R63E\_92.

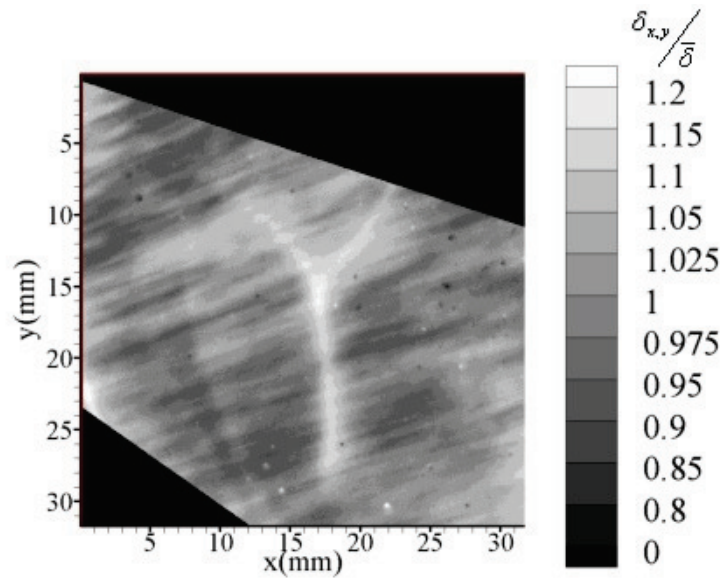


Figure 5.12. Map of the normalized boundary layer thickness for image R63E\_92.

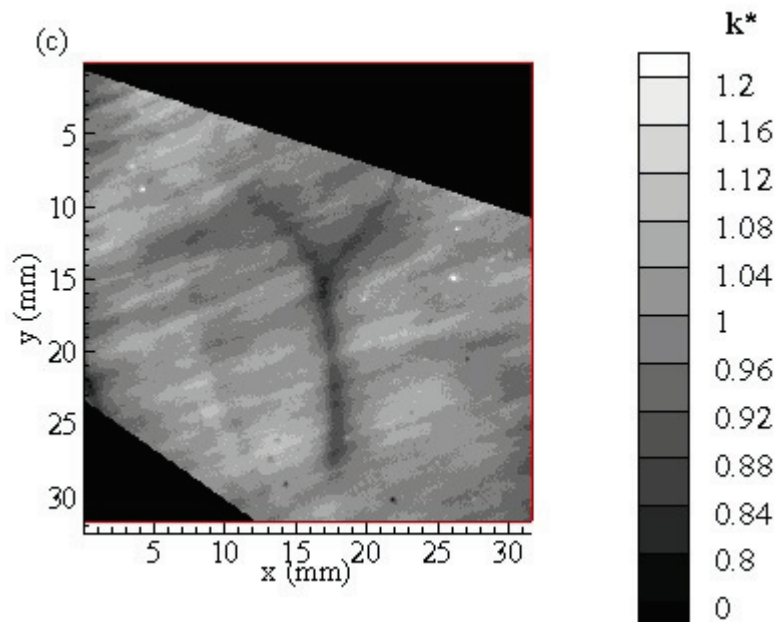


Figure 5.13. Grayscale plot of the dimensionless mass transfer coefficient values for image R63E\_92.

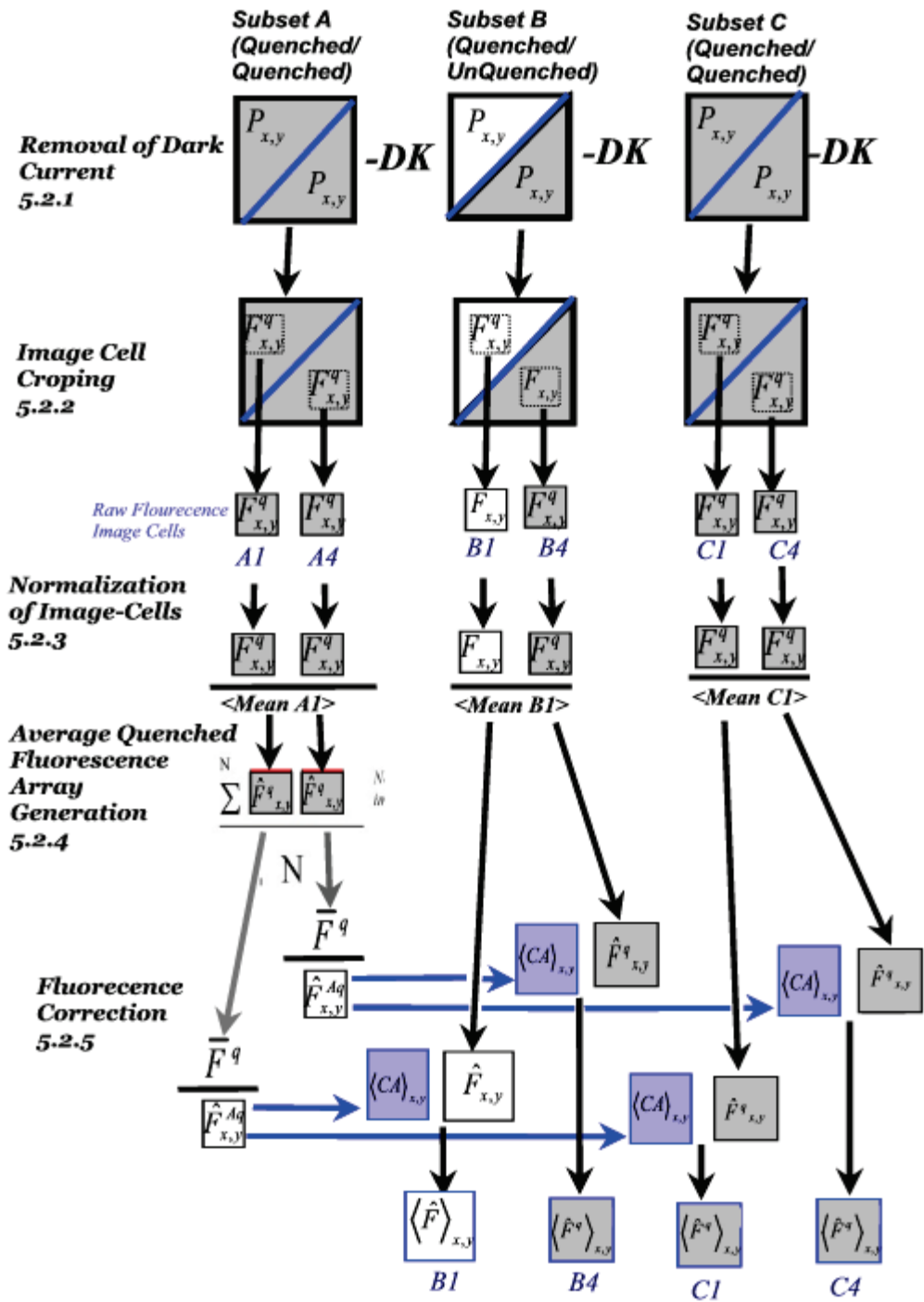


Figure 5.14. SLIF verification study image processing diagram.

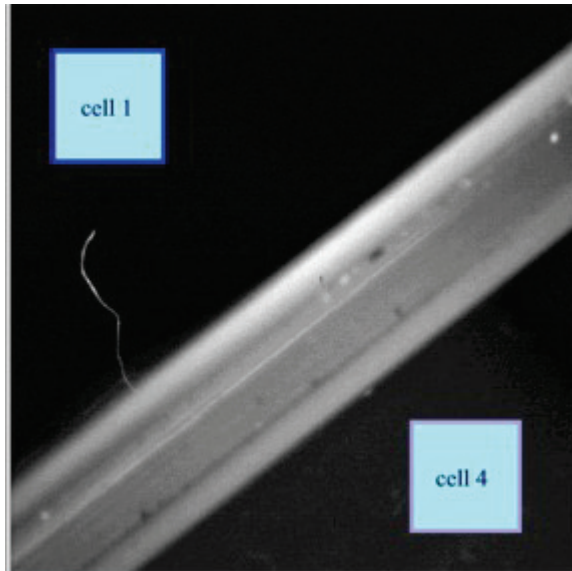


Figure 5.15. Image indicating location of image cells in regards to tank features.

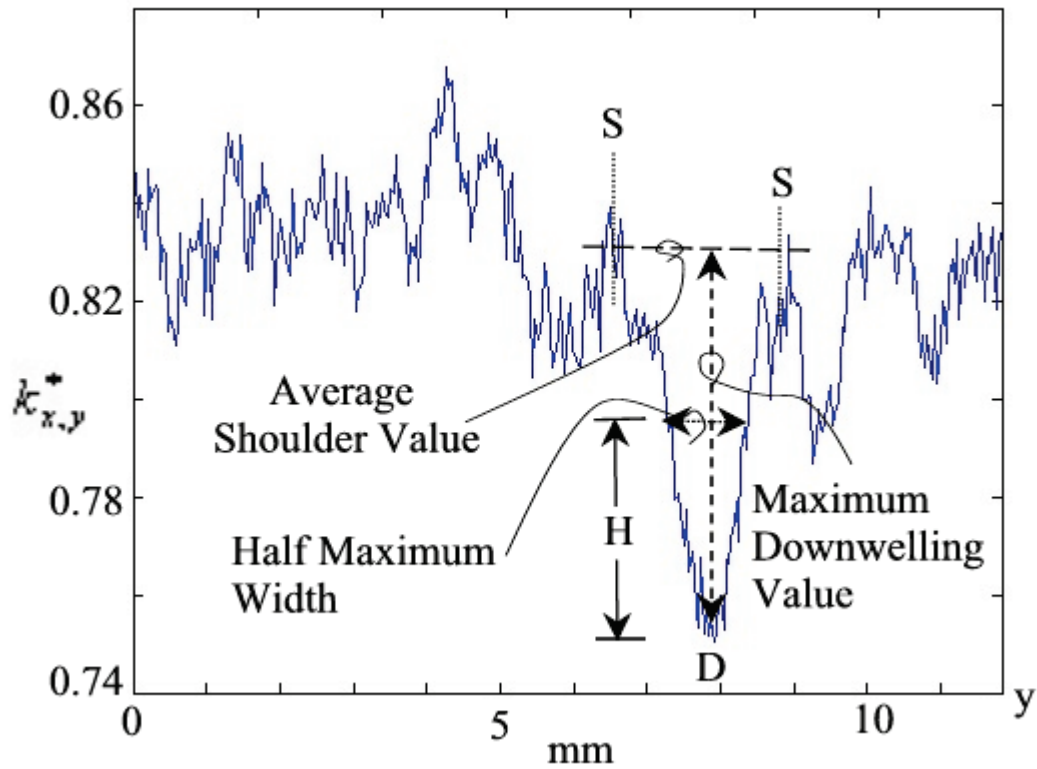


Figure 5.16. Cross-section of dimensionless mass transfer coefficient data for image R63E\_92 at  $x=200$ .

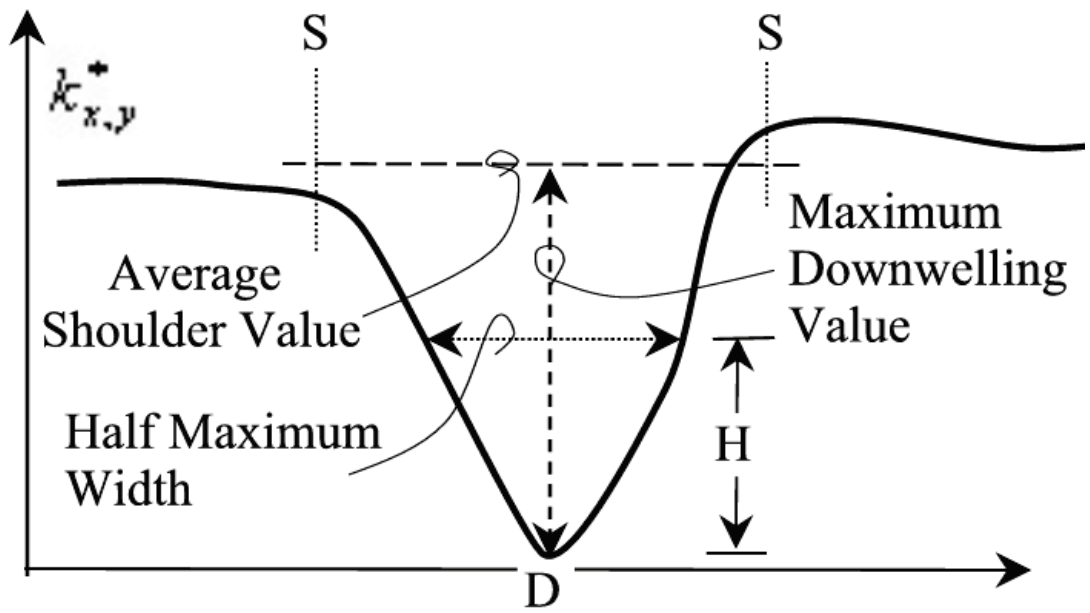


Figure 5.17. Ideal cross-section of dimensionless mass transfer coefficient data

## 6. RESULTS AND DISCUSSION:

### SURFACE LASER INDUCED FLUORESCENCE VERIFICATION STUDY

#### 6.1. SLIF verification study results

The SLIF verification study was designed to verify that the SLIF system could detect the differences in fluorescence caused by differences in the oxygen concentration near the interface. The verification study was designed to acquire images that contained the near surface fluorescence from both oxygen saturated and an oxygen depleted water sample. The verification study images contain two tanks with independent oxygen concentrations. The verification study analyzed the fluorescence intensity within two image cells cropped from the original image. The verification study was conducted using two tank systems as discussed in section 4.6. One set of verification study experiments were conducted using a 7 mm deep wave tank with a 4.5 mm deep inner tank. A second set of experiments were conducted in a 50 mm deep wave tank, with a 40 mm deep inner tank. As discussed in section 5.2, two 65 pixel by 65 pixel image cells were cropped from the overall 512 pixel by 512 pixel image and used in the image analysis. The image cell locations were selected to avoid effects from the inner tank wall or beam edges.

Figure 6.1 illustrates the general layout of the two tank images in the study. The locations of the inner tank wall and image cells, for both the 7 mm and 50 mm deep two tank systems, are labeled in the illustration. The dark region that separates the image in

half is the inner tank wall. The liquid level was set at the height of the inner tank wall within all of the 7 mm deep verification study images, while the tank wall in 50 mm deep tank was approximately 5 mm higher than the liquid level. The height of the outer tank wall for both the 7 mm deep and 50 mm deep two-tank apparatus was greater than the inner tank wall height. In all of the experiments detailed in this chapter, the inner tank was fully saturated with oxygen.

The image cell locations for the first set of verification experiments are illustrated in Figure 6.2 and are located where a 50% reduced intensity filter has not been applied. Figure 6.2 is of the intensity image Ttest9\_9. Ttest9\_9 is an 8.6 mm by 8.6 mm image containing a 5 mm deep outer liquid level and a 4.5 mm deep inner liquid level. The oxygen concentration was at saturation in both the inner and outer tanks. The image cell locations shown in Figure 6.2 are placed along the centerline of the beam spot while avoiding the inner tank wall. image cell 1 is located over the outer tank near the brightest location of the excitation laser beam spot. image cell 4 was located over the inner tank. image cell 4 was centered between the inner tank wall and the edges of the excitation laser beam spot.

### 6.1.1. Verification experiment images, 7mm tank

A list of the verification experiment image sets taken in the 7 mm deep wave tank is given in Table 6.1. For the image sets taken on the 7 mm wave tank, the outer liquid layer is 5 mm deep with the inner tank having a liquid depth of approximately 4.5 mm.

Image Set Label	Number of images in set	Oxygen Level Inner Tank	Oxygen Level Outer Tank	Outer Tank Depth (mm)	Inner Tank Depth (mm)	Comments
Ttest1_[n]	5	Saturated	Saturated	5	4.5	
Ttest2_[n]	10	Saturated	Depleted	5	4.5	Uneven liquid level
Ttest3_[n]	10	Saturated	Depleted	5	4.5	
Ttest4_[n]	10	Saturated	Depleted	5	4.5	long exposure
Ttest5_[n]	10	Saturated	Saturated	5	4.5	
Ttest6_[n]	8	Saturated	Depleted	5	4.5	
Ttest7_[n]	20	Saturated	Depleted	5	4.5	
Ttest8_[n]	35	Saturated	Saturated	5	4.5	See TTEST7
Ttest9_[n]	45	Saturated	Saturated	5	4.5	See TTEST7
Ttest10_[n]	5	Saturated	Depleted	5	4.5	Repeat TTEST7

Table 6.1. List of two tank experiments using 7 mm wave tank.

Table 6.1 details for each validation image set the image set label, the number of images in the set, the oxygen level of the inner and outer tanks, the depth of the inner and outer tanks, and comments about the data set. Macroscopic oxygen measurements were not taken in the wave tank to avoid unwanted stirring. Also, the depth was insufficient to use the oxygen probe as mentioned in section 4.6. In those sets with the outer tank liquid is unquenched, the liquid was sparged with nitrogen at atmospheric pressure for fifteen minutes. The average oxygen concentration within the sparging tank was found to be approximately 0.5 mg/L before transfer to the wave tank. The area of each intensity image is 8.6 mm by 8.6 mm.

Figures 6.3 through 6.10 are example intensity images acquired of the near surface fluorescence 7 mm deep tank system.

Figure 6.3 is the same image displayed in Figure 6.2 (Ttest9\_9) without the image-cells marked.

Figure 6.4 is an intensity image of Ttest9\_1 obtained in the 7 mm deep two tank apparatus. The liquids in both the inner and outer tanks were saturated with dissolved oxygen. The liquid depth in the outer tank was 5 mm and 4.5 mm in the inner tank.

Figure 6.5 is an intensity image of Ttest9\_29 obtained in the 7 mm deep two tank apparatus. The liquids in both the inner and outer tanks were saturated with dissolved oxygen. The liquid depth in the outer tank was 5 mm and 4.5 mm in the inner tank.

Figure 6.6 is an intensity image of Ttest9\_15 obtained in the 7 mm deep two tank apparatus. The liquids in both the inner and outer tanks were saturated with dissolved oxygen. The liquid depth in the outer tank was 5 mm and 4.5 mm in the inner tank.

Figures 6.3 through 6.6 demonstrate the ability of the SLIF system to take focused, repetitive images of a surface. In each of the images presented we can

In the images presented in 6.1 thru 6.9 the liquid level was to the top of the inner tank wall.

Figure 6.7 is an intensity image of Ttest7\_2. The image is of an 8.6 mm by 8.6 mm area of the 7 mm deep two tank apparatus. The dissolved oxygen concentration in the inner tank was depleted. The dissolved oxygen concentration in the outer tank was saturated. The liquid depth in the outer tank was 5 mm and 4.5 mm in the inner tank.

Figure 6.8 is an intensity image of Ttest7\_3. The image is of an 8.6 mm by 8.6 mm area of the 7 mm deep two tank apparatus. The dissolved oxygen concentration in

the inner tank was depleted. The dissolved oxygen concentration in the outer tank was saturated. The liquid depth in the outer tank was 5 mm and 4.5 mm in the inner tank.

Figure 6.9 is an intensity image of Ttest7\_4. The image is of an 8.6 mm by 8.6 mm area of the 7 mm deep two tank apparatus. The dissolved oxygen concentration in the inner tank was depleted. The dissolved oxygen concentration in the outer tank was saturated. The liquid depth in the outer tank was 5 mm and 4.5 mm in the inner tank.

Figure 6.10 is an intensity image of Ttest7\_5. The image is of an 8.6 mm by 8.6 mm area of the 7 mm deep two tank apparatus. The dissolved oxygen concentration in the inner tank was depleted. The dissolved oxygen concentration in the outer tank was saturated. The liquid depth in the outer tank was 5 mm and 4.5 mm in the inner tank.

Figure 6.11 is an intensity image of Ttest7\_12. The image is of an 8.6 mm by 8.6 mm area of the 7 mm two tank apparatus. The dissolved oxygen concentration in the inner tank was unquenched. The dissolved oxygen concentration in the outer tank was saturated. The liquid depth in the outer tank was 5 mm and 4.5 mm in the inner tank.

Figures 6.7 through 6.11 have little apparent difference from those seen in Figures 6.3 through 6.6. The actual difference between the mean value of the image cells is detailed in section 6.1.3.

### 6.1.2. Verification experimental images, 50mm tank

A list of the verification experiment image sets using the 50 mm deep wave tank is given in Table 6.2.

Image Set Label	Number of images in set	Oxygen Level Inner Tank	Oxygen Level Outer Tank	Outer Tank Depth (mm)	Inner Tank Depth (mm)	Comments
TT902T_[n]	5	Saturated	Saturated	35	35	Wall alignment
T1002B_[n]	9	Saturated	Saturated	35	35	Focusing Image
F1002C_[n]	10	Saturated	Depleted	35	35	
1002D_[n]	10	Saturated	Saturated	35	35	
1002E_[n]	22	Saturated	Saturated	35	35	
1002F_[n]	29	Saturated	Depleted	35	35	
1002G_[n]	26	Saturated	saturated	35	35	
1002H_[n]	5	Saturated	Saturated	35	35	Laser problems
1002I_[n]	9	Saturated	Depleted	35	35	Laser problems
1002K_[n]	60	Saturated	Saturated	35	35	Setting changed
1002M_[n]	45	Saturated	Saturated	35	35	
1002N_[n]	54	Saturated	Depleted	35	35	

Table 6.2. List of verification study experiments using 50 mm deep wave tank.

For the image sets listed in Table 6.2, the liquid depth was 35 mm in both tanks. Table 6.2 details for each 50 mm deep wave tank validation image set: the image set label, the number of images in the set, the oxygen level of the inner tank, the oxygen level of the outer tank, the liquid depth in the outer tank, the liquid depth in the inner tank and comments about the set. Macroscopic oxygen measurements were not taken in the wave

tank to avoid undesired ripples. The depleted liquid was produced in the same manner as for the 7 mm deep wave tank experiments, again the liquid was found to have an oxygen level of approximately 0.5 mg/L.

Figure 6.12 illustrates the locations of the inner tank wall and the image cells in the 50 mm deep two tank experiments. Figure 6.12 is of the intensity image 1002M\_5. The image 1002M\_5 is of an 8.6 mm by 8.6 mm area of the 50 mm deep two tank apparatus. The depth of the liquid in both tanks was approximately 35 mm. In Figure 6.12 the areas outside the image cells are reduced in intensity by 50% as in Figure 6.2. Compared with Figure 6.2, image cell 4 was much closer to the wall in Figure 6.12. The wall edge was not in focus in this image since it was approximately 5 mm above the surface. The water in both tanks was saturated with oxygen.

Figure 6.13 is an intensity image of 1002M\_30. The image is of an 8.6 mm by 8.6 mm area of the 50 mm two tank apparatus. The 35 mm deep liquids in both tanks were saturated with oxygen.

Figure 6.14 is an intensity image of 1002M\_36. The image is of an 8.6 mm by 8.6 mm area of the 50 mm two tank apparatus. The 35 mm deep liquids in both tanks were quenched.

Figure 6.15 is an intensity image of 1002M\_41. The image is of an 8.6 mm by 8.6 mm area of the 50 mm two tank apparatus. The 35 mm deep liquids in both tanks were quenched.

Figure 6.16 is an intensity image of 1002N\_1. The image is of an 8.6 mm by 8.6 mm area of the 50 mm deep two tank apparatus. The liquid in the outer tank was unquenched. The liquid in the inner tank was quenched. The liquids in both tanks were 35 mm deep.

Figure 6.17 is an intensity image of 1002N\_4. The image is of an 8.6 mm by 8.6 mm area of the 50 mm deep two tank apparatus. The liquid in the outer tank was unquenched. The liquid in the inner tank was quenched. The liquids in both tanks were 35 mm deep.

Figure 6.18 is an intensity image of 1002N\_7. The image is of an 8.6 mm by 8.6 mm area of the 50 mm deep two tank apparatus. The liquid in the outer tank was unquenched. The liquid in the inner tank was quenched. The liquids in both tanks were 35 mm deep.

Figure 6.19 is an intensity image of 1002N\_10. The image is of an 8.6 mm by 8.6 mm area of the 50 mm deep two tank apparatus. The liquid in the outer tank was unquenched. The liquid in the inner tank was quenched. The liquids in both tanks were 35 mm deep.

Figure 6.20 is an intensity image of 1002N\_30. The image is of an 8.6 mm by 8.6 mm area of the 50 mm deep two tank apparatus. The liquid in the outer tank was unquenched. The liquid in the inner tank was quenched. The liquids in both tanks were 35 mm deep.

### 6.1.3. Image-cell intensity measurements and analysis

Table 6.3 lists the mean intensity values of the image cells from the selected images of image set Ttest9. The selected images are the examples shown in section 6.1.1.

Image Label .TIFF	Cell 1 Quenched $F_{x,y}$ (Intensity Units)		Cell 4 Quenched $F_{x,y}$ (Intensity Units)		Cell1 Quenched $\langle \hat{F} \rangle_{x,y}$ (Dimensionless)		Cell 4 Quenched $\langle \hat{F} \rangle_{x,y}$ (Dimensionless)	
	Mean	Std	Mean	Std	Mean	Std	Mean	Std
	Ttest9_9	1870	91	1240	86	1.38	0.042	1.001
Ttest9_4	2170	101	1430	100	1.40	0.039	1.000	0.038
Ttest9_1	2120	89.3	1320	83	1.58	0.019	1.000	0.024
Ttest9_29	2230	122	1220	116	2.03	0.032	0.998	0.022
Ttest9_15	1840	116	994	99	2.31	0.021	0.998	0.052

Table 6.3. Selected quenched/quenched image cell pairs from image set Ttest9.

Table 6.4 lists the selected image cells from the image set TTEST7. The selected images are shown in section 6.1.1

Image Label .TIFF	Cell 1 Unquenched $F_{x,y}$ (Intensity Units)		Cell 4 Quenched $F_{x,y}$ (Intensity Units)		Cell1 Unquenched $\langle \hat{F} \rangle_{x,y}$ (Dimensionless)		Cell 4 Quenched $\langle \hat{F} \rangle_{x,y}$ (Dimensionless)	
	Mean	Std	Mean	Std	Mean	Std	Mean	Std
	Ttest7_2	3250	95.8	1640	80.2	2.39	0.037	1.002
Ttest7_3	2310	110	1050	105	2.99	0.039	1.001	0.033
Ttest7_4	2520	113	1210	117	3.39	0.026	1.001	0.022
Ttest7_5	2950	123	1340	118	2.45	0.042	1.001	0.032
Ttest7_12	2200	110	1310	98.8	1.71	0.041	1.002	0.032

Table 6.4. Selected unquenched/quenched image cell pairs from image set Ttest7.

Tables 6.3 and 6.4 list the mean raw fluorescence  $F_{x,y}$  intensity values and the mean corrected fluorescence  $\langle \hat{F} \rangle_{x,y}$  intensity values for image cells 1 and 4. The first column in both tables lists the example image name. The second column lists the mean raw fluorescence  $F_{x,y}$  for the 65 pixel by 65 pixel image cell 1 in intensity units. The third column lists the standard deviation of the raw fluorescence intensity within image cell 1. The fourth column lists the mean raw fluorescence of image cell 4 in intensity units. The fifth column lists the standard deviation of the raw fluorescence of image cell 4. The sixth column lists the mean corrected fluorescence  $\langle \hat{F} \rangle_{x,y}$  for the 65 pixel by 65 pixel image cell 1. The seventh column in Tables 6.3 and 6.4 lists the standard deviation of the corrected fluorescence for image cell 1. The eighth column lists the mean normalized corrected fluorescence of image cell 4. The ninth column lists the standard deviation of the normalized corrected fluorescence for image cell 4.

In Table 6.3, image cell 1 contains mean fluorescence intensity values and standard deviations of fluorescence for saturated liquid. In Table 6.4, image cell 1 contains mean fluorescence intensity values and standard deviations of fluorescence for an unquenched liquid.

Figure 6.20 plots thirty mean corrected fluorescence intensity values from Ttest7 and Ttest9 including image cell 1 and image cell 4. The data corresponding to the sixth column in Table 6.3, the mean corrected fluorescence of image cell 1 of a quenched liquid is plotted as open diamonds in Figure 6.20. The mean corrected fluorescence intensity values for image cell 4 from Ttest9 is represented by a dark square. The

corrected fluorescence intensity values for image cell 1 of Ttest7 is represented by an open triangle in the figure. Image cell 1 of Ttest7 is of an depleted liquid. An x represents the corrected fluorescence data for image cell 4 of Ttest7. The x-axis stated in imaging cycles, the number of image cycles could give an approximate time for each image, with an average 35 seconds between each successive image.

The data in Tables 6.3, 6.4 and Figure 6.1 illustrate the problems encountered with the 5mm deep liquid level. The range of corrected fluorescence intensity values for both the unquenched image cell 1 and the quenched image cell 1 were found to overlap, with intensity values from both sets falling in between intensity values of the other set. The overlap of ranges between quenched and unquenched image cell intensity values indicated that the SLIF apparatus could not detect differences in fluorescence levels due to differences in the oxygen mass transfer boundary layer. When examining the apparatus to correct the problem, we proposed that the overlap was caused by the height difference between the two tanks.

Table 6.5 lists a selection of images from the image sets 1002M. Both liquids imaged in this experiment were quenched. The images listed are from an experiment conducted using the 50mm deep wave tank.

Image	Cell 1 Quenched		Cell 4 Quenched		Cell1 Quenched		Cell 4 Quenched	
	$F_{x,y}$ (Intensity Units)		$F_{x,y}$ (Intensity Units)		$\langle \hat{F} \rangle_{x,y}$ (Dimensionless)		$\langle \hat{F} \rangle_{x,y}$ (Dimensionless)	
Label .TIFF	Mean	STD	Mean	STD	Mean	STD	Mean	STD
1002M_5	12320	218	9136	190	0.974	0.0064	1.003	0.012
1002M_15	7152	97.6	5268	108	0.998	0.0077	0.994	0.020
1002M_30	13220	210	9904	107	0.971	0.0047	1.001	0.0083
1002M_36	13210	240	9883	110	0.973	0.0057	1.001	0.0064
1002M_41	11530	225	8134	235	1.032	0.0064	0.998	0.012

Table 6.5. Selected quenched/quenched image cell pairs from image set 1002M

Table 6.6 lists a selection of cell sets from the image set 1002N, the outer liquid was unquenched while the inner tank liquid was quenched. The images listed are from an experiment conducted using the 50mm deep wave tank.

Image	Cell 1 Unquenched		Cell 4 Quenched		Cell1 Unquenched		Cell 4 Quenched	
	$F_{x,y}$ (Intensity Units)		$F_{x,y}$ (Intensity Units)		$\langle \hat{F} \rangle_{x,y}$ (Dimensionless)		$\langle \hat{F} \rangle_{x,y}$ (Dimensionless)	
Label.TIFF	Mean	STD	Mean	STD	Mean	STD	Mean	STD
1002N_1	18840	210	8753	101	1.567	0.018	1.034	0.012
1002N_4	16500	340	8266	96	1.419	0.029	1.036	0.012
1002N_7	16690	150	8534	107	1.423	0.014	1.036	0.013
1002N_10	18360	270	8960	95	1.493	0.022	1.035	0.011
1002N_30	18600	270	8854	103	1.492	0.022	1.033	0.012

Table 6.6. Selected unquenched/quenched image cell pairs from image set 1002N

Figure 6.21 presents fourteen mean corrected fluorescence intensity values from both 1002M and 1002N, plotting the intensity values for image cell 1 and image cell 4. The data corresponding to the second column in Table 6.5, image cell 1 with a quenched liquid is plotted as open diamonds in Figure 6.21. The corrected fluorescence intensity values for image cell 4 of 1002M is represented by a dark square. The corrected fluorescence intensity values for image cell 1 of 1002N is represented by an open triangle in the figure. The intensity values of image cell 1 of image sets 1002N are of the quenched liquid. The corrected fluorescence data for image cell 4 of 1002N is represented by an x. The x axis is in terms of imaging cycles which can be translated to image number. The number of image cycles is analogous to time, with approximately 35 seconds between each successive image.

The data in Tables 6.5, 6.6 and Figure 6.21 demonstrate the difference in corrected fluorescence intensity values between quenched and unquenched liquids, with approximately the same depth of liquid in both liquids. The range of mean corrected fluorescence intensity values for both the unquenched image cell 1 and the quenched image cell 1 were found not to overlap. The corrected fluorescence intensity values for an unquenched liquid were approximately 50% higher than for quenched liquids.

## 6.2. Discussion of SLIF verification

### 6.2.1. Intensity images from verification experiment

The images of fluorescence acquired by the SLIF apparatus were clear and focused. In the intensity images 6.3 through 6.20 the variance in the intensity could clearly be distinguished. Image features at the air-water interface, such as the inner-tank wall in Figures 6.3 through 6.11, were distinct. Image features above the air-water interface were not distinct. In the image 1002N\_7, (Figure 6.17) the levels of fluorescence intensity clearly decreased as they approached the inner tank wall. The sides of the inner tank wall were difficult to accurately define in Figures 6.12 through 6.20 as they merge with the nearby fluorescence. The inner tank wall in Figures 6.12 through 6.20 was 5 mm above the air-water interface and outside of the depth of field for the CCD camera. In comparison, the small piece of debris attached to the inner tank wall in image 1002N\_7 could be clearly made out from the surrounding fluorescence. The ability of the SLIF system to acquire clear, focused images of near surface fluorescence allowed for the analysis of image features and variances in the fluorescence across the surface of the air-water interface.

### 6.2.2. Discussion of image cell data

The changes in fluorescence intensity due to variations in the boundary layer thickness were larger than the general level of noise, and other small-scale variances, found in the area of the image cells. The intensity values of raw fluorescence for the example image cells listed in Tables 6.3 through 6.6 vary both spatially and temporally.

Both spatial variations and temporal variations consisted of large-scale variations and small-scale variations. The differences in raw fluorescence in Tables 6.5 and 6.6 were examined in terms of source and scale.

The variations in fluorescence in the image cells can be defined as either large scale or small scale. The large-scale variations in fluorescence were measured in the mean raw fluorescence intensity values and were defined as effects of the uneven distribution of excitation energy across the surface, changes in the quencher concentration, or variations in the mean level of excitation energy. Small-scale variations in fluorescence were measured by finding the standard deviation of the fluorescence in the image cells and were defined as noise or other small-scale variations.

The difference between small-scale and large-scale variations was important as it defined the ability to differentiate mass transfer phenomena. If we consider the primary component of small-scale variations to be noise, then the ability of the SLIF technique to differentiate between possible mass transfer affecting phenomena from the background noise was related to the difference in magnitude between the small-scale variations and the large-scale variations. If the small-scale variations were much smaller in magnitude than the large-scale variations, the SLIF technique would more easily define image features and oxygen boundary layer thickness differences. If the small-scale variations were the same magnitude as the large scale variations, the SLIF technique could not separate the variations in fluorescence caused by defined image features and oxygen boundary layer thickness differences from the noise of the fluorescence.

The large-scale spatial variations in mean raw fluorescence were found to be a magnitude larger than the standard deviations within the image cells. The changes of the

raw fluorescence intensity across the surface between the inner and outer tank were caused by the uneven distribution of excitation energy across the surface. In Table 6.5 the average difference between the mean raw fluorescence value of image cell 1 and image cell 4 was 2820 intensity units, with a range from 1880 intensity units to 3400 intensity units. The average standard deviation of image cell 1 in Table 6.5 was 197 intensity units and the average standard deviation of image cell 4 was 150 intensity units. The intensity values of standard deviation for both image cells in Table 6.5 were not larger than 240 intensity units. Since the difference in mean raw fluorescence intensity between the image cells is an order of magnitude greater than the standard deviation of fluorescence intensity within the image cells, the variation in fluorescence intensity caused by the excitation energy distribution could be separated from the background noise of the SLIF system.

It was found that the variation between the quenched fluorescence and unquenched fluorescence of the image cells was a magnitude larger than the standard deviation of fluorescence for the image cells. In Table 6.6 the average difference between the mean raw fluorescence value of image cell 1 and image cell 4 was 9140 intensity units, with a range from 10,090 intensity units to 8,136 intensity units. The average standard deviation of raw fluorescence intensity for image cell 1, in Table 6.6, was 248 intensity units and the average standard deviation of raw fluorescence for image cell 4 was 101 intensity units. The standard deviations of raw fluorescence intensity for both image cells in Table 6.6 were not larger than 340 intensity units. The difference in the mean raw fluorescence of the unquenched image cell 1 to the quenched image cell 4 (Tables 6.4 and 6.6) could be considered comprised of both spatial effects and oxygen

concentration effects. As explained in section 3.2 and section 5.2 the raw fluorescence intensity values are processed into corrected fluorescence intensity values to correct for this problem. In Table 6.6 the average difference between the mean normalized corrected fluorescence intensity values of image cell 1 and image cell 4 was 0.44. The difference ranged from 0.533 to 0.383. The average standard deviation of normalized corrected fluorescence for image cell 1 in Table 6.6 was 0.021 and the average standard deviation of normalized corrected fluorescence for image cell 4 was 0.012 intensity units. The intensity values of standard deviation of normalized corrected fluorescence for both image cells in Table 6.6 were not larger than 0.029. The large difference in ranges between the variation in fluorescence generated by variations in the boundary layer thickness and the approximate noise levels of the SLIF technique demonstrate that we could separate out large changes in mass transfer from the surrounding noise.

### 6.2.3. Comparison of quenched/unquenched and quenched/quenched image cell sets

The SLIF system was designed to image variances in the concentration boundary layer thickness across the surface of a liquid. The goal of the verification study was to prove the SLIF system could detect the variances of surface fluorescence directly attributable to differences in the near surface oxygen concentration and the concentration boundary layer thickness. The theoretical relationship between the corrected fluorescence  $\langle \hat{F}_{x,y} \rangle$  and the dissolved oxygen concentration  $[Ox]$  is described by equation 3.36. The relationship necessitates correction of the raw fluorescence for the excitation energy distribution as described in section 3.3.4.

The SLIF system produced images with a measurable difference in the corrected

fluorescence intensity values attributable to differences in the near surface oxygen concentration boundary layer thickness. The SLIF system produced raw fluorescence images where the observed differences in raw fluorescence intensity between oxygen saturated and depleted liquids appeared to correspond to the dissolved oxygen concentration. Comparison of the mean raw fluorescence intensity values of deoxygenated liquids and fully oxygen saturated liquids showed a much larger difference than the difference between the mean fluorescence intensity values of oxygenated liquids. A comparison of the mean raw fluorescence intensity values from deoxygenated liquids and fully oxygen saturated liquids allowed us to find the range of system response between them.

The observable differences in raw fluorescence between saturated and depleted liquids demonstrate the relationship between raw fluorescence intensity and oxygen boundary layer thickness. In the validation experiments, the two tanks were either filled with water that had been purged of oxygen by bubbling nitrogen through it, or was fully saturated. Acquiring images of liquid that had been purged of oxygen allowed us to find the approximate level of fluorescence intensity with no concentration boundary layer present, since there was a very low oxygen concentration. Acquiring images of liquid that was fully saturated allowed us to find the approximate level of fluorescence intensity with a very large boundary layer thickness. In Figures 6.12 through 6.15 showed a comparison of quenched and quenched fluorescence in both 50 mm deep tanks. In intensity image 1002M\_41 (Figure 6.15) the intensity from both the inner and outer tank appear equal. In Figures 6.16 through 6.19 showed a comparison of unquenched and quenched fluorescence from the 50 mm deep two tank apparatus. In intensity image

1002N\_1 the raw fluorescence from the depleted liquid in the outer tank appears to have a greater intensity than the raw fluorescence from the fully saturated inner tank. Both the ability to see the same approximate level of intensity between two fully oxygen saturated liquids, and the ability to see a difference between fully oxygen saturated liquids and oxygen depleted liquids indicates that the SLIF should be able to find differences in corrected fluorescence levels.

The ability of the SLIF apparatus to acquire images with differences in raw fluorescence corresponding to boundary layer thickness was demonstrated by the raw fluorescence intensity values of the image cell data. The difference between the raw fluorescence intensity values of a deoxygenated liquid to that of fully oxygen saturated liquids was much larger than the difference between two fully oxygen saturated liquids in both tanks. The mean raw fluorescence intensity values for image cell 1 for the selected images of image set 1002M (Table 6.5) was for a fully oxygen saturated, or quenched, liquid and varied from 7,152 intensity units to 13,220 intensity units. The mean raw fluorescence intensity values for image cell 4 of image set 1002M varied from 5,268 intensity units to 9,883 intensity units. The mean raw fluorescence intensity values for image cell 1 for the selected images of image set 1002N (Table 6.6) was for a deoxygenated liquid and varied from 16,500 intensity units to 18,600 intensity units. The mean raw fluorescence intensity values for image cell 4 of image set 1002N was for a fully oxygen saturated liquid and varied from 8,226 intensity units to 8,960 intensity units. In Table 6.5, the mean raw fluorescence intensity values of image cell 1 and image cell 4 have an average difference of 2,200 intensity units or approximately 24.3% of the average mean raw fluorescence intensity values of image cell 4. In Table 6.6, the mean

raw fluorescence intensity values of image cell 1 and image cell 4 have an average difference of 9,125 or approximately 106% of the average mean raw fluorescence intensity values of image cell 4. The qualitative intensity values of raw fluorescence show the increase in fluorescence intensity due to decrease in dissolved oxygen concentration and the concentration boundary layer.

The ability of the SLIF technique to produce intensity values of corrected fluorescence corresponding to the concentration boundary layer thickness was demonstrated in the SLIF verification study. The mean fluorescence intensities of corrected images from fully oxygen saturated, or quenched, liquids was smaller than the mean intensity values of corrected fluorescence for a deoxygenated, or unquenched, liquid. The SLIF technique gain, the difference between the quenched corrected fluorescence intensity values and the unquenched corrected fluorescence intensity values, was found to be a 43.2% of the quenched corrected fluorescence intensity values. The mean corrected fluorescence intensity values for image cell 1 and image cell 4 of image set 1002M (Table 6.5) varied from 1.032 to 0.974. The mean corrected fluorescence intensity values for image cell 4 of image set 1002N varied from 1.034 to 1.036. The mean corrected fluorescence intensity values for image cell 1 of image set 1002N, which are unquenched fluorescence intensity values, varied from 1.416 to 1.567. The average difference between the mean corrected fluorescence intensity values for both image cells of image set 1002M was 0.025, or 2.5% of the mean corrected fluorescence intensity values for image cell 4. The average difference between the mean corrected fluorescence intensity values of the quenched image cells and unquenched image cell was 0.444, or 43.2% of the average mean corrected fluorescence value for image cell 4. The difference

between the mean intensity values of quenched corrected fluorescence and unquenched corrected fluorescence was illustrated in Figure 6.21. In Figure 6.21, the mean intensity values of unquenched corrected fluorescence range from 1.6 to 1.4 while the mean intensity values of quenched data are found to vary from 0.996 to 1.036. The gain between mean intensity values of corrected quenched and unquenched fluorescence was the change in SLIF fluorescence response between a boundary layer of very small thickness and a concentration boundary layer that was almost 30 mm.

The SLIF technique gain illustrated in Table 6.5, Table 6.6 and Figure 6.21 was small compared to the expected SLIF technique gain. The actual SLIF technique gain was found to be smaller than the SLIF technique gain predicted by the Stern-Vollmer relationship, presented in equation 3.3. We used an estimated saturated oxygen concentration of approximately 8.6 mg/L in the Stern-Vollmer relationship to predict an SLIF technique gain of 2.5, or an increase of 150%, between the corrected fluorescence intensity values from a quenched and unquenched liquid. The predicted value of SLIF technique gain was larger than the gain of 1.48 experimentally determined. The larger the SLIF technique gain, the better the ability of the SLIF technique would identify mass transfer affecting phenomena below the surface. The smaller SLIF technique gain was possibly due to the refraction of some fluorescence as it crossed the air-water boundary, which spread some fluorescence intensity across the entire imaged area. The reduced gain represents the actual ability of the SLIF technique to identify mass transfer affecting phenomena.

The ability of the SLIF technique to produce a range of both raw fluorescence intensity values and corrected fluorescence intensity values corresponding to the boundary layer thickness at the air-water interface demonstrated that the SLIF system could investigate mass transfer affecting phenomena across the air water interface. The SLIF technique gain between corrected fluorescence intensity values for oxygen saturated and depleted liquids allowed for SLIF analysis of the underlying concentration boundary layer. Although the experimental SLIF technique gain was smaller than the theoretical SLIF technique gain, the SLIF technique could still find differences in boundary layer thickness across the surface of the air-water interface. The ability of the SLIF technique to have a gain between the quenched and unquenched intensities of correction fluorescence demonstrates that theory described in section 3.3.4 can be successfully implemented by the fluorescence correction theory described in sections 5.1.5 and 5.2.3.

#### 6.2.4. SLIF improvements

Several key improvements were made during the course of the verification experiment. The primary change was the replacement of the 7 mm deep two tank system for the 50 mm deep two tank system. At the same time improvements in alignment, excitation beam spot size and camera settings were made.

The replacement of the 7 mm deep two tank system with the 50 mm two tank system was due to the problems in obtaining a useful SLIF technique gain. The example data presented in Tables 6.3 and 6.4 showed almost identical differences between the mean intensity values of quenched fluorescence for both image cells of the

quenched/quenched data set and the unquenched/quenched data set. The lack of a discernable difference between the mean intensity values of corrected unquenched fluorescence to the mean intensity values of corrected quenched fluorescence was illustrated in Figure 6.20, where the intensity values of image cell 1, both quenched and unquenched, were approximately 1.5 times the intensity values for image cell 4. The 0.5 mm difference in depth between the inner tank and the outer tank might be the cause of the problem, as detailed in Chapter 4.

The problem can be explained in terms of the depth of penetration of the excitation radiation  $d$ . The correction array theory discussed in section 3.3.4 was based on the assumption that the variation in the penetration depth  $d$  was only a function of the excitation radiation  $I_{xy}$ . In the 7 mm deep two tank system, the excitation radiation was penetrating the full depth of both the inner and outer tank. The outer tank was deeper, and had a larger depth of penetration than the inner tank. The result was that the outer tank would always produce more fluorescence since the extra depth of water would produce additional fluorescence, even when saturated with oxygen and the amount of extra radiation would be independent of the excitation radiation distribution. The effect could be seen in the mean corrected fluorescence intensity values of the 7 mm two tank system (Figure 6.20). The corrected fluorescence intensity values of both image cell 1, for both the fully oxygen saturated and depleted liquids was much larger than the mean corrected fluorescence intensity values of image cell 4. However, when we examined the mean intensity values of corrected fluorescence in the corresponding tables (Tables 6.3 and 6.4) the range of the unquenched fluorescence from image cell 4 only overlapped the quenched fluorescence from image cell 4.

The 50 mm two tank apparatus was designed so that there was no difference in depth between the two tanks. Comparing the mean corrected fluorescence intensity values of the 7 mm two tank system (Figure 6.20) to the mean corrected fluorescence intensity values of the 50 mm tank system presented in Figure 6.21 demonstrates that the new system can generate usable corrected fluorescence data. In Figure 6.20, there was a large difference, corresponding to the SLIF apparatus gain, between the corrected fluorescence data for image cell 1, both for quenched and unquenched fluorescence, and image cell 4. Examining the intensity values plotted in Figure 6.21, there was a large difference, 0.44 between the set of mean unquenched corrected fluorescence intensity values and the three sets of mean quenched corrected fluorescence intensity values. The corresponding difference between the mean intensity values of quenched corrected fluorescence for image cell 4 and image cell 1 was much smaller, a value of 0.023 approximately.

Several other changes to the SLIF apparatus were also made. The SLIF apparatus moved to a new laboratory with better environmental control. The mirror support was made more robust by installing a larger ball joint, allowing the targeting mirror to maintain a larger number of possible angles. The excitation beam spot projection was spread out over a larger area, as could be seen between the Figures attributed to the 7 mm tank and those attributed to the 50 mm wave tank. The new inner tank wall was aligned to the incoming laser beam, reducing the amount of shadow it created, and a thinner inner tank wall used.

### 6.3. SLIF verification study conclusions

The SLIF verification study provided insight into the capabilities of the SLIF system and into theory that underlies SLIF. In general the SLIF system produced clear, focused images of a liquid surface undergoing mass transfer, as seen in Figures 6.3 to 6.19. The SLIF apparatus could acquire images that large-scale variations in fluorescence could be distinguished from small-scale variations in fluorescence, such as noise. The SLIF system produced images with a measurable difference in the corrected fluorescence intensity values attributable to differences in the near surface oxygen concentration boundary layer thickness. The SLIF verification study apparatus was improved to acquire images with differences in normalized quenched fluorescence attributable only to differences in dissolved oxygen concentration.

The SLIF system needed to produce clear, focused images of the liquid surface. With clear, focused images of the liquid surface and the near surface fluorescence, we could spatially analyze the changes in near surface fluorescence.

We can see from Tables 6.3, 6.4, 6.5 and 6.6 that the raw fluorescence intensity levels vary from image to image and across the imaged area. The variations in fluorescence can be defined as either small-scale or large-scale. Analysis of the raw fluorescence intensity values presented in Table 6.5 demonstrated that the variations in fluorescence caused by the distribution of excitation energy were an order of magnitude larger than the small-scale variations in the image cells. Analysis of the raw fluorescence intensity values, and normalized corrected fluorescence intensity values, in Table 6.6 showed that the variations in fluorescence caused by differences in the oxygen

boundary layer thickness were a magnitude larger than the small-scale variations in the image cells. The large difference between these large-scale variations and small-scale variations showed that we can separate out data on the excitation distribution and the oxygen boundary layer from the background noise.

The ability of the SLIF image processing procedure to produce corrected fluorescence intensity values from raw fluorescence intensity values that contains differences relating to boundary layer thickness was demonstrated. Tables 6.5 and 6.6 showed that the correction process would remove the difference in raw fluorescence generated by excitation energy distribution, while leaving the difference generated by variations in the oxygen boundary layer thickness. The full sets of data were compared in Figure 6.21. It was also found that the SLIF technique gain was approximately 1.48 between quenched and unquenched normalized corrected fluorescence intensity values. This is in comparison to the theoretical gain of 2.5 predicted by the Stern-Vollmer relationship.

Chapter 6 figures

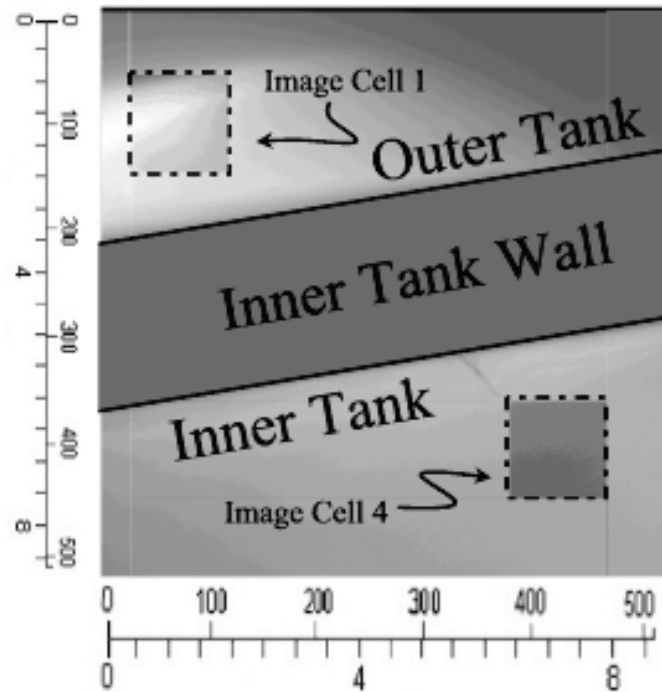


Figure 6.1. General layout of the two tank images; TTEST8\_1; outer tank, oxygen saturated, depth 5 mm; inner tanks oxygen saturated, depth 4.5 mm.

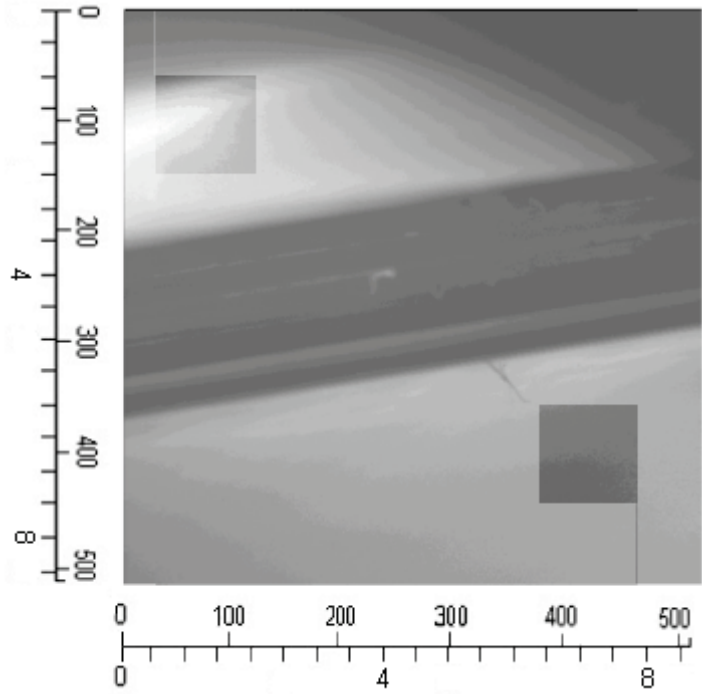


Figure 6.2. Intensity image of Ttest9\_9 with cell cropping locations indicated on the image by reducing the intensity for all excluded points; outer tank, oxygen saturated, depth 5 mm; inner tank, oxygen saturated, depth 4.5 mm.

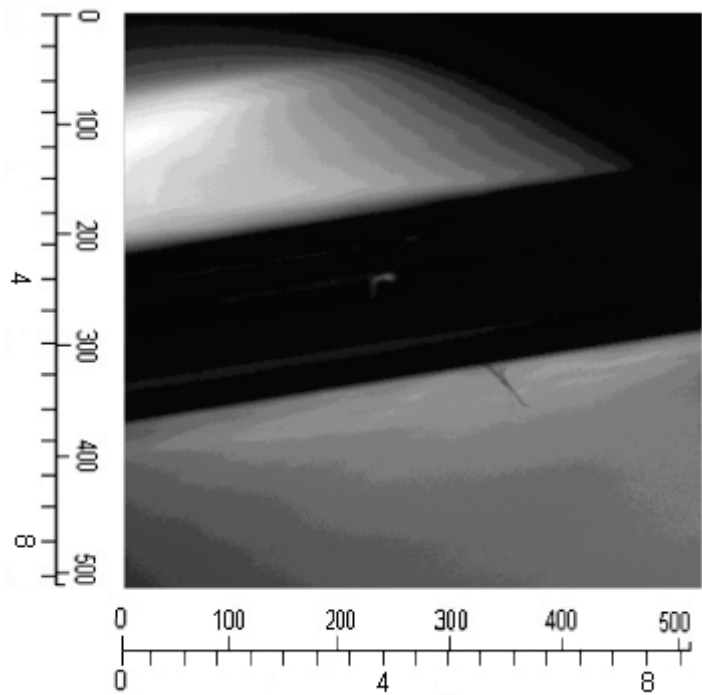


Figure 6.3. Intensity image of TTEST 9\_9 without shading.

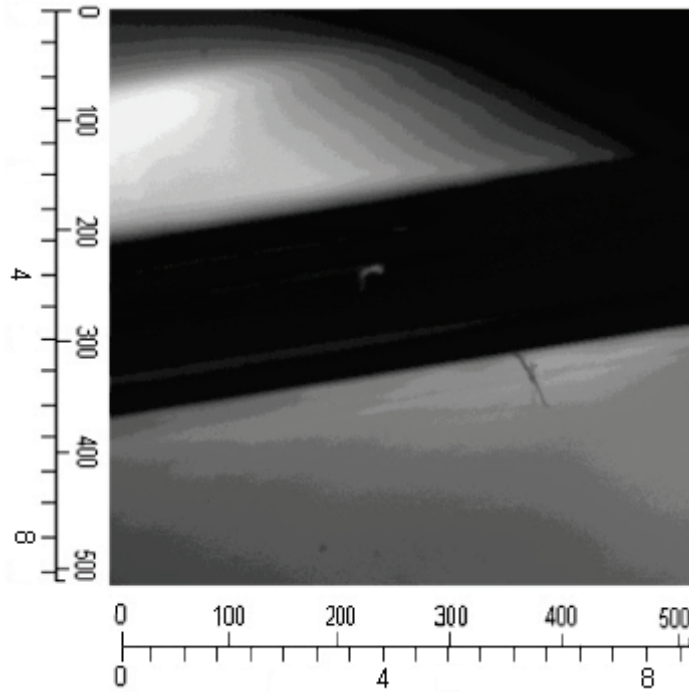


Figure 6.4. Intensity image of TTEST 9\_1; outer tank, oxygen saturated, depth 5 mm; inner tank, oxygen saturated, depth 4.5 mm.

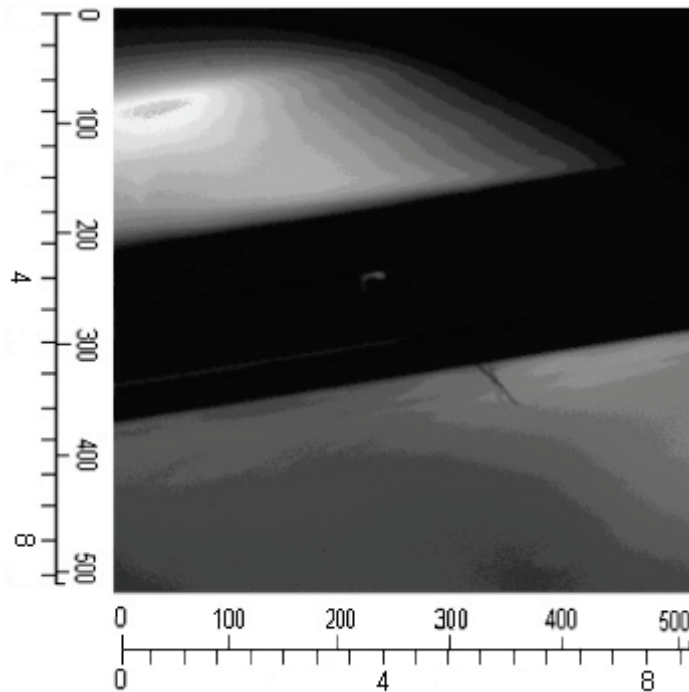


Figure 6.5. Intensity image of Ttest9\_29 outer tank, oxygen saturated, depth 5 mm; inner tank, oxygen saturated, depth 4.5 mm.

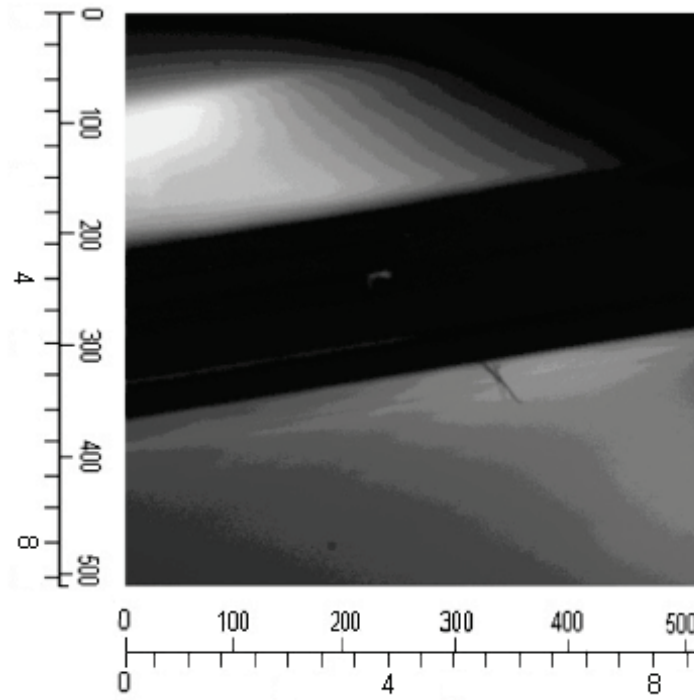


Figure 6.6. Intensity image of Ttest9\_15; outer tank, oxygen saturated, depth 5 mm; inner tank, oxygen saturated, depth 4.5 mm.

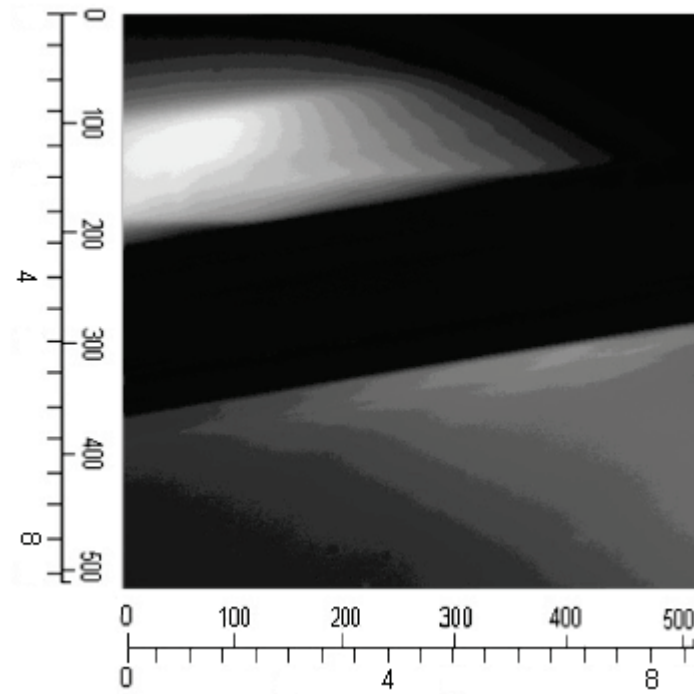


Figure 6.7. Intensity Image of Ttest7\_2; outer tank, oxygen depleted, depth 5 mm; inner tank, oxygen saturated, depth 4.5 mm.

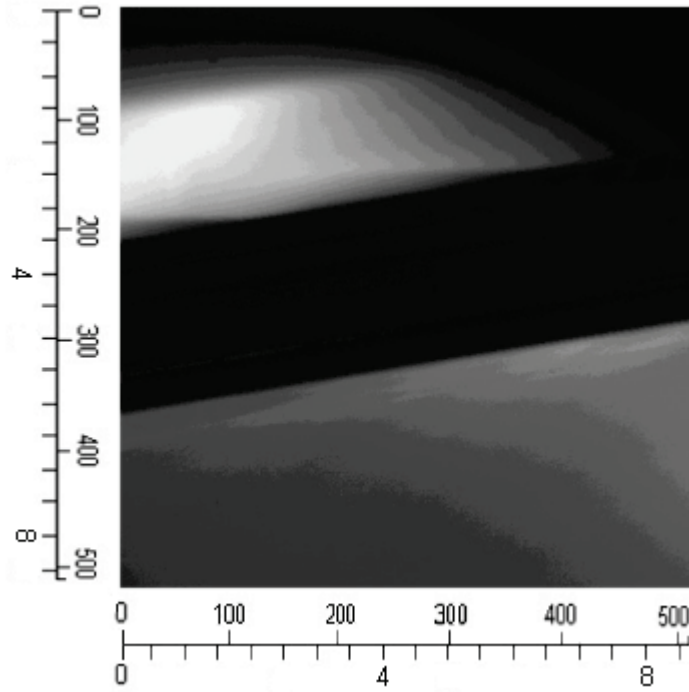


Figure 6.8. Intensity image of Ttest7\_3; outer tank, oxygen depleted, depth 5 mm; inner tank, oxygen saturated, depth 4.5 mm.

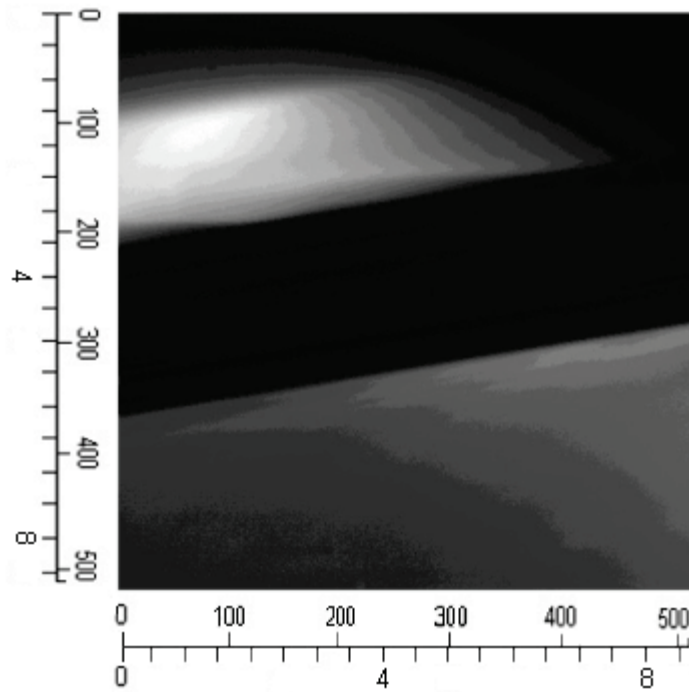


Figure 6.9. Intensity image of Ttest7\_4; outer tank, oxygen depleted, depth 5 mm; inner tank, oxygen unsaturated, depth 4.5 mm.

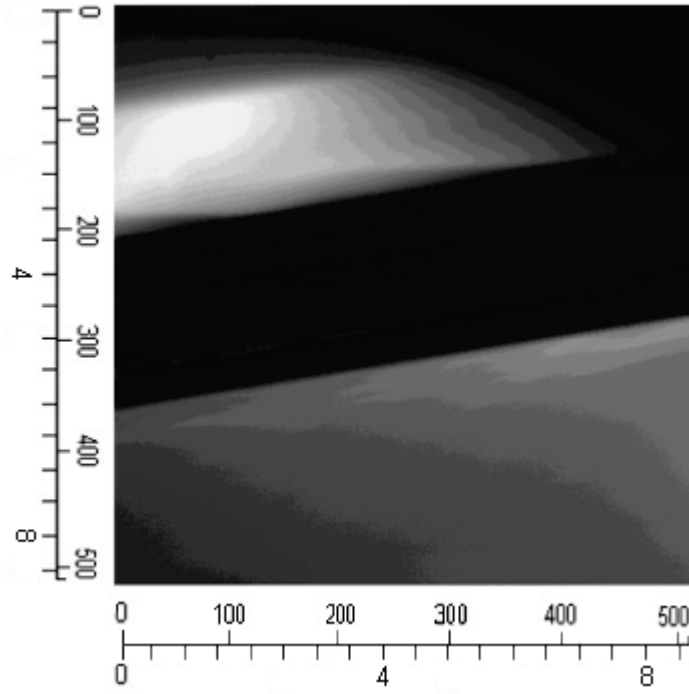


Figure 6.10. Intensity image of Ttest7\_5; outer tank, oxygen depleted, depth 5 mm; inner tank, oxygen saturated, depth 4.5 mm.

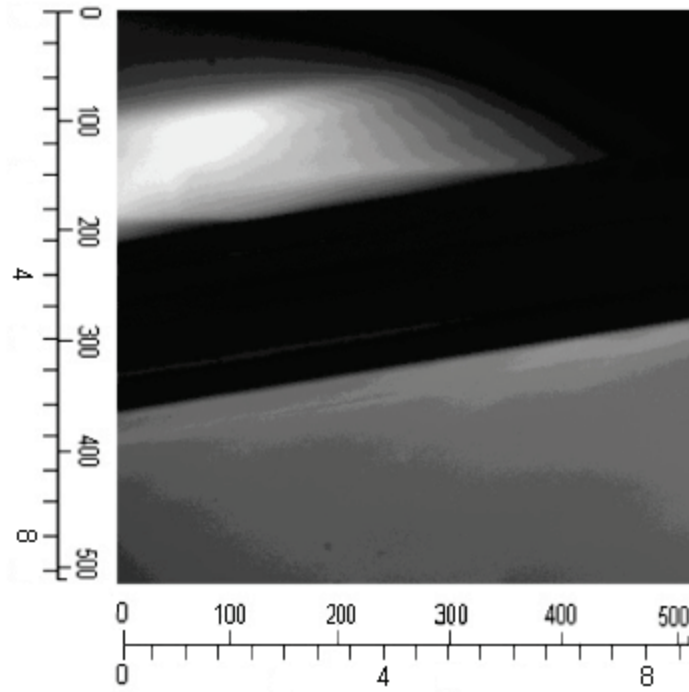


Figure 6.11. Intensity image of Ttest7\_12; outer tank, oxygen depleted, depth 5 mm; inner tank, oxygen saturated, depth 4.5 mm.

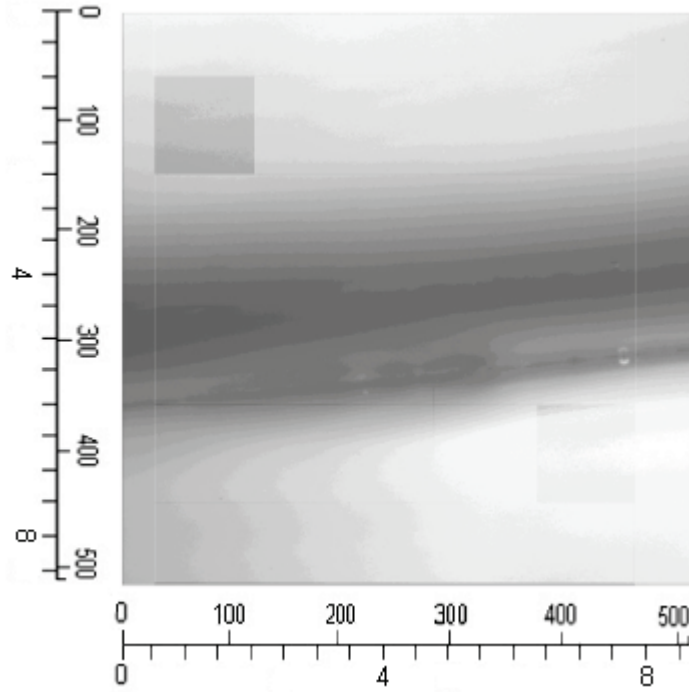


Figure 6.12. Intensity image of 1002M\_5 with cell cropping locations indicated on the image by reducing the intensity for all excluded points; outer tank, oxygen saturated, depth 35 mm; inner tank, oxygen saturated, depth 35 mm.

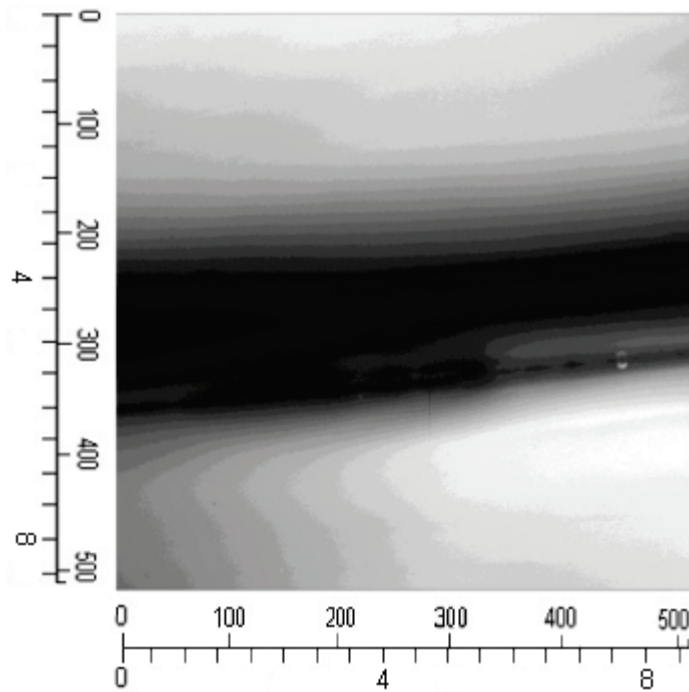


Figure 6.13. Intensity image of 1002M\_30; outer tank, oxygen saturated, depth 35 mm; inner tank, oxygen saturated, depth 35 mm.

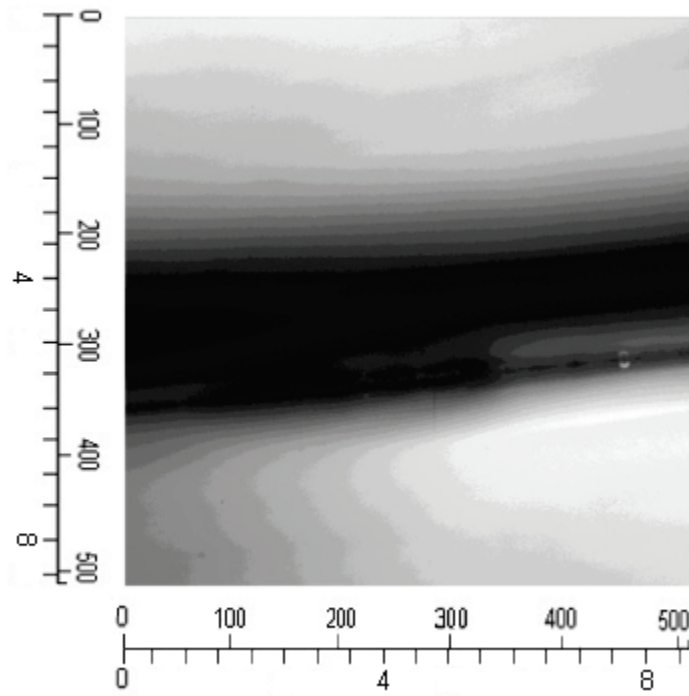


Figure 6.14. Intensity image of 1002M\_36; outer tank, oxygen saturated, depth 35 mm; inner tank, oxygen saturated, depth 35 mm.

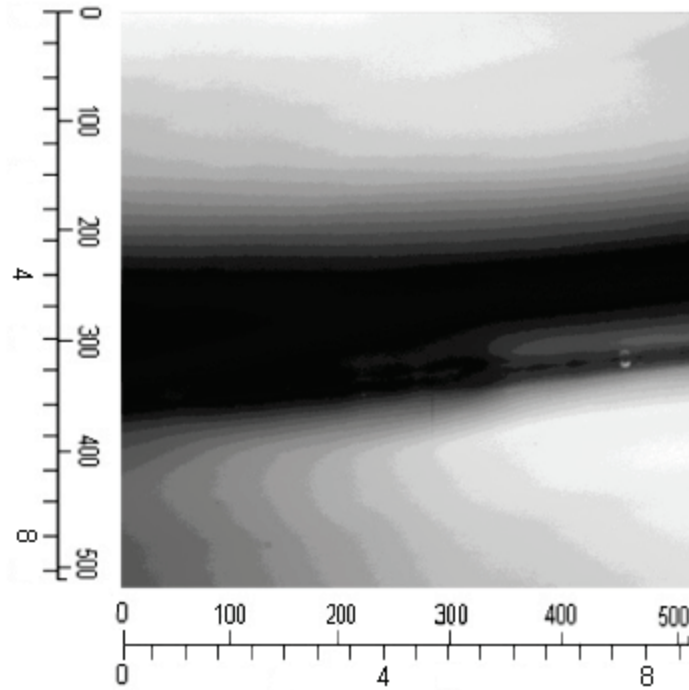


Figure 6.15. Intensity image of 1002M\_41; outer tank, oxygen saturated, depth 35 mm; inner tank, oxygen saturated, depth 35 mm.

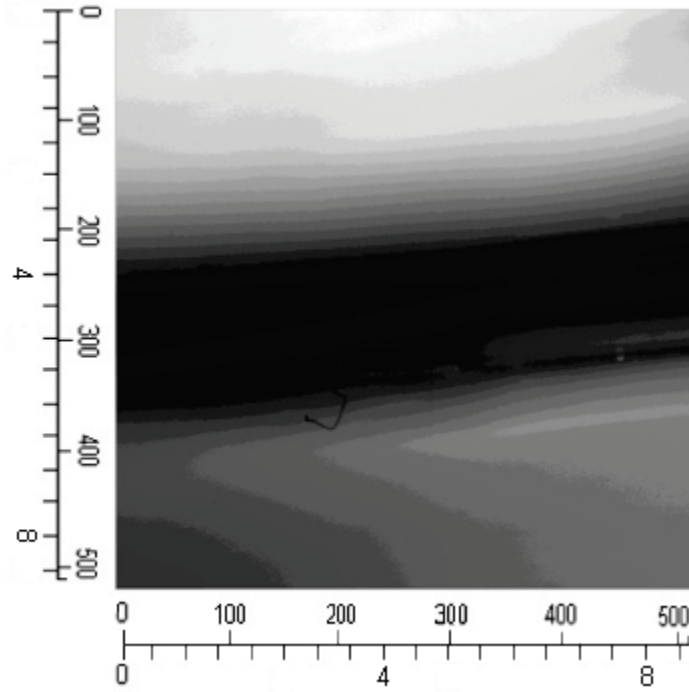


Figure 6.16. Intensity image of 1002N\_1; outer tank, oxygen depleted, depth 35 mm; inner tank, oxygen saturated, depth 35 mm.

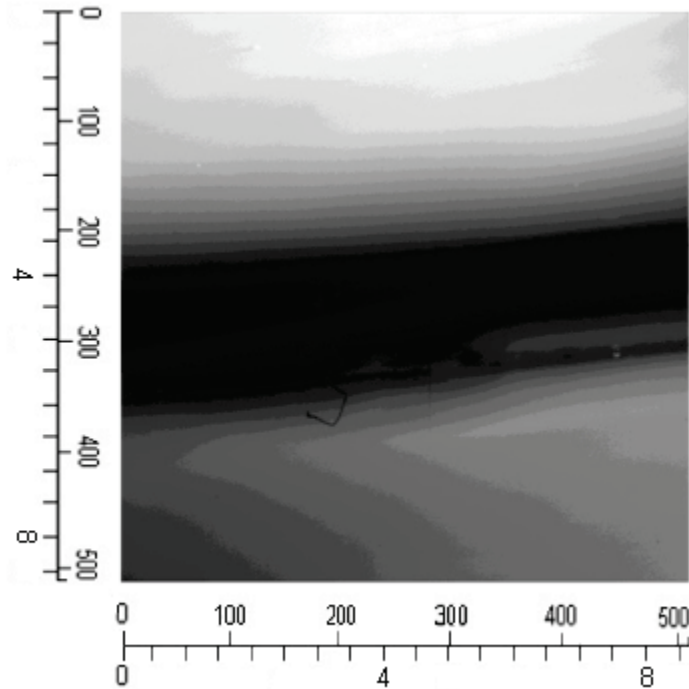


Figure 6.17. Intensity image of 1002N\_4; outer tank, oxygen depleted, depth 35 mm; inner tank, oxygen saturated, depth 35 mm.

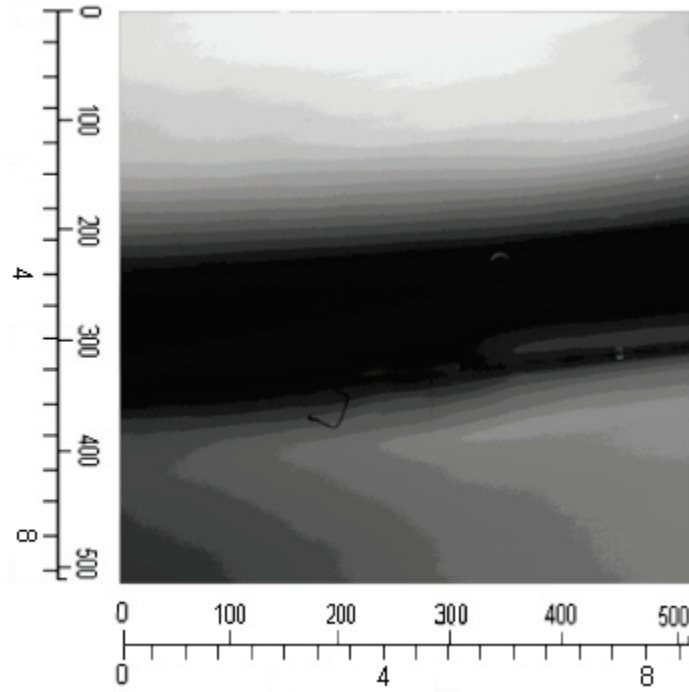


Figure 6.18. Intensity image of 1002N\_7; outer tank, oxygen depleted, depth 35 mm; inner tank, oxygen saturated, depth 35 mm.

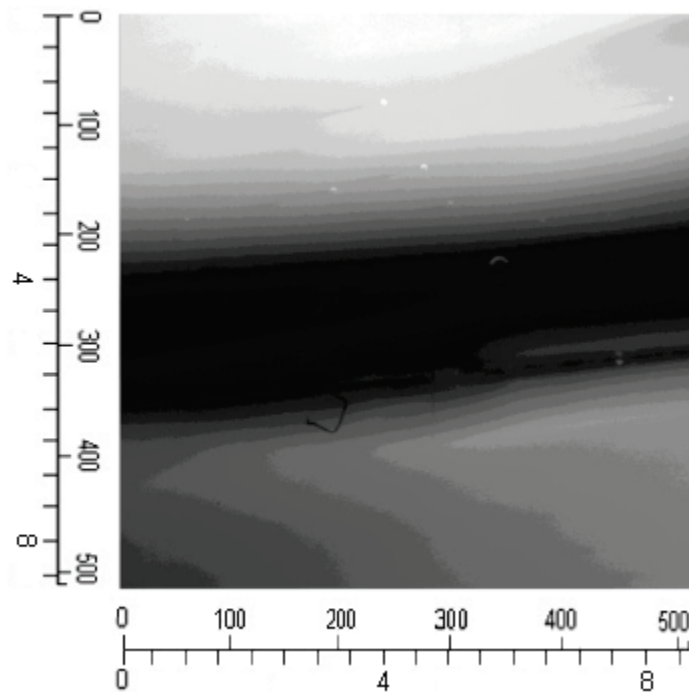


Figure 6.19. Intensity image of 1002N\_10; outer tank, oxygen depleted, depth 35 mm; inner tank, oxygen saturated, depth 35 mm.

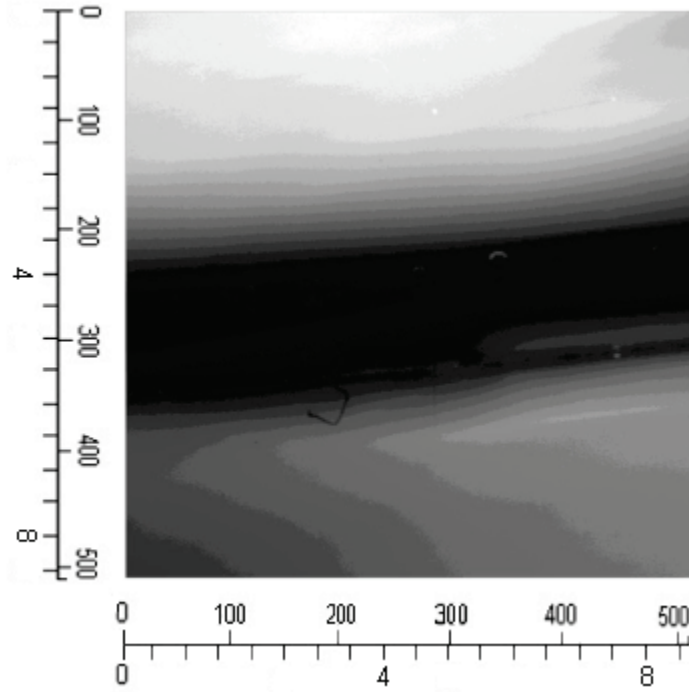


Figure 6.20. Intensity image of 1002N\_30; outer tank, oxygen depleted, depth 35 mm; inner tank, oxygen saturated, depth 35 mm.

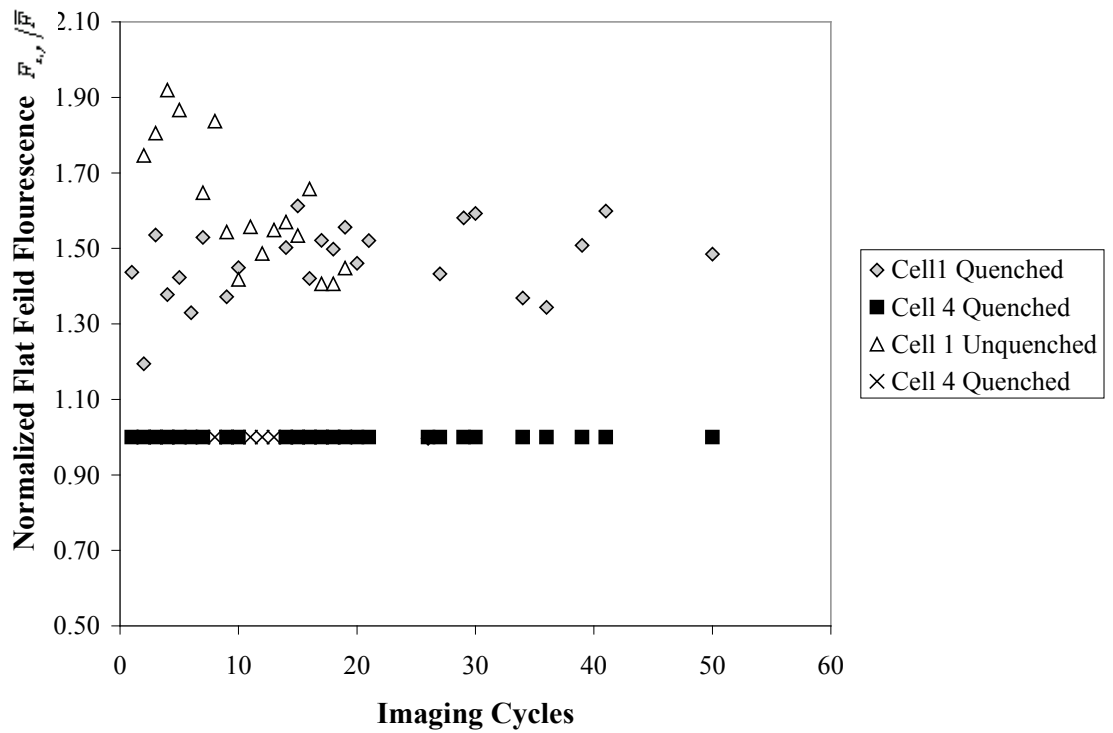


Figure 6.21. Plot of mean corrected fluorescence values, 7 mm deep two tank system.

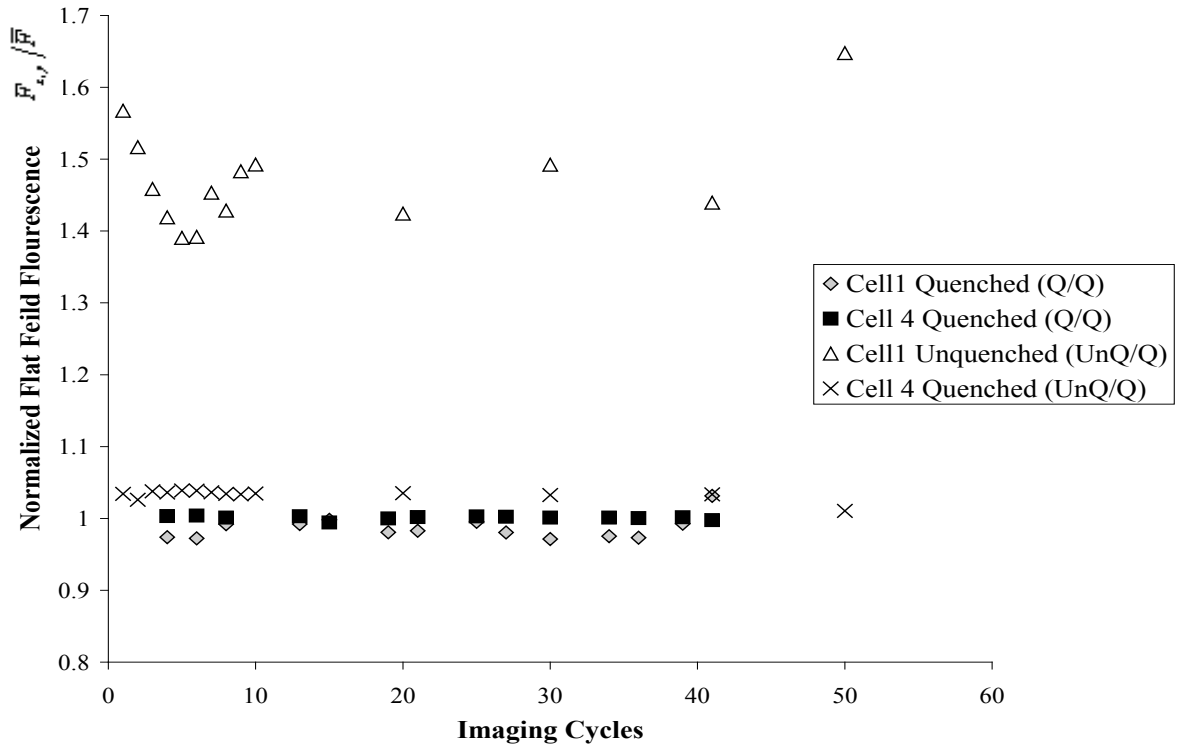


Figure 6.22. Plot of mean corrected fluorescence values, 50 mm deep two tank system.

## 7. RESULTS AND DISCUSSION:

### SLIF DEVELOPMENT STUDY

The SLIF system was designed for the study of mass transport across air-water interfaces. In Chapter 6, the SLIF verification study demonstrates that the SLIF system detects differences in fluorescence caused by differences in the near surface oxygen concentration. Chapter 7 describes the development of the SLIF technique to study oxygen mass transfer across flat air-water interfaces. Chapter 7 illustrates the development of the methods described in Chapter 4. Chapter 7 also details the progressive design of the SLIF image processing technique in Chapter 5.

#### 7.1. SLIF results for development study

The SLIF data consists of intensity images, raw fluorescence contour plots, profile images of fluorescence, contour plots of corrected fluorescence, maps of relative boundary layer thickness, maps of relative mass transfer coefficients, and profile plots of relative mass transfer coefficients. In Chapter 7, the SLIF data is presented as intensity images, contour plots, and dimensionless mass transfer coefficient maps. The orientation of the images is presented in Figure 7.1. Images and contour plots are presented in matrix format; the origin located in the upper right corner, the  $x$ -axis is located along the vertical and the  $y$ -axis is presented along the horizontal axis. In this format, the  $x$  and  $y$

axis retain their locations relative to the origin, but appear to be rotated 90 degrees to conventional plots. The  $x$ -axis is along the fetch of the wave tank from the wave generator. The  $y$ -axis is across the width of the tank. A vertical dotted line in Figure 7.1 shows the approximate location of the plane where Woodrow (2001) obtained PLIF images; waves produced for the Woodrow study travel from the top to bottom of the SLIF image orientation. Objects in the images are located by stating the  $x$  pixel coordinate and the  $y$  pixel coordinate or by their distance from the origin point of the image in millimeters. An example surface object, a black particle, is shown in Figure 7.1 centered on location ( $x=415, y=398$ ). Figure 7.1 also illustrates three components of a contour plot: contour lines, valleys, and ridges. Each of the thin, irregular circles is a contour line. In the contour lines there are several v shaped structures that indicate either a valley or ridge. In contour plots, valleys appear as v shaped structures with the tip of the v pointing towards the higher contour levels while ridges appear as v shaped structures with the tip pointing towards lower contour levels.

#### 7.1.1. Data used for SLIF development

Intensity image sets produced for the developmental SLIF study are listed in Table 7.1. Table 7.1 does not include quenched data sets. Table 7.1 lists the image numbers, conditions of the atmosphere when the image was acquired (room temperature, barometric pressure, relative humidity), the approximate width of the area imaged, the saturated dissolved oxygen concentration ( $[Ox]'$ ), and comments about the image set. The saturated oxygen concentration is calculated from the room temperature and barometric pressure, using Table C.2 in Appendix C.

The presentation labels found within the text are comprised of three parts: the data set label, the image set label, and the image number. The data set label contains what study the image was generated in, the relative humidity of the atmosphere and which data set at that relative humidity the image belongs. For example D32B is the second data set acquired at 32% relative humidity. The image label and image number divide each data set into blocks of less than 99 images, which was the limit of the acquisition labels generated by V for Windows. The original image blocking is maintained to allow reference between this document and the original data files. The corresponding acquisition labels are detailed in Appendix D.

A special presentation label is used for the image sets created during design of the beam expansion and density filter experiments. The data set label is DBA for data of type B, or design data with A representing the alpha, or first, data set. Likewise the image set number is not a letter but a number to further differentiate these image sets from other image sets. Atmospheric humidity and temperature were not recorded since the wave tank was continually perturbed and the oxygen level of the water was near saturation.

Data Set	Image Set	Number range of images #	Temp °C	Pressure inHg	Atmospheric Humidity	Image width mm	Ox' mg/L	Comments
D21A	A_[n]	0-63	25	30.30	21%	17.2	8.45	Downwelling
D21A	B_[n]	0-99	25	30.30	21%	17.2	8.45	Downwelling
D21B	A_[n]	0-24	25	30.36	21%	17.2	8.74	Downwelling
D21B	B_[n]	0-78	25	30.36	21%	17.2	8.74	
D21B	C_[n]	0-99	25	30.36	21%	17.2	8.74	Downwelling
D32A	A_[n]	0-95	23	30.27	32%	17.2	8.64	Downwelling
D32A	B_[n]	0-35	23	30.27	32%	17.2	8.64	
D32A	C_[n]	0-87	23	30.27	32%	17.2	8.64	Downwelling
D36A	A_[n]	0-77	24.5	30.21	36%	17.2	8.48	Downwelling
D29A	A_[n]	31-42	24	30.39	29%	28.4	8.61	
D29A	B_[n]	0-36	24	30.39	29%	28.4	8.61	
D29A	C_[n]	0-99	24	30.39	29%	28.4	8.61	
D29A	D_[n]	0-99	24	30.39	29%	28.4	8.61	
D46A	A_[n]	0-64	22.5	29.83	46%	17.2	8.69	Scale (mm)
D46A	B_[n]	2-99	22.5	29.83	46%	17.2	8.69	
D46A	C_[n]	1-99	22.5	29.83	46%	17.2	8.69	Dark
D46A	D_[n]	0-39	22.5	29.83	46%	17.2	8.69	
D46A	E_[n]	0-32	22.5	29.83	46%	17.2	8.69	Dirty
D46B	A_[n]	0-91	22	29.83	46%	17.2	8.69	D46BA/D46BB
D46B	B_[n]	0-91	22	29.83	46%	28.4	8.69	Div by scale
D46C	A_[n]	1-9	22	29.83	46%	28.4	8.69	
D46C	B_[n]	0-9	22	29.83	46%	28.4	8.69	
D46C	C_[n]	0-9	22	29.83	46%	28.4	8.69	
D46C	D_[n]	0-9	22	29.83	46%	28.4	8.69	
D46C	E_[n]	1-9	22	29.83	46%	28.4	8.69	
DBA	1_[n]	0-46	N/A	N/A	N/A	28.4	N/A	Exp Design
DBA	2_[n]	0-10	N/A	N/A	N/A	28.4	N/A	0.1 D Filter
DBA	3_[n]	0-22	N/A	N/A	N/A	28.4	N/A	0.3 D Filter
DBA	4_[n]	0-5	N/A	N/A	N/A	28.4	N/A	Both Filters
D36B	A_[n]	0-99	22	30.39	36%	17.2	8.95	
D36B	B_[n]	0-98	22	30.39	36%	17.2	8.95	Downwelling
D42A	A_[n]	0-98	21	30.33	42%	17.2	9.09	
D42A	B_[n]	0-96	21	30.33	42%	17.2	9.09	Downwelling

Table 7.1. Unquenched SLIF images for flat surfaces.

### 7.1.2. Examples of SLIF data

In this section a series of images are presented to illustrate typical image features found in the SLIF data for flat air-water interfaces. Figure 7.2 presents an intensity image, D21AA\_60. The image was of a 17.2-mm by 17.2-mm area. The image was acquired under evaporative conditions. Evaporative conditions occur when the atmospheric conditions are at levels where evaporation model of Jones et al. (1993) predicts that water will evaporate; equation 2.42. The evaporation rate is based on room temperature, barometric pressure, and the atmospheric humidity. The atmospheric humidity is given in terms of the relative humidity of the air surrounding the wave tank. For data set D21A, the room temperature was 25 °C, the barometric pressure was 30.36 inHg and atmospheric humidity was 21%. The faint ridge line running from location  $(x=512, y=340)$  to location  $(x=260, y=340)$  is an image feature generated by a scratch on the bottom of the wave tank.

Figure 7.3 presents a false color contour plot of the raw fluorescence,  $P_{x,y}$  for image D21AA\_60. The values of raw fluorescence intensity varied from 2,560 to 10,900. The contour plot is presented with twenty levels of intensity marked by black contour lines. A ridge is located from coordinates  $(x=512, y=340)$  to  $(x=260, y=340)$ . Again, this was identified as a scratch on the bottom of the wave tank.

Figure 7.4 is intensity image, D21BA\_60. The image was acquired under evaporative conditions, with a room temperature of 25 °C, a barometric pressure of 30.36 inHg and an atmospheric humidity of 21%. A dark streak was seen in the image from location  $(x=0, y=210)$  to  $(x=512, y=500)$  and is indicated by a red arrow. There were

several bubbles in the image, including a cluster of bubbles at location  $(x=30, y=100)$  that cast a shadow.

Figure 7.5 is of a color contour plot of the raw fluorescence D21BA\_60. The values of raw fluorescence varied from 1,510 to 14,300. A 'valley' feature is located on each contour line indicating the dark streak seen in Figure 7.4. The cluster of bubbles at locations  $(x=30, y=100)$  and  $(x=500, y=290)$  appear as black spots in the raw fluorescence contour plot. Their appearance as black spots is due to each bubble appearing to have the interior of one to two pixels in diameter with the bubble wall appearing equally thick. The Matlab function *contourf*, which produced the contour plot, marked the contours of the bubbles with black points as described in section 5.1.1. This level marking has made the bubbles appear as dark spots within this contour plot. The shadows created by the bubbles appeared as 'valleys' within the raw fluorescence contour plot.

Figure 7.6 shows an intensity image, D32AA\_79. The image was acquired under evaporative conditions, with a room temperature of 23 °C, a barometric pressure of 30.27 inHg and an atmospheric humidity of 32%. A dark streak was located along the line  $y=200$ . An arrow indicates the dark streak. No bubbles were present within the image.

Figure 7.7 is a color contour plot of the raw fluorescence D32AA\_89. The raw fluorescence varied from 960 to 10,300. The image was acquired under evaporative conditions, with a room temperature of 23 °C, a barometric pressure of 30.27 inHg and

an atmospheric humidity of 32%. A dark streak was located starting at  $(x=0, y=200)$  and curving to  $(x=512, y=100)$ . This image was captured approximately 130 seconds after D32AA\_79, presented in Figure 7.6.

Figure 7.8 illustrates the movement of a dark streak across the imaged surface. Figure 7.8 contains four intensity images, D32AC\_45, D32AC\_48, D32AC\_52, and D32AC\_56. The images were of a 17.2-mm by 17.2-mm area. The atmospheric humidity was 32%. The room temperature for the four images was 23 °C. The barometric pressure was 30.27 inHg. An arrow indicates the dark streak found in each image. The dark streak moved across this series of images at an estimated speed of 0.03mm/sec.

Figure 7.9 consists of two intensity images, D46BA\_16 and D46BA\_25. The images were acquired under evaporative conditions with the room temperature of 22 °C, a barometric pressure of 29.83 inHg and an atmospheric humidity of 46%. Figure 7.9(a), D46AF\_16 was of a 17.2-mm by 17.2-mm area. A dark streak was found from location  $(x=0, y=150)$  to location  $(x=512, y=400)$  and is indicated by an arrow. Figure 7.9(b) D46AF\_25 was of a 28.4-mm by 28.4-mm image area. The image contained a dark streak that divided into two, thinner dark streaks at location  $(x=210, y=210)$ . Arrows in the figure indicate the dark streaks. D46AF\_25, Figure 7.9(b) was acquired by decreasing the magnification of the imaging area on the surface after acquiring the intensity image shown in Figure 7.9(a). The dark streak in D46AF\_16 was approximately 0.75-mm in thickness. The dark streak in D46AF\_25 was found to be approximately 0.8-mm in thickness at location  $(x=410, y=420)$ .

Figures 7.2 through 7.9 illustrated the three categories of image features found in the SLIF data: surface objects, equipment features, and undefined features. The image features were categorized by their source. Surface objects were objects on the liquid surface, including bubbles and debris. Figures 7.4., 7.5 and 7.8 illustrate the shadow effect generated by surface objects. Surface objects were most notable for the shadow effect created by a decrease in the excitation energy caused by the surface object being in the laser beam path. The shadows were directly opposite the targeting mirror. Surface objects generally appeared as black spots within the contour plots of the raw fluorescence; although bubbles would appear as small, bright circles if they were larger than two to three pixels. Equipment features were image features, such as the faint line in Figures 7.2 and 7.3, generated by the SLIF apparatus itself. The faint line in Figures 7.2 and 7.3 was generated by a scratch on the bottom of the wave tank. Equipment features were found to only vary with changes in the physical settings of the SLIF apparatus. In Figures 7.4 and 7.5 the imaging area had been translated to avoid capturing the scratch mark. The dark streaks shown in Figures 7.2, 7.4, 7.8, and 7.9 were classified as undefined features. Image features were classified as undefined if they could not be attributed to objects on the liquid surface or the SLIF apparatus. The dark streaks are further examined in section 7.2.

### 7.1.3. Adjustment of the SLIF excitation beam

In the developmental SLIF study of flat air-water interfaces, it was concluded that the depth of penetration,  $d$ , was too large. The large depth of penetration was causing the SLIF camera to capture a large amount of background fluorescence and the bottom of the wave tank. After the problem was discovered, adjustments were made to correct the problem; images presented in this section illustrate the changes made to reduce the depth of penetration. The images show the effect of each change on the SLIF system and the SLIF data. These images illustrate why the changes were included in the SLIF experimental methods (Chapter 4).

The ability of the SLIF system to capture differences in the effective boundary layer thickness was adversely affected by the large depth of penetration. The greater the depth of penetration, the larger the background fluorescence level is in comparison to the signal fluorescence level; the difference between areas with a thick effective boundary layers versus those with a thin effective boundary layer. Figure 7.10 is a profile image of the initial designed fluorescence spot showing the depth of penetration of the excitation laser beam. The image was acquired through the transparent side-wall of the wave tank using a Kodak Digital Camera. Lines on the image indicate the location of the air-water interface and the location of the tank bottom. The liquid depth was 10-mm. In Figure 7.10, the excitation laser beam spot was approximately 25-mm by 20-mm before being reflected by the targeting mirror. The beam expander did not have the neutral density filters detailed in section 4.1.1 installed.

The first corrective action was to alter the expansion of the incident radiation laser beam. Figure 7.11 is a profile image of the fluorescence spot after altering the expansion of the incident radiation laser beam. Lines indicate the location of the air-water interface and the location of the wave tank bottom. The liquid depth was 10-mm. In Figure 7.11, the beam expander detailed in section 4.1.1 was adjusted to allow continued beam expansion as it approached the targeting mirror, reducing the intensity of laser beam at any given point on the liquid surface. The beam expander did not have the neutral density filters described in section 4.1.1 installed.

The second corrective action was to introduce a series of neutral density filters that were described in section 4.1.1. Figure 7.12 is a profile image of the fluorescence spot after altering the expansion of the incident radiation laser beam and installing the neutral density filters. The neutral density filters are detailed in section 4.1.1. The liquid depth is 10-mm.

Figures 7.11 through 7.12 illustrated changes made to the SLIF system over the course of the development of SLIF flat-air water interface experiments. Broadening the incident radiation laser beam and installing neutral density filters reduced the penetration depth of the incident radiation; decreasing the background fluorescence in comparison to the signal fluorescence. These changes increased the ability of the SLIF apparatus to resolve differences in the resolution oxygen concentration gradient. An example image after these corrections is presented in Figures 7.13 and 7.14(a).

Figures 7.13 and 7.14(a) illustrate the changes in SLIF intensity after the corrections. In these figures the 'rolling' background, created by the surface of the wave tank during extrusion is attenuated. Second, the beam expansion has allowed for a much

larger area to be illuminated with most of the poorly illuminated corners now fully illuminated by the laser beam. The most important correction, the moving dark feature mentioned in section 7.1.2 can be more easily differentiated from the surrounding fluid in Figure 7.14(a) than in the previous SLIF image sets.

#### 7.1.4. Data acquired after SLIF excitation beam adjustments

A set of SLIF experiments were conducted to study the effect of humidity on mass transfer. The set of experiments, listed in Table 7.2, utilized the expanded beam and neutral density filters described in section 7.1.2. The image area size was increased from 17.4 mm to 31.4 mm. The set of experiments were conducted over a relative humidity range of 27% to 96%. The humidity range and image area were selected to meet the experimental design requirements of the atmospheric humidity study discussed in Chapter 8.

The set of experiments was used to refine the SLIF image processing technique. Analysis of the images produced after the alterations to the laser beam revealed that polishing steps were needed as part of the image processing procedure. Chapter 5 describes the full image processing procedure, but in this section we will discuss the reasoning and development of those steps not directly based on theory (Chapter 3) but from application. Specifically, two new image processing steps were developed and applied to the SLIF data: cropping and secondary background correction. The two new image processing steps were developed to address problems that had been identified in translating raw intensity values to dimensionless mass transfer maps. Some of the example images presented here were first presented as illustrative examples in Chapter 5. Chapter 8 will discuss the mass transfer aspects of the data presented in this section.

Data Set	Image set	Number range of images	Temp °C	Pressure inHg	Relative Humidity	Image size Mm	Ox' Mg/L	Comments
R27	A_[n]	0-98	22	29.96	27%	31.75	8.45	60% quenched
R27	B_[n]	0-22	22	29.96	27%	31.75	8.45	60% quenched
R27	C_[n]	0-94	22	29.96	27%	31.75	8.45	Downwelling
R27	D_[n]	0-27	22	29.96	27%	31.75	8.45	Downwelling
R27	E_[n]	0-99	22	29.96	27%	31.75	8.45	Downwelling
R27	F_[n]	0-99	22	29.96	27%	31.75	8.45	Downwelling
R27	G_[n]	0-60	22	29.96	27%	31.75	8.45	
R27	H_[n]	0-40	22	29.96	27%	31.75	8.45	Downwelling
R27	I_[n]	0-99	22	29.96	27%	31.75	8.45	Quenched
R29	A_[n]	31-42	24	30.39	29%	31.75	8.61	
R61	A_[n]	0-25	21.5	29.71	61%	31.75	8.82	Ruler
R58	A_[n]	0-99	22.0	29.71	58%	31.75	8.74	Downwelling
R58	B_[n]	0-99	22.0	29.71	58%	31.75	8.74	
R58	C_[n]	0-99	22.0	29.71	58%	31.75	8.74	Downwelling
R58	D_[n]	0-99	22.0	29.71	58%	31.75	8.74	Downwelling
R58	E_[n]	0-99	22.0	29.71	58%	31.75	8.74	
R63	A_[n]	0-99	21.5	29.71	63%	31.75	8.82	Downwelling
R63	B_[n]	0-99	21.5	29.71	63%	31.75	8.82	Downwelling
R63	C_[n]	0-99	21.5	29.71	63%	31.75	8.82	Downwelling
R63	D_[n]	0-99	21.5	29.71	63%	31.75	8.82	Downwelling
R63	E_[n]	0-99	21.5	29.71	63%	31.75	8.82	Downwelling
R63	F_[n]	0-68	21.5	29.71	63%	31.75	8.82	Downwelling
R96	A_[n]	0-95	23.0	29.72	96%	31.75	8.58	
R96	B_[n]	4-103	23.0	29.72	96%	31.75	8.58	
R96	C_[n]	6-98	23.0	29.72	96%	31.75	8.58	
R96	D_[n]	7-100	23.0	29.72	96%	31.75	8.58	
R96	E_[n]	5-63	23.0	29.72	96%	31.75	8.58	Downwelling
R96	F_[n]	2-36	23.0	29.72	96%	31.75	8.58	Downwelling
R91	A_[n]	1-81	23.0	29.72	91%	31.75	8.58	
R91	B_[n]	0-99	23.0	29.72	91%	31.75	8.58	
R91	C_[n]	0-97	23.0	29.72	91%	31.75	8.58	
R91	D_[n]	0-22	23.0	29.72	91%	31.75	8.58	
R46	A_[n]	7-92	21.0	29.70	46%	31.75	8.91	
R46	B_[n]	4-92	21.0	29.70	46%	31.75	8.91	
R46	C_[n]	0-100	21.0	29.70	46%	31.75	8.91	
R46	D_[n]	1-99	21.0	29.70	46%	31.75	8.91	

Table 7.2. SLIF images for humidity experiments.

#### 7.1.5. Refinement of SLIF image processing

The image processing steps first developed for SLIF were designed from SLIF theory, detailed in Chapter 3. These steps allowed for the raw fluorescence images to be translated into contour plots of the relative mass transfer boundary layer thickness (Figure 7.14) and contour plots of dimensionless mass transfer coefficient values (Figure 7.15). These image processing steps were primarily based on SLIF theory. Additional image processing was needed to refine the SLIF data and remove two artifacts of the SLIF apparatus that were hindering the image processing procedure: some poorly illuminated areas at the corners of the images and an apparent vibration effect altering the alignment of the laser beam between consecutive images. The additional image processing steps were: cropping and a secondary background correction.

Cropping of the raw fluorescence images was introduced to deal with poor illumination of the liquid surface within the imaging area. To investigate a set of image features labeled dark streaks, the imaging area was increased from 17.4 mm to 38.2 mm. The liquid surface area that the laser beam could illuminate was limited by the targeting mirror size of 100mm by 100 mm; leaving areas of poor illumination at the upper right and lower left corners of the SLIF raw fluorescence data, as shown in Figure 7.16. These poorly illuminated areas were cropped out of the raw fluorescence images, as in Figure 7.17. The procedure for identifying and cropping poorly illuminated areas is detailed in section 5.1.3.

A secondary background correction procedure was added to the SLIF image processing to remove ‘slopes’ from within the contour plots of relative boundary layer

thickness and dimensionless mass transfer coefficients. Examining the relative boundary layer thickness contour plot presented in Figure 7.14(b), there is an apparent ‘slope’ of the boundary layer thickness across the plot. The ‘slope’ is more discernable in a cross sectional plot such as Figure 7.18. This ‘slope’ became more pronounced as the imaging area size was increased. We attributed the ‘slope’ to misalignment between the normalized incident radiation distribution and the incident radiation distribution of a given SLIF image, caused by the targeting mirror vibrating. The implementation of the secondary background correction is detailed in section 5.1.6. Figure 7.19 presents the secondary background correction array for R63E\_92. Figure 7.20 presents R63E\_92 before (a) and after (b) the secondary background correction.

The additional image processing steps of cropping and secondary background correction allowed us to generate dimensionless mass transfer coefficient plots from SLIF raw fluorescence images. Figure 7.21, Figure 7.22 and Figure 7.23 are examples of the dimensionless mass transfer coefficient plots that the SLIF technique produced. These images illustrate the variation in the values of dimensionless mass transfer using gray scale intensity and are not broken into various levels by contour lines such as Figure 7.15.

## 7.2. Image feature analysis

Figures 7.2 through 7.9 illustrate the image feature types found within the SLIF data: surface objects, equipment features, and undefined features. It is the undefined features, specifically the dark streaks, which may illustrate a potential mass transfer affecting event. Although bubbles and surface contamination will affect the mass transfer rate, the dark streaks held the potential of a much larger effect. Section 7.2 discusses the methodology of SLIF image feature analysis and uses these dark streaks as the example.

The work and ideas presented in sections 7.2 and 8.1 were conducted in a parallel, integrated process. The development of the SLIF technique occurred from analysis of the images captured on air-water mass transfer. Section 7.2 covers those aspects that are universal to any application of the SLIF technique. Section 8.1 specifically focuses on the analysis of the dark streaks themselves and the fluid mechanical phenomena they indicate. The identification of the sources of image features is universal to any application of the SLIF technique and is therefore described in this chapter. However, the dark streaks seen in the previous images are specific to the study of Raleigh-Bernard circulations. Section 7.2.2 discusses the creation of the data analysis subroutines presented in section 5.3. Though they are specific to Rayleigh-Benard downwelling zones, the methodology in development of the subroutines is universal to any SLIF data analysis.

### 7.2.1. Analysis of undefined features

In the Planar Laser Induced Fluorescence study of flat air-water interfaces (Woodrow 2001) there were several cross sections of the mass transfer boundary layer that showed increased thickness at locations. Woodrow attributed these to thermally driven circulations in water; specifically that the boundary layer thickness was increasing due to downwelling, where cool surface liquid collects and returns to the bulk fluid. We expected that like Woodrow, that these downwelling zones would have observable affect upon the SLIF generated relative mass transfer data. Within the SLIF data, there appeared a series of dark streaks similar to the downwelling zones seen by Spangenburg and Rowland (1965) in their study of thermally driven circulations. Examples of these dark streaks in the SLIF data can be found in Figures 7.4, 7.6, 7.8, 7.9, 7.13, and 7.15. The data sets from the SLIF developmental study (Table 7.1) that contained dark streaks are listed in table 7.3.

Data Set Name	Relative Humidity %	Temperature °C	Atmospheric Pressure InHg
D21A	21	25	30.30
D21B	21	25	30.36
D29A	29	24	29.96
D32A	32	23	20.27
D36A	36	25	30.21
D36B	36	22	30.39
D42A	42	21	30.33
D46A	46	23	29.83

Table 7.3. List of conditions in which dark streaks were located within data images.

The dark streaks appeared as valleys in the contour plots of the raw fluorescence and as areas of low mass transfer rate in the dimensionless mass transfer rate contour plots. In the flat air-water study, the water depth was 10 mm. The range of relative humidity surrounding the wave tank varied from 21% to 46%. The dark streaks were seen in the SLIF development data across the entire range, but not in all images. However, the source of the dark streaks could not be immediately described to downwelling zones. First there were a few other possible sources for the dark streaks that needed to be eliminated: surface objects, the SLIF apparatus, or waves. By using a process of elimination to reject the other sources, we were able to attribute these dark streaks directly to being increases in the mass transfer boundary layer thickness. The second step of relating the increases in the mass transfer boundary layer thickness to Rayleigh-Bénard circulations is detailed as part of the mass transfer study discussed in Chapter 8.

The possible sources that the dark streaks could be attributed to were investigated. The dark streaks could have been: shadows generated by surface objects, shadows created by the SLIF apparatus, a defect within the imaging system, shadows generated by waves, or a variation in the dissolved oxygen gradient beneath the surface of the liquid. The source of the dark streaks was attributed to a variation in the dissolved oxygen concentration gradient by comparing the behavior of the dark streaks to the observed and expected behavior of the other possible sources and eliminating them.

Surface objects were determined not to be a possible source of the dark streaks. First, the dark streaks appeared as dark lines, or valleys, within the SLIF data rather than as objects on the surface such as bubbles (Figures 7.2 thru 7.4) or particles (Figures 7.2

and 7.3). Both bubbles and particles appeared as black spots within the raw fluorescence contour plots. Bubbles could clearly be distinguished within the raw fluorescence images (Figures 7.4, 7.8, 7.9, 7.13). Second, examining Figures 7.2 thru 7.4 illustrated the differences between shadows generated by particles and bubbles and the dark streaks. The axes of the shadows generated by bubbles were oriented directly away from the laser targeting mirror, since the bubbles interfered in transmission of laser light. In Figure 7.4, the dark streak was almost perpendicular to the shadows generated by the bubbles within the image. Third, the presence of dark streaks was independent of the presence of objects on the surface. Both surface objects and dark streaks were found in the some of the same intensity images, illustrated in Figure 7.8. In other images, such as presented in Figures 7.13 and 7.16, dark streaks were not found with surface objects present.

The dark streaks were determined not to be an equipment feature generated by the SLIF apparatus. The dark streaks exhibited behavior not associated with equipment features such as movement over time. Figure 7.8 presents four intensity images taken over a period of several minutes. The dark streak within the images moves across the imaging area at approximately 0.3 mm/min while the SLIF apparatus was stationary. Unlike Figure 7.8, a shadow created by equipment in the excitation radiation path would not move between acquired images of an image set.

The dark streaks were not related to the imaging system, either through the camera head or camera lens. Figure 7.9 shows the same dark streak, in images D46BA\_16 and D46BA\_25 with a decrease in magnification of 65%. The measured

thickness remained approximately 0.8 mm in both images. An artifact of the imaging system would have had an identical pixel width with an apparent increase in the determined thickness of approximately 65%.

The dark streaks were not generated by waves, or ripples, moving across the surface. The dark streaks moved and flexed across the surface of the water, which could be explained as a series of waves with a frequency slightly greater or larger than the frequency of the SLIF image capture rate. However, when examining the right hand intensity image within Figure 7.9, the dark streak reforms into two dark streaks. Although it is possible for two waves to form a “Y” structure in rare instances, the merging point of the two waves would have amplitude of both waves together. In Figure 7.9 the amplitude of the dark streak appeared to decrease rather than increase at the meeting location. This lack of any apparent increase in amplitude demonstrated that the dark streaks were not related to waves on the surface.

The remaining source for the dark streaks in the SLIF data was a change in the dissolved oxygen concentration gradient near the surface. Based on equation 3.13, the decrease in fluorescence represents a decrease in the slope of the dissolved oxygen concentration gradient where the dark streaks appear. The decrease in the dissolved oxygen concentration gradient was treated as an increase in the effective mass transfer boundary layer thickness, equation 3.34.

#### 7.2.2. Development of image analysis programs

The study of the effect of atmospheric humidity on mass transfer focuses on the dark streaks, or thick boundary layer zones, that appeared in the developmental SLIF study. As mentioned before, the previous section 7.2.1 only focuses on illustrating the

analysis for identifying the source of an undefined feature. A set of image analysis functions, detailed in Chapter 5, were developed to help standardize and expedite the analysis of these image features. The image analysis functions and their structure are detailed in Chapter 5 while their implementation is detailed in Chapter 8; in this section the development of these image analysis functions is discussed. To develop the image analysis routines detailed in section 5.3, a basic understanding of the expected and observed structure and behavior of the dark streaks was needed.

As was illustrated in Figures 7.14 and 7.15, the dark streaks were related to an increase in the oxygen mass transfer boundary layer thickness, and a decrease in the dimensionless mass transfer coefficient. In Chapter 8, a detailed study of the dark streaks attributes them to the collection of cool, oxygen rich water near the surface at Rayleigh-Bénard downwelling zones. Rayleigh-Bénard circulations were the focus of the study of the effect of atmospheric humidity on mass transfer of oxygen in Chapter 8.

Rayleigh-Bénard circulations, as discussed in section 2.3, are formed by thermal instability, in this instance a thermal instability rising out of the evaporative cooling at the surface. An attribute of liquids undergoing Rayleigh-Bénard circulation in water was the presence of downwelling zones, where cool surface liquid collected and plunged back into the bulk fluid (Berg, 1965). The downwelling zones then would form a thick boundary layer where oxygenated surface liquid was swept into them. Rayleigh-Bénard circulations were found to form in evaporating liquids where the stability values, the modified Rayleigh  $Ra^*$  and Marangoni  $Ma^*$  numbers detailed in section 2.4, exceeded the meta-stable point represented by the critical values  $(Ma_c, Ra_c)$ . The stability values

shown in Table 7.4 indicated that, for all of the experiments listed in Table 7.1, Rayleigh-Bénard circulation could have been present since the range of modified Rayleigh and Marangoni number values for these experiments exceed the critical values as shown in Table 7.4.

Atmospheric Humidity	Evaporation Rate (kg/m <sup>2</sup> s)	$Ra^*$	$Ma^*$
20.0%	6.7E-4	2,000,000	390,000
30.0%	5.9E-4	1,700,000	340,000
40.0%	5.0E-4	1,500,000	290,000
50.0%	4.1E-4	1,200,000	250,000
Critical Values (Koschmieder, 1993)			
	$Ra_c$	1100.7	
	$Ma_c$		79.607

Table 7.4. Stability values for a 10-mm deep open tank of water.

Table 7.4 lists the modified Rayleigh, modified Marangoni, critical Rayleigh, and critical Marangoni numbers for an open tank of water 10-mm in depth  $\delta_s$  for atmospheric evaporation from 20% to 50% relative humidity.

The image analysis functions, detailed in section 5.3, needed to be able to capture important details of the downwelling zones such as width, dimensionless mass transfer value, location and area while dealing with other artifacts of the SLIF data. The image analysis functions also needed to allow for calculating the rate of downwelling movement between SLIF data images.

How the SLIF image analysis functions calculate the width, dimensionless mass transfer value, location and area are detailed in Chapters 5. Why these attributes were

selected for analysis is detailed in section 8.2; which explains the experimental design of the atmospheric humidity study. What was desired, from an image analysis standpoint, was a set of image analysis functions that would generate measurements of width, the dimensionless mass transfer value, and location at both the pixel and image level. Image level values of the width and dimensionless mass transfer value were simply averages of the pixel values.

The image analysis function *dwlocate*, detailed in section 5.3.1., had to be robust enough to identify downwelling zones with the variances in how dark streaks, or downwelling zones, appeared within the SLIF data. Figure 7.21 illustrates that the downwelling zones did form continuous lines, but they might have sharp bends or curves that the analysis technique had to be robust enough to deal with. In the function *dwlocate*, the function utilizes a custom line enhancement routine *Zline* based on a five by five pixel kernel versus a traditional three by three pixel kernel, allowing for more abrupt corner pixel variations. Not all the SLIF data contained downwelling zones, as shown in Figure 7.22. By utilizing a continuity test, the image analysis function would ignore points that were noise, and not apply a downwelling zone to images lacking one. In some examples, such as Figure 7.23, the downwelling zones were not the image minima. By utilizing a derivative derived minima location routine, the image analysis functions could highlight local minima that had a narrow width and remove noise from the detection process.

The image analysis function *SlifRBanalysis* was designed to maintain a record for each image of the downwelling zone locations, and other attributes. The saved data allowed for analysis of downwelling movement between consecutive images, as shown in

Figure 7.24, where a series of SLIF contour plots over time are presented. Unfortunately only a rough estimate could be made about the rate of downwelling movement due to the changing shape of the downwelling zones as illustrated in Figure 7.25.

### 7.3. Evaluation of SLIF technique

The SLIF system was designed to measure the spatial variation in mass transfer across the air-water interface. The verification of the SLIF concept is presented in Chapter 6. Evaluation of the SLIF technique at generating insights and mass transfer data for flat air-water interfaces is presented in this section. The evaluation of SLIF technique is discussed in three parts: qualitative analysis of unprocessed data, evaluation of the improvements made to the SLIF apparatus during the study of flat air-water interfaces and assessment of the SLIF technique to produce data on the spatial variation of mass transfer across the air-water interface.

#### 7.3.1. Evaluation of qualitative analysis

The SLIF system produced data which allowed for qualitative analysis of image features. This qualitative analysis included: evaluating changes in image features, relationships between different image features, and determining the source of many image features. The SLIF system allowed the user to conduct qualitative analysis using both processed and unprocessed data.

The SLIF system acquired intensity values of fluorescence. The prototype SLIF unit displayed intensity images of fluorescence in real time, Figure 7.2. These acquired intensity values  $P_{x,y}$  were converted to the raw fluorescence value  $F_{x,y}$  by removing the

dark current, as detailed in section 5.1.1. The intensity values and the raw fluorescence values were considered unprocessed data. Raw fluorescence  $F_{x,y}$  values were presented in false color contour plots such as Figure 7.3. The SLIF prototype allowed for qualitative analysis to be conducted utilizing the unprocessed SLIF data.

Qualitative analysis of unprocessed data excluded blank images, identified image features and helped identify the sources of image features. Blank images occur where little or no fluorescence was captured by the CCD. Image features, such as surface objects, equipment features, and downwelling were detailed in sections 7.1. and 7.2. The image features were classified by source. The sources of the image features were identified by observing their behavior between: successive images, images of different scale, and images with over different air-water surface locations.

Blank images were identified during operation of the SLIF apparatus. The SLIF apparatus would display the last captured image on the screen of the PC, allowing the user to note which images appeared to be blank, or primarily dark current noise. Blank images were generated when the laser misfired and low levels of excitation energy were generated. Blank images were discarded from the image processing queue. Image features were identified by visual inspection. The use of unprocessed SLIF data allows for monitoring of the data being generated and the removal of images with low light levels from the image processing queue.

An example of qualitatively analyzing an image features was detailed in section 7.2.1. The SLIF system allowed the user to: examine image features in-situ, examine image features over time, and examine image features under varying magnification. The user could determine presence of surface objects such as bubbles or particles within the

intensity images by examining the liquid surface in natural light during the experiment. Examples of image features created by surface objects were presented in Figures 7.3 through 7.7. The shadows generated by unwanted surface objects could then be ignored or removed in future analysis. The ability to qualitatively analyze image features over time is illustrated in Figures 7.8, 7.24 and 7.25. By capturing sequential images of the same location, the SLIF system could separate equipment features, such as the bright line found in Figure 7.2, from other image features. Equipment features, such as the bright line from location  $(x=300, y=300)$  to location  $(x=512, y=300)$  in Figure 7.2, could only be removed by adjustment of the SLIF system. Surface objects tended to move between sequential images and contour plots. Analysis of image features could be done by using the ability to change imaging scale of SLIF images without affecting the contents of the wave tank. The ability to quickly alter the camera lens system of the SLIF prototype, allowed for examination of the same image feature at differing scales. The SLIF apparatus had a close focus point and a far focus point. By simply moving the camera up or down the camera stand and inserting, or removing, an extension ring between the camera lens and camera body, the surface area of the SLIF imaging area could be changed. An example is shown in Figure 7.9. Figure 7.9 shows the intensity images D46BA\_16 and D46BA\_25. The thickness of the dark streak seen in D46BA\_16 at a magnification 0.034 mm/pixel was the same as the dark streak seen in Figure D46BA\_25 at a magnification of 0.056 mm/pixel.

Establishment of procedures for qualitative analysis of unprocessed data was critical to development of SLIF for the investigation of mass transfer across the air-water interface. First, qualitative analysis of unprocessed data identifies blank images that are

unusable in image processing. Second, qualitative analysis of unprocessed images identifies changes in the raw fluorescence values attributable to sources other than changes in the mass transfer boundary layer thickness. Image features identified in the unprocessed data can be investigated to determine their source, allowing the user to focus on features of interest. Image features that were generated by surface objects or equipment features can either be removed from future images, or omitted when examining mass transfer coefficient data.

### 7.3.2. Benefit of alterations to the SLIF system

Alterations were made to the SLIF system to reduce the amount of excitation energy at any given location of the imaged surface. The alterations were done to improve the system resolution and reduce background features found in some early images. Examining some early SLIF flat air-water interface data sets, small narrow lines were found within the intensity images (Figure 7.3). Examination of raw fluorescence contour plots and imaging the cross section of the laser zone (Figure 7.10) indicated that the source of these small, narrow image features was excitation radiation illuminating the bottom of the wave tank. The refraction of the fluorescence by the bottom of the wave tank caused the apparent spread at the bottom of the tank seen in Figure 7.10. The fluorescence also had a bright spot at the air-water interface. The fluorescence correction theory, used in image processing and discussed in sections 3.3.4 and 6.2, assumes that the penetration depth  $d$  is dependent only on the excitation radiation  $I_{x,y}$ . The solution to the problem was expanding and filtering the excitation radiation beam to prevent the excitation radiation from illuminating the bottom of the wave tank.

Figure 7.11 illustrates the first alternation made to decrease the excitation radiation intensity across the surface and decrease the depth of penetration; expanding the laser beam spot. In the initial SLIF design, the beam expander detailed in section 4.1.2 was designed to generate a columnar beam of laser light. By reducing the distance between the concave and convex lenses of the beam expander, the beam continued to spread after the concave lens of the beam expander. The expanding laser beam was then projected onto a much larger area of the liquid surface, reducing the excitation radiation at any given location of  $x,y$ . The larger beam generated fluorescence over a much larger area. At the same time, the generated fluorescence was much less intense at the air-water interface. However, the generated fluorescence still substantially illuminated the bottom of the wave tank.

The second alteration made was to add two neutral density filters, described in section 4.1.2, to reduce the overall excitation radiation  $I$  reaching the liquid surface. Both a neutral density filter of 0.6 D and a filter of 0.4 D were installed in the beam expander cage. The use of both filters reduced the intensity of the UV beam by an estimated 75% of the original laser beam strength. Figure 7.12 showed the fluorescence profile with both ND filters installed. The penetration depth, illustrated by the thickness of the fluorescence profile, had decreased significantly when compared with Figures 7.10 and 7.11. In the intensity image D36BA\_10, Figure 7.13, the streaky structure illustrated in Figure 7.2 was no longer apparent.

### 7.3.3. Evaluation of image processing

As discussed in Chapter 3 and Chapter 5, the SLIF image processing procedure was designed to convert raw fluorescence values  $F_{x,y}$  into dimensionless mass transfer coefficients  $k^*_{x,y}$  in four steps: normalization, fluorescence correction, calculation of the relative boundary layer thickness, and calculation of the dimensionless mass transfer values. Raw fluorescence data was normalized by dividing the data by the mean fluorescence of the image. The correction procedure, discussed in section 5.1.4, corrected the raw fluorescence values by removing the excitation radiation distribution. As described in section 5.1.5, equation 3.43 was implemented using the corrected fluorescence values and saturated oxygen concentration to find the values of relative boundary layer thickness  $\delta_{x,y}/\delta$ . The values of relative boundary layer thickness were inverted to find the values of relative mass transfer coefficient across the surface of the air-water interface. The SLIF technique was first examined in the verification study, presented in Chapter 6, using a modified image processing procedure. The modified image processing procedure consisted of normalization and fluorescence correction of two 65 pixel by 65 pixel image cells from an overall 512 pixel by 512 pixel image. The primary background correction procedure was evaluated in terms of producing mean corrected fluorescence values for each image cell with a known oxygen concentration.

The primary background correction was a critical step in the image processing procedure since it removed the distribution in fluorescence generated by the excitation radiation distribution and produced a uniform basis for the relative boundary layer

thickness values. In the validation study, the fluorescence correction step generated corrected fluorescence values that represented the dissolved oxygen levels in the two separate tanks. For the intensity image R63E\_92 (Figure 7.17), the excitation distribution was removed from the raw fluorescence values to find the corrected normalized fluorescence values (Figure 7.26). In the example of fluorescence correction for image R63E\_92, the  $y$  shaped shadow became an area of high intensity. At the same time, the bright area of intensity centered at location ( $x=25$  mm,  $y=30$  mm) was evened out with the surrounding fluorescence.

The secondary background correction removed an apparent shift, or ‘slope’ caused by low frequency vibrations. As discussed in chapter 5, the alignment between each images individual excitation radiation distribution and the normalized radiation distribution needed to be corrected. The secondary background correction, illustrated in Figure 7.19, was removed from R63E\_92 after normalization and primary background correction. The resulting normalized corrected fluorescence image is shown in Figure 7.27.

The background correction process enhanced the resolution of image features. The split in dark streak in the intensity image R63E\_92 was unobserved in the raw intensity contour plot (Figure 7.17). The branching of the dark streak appears only as a large spot upon the dark streak after primary background correction (Figure 7.27). The secondary background correction reveals even more of the branched structure (Figures 7.20, 7.26, and 7.27). The background correction process removed the overlying excitation radiation that was obscuring the structure of the dark streak phenomena in the image.

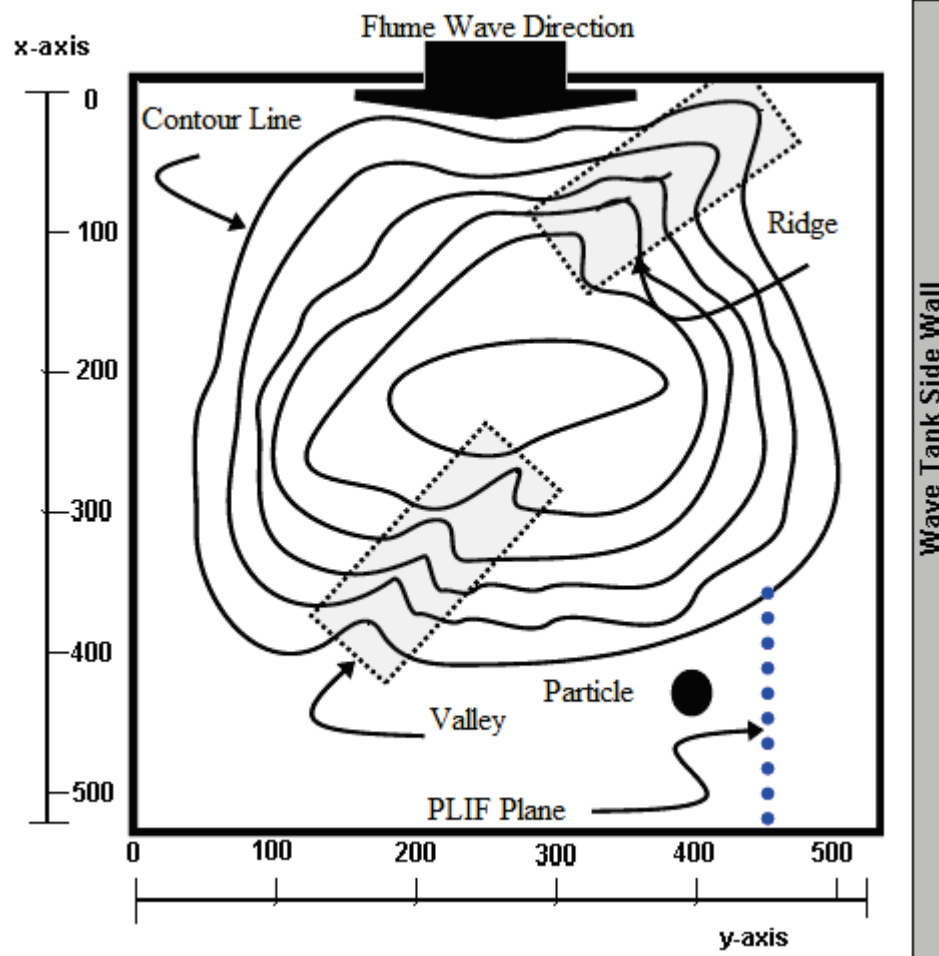


Figure 7.1. Diagram of an example image.

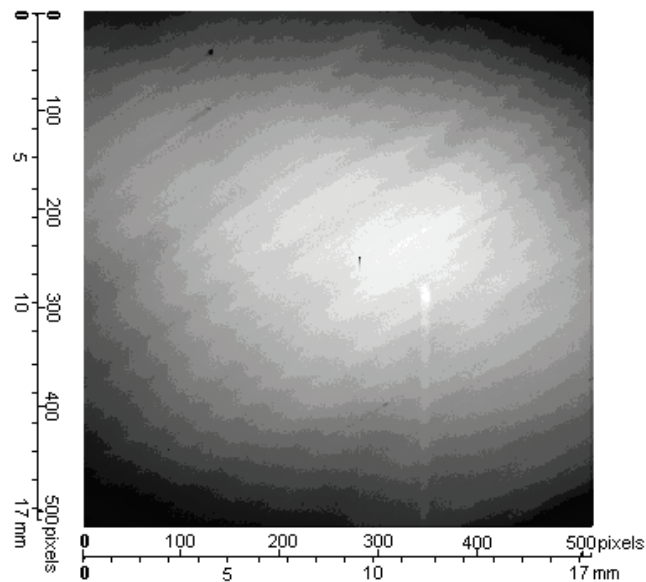


Figure 7.2. Intensity image D21AA\_60; temperature 25 °C; pressure 30.33inHg, humidity 21%, width 17.2 mm.

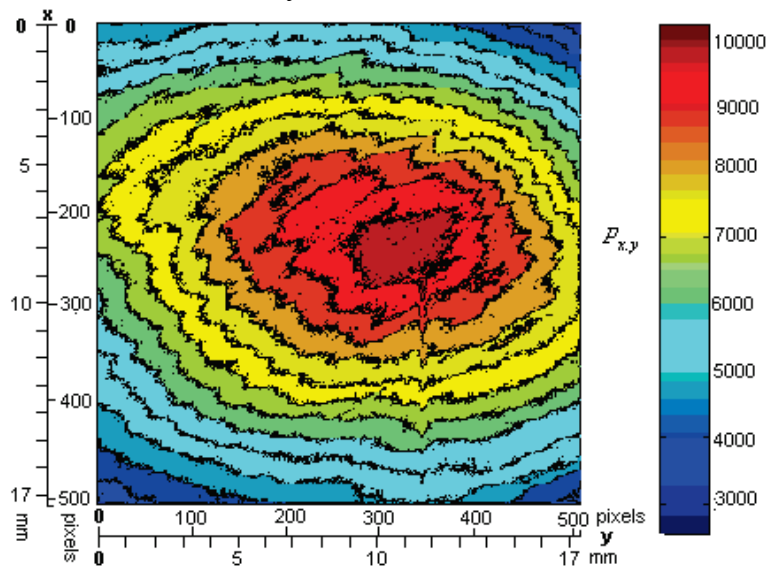


Figure 7.3. False color contour plot of raw fluorescence values for image D21AA\_60.

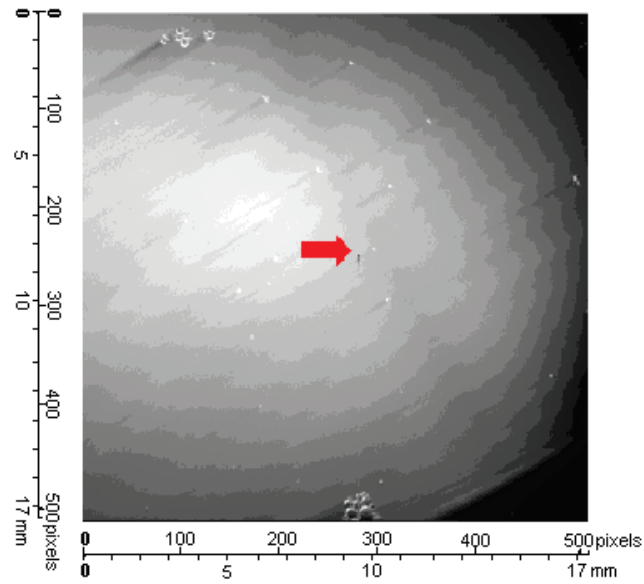


Figure 7.4. Intensity image of D21AB\_60; temperature 25 °C, pressure 30.36inHg, humidity 21%, width 17.2 mm.

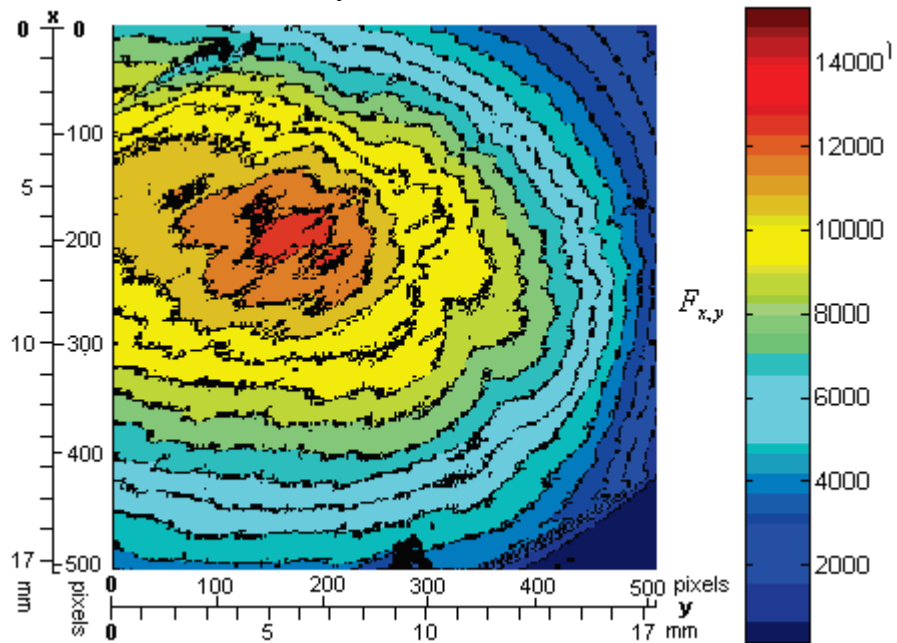


Figure 7.5. False color contour plot of raw fluorescence values for image D21AB\_60.

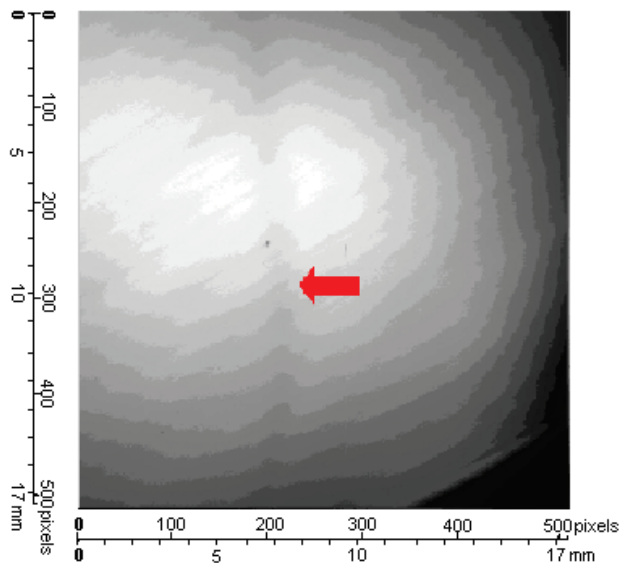


Figure 7.6. Intensity image D32AA\_79; temperature 23 °C, pressure 30.27inHg, humidity 32%, width 17.2 mm.

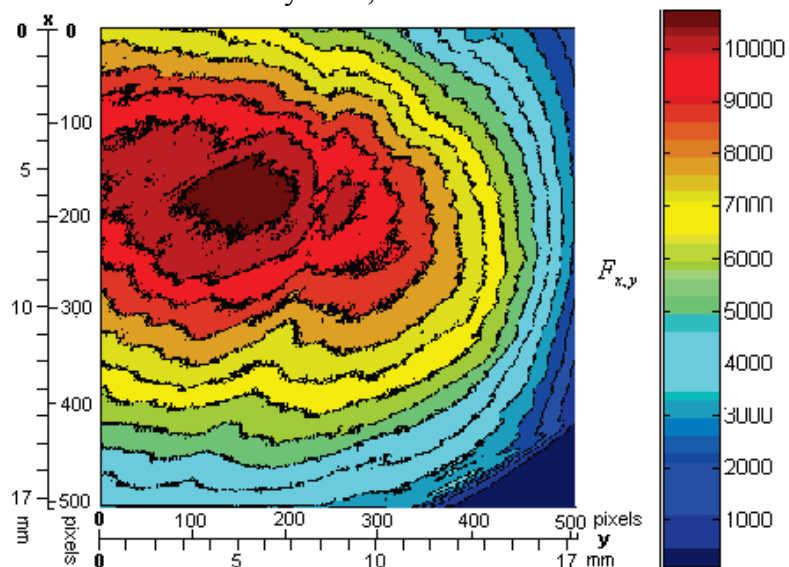


Figure 7.7. False color contour plot of raw fluorescence values for image D32AA\_89; temperature 23 °C, pressure 30.27inHg, humidity 32%, width 17.2 mm.

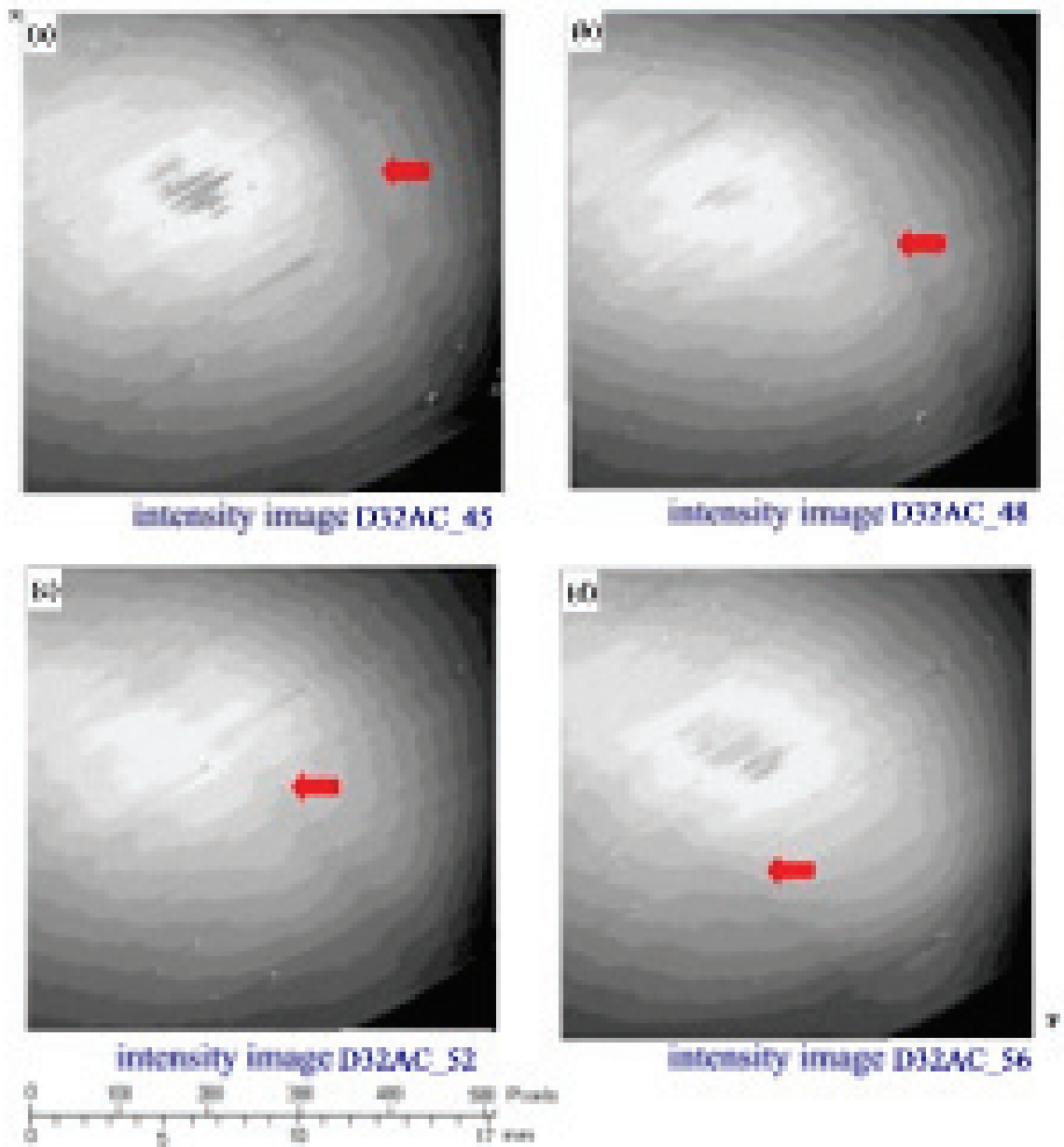


Figure 7.8. Intensity image of D32AC\_45, (a); 48, (b); 52, (c); and 56, (d); temperature 23 °C, pressure 30.27 inHg, humidity 32%, width 17.2 mm.

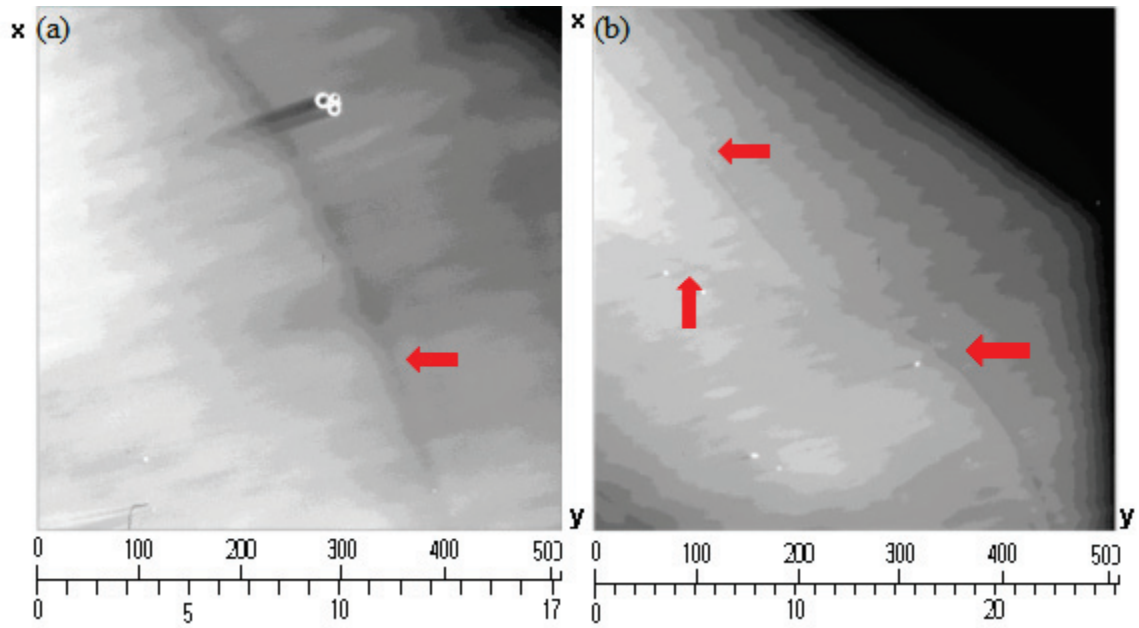


Figure 7.9. (a) Intensity image of D46BA\_16, width 17.2 mm, (b) D46BA\_25, width 26.4 mm; temperature 22 °C, pressure 29.83inHg, humidity 46%.

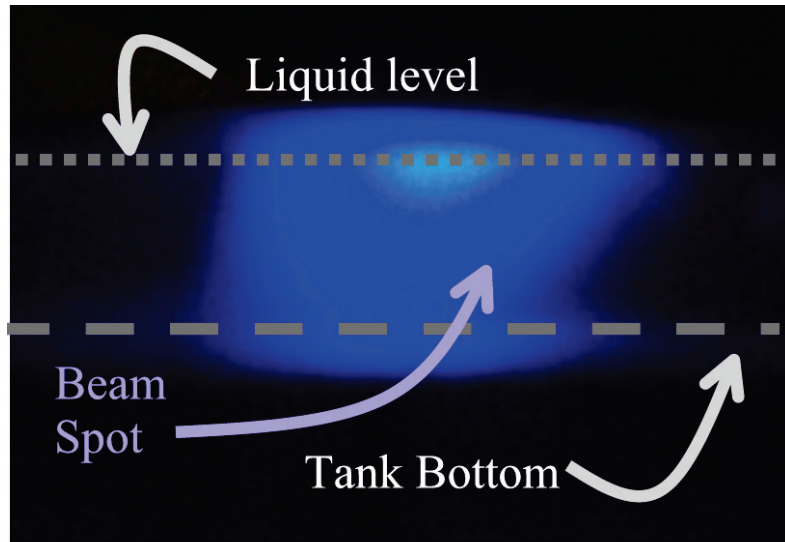


Figure 7.10. Profile view of fluorescence before beam adjustments.

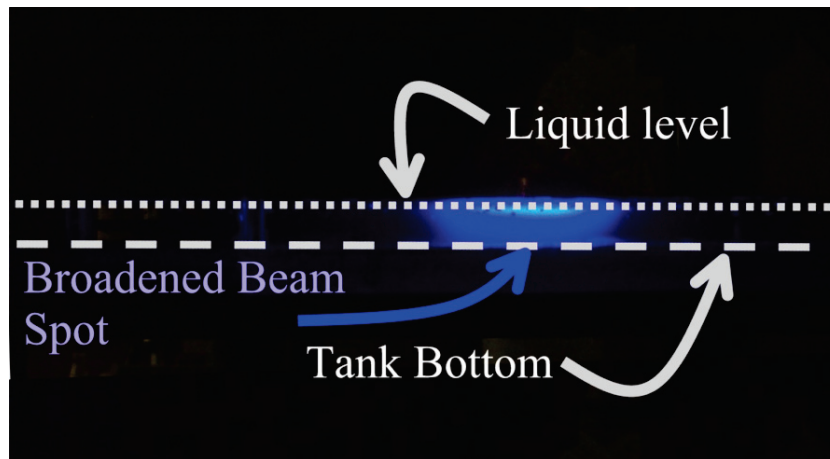


Figure 7.11. Profile view of fluorescence after laser beam was broadened.

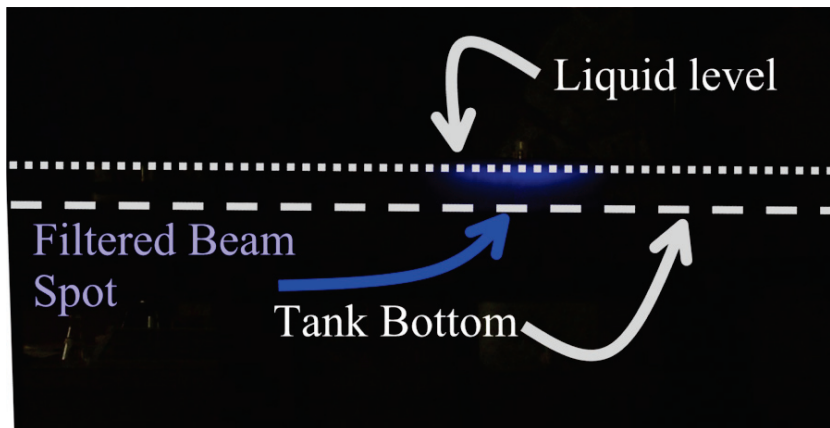


Figure 7.12. Profile view of fluorescence after addition of neutral density filters.

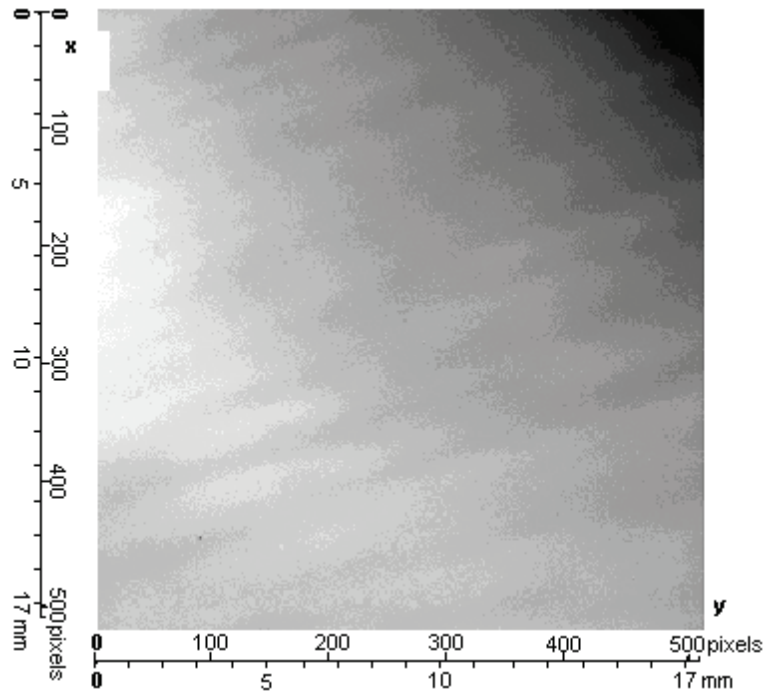


Figure 7.13. Intensity image after laser beam expansion and correction, D36BA\_10; temperature 22°C, pressure 30.39 inHg, humidity 36%, width 17.2 mm.

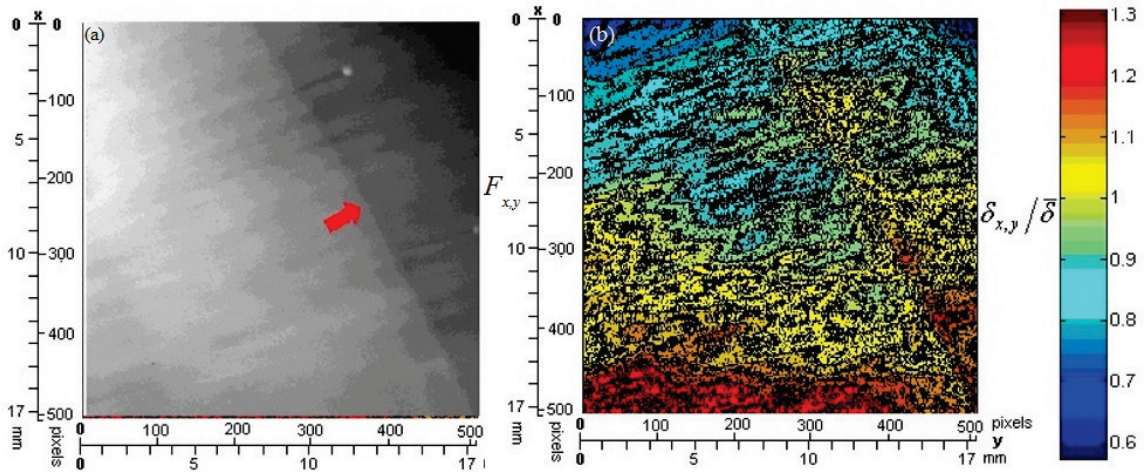


Figure 7.14. (a) Intensity image of D42AB\_34; (b) Contour plot of relative boundary layer thickness, D42AB\_34; temperature 21 °C, pressure 30.33inHg, humidity 42%, width 17.4 mm. These figures compare the appearance in intensity of a dark streak versus the corresponding boundary layer thickness of the same dark streak. D42AB\_34 has not undergone secondary background correction in the contour plot of relative boundary layer thickness;

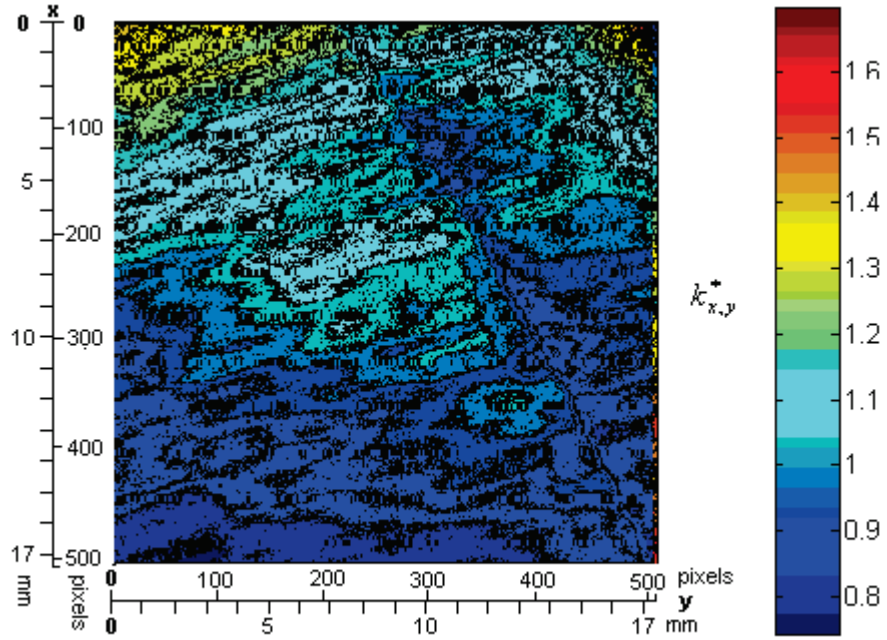


Figure 7.15. Contour plot of dimensionless mass transfer coefficient values for image D42AB\_34 using image processing developed from SLIF theory.

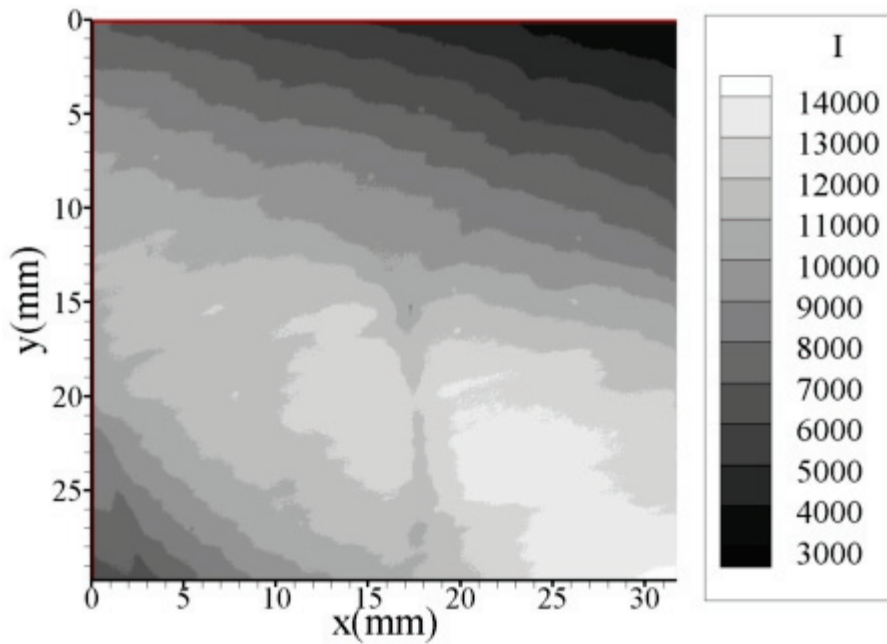


Figure 7.16. Raw fluorescence image showing poor illumination, R63E\_92; temperature 21.5 °C, pressure 29.71 inHg, humidity 63%, width 31.75 mm.

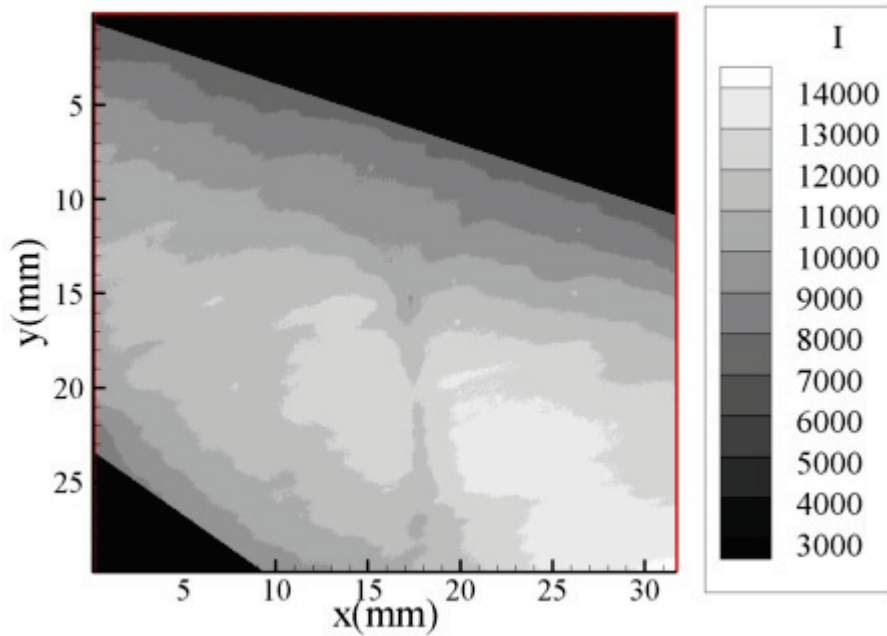


Figure 7.17. Cropped raw fluorescence image of R63E\_92.

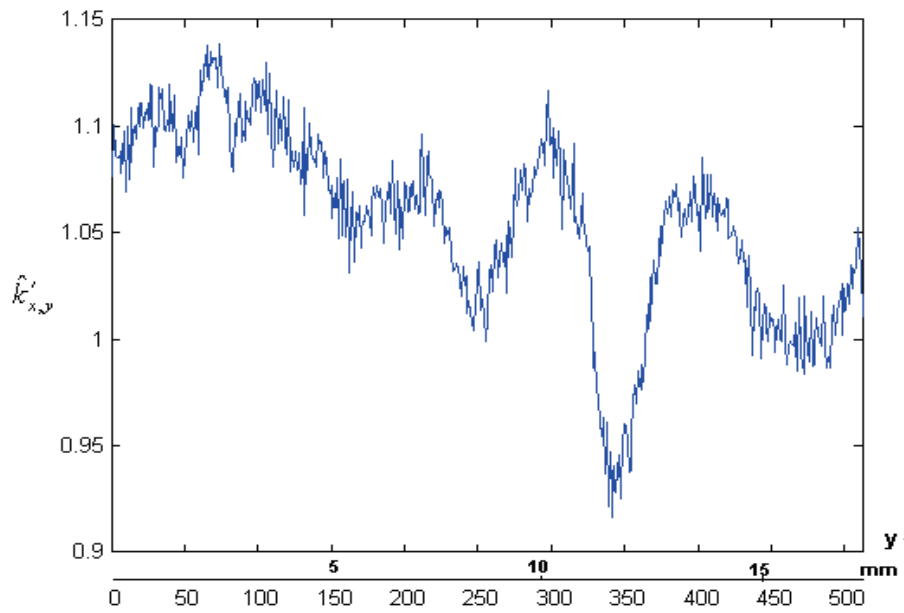


Figure 7.18. Cross-sectional plot of relative mass transfer values for image D42AB\_64 at  $x=180$ ; temperature 21 °C, pressure 30.33inHg, humidity 42%, width 17.4 mm.

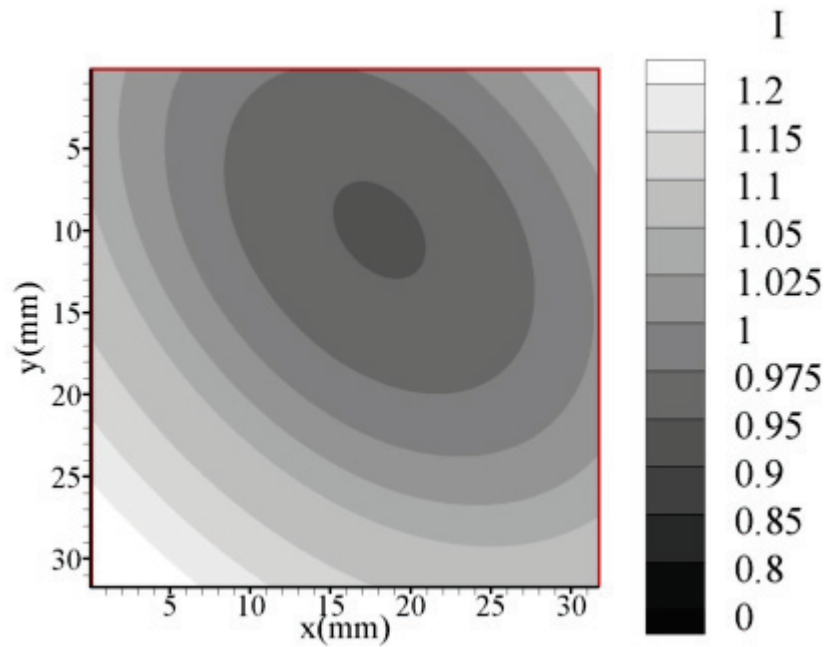


Figure 7.19. Secondary background correction array values for image R63E\_92.

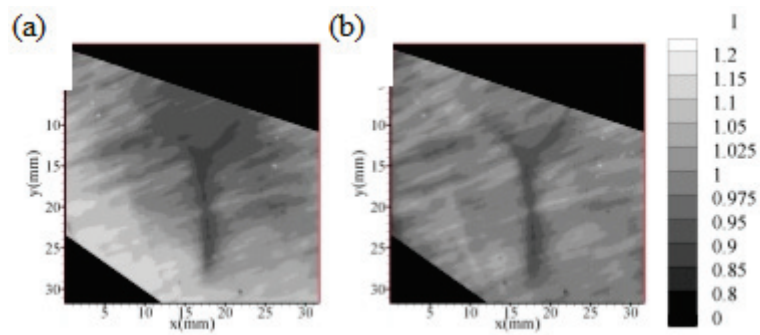


Figure 7.20. Comparison of R63E\_92 fluorescence intensity before (a) and after (b) secondary background correction.

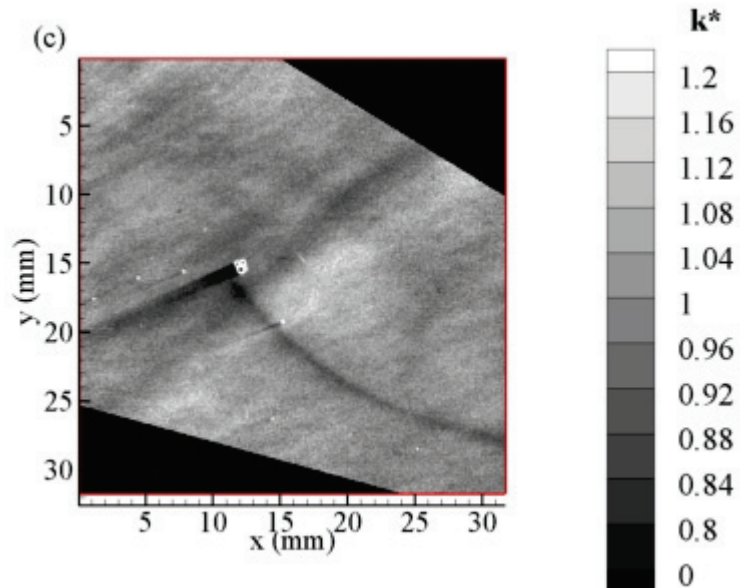


Figure 7.21. Contour plot of dimensionless mass transfer coefficient values for the image R27E\_23; temperature 22 °C, pressure 29.96 inHg, humidity 27%, width 31.75 mm.

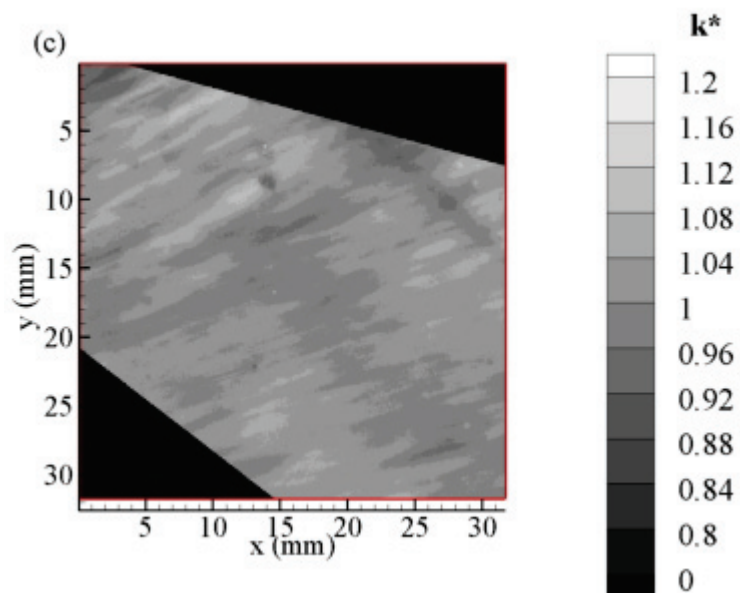


Figure 7.22. Contour plot of dimensionless mass transfer coefficient values for the image R46A\_31; temperature 21 °C, pressure 29.70 inHg, humidity 46%, width 31.75 mm.

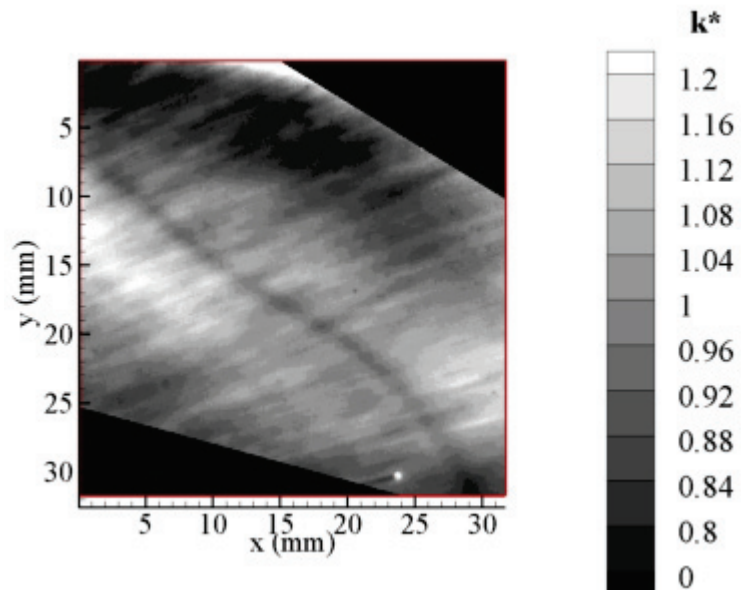


Figure 7.23. Grayscale plot of dimensionless mass transfer coefficient values for the image R58E\_86; temperature 22 °C, pressure 29.71 inHg, humidity 58%, width 31.75 mm.

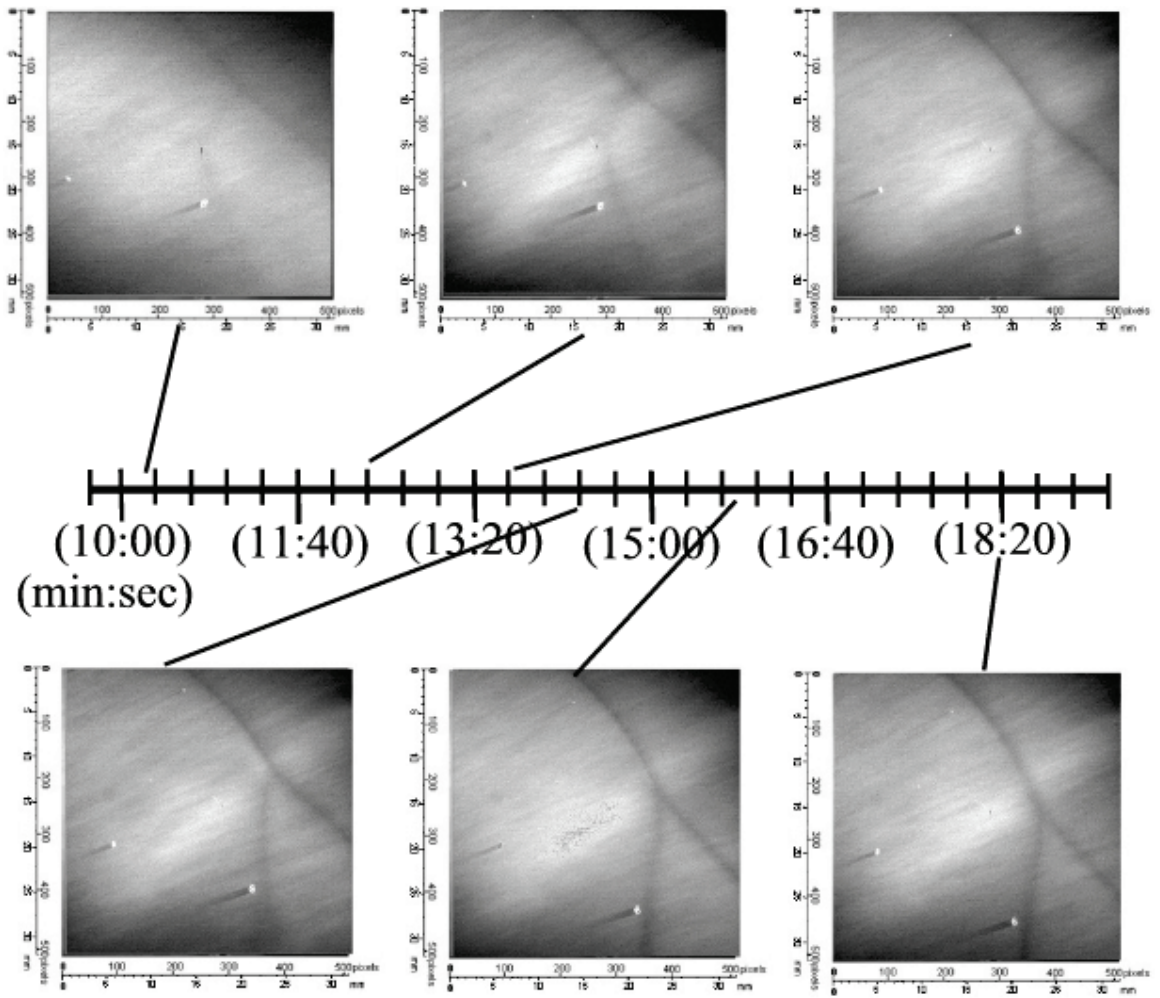


Figure 7.24. Composite intensity images of dark streaks reforming over time, (taken from data set R63)

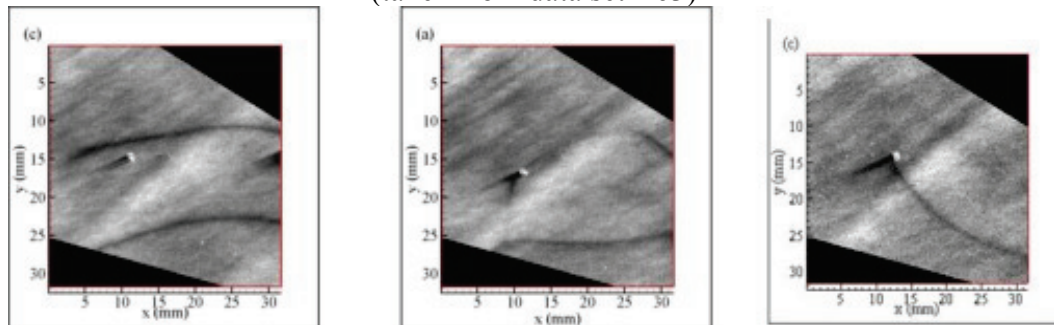


Figure 7.25 Illustration of cell formation and destruction from image set R27.

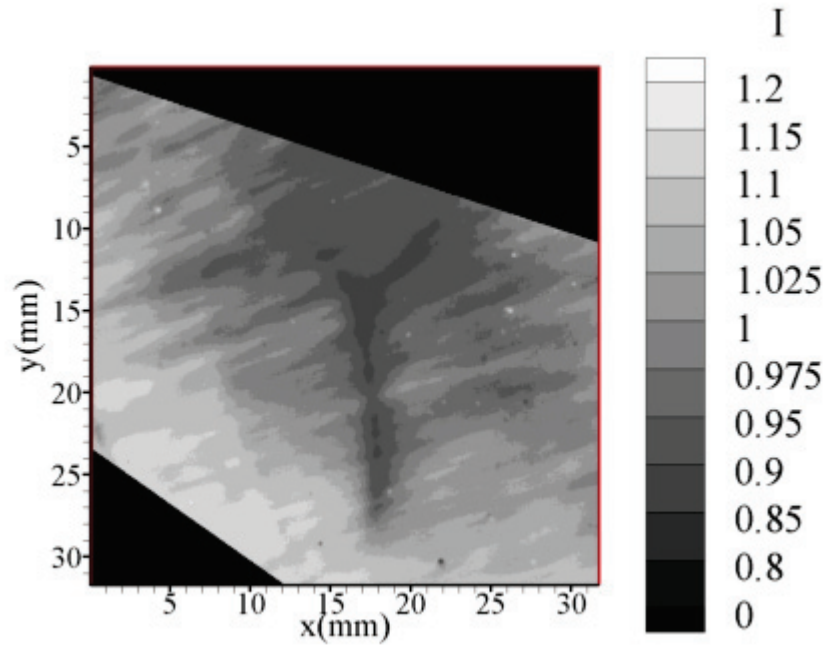


Figure 7.26. Contour plot of normalized fluorescence values for R63E\_92 before secondary correction.

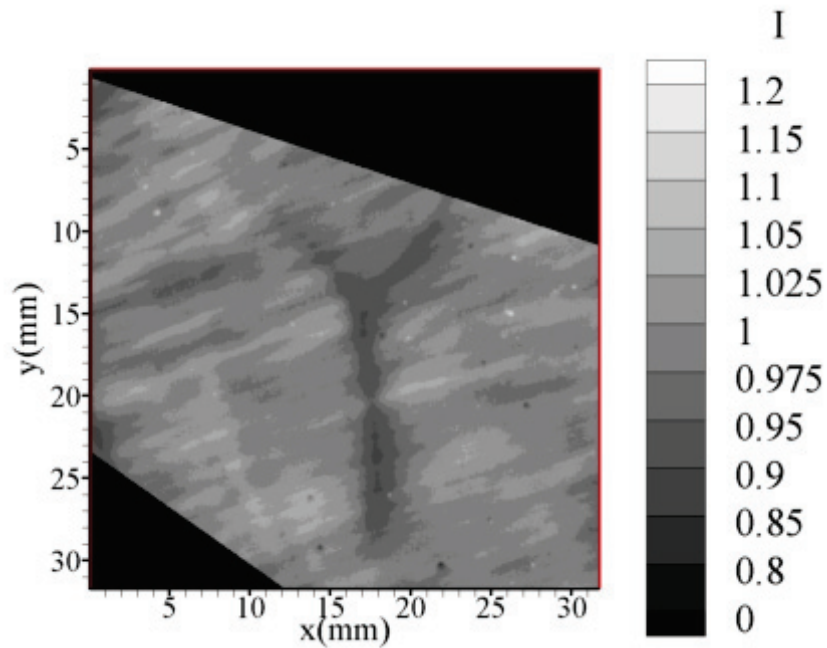


Figure 7.27. Contour plot of normalized corrected fluorescence values for the image R63E\_92 after secondary correction.

## 8. RESULTS AND DISCUSSION:

### THE EFFECT OF ATMOSPHERIC HUMIDITY ON OXYGEN MASS TRANSFER

The SLIF technique was used to study flat, air-water interfaces. The study focuses on how changes in atmospheric humidity affects the mass transfer of oxygen across the air-water interface via evaporation induced circulation. The phenomena indicative of these circulations is downwelling: referred to as dark streaks in Chapter 7 and identified in section 8.1. Chapter 8 utilizes the behavior, shape, and size of these downwelling zones to generate an understanding of the evaporation-induced circulations and their effect on mass transfer into the bulk fluid.

It is typically assumed that a flat, unperturbed body of liquid is stagnant (Thibodeaux, 1996) or quiescent, and that the applicable mass transfer model is simply the Whitmann model (Eq. 2.14). However, there have been several studies that indicate there are phenomena affecting the local mass transfer rates across flat surfaces, including Woodrow (2001 and 2002). Woodrow's Planar Laser Induced Fluorescence (PLIF) work included imaging the concentration gradient below an unperturbed, or flat, surface. In several of Woodrow's images the thickness of the oxygen concentration gradient varies dramatically: under some parts of surface the concentration gradient would be three to four times thicker than the concentration gradient under the adjacent surface. Woodrow

attributed these near surface regions to downwelling zones generated by Rayleigh-Bénard circulations. Woodrow speculated that the circulations were driven by unstable temperature gradients generated through evaporative cooling at the surface. Woodrow supported his case by demonstrating that with evaporation occurring, his system was theoretically unstable and could be characterized by circulations.

In sections 7.2.1 and 7.2.2, the image features labeled as dark streaks were identified as thick boundary layer zones. We speculate that they were created by the downwelling phenomena of Rayleigh-Bénard circulations. In section 8.1, the connections between dark streaks and Rayleigh-Bénard circulations are examined. In section 8.2, results are presented that examine the effects of evaporation driven circulations on oxygen mass transfer by controlling the atmospheric relative humidity.

### 8.1. Evaluation of SLIF development data

One of the features of the SLIF development data were dark streaks which could be attributed to thick mass transfer boundary layers near the surface. In section 7.2, the dark streaks were examined in terms of possible sources with a thickening of the mass transfer boundary layer being identified as the probable source. It was theorized that the dark streaks, or thick boundary layer zones, were created by Rayleigh-Bénard circulations, where cooler, oxygen rich, surface liquid plunged back into the bulk fluid. In this section we analyze the dark streaks of section 7.2 to determine if they are downwelling zones by: comparisons with studies similar to the developmental SLIF study, investigating the conditions of the developmental study, and comparing the dark

streaks to Rayleigh-Bénard and Marangoni phenomena found in the literature. The analysis supports that the dark streaks are attributed to being Rayleigh-Bénard downwelling zones where the oxygen rich surface liquid returns to the bulk fluid.

The conditions during the developmental SLIF study were conducive to the formation of Rayleigh-Bénard circulations. The conditions of atmospheric temperature and humidity were conducive to evaporation of water from the surface and the formation of an unstable thermal gradient. As detailed in section 2.3 and 2.4, thermal circulation can occur through mechanisms utilizing either surface tension or density. The Rayleigh  $Ra$  and Marangoni  $Ma$  numbers are the measures of instability for a liquid. If either, or both, of these values supersede their critical values, the system is unstable and may form self-sustaining circulation. Traditional and modified forms exist for Rayleigh-Bénard and Marangoni-Bénard equations, as detailed in section 2.4.

The traditional Rayleigh number  $Ra$  is given by the equation

$$Ra = \frac{\delta_s^3 \rho g \alpha \Delta T C_p}{\mu k^T} \quad (2.24)$$

which is described in section 2.4.1. The traditional Marangoni number  $Ma$  is given by the equation

$$Ma = \frac{S \delta_s \rho C_p \Delta T}{\mu k^T} \quad (2.29)$$

which is described in section 2.4.2. The modified Rayleigh  $Ra^*$  and modified Marangoni  $Ma^*$  numbers are, respectively

$$Ra^* = \frac{\beta \rho g \Delta T \delta_s^3}{\mu k^T} + \frac{\beta \rho g \dot{V} \Delta h_v \delta_s^4}{\mu C_p (k^T)^2} \quad (2.40)$$

$$Ma^* = \frac{S \Delta T \delta_s}{\mu k^T} + \frac{S \dot{V} \Delta h_v \delta_s^2}{\mu C_p (k^T)^2} \quad (2.39)$$

The equations are described in section 2.4.3. The modified values have been found to be valid in systems where the liquid is evaporating (Zhang et al., 2002). The Bond number,  $Bo_D$ , represents the ratio between the forces generated by surface tension and those generated by density (Neild, 1964),

$$Bo_D = Ra / Ma = Ra^* / Ma^* \quad (2.36)$$

For the SLIF developmental study, the applicable constants for water are listed in Table 8.1 (Lide, 2001).

$S$	$\rho$	$\beta$	$\mu$	$k^T$	$\Delta h_v$	$C_p$
(mN/m °K)	(g/cm <sup>3</sup> )	(°K <sup>-1</sup> )	(mN s/m <sup>2</sup> )	(m <sup>2</sup> /s)	(kJ/kg)	(kJ/kg °K)
-1.55x10 <sup>-4</sup>	0.9982	0.207	9.81x10 <sup>-4</sup>	1.43x10 <sup>-7</sup>	2444	4.1818

Table 8.1. Applicable constants for water near 25 °C.

Table 8.2 lists the Rayleigh, Marangoni, modified Rayleigh, modified Marangoni, Bond, critical Rayleigh, and critical Marangoni numbers for an open tank of water 10-mm in depth  $\delta_s$ . The modified stability values assume no applied temperature gradient,  $\Delta T$ , the temperature gradient only being generated by evaporation.

---

Relative humidity (%)	Evaporation rate (kg/m <sup>2</sup> s)	$Ra^*$	$Ma^*$	$Bo_D$
20.0	6.7E-4	2,000,000	390,000	5.1
30.0	5.9E-4	1,700,000	340,000	5.0
40.0	5.0E-4	1,500,000	290,000	5.2
50.0	4.1E-4	1,200,000	250,000	4.8
60.0	3.3E-4	1,000,000	200,000	5.0
70.0	2.5E-4	700,000	150,000	4.7
80.0	1.6E-4	460,000	104,000	4.4
90.0	7.7E-5	210,000	57,000	3.6
96.0	2.6E-5	54,000	28,000	1.9
97.0	1.5E-5	22,000	22,000	1.0
99.0	8.6E-6	3,400	19,000	0.2
Critical Values (Koschmieder, 1993)				
	$Ra_c$	1100.7		
	$Ma_c$		79.607	

---

Table 8.2. Stability values for a 10-mm deep open tank of water.

Values for modified stability numbers are shown for different relative humidity and evaporation rate values. The evaporation rates in Table 8.2 are estimated from the model presented by Jones et al. (1993), and detailed in equation 2.42. The critical values were taken from Koschmieder (1993).

The traditional and modified stability values presented in Table 8.2 suggest that the air-water interface for the experiments listed in Table 7.1 should be evaporating and unstable. The traditional Rayleigh number, using an estimated temperature gradient exceeds the critical value of  $Ra_c=1100.7$  for a system with a free surface and rigid bottom. The modified Rayleigh numbers, based on the range of 21 to 46 percent relative

humidity of the developmental experiments, varied from  $2 \times 10^6$  to  $1.2 \times 10^6$ . The modified Marangoni numbers varied from  $3.9 \times 10^5$  to  $2.6 \times 10^5$ . Both the modified and traditional Marangoni numbers exceed the critical value of  $Ma_c = 79.607$ .

Table 8.2 indicates that the phenomena listed in Table 7.1 were generated by the Rayleigh-Bénard mechanism rather than the Marangoni mechanism. The dynamic bond numbers,  $Bo_D$ , listed in Table 8.2 were approximately five between 20% to 50% relative humidity. As noted by Neild (1964), a dynamic bond number of four to five indicates that thermally driven circulation are dominated by the Rayleigh-Bénard buoyancy driven flow while the Marangoni surface tension driven flow would be comparatively weak and unobserved.

A comparison of the characteristics and behavior of the thick boundary layer zones to that reported in the literature on Rayleigh-Bénard circulation in water (Spangenburg and Rowland, 1961; Berg et al., 1966a; Theerthan and Arekeri, 1994; Heidel and Knobler, 1998; Yamamura et al., 2003) supports the hypotheses that they are generated by Rayleigh-Bénard circulation. The thick boundary layer zones appear to be similar to those reported by Spangenburg and Rowland (1961). Spangenburg and Rowland imaged the variances in the water density across the surface of an open tank of water with an inverted temperature gradient by applying the Schilleren technique. Spangenburg and Rowland found the presence of dark streaks of dense fluid across the surface in their images. Berg et al. (1966a) observed dark lines in evaporating water where colder, denser fluid was collecting at the surface and flowing towards the bulk of the fluid. The SLIF data does not show bright locations consistent with a counter-current upwelling from the liquid bulk. Berg noted the absence of apparent upwelling zones and

Spangenburg and Rowland noted that water only showed downwelling zones or cold streamers. In Figure 7.8, the dark streaks are moving across the surface in a series of images from data set D32A taken at 32% humidity. In Figure 8.1, we see similar behavior of the dark areas of fluorescence intensity caused by the thick boundary layer zones, moving over a period of time at 63% relative humidity. The movement of the thick boundary layer zones is similar to reports in literature that note the movement of downwelling zones across the liquid (Spangenburg and Rowland, 1961; Theerthan and Arekeri, 1994; Heidel and Knobler, 1998). In Figure 8.2 a series of dimensionless mass transfer coefficient contour plots presents a disordered cell pattern appearing and then disappearing, similar to downwelling zones reported by Berg (1966b) and Yamamura et al., (2003). Only Block (1956) and Anisimova et al. (2001) have seen indications of Marangoni driven circulation in water.

The dark streaks imaged in the SLIF development study, presented in Chapter 7, are downwelling zones created by Rayleigh-Bénard circulations. The Rayleigh- Bénard downwelling zones are where cool, oxygen rich surface liquid collects and returns to the bulk fluid. These appear as areas of high boundary layer thickness, or low dimensionless mass transfer coefficient values within the SLIF data.

## 8.2. Study of mass transfer and atmospheric humidity

A set of SLIF experiments were designed primarily to study evaporation induced Rayleigh-Bénard circulations and their effect upon the mass transfer of oxygen across the air-water interface. The SLIF technique and apparatus allowed for the direct investigation of how thermally driven circulations affect the mass transport of gases into liquids. The data sets produced for the SLIF study of atmospheric humidity and mass transfer are listed in Table 8.3. Table 8.3 lists the data set label, the image set label, the number of images in the set, the lab temperature, the barometric pressure, the atmospheric humidity, the approximate width of the area imaged, the saturated dissolved oxygen concentration ( $Ox'$ ), and comments about the image set. The comments note important details about particular data sets. The saturated oxygen concentration was estimated from the room temperature and barometric pressure, using Table A.2 in Appendix A. Additional information on the data sets presented in Table 8.3 are presented in Table 7.2.

Data set	Image Sets	Temp (°C)	Pressure (inHg)	Relative humidity (%)	Image size (mm)	$Ox'$ (mg/L)	Comments
R27	A-H	22	29.96	27	31.75	8.45	Downwelling
R29	A	24	30.39	29	31.75	8.61	
R61	A	22	29.71	61	31.75	8.82	Ruler
R46	A-D	21	29.70	46	31.75	8.91	
R58	A-E	22	29.71	58	31.75	8.74	Downwelling
R63	A-F	22	29.71	63	31.75	8.82	Downwelling
R91	A-D	23	29.72	91	31.75	8.58	
R96	A-F	23	29.72	96	31.75	8.58	Downwelling

Table 8.3. Data sets for humidity experiments. Data sets are detailed in Table 7.2.

Atmospheric humidity was chosen as the control factor or controlling variable, for the experiment. Atmospheric humidity was found to be the factor with the greatest effect that could easily be controlled. Other factors such as the atmospheric temperature, and atmospheric pressure were more difficult to control and theoretically needed greater ranges to have the same effect in superseding the meta-stable limit.

For the modified stability equations, 8.3 and 8.4, the two ‘driving forces’ are the applied liquid temperature gradient  $\Delta T$  and the evaporation rate,  $\dot{V}$ . For the SLIF apparatus it would have been difficult to remove evaporation from the study and control the instability through an applied temperature gradient. The evaporation rate of water from the surface could be easily controlled by controlling the atmospheric humidity, while the temperature gradient between the surface and the liquid would be harder to control and have the same overall effect on the evaporation rate from the surface. The effect of increasing relative humidity on the evaporation rate, the modified Rayleigh number, the modified Marangoni number and the Bond number for the SLIF wave tank is presented in Table 8.1.

The dynamic Bond number  $Bo_D$  represents the relative ‘strength’ of the Rayleigh-Bénard density mechanism to that of the Marangoni-Bénard surface tension mechanism. A dynamic Bond number greater than one shows that the density driven mechanism should dominate within the fluid while a dynamic Bond number of less than one indicates a liquid where the surface tension driven mechanism should dominate (Neild, 1965). Above 90% relative humidity, the Maragnoni mechanism becomes

stronger in relation to the Rayleigh-Bénard mechanism, as represented by the dynamic Bond number. Most previous investigations of thermal instability in water have found that the Rayleigh-Bénard mechanism usually dominates, as discussed in section 2.4.4.

The rigor of the thermal circulations is represented by the difference between the liquid stability and the meta-stable liquid moment, evaluated in the reduced Rayleigh and Marangoni numbers. The reduced Rayleigh,  $Ra_r$ , and reduced Marangoni numbers,  $Ma_r$ , are presented in equations 8.1 and 8.2,

$$Ra_r^* = Ra^* / Ra_c \quad (8.1)$$

$$Ma_r^* = Ma^* / Ma_c \quad (8.2)$$

where the modified Rayleigh and Marangoni numbers represent the liquid stability and the critical Rayleigh and Marangoni numbers represent the liquid's meta-stable moment.

The relationship between the reduced stability values and the atmospheric humidity are presented in Table 8.4.

Relative humidity	Evaporation rate (kg/m <sup>2</sup> s)	$Ra_r^*$	$Bo_D$
20.0%	6.7E-4	1800	5.1
30.0%	5.9E-4	1500	5.0
40.0%	5.0E-4	1400	5.2
50.0%	4.1E-4	1100	4.8
60.0%	3.3E-4	910	5.0
70.0%	2.5E-4	640	4.7
80.0%	1.6E-4	420	4.4
90.0%	7.7E-5	190	3.6
96.0%	2.6E-5	49	1.9
97.0%	1.5E-5	20	1.0
99.0%	8.6E-6	3.1	0.2

Table 8.4. Reduced Rayleigh numbers for a 10-mm deep open tank of water.

Table 8.4 indicates that circulations occurring at a lower relative humidity should have more rigorous circulation.

### 8.2.1. Example SLIF data from evaporation and oxygen mass transfer experiments

Figures 8.3 through 8.8 are sample dimensionless mass transfer contour plots for the six data sets that the SLIF humidity study generated. The factors of lab temperature, barometric pressure and relative humidity are listed for Figures 8.1 thru 8.6 in Table 8.5.

Figure	Image label	Room temp (°C)	Barometric pressure (inHg)	Relative humidity (%)
8.3	R27D_23	22	29.96	27
8.4	R46A_31	21	29.70	46
8.5	R63D_30	22	29.71	63
8.6	R58C_96	23	29.71	58
8.7	R91C_41	23	29.72	91
8.8	R96A_96	23	29.72	96

Table 8.5. List of example images for data sets listed in table 8.2.

### 8.2.2. Results, SLIF study of atmospheric humidity and oxygen mass transfer

The SLIF study of flat interfaces under varying atmospheric humidity examined the behavior of Rayleigh-Bénard circulations and how the behavior of the Rayleigh-Bénard circulations affected the mass transfer across the air-water interface. The effect of humidity on behavior of the circulation cells was examined through the frequency of appearance of the downwelling zones, the initial appearance time of the downwelling zones, the width of the downwelling zones, and the speed of movement of the downwelling area within the imaging area. The effect of humidity on the relative mass transfer across the surface was examined by observing changes in the dimensionless mass transfer rates across the downwelling zones compared to the dimensionless mass transfer rates across the remaining surface.

Table 8.6 illustrates the frequency of the downwelling cells for each image set. In Table 8.6, the relative humidity, number of viable images, number of images with downwelling, frequency and the initial appearance time are presented for the six data sets. The viable image term represents the number of data images without serious defects due to poor illumination for that data set. The downwelling image number is the number

of images within the data set that a downwelling zone appears. The frequency is given as a percentage of the total number of viable images in which downwelling appears. All of the images are presented in Appendix C.

Data set	Relative humidity	Number of viable images	Number of images with downwelling	Frequency	Initial appearance time
	(%)	(#)	(#)	(%)	(sec)
R27	27	103	103	100	20
R46	46	130	0	0	--
R58	58	169	23	14	608
R63	63	136	54	40	510
R91	91	90	0	0	--
R96	96	125	5	4	3210

Table 8.6. Frequency and start times for humidity study data sets.

Figure 8.9 illustrates the frequency of the data sets over the time from the start of SLIF image capture. Figure 8.10 illustrates the relationship between humidity and frequency. Figures 8.9 and 8.10 show the rather complex nature of the frequency of the downwelling zones to the atmospheric humidity.

Figure 8.11 illustrates the relationship between the initial appearance time for downwelling and the relative humidity. The start times show an logarithmic relationship to the increasing atmospheric humidity. The relationship between initial appearance time and atmospheric humidity indicates a relationship between the evaporation rate and the liquid stability. For lower evaporation rates, the time for a destabilizing temperature gradient to form at the surface becomes longer, therefore the time for appearance of downwelling zones will also increase.

The average, maximum, and minimum values for the width of the downwelling zone are presented in Table 8.7.

Data set	Relative humidity (%)	Average width (mm)	Minimum width (mm)	Maximum width (mm)
R27	27%	1.59	0.87	2.17
R46	46%		(no downwelling observed)	
R63	63%	1.96	1.40	2.54
R58	58%	1.90	1.22	2.36
R91	91%		(no downwelling observed)	
R96	96%	1.01	0.93	1.12

Table 8.7. Width measurements for data sets of the evaporation and oxygen mass transfer study

In Table 8.7 the width reported is the width at half maximum described in section 5.3. The half maximum width is calculated by the data analysis subroutines described in section 5.3.4. Figure 8.12 illustrates a width measurement for an idealized cross section. Figure 8.13 illustrates the same measurements on a cross section of SLIF data.

Figure 8.14 illustrates the relationship between humidity and the average width. There does not appear to be any discernable relationship between relative humidity and the width of the downwelling zones. Although the initial three sets show a linear trend with increasing width with increasing humidity, the fourth set has the narrowest downwelling zone width recorded. Further there is no apparent relationship between the width of the downwelling zone and the time of the experiment as shown in Figure 8.15. In Figure 8.15 the half maximum width values for the downwelling zones appear to vary

from 1 mm to 2.5 mm over the 4,500 seconds of images captured. Figure 8.16 shows the same relationship as Figure 8.15, but considers the time after the appearance of downwelling rather than the end of sparging.

Figure 8.17 illustrates the relationship between the width and the normalized dimensionless mass transfer coefficient of the downwelling. In Figure 8.17 the sampled data shows no relationship between the width of the downwelling and the dimensionless mass transfer coefficient.

Table 8.8 illustrates the relationship between humidity and rate of movement downwelling zones across the surface. The rate of movement of the downwelling zones was estimated between images using the displacement of several points along the downwelling zone between successive images and dividing by the approximate time difference between the images. Table 8.8 details the average rate of movement for each data set that contains downwelling zones, the minimum rate of movement for each data set, and the maximum rate of movement of each set.

Data set	Relative humidity	Avg. rate of movement	Min rate of movement	Max rate of movement
Label	(%)	(mm/min)	(mm/min)	(mm/min)
R27	27%	1.1	0.0	4.2
R58	58%	1.4	0.6	5.9
R63	63%	4.8	0.1	12
R96	96%	7.1	3.5	12.5

Table 8.8. Comparison of downwelling movement speed to relative humidity.

The rate of movement of the downwelling zones versus relative humidity is shown in Figure 8.18. Although the average rate of movement appears to increase with

increasing relative humidity, the overlap of the ranges is substantial. Further, there is a large difference in the average movement rates recorded at 58% relative humidity and 63% relative humidity, while there is only a small difference in the movement rates from 27% to 63% relative humidity.

The rate of movement of downwelling zones over time for each of the four sets is shown in Figure 8.19. There is no discernable pattern to the rate of movement of the downwelling zones over the duration of the experiments.

Table 8.9 details the humidity study results in terms of mass transfer. Table 8.9 lists the average values of the dimensionless transfer coefficients for both the upwelling and downwelling areas, and the standard deviation of the dimensionless mass transfer coefficients. Figure 8.20 illustrates the changes in dimensionless mass transfer coefficient values of the downwelling zones over time. Figure 8.21 illustrates the relationship between relative humidity and the dimensionless mass transfer coefficients for the downwelling area.

Relative humidity	Image label	Reduced Rayleigh number $Ra/Ra_c$	Dimensionless mass transfer coefficient upwelling $k_u^*$		Dimensionless mass transfer coefficient downwelling $k_{dw}^*$	
			Average	Standard Deviation	Average	Standard deviation
27%	R27	1641	1.03	0.011	0.882	0.118
46%	R46	1204	1.02	0.011		
58%	R58	928	0.99	0.012	0.905	0.095
63%	R63	812	1.00	0.011	0.900	0.100
91%	R91	168	0.99	0.011		
96%	R96	53	0.99	0.029	0.955	0.045

Table 8.9. Dimensionless mass transfer coefficient values for SLIF data

### 8.3. Discussion of evaporation induced thermal circulations

The first application of the SLIF system was to study the effects of evaporation induced thermal circulation on oxygen mass transfer by varying the atmospheric humidity. The study of evaporation induced Rayleigh-Bénard circulation provides insight into the behavior of Rayleigh-Bénard circulations in water and their effect on oxygen mass transfer. In many situations, an unperturbed open tank of liquid would be treated as a stagnant fluid (Thibodeaux, 1996), and the mass transfer model applied would be the Whitmann model (Eq. 2.14). In section 7.2, dark streaks found within SLIF data of flat, unperturbed were attributed to being areas of high oxygen concentration generated by thermal circulations. In this situation, the unperturbed liquid was not quiescent as was usually assumed. In Chapter 8 we examine the effect of atmospheric humidity and time on Rayleigh-Bénard circulations in water and how Rayleigh-Bénard circulations affect the mass transfer across the air-water interface.

#### 8.3.1. Atmospheric humidity and thermal circulation.

The humidity experiments described in section 8.1.1 investigated quantifiable characteristics of thermal circulations in water and how changes in the controlling variable, atmospheric humidity, affected these characteristics. Downwelling zones are the most identifiable feature of thermally driven circulations and are utilized throughout the literature as the basis for analysis of thermally driven circulations. The traditional quantitative parameters in for the study of thermally driven circulations were cell size and cell shape. Cell size,  $\lambda$ , of thermally driven circulation is focused upon in traditional

studies since it can be directly related to the solutions of the mathematical models, such as equation 2.32. However, thermally driven circulation in water does not form a regular, or rigid, cell structure, as discussed in sections 2.2.4. Therefore, non-traditional measures for the dynamics of cell circulation were chosen: downwelling zones observed frequency, time of initial detection movement speed, and downwelling zone width. The observed frequency is the amount of time that the SLIF system captured a downwelling zone during an experiment. The downwelling zone movement speed is the rate that the downwelling moves across the surface as measured from consecutive images. The width is defined by the half maximum width as discussed in the proceeding section.

The downwelling frequency appears to decrease with increasing humidity. However the results are too erratic to make any real determination. The frequency of the downwelling zones is strongly influenced by the ‘rough’ cell size and the movement of the downwelling zones. The rough cell size of the downwelling zones is the average distance between roughly parallel downwelling zones that define a ‘cell’. The rough cell size may be significantly larger than the SLIF imaging area of 31.75mm. Further, the speed of movement of the cell likewise affects the frequency by determining the ‘residence’ time of a downwelling zone in, and out, the SLIF imaging area.

The erratic results for downwelling frequency are illustrated by data sets R27, and R43. Both data sets image flat surfaces under low atmospheric humidity, at 27% and 43% respectively. But the R27 data set has an apparent downwelling frequency of 100% versus the R43 data set having an apparent downwelling frequency of 0%. The difference in frequency could be explained by the size of the SLIF imaging area and the rate of downwelling movement. In Table 8.7, the average speed at low at low

atmospheric humidity was found to be 1.1 mm/min. At that rate of movement, it would take 25 minutes for a downwelling zone to cross the distance of 24.5 mm. If one of the 'rough' cell dimensions was greater than three inches, the ability to capture one of the two downwelling zones within 50 minutes would be less than 50%.

An increase in the time of appearance of the downwelling zones appeared to relate to an increase in the relative humidity. Figure 8.11 illustrates the relationship between the initial appearance of downwelling and the atmospheric humidity. The increasing appearance time for downwelling zones can be explained by the increasing time for the liquid to achieve a critical temperature gradient,  $\Delta T_c$ . The critical temperature gradient is defined as the minimum temperature gradient needed to achieve the critical Rayleigh or Marangoni value. As the relative humidity above the liquid surface increases, the evaporation rate  $\dot{V}$  decreases as does the rate of heat loss due to evaporation,  $\dot{V}h_v$ . Since the rate of heat loss decreases, the time for system to surpass the critical point also increases.

There appears to be no relationship between the width of the downwelling zone and the relative humidity. The width, or half max width, of the down-welling zones appears to vary from approximately 0.7 mm to 2.25 mm, as presented in Figure 8.14. Figure 8.14 shows that the variance in downwelling thickness at first increases, and then decreases with increasing humidity. Figure 8.15 illustrates the lack of any apparent relationship between the start time of the experiment and the width of the downwelling zones. Figure 8.14 shows no relationship between the downwelling zone width and the

initial appearance time. Examining the relationship between the measured width and the dimensionless mass transfer coefficient, Figure 8.17, demonstrates that there is no discernable relationship between the two.

The rate of movement of the downwelling zones across the surface appears to have no relationship with increasing humidity. As shown in Figure 8.22 the downwelling zones change shape as they move. However, a general rate of movement can be calculated by measuring certain points along the zones over each sequential image. Table 8.7 lists the controlled humidity data sets, the relative humidity of the sets, the average rate of movement found within the sets, and the minimum and maximum movement rate for each set. The average rate of downwelling movement versus the relative humidity is shown in Figure 8.18. The range of rate of movement at both 30% humidity and 63% humidity were relatively close. However, the range of the rate of movement recorded at 65% relative humidity was much greater. The measured rate of downwelling movement over time for all of the data sets is shown in Figure 8.19. The rate of movement of the downwelling appeared to be independent of time in the three available data sets. These results support the theory that the movement of the downwelling zones across the surface is independent of the evaporation rate of liquid from the surface. First, the rate of movement appeared to be independent of the atmospheric relative humidity. Second, the rate of movement appeared to be independent of time in each set.

The thermal circulations imaged by the SLIF technique appeared to be solely Rayleigh-Bénard circulations. For most of the experiments described in Table 8.3 the Rayleigh-Bénard mechanism was going to dominate based on the dynamic Bond number,

$Bo_D$ . As noted by Neild (1964), a dynamic bond number of four to five indicates that any thermally driven circulation will be dominated by the Rayleigh-Bénard mechanism while the Marangoni mechanism would be comparatively weak and unobserved. Referring to Table 8.2, only the experiments occurring with an atmospheric humidity greater than 90% relative would we expect the Maragnoni mechanism to become stronger in relation to the Rayleigh-Bénard mechanism. There is no indication that the downwelling zones imaged at 96% relative humidity were any different that those captured at lower relative humidity rates. Previous investigations of thermal instability in water have found that the Rayleigh-Bénard mechanism usually dominates, as discussed in section 2.4.4. Only Block (1956) and Anisimova et. al. (2001) have reported indications of Marangoni driven circulation in water. Therefore it is most likely that the few downwelling zones captured at 96% relative humidity were generated by Rayleigh-Bénard circulations.

### 8.3.2. Rayleigh-Bénard effects on oxygen mass transfer

We investigated the effect that the Rayleigh-Bénard circulations caught within the SLIF imaging area had on the mass transfer rates of oxygen across the surface. The dimensionless mass transfer coefficient for the downwelling zones,  $k_{dw}^*$ , is a good gauge of the effect of circulation on the mass transfer across the surface. By examining the behavior of the dimensionless mass transfer coefficient for the downwelling zones we found that the effect of Rayleigh-Bénard circulations on the air-water mass transfer trends with the reduced Rayleigh term,  $Ra/Ra_c$ .

Rayleigh-Bénard circulations affect the rate of mass transfer across the air water interface by inducing liquid side mass transport beneath the liquid surface. The current theory of Rayleigh-Bénard circulation is that the upwelling of the warm liquid occurs across the surface of the liquid while the cold liquid is returned to the bulk via the downwelling plumes. The contour plots of dimensionless mass transfer coefficients indicate that the surface area is nearly identical in mass transfer resistance and boundary layer thickness except where there is downwelling. Downwelling zones are marked by a sharp decrease in the values of dimensionless mass transfer coefficients compared with the upwelling areas that mark the rest of the surface. A cross section of a dimensionless mass transfer contour plot is shown in Figure 8.23.

From the model of Rayleigh-Bénard circulation, presented in Figure 8.24, we can generate a few basic concepts about mass transfer under Rayleigh-Bénard circulation, and demonstrate that the dimensionless mass transfer coefficient of the downwelling zone  $k_{aw}^*$  is a good measure of how much mass transfer is occurring due to convection. As theory holds, fluid from the bulk liquid flows through the upwelling zone and into the downwelling zone. As it does this it will ‘pick up’ oxygen from the near surface of the liquid and convectively transfer it to the downwelling zone. The maximum boundary layer thickness possible at the upwelling zone  $\delta_u$  is the diffusive boundary layer thickness  $\delta_{diff}$  since a diffusive boundary layer represents the lowest mass transfer rates and the highest mass transfer resistance possible. If the upwelling zone boundary layer thickness is completely diffusive, then the thickness of the concentration gradient under the downwelling zone  $\delta_{dw}$  that is greater than the diffusive layer  $\delta_{diff}$  represents the

excess oxygen transferred to the liquid due to convection. In the case that the upwelling boundary layer thickness is less than the diffusive layer thickness, the concentration gradient less the upwelling gradient represents the excess oxygen transferred to the liquid due to convection.

The changes in the dimensionless mass transfer coefficient values for the downwelling zone over time are shown in Figure 8.20. The dimensionless mass transfer coefficient values for downwelling zones form are roughly equivalent for most of the images, but then begin to approach the values for upwelling near 4000 seconds, or approximately an hour. This at first glance appears to be similar to results reported by Woodrow (2001), who noted a fairly flat ‘plateau’ of values for the boundary layer thickness after a few minutes. However, Woodrow did not go to over an hour of image capture time in his flat interface study. Additionally it is impossible to differentiate this data from the humidity data since the few data points of lower value occurred at high atmospheric humidity. We would expect for the dimensionless mass transport values at the downwelling and upwelling to approach each other as the bulk oxygen concentration increases. As such, a decrease in the difference between these two dimensionless mass transport values represents the oxygenation of the liquid rather than a decrease in circulation.

The changes in the average dimensionless mass transfer coefficient value for the downwelling zones over time are shown in Figure 8.21. The dimensionless mass transfer coefficient values for downwelling zones increase with increasing humidity. This behavior is consistent with decreasing convective mass transfer due to decreasing rigor of the Rayleigh-Bénard circulation beneath the surface. Figure 8.25 presents the same data

in terms of the reduced Rayleigh number,  $Ra/Ra_c$ , which is typically considered to be the measure of the strength, or rigor, of the Rayleigh-Bénard circulation. Figure 8.25 shows decreasing values for the dimensionless mass transfer coefficient of the downwelling zone compared as the reduced Rayleigh number increases. The relationship demonstrates that as the strength of the Rayleigh-Bénard circulation increases the oxygen mass transfer rate also increases.

Chapter 8 figures

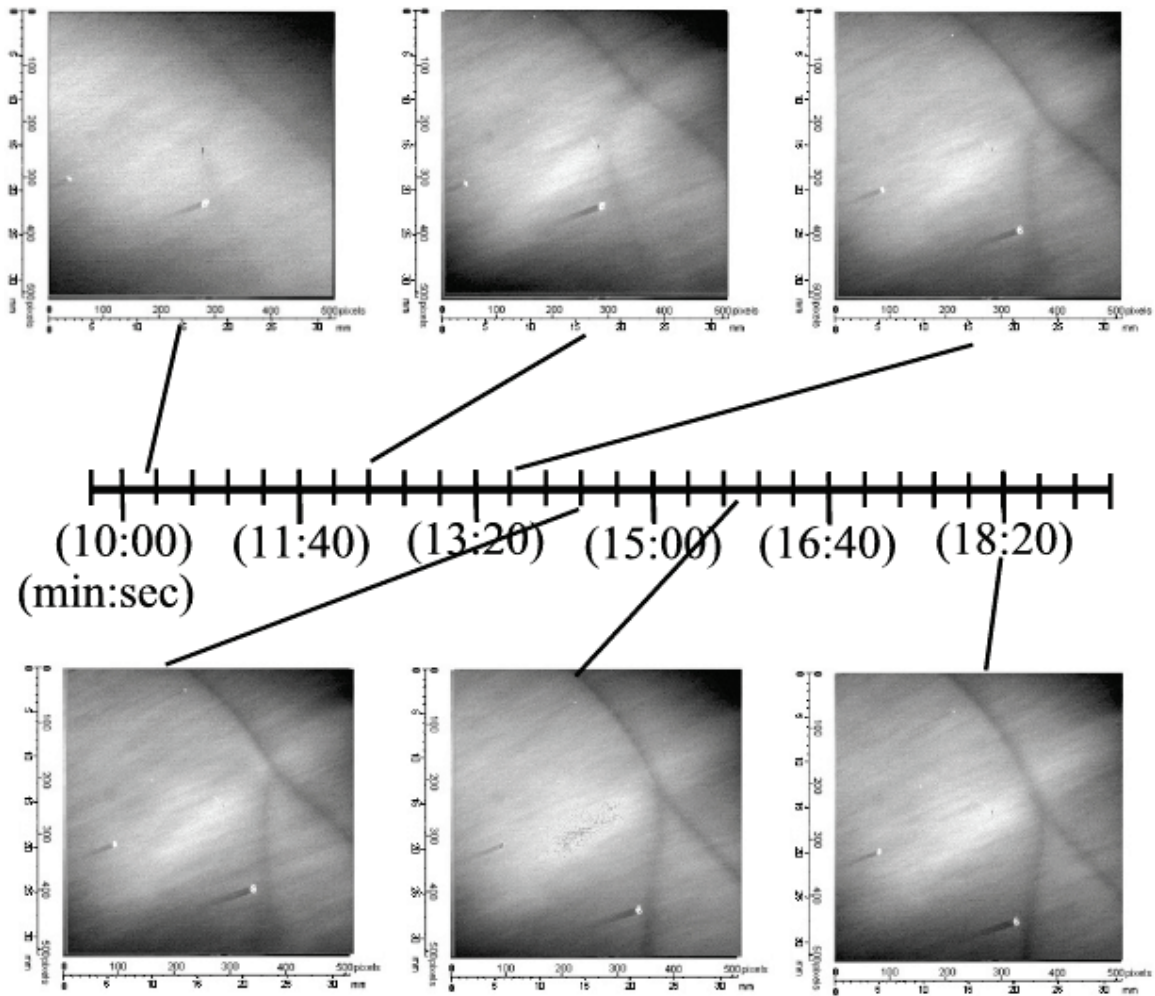


Figure 8.1. Intensity images from data set R63; temperature 21.5 °C, pressure 29.71 inHg, humidity 63%, size 31.75 mm. The series of images show dark streaks combining over time.

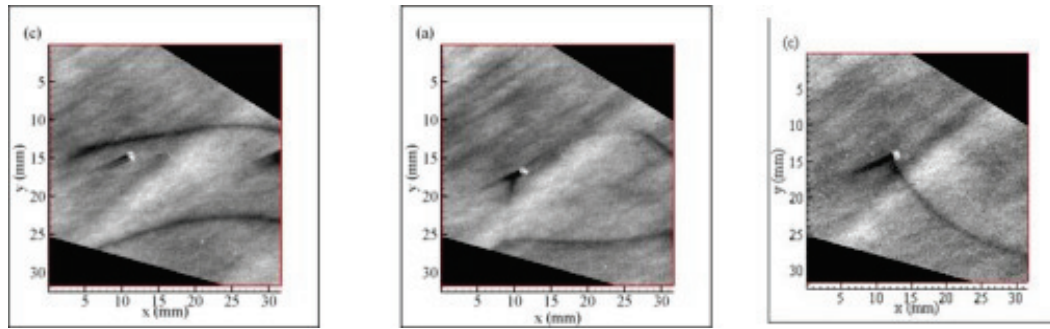


Figure 8.2. Dimensionless mass transfer coefficient plots from data set R27; temperature 22 °C, pressure 29.96 inHg, humidity 27%, size 31.75 mm. The images illustrate cell formation and destruction from image set R27.

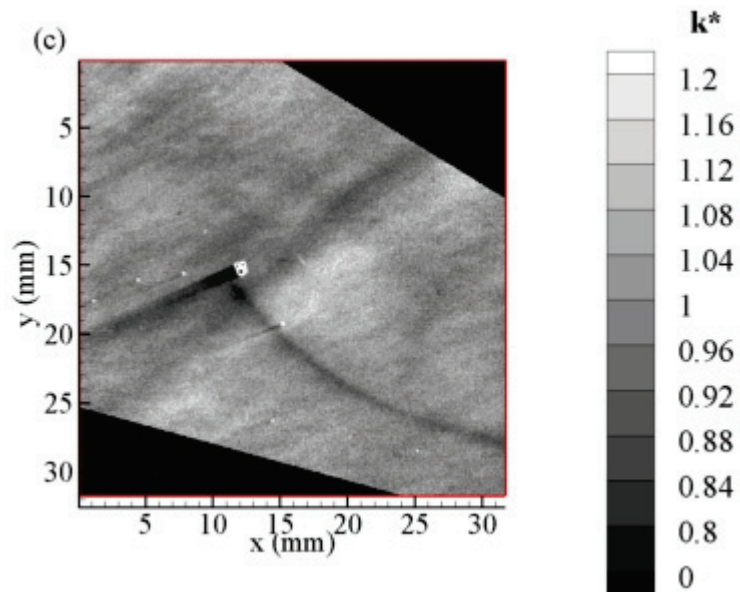


Figure 8.3. Grayscale plot of dimensionless mass transfer coefficient values for the image R27D\_23; temperature 22 °C, pressure 29.96 inHg, humidity 27%, size 31.75 mm.

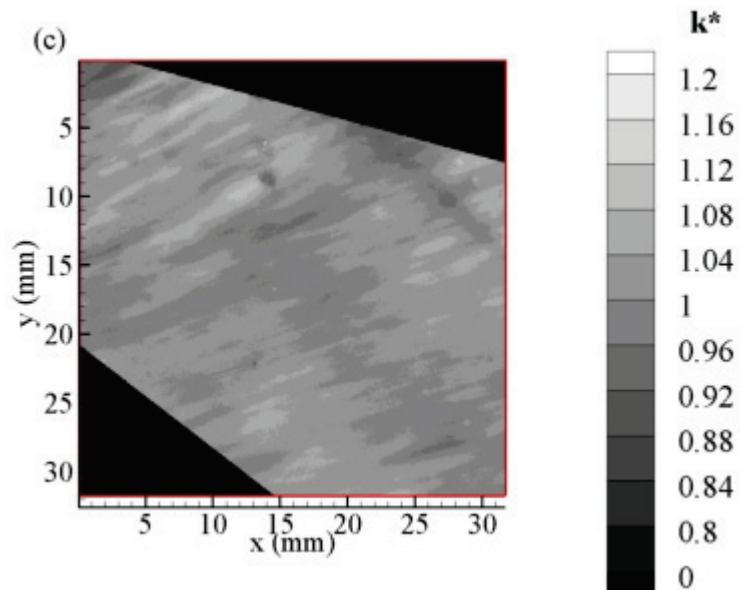


Figure 8.4. Grayscale plot of dimensionless mass transfer coefficient values for the image R46A\_31; temperature 21.0 °C, pressure 29.70 inHg, humidity 46%, size 31.75 mm.

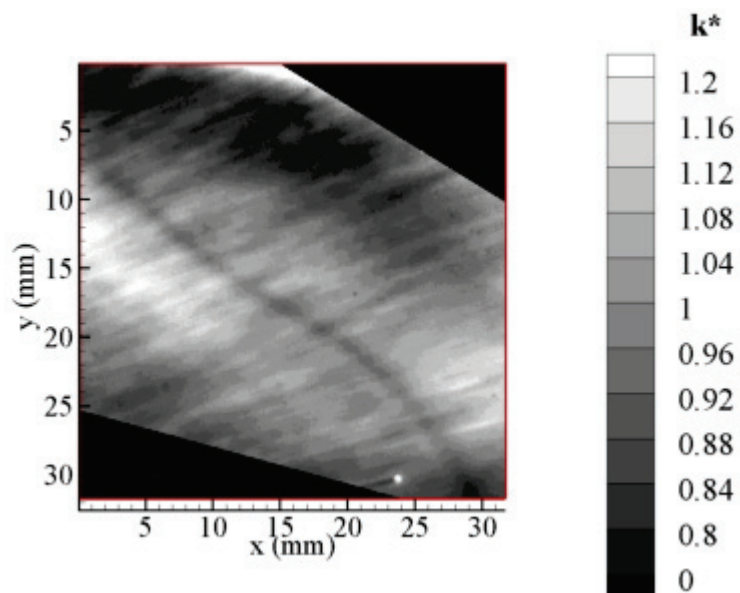


Figure 8.5. Grayscale plot of dimensionless mass transfer coefficient values for the image R58C\_86; Temperature 22.0 °C, pressure 29.71 inHg, humidity 58%, size 31.75 mm.

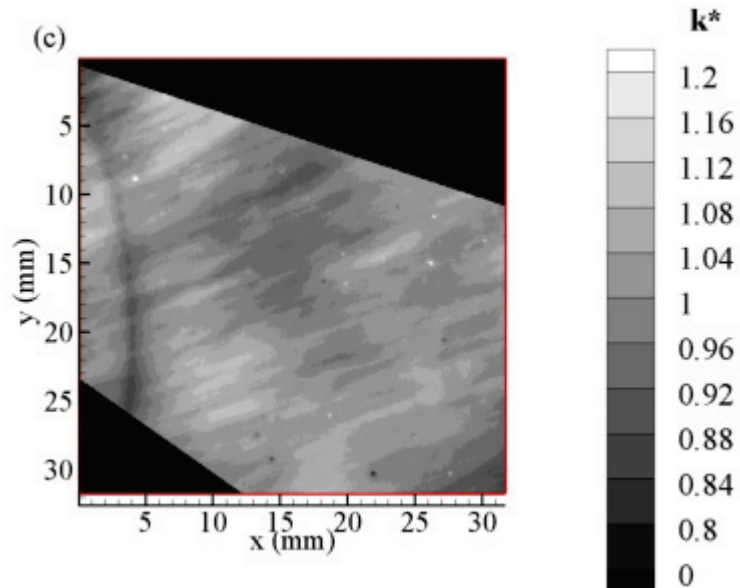


Figure 8.6. Grayscale plot of dimensionless mass transfer coefficient values for the image R63D\_30; temperature 21.5 °C, pressure 29.71 inHg, humidity 63%, size 31.75 mm.

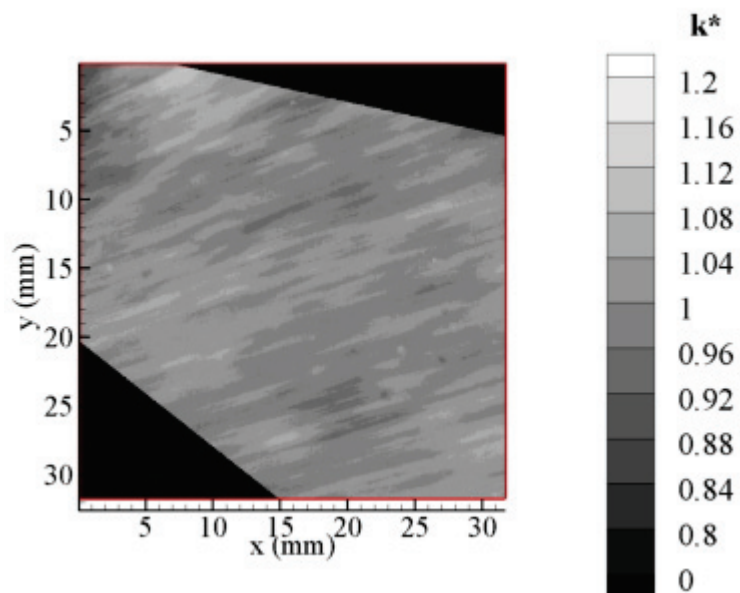


Figure 8.7. Grayscale plot of dimensionless mass transfer coefficient values for the image R91C\_41; temperature 21.0 °C, pressure 29.72 inHg, humidity 91%, size 31.75 mm.

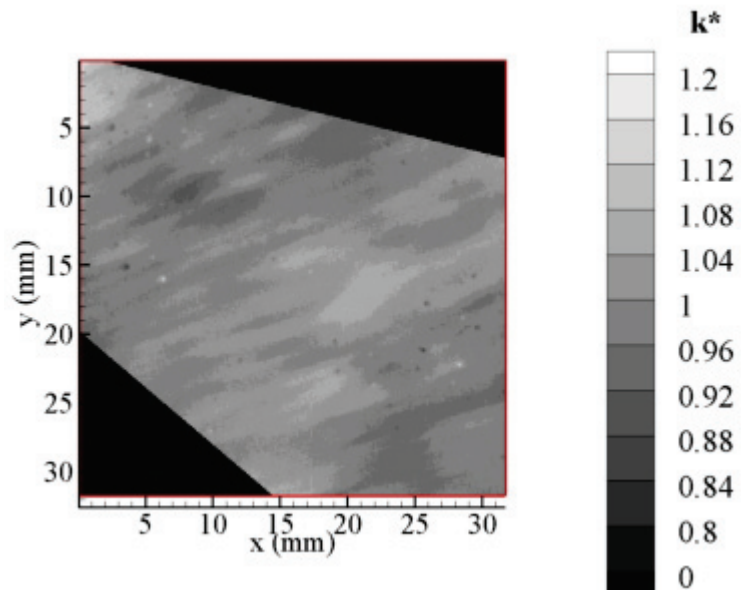


Figure 8.8. Grayscale plot of dimensionless mass transfer coefficient values for the image R96A\_96; temperature 22.0 °C, pressure 29.72 inHg, humidity 96%, size 31.75 mm.

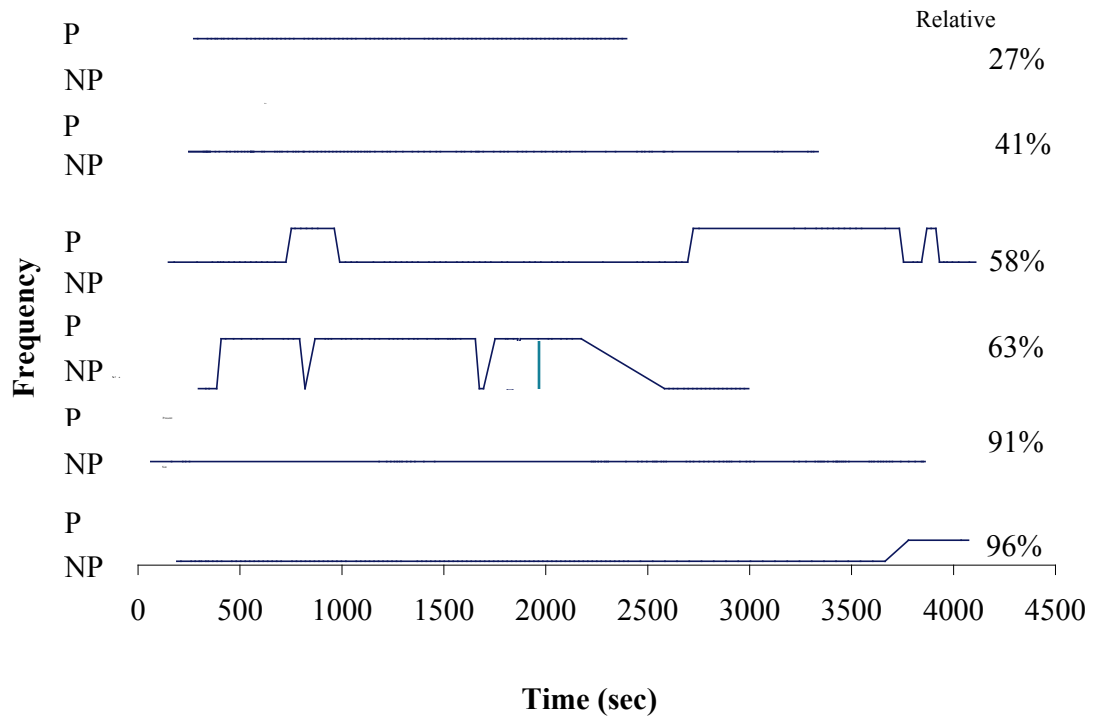


Figure 8.9. Plot of downwelling frequency within all image sets for relative humidity from 27% to 96%. P indicates downwelling present while NP indicated downwelling not present.

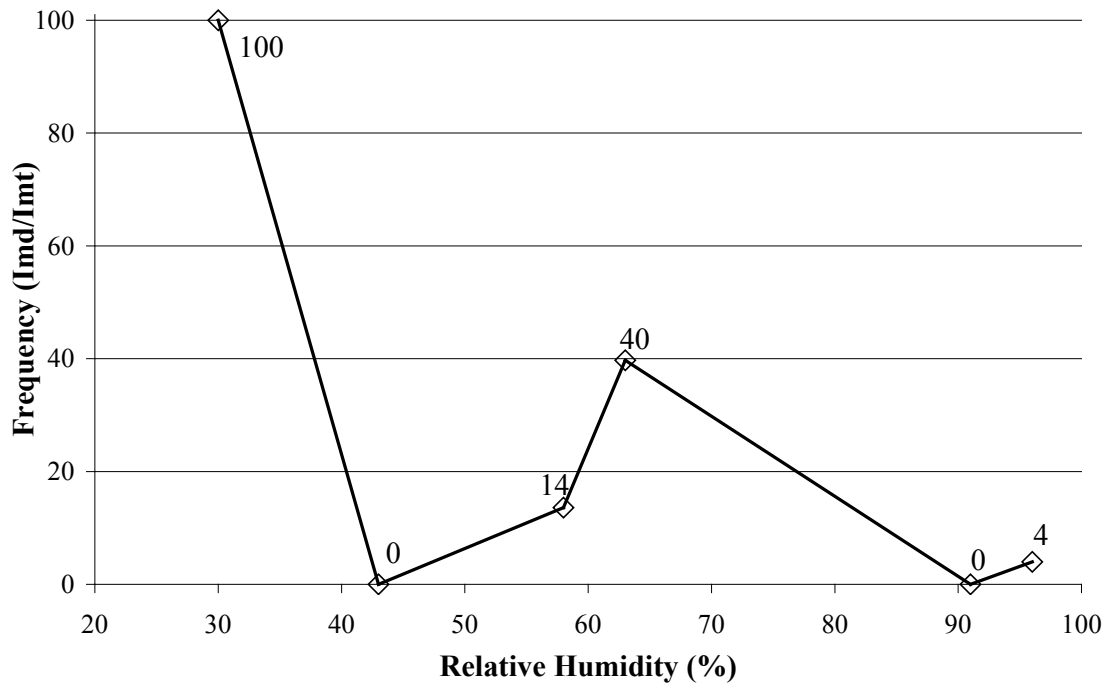


Figure 8.10. Plot of overall downwelling frequency with to relative humidity. Imd is the number of images within the data set with downwelling; Imt is the total number of images in the data set.

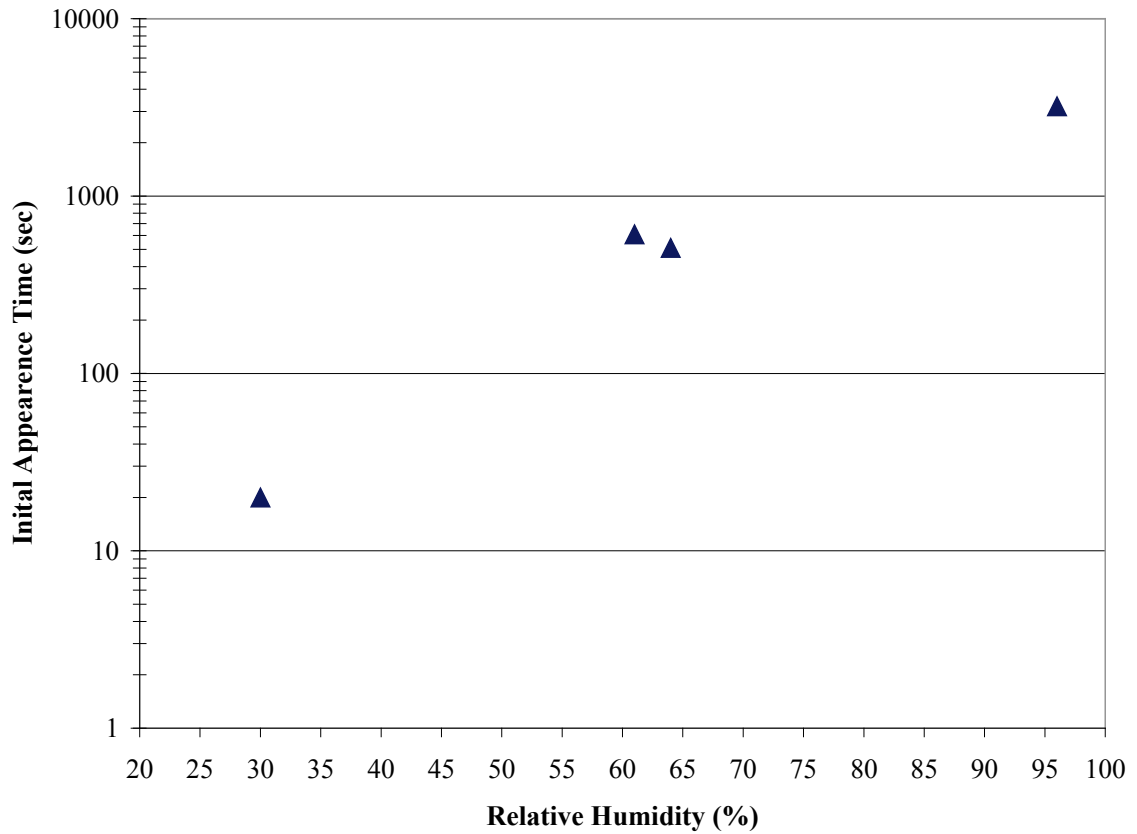


Figure 8.11. Plot of initial appearance time versus relative humidity for humidity levels of 27%, 58%, 63% and 96%.

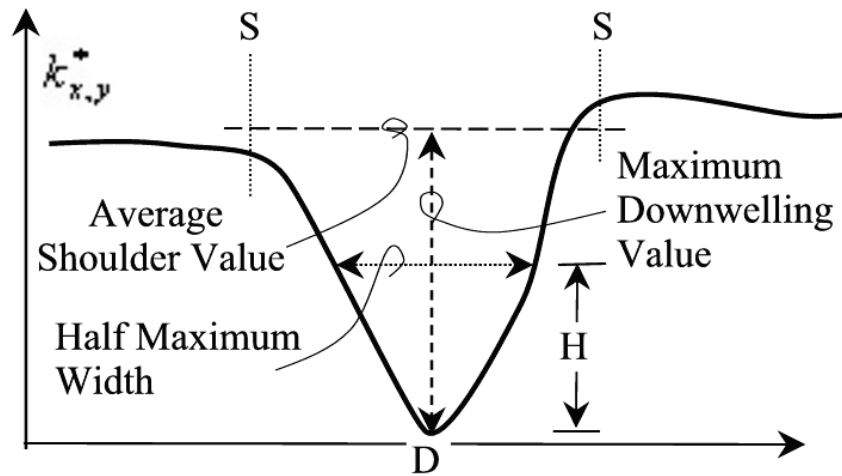


Figure 8.12. Idealized dimensionless mass transfer value cross section illustrating downwelling parameters.

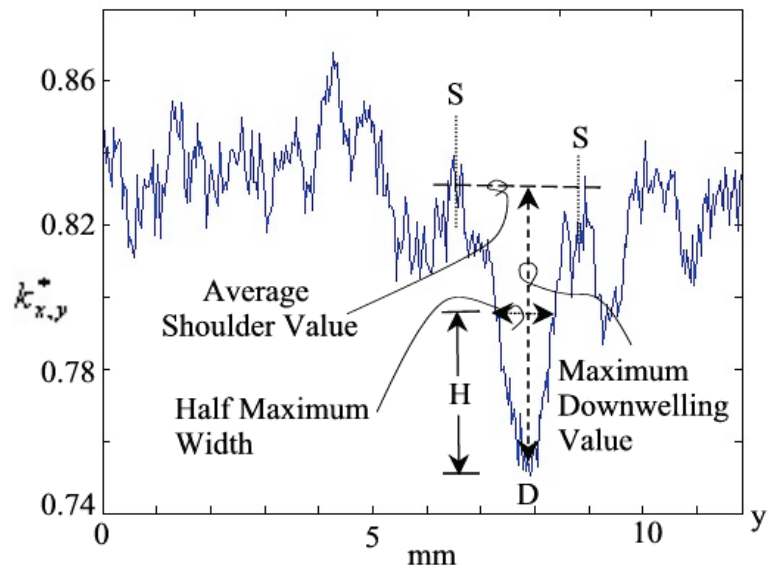


Figure 8.13. Cross-section of R63E\_92 at x=200; Temperature 21.5 °C, pressure 29.71 inHg, humidity 63%, width 31.75mm.

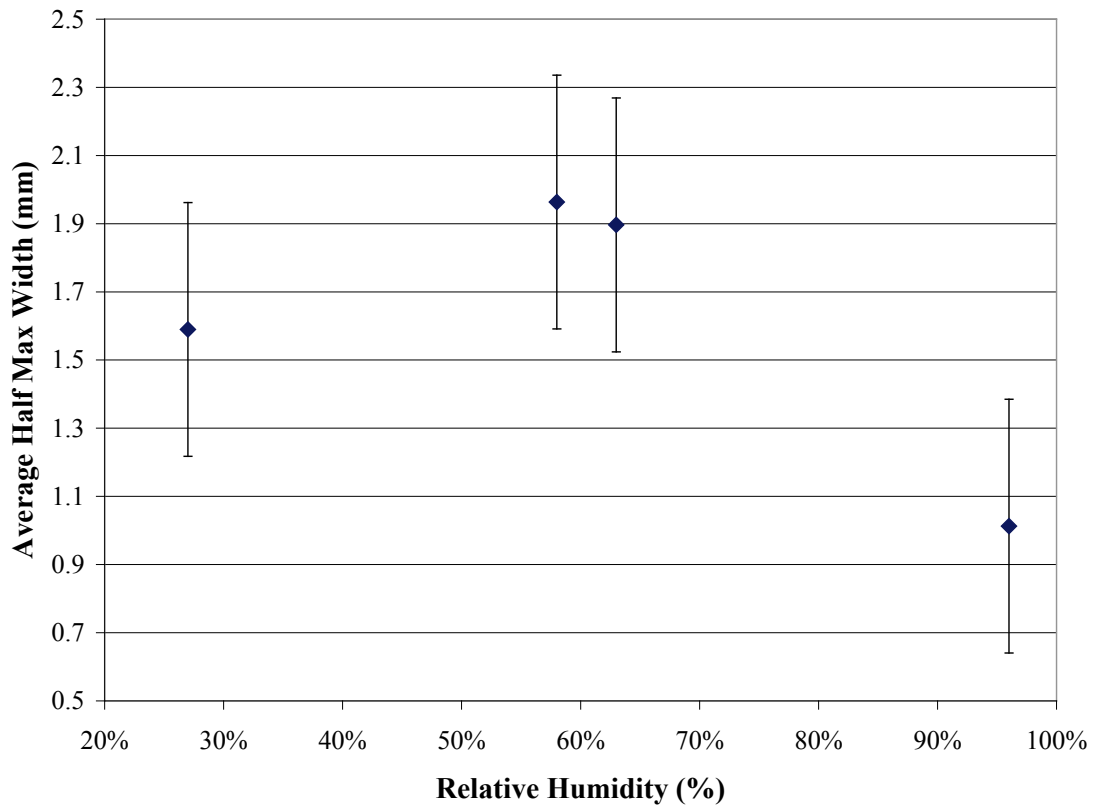


Figure 8.14. Average downwelling width versus humidity for humidity levels of 27%, 58%, 63% and 96%.

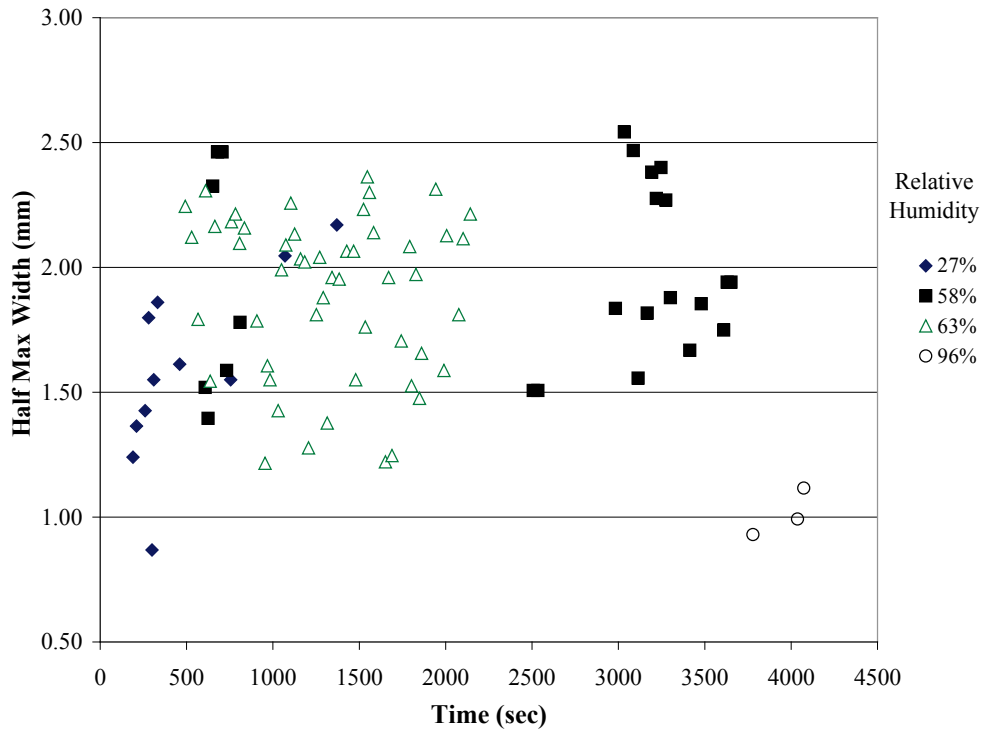


Figure 8.15. Average downwelling width over time from start of experiment for humidity levels of 27%, 58%, 63% and 96%.

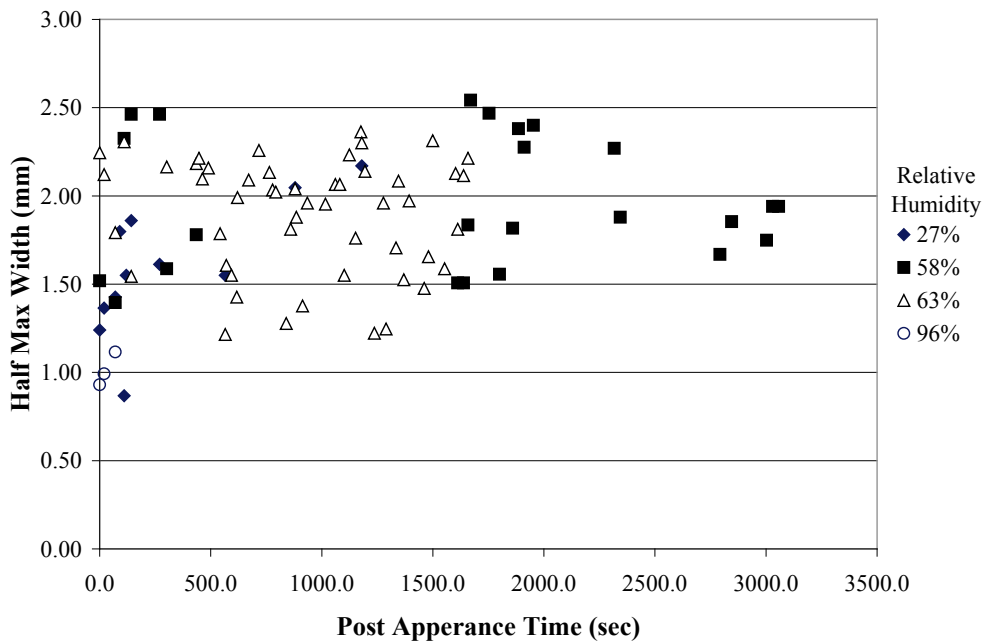


Figure 8.16. Average downwelling width over time from initial appearance, post appearance time of downwelling for humidity levels of 27%, 58%, 63%, and 96%.

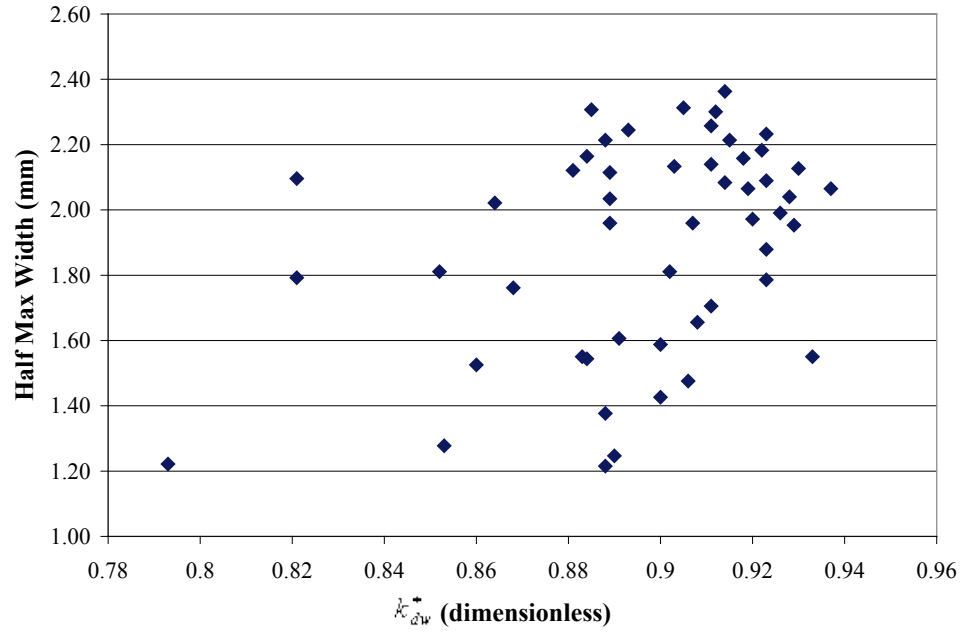


Figure 8.17. Comparison of average dimensionless mass transfer value of the downwelling zone to the width of the downwelling zone for humidity levels of 27%, 58%, 63%, and 96%.

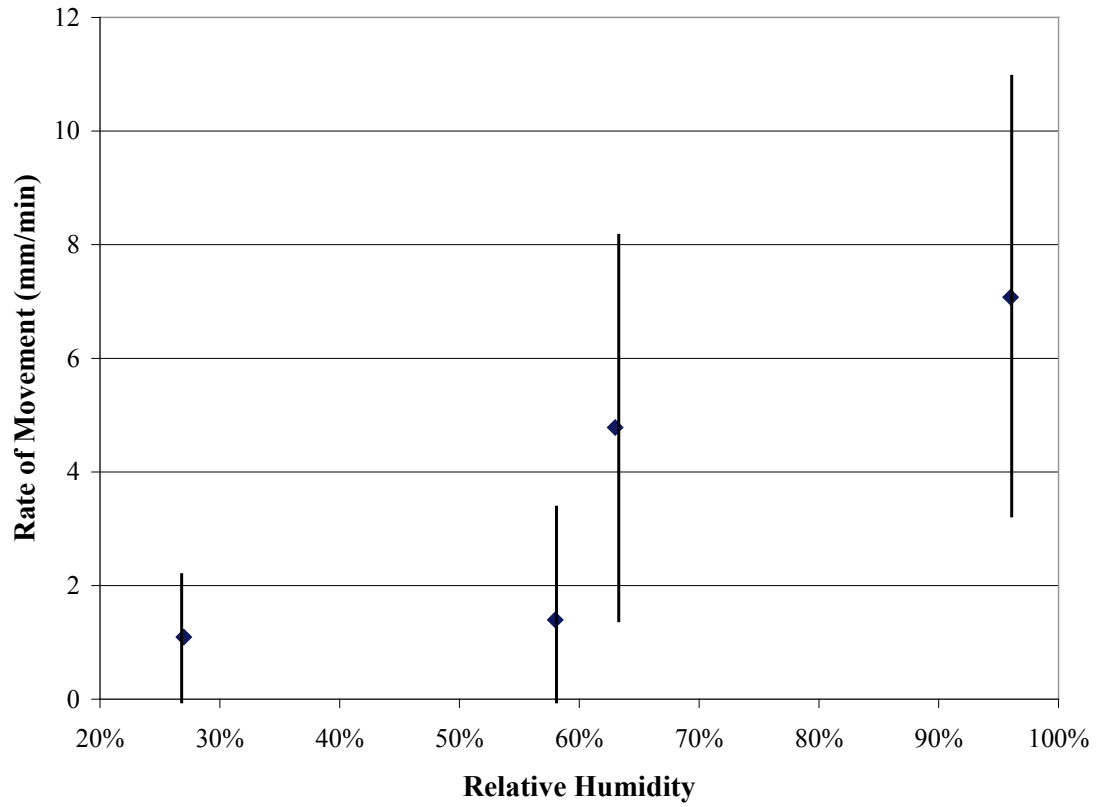


Figure 8.18. Comparison of average rate of downwelling movement to the relative humidity for humidity levels 27%, 58%, 63% and 96%.

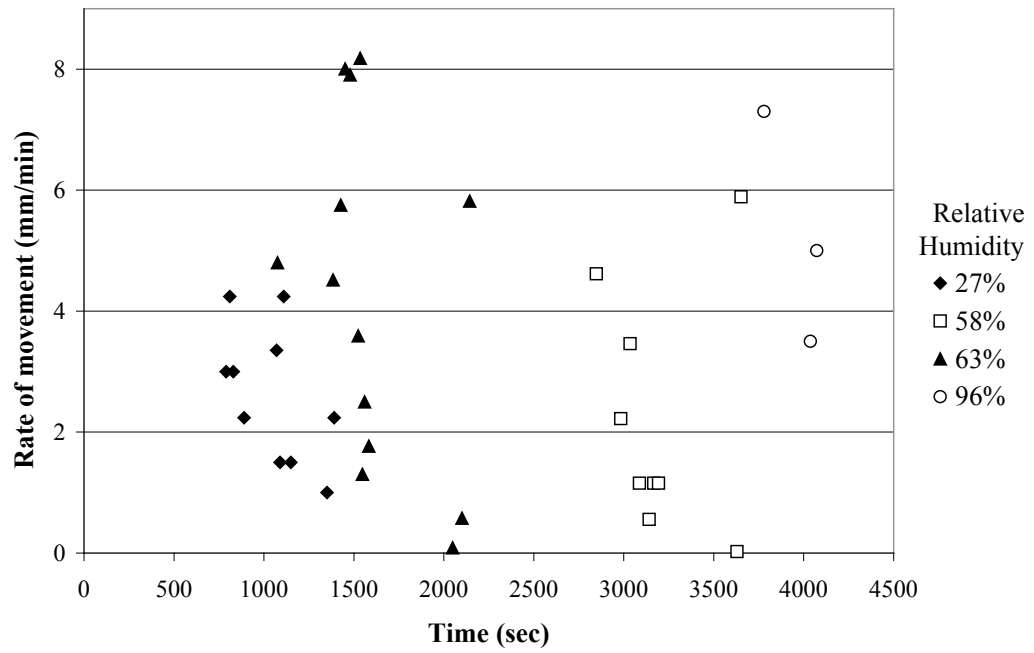


Figure 8.19. Rate of downwelling movement over time for humidity levels of 27%, 58%, 63% and 96%.

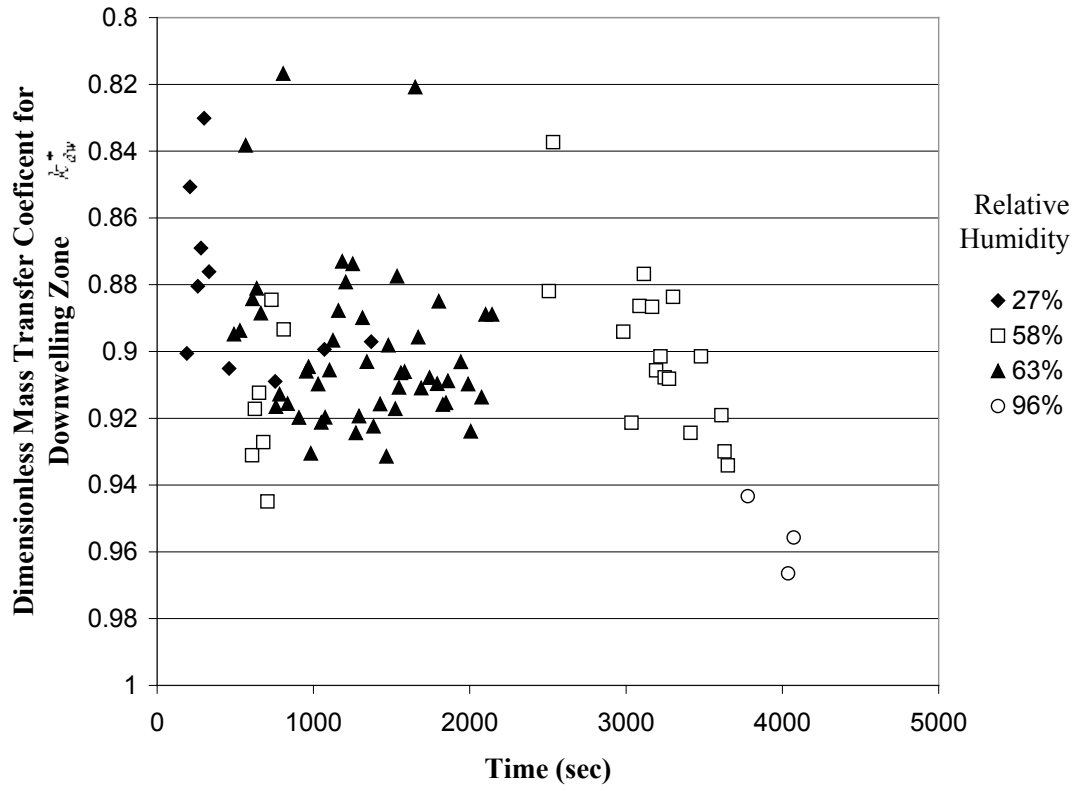


Figure 8.20. Dimensionless relative mass transfer coefficient values for downwelling areas over time for humidity levels of 27%, 58%, 63%, and 96%.

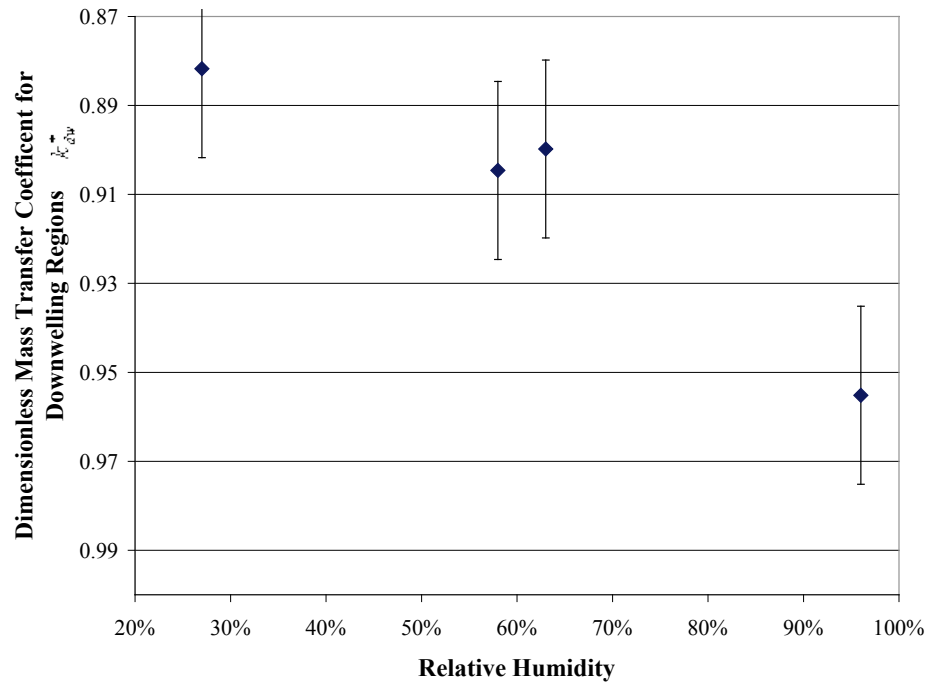


Figure 8.21. Average dimensionless relative mass transfer coefficient values for downwelling areas over relative humidity from 27 to 96%.

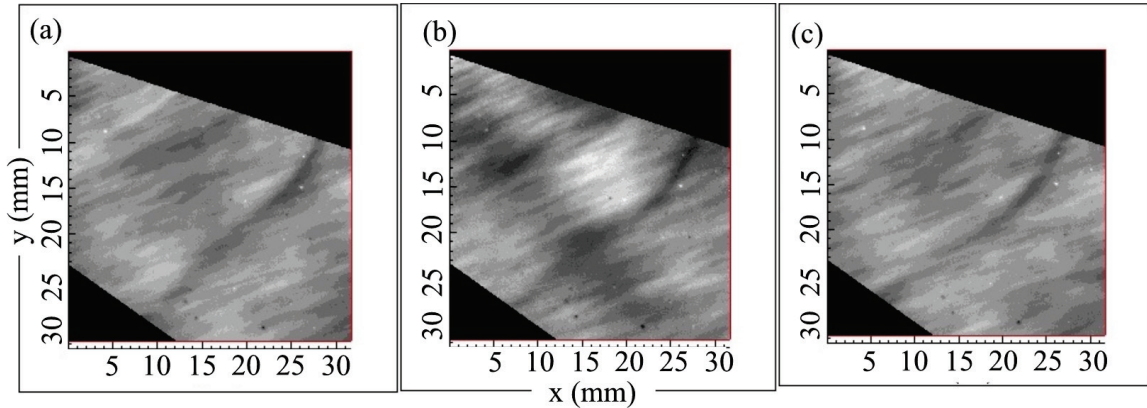


Figure 8.22. Dimensionless mass transfer coefficient plots from data set R63 at times of (a)R63B\_22, 19 min, 24 sec, (b)R63B\_24, 19 min, 35 sec, (c)R63B\_25, 19 min, 47 sec; temperature 21.5 °C, pressure 29.71 inHg, humidity 63%, size 31.75 mm. The images illustrate the change of shape in a downwelling zone over time.

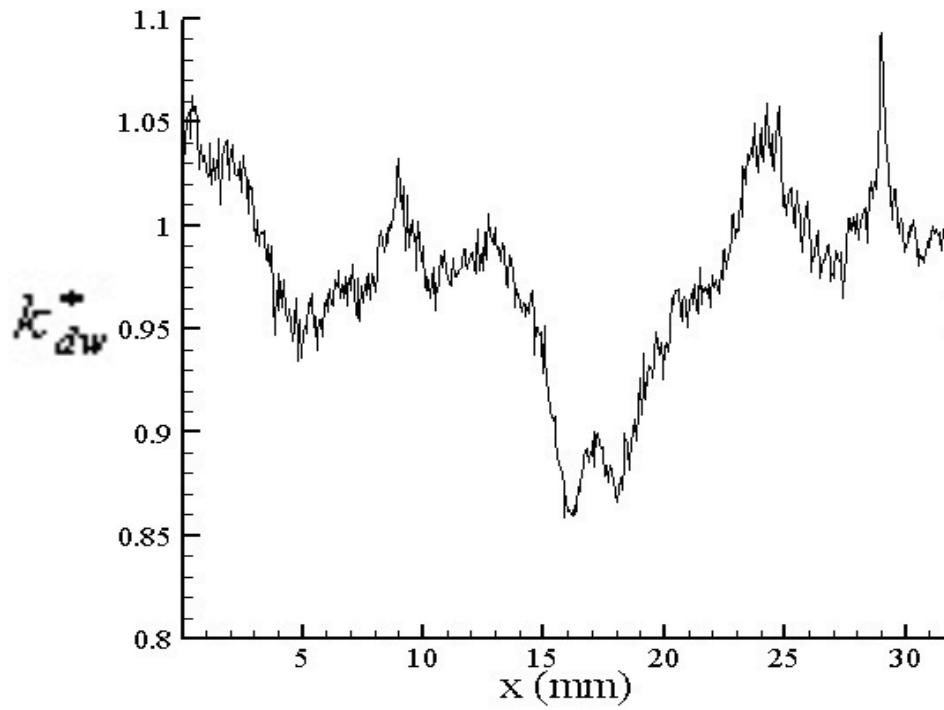


Figure 8.23 Cross sectional plot of dimensionless mass transfer coefficient values at  $y = 13.6$  mm for R63E\_92. The cross section illustrates the value difference in dimensionless mass transfer coefficient values for downwelling zones (between 15 and 19 mm) and the surrounding liquid.

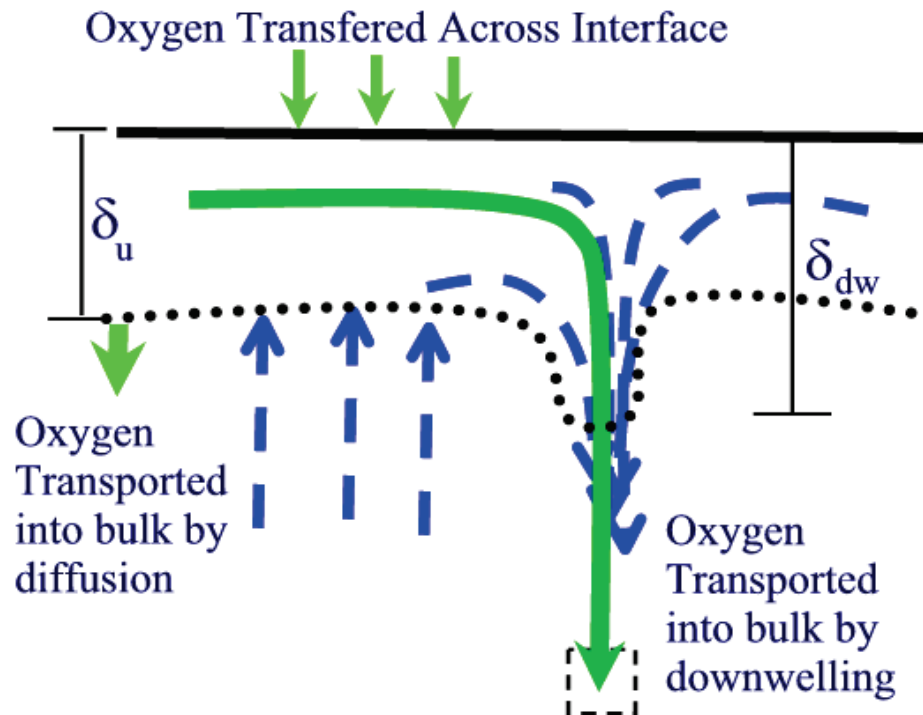


Figure 8.24. Proposed model of Rayleigh-Bénard affected mass transport.

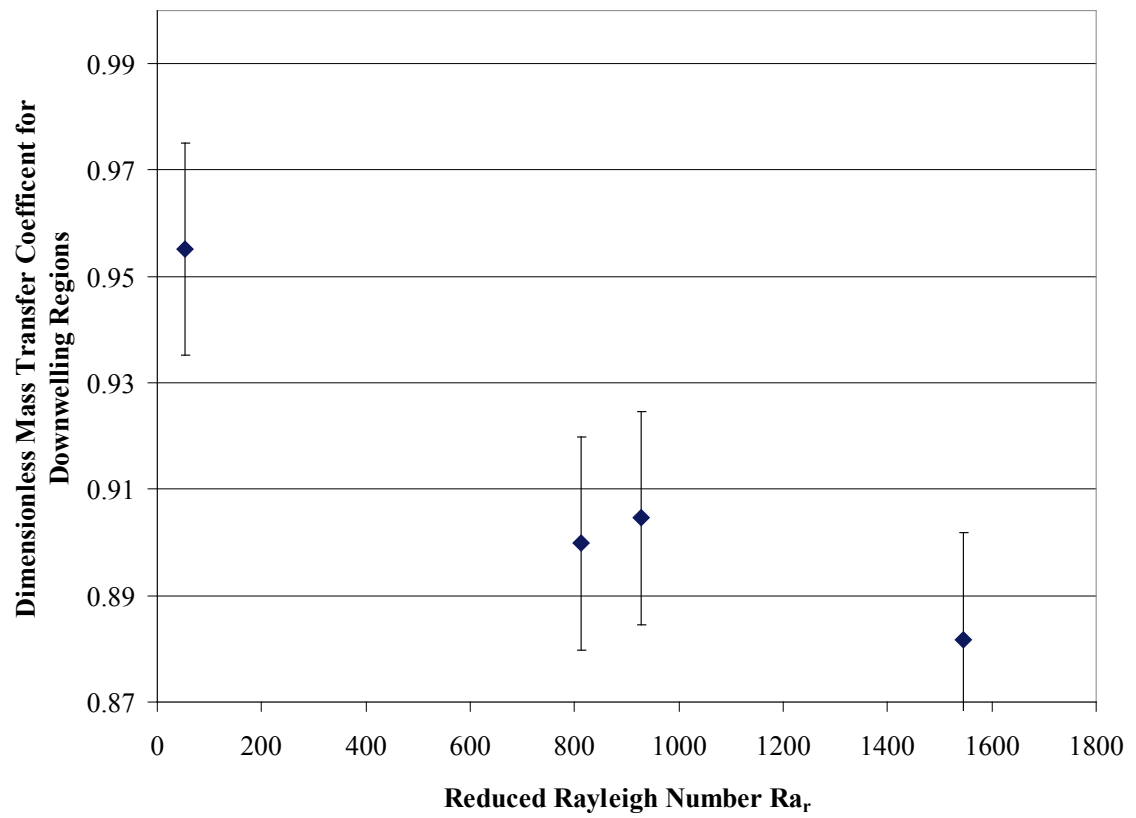


Figure 8.25. Comparison of mass transfer coefficient to reduced Rayleigh number.

## 9. CONCLUSIONS

The Surface Laser Induced Fluorescence (SLIF) technique investigated the spatial variation in air-water mass transfer and has been applied to determine the effect of evaporation on air-water mass transfer. The SLIF technique and apparatus were demonstrated to be unique in measuring the variation in the oxygen concentration gradient across the surface of a liquid, rather than a profile of the concentration gradient as in Planar Laser Induced Fluorescence (Wolf et al., 1991, Wolf and Hanratty, 1994; Duke, 1996; Münsterer, 1996; Münsterer and Jähne, 1998; Woodrow et al., 2001; Woodrow and Duke, 2001; Woodrow, 2001). The SLIF technique can classify and investigate the features and phenomena that fall within the imaging area. The SLIF technique was applied to investigating a possible relationship between atmospheric humidity and oxygen air-water mass transfer via Rayleigh-Bénard circulations.

The Surface Laser Induced Fluorescence technique has the proven ability to measure the spatial variation of the oxygen concentration gradient across the surface of a liquid. Table 6.6 illustrates the difference in fluorescence captured by the SLIF system between a thin and thick concentration gradient. The ability of the SLIF system to capture the differences in the concentration gradient was shown to be independent of any variation in the laser intensity. A dual tank system allowed for the SLIF visualization of fluorescence from both oxygen saturated and unsaturated water at the same time. The SLIF concept was proven by demonstrating that the changes in measured fluorescence

intensity in SLIF data were directly related to predetermined differences in the oxygen concentration gradient thickness.

The abilities of SLIF technique to investigate mass transfer phenomena were demonstrated by application to the study of flat air-water interfaces. The refinement of the SLIF technique to image near surface phenomena was discussed. The SLIF methodology for identifying image features and classifying them based on their source was also demonstrated. The methodology for investigating phenomena was illustrated by proving that downwelling zones captured in the SLIF images could only be caused by an increase in the boundary layer thickness. The final development of the SLIF image processing steps to investigate these downwelling zones was discussed. Figure 7.27 illustrates the data produced by the SLIF apparatus while Figure 7.28 illustrates the final state of the data produced by the SLIF image processing algorithms.

The SLIF data provided clear evidence that the atmospheric humidity above a liquid body has an impact on mass transfer into a water body by controlling the presence of evaporation-induced circulations. Comparison with research in both Rayleigh-Bénard and Marangoni driven circulations showed that the evaporative cooling of the surface generated convective circulations. Based on the presence and behavior of downwelling zones, the convective circulations in this study were primarily buoyancy driven, Rayleigh-Bénard circulations. It was shown that the downwelling zones had a greater oxygen concentration gradient than the surrounding liquid. This reduced the dimensionless mass transfer of oxygen across these regions. It was theorized that these

downwelling zones would increase the mass transfer rate across the remaining surface by reducing resistance to air-water mass transfer. The effect of Rayleigh-Bénard circulations on oxygen mass transfer was illustrated by Figure 8.24. It was shown that as the strength, or rigor, of the Rayleigh-Bénard circulations increased, the mass transfer due to evaporative convection increased.

## REFERENCES

- Adrian, RJ; Ferreira, RT; Boberg, T; 1986, Turbulent thermal convection in wide horizontal fluid layers, *Experiments in Fluids*, **4**, 121-141.
- Alaee, M; Donelan, MA; Strachan, WM; 1995, Wind and wave effects on mass transfer velocities of halomethanes and SF<sub>6</sub> measured in a gas transfer flume, *Air-Water Gas Transfer*, (ed: Jähne B, Monahan EC), 3<sup>rd</sup> symp. on Air-Water Gas Transfer, Heidelberg July 1995, 617-626, AEON: Hanau.
- Anisimova, EP; Petrenko, IV; Speranskaya, AA; Dikarev, SN; Speranskaya, OA; 2001, On the mechanisms of the origin and development of free convective motion in water cooled from the surface, *Oceanology*, **41**:2,176-183.
- Atkins, PW; 1994, *Physical Chemistry*, 5<sup>th</sup> ed., Oxford University Press, Oxford.
- Barnes, GT; Hunter, DS; 1982, Heat conduction during the measurement of the evaporation resistances of monolayers, *Journal of Colloid and Interface Science*, **88**:2, 437-443.
- Barnes, GT; Cammenga, HK; Schreiber, D; Hunter, DS; 1984, On Marangoni convection during the evaporation of water, *Journal of Colloid and Interface Science*, **98**:2, 585-586.
- Bedeaux, D; Kjelstrup, S; 1999, Transfer coefficients for evaporation, *Physica A*, **270**, 413-426.
- Bernaz, L; Bonnet, JM; Seiler, JM; 2001, Investigation of natural convection heat transfer to the cooled top boundary of a heated pool, *Nuclear Engineering and Design*, **204**, 413-427.
- Berg, JC; Acrivos, A; Boudart, M; 1966a, Evaporative convection. *Advances in Chemical Engineering*, ed. Drew et al., 61-123, New York: Academic Press.
- Berg, JC; Boudart, M; Acrivos, A; 1966b, Natural convection in pools of evaporating liquids, *Journal of Fluid Mechanics*, **24**:4, 721-735.

- Berg, JC; Morig, CR; 1969, Density effects in interfacial convection, *Chemical Engineering Science*, **24**,937-946.
- Berg, JC; Haselberger, GS; 1971, Mass transfer during interfacial convection, *Chemical Engineering Science*,**26**, 481-485.
- Bird, BR; Stewart, WE; Lightfoot, EN; 1960, *Transport Phenomena*, 2<sup>nd</sup> ed., New York: John Wiley and Sons.
- Block, MJ; 1956, Surface tension as the cause of Bénard cells and surface deformation in a liquid film, *Nature*, **178**, 650-651.
- Boyadjiev, C; 2000, On the mechanism and kinetics of the transport processes in systems with intensive interphase mass transfer: 2 stability, *International Journal of Heat and Mass Transfer*, **43**, 2759-2766.
- Boyadjiev, C; Halatchev, I; 1998, Non-linear mass transfer and Marangoni effect in gas-liquid systems, *International Journal of Heat and Mass Transfer*, **41**:1, 197-202.
- Broecker, HC; Petermann, J; Siems, W; 1978, The influence of wind on carbon dioxide exchange in a wind-wave tunnel. *Journal of Marine Research*, **36**, 595-610.
- Butler, WL; Hopkins, DW; 1970; Higher derivative analysis of complex absorption spectra, *Photochemistry and Photobiology*, **12**, 439-450.
- Cammenga, HK; Schreiber, D; Rudolph, B.E.; 1983, Two methods for measuring the surface temperature of evaporating liquid and results obtained with water, *Journal of Colloid and Interface Science*, **92**:1, 181-188.
- Chai, A; Zhang, N; 1998, Experimental study of Marangoni-Bénard convection in a liquid layer induced by evaporation, *Experimental Heat Transfer*, **11**, 187-205.
- Chandrasekhar, S; 1961, *Hydrodynamic and Hydromagnetic Stability*, Clarendon Press: Oxford.
- Chu, TY; Goldstein, RJ; 1973, Turbulent convection in a horizontal layer of water, *Journal of Fluid Mechanics*, **60**:1, 141-159.
- Dankwerts, PV; 1951, Significance of liquid-film coefficients in gas absorption, *Industrial Engineering Chemistry*, **43**:6, 1469-1452.
- Daniil, E; Gulliver, JS; 1991, Influence of waves on air-water gas transfer, *Journal of Environmental Engineering*, **117**:5, 522-539.

- Donelan, MA; Wanninkhof, R; 2002, Gas transfer at water surfaces: Concepts and issues, *Gas Transfer at Water Surfaces: Geophysical Monograph 127*, ed. Donelan, Drennan, Saltzman, and Wanninkhof; 3-12. Washington, DC: American Geophysical Union.
- Dijkstra, HA; Van de Vooren, AI; 1985, Initial flow development due to Marangoni convection in a mass transfer system, *International Journal of Heat and Mass Transfer*, **28**, 2315-2322.
- Duckworth, J; 2004, Mathematical Data Preprocessing, *Near-Infrared Spectroscopy in Agriculture*, Roberts, C.A.; Workman, J. Reeves, J.B. ed. 115-132.
- Duke, SR; Wolff, LM; Hanratty, TJ; 1995, Slopes of small-scale wind waves and their relation to mass transfer rates, *Experiments in Fluids*, **19**, 280-292.
- Duke, SR; 1996, *Air-Water Transfer at Wavy Interfaces*, Ph.D. Dissertation, University of Illinois and Urbana-Champaign, Illinois.
- Emery, AF; Lee, JW; 1999, The effect of property variations on natural convection in a square enclosure, *Journal of Heat Transfer*, **121**, 57-62.
- Fang, G; Ward CA; 1999, Examination of the statistical rate theory expression for liquid evaporation rates, *Physical Review E*, **59**, 441-453.
- Finkel, J; 1982, *CRC Handbook of Irrigation Technology*, **1**, CRC Press: Boca Raton.
- Fortescue, GE; Pearson, JRA; 1967, On gas absorption into a turbulent liquid, *Chemical Engineering Science*, **22**, 1163-1176.
- Getling, AV; 1998, *Rayleigh-Bénard Convection, Structures and Dynamics*, World Scientific: London.
- George, J; Caussade, B; Masbernat; 1995, Conceptual modeling of interfacial gas-liquid mass transfer, *Air-Water Gas Transfer*, ed: Jähne B, Monahan EC, 3<sup>rd</sup> symposium on Air-Water Gas Transfer, Heidelberg July 1995, 69-78, AEON: Hanau.
- Golovin, AA; 1992, Mass transfer under interfacial turbulence, kinetic regularities, *Chemical Engineering Science*, **47**:8, 2069-2080.
- Guilbault, GG; 1990 *Practical Fluorescence*, 2<sup>nd</sup> edition, Marcel Dekker: New York.
- Ha, V; Lai, C; 1998, Study of Marangoni instability of an evaporating liquid layer, *Journal of the Chinese Institute of Engineers*, **21**:5, 547-562.

- Hanratty, TJ; 1991, Effect of gas flow on physical absorption, *Air-Water Mass Transfer: 2<sup>nd</sup> International Symposium on Gas Transfer at Water interfaces*. ed: Wilheims , Gulliver; A.S.C.E: New York.
- Heidel, B; Knobler, CM; 1998, Pattern formation at liquid interfaces, *Physical Review Letters*, **60**, 2492-2495.
- Heise, HM; Winzen,R; 2002, Chemometrics in near-infrared spectroscopy, *Near-Infrared Spectroscopy*, Siesler, HW et. al. ed. Wiley-VCH.
- Hemstead, M; 1993, Determination of diffusion profiles of neodymium in lithium niobate by means of spatially resolved fluorescence measurements, *Journal of Applied Physics*, **74**:9,5483-5492.
- Higbie, R; 1935, The role of absorption of a pure gas into a still liquid during short periods of exposure, *Transactions American Institute of Chemical Engineering*, **35**, 365-375.
- Jain, AK; 1989, *Fundamentals of Digital Image Processing*, Prentice Hall, NJ.
- Jähne, B; 1995, Impact of Quantitative Visualization and Image Processing on the Study of Small-Scale Air-Sea Interactions, *Air-Water Gas Transfer*, ed: Jähne, Monahan; 3<sup>rd</sup> sym on Air-Water Gas Transfer, Heidelberg July 1995, 3-12 AEON: Hanau.
- Jähne, B; 1997, *Practical Handbook on Image Processing for Scientific Applications*, CRC Press, Boca Raton NY.
- Jähne, B; Haußeker, H; 1998, Air-Water Gas Exchange, *Annual Review of Fluid Mechanics*, **30**, 443-468.
- Jones, R; Smith, CC; Löf, G; 1993, Measurement and analysis of evaporation from an inactive outdoor swimming pool, *Proceeding of 1993 Annual Conference American Solar Energy Society*, 399-404, Washington D.C., April 25-28<sup>th</sup>.
- Koschmeider, EL; 1993. *Bernard Cells and Taylor Vortices*, Cambridge University Press: Victoria Australia.
- Lakowicz, JR; 1983, *Principles of Fluorescence Spectroscopy*, Plenum Press.
- Lewis, WK; Whitman, WG; 1924, Principles of Gas Absorption, *Industrial and Engineering Chemistry*, **16**:12, 1215-1220.
- Lide, RD; 2001, *CRC Handbook of Chemistry and Physics*, 82<sup>nd</sup> Edition. CRC Press: Boca Raton.

- Liss, PS; Merlivat, L; 1986, Air-sea exchange rates: introduction and synthesis, in *The Role of Air-Gas Exchange in Geochemical Cycling*, ed. Beat-Menard; 113-129, Ridel:Boston.
- Macintyre, S; Eugster, W; Kling, GW; 2002, The critical importance of buoyancy flux for gas flux across the air-water interface, *Gas Transfer and Water Surfaces: Geophysical Monograph 127*, ed. Donelan, Drennan, Saltzman, Wanninkhof; 135-139, American Geophysical Union: Washington, DC.
- Magnaudet, J; George, J; Masbernat, L; Caussade, B; 1991, Turbulence level below the waves and its relation to absorption, *Air-Water Gas Transfer*, ed: Wilhelms; Gulliver; 2nd symposium on Air-Water Gas Transfer, Minneapolis, September, 1990, 593-607, AEON: Hanau.
- McKenna, SP; McGillis, WR; 2002, Surface divergence and air-water gas transfer, *Gas Transfer and Water Surfaces: Geophysical Monograph 127*, ed. Donelan, Drennan, Saltzman, Wanninkhof; 129-134, American Geophysical Union: Washington, DC.
- Moog, DB; Jirka, GH; 1998; Analysis of re-creation equations using mean multiplicative error, *Journal of Environmental Engineering*, **124**:104-110.
- Münsterer, T; 1996, *LIF Investigation of the Mechanisms Controlling Air-Water Mass Transfer at a Free Interface*, Ph.D. Dissertation, University of Heidelberg, Germany.
- Münsterer, T; Jähne, B; 1998, LIF measurements of concentration profiles in the aqueous mass boundary layer, *Experiments in Fluids*, **25**, 190-196.
- Navon, U; Fenn, JB; 1971, Interfacial mass and heat transfer during evaporation, *AIChE Journal*, **17**:1, 131-136.
- Nield, DA; 1964, Surface tension and buoyancy effects in cellular convection, *Journal of Fluid Mechanics*, **19**, 341-352.
- Okhotsimskii, A.; Hozawa, M.; 1998, Schlieren visualization of natural convection in binary gas-liquid systems, *Chemical Engineering Science*, **53**:14, 2547-2573.
- Pearson, JRA; 1958, On convection cells induced by surface tension, *Journal of Fluid Mechanics*, **4**, 489-500.

- Panin, GN; Nasonov, AE; Sarkisian, SG; 2002, Air-lake interaction and surface layer processes, *Gas Transfer and Water Surfaces :Geophysical Monograph 127* ed. Donelan, Drennan, Saltzman, Wanninkhof; 147-151, American Geophysical Union: Washington, DC.
- Quinn, GP; Saville, DA; 1976, Marangoni instability with an evaporating interface, *Letters in Heat and Mass Transfer*, **3**, 309-318.
- Rayleigh, L; 1916, On the convection currents in a horizontal layer of fluid when the higher temperature is on the under side, *Philosophy Magazine* **32**, 529-46.
- Rashidi, M; Hetsroni, G; Banerjee, S; 1991, Mechanisms of heat and mass transport at the gas-liquid interfaces, *International Journal of Heat and Mass Transfer*, **34**:7, 1799-1810.
- Redfern, D; Campbell C; 1998, *The Matlab 5 Handbook*, Springer-Verlag, New York.
- Ruckenstein, E; 1971, Mass transfer into a horizontal layer of stagnant liquid under the action of instabilities, *Canadian Journal of Chemical Engineering*, **49**, 62-66.
- Russ, JC; 2002, *The Image Processing Handbook*, 4<sup>th</sup> ed. CRC Press, Boca Raton.
- Schatz, MF; Neitzel, GP; 2001, Experiments on thermocapillary instabilities, *Annual Review Fluid Mechanics*, **33**, 93-129.
- Schreiber, D; Cammenga, HK; 1981; Conductive and convective heat transfer below evaporating liquid surfaces, *Ber. Bunsenges. Physical Chemistry*, **85**, 909-914.
- Scriven, LE; 1968, Flow and transfer at fluid interfaces, Part I, *Chemical Engineering Education*, **15**, 50-155.
- Scriven, LE; 1969a, Flow and transfer at fluid interfaces, Part II, *Chemical Engineering Education*, **16**, 26-29.
- Scriven, LE; 1969b, Flow and transfer at fluid interfaces, Part III, *Chemical Engineering Education*, **16**: 94-98.
- Sharma, A; Schulman, SG; 1999, *Fluorescence Spectroscopy*, John Wiley and Sons: New York.
- Shenk, JS; Workman, JJ; Westerhaus, MO; 2001, Application of NIR spectroscopy to agricultural products, *Handbook of Near-Infrared Analysis* 2<sup>nd</sup> ed. Burns, D.A.; Ciurczak, E.W. ed. Marcel Dekker, NY.

- Shimpf, U; Haußeker, H; Jähne, B; 1999, Air-sea gas transfer and micro turbulence at the ocean surface using infrared image processing, *Proceedings of the 1999 IEEE International Geoscience and Remote Sensing Symposium, 1999, Hamburg*, 11-13, IEEE: Piscaway, NJ.
- Shimpf, U; Haußeker, H; Jähne, B; 2000, On the investigation of micro turbulence at the water Surface using infrared imaging, *International Geoscience and Remote Sensing Symposium*, **3**, 1274-1276.
- Spangenberg, WG; Rowland, WR; 1961, Convective circulation in water induced by evaporative cooling, *Physics of Fluids*, **4**:6, 743-750.
- Sparrow, EM; Goldstein, RJ; Jonsson, VK; 1964, Thermal instability in a horizontal fluid layer, effect of boundary conditions and non-linear temperature profile, *Journal of Fluid Mechanics*, **35**, 513-527.
- Sparrow, EM; Husar, RB; Goldstein, RJ; 1970, Observations and other characteristics of thermals, *Journal of Fluid Mechanics*, **41**:4, 793-800.
- Stauffer, FR; Sakai, H; 1968, Derivative spectroscopy, *Applied Optics*, **7**:1, 61-66.
- Stolzer, S; Johnsen, O; Bapst, F; Ingold, R; 2006, Groove extraction of phonographic records, *Lecture Notes In Computer Science* **3872**: 529-540.
- Takehara, K; Etoh, GT; 2002, A direct visualization method of carbon dioxide gas transfer at water surface driven by wind waves, *Gas Transfer and Water Surfaces: Geophysical Monograph 127*, ed. Donelan, Drennan, Saltzman, Wanninkhof; 89-95, American Geophysical Union: Washington, DC.
- Theerthan, SA; Arekeri, JH; 1994 Planform Structure of turbulent Rayleigh-Bénard convection, *International Communications in Heat and Mass Transfer*, **21**:4, 561-572.
- Thibodeaux, LJ; 1996, *Environmental Chemodynamics*, 2<sup>nd</sup> ed, John Wiley and Sons, New York.
- Torii, S; Yang, W; 1999, Numerical flow visualization and thermal transport phenomenon of Bénard convection in a thin liquid layer induced by evaporation, *Journal of Flow Visualization and Image Processing*, **6**, 95-104.
- Torii, S; Yang, WJ; 2003, Evaporation-induced Bénard convection in a thin liquid layer, *International Journal of Energy Research*, **27**, 255-264.
- U.S. Geological Survey, 2006; Dissolved oxygen, *Handbooks for Water-Resources Investigations*, ed. M.E.Lewis.

- Valeur, B; 2002, *Molecular Fluorescence*, Wiley-VCH, Weinheim.
- Vaughan, WM; Weber, G; 1970, Oxygen quenching of pyrenebutyric acid fluorescence in water, *Biochemistry*, **9**, 464-473.
- Vázquez, G; Anorrena, G; Navaza, JM; Santos, V; 1996, Absorption of CO<sub>2</sub> by water and surfactant solutions in the presence of induced Marangoni effect, *Chemical Engineering Science*, **51**:12, 3317-3324.
- Vidal, A; Acrivos, A; 1966, Nature of the neutral state in surface-tension driven convection, *Physics of Fluids*, **9**:3, 615-616.
- Vidal, A; Acrivos, A; 1968, Effect of nonlinear temperature profiles on the onset of convection driven by surface tension gradients, *Industrial and Engineering Chemistry Fundamentals*, **7**:1, 53-58.
- Ward, CA; Fang G; 1999, Expression for predicting liquid evaporation flux: Statistical rate theory approach, *Physical Review E*, **59**, 429-440.
- Ward, CA; Stanga, D; 2001, Interfacial conditions during evaporation or condensation of water, *Physical Review E*, **64**, 0515091-0515099.
- Weeks, AR; 1996, *Fundamentals of Electronic Image Processing*, IEEE Press, NJ
- Whitman, WG; 1923, A preliminary experimental confirmation of the two-film theory of gas absorption, *Chemical and Metallurgical Engineering*, **29**, pp. 146-148.
- Wolff, LM.; Liu, Z; Hanratty, TJ; 1991, A fluorescence technique to measure concentration gradients near an interface. *Gas Transfer at Water Surfaces* ed. Gulliver, et al.; 210-218, ASCE: New York.
- Wolff, LM; Hanratty, TJ; 1994, Instantaneous concentration profiles of oxygen accompanying absorption in stratified flow. *Experiments in Fluids*, **16**, 385-392.
- Woodrow, PT; 2001, *Laser-Induced Fluorescence Studies of Oxygen Transfer Across an Air-Water Interface*, Ph.D. Dissertation, Auburn University, Alabama.
- Woodrow, PT; Donath, GW; Duke, SR; 2001, LIF measurements of oxygen concentration gradients beneath flat and wavy air-water interfaces, *Proceedings of the ICMF-2001: 4th International Conference on Multiphase Flows*, **1**, paper 421.
- Woodrow, PT; Duke SR; 2001, Laser-Induced fluorescence studies of oxygen transfer across unsheared flat and wavy air-water Interfaces, *Industrial and Engineering Chemistry Research*, **40**, 1985-1995.

- Yamamura, M; Nagai, K; Toshihisa, K; Adachi, K; 2003; Stripe pattern breakup in evaporating liquid layer on a plate with horizontal temperature gradient, *Chemical Engineering and Processing*, **42**, 395-402.
- Yang, WJ; Guo, K.; Sakamoto, M.; 1997, Evaporation-induced cellular convection in thin liquid layers, *Experimental Heat Transfer*, **10**, 191-205.
- Yang, W; Torii, S; 2002, Evaporation-induced Bénard convection in a thin liquid layer, *International Journal of Energy Research*, **27**, 255-246.
- Zhang, N; Chao, DF; 1999, Mechanisms of convection instability in thin liquid layers induced by evaporation, *International Communications of Heat and Mass Transfer*, **26**:8,1069-1080.
- Zhang, N; Chao, DF; Yang, WJ; 2002, Convective instability in transient evaporating thin liquid layers, *Journal of Non-Equilibrium Thermodynamics*, **27**, 71-89.
- Zheng, GS; Worek, WM; 1996, Method of heat and mass transfer enhancement in film evaporation, *International Journal of Heat and Mass Transfer*, **39**:1, 97-108.

## APPENDIX A: SUPPLIMENTS TO RESEARCH METHODS

### A.1. Probe calibration in air

These instructions are taken from YSI, 1996; YSI Model 52 Dissolved Oxygen Meter Manual.

To calibrate in air:

1. Place a prepared probe in air at 100% relative humidity. To achieve this, BOD probes can be placed in a BOD bottle with approximately 1" of water. Field probes can be placed in the plastic calibration bottle with a moistened sponge, or calibrated with the 5075A Calibration Chamber.
2. Switch to CALIBRATE. The display will read:

*Calibrate in percent?*

Select percent calibration by pressing CONFIRM. A display similar to the one below will be shown.

*Enter cal value Last = 94.4 %*

3. Using the up arrow and the down arrow adjust the number to the calibration value determined from the altitude or pressure chart on the back of the Model 52. SKIP sets the value to 100.0%; and shows the following display:

*Enter cal value Sat. = 100%*

you may wish to do this to bring the setting quickly to a value near the one you want, then continue with the up arrow and the down arrow. Pressing SKIP again sets the value to 0.0% . Pressing SKIP a third time brings it back to the last calibration value.

Pressure		Altitude		Calibration value
(mmHg)	(kPa)	(ft)	(m)	(%)
768	102.3	-276	-84	101
760	101.3	0	0	100
752	100.3	278	85	99
745	99.3	558	170	98
737	98.3	841	256	97
730	97.3	1126	343	96
722	96.3	1413	431	95
714	95.2	1703	519	94
707	94.2	1995	608	93
699	93.2	2290	698	92
692	92.2	2587	789	91
684	91.2	2887	880	90
676	90.2	3190	972	89
669	89.2	3496	1066	88
661	88.2	3804	1160	87
654	87.1	4115	1254	86
646	86.1	4430	1350	85
638	85.1	4747	1447	84
631	84.1	5067	1544	83
623	83.1	5391	1643	82
616	82.1	6047	1743	81
608	81.1	6047	1843	80
600	80.0	6381	1945	79
593	79.0	6717	2047	78
585	78.0	7058	2151	77
578	77.0	7401	2256	76
570	76.0	7749	2362	75
562	75.0	8100	2469	74
555	74.0	8455	2577	73
547	73.0	8815	2687	72
540	71.9	9178	2727	71
532	70.9	9545	2909	70
524	69.9	9917	3023	69
517	68.9	10293	3137	68
509	67.9	10673	3253	67

Table A.1 Calibration data for YSI 52 dissolved oxygen meter and YSI 5792 field probe.

A.2. Dissolved oxygen concentration

T (°C)	Atmospheric pressure (millimeters of mercury)											
	795	790	785	780	775	770	765	760	755	750	745	740
10	11.8	11.8	11.7	11.6	11.5	11.5	11.4	11.3	11.2	11.2	11.1	11.0
11	11.6	11.5	11.4	11.4	11.3	11.2	11.1	11.1	11.0	10.9	10.8	10.8
12	11.3	11.2	11.2	11.1	11.0	11.0	10.9	10.8	10.7	10.7	10.6	10.5
13	11.1	11.0	10.9	10.9	10.8	10.7	10.6	10.6	10.5	10.4	10.4	10.3
14	10.8	10.8	10.7	10.6	10.6	10.5	10.4	10.3	10.3	10.2	10.1	10.1
15	10.6	10.5	10.5	10.4	10.3	10.3	10.2	10.1	10.1	10.0	9.93	9.86
16	10.4	10.3	10.3	10.2	10.1	10.1	10.0	9.92	9.86	9.79	9.72	9.66
17	10.2	10.1	10.0	10.0	9.92	9.85	9.78	9.72	9.65	9.59	9.52	9.46
18	10.0	9.91	9.84	9.78	9.72	9.65	9.59	9.52	9.46	9.40	9.33	9.27
19	9.77	9.71	9.65	9.59	9.52	9.46	9.40	9.34	9.27	9.21	9.15	9.08
20	9.58	9.52	9.46	9.40	9.34	9.28	9.21	9.15	9.09	9.03	8.97	8.91
21	9.40	9.34	9.28	9.22	9.16	9.10	9.04	8.98	8.91	8.85	8.79	8.73
22	9.22	9.16	9.10	9.04	8.98	8.92	8.86	8.80	8.74	8.69	8.63	8.57
23	9.05	8.99	8.93	8.87	8.81	8.75	8.70	8.64	8.58	8.52	8.46	8.40
24	8.88	8.82	8.76	8.71	8.65	8.59	8.53	8.48	8.42	8.36	8.30	8.25
25	8.71	8.66	8.60	8.55	8.49	8.43	8.38	8.32	8.26	8.21	8.15	8.09
26	8.56	8.50	8.44	8.39	8.33	8.28	8.22	8.17	8.11	8.06	8.00	7.94
27	8.40	8.35	8.29	8.24	8.18	8.13	8.07	8.02	7.96	7.91	7.85	7.80
28	8.25	8.20	8.14	8.09	8.04	7.98	7.93	7.87	7.82	7.77	7.71	7.66
29	8.10	8.05	8.00	7.95	7.89	7.84	7.79	7.73	7.68	7.63	7.57	7.52
30	7.99	7.94	7.88	7.83	7.78	7.73	7.68	7.62	7.57	7.52	7.47	7.41
31	7.87	7.82	7.77	7.72	7.66	7.61	7.56	7.51	7.46	7.40	7.35	7.30
32	7.75	7.70	7.65	7.60	7.55	7.50	7.45	7.40	7.34	7.29	7.24	7.19
33	7.64	7.59	7.54	7.49	7.44	7.39	7.33	7.28	7.23	7.18	7.13	7.08
34	7.52	7.47	7.42	7.37	7.32	7.27	7.22	7.17	7.13	7.08	7.03	6.98
35	7.41	7.36	7.31	7.26	7.22	7.17	7.12	7.07	7.02	6.97	6.92	6.87
36	7.30	7.25	7.20	7.16	7.11	7.06	7.01	6.96	6.91	6.86	6.81	6.77
37	7.19	7.14	7.10	7.05	7.00	6.95	6.90	6.86	6.81	6.76	6.71	6.66
38	7.09	7.04	6.99	6.94	6.89	6.85	6.80	6.75	6.70	6.66	6.61	6.56
39	6.98	6.93	6.88	6.84	6.79	6.74	6.70	6.65	6.60	6.56	6.51	6.46
40	6.87	6.83	6.78	6.73	6.69	6.64	6.59	6.55	6.50	6.46	6.41	6.36

Table A.2. Dissolved Oxygen Concentration in mg/L for distilled water from 795 mmHg to 740 mmHg and from 10°C to 40°C (U.S. Geological Survey, 2006)

### A.3. Camera controller Input/Output status connector pinout



Figure A.1. Diagram of Photometrics 300 CCD camera controller outputs and inputs.

All inputs are pulled up to +5V through 10k ohm resistors. Outputs are driven by a 74HCT244 driver. Inputs must be at least 3.15V for a high and less than 0.9V for a low. The numbers on the trigger connector diagram correspond to the numbers given to the definition of each of the pins. The I/O connector is a female, D-subminiature 9-pin connector.

#### 1. WAIT FOR TRIGGER OUTPUT

Active high. A high level on this output indicates that the camera is waiting for a trigger input.

## **2. SHUTTER MOVING OUTPUT**

Active high. A high level on this output indicates that the shutter is opening or closing. The output is low when the shutter is completely open or completely closed. The length of time this signal is held high is specified in PVCAM or by the Shutter Open Delay and Shutter Close Delay functions in the software program.

## **3 CAMERA EXPOSING OUTPUT**

Active high. A high level on this output indicates that the camera is exposing (integrating).

## **4 FLASH OUTPUT**

This pin is an output that can be controlled in PVCAM with the FLASH\_MODE constant.

## **5 FACTORY SETUP**

This pin is reserved for factory setup.

## **6 FILTERED TRIGGER INPUT**

This input has an RC filter inline to reduce noise on the trigger input. The input is pulled low to initiate a trigger (default). If nothing is connected to the input, it is pulled high to prevent the system from getting false triggers. To change the state of this input see TRIGGER INVERT INPUT (8). (The inputs are internally pulled up, therefore it is recommended to drive them with an open collector driver.)

## **7 TRIGGER INHIBIT INPUT**

This input inhibits all trigger signals. If the input is pulled low, trigger activity is disabled. By default, the input is pulled high so the trigger circuitry is enabled. (The inputs are internally pulled up, therefore it is recommended to drive them with an open collector driver.)

## **8 TRIGGER INVERT INPUT**

Active low. A low on this input inverts the state of FILTERED TRIGGER INPUT (6) and TRIGGER CONNECTOR (see below), causing a high level to cause a trigger. (The inputs are internally pulled up, therefore it is recommended to drive them with an open collector driver.)

## **9 GROUND**

System digital ground. Any external circuitry intended to interface with the trigger control signals must reference this ground connection.

### Trigger Connector

This input uses a TTL voltage level to trigger the camera. The input is pulled low to initiate a trigger (default). If nothing is connected to the input, it is pulled high to prevent the system from getting false triggers. To change the state of this input see TRIGGER INVERT INPUT (I/O Status 8). (The inputs are internally pulled up, so it is recommended to drive them with an open collector driver.)

### Shutter Status Connector

Active low. A low level on this output indicates that the shutter is open or in motion. A high level output indicates that the shutter is closed or in motion.

## APPENDIX B: GENERATED MATLAB FUNCTIONS

```
function F=2poly(A,data)
% F=Function 2poly(A,D) is used to solve the equation
%  $A(1)+A(2)*x+A(3)*y+A(4)*x.^2+A(5)*y.^2+A(6)*x.*y$ 
% using the x and y values provided in data
%
% Copyright 2006, G.W. Donath
% All Rights Reserved
%
x=data(1,:);
y=data(2,:);
%
F=A(1)+A(2)*x.+A(3)*y.+A(4)*x.^2+A(5)*y.^2+A(6)*x.*y.;

function B=B2Dfind(I,CA);
%
%
%
%
C1=10000;
k=1;
I=I.*C1;
%set number of iterations for B
options=optimset('MaxFunEvals',1000000,'MaxIter',1500000,'LargeScale','off');
for i=1:18:500
    for j=1:18:500
        i2=i+17;
        j2=j+17;
        Z=I(i:i2,j:j2);
        F=max(max(Z));
        if F>0
            [L1,L2]=find(Z==F);
            xydata(1,k)=9+i;
            xydata(2,k)=9+j;
            Idata(k)=F;
            k=k+1;
        end
    end
end
```

```

end

Ao=
[0,0,0,0,0,0];
%
[B1]=lsqcurvefit(@varB1C,Ao,xydata,Idata,[],[],options);
B=B1./C1;

function [Y,C]=B2filter(B,Iin);
% The function [Y,C]=B2filter(B,Iin) is designed to translate the values found in B2Find
%(Iin) into an array of values of the second background correction array © that are
%subtracted from the image (B) to generated the secondary background corrected values
%(Y),
% Copyright 2006, G.W. Donath
% All Rights Reserved
%first step reform Iin
[I,J]=size(Iin);
C=zeros(I,J);
Y=zeros(I,J);
K=I*J;
for i=1:I,
    for j=1:J,
        C(i,j)=varB1C(B,[i,j]);
    end
end
Y=Iin./C;

function [Z]=batchline(A);
% The batchline function creates a series of possible line connections in a three by three
% array allowing the continuous points of a downwelling line to have a gain of 5 and be
% detectable
% Copyright G.W. Donath 2005
%
L5=-1.*ones(5,5);
v=[0 0 5 0 0; 0 0 5 0 0; 0 0 5 0 0; 0 0 5 0 0; 0 0 5 0 0];
L5v=L5+v;
L5h=L5v';
L545=[5 0 0 0 0; 0 5 0 0 0; 0 0 5 0 0; 0 0 0 5 0; 0 0 0 0 5];
L545=L545+L5;

```

```

L5135=rot90(L545);
L5A1=[0 5 0 0 0; 0 5 0 0 0; 0 0 5 0 0; 0 0 0 5 0; 0 0 0 0 5]+L5;
L5A2=fliplr(L5A1);
L5A3=flipud(L5A1);
L5A4=flipud(L5A2);
L5A5=L5A1';
L5A6=L5A2';
L5A7=L5A3';
L5A8=L5A4';
L5A9=[0 0 5 0 0; 0 0 5 0 0; 0 0 5 0 0; 0 0 0 5 0; 0 0 0 0 5]+L5;
L5A10=fliplr(L5A9);
L5A11=flipud(L5A9);
L5A12=flipud(L5A11);
L5A13=L5A9';
L5A14=L5A10';
L5A15=L5A11';
L5A16=L5A12';
L5A17=[0 5 0 0 0; 0 5 0 0 0; 0 0 5 0 0; 0 0 0 5 0; 0 0 0 5 0]+L5;
L5A18=fliplr(L5A17);
L5A19=flipud(L5A17);
L5A20=flipud(L5A18);
L5A21=L5A17';
L5A22=L5A18';
L5A23=L5A19';
L5A24=L5A20';
L5A25=[0 5 0 0 0; 0 0 5 0 0; 0 0 5 0 0; 0 0 0 5 0; 0 0 5 0 0]+L5;
L5A26=fliplr(L5A25);
L5A27=flipud(L5A25);
L5A28=flipud(L5A26);
L5A29=L5A25';
L5A30=L5A26';
L5A31=L5A27';
L5A32=L5A28';
%
L5A33=[0 5 0 0 0; 0 0 5 0 0; 0 0 5 0 0; 0 0 0 5 0; 0 0 0 0 5]+L5;
L5A34=fliplr(L5A33);
L5A35=flipud(L5A33);
L5A36=flipud(L5A34);
L5A37=L5A33';
L5A38=L5A34';
L5A39=L5A35';
L5A40=L5A36';
%
L5A41=[0 0 5 0 0; 0 0 5 0 0; 0 0 5 0 0; 0 0 0 5 0; 0 0 0 5 0]+L5;

```

```

L5A42=flipr(L5A41);
L5A43=flipud(L5A41);
L5A44=flipud(L5A42);
L5A45=L5A41';
L5A46=L5A42';
L5A47=L5A43';
L5A48=L5A44';
L5C1=[0 5 0 0 0; 0 5 0 0 0; 0 0 5 0 0; 0 5 0 0 0; 0 5 0 0 0]+L5;
L5C2=flipr(L5C1);
L5C3=flipud(L5C1);
L5C4=flipud(L5C2);
L5C5=L5C1';
L5C6=L5C2';
L5C7=L5C3';
L5C8=L5C4';
L5C9=[5 0 0 0 0; 0 5 0 0 0; 0 0 5 0 0; 0 5 0 0 0; 5 0 0 0 0]+L5;
L5C10=flipr(L5C9);
L5C11=flipud(L5C9);
L5C12=flipud(L5C10);
L5C13=L5C9';
L5C14=L5C10';
L5C15=L5C11';
L5C16=L5C12';
L5C17=[0 0 5 0 0; 0 0 0 5 0; 0 0 5 0 0; 0 5 0 0 0; 0 0 5 0 0]+L5;
L5C18=flipr(L5C17);
L5C19=flipud(L5C17);
L5C20=flipud(L5C18);
L5C21=L5C17';
L5C22=L5C18';
L5C23=L5C19';
L5C24=L5C20';
%
L5C25=[0 0 5 0 0; 0 0 0 5 0; 0 0 5 0 0; 0 0 0 5 0; 0 0 5 0 0]+L5;
L5C26=flipr(L5C25);
L5C27=flipud(L5C25);
L5C28=flipud(L5C26);
L5C29=L5C25';
L5C30=L5C26';
L5C31=L5C27';
L5C32=L5C28';
%
L5C33=[0 0 5 0 0; 0 0 5 0 0; 0 0 5 0 0; 0 0 0 5 0; 0 0 5 0 0]+L5;
L5C34=flipr(L5C33);
L5C35=flipud(L5C33);

```

```

L5C36=flipud(L5C34);
L5C37=L5C33';
L5C38=L5C34';
L5C39=L5C35';
L5C40=L5C36';
%
Egr=A;
LT=zeros(512,512,92);
LT(:,:,1)=imfilter(Egr,L5v,'replicate');
LT(:,:,2)=imfilter(Egr,L5h,'replicate');
LT(:,:,3)=imfilter(Egr,L545,'replicate');
LT(:,:,4)=imfilter(Egr,L5135,'replicate');
LT(:,:,5)=imfilter(Egr,L5A1,'replicate');
LT(:,:,6)=imfilter(Egr,L5A2,'replicate');
LT(:,:,7)=imfilter(Egr,L5A3,'replicate');
LT(:,:,8)=imfilter(Egr,L5A4,'replicate');
LT(:,:,9)=imfilter(Egr,L5A5,'replicate');
LT(:,:,10)=imfilter(Egr,L5A6,'replicate');
LT(:,:,11)=imfilter(Egr,L5A7,'replicate');
LT(:,:,12)=imfilter(Egr,L5A8,'replicate');
LT(:,:,13)=imfilter(Egr,L5A9,'replicate');
LT(:,:,14)=imfilter(Egr,L5A10,'replicate');
LT(:,:,15)=imfilter(Egr,L5A11,'replicate');
LT(:,:,16)=imfilter(Egr,L5A12,'replicate');
LT(:,:,17)=imfilter(Egr,L5A13,'replicate');
LT(:,:,18)=imfilter(Egr,L5A14,'replicate');
LT(:,:,19)=imfilter(Egr,L5A15,'replicate');
LT(:,:,20)=imfilter(Egr,L5A16,'replicate');
LT(:,:,21)=imfilter(Egr,L5A17,'replicate');
LT(:,:,22)=imfilter(Egr,L5A18,'replicate');
LT(:,:,23)=imfilter(Egr,L5A19,'replicate');
LT(:,:,24)=imfilter(Egr,L5A20,'replicate');
LT(:,:,25)=imfilter(Egr,L5A21,'replicate');
LT(:,:,26)=imfilter(Egr,L5A22,'replicate');
LT(:,:,27)=imfilter(Egr,L5A23,'replicate');
LT(:,:,28)=imfilter(Egr,L5A24,'replicate');
LT(:,:,29)=imfilter(Egr,L5A25,'replicate');
LT(:,:,30)=imfilter(Egr,L5A26,'replicate');
LT(:,:,31)=imfilter(Egr,L5A27,'replicate');
LT(:,:,32)=imfilter(Egr,L5A28,'replicate');
LT(:,:,33)=imfilter(Egr,L5A29,'replicate');
LT(:,:,34)=imfilter(Egr,L5A30,'replicate');
LT(:,:,35)=imfilter(Egr,L5A31,'replicate');
LT(:,:,36)=imfilter(Egr,L5A32,'replicate');

```

```
LT(:,37)=imfilter(Egr,L5A33,'replicate');
LT(:,38)=imfilter(Egr,L5A34,'replicate');
LT(:,39)=imfilter(Egr,L5A35,'replicate');
LT(:,40)=imfilter(Egr,L5A36,'replicate');
LT(:,41)=imfilter(Egr,L5A37,'replicate');
LT(:,42)=imfilter(Egr,L5A38,'replicate');
LT(:,43)=imfilter(Egr,L5A39,'replicate');
LT(:,44)=imfilter(Egr,L5A40,'replicate');
LT(:,45)=imfilter(Egr,L5A41,'replicate');
LT(:,46)=imfilter(Egr,L5A42,'replicate');
LT(:,47)=imfilter(Egr,L5A43,'replicate');
LT(:,48)=imfilter(Egr,L5A44,'replicate');
LT(:,49)=imfilter(Egr,L5A45,'replicate');
LT(:,50)=imfilter(Egr,L5A46,'replicate');
LT(:,51)=imfilter(Egr,L5A47,'replicate');
LT(:,52)=imfilter(Egr,L5A48,'replicate');
LT(:,53)=imfilter(Egr,L5C1,'replicate');
LT(:,54)=imfilter(Egr,L5C2,'replicate');
LT(:,55)=imfilter(Egr,L5C3,'replicate');
LT(:,56)=imfilter(Egr,L5C4,'replicate');
LT(:,57)=imfilter(Egr,L5C5,'replicate');
LT(:,58)=imfilter(Egr,L5C6,'replicate');
LT(:,59)=imfilter(Egr,L5C7,'replicate');
LT(:,60)=imfilter(Egr,L5C8,'replicate');
LT(:,61)=imfilter(Egr,L5C9,'replicate');
LT(:,62)=imfilter(Egr,L5C10,'replicate');
LT(:,63)=imfilter(Egr,L5C11,'replicate');
LT(:,64)=imfilter(Egr,L5C12,'replicate');
LT(:,65)=imfilter(Egr,L5C13,'replicate');
LT(:,66)=imfilter(Egr,L5C14,'replicate');
LT(:,67)=imfilter(Egr,L5C15,'replicate');
LT(:,68)=imfilter(Egr,L5C16,'replicate');
LT(:,69)=imfilter(Egr,L5C17,'replicate');
LT(:,70)=imfilter(Egr,L5C18,'replicate');
LT(:,71)=imfilter(Egr,L5C19,'replicate');
LT(:,72)=imfilter(Egr,L5C20,'replicate');
LT(:,73)=imfilter(Egr,L5C21,'replicate');
LT(:,74)=imfilter(Egr,L5C22,'replicate');
LT(:,75)=imfilter(Egr,L5C23,'replicate');
LT(:,76)=imfilter(Egr,L5C24,'replicate');
LT(:,77)=imfilter(Egr,L5C25,'replicate');
LT(:,78)=imfilter(Egr,L5C26,'replicate');
LT(:,79)=imfilter(Egr,L5C27,'replicate');
LT(:,80)=imfilter(Egr,L5C28,'replicate');
```

```

LT(:,:,81)=imfilter(Egr,L5C29,'replicate');
LT(:,:,82)=imfilter(Egr,L5C30,'replicate');
LT(:,:,83)=imfilter(Egr,L5C31,'replicate');
LT(:,:,84)=imfilter(Egr,L5C32,'replicate');
LT(:,:,85)=imfilter(Egr,L5C33,'replicate');
LT(:,:,86)=imfilter(Egr,L5C34,'replicate');
LT(:,:,87)=imfilter(Egr,L5C35,'replicate');
LT(:,:,88)=imfilter(Egr,L5C36,'replicate');
LT(:,:,89)=imfilter(Egr,L5C37,'replicate');
LT(:,:,90)=imfilter(Egr,L5C38,'replicate');
LT(:,:,91)=imfilter(Egr,L5C39,'replicate');
LT(:,:,92)=imfilter(Egr,L5C40,'replicate');
%
for i=1:512,
    for j=1:512,
        Z(i,j)=max(LT(i,j,:));
    end
end

function [M]=boundarylayer(NFF,NFQ,Ox)
%boundarylayer(NFF, NFQ, Ox) is designed to find the normalized boundary layer
thickness
%of a Corrected Fluorescence Image, NFF, a Normalized Quenched Image NFQ,
%and the saturated oxygen concentration, Ox in mg/L
A=(1+176*(Ox/1000))/(176*(Ox/1000));
B=1/(176*(Ox/1000));
C=zeros(512,512);
for i=1:512,
    for j=1:512,
        if NFF(i,j)>0;
C(i,j)=(NFQ(i,j)./NFF(i,j)).*A;
M(i,j)=C(i,j)-B;
        end
    end
end

function [cell1,cell4]=cellmean(Y)
%[cell1,cell4]=cellmean(Y) is designed to find the mean values of the image cells
%used in the SLIF verification study
% Copyright G.W.Donath 2000
A=Y(24:89,24:89);
B=Y(296:361,396:461);
cell1=mean2(A)
cell4=mean2(B)

```

```

function [D]=cropset(L1,L2);
%G.W. Donath
%
%
%
i=1;
j=1;
B=ones(512,512);
%
C=ones(512,512);
for i=1:512;
    for j=1:512;
        if (i <= round(L1(1)*j+L1(2))),
            B(i,j)=0;
        end
    end
end
end
%
%
C=cropset2(L2);
%
%
%
D=B.*C;

function C = cropset2(L2);
C=ones(512,512);
%
%
clear i j
%
%
for j=1:512;
    for i=1:512;
        if (i > round((L2(1)*j)+L2(2)));
            C(i,j)=0;
        end
    end
end
end
end

```

```

function [B]=correct3(A,C2,CA,R1b);
%G.W.Donath 8/05
%This function is designed to follow [A1,A2,A3,A4]=correct2(A,CA,CAb)to
%rescale normalized image A in terms of correction arrays CA, and CAb using
%both the values of normalized range, and normalized standard deviation found by
%std2.
%A1 is set to the range of CA DI"/I'
%A2 is set to the range of CA std2
%A3 is set to the range of CAb DI"/I'
%A4 is set to the range of CAb std2
A1=scratchcorrect2(A,150,400);
A2=A1.*C2;
A3=A2/mean2b(A1);
RA=std2b(A3)
%
%
B1=blkproc(A,[1,1],'scale3',R1b,RA);
%
B2=t2filter(CA,B1);
%
%
```

```

function [B,C]=correctBF(A,C2,CA);
%G.W.Donath 8/05
%This function is designed to correct images as instructed, it will remove
%scratches, crop by C2, normalize by the mean, scale by the std2b of CA,
%and then correct by CA in t3filter
%
A1=scratchcorrection2(A,150,400);
A2=A1.*C2;
A3=A2/mean2b(A2);
RA=std2b(A3);
Rb=std2b(CA);
z=1;
%
%
CAs=blkproc(CA,[1 1],'scale4',RA,Rb);
%flat feild correction
B1=t3filter(CAs,A3);
%
%Find remainder background
D1=B2Dfind(B1,B1);
%
%remainder background subtraction
```

```
[B,C]=B2filter(D1,B1);
%
mean2b(B),std2b(B)
```

```
function [D]=cropset(L1,L2);
% This function along with cropset2 are designed to generate the crop % array from the
line arrays generated elsewhere
% G.W. Donath 2006
i=1;
j=1;
B=ones(512,512);
%
```

```
C=ones(512,512);
for i=1:512;
    for j=1:512;
        if (i <= round(L1(1)*j+L1(2))),
            B(i,j)=0;
        end
    end
end
end
%
%
C=cropset2(L2);
%
%
%
D=B.*C;
```

```
function C = cropset2(L2);
C=ones(512,512);
% Sub-function of cropset
% G.W. Donath 2006
clear i j
%
%
for j=1:512;
    for i=1:512;
        if (i > round((L2(1)*j)+L2(2)));
            C(i,j)=0;
        end
    end
end
end
```

```

function [Z]=crosscheck(A)
%G.W.Donath 05/18/06
%Designed to find the best possible location of zero crossing for a given
%function A is a 2x1 matrix, Z is the 2x1 response
%
Te=A(1).*A(2);
if Te>0,
    Z=[0 0];
elseif Te<0,
    R=min(abs(A));
    j=find(abs(A)==R);
    Z(j)=1;
else
    R=min(A);
    j=find(A==R);
    Z(j)=1;
end

```

```

function [J,Z,D1D2map]=dwavgayls(A,name);
% This function is designed to find the downwelling zones and %calculate the average
width (J), average dimensionless mass transfer %value Z, and D1D2 which is the map of
the downwelling zone
% G.W. Donath 2006
[W1,D1D2map,D2,W3]=dwlocate(A);
Ab=(A==0);
Az=(A+Ab)<0.96;
W2=W1.*Az;
AB=ones(512,512);
AB(1:5,:)=0;
AB(507:512,:)=0;
AB(:,1:5)=0;
AB(:,507:512)=0;
W3=W2.*AB;
%
[lr,lc]=find(W3>0);
ls=length(lr);
lz=ls+3;
JT=zeros(lz,13);
%
LIRA=linerank(W1,lr,lc);
%

```

```

for i=1:ls
    iv=i+3
    ri=lr(i);
    ci=lc(i);
    JT(iv,1)=ri;
    JT(iv,2)=ci;
    %
    if D1D2map(ri,ci)==1.5;
        BA=dwlc1(A(ri,:),ci);
        BL=ci;
    elseif D1D2map(ri,ci)==1;
        [BA,BL]=dwlc2(A(ri,:),D1D2map(ri,:),ci);
        if BL<1;
            BL=1;
        end
    else
        break
    end
    JT(iv,3)=BL;
    JT(iv,4)=BA;
    %
    D2R=imregionalmin(D2(ri,:));
    [M1,M2,M1V,M2V]=shoulderfind(D2R,A(ri,:),BL);
    JT(iv,5)=M1;
    JT(iv,6)=M2;
    Mx=max([M1V,M2V]);
    JT(iv,7)=Mx;
    dH=Mx-min([M1V,M2V]);
    JT(iv,8)=dH;
    %
    HMWV=((Mx-BA)/2)+BA;
    JT(iv,11)=HMWV;
    V=A(ri,:);
    size(V)
    size(BL)
    HMWV;
    M1V;
    M2V;
    M1;
    M2;
    %
    [wid,S1,S2]=zmaxhalfwidth(V,BL,HMWV,M1V,M2V,M1,M2);
    JT(iv,10)=LIRA(ri,ci);
    JT(iv,9)=wid;

```



```

%
%
DKA=imfilter(A2,hd1,'replicate');
D2KA=imfilter(DKA,hd2,'replicate');
ZM=(zeromap(DKA)).*0.5;
%
%Plot maxima
for i=1:512;
    T(i,:)=imregionalmax(D2KA(i,:));
end
%
Er=T.*D2KA;
Eg=Er>0.75;
ZM=Eg+ZM;
Egr=Er.*Eg;
%
LA=Zline(Egr);
%
Ert=abs(Er);
ZLS=nlfilter(Ert,[3 17],'polymut');
ZLSn=ZLS>0;
LA2=LA.*ZLSn;
LA3=LA2>25;
%
MG=findcontpoints(LA3);
Z=MG>4;

function [Z]=findcontpoints(A);
%G.W. Donath 05/29/06
%[Z]=findcontpoints(A)
%A=Data (should be made up of 1/0
%Z=output various 'regions' ranked by multiplying by their region ranking
%
%
%
set(0,'RecursionLimit',1000);
G=A;
[l,m]=size(A);
B=ones(1,m);
Rmt=zeros(1,m);
A=A>0;
A=double(A);
[xp,yp]=find(A>0);
ul=length(xp);

```

```

ky=(length(xp));
k=1;
while ky>0;
    Rk=zeros(1,m);
    I=xp(1);
    J=yp(1);
    Rk(I,J)=1;
    Ra=0;
    Rm=zeros(1,m);
    [xt,yt]=find((Rk.*B)>0);
    Ne=length(xt);
    while Ne>0;
        I1=xt(1);
        J1=yt(1);
        Rk(I1,J1)=0;
        [B,Rm,Ra,Rk]=searchpoints(I1,J1,A,B,Rm,Ra,Rk);
        [xt,yt]=find((Rk.*B)>0);
        Ne=length(xt);
    end
    Ac=B.*A;
    [xp,yp]=find(Ac>0);
    ky=length(xp);
    Rmt=Rmt+(Rm.*Ra.*G);
    %
    Ra;
    k=k+1;
end
Z=Rmt;

function [M1,M2,DM]=findminmax(A,z1,z2);
% G Donath 07/22/05
% [M1,M2,DM]=findminmax(A,z1,z2);
% M1=minimum at Z1 from bottom
% M2=maximum at Z2 from top
% DM
% Z1 percentage (as % of the number of values) from the absolute maximum value
% Z2 percentage (as % of the number of values) from the absolute minimum value
% A is the array that you wish to process
y1=size(A);
y2=y1(1)*y1(2);
A2=reshape(A,y2,1); % Create a linear string
A2=sort(A2);
x1=round(z1/100*y2); % find the point of Z1 in the string
x2=(y2-round(z2/100*y2)); % find the point of Z2 in the string

```

```

M1=A2(x1);
M2=A2(x2);
DM=M2-M1;

```

```

function Z=halfmaxwidth(A,ci,HMWV,M1V,M2V,M1,M2);
% The function halfmaxwidth calculates the half max width of a
% downwelling zone based on the location of the peaks or shoulders
% to the left and right of the downwelling zone.
%
%
k=0;
i=0;
g1=1;
g2=1;
if HMWV>M1V,
    k=0.5
    g1=0;
    S1=M1;
elseif HMWV>M2V,
    k=0.5
    g2=0;
    S2=M2;
end
%
while k<1;
    i=i+1;
    il=ci-i;
    il1=il;
    il2=il+1;
    if il<1;
        il=1;
        il1=1;
        if g1>0;
            S1=il;
            k=k+0.5;
            g1=0;
        end
    end
end
    iu=ci+i;
    iu1=iu;
    iu2=iu+1;
    if iu>512;
        iu=511;
        iu2=512;
    end
end

```

```

        if g2>0;
        S2=il;
        k=k+0.5;
        g2=0;
        end
    end
    %
    ilm=A(il1:il2).*g1;
    ium=A(iu1:iu2).*g2;
    if max(ilm)>=HMWV,
        if min(ilm)<=HMWV
            z1=ilm-HMWV;
            t=(find(min(abs(z1))));
            k=k+0.5;
            g1=0;
            if t==1;
                S1=il1;
            else
                S1=il2;
            end
        end
    end
    if max(ium)>=HMWV,
        if min(ium)<=HMWV
            z1=iium-HMWV;
            t=(find(min(abs(z1))));
            k=k+0.5;
            g2=0;
            if t==1;
                S2=iu1;
            else
                S2=iu2;
            end
        end
    end
    end
    Z=abs((S2-S1));

```

```

function [M,K,J,G,H,I]=imnorm(A1)
%imnorm is designed to quickly implement the basic function
%M=A1/mean2(A1); Where A1 is a double precision array. The output [M,K,J,G]
includes
%K the min(min(M)) and J the max(max(M)) G is the mean2(M)
M=A1/mean2(A1);

```

```

K=min(min(M))
J=max(max(M))
G=mean2(M)

```

```

function [A]=Inv3(M)
%The function needed for t2filter to calculate 1/x for all points
A=blkproc(M,[1 1],'gwd3',1);

```

```

function B=invertignorezero(A1)
%The function is designed to invert an array of data but ignore the cropped
%points of the image that are zero
%
%
[I,J]=size(A1);
C=zeros(I,J);
%
for i=1:I,
    for j=1:J,
        if A1(i,j)>0
            C(i,j)=(1/A1(i,j));
        else
            C(i,j)=0;
        end
    end
end
end
B=C;

```

```

function [L1,L2,A3,A4]=linefind(Ii,leveli)
% the function linefind calculates the line values for cropping using
% the data set Ii at a level (leveli)%
%Divide image into upper and lower half
Iil=Ii(1:250,:);
Iiu=Ii(251:512,:);
%
%Calculate levels based on each half
%
A1=contourc(Iil,[leveli leveli]);
A2=contourc(Iiu,[leveli leveli]);
%
LT1=A1(2,1)+1;
LT2=A2(2,1)+1;
%remove first set of data
%
A3=zeros(2,(LT1-1));

```

```

%
A4=zeros(2,(LT2-1));
for i=2:LT1
    A3(:,(i-1))=A1(:,i);
end
%
for i=2:LT2
    A4(:,(i-1))=A2(:,i);
    %
    A4(2,(i-1))=A4(2,(i-1))+250;
end
%Find slope and intercept for lines
%
%
A3=sort(A3,2);
A4=sort(A4,2);
S1=polyfit(A3(1,:),A3(2,:),1);
S2=polyfit(A4(1,:),A4(2,:),1);
%
L1=rint(A3,S1);
L2=rint(A4,S2);

```

```

function Z=linerank(A,rl,cl);

```

% This function adds the contious points during the downwelling %location process and gives each line segment a rank equivalent to the %number of points within the line segment.

```

%
%
[j,k]=size(A);
B=ones(j,k);
E=zeros(j,k);
Zi=zeros(j,k);
y=length(rl);
%
for i=1:y,
    ri=rl(i);
    ci=cl(i);
    r1=rl(i)-4;
    r2=rl(i)+4;
    c1=cl(i)-4;
    c2=cl(i)+4;
    U1=A(r1:r2,c1:c2);
    U2=B(r1:r2,c1:c2);
    UE=E(r1:r2,c1:c2);

```

```

    E(ri,ci)=sum(sum(U1.*U2))+max(max(UE));
    B(r1:r2,c1:c2)=zeros(9,9);
end
ru=flipud(rl);
cu=flipud(cl);
for f=1:y,
    ri=ru(f);
    ci=cu(f);
    r1=ru(f)-4;
    r2=ru(f)+4;
    c1=cu(f)-4;
    c2=cu(f)+4;
    U3=E(r1:r2,c1:c2);
    Zi(ri,ci)=max(max(U3));
end
Z=Zi;

```

```

function [B]=locatemaxima(A)
% G.W. Donath 04/22/06 [B]=locatemaxima(A);
% This function locates the minima and maxima of a profile from the % %image
%
%
%
%
P1=imregionalmax(A);
P2=find(P1>0.9);
Iz=length(P2);
for i=1:Iz
    j=P2(i);
    P3(1,i)=A(j);
    P3(2,i)=P2(i);
end
%
%
P4=P3';
P5=sortrows(P4,1);
B=(flipud(P5))';

```

```

function m=mean2b(A);
% Calculates the two dimensional mean after removing the zeros from the % cropped
image
B=rmvzeros(A);
m=mean(B);

```

```

function m=min2b(A);
% Calculates the minima of the image after removing the zeros from the % cropped
image
B=rmvzeros(A);
m=min(B);

```

```

function [M]=minmap(A,B)
%minmap generates a map of the image A finding points where they are less than Z
%and then plotting them as an array of the same size as A with ones
A2=zeros(size(A));
[j,k]=find(A < B);
for u=1:length(j);
    A2(j(u),k(u))=1;
end
M=A2;

```

```

function [C]=plotmaxima(B,S)
%G.W. Donath 04/22/06
% Subfunction of the function dwlocate which plots the location of the
% maxima and minima of the image before being ranked and filtered
%
P1=zeros(1,S);
J=length(B);
if J>10,
    J=10;
end
%
for i=1:J;
    if (B(1,i))>0,
        P1(B(2,i))=B(1,i);
    else
        P1(B(2,i))=0;
    end
end
C=P1;

```

```

function B=rmvzeros(A);
% removes the zero values from a cropped image so that the next % %function will not
include cropped values of zero in its calculation
[r,c]=size(A);
t=r*c;
%
A1=zeros(1,t);

```

```

A1=reshape(A,t,1);
%
A2=sort(A1,'descend');
if min(A2)>0;
    c=t+1;
else
c=find((A2==0),1,'first');
end
%
B=A2(1:c-1);

function [A,B]=linest(Im,CA)
% Estimates the line values for analysis
%
[s1,s2]=size(Im);
%produce the horizontal index
for i=1:s2, In1(1,i)=i;end
% produce the vertical index
for i=1:s1, In2(i,1)=i;end
%
%allocate memory
DH=zeros(3,s2);
DV=zeros(3,s1);
HD=zeros(s1,3);
HD(:,1)=In2;
VD=zeros(3,s2);
VD(1,:)=In1;
%
%send data to proper location
%horizontal data
for j=1:s1;
    DH(3,:)=In1;
    DH(2,:)=Im(j,:);
    DH(1,:)=CA(j,:);
    HD(j,2:3)=thetacalc(DH,s2)
end
%Vertical data
for m=1:s2;
    DV(3,:)=In2';
    DV(2,:)=Im(:,m)';
    DV(1,:)=CA(:,m)';
    VD(2:3,m)=(thetacalc(DV,s1))';
end
%

```

```

%Now to find the locus
[a1,b1]=polyfit(VD(3,:),VD(1,:),1);
[a2,b2]=polyfit(HD(:,3),HD(:,1),1);
%
xx=(b2-b1)/(a1-a2);
yy=a1*xx+b2;
%
%Now to estimate the angles
%alpha
alpha=mean(HD(:,2));
beta=mean(VD(2,:));
%
A=[xx yy];
B=[alpha beta];

function [v]=scale4(u,R1,Ri)
%G.W. Donath 8/05
%This function is designed to rescale the point value u to v based on the
%scale Ri and R1. Where Ri is the original range for values of u and R1 is
%the desired range of values of v.

if u==0,
    v=0;
elseif u < 1
    v=((R1/Ri)*(u-1))+1;
elseif u > 1
    v=((R1/Ri)*(u-1))+1;
else
    v=u;
end

function I2=scratchcorrection2(I1,K1,K2,C)
% Removes a scratch from image I1 along from pixels K1 to K2 along
% column C
%
while K1 <= K2,
    I1(K1,C)=(I1(K1,C-1)/2+I1(K1,C+1)/2);
    K1=K1+1;
end
I2=I1;

```

```

function [Bo,Rmo,Rao,Rlo]=searchpoints(I,J,A,B,Rm,Ra,RI);
%G.W.Donath 05/29/06
%[Bo,Rmo,Rao]=searchpoints(I,J,A,B,Rm,Ra);
%A=data
%B=Used points map
%C=linecurvepoints map (removed)
%Rm=region points map
%Ra=Rank of region
%I=row
%J=column
%Rm=region map
M=[1 1 1 1 1 1 1; 1 1 1 0 1 1 1; 1 1 1 1 1 1 1];
B(I,J)=0;
Rm(I,J)=1;
x=I-1;
y=J-3;
y2=y+6;
x2=x+2;
z=0;
if y2>512;
    y2=512;
    z=1;
end
if x2>512;
    x2=512;
    z=1;
end
if x<1;
    x=1;
    z=1;
end
if y<1;
    y=1;
    z=1;
end
PB=B(x:(x2),y:(y2));
PA=A(x:(x2),y:(y2));
%PC=C(x:(x+2),y:(y+6));
if z==1;
[x3,y3]=size(PB);
Mt=ones(x3,y3);
PT=(Mt.*PA.*PB);
else
PT=(M.*PA.*PB);

```

```

end
Sa=sum(sum(PT));
if(Sa>0);
[l1,m1]=size(Rl);
Rc=zeros(l1,m1);
Rc(x:x2,y:y2)=PT;
Rlo=Rl+Rc;
Ra=Ra+1;
else
Rlo=Rl;
end
Bo=B;
Rao=Ra;
Rmo=Rm;

function [M1,M2,M1V,M2V]=shoulderfind(A,B,ci);
% Locates the two shoulder locations for a downwelling zone based on %the first
% derivative crossing A and the second derivative crossing B
% to the downwelling location ci;
%
%
%
M1=ci;
M2=ci;
M1V=B(ci);
M2V=B(ci);
k=0;
i=0;
g1=1;
g2=1;
s1=0;
su=0;
j=0;
while k<1;
    j=j+1;
    ci=round(ci);
    i=i+1;
    il=ci-i;
    il1=il-1;
    il2=il+1;
    if il1<1;
        il=1;
        il1=1;
        s1=1*g1;

```

```

    end
iu=ci+i;
iu1=iu-1;
iu2=iu+1;
    if iu2>512;
        iu=512;
        iu2=512;
        su=1*g2;
    end
ci;
il1;
il2;
%
ilm=A(il).*g1;
ium=A(iu).*g2;
if ilm==1;
    M1V=mean(B(il1:il2));
    M1=il;
    k=k+0.5;
    g1=0;
    s1=0;
end
if ium==1,
    M2V=(B(iu1:iu2))/3;
    M2=iu;
    k=k+0.5;
    g2=0;
    su=0;
end
if s1==1,
    M1V=mean(B(il1:il2));
    M1=il;
    k=k+0.5;
    g1=0;
end
if su==1;
    M1V=(B(il1:il2))/3;
    M2=il;
    k=k+0.5;
    g1=0;
end
if j>1000;
    n='Error point at',
    k=1;

```

```

    M1=ci;
    M2=ci;
    M1V=B(ci);
    M2V=B(ci);
end
end

```

```

function C=std2b(A);
%Calculates the standard deviation after removing the cropped (zero)
% values of the image from consideration.
B=rmvzeros(A);
C=std(B);

```

```

function [K,I,J,L]=t2filter(A2,A3)
%This function is to take an average image and create an inversed normalized
%image functions that can be used in d2filter not dfilter A=invdfilter(A2)
%elsewhere
fA2=double(A2);
fA3=double(A3);
fA3=fA3/(mean2(fA3));
G=fA2<=0.0;
L=0;
[I,J]=find(G);
c=length(I);
for n=1:c,
    if I(n)==1,
        a=2;
    elseif I(n)==512,
        a=0;
    else
        a=1;
    end

% next part
    if J(n)==1,
        b=2;
    elseif J(n)==512
        b=0;
    else
        b=1;
    end
    Q=mean2(fA2((I(n)-2+a):(I(n)+a),(J(n)-2+b):(J(n)+b)));
    fA2(I(n),J(n))=Q;
    L=L+1;
end

```

```

    end
    imean=1.000;
    ifA2=blkproc(fA2,[1 1],'gwd3',imean);
    S=fA3.*ifA2;
    if S < 0;
        K=0;
    else
        K=S;
    end
end

```

```

function B=tagremove(A,level);
%G.W. Donath
% Removes data tags before processing the given set of data
%
%
m=1;
n=1;
%
%
while n < length(A),
    if A(1,n)==level,
        c=(A(2,n));
        B(:,m:(m+c-1))=A(:,(n+1):(n+c));
        n=n+c+1;
        m=m+c;
    else
        B(:,m)=A(:,n);
        m=m+1;
        n=n+1;
    end
end
end
%techform.m
%function to convert matrix of data to a single column of data to use in techplot

```

```

function mtxcol=techform(A)
[r,c]=size(A);
mtxcol=reshape(A,r*c,1);

```

```

function F=var2B(A,data)
% This is the function that represents a two-dimensional planar
% rotation
x=data(1,:);

```



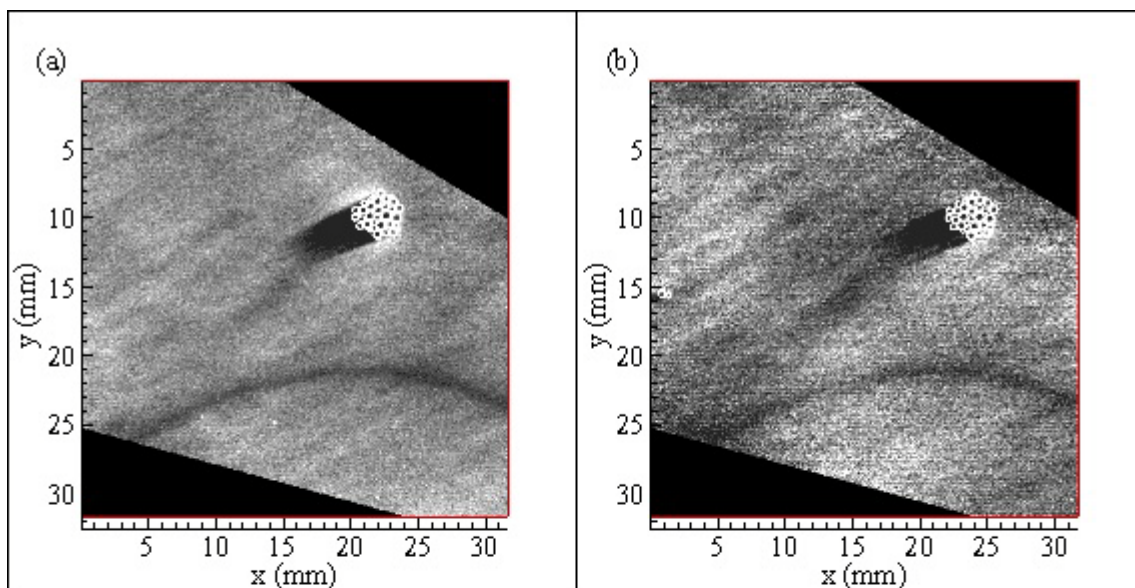
```

function [Z]=zeromap(A);
%G.W. Donath
%[Z]=zeromap(A) is designed to find the zero points or zero value crossings
%of the Array (A) A is to be 512 by 512
%Z shall plot a one at each approximate zero value and at the value closest
%to the axis at the zero crossing
%
[y1,y2]=size(A);
Z=zeros(y1,y2);
K=y2-1;
for i=1:y1,
    for j=1:K
        if max(Z(i,j:j+1))<0.5;
            A2=A(i,j:j+1);
            Z(i,j:j+1)=crosscheck(A2);
        end
    end
end
end

```

## APPENDIX C: SELECTED DIMENSIONLESS MASS TRANSFER PLOTS

The dimensionless mass transfer plots for R27, R42, R58, R63, R91, and R96 are presented here for reference. The data set R29 is not presented due to the high dissolved oxygen concentration of the water removed the possibility of imaging any differences in the oxygen concentration gradient. The data set R61 is not included due to its relatively small size (25 images) and the presence of objects within the images. In some instances, such as the plots presented for R27, there is a long delay time between the start of the image capture process and the capturing of a usable image.



$k^*$ : 0 0.8 0.84 0.88 0.92 0.96 1 1.04 1.08 1.12 1.16 1.2

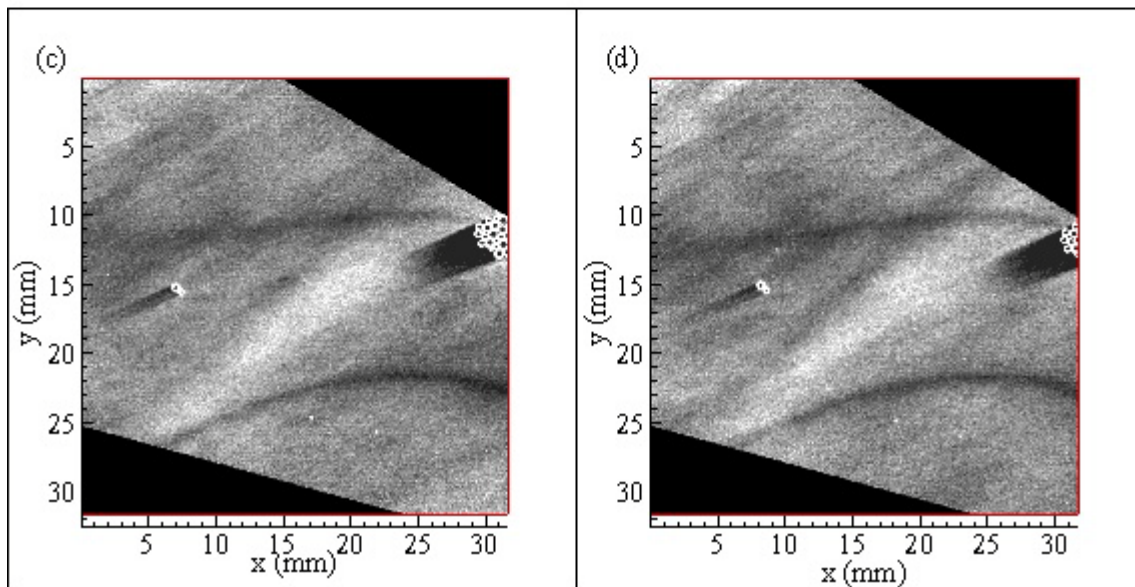
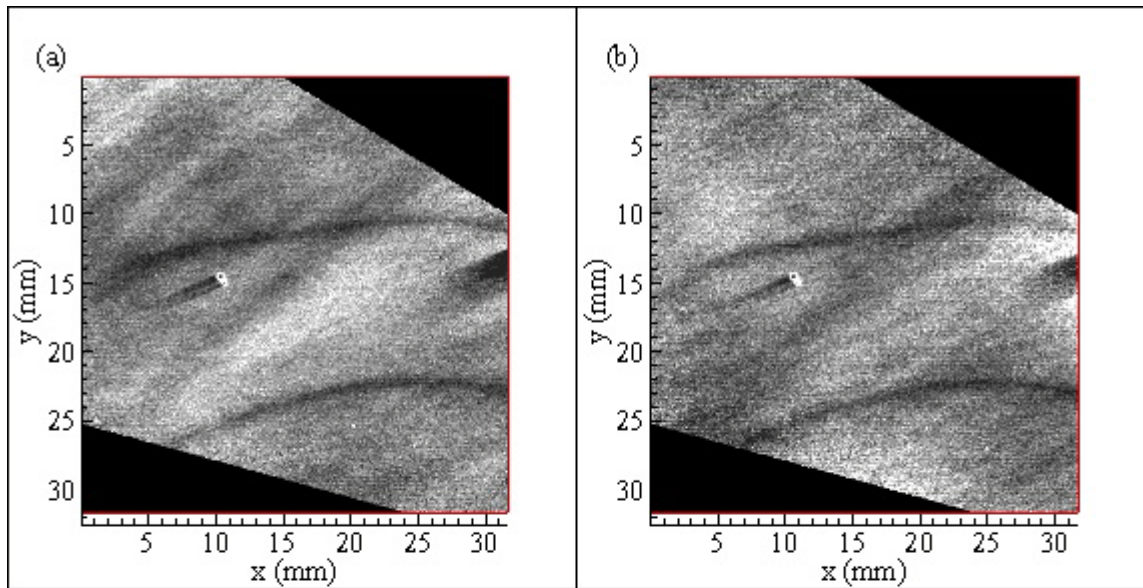


Figure C.1. Grayscale plots of normalized dimensionless mass transfer coefficient values at 27% relative humidity: (a) R27C\_23; 3 min.: 10 sec., (b) R27C\_24; 3 min.: 30 sec., (c) R27C\_34; 4 min.: 20 sec., (d) R27C\_36; 4 min.: 40 sec.



$k^*$ : 0 0.8 0.84 0.88 0.92 0.96 1 1.04 1.08 1.12 1.16 1.2

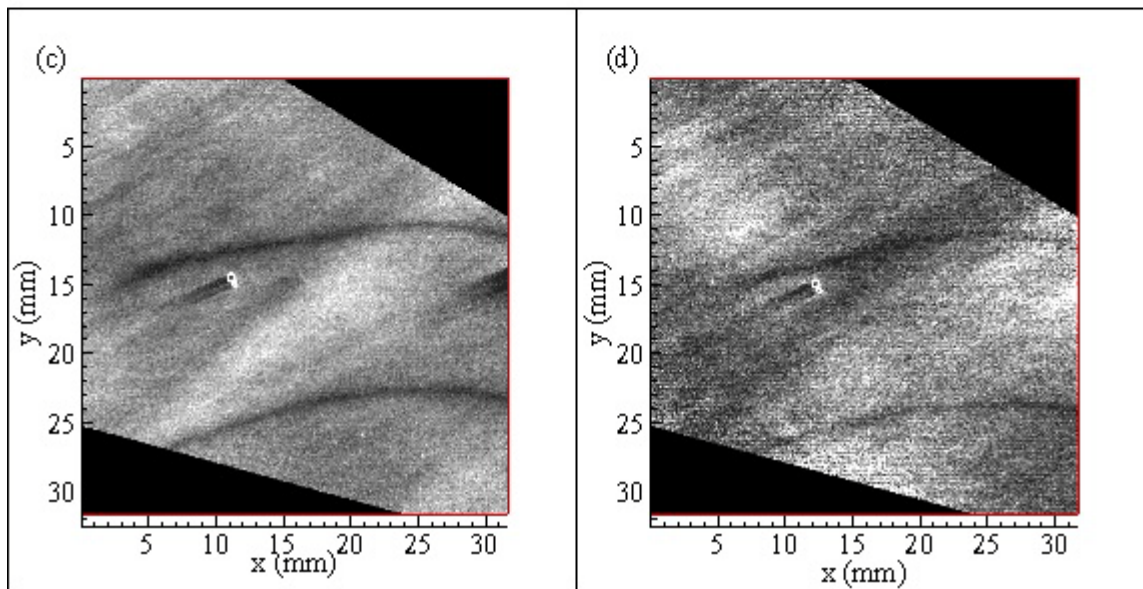
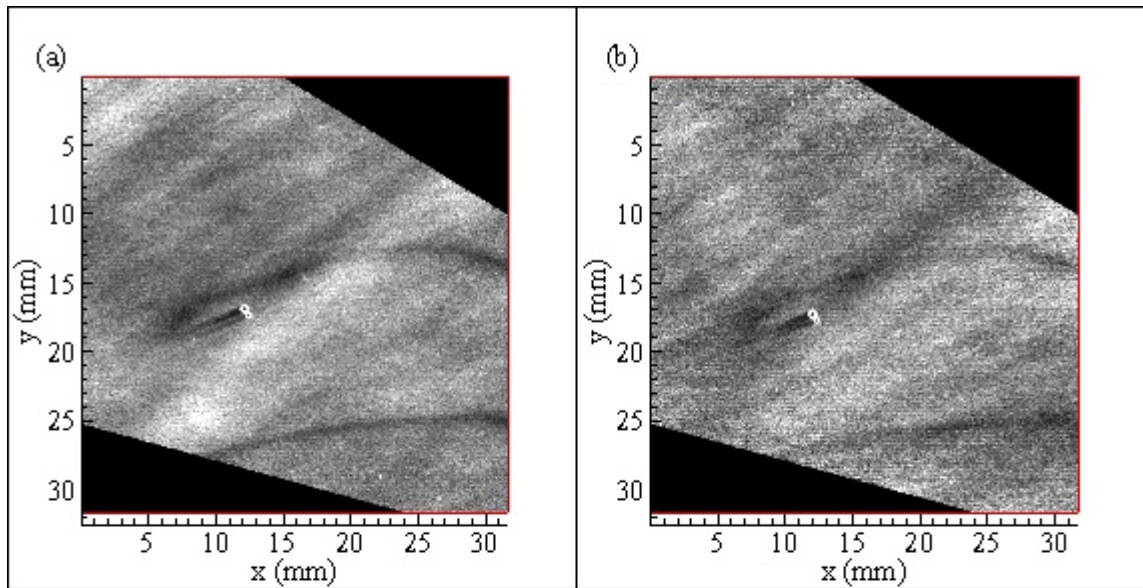


Figure C.2. Grayscale plots of normalized dimensionless mass transfer coefficient values at 30% relative humidity: (a) R27C\_43; 5 min.: 00 sec., (b) R27C\_44; 5 min.: 10 sec., (c) R27C\_47; 5 min.: 20 sec., (d) R27C\_54; 5 min.: 50 sec.



$k^*$ : 0 0.8 0.84 0.88 0.92 0.96 1 1.04 1.08 1.12 1.16 1.2

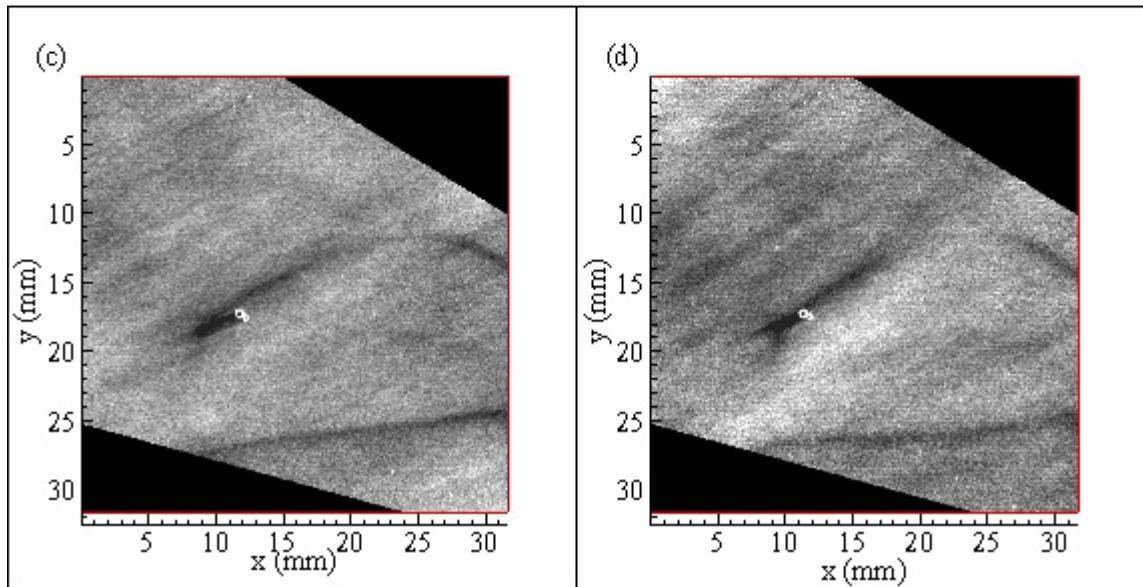


Figure C.3. Contour Plots of normalized dimensionless mass transfer coefficient values at 30% relative humidity: (a) R27C\_64; 6 min.: 30 sec., (b) R27C\_66; 7 min.: 00 sec., (c) R27C\_81; 7 min.: 33 sec., (d) R27C\_82; 7 min.: 40 sec.

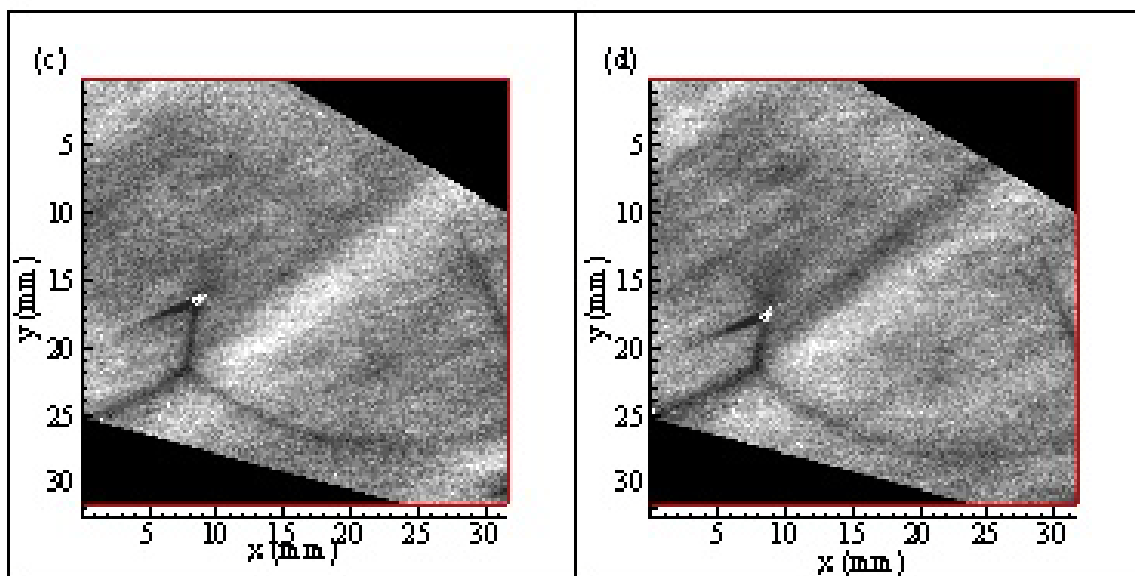
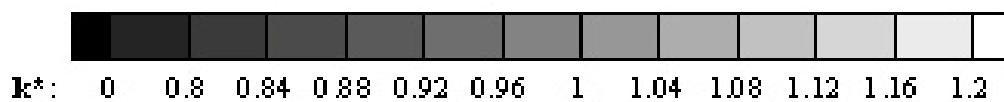
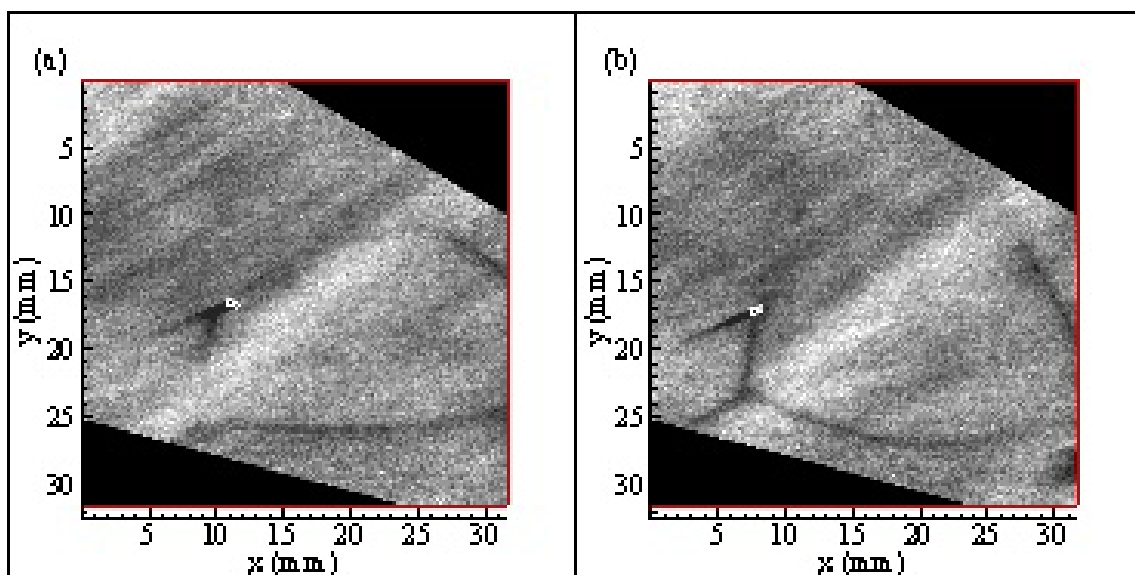


Figure C.5. Grayscale plots of normalized dimensionless mass transfer coefficient values at 30% relative humidity: (a) R27D\_1; 9 min.: 22 sec., (b) R27E\_8; 9 min.: 34 sec., (c) R27E\_10; 9 min.: 52 sec., (d) R27E\_13; 10 min.: 06 sec.

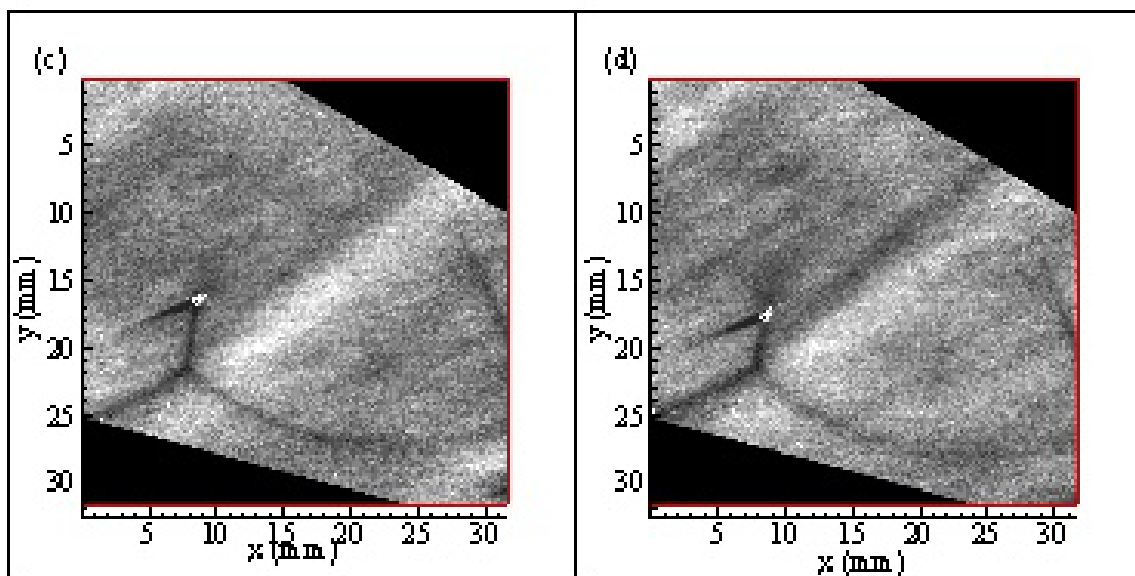
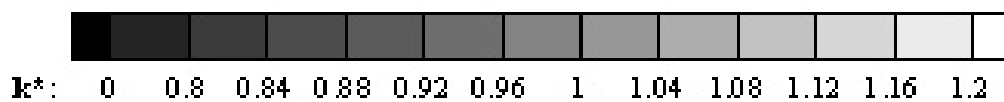
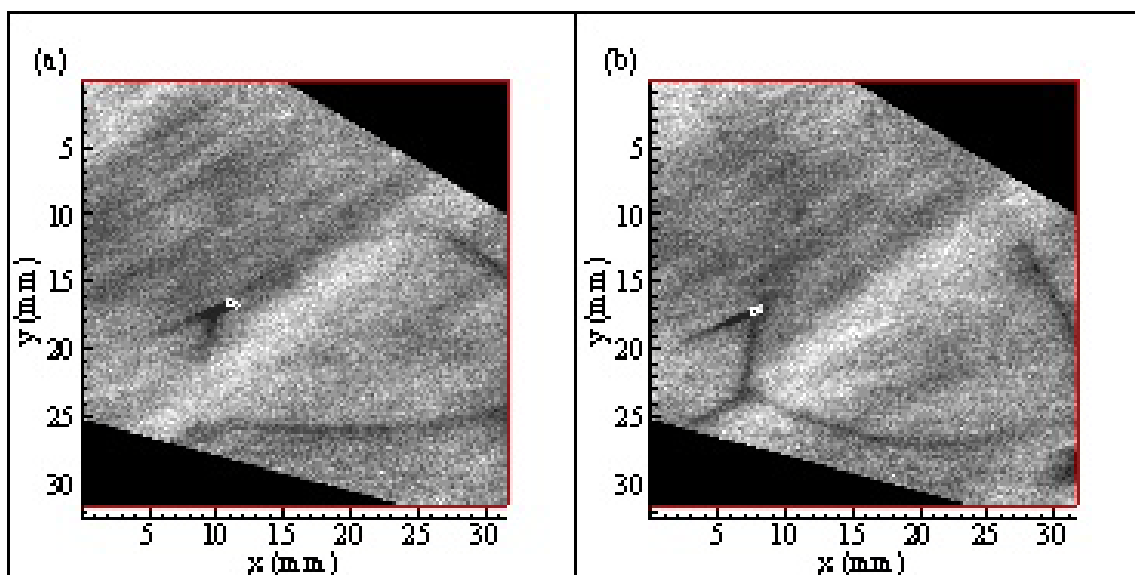
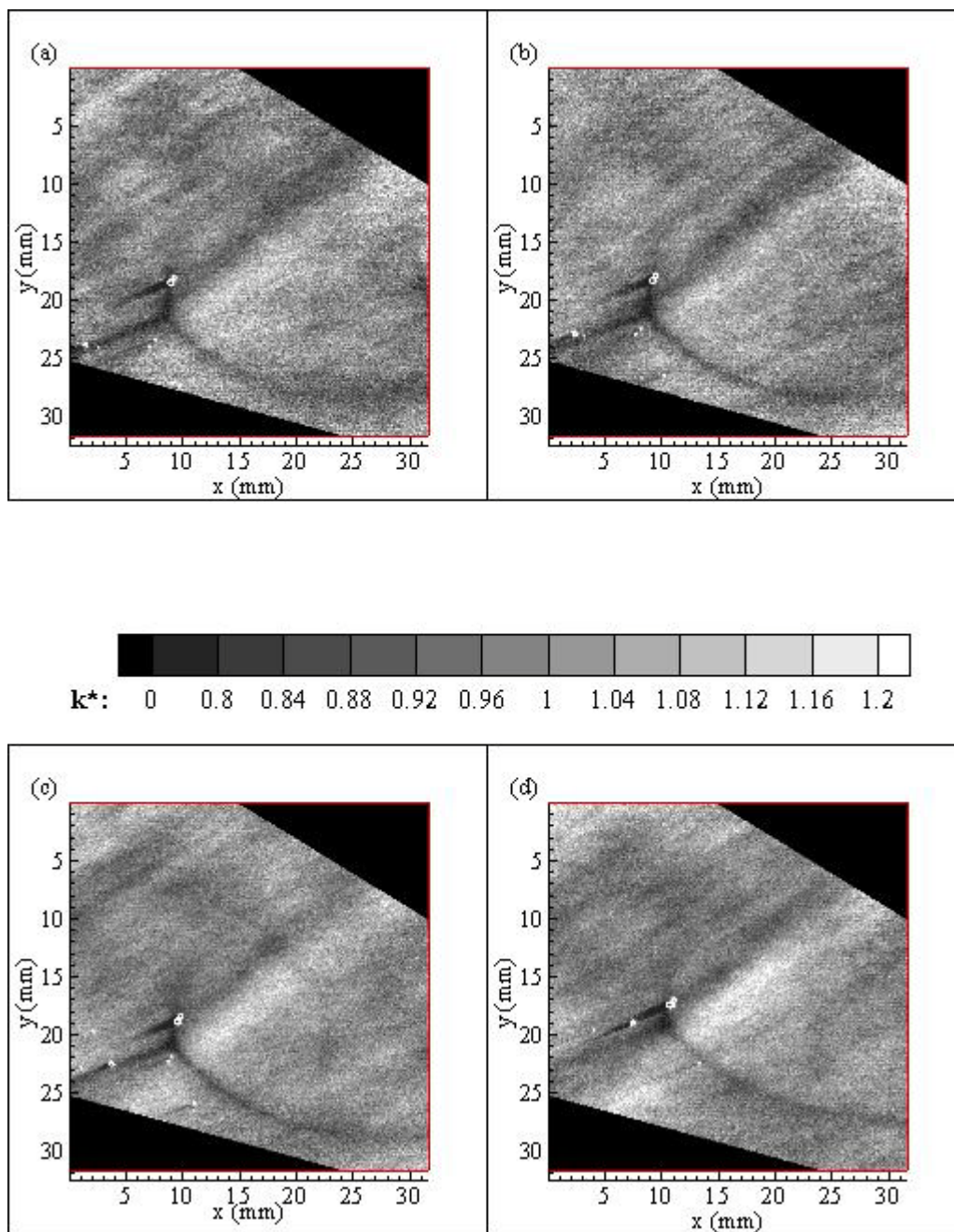
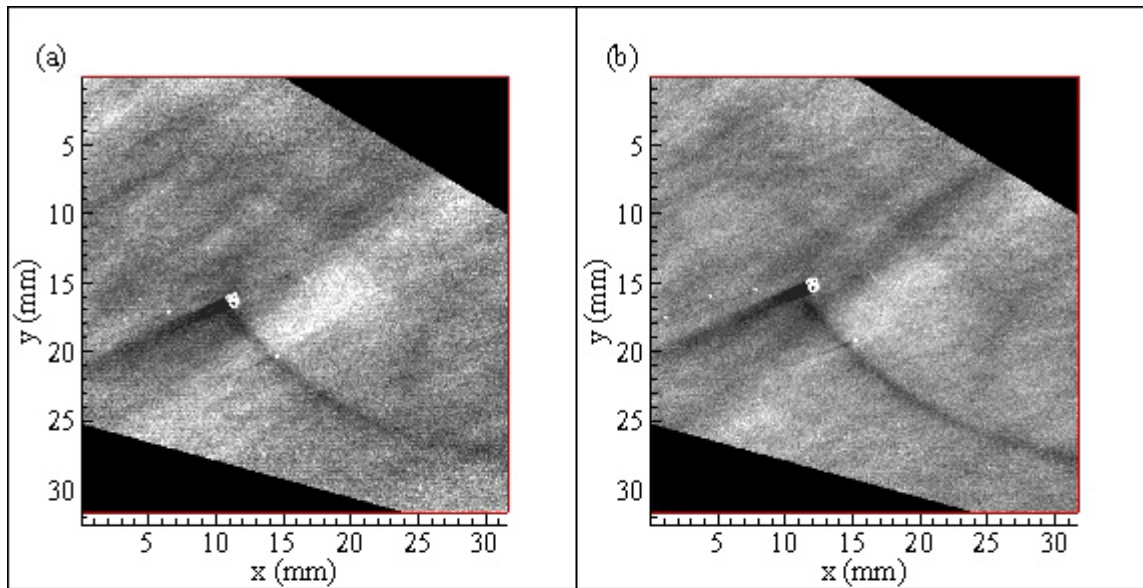


Figure C.5. Grayscale plot of normalized dimensionless mass transfer coefficient values at 30% relative humidity: (a) R27D\_1; 9 min.: 22 sec., (b) R27D\_8; 9 min.: 34 sec., (c) R27D\_10; 9 min.: 52 sec., (d) R27D\_13; 10 min.: 06 sec.





$k^*$ : 0 0.8 0.84 0.88 0.92 0.96 1 1.04 1.08 1.12 1.16 1.2

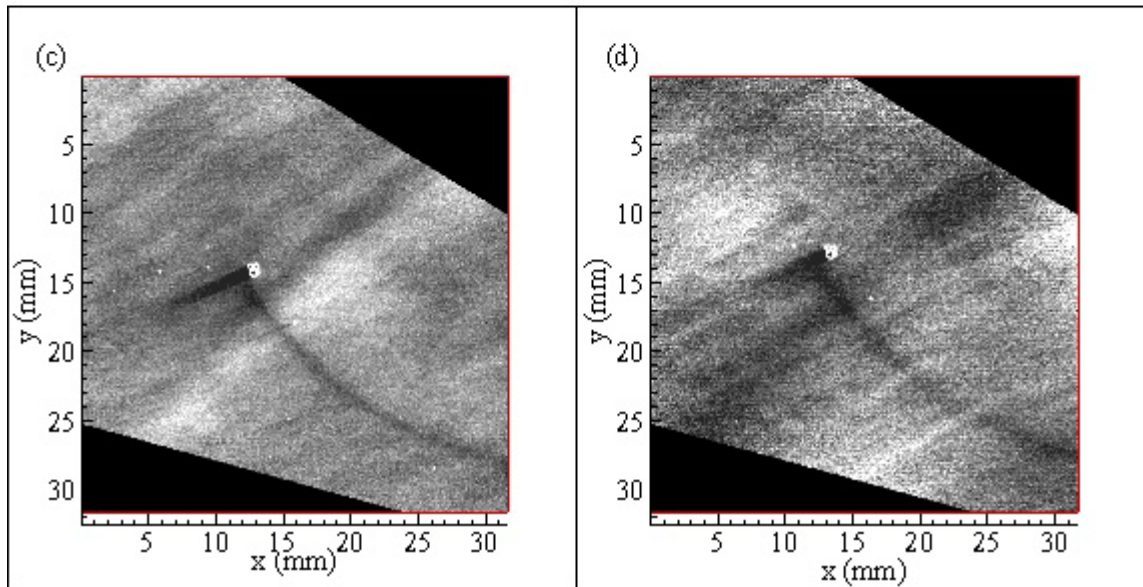
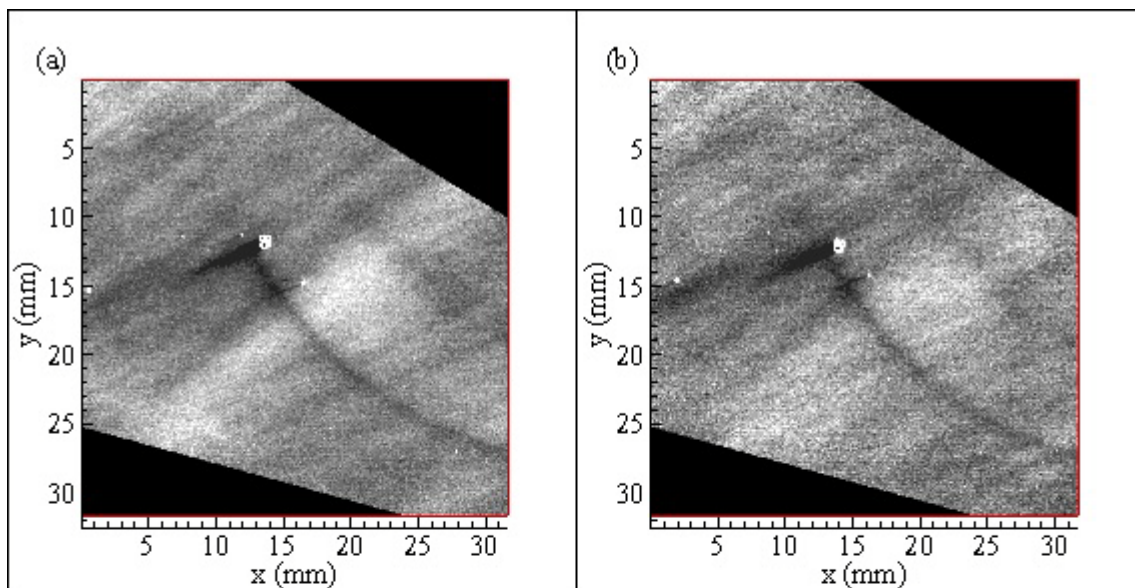


Figure C.7. Grayscale plots of normalized dimensionless mass transfer coefficient values at 27% relative humidity. (a) R27E\_18; 12 min.: 50 sec., (b) R27E\_23; 13 min.: 10 sec., (c) R27E\_27; 13 min.: 30 sec., (d) R27E\_7; 13 min.: 50 sec.



$k^*$ : 0 0.8 0.84 0.88 0.92 0.96 1 1.04 1.08 1.12 1.16 1.2

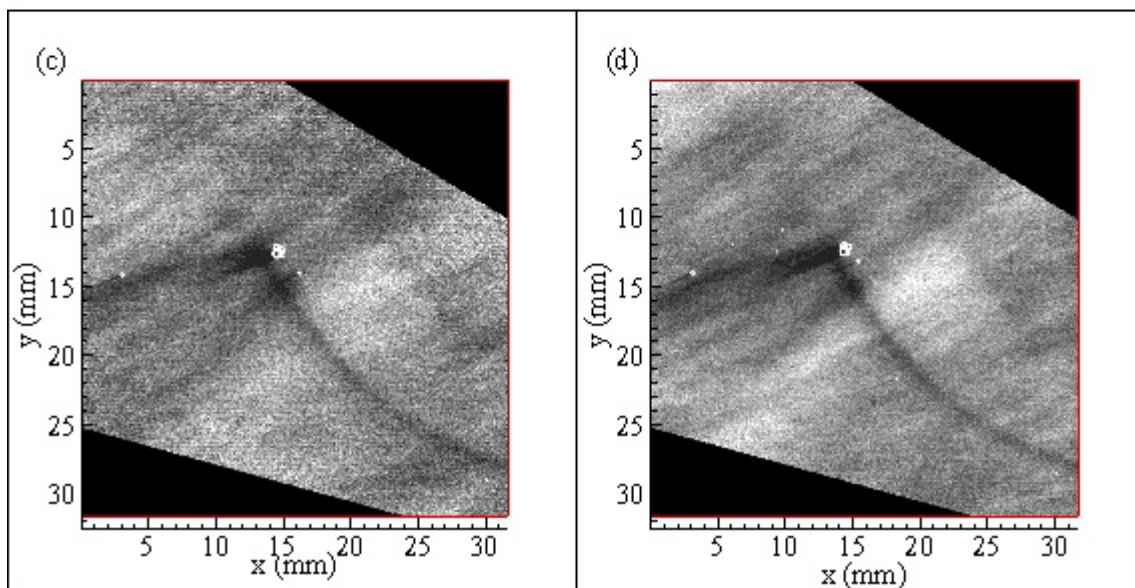
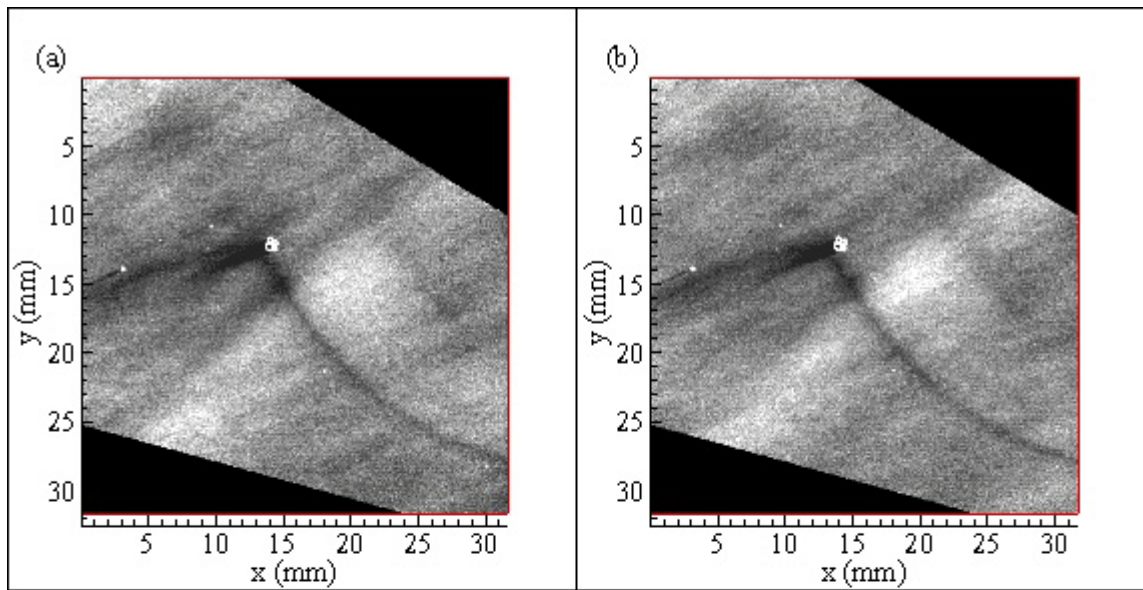


Figure C.8. Grayscale plots of normalized dimensionless mass transfer coefficient values at 27% relative humidity: (a) R27E\_46; 14 min.: 10 sec., (b) R27E\_62; 14 min.: 30 sec., (c) R27E\_69; 14 min.: 54 sec., (d) R27E\_73; 15 min.: 00 sec.



$k^*$ : 0 0.8 0.84 0.88 0.92 0.96 1 1.04 1.08 1.12 1.16 1.2

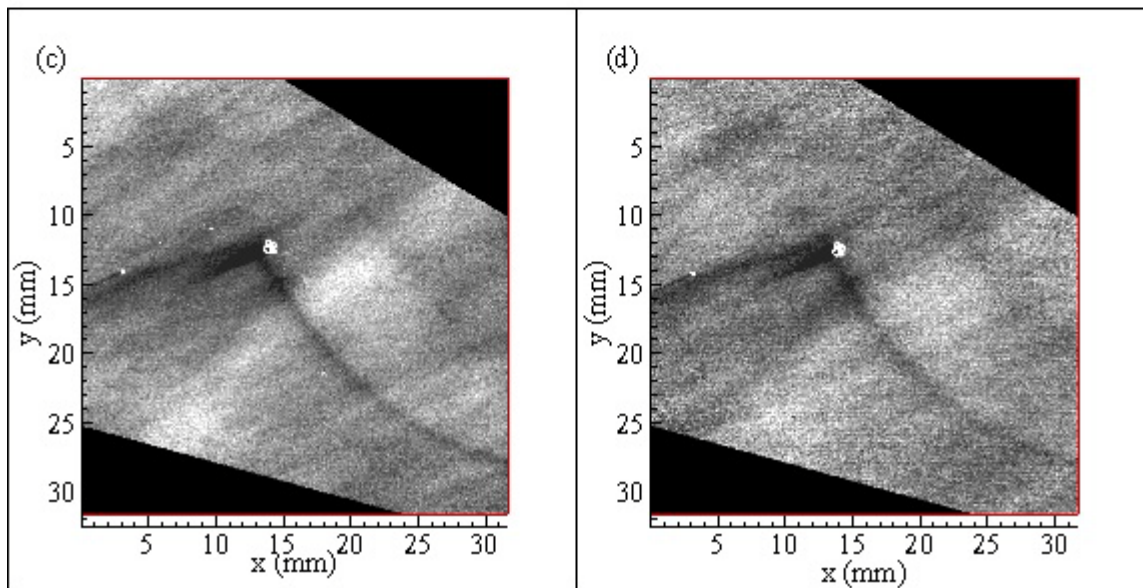
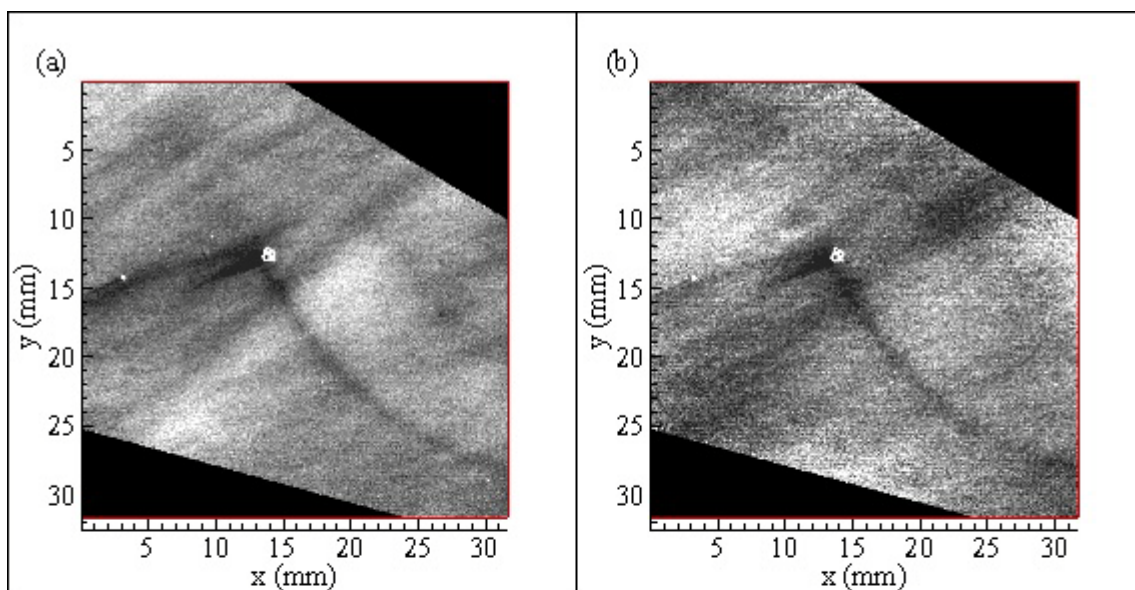


Figure C.9. Grayscale plots of normalized dimensionless mass transfer coefficient values at 27% relative humidity: (a) R7E\_78; 15 min.: 40 sec., (b) R27E\_79; 15 min.: 50 sec., (c) R27E\_80; 16 min.: 00 sec., (d) R27E\_81; 16 min.: 10 sec.



$k^*$ : 0 0.8 0.84 0.88 0.92 0.96 1 1.04 1.08 1.12 1.16 1.2

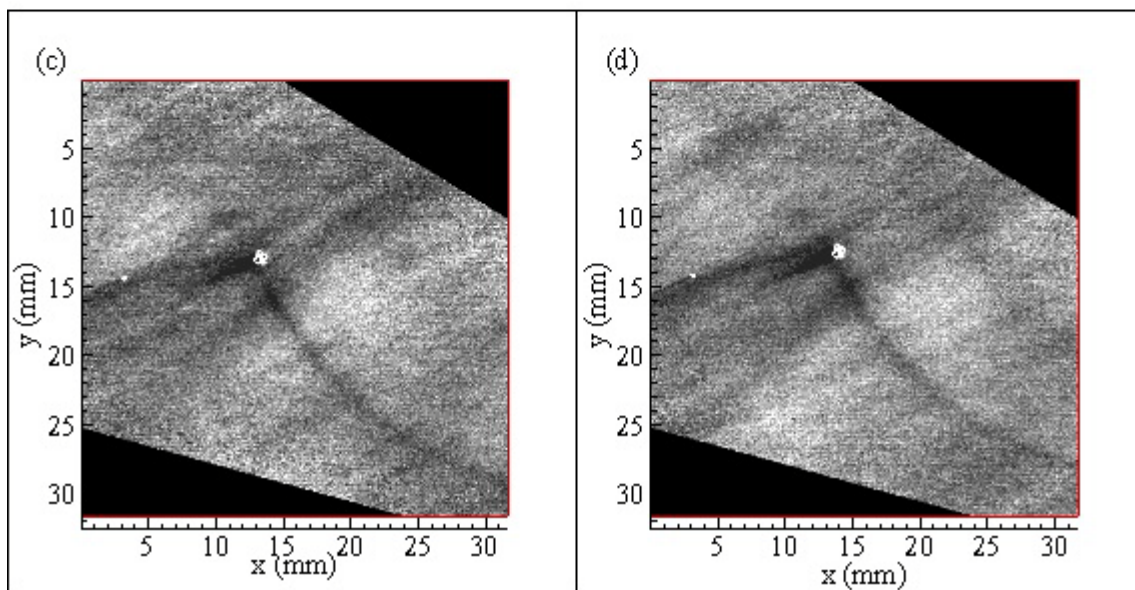


Figure C.10. Grayscale plots of normalized dimensionless mass transfer coefficient values at 27% relative humidity: (a) R27E\_82; 16 min.: 20 sec., (b) R27E\_83; 16 min.: 30 sec., (c) R27E\_84; 16 min.: 50 sec., (d) R27E\_94; 17 min.: 30 sec.

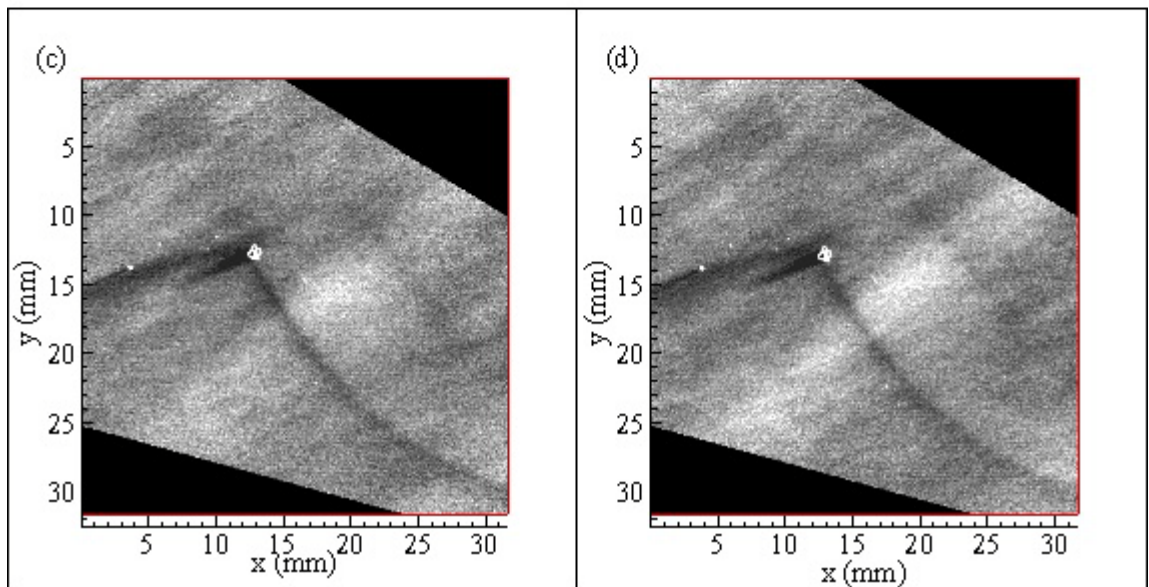
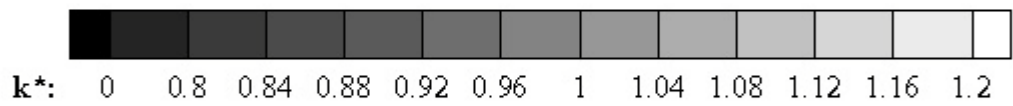
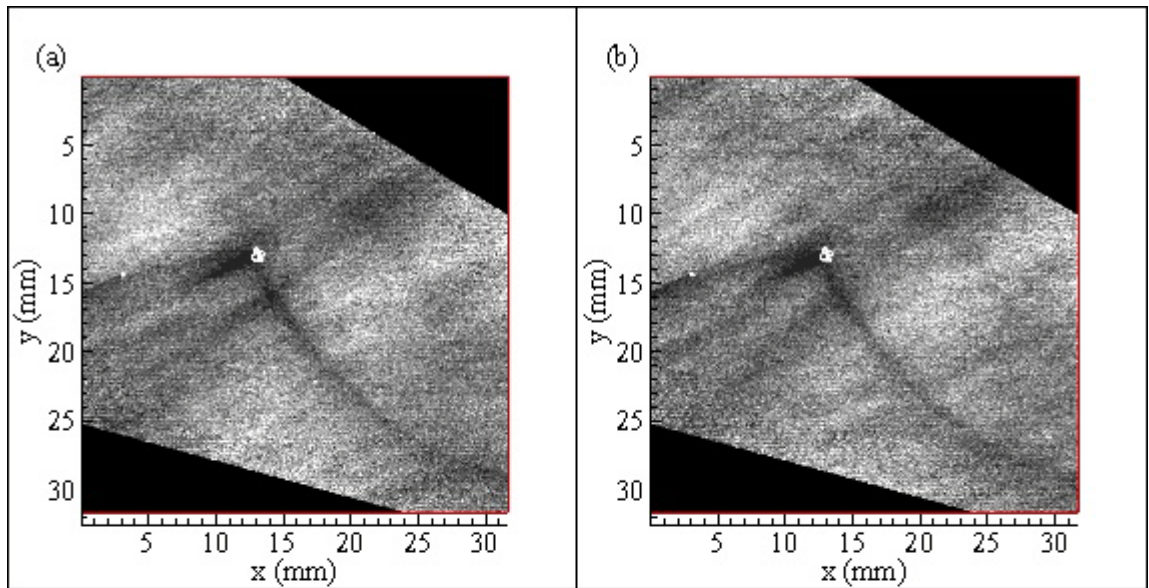
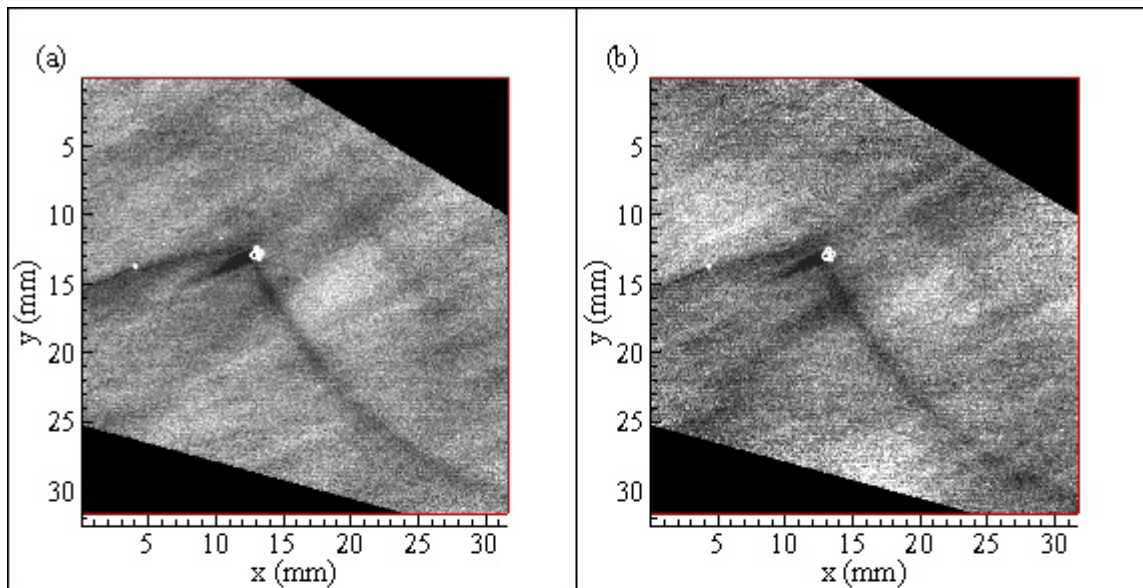


Figure C.11. Grayscale plots of normalized dimensionless mass transfer coefficient values at 27% relative humidity: (a) R27E\_95; 17 min.: 50 sec., (b) R27F\_1; 18 min.: 10 sec., (c) R27F\_2; 18 min.: 20 sec., (d) R27F\_4; 18 min.: 50 sec.



$k^*$ : 0 0.8 0.84 0.88 0.92 0.96 1 1.04 1.08 1.12 1.16 1.2

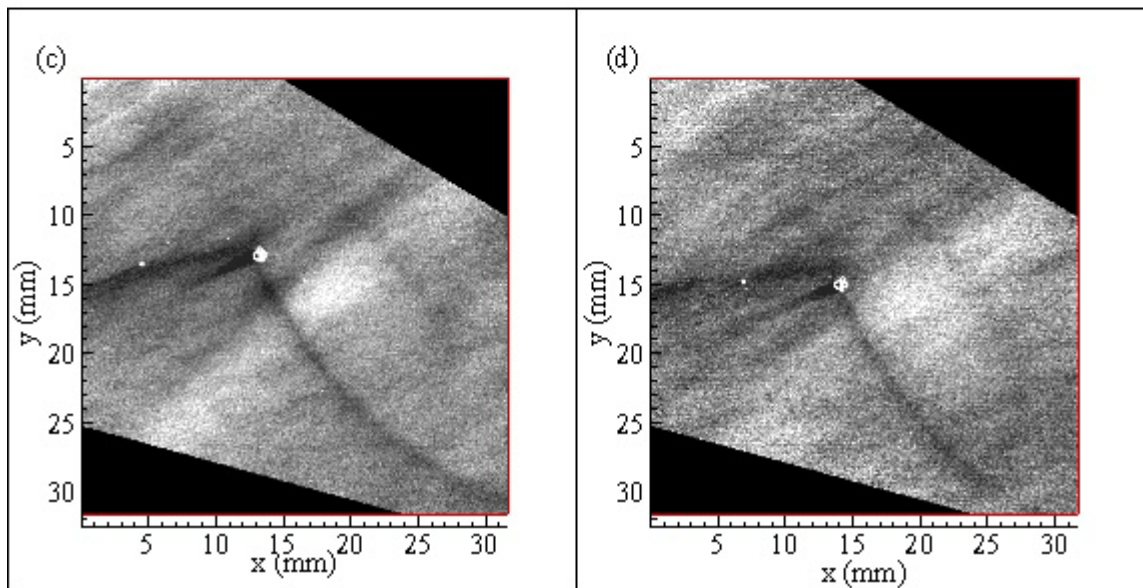


Figure C.12. Grayscale plots of normalized dimensionless mass transfer coefficient values at 27% relative humidity: (a) R27F\_5; 19 min.: 30 sec., (b) R27F\_10; 19 min.: 50 sec., (c) R27F\_20; 20 min.: 20 sec., (d) R27F\_25; 21 min.: 00 sec.

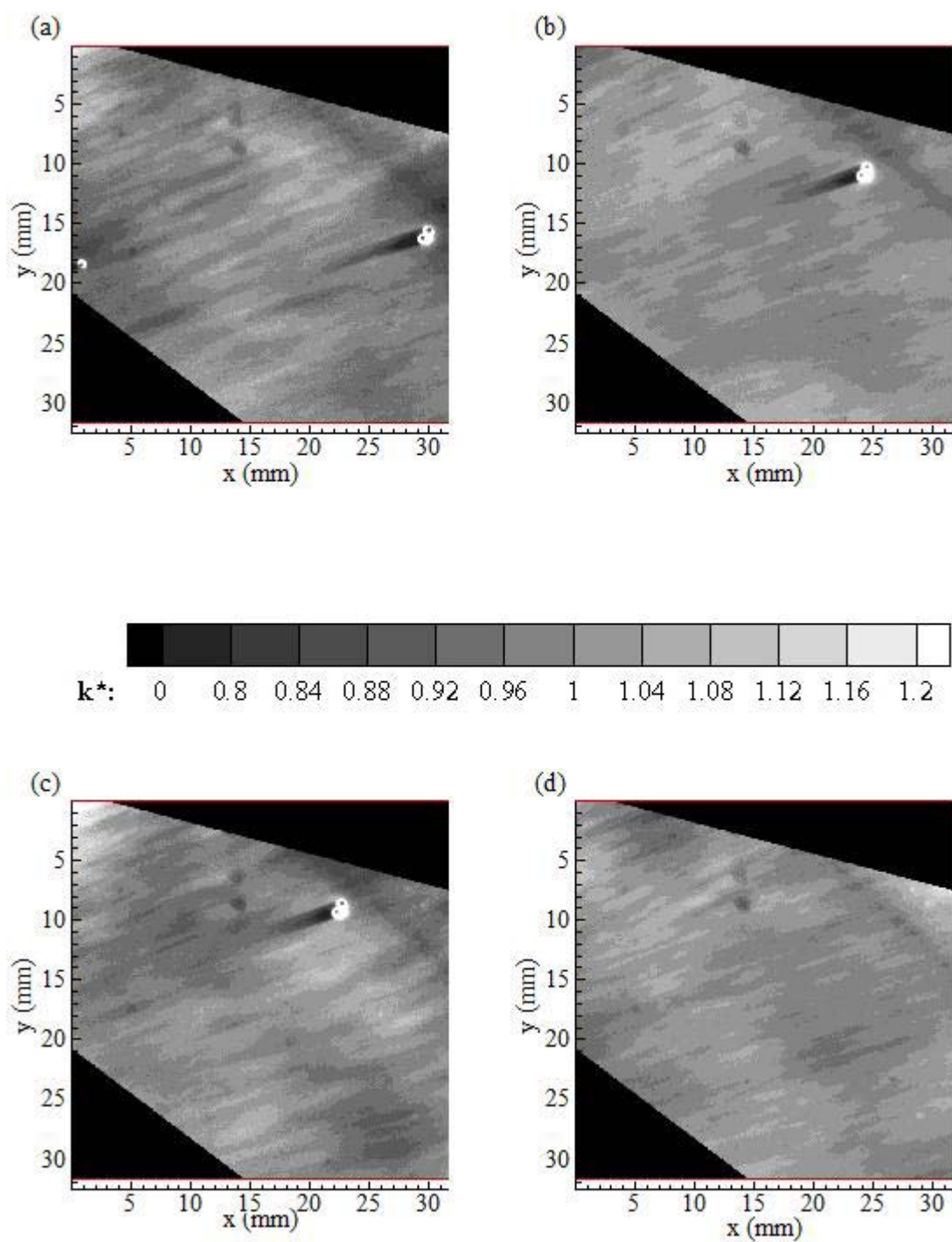


Figure C.13. Grayscale plots of normalized dimensionless mass transfer coefficient values at 46% relative humidity: (a) R46A\_16; 2 min.: 00 sec., (b) R46A\_18; 2 min.: 30 sec., (c) R46A\_19; 2 min.: 40 sec., (d) R46A\_28; 3 min.: 20 sec.

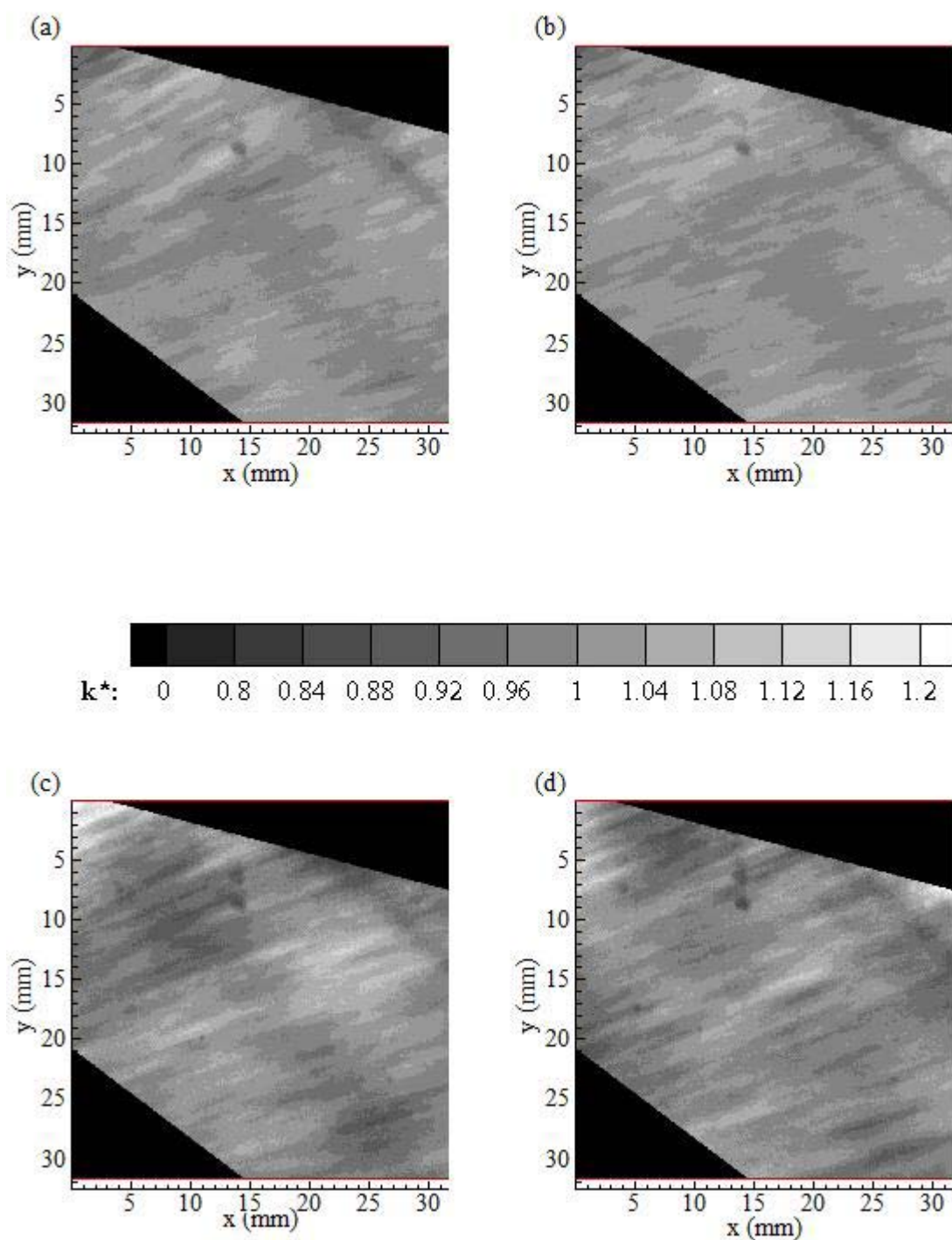


Figure C.14. Grayscale plots of normalized dimensionless mass transfer coefficient values at 46% relative humidity: (a) R46A\_31; 3 min.: 30 sec., (b) R46A\_34; 3 min.: 50 sec., (c) R46A\_35; 4 min.: 00 sec., (d) R46A\_37; 4 min.: 20 sec.

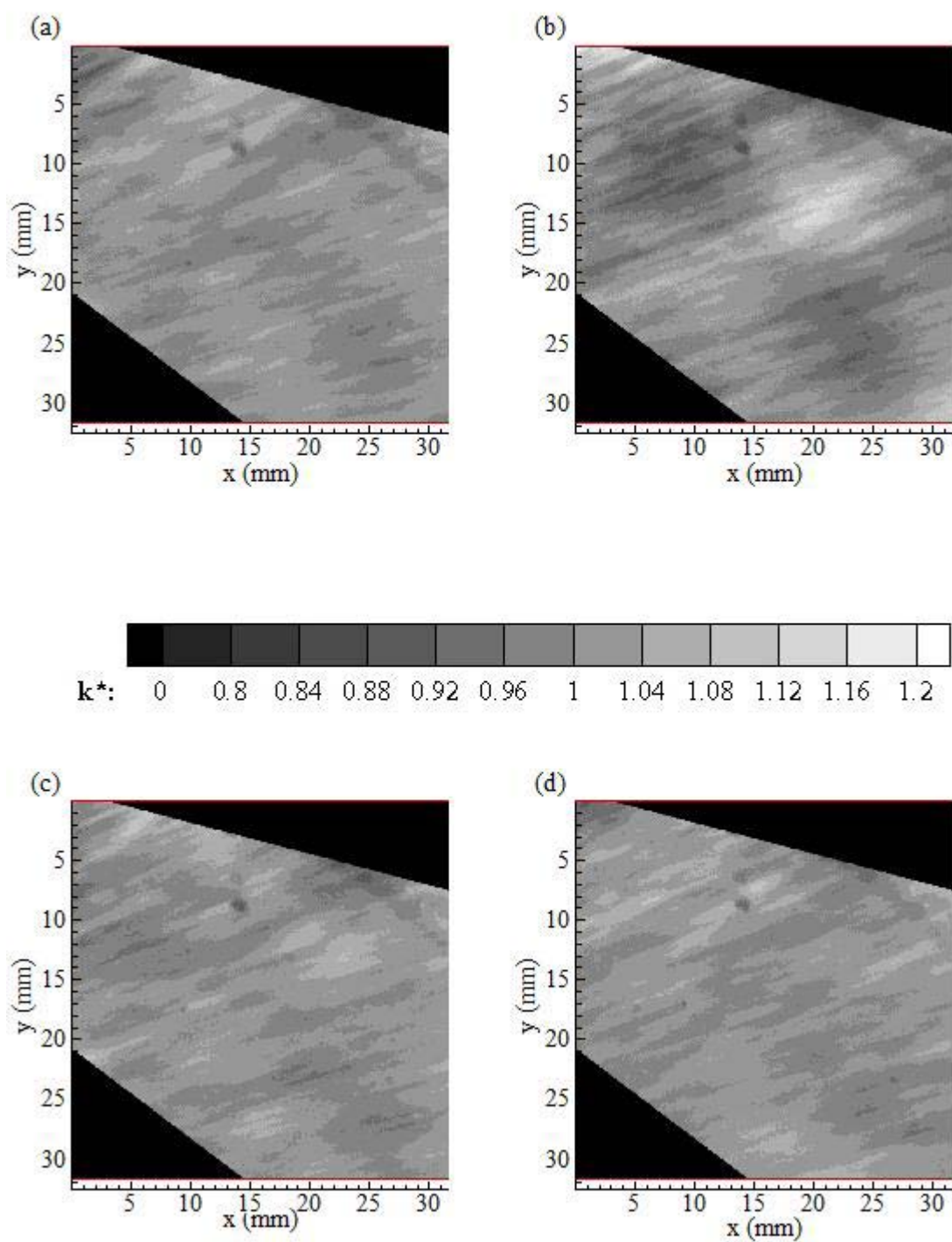


Figure C.15. Grayscale plots of normalized dimensionless mass transfer coefficient values at 46% relative humidity: (a) R46A\_40; 5 min.: 00 sec., (b) R46A\_43; 5 min.: 10 sec., (c) R46A\_44; 5 min.: 30 sec., (d) R46A\_45; 5 min.: 40 sec.

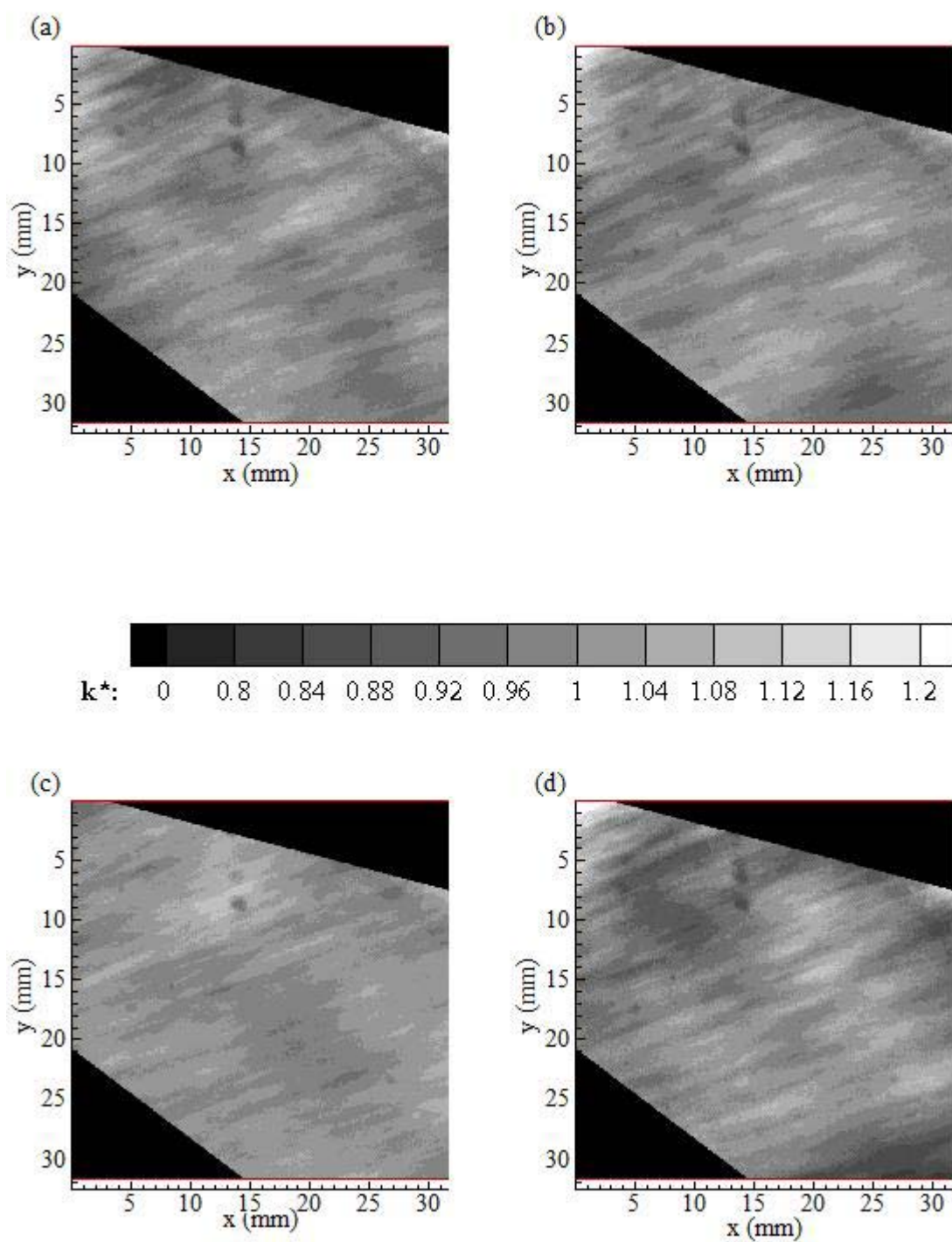
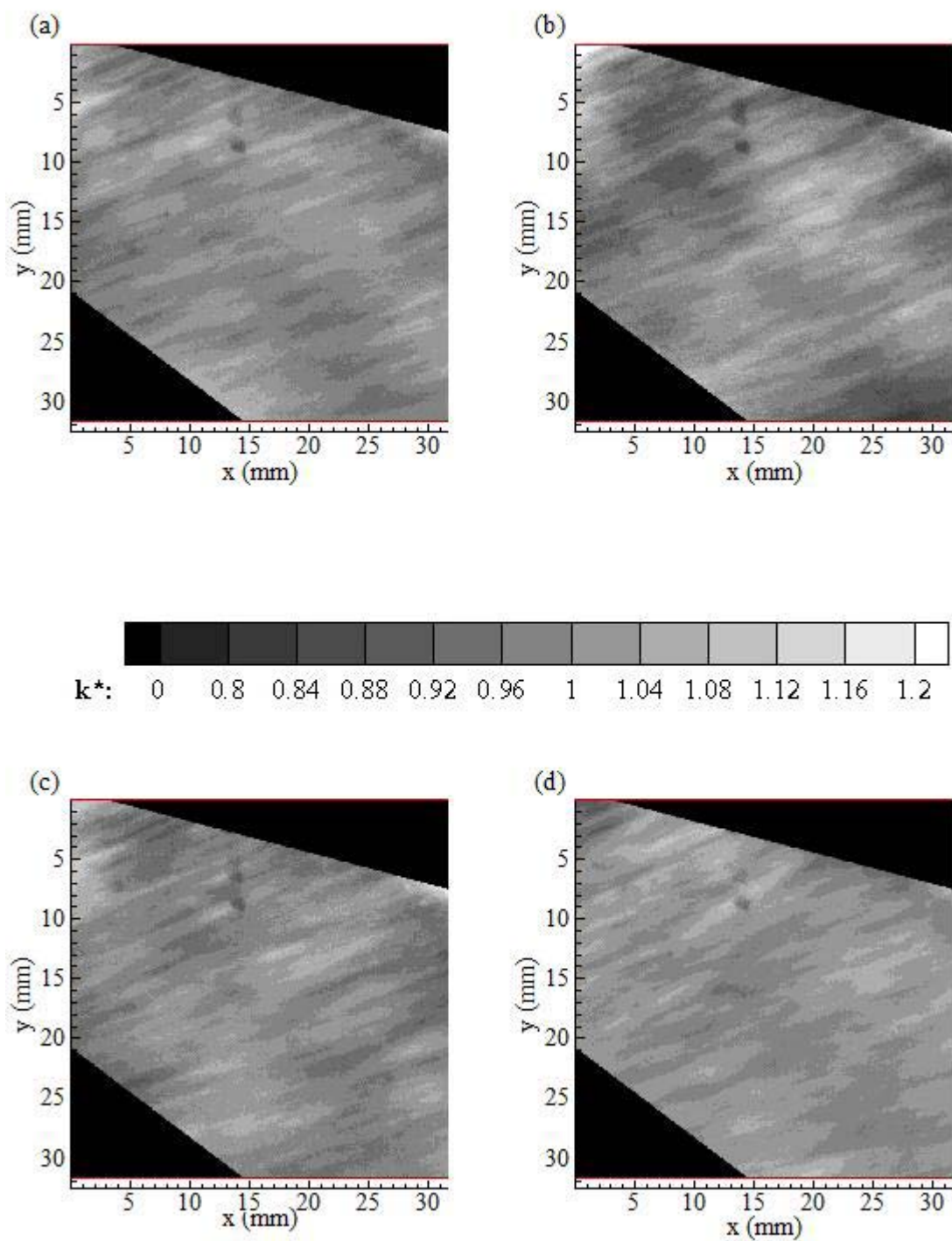


Figure C.16. Grayscale plots of normalized dimensionless mass transfer coefficient values at 46% relative humidity: (a) R46A\_48; 5 min.: 10 sec., (b) R46A\_53; 6 min.: 30 sec., (c) R46A\_57; 6 min.: 40 sec., (d) R46A\_60; 6 min.: 50 sec.



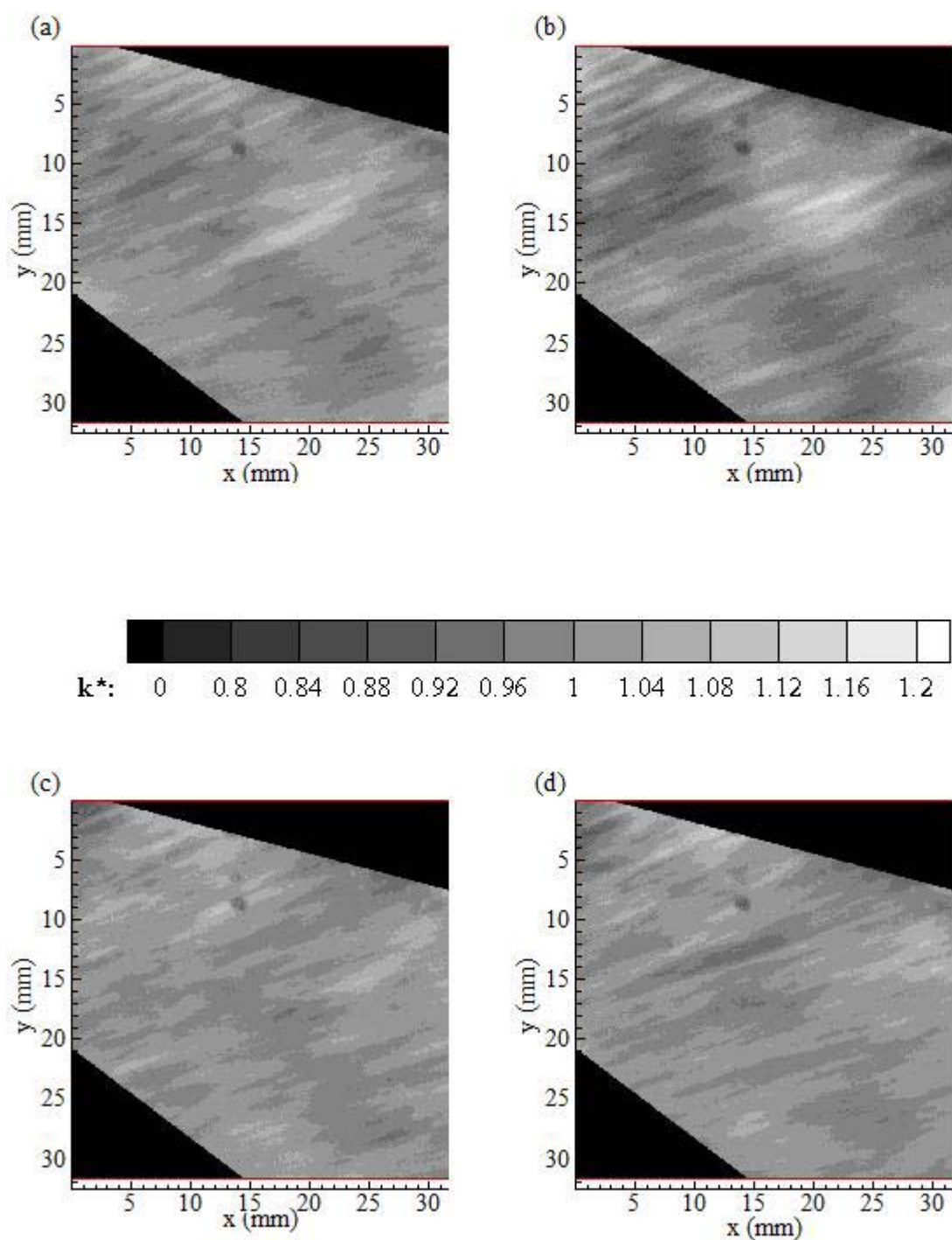


Figure C.18. grayscale plots of normalized dimensionless mass transfer coefficient values at 46% relative humidity: (a) R46A\_75; 8 min.: 30 sec., (b) R46A\_76; 8 min.: 40 sec., (c) R46A\_77; 9 min.: 00 sec., (d) R46A\_80; 9 min.: 20 sec.

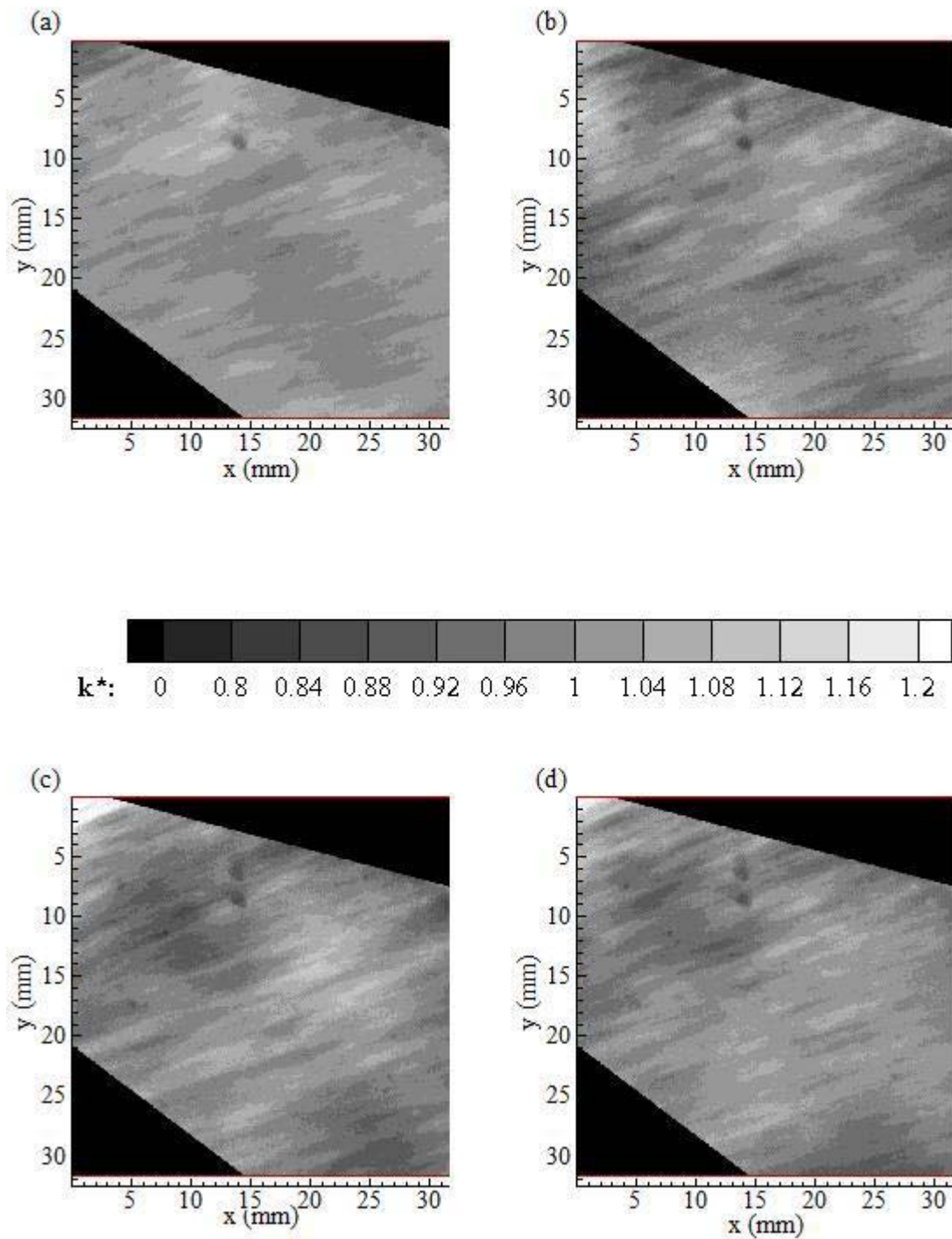


Figure C.19. grayscale plots of normalized dimensionless mass transfer coefficient values at 46% relative humidity: (a) R46A\_81; 9 min.: 30 sec., (b) R46A\_84; 9 min.: 50 sec., (c) R46A\_86; 10 min.: 20 sec., (d) R46A\_88; 10 min.: 30 sec.

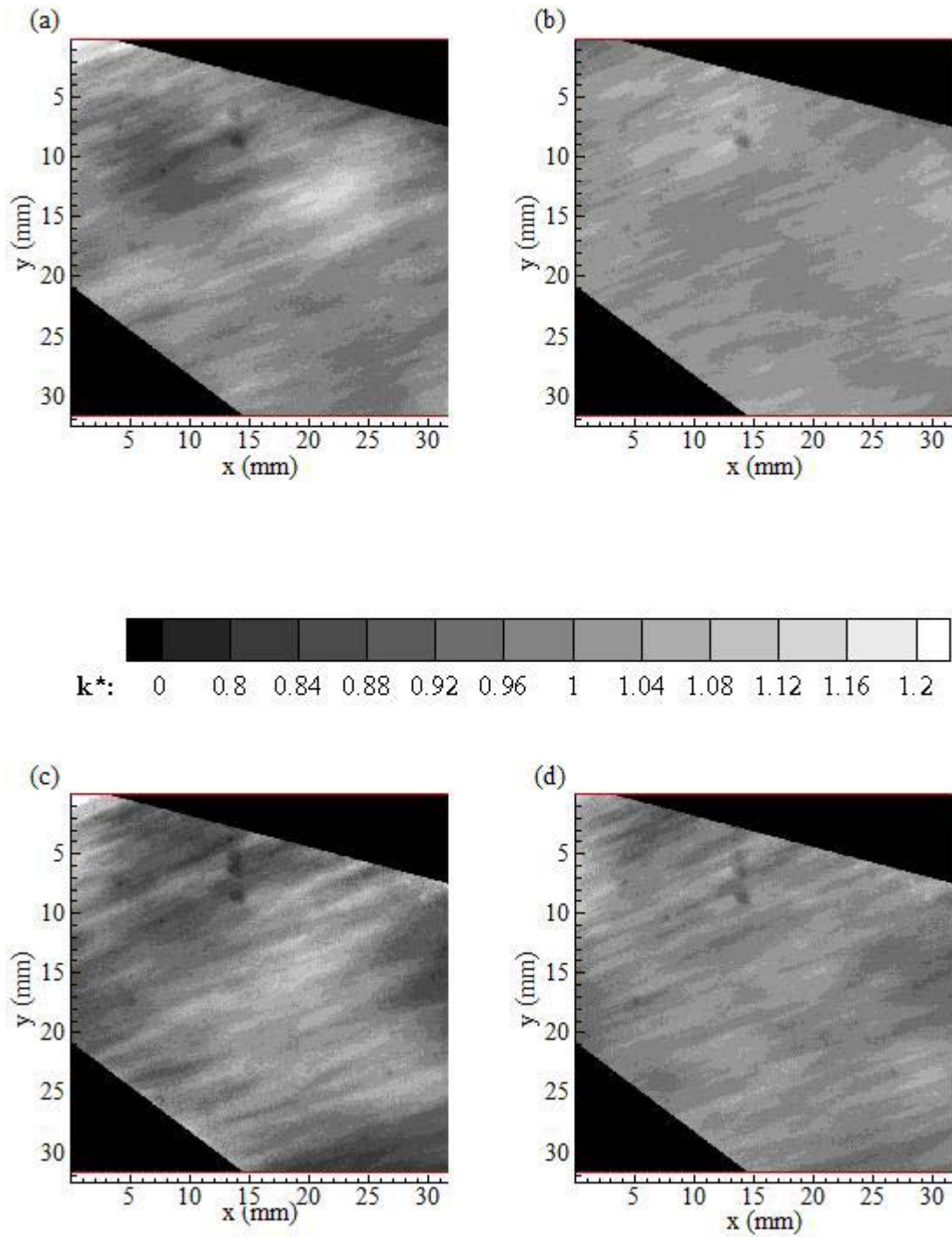


Figure C.20. grayscale plots of normalized dimensionless mass transfer coefficient values at 46% relative humidity: (a) R46A\_92; 10 min.: 40 sec., (b) R46A\_93; 10 min.: 50 sec., (c) R46A\_95; 11 min.: 10 sec., (d) R46B\_1; 11 min.: 40 sec.

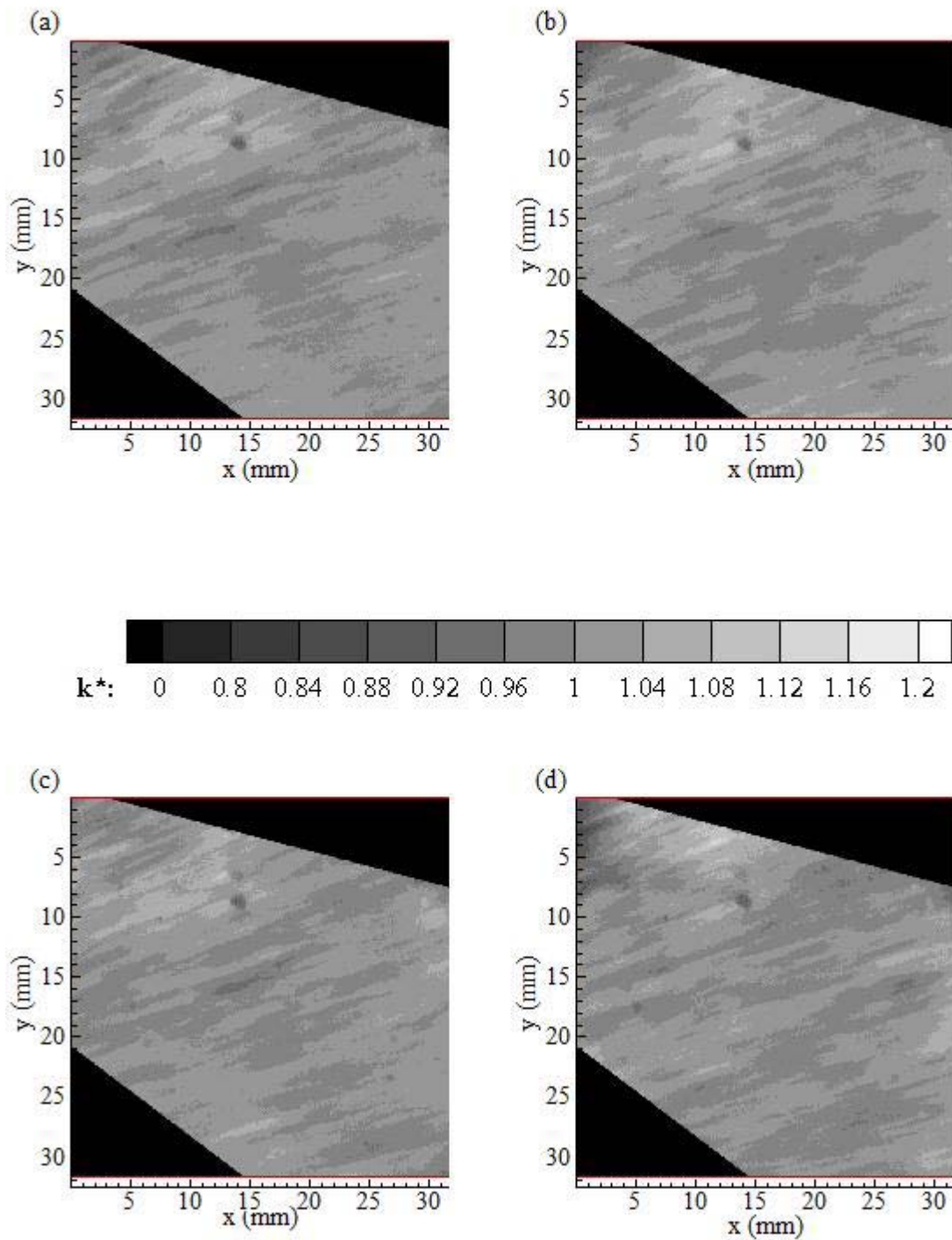


Figure C.21. Grayscale plots of normalized dimensionless mass transfer coefficient values at 46% relative humidity: (a) R46B\_4; 11 min.: 50 sec., (b) R46B\_6; 12 min.: 00 sec., (c) R46B\_7; 12 min.: 10 sec., (d) R46B\_10; 12 min.: 30 sec.

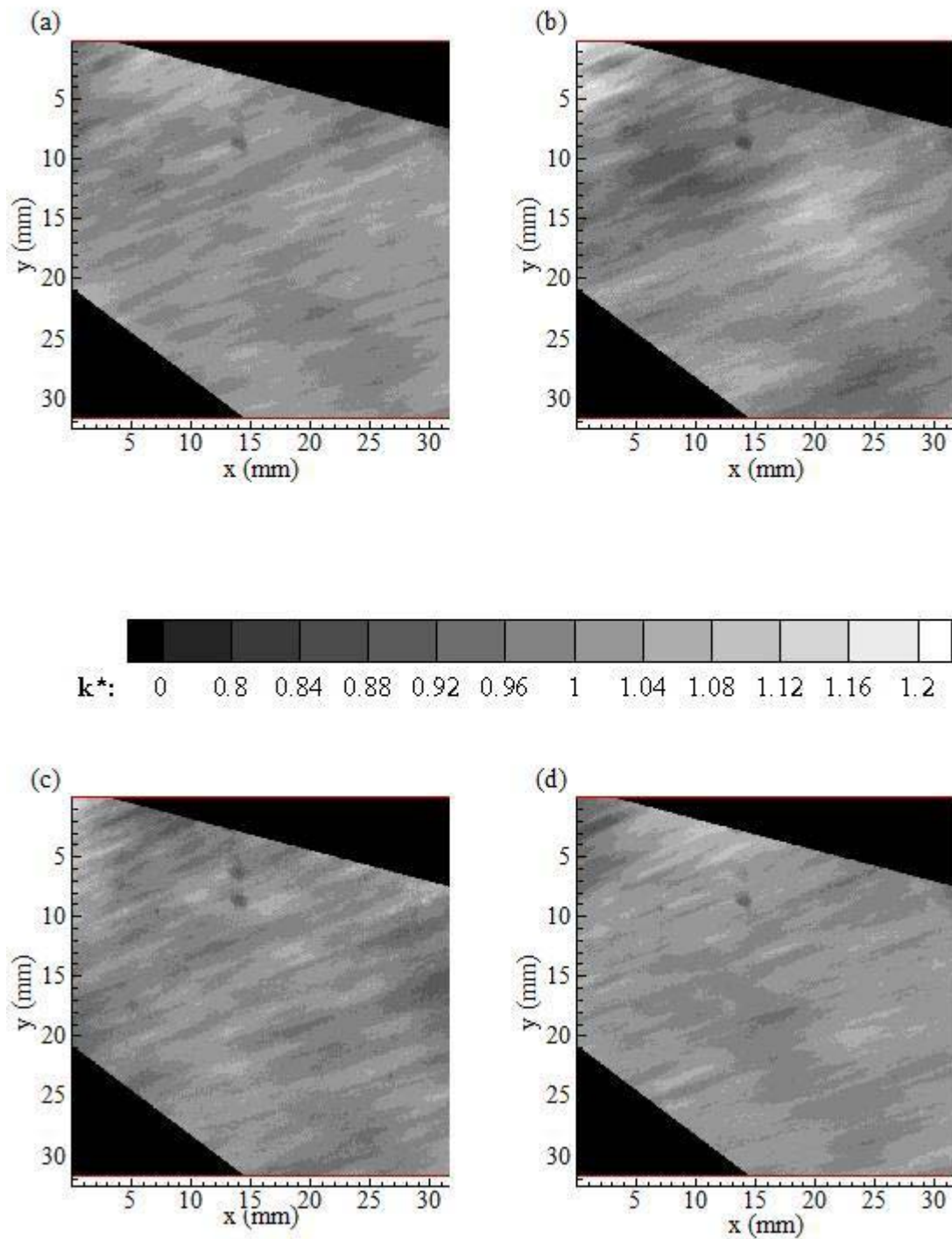


Figure C.22. Grayscale plots of normalized dimensionless mass transfer coefficient values at 46% relative humidity: (a) R46B\_11; 12 min.: 40 sec., (b) R46B\_13; 13 min.: 00 sec., (c) R46B\_15; 13 min.: 20 sec., (d) R46B\_26; 13 min.: 50 sec.

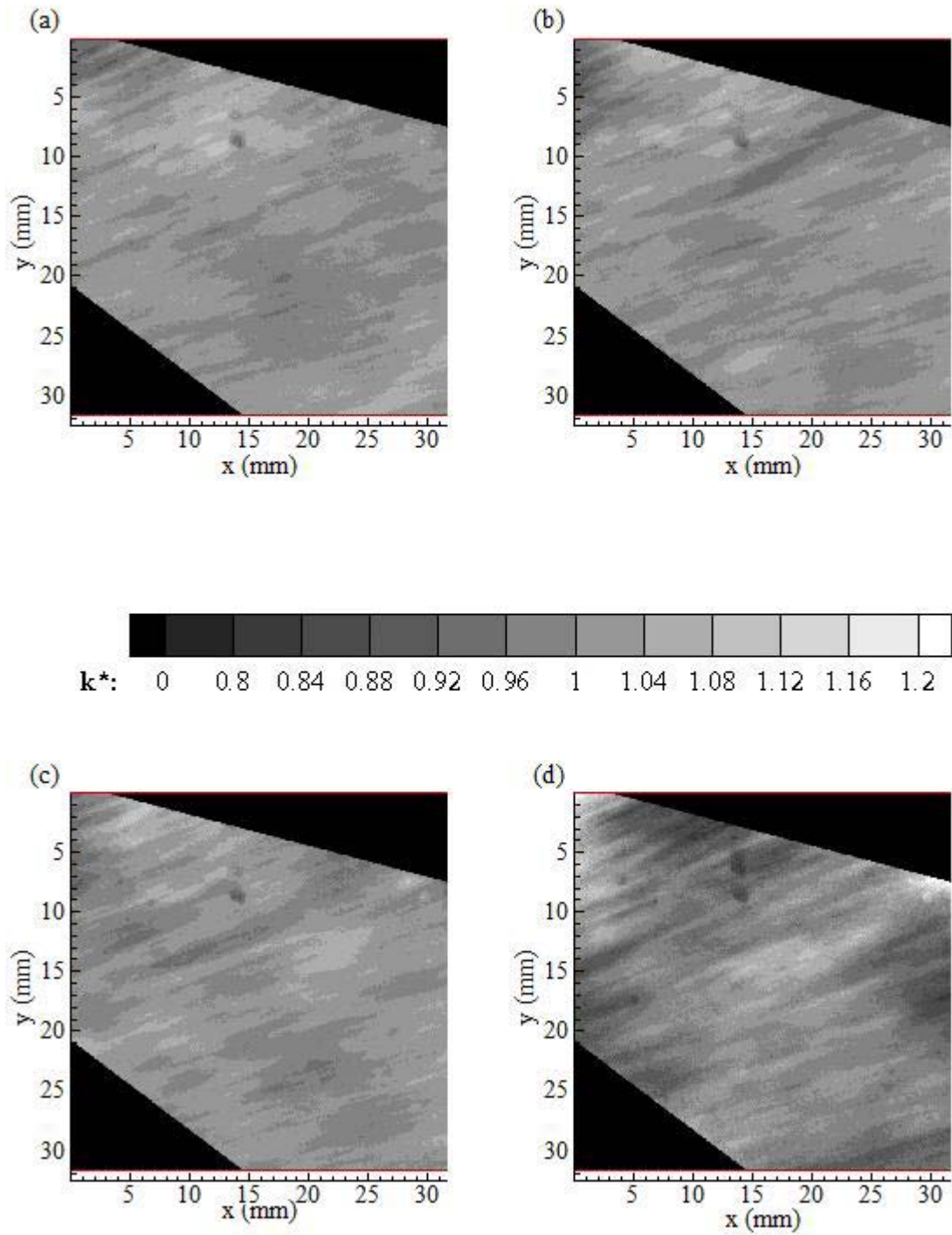


Figure C.23. Grayscale plots of normalized dimensionless mass transfer coefficient values at 46% relative humidity: (a) R46B\_27; 14 min.: 00 sec., (b) R46B\_28; 14 min.: 10 sec., (c) R46B\_29; 14 min.: 20 sec., (d) R46B\_30; 14 min.: 30 sec.

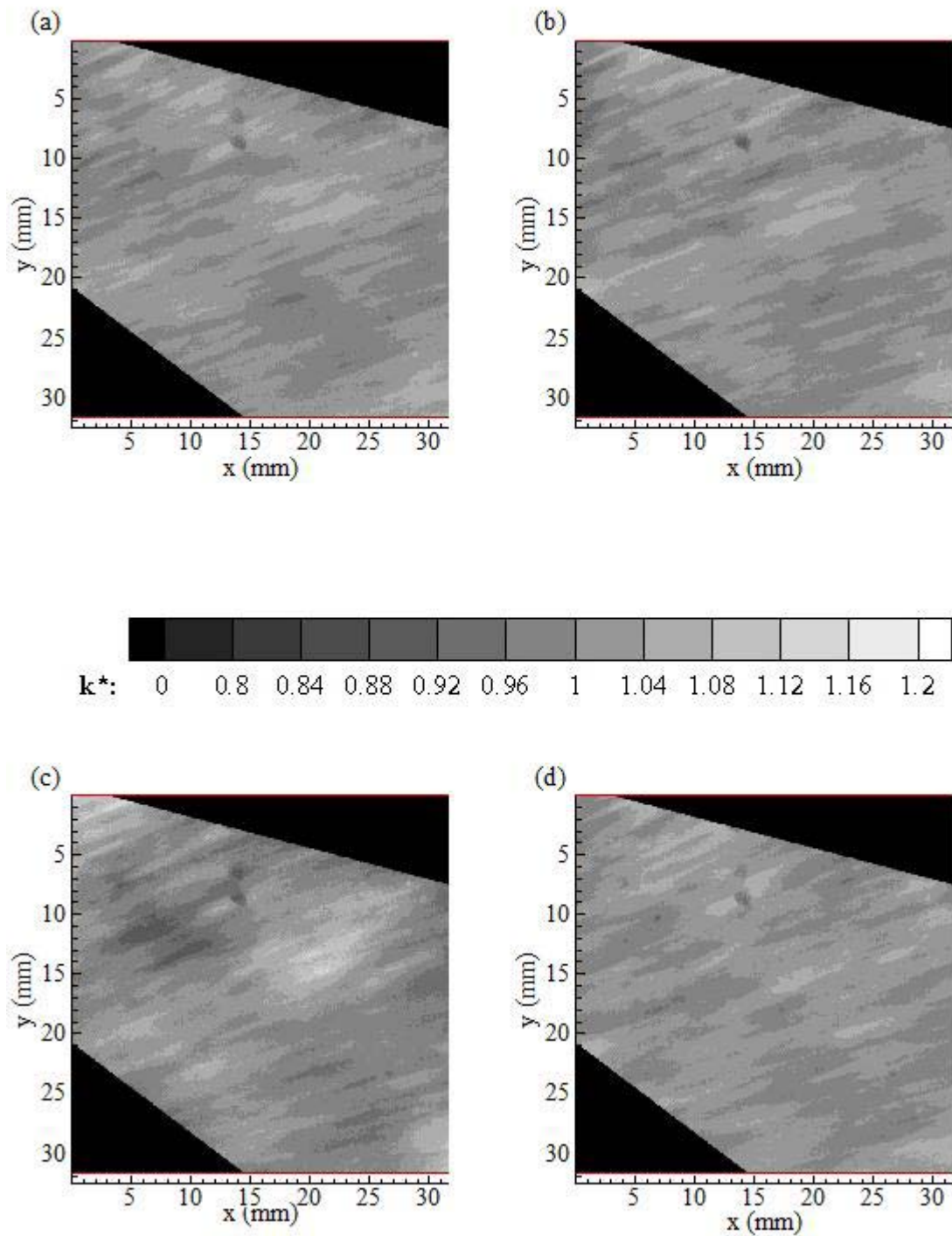


Figure C.24. Grayscale plots of normalized dimensionless mass transfer coefficient values at 46% relative humidity: (a) R46B\_47; 15 min.: 10 sec., (b) R46B\_28; 15 min.: 30 sec., (c) R46B\_50; 15 min.: 40 sec., (d) R46B\_55; 16 min.: 10 sec.

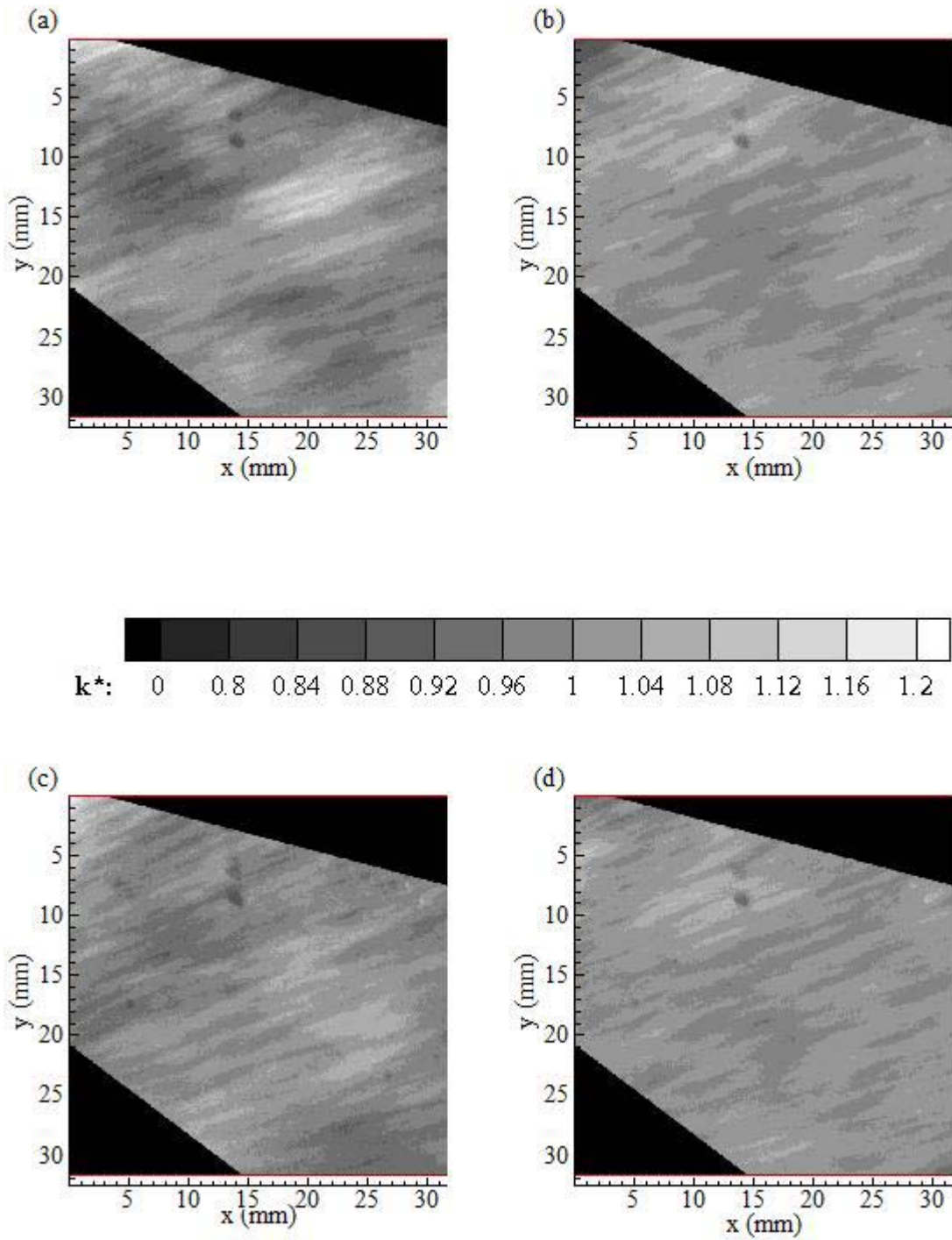


Figure C.25. Grayscale plots of normalized dimensionless mass transfer coefficient values at 46% relative humidity: (a) R46B\_62; 16 min.: 30 sec., (b) R46B\_64; 16 min.: 40 sec., (c) R46B\_67; 17 min.: 00 sec., (d) R46B\_78; 17 min.: 40 sec.

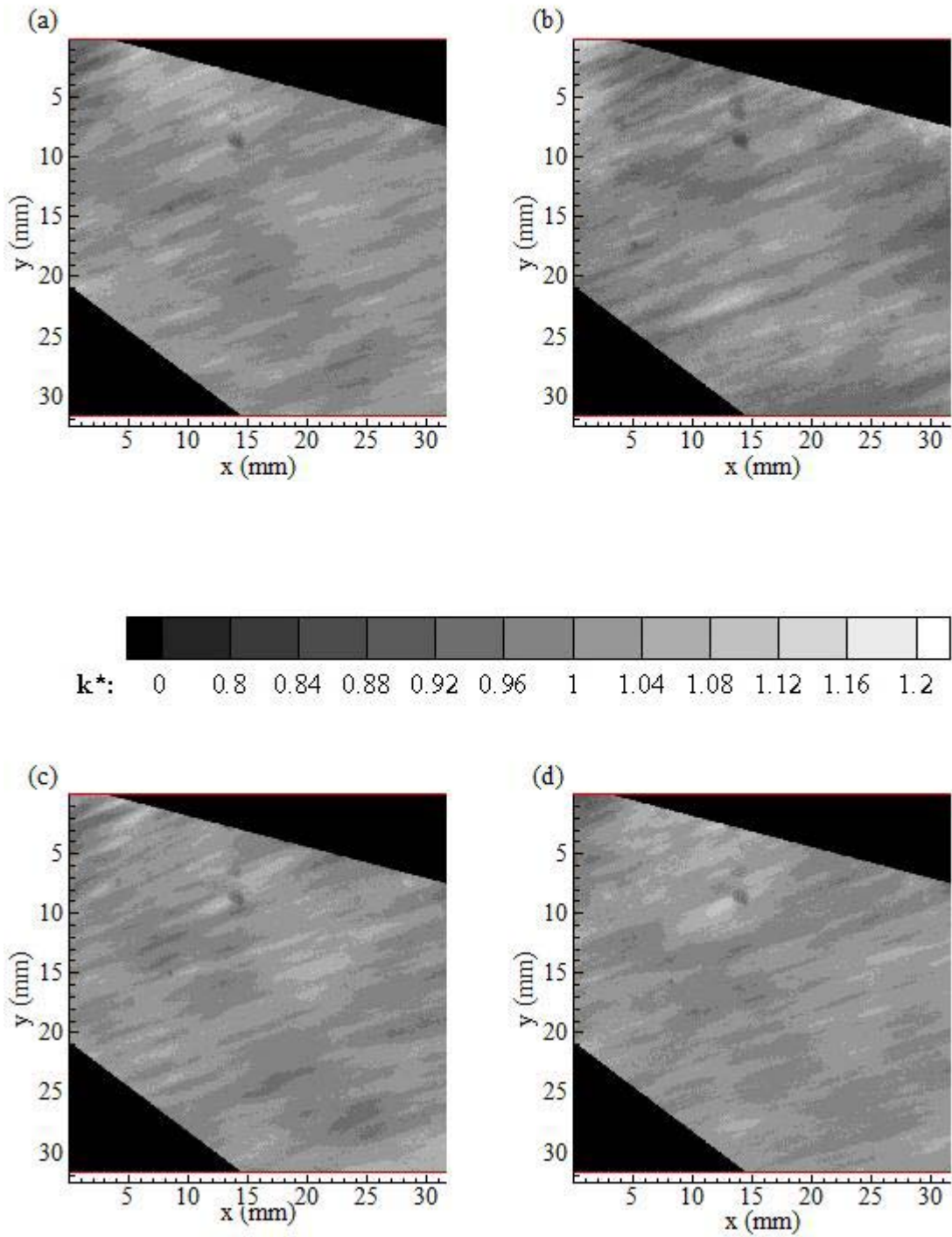


Figure C.26. Grayscale plots of normalized dimensionless mass transfer coefficient values at 46% relative humidity: (a) R46B\_86; 18 min.: 20 sec., (b) R46B\_92; 18 min.: 50 sec., (c) R46C\_1; 19 min.: 10 sec., (d) R46C\_4; 19 min.: 20 sec.

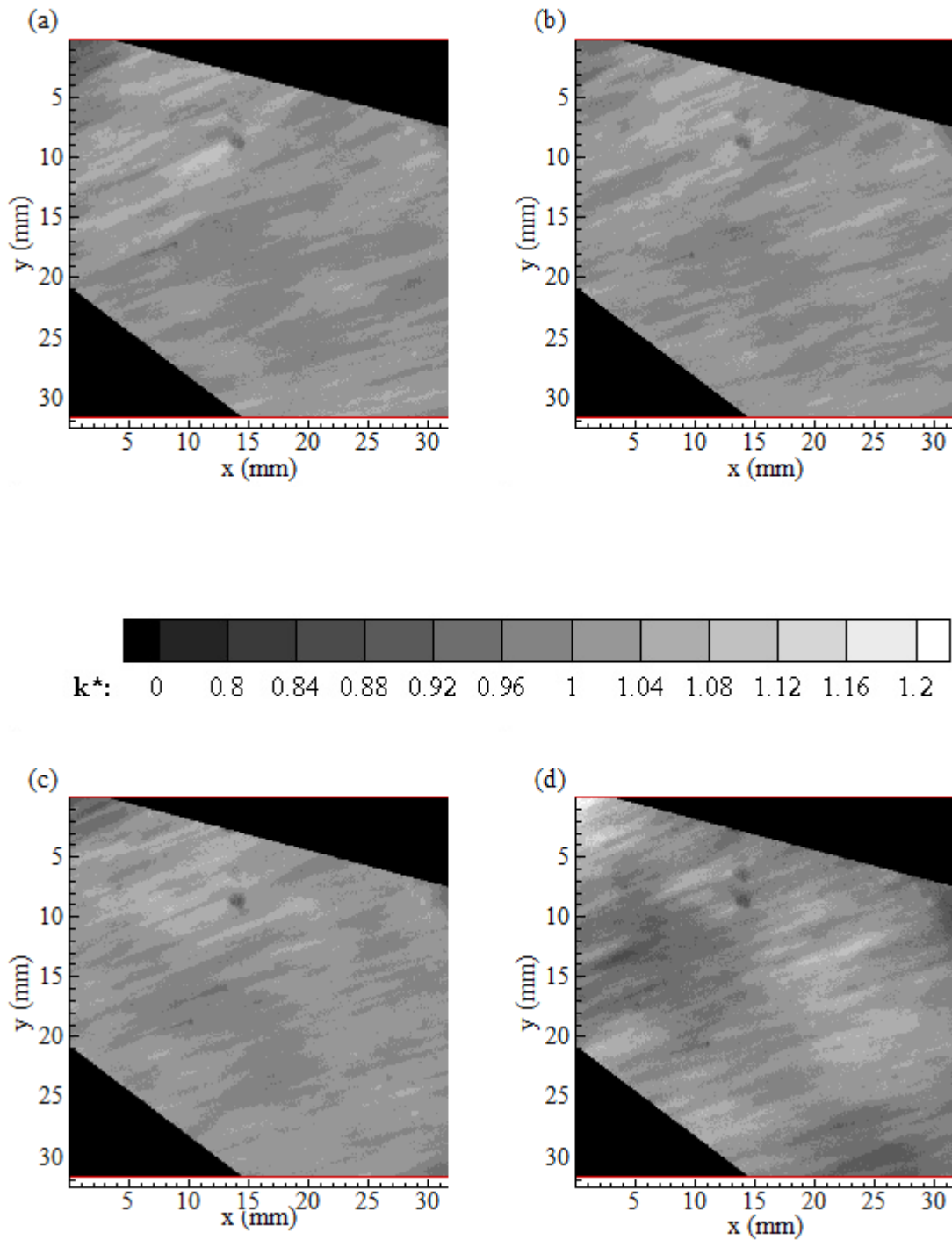


Figure C.27. Grayscale plots of normalized dimensionless mass transfer coefficient values at 46% relative humidity: (a) R46C\_20; 20 min.: 50 sec., (b) R46C\_24; 21 min.: 40 sec., (c) R46C\_28; 22 min.: 30 sec., (d) R46C\_29; 22 min.: 50 sec.

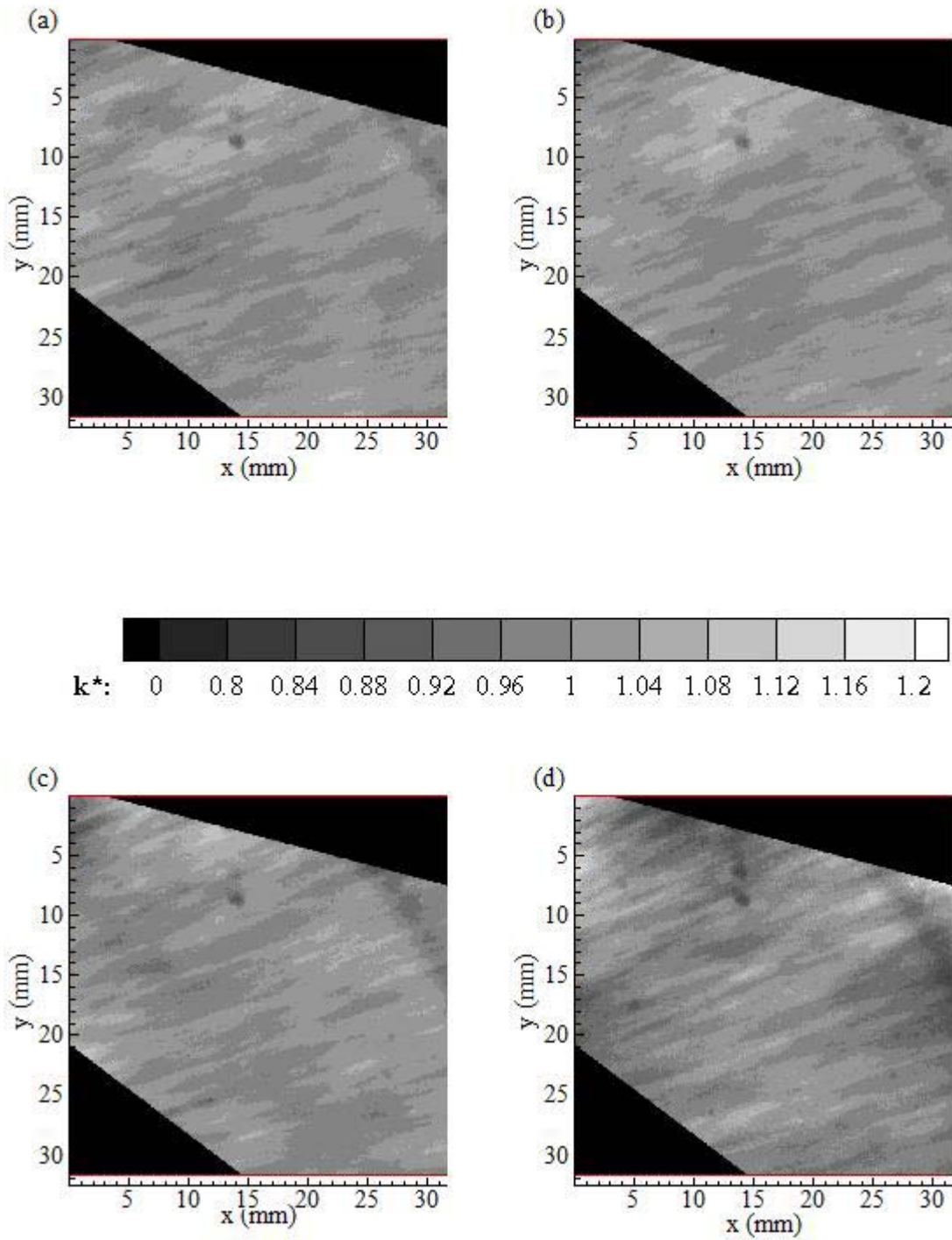


Figure C.28. Grayscale plots of normalized dimensionless mass transfer coefficient values at 46% relative humidity: (a) R46C\_48; 24 min.: 40 sec., (b) R46C\_50; 26 min.: 10 sec., (c) R46C\_52; 26 min.: 40 sec., (d) R46C\_57; 28 min.: 00 sec.

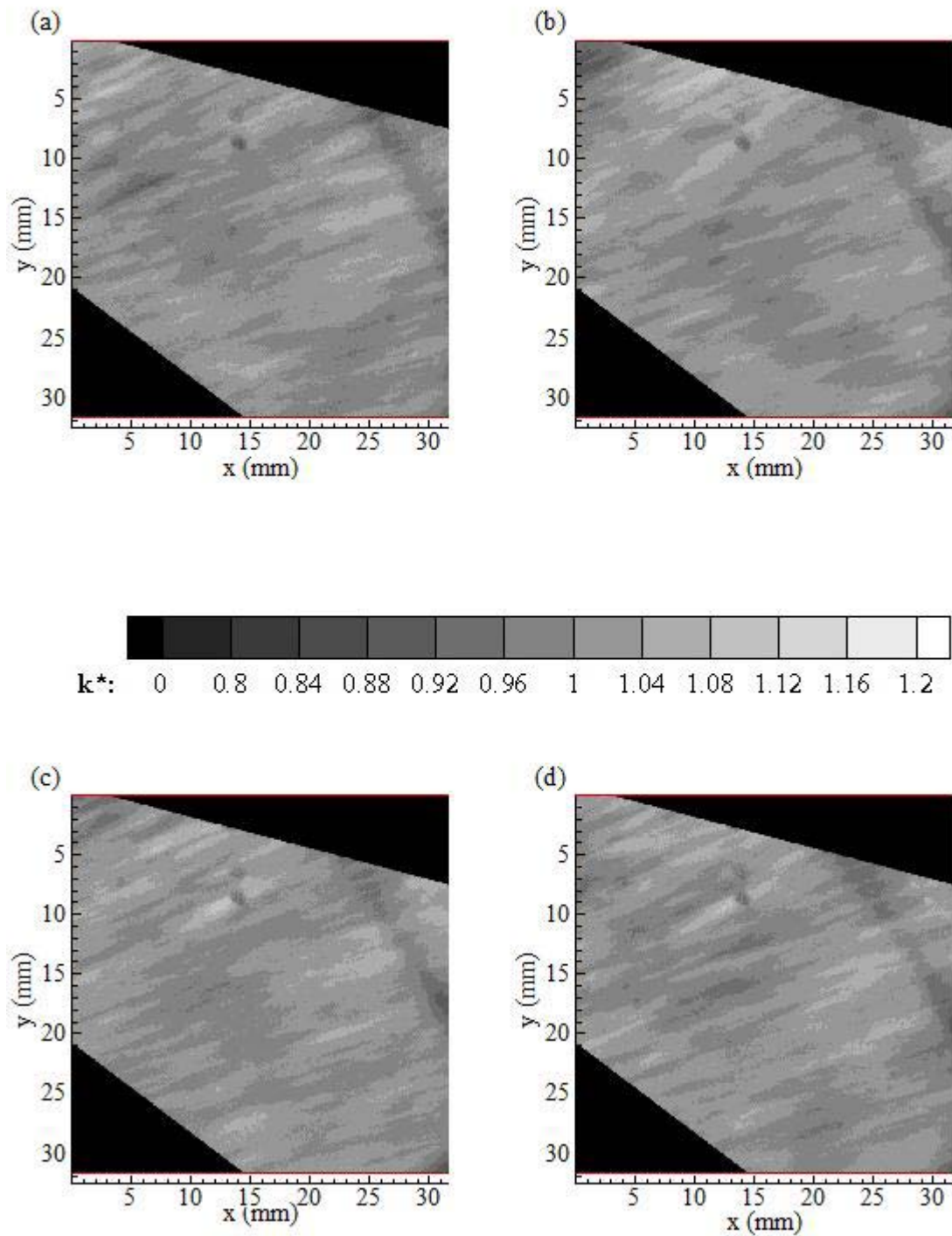


Figure C.29. Grayscale plots of normalized dimensionless mass transfer coefficient values at 46% relative humidity: (a) R46C\_67; 30 min.: 40 sec., (b) R46C\_69; 31 min.: 50 sec., (c) R46C\_72; 33 min.: 10 sec., (d) R46C\_78; 34 min.: 40 sec.

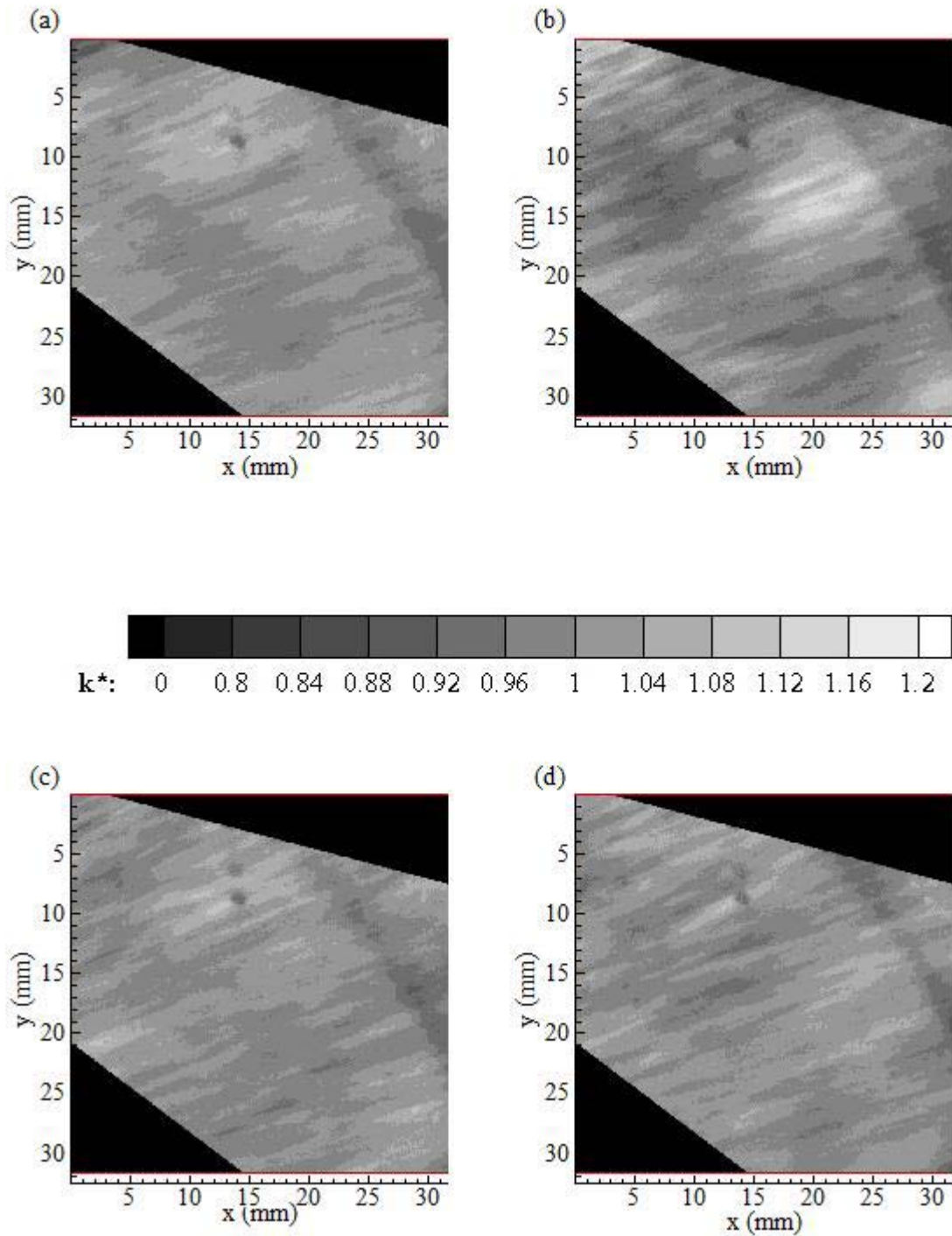


Figure C.30. Grayscale plots of normalized dimensionless mass transfer coefficient values at 46% relative humidity: (a) R46C\_90; 36 min.: 00 sec., (b) R46C\_95; 37 min.: 40 sec., (c) R46D\_4; 38 min.: 10 sec., (d) R46D\_10; 39 min.: 30 sec.

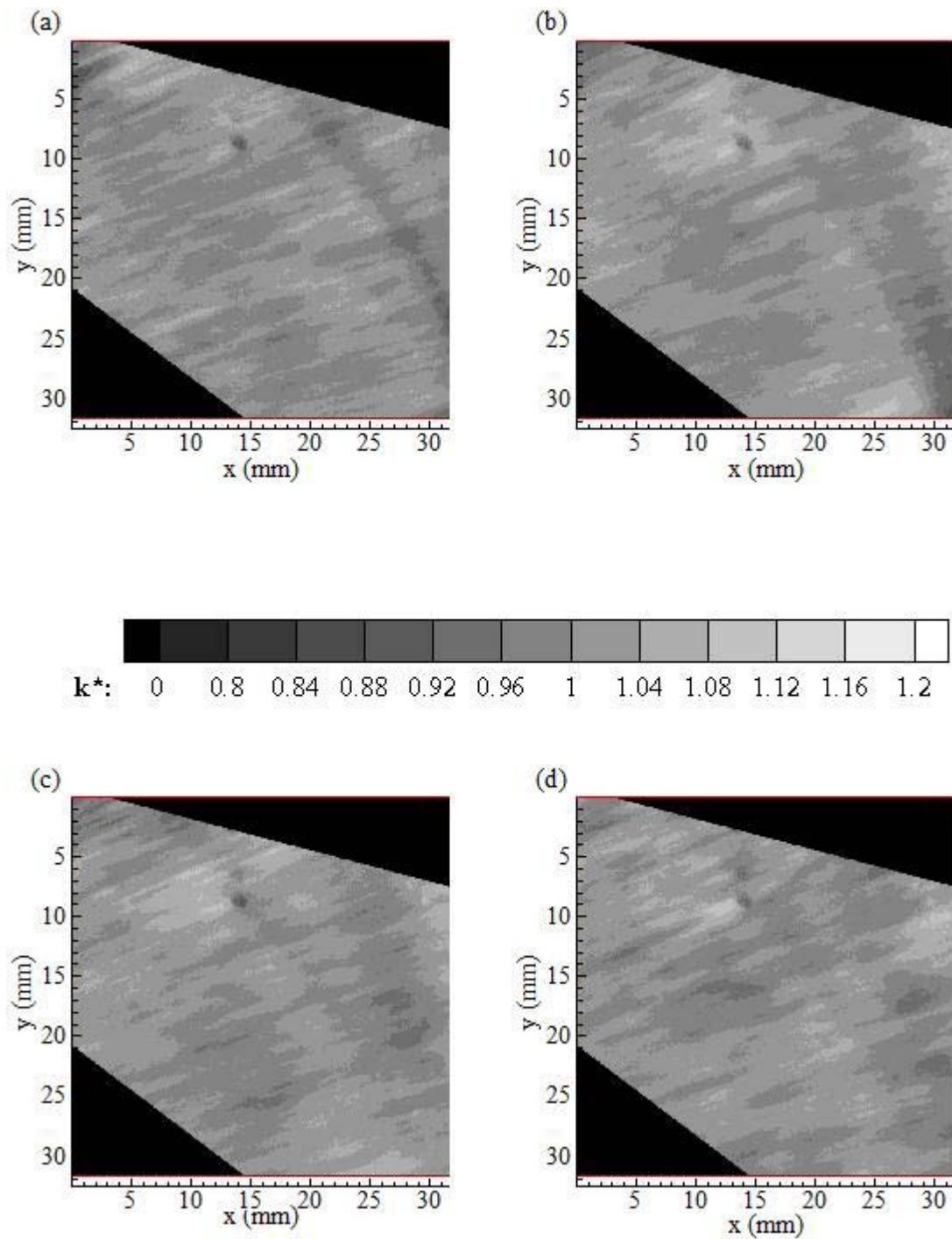


Figure C.28. Grayscale plots of normalized dimensionless mass transfer coefficient values at 46% relative humidity: (a) R46D\_20; 40 min.: 30 sec., (b) R46D\_35; 41 min.: 10 sec., (c) R46D\_30; 42 min.: 50 sec., (d) R46D\_44; 46 min.: 10 sec.

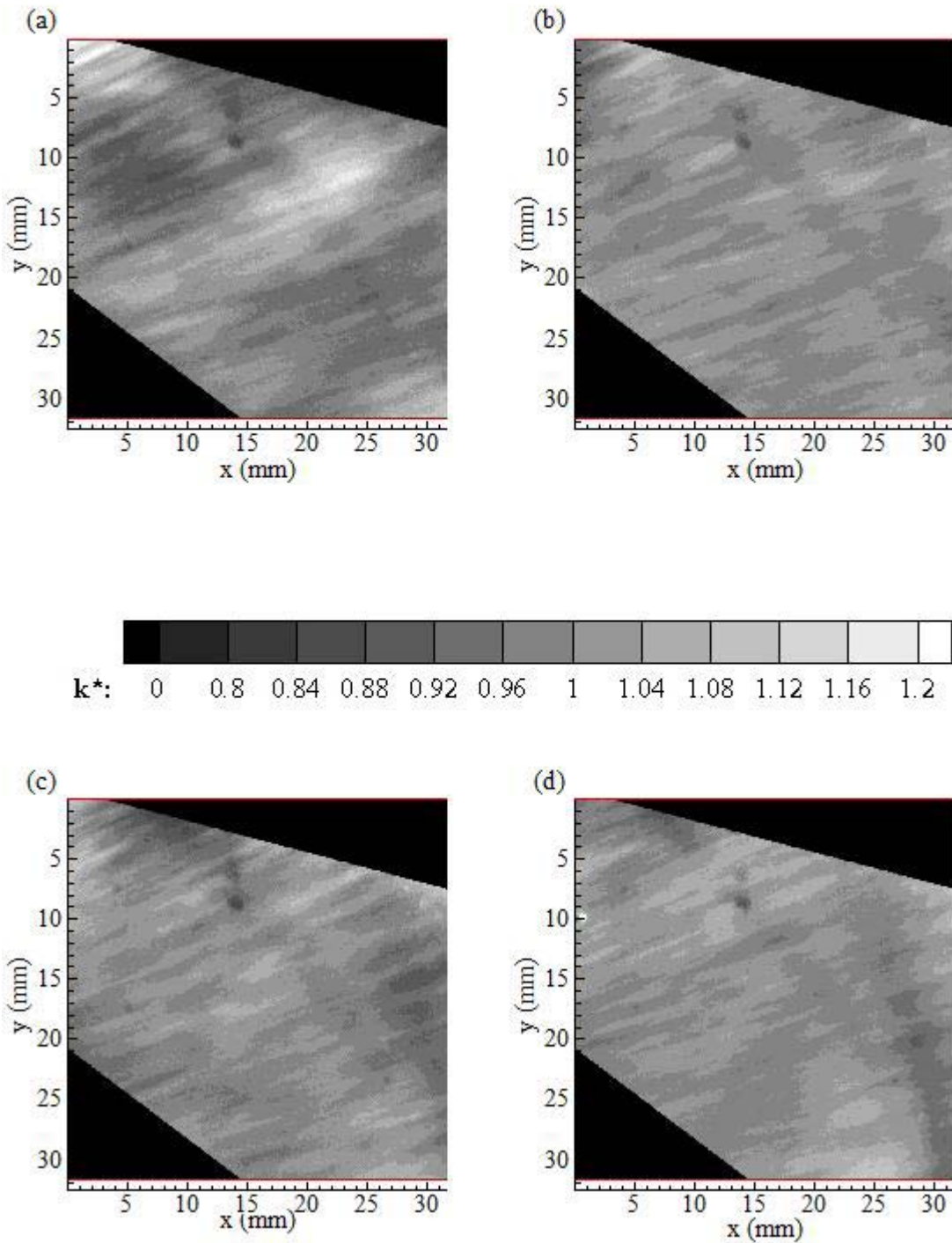


Figure C.28. Grayscale plots of normalized dimensionless mass transfer coefficient values at 46% relative humidity: (a) R46D\_48; 48 min.: 40 sec., (b) R46D\_50; 49 min.: 10 sec., (c) R46D\_52; 51 min.: 40 sec., (d) R46D\_55; 52 min.: 10 sec.

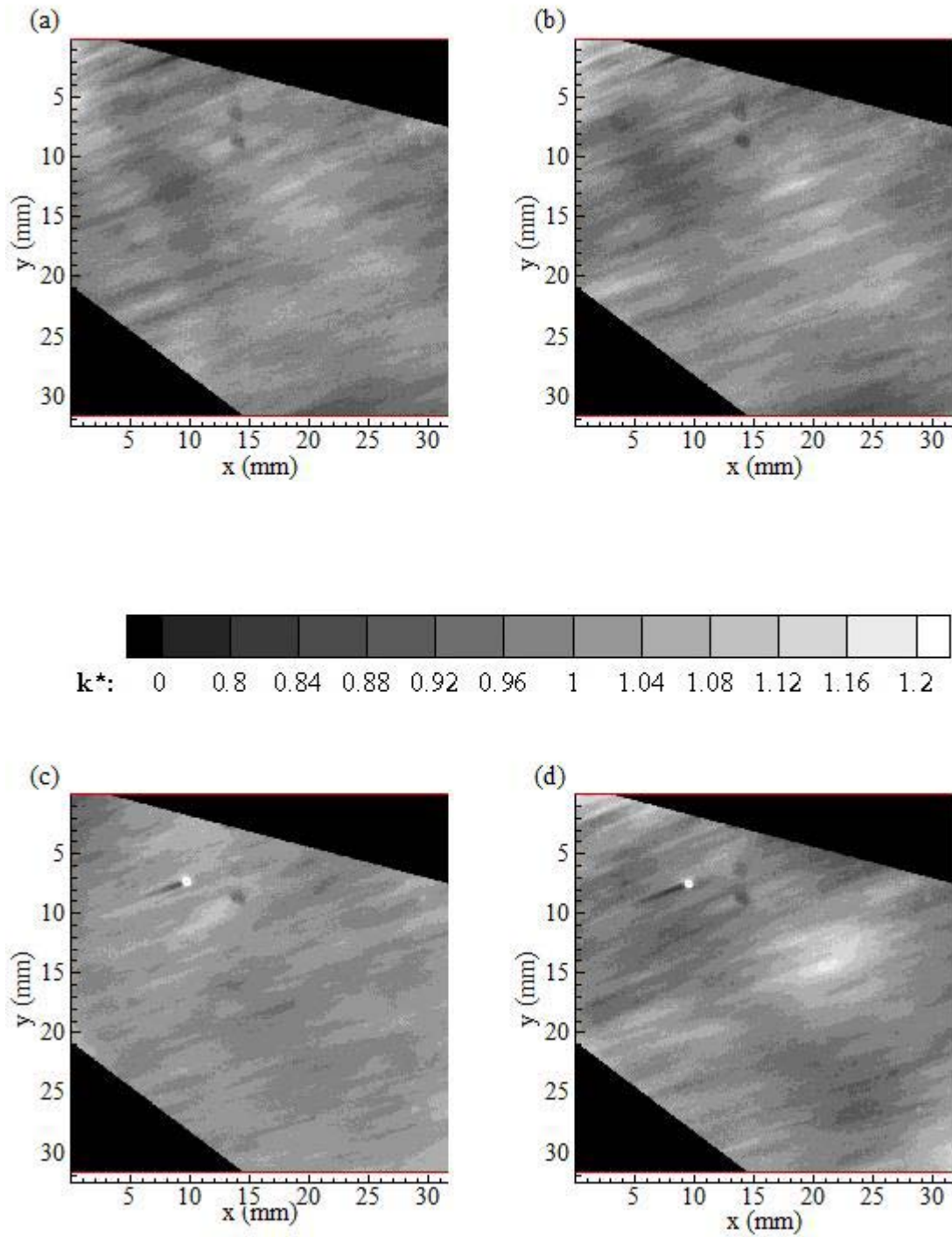


Figure C.28. Grayscale plots of normalized dimensionless mass transfer coefficient values at 46% relative humidity: (a) R46D\_56; 55 min.: 10 sec., (b) R46D\_58; 55 min.: 40 sec., (c) R46C\_60; 56 min.: 50 sec., (d) R46D\_62; 57 min.: 20 sec.

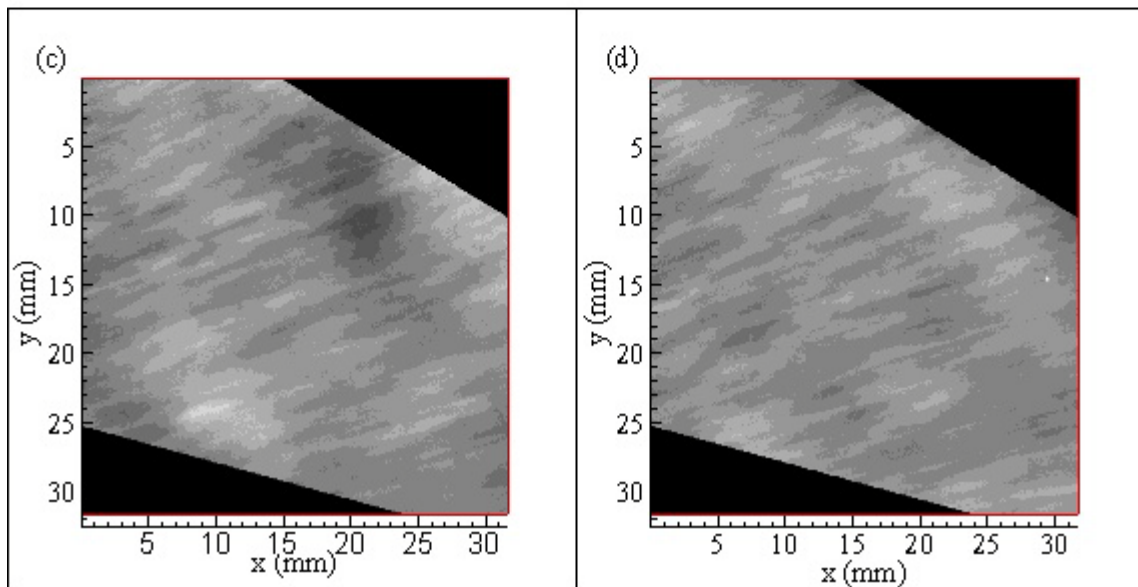
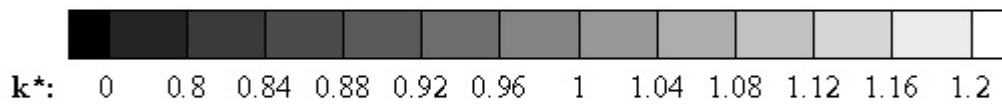
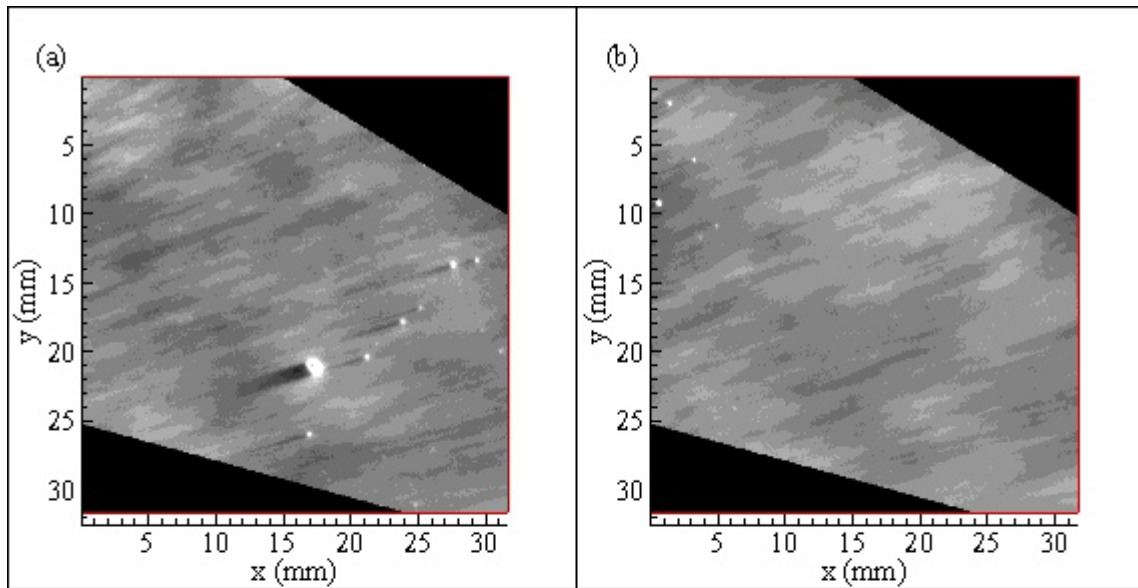


Figure C.34. Grayscale plots of normalized dimensionless mass transfer coefficient values at 58% relative humidity: (a) R58A\_1; 0 min.: 30 sec., (b) R58A\_5; 0 min.: 50 sec., (c) R58A\_9; 2 min.: 40 sec., (d) R58A\_13; 3 min.: 50 sec.

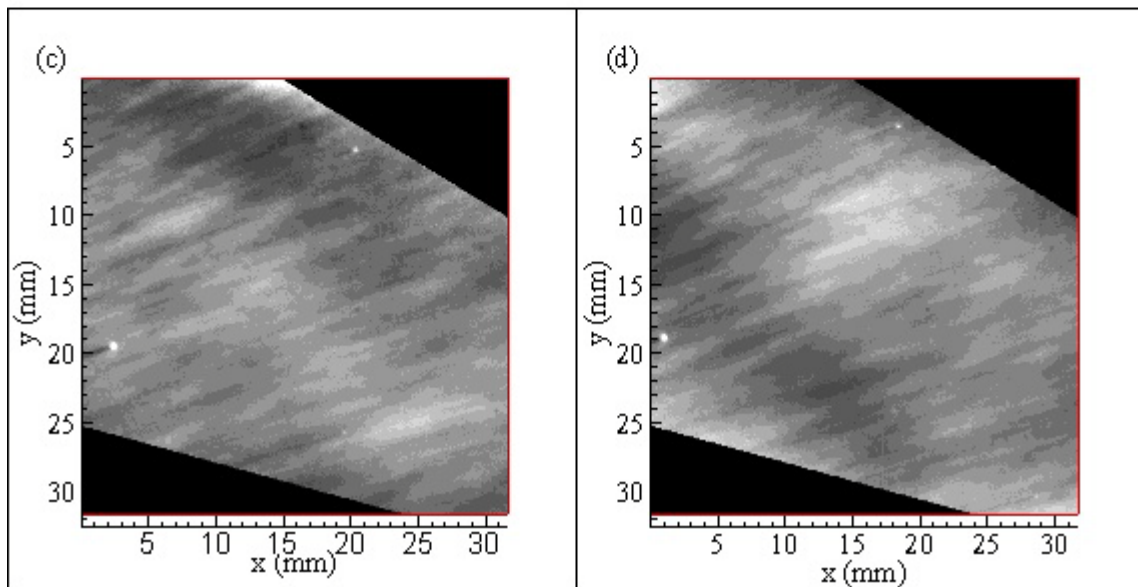
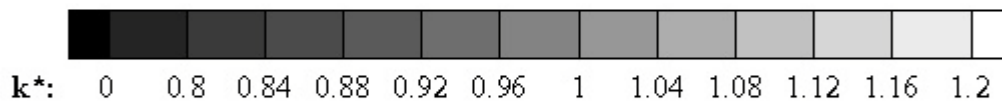
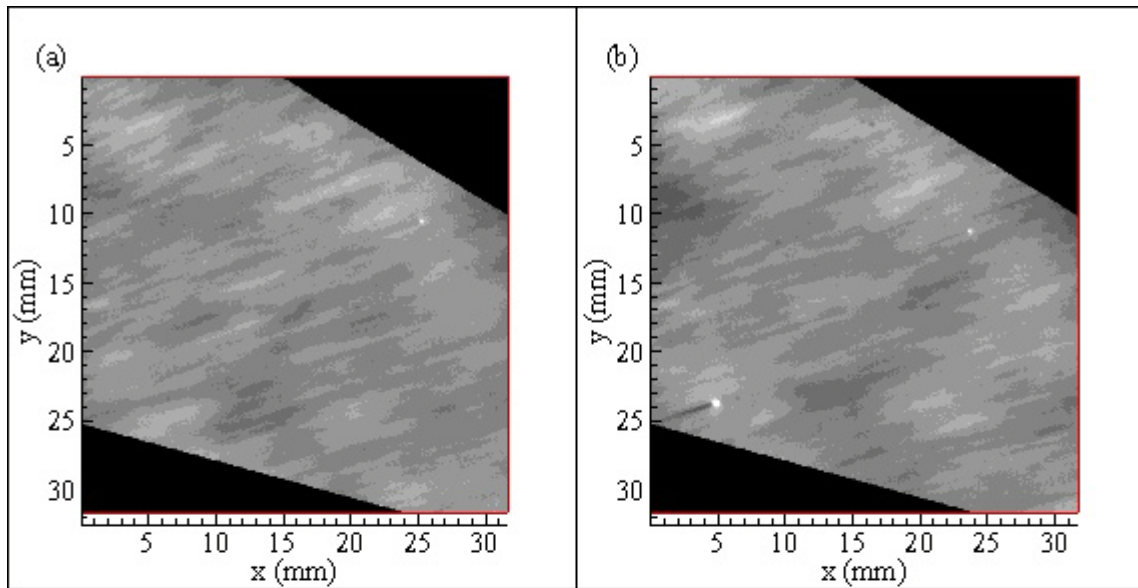


Figure C.35. Grayscale plots of normalized dimensionless mass transfer coefficient values at 58% relative humidity: (a) R58A\_14; 4 min.: 20 sec., (b) R58A\_18; 4 min.: 50 sec., (c) R58A\_19; 5 min.: 10 sec., (d) R58A\_20; 5 min.: 40 sec.,

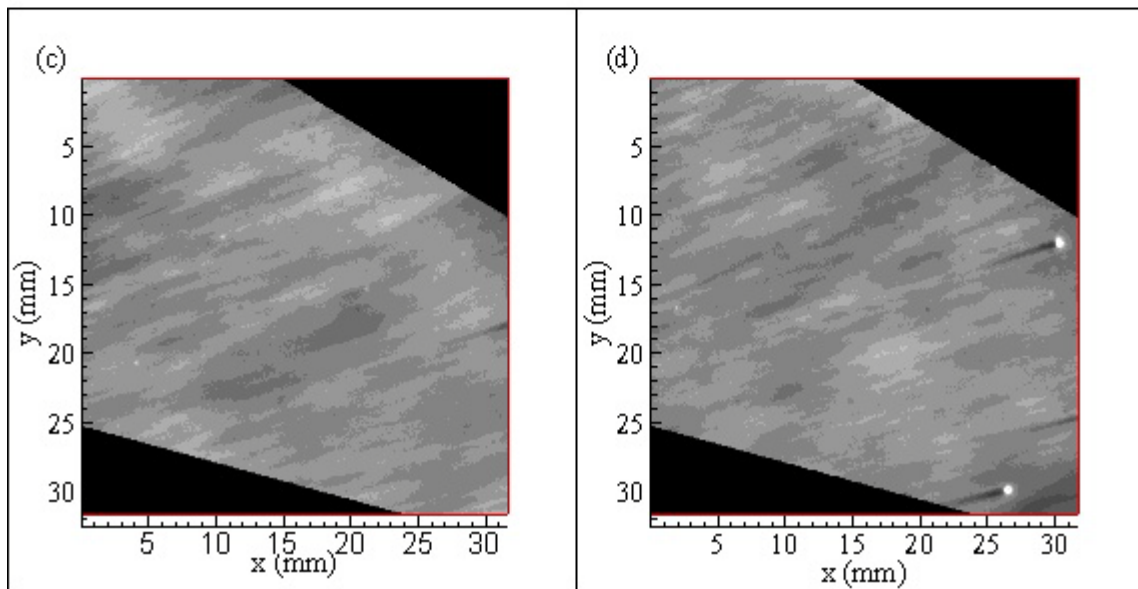
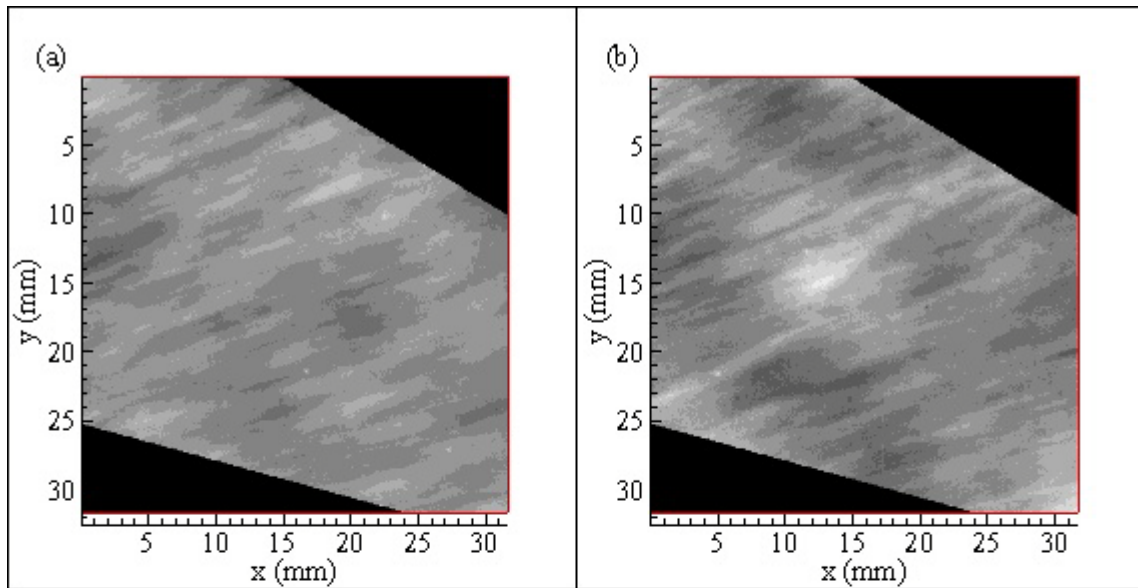


Figure C.36. Grayscale plots of normalized dimensionless mass transfer coefficient values at 58% relative humidity: (a) R58A\_21; 6 min.: 0 sec., (b) R58A\_24; 6 min.: 30 sec., (c) R58A\_25; 7 min.: 00 sec., (d) R58A\_27; 7 min.: 22 sec.

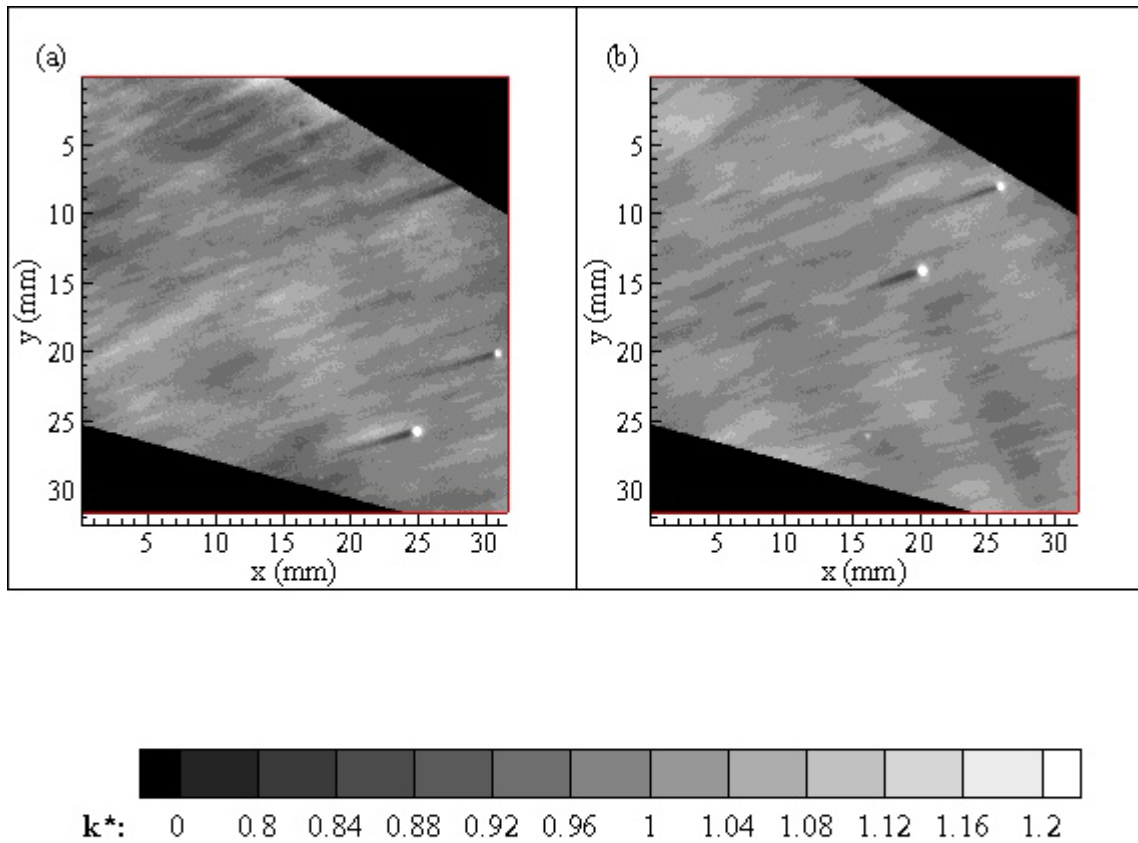


Figure C.37. Grayscale plots of normalized dimensionless mass transfer coefficient values at 58% relative humidity: (a) R58A\_28; 7 min.: 50 sec., (b) R58A\_36; 8min.: 10 sec.

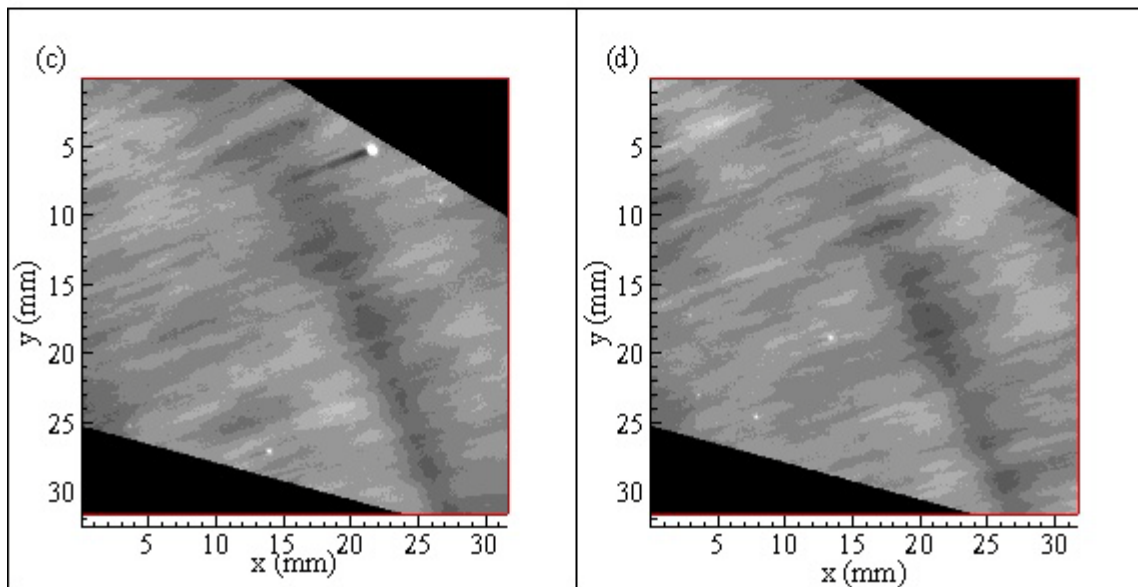
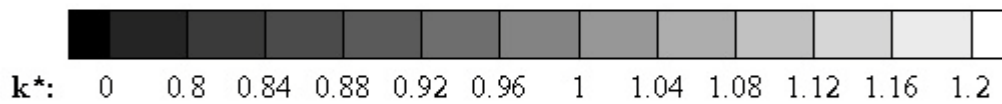
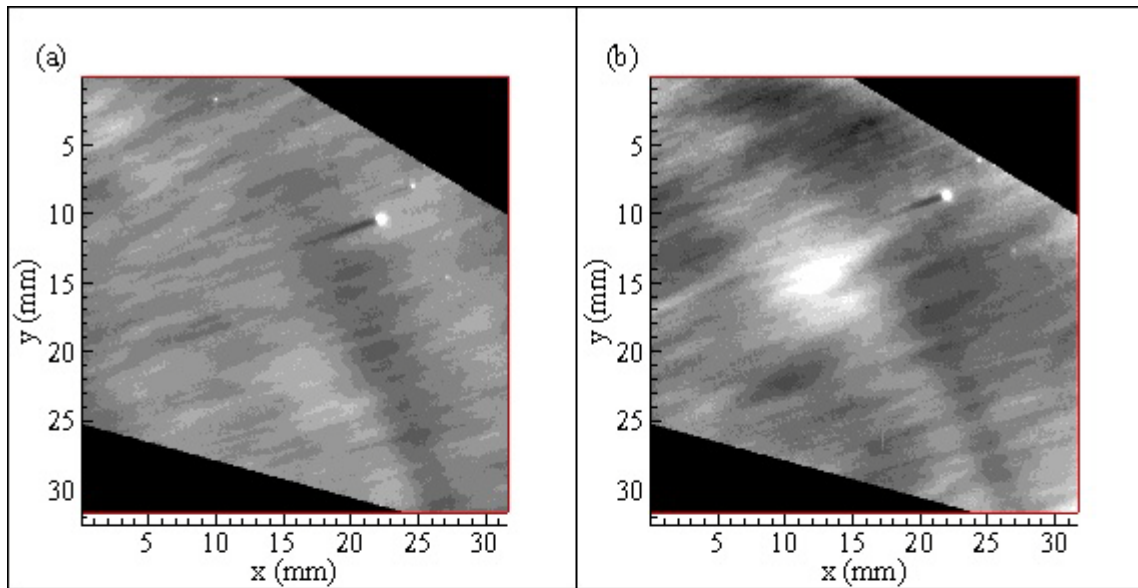


Figure C.38. Grayscale plots of normalized dimensionless mass transfer coefficient values at 58% relative humidity: (a) R58A\_59; 10 min: 10 sec., (b) R58A\_60; 10 min.: 30 sec., (c) R58A\_65; 10 min.: 50 sec., (d) R58A\_75; 11 min.: 20 sec.

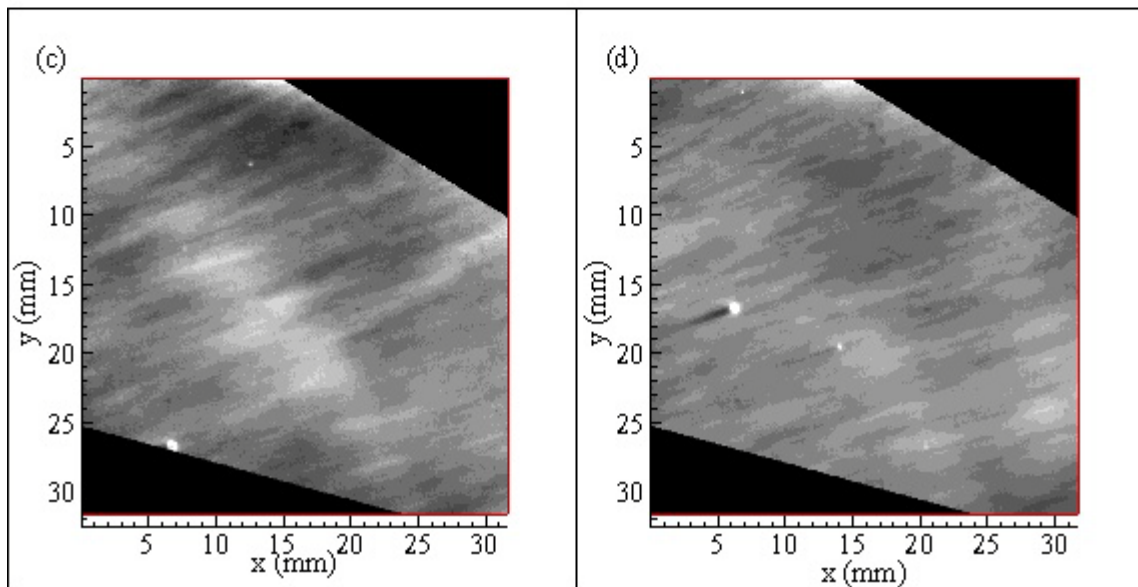
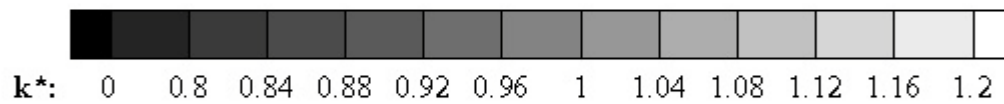
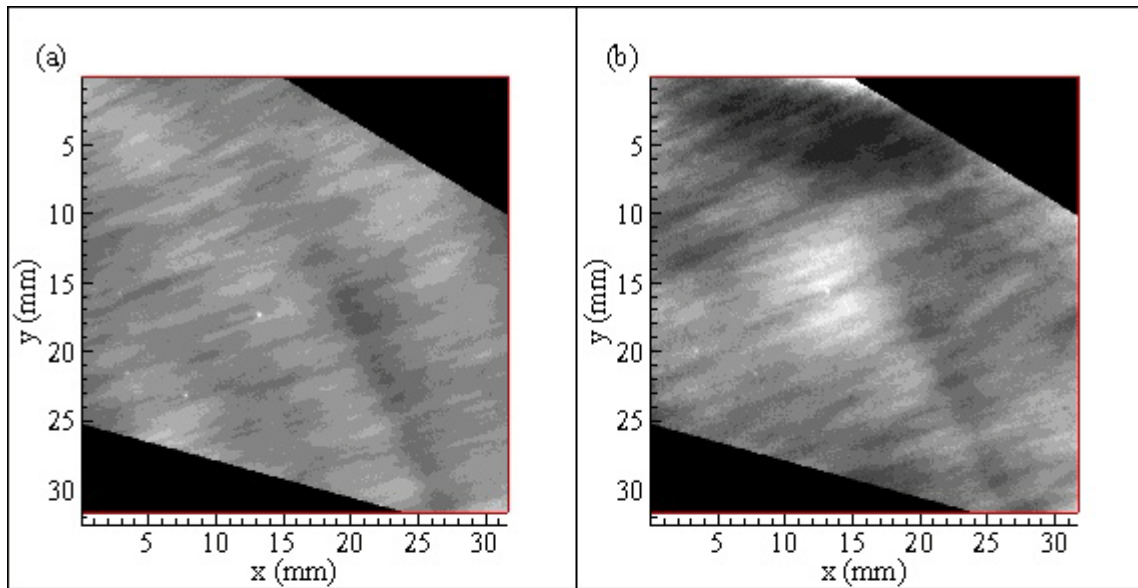


Figure C.39. Grayscale plot of normalized dimensionless mass transfer coefficient values at 58% relative humidity (a) R58A\_77; 11 min : 46 sec, (b) R58A\_79; 12 min : 12 sec (c) R58A\_94; 13 min : 30 sec (d) R58A\_7; 13 min : 56 sec,

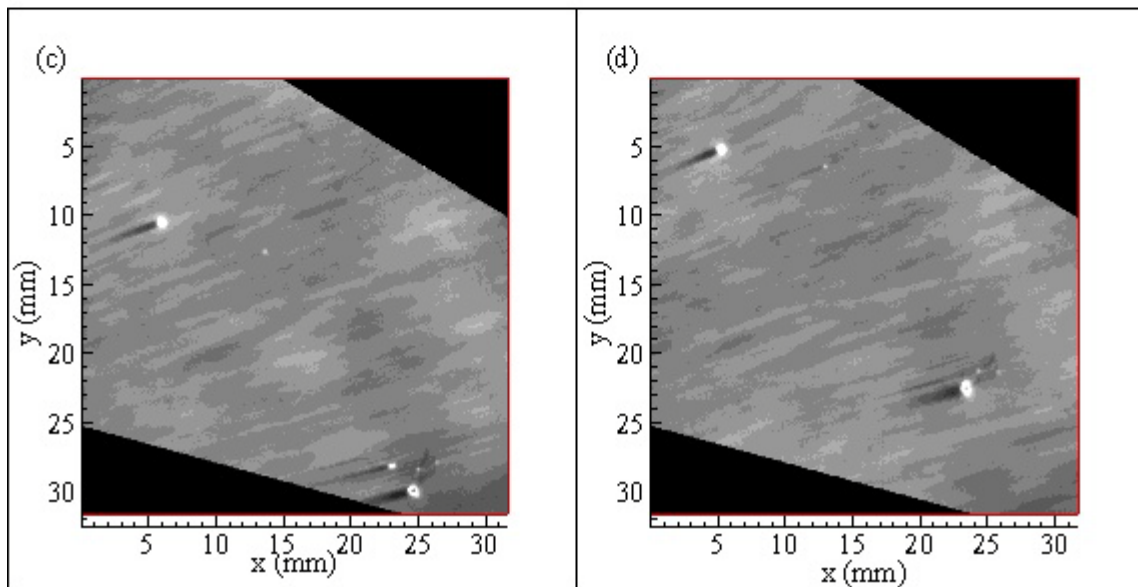
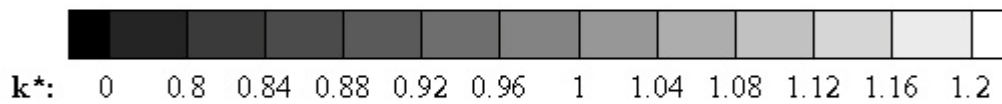
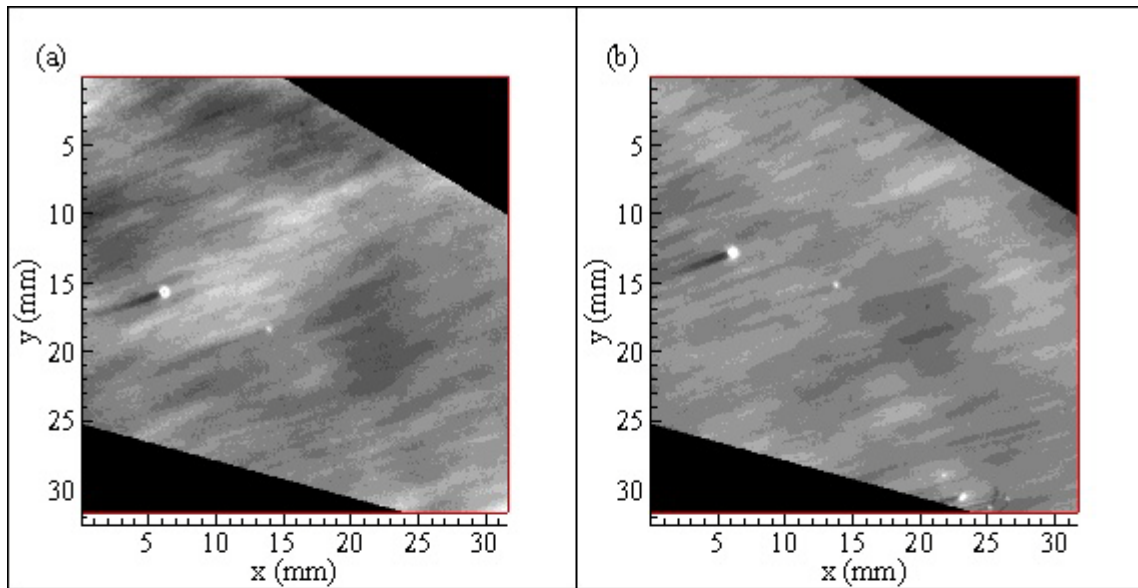


Figure C.40. Grayscale plot of normalized dimensionless mass transfer coefficient values at 58% relative humidity. (a) R58B\_9; 14 min: 23 sec; (b) R58B\_17; 14 min :50 sec; (c) R58B\_24; 15 min: 17 sec; (d) R58B\_47; 16 min: 35 sec.

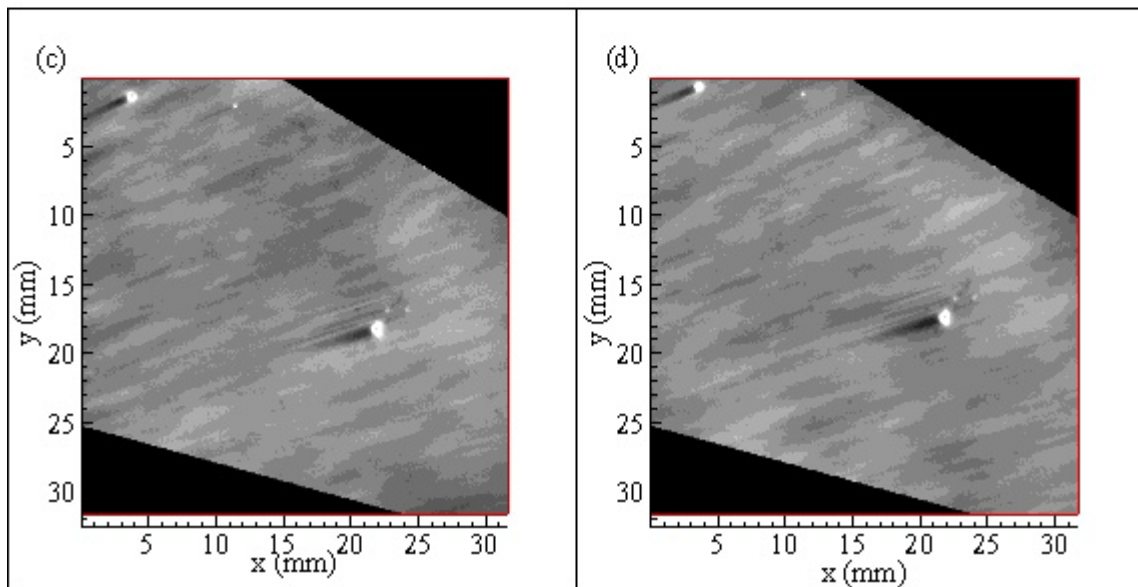
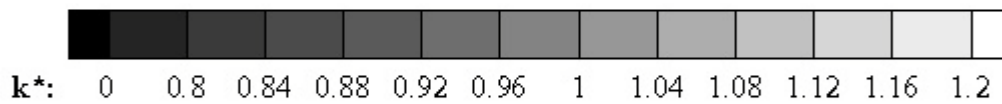
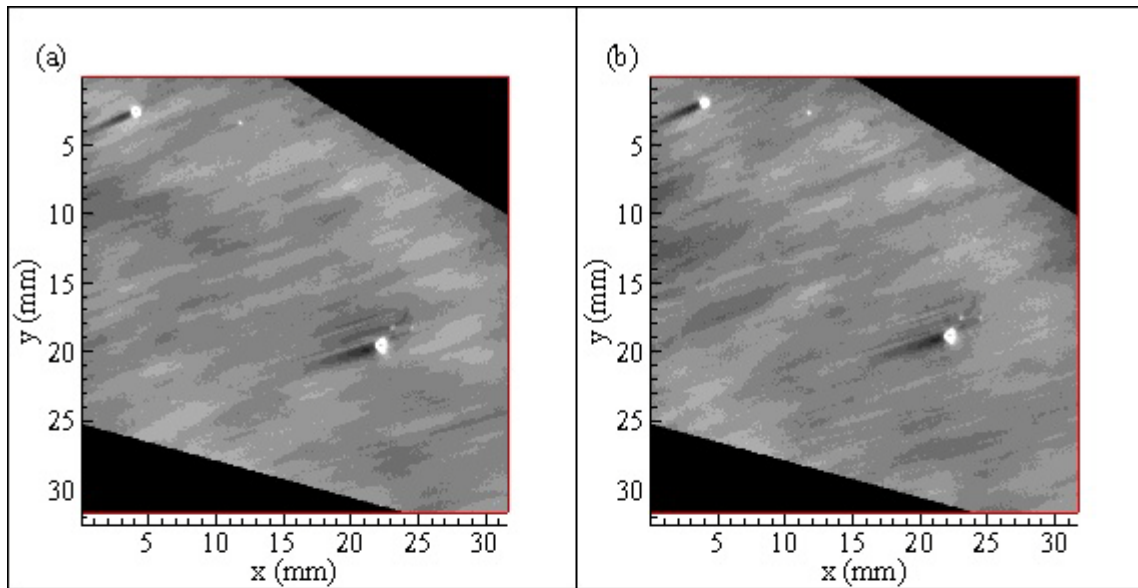


Figure C.41. Grayscale plot of normalized dimensionless mass transfer coefficient values at 58% relative humidity. (a) R58B\_61; 17 min.: 30 sec., (b) R58B\_63; 17 min.: 50 sec., (c) R58B\_65; 18 min.: 20 sec., (d) R58B\_67; 18 min.: 50 sec.

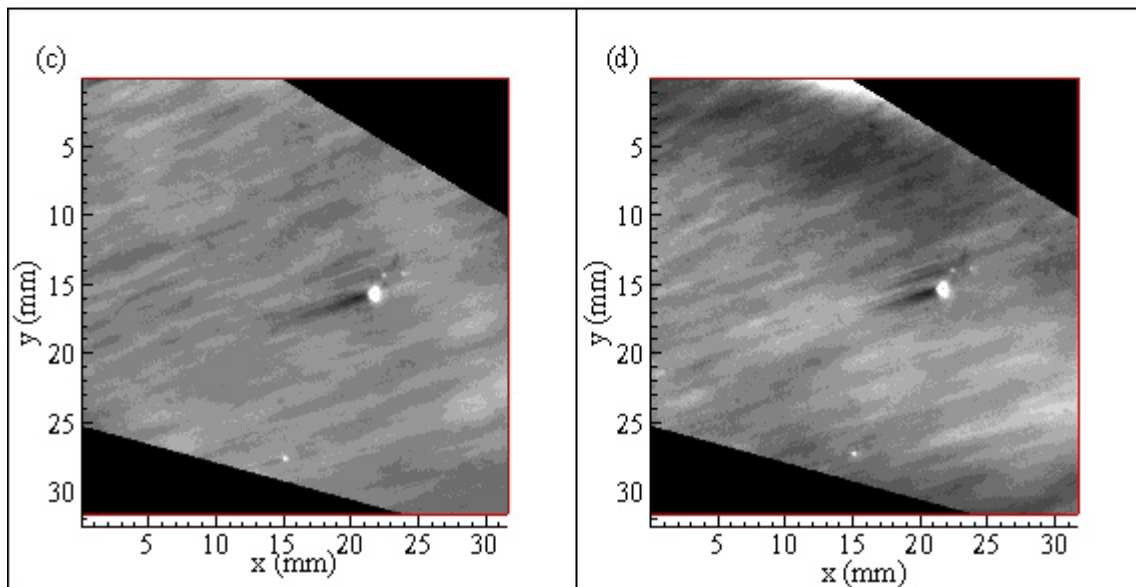
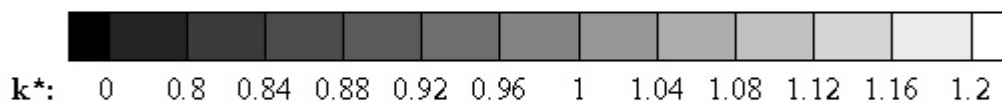
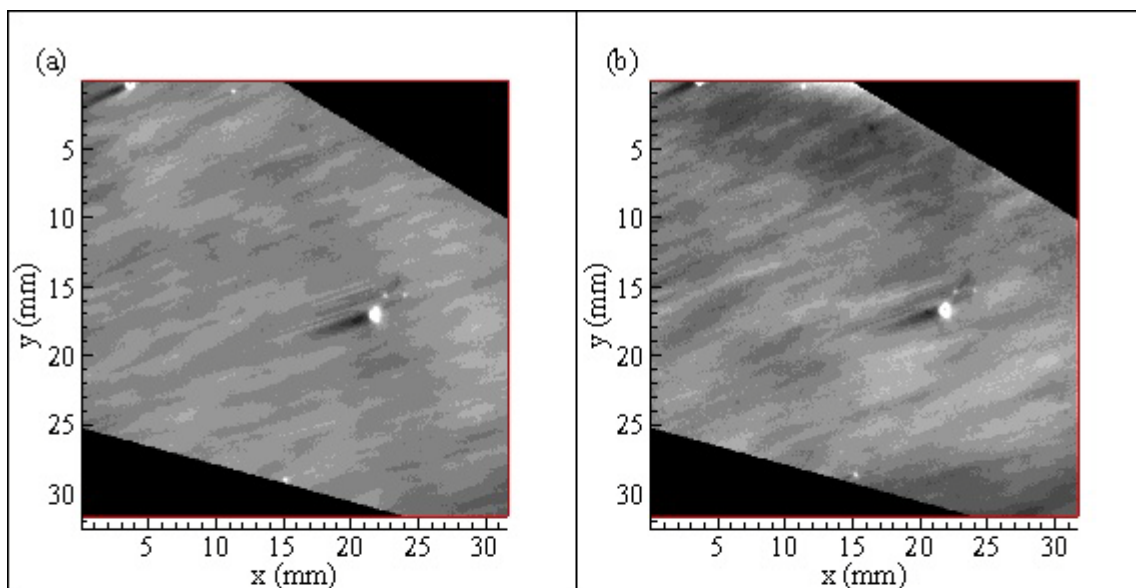


Figure C.42. Grayscale plots of normalized dimensionless mass transfer coefficient values at 58% relative humidity: (a) R58B\_68; 19 min.:10 sec., (b) R58B\_69; 19 min.: 40 sec., (c) R58B\_71; 20 min.: 10 sec., (d) R58B\_74; 21 min.: 00 sec.

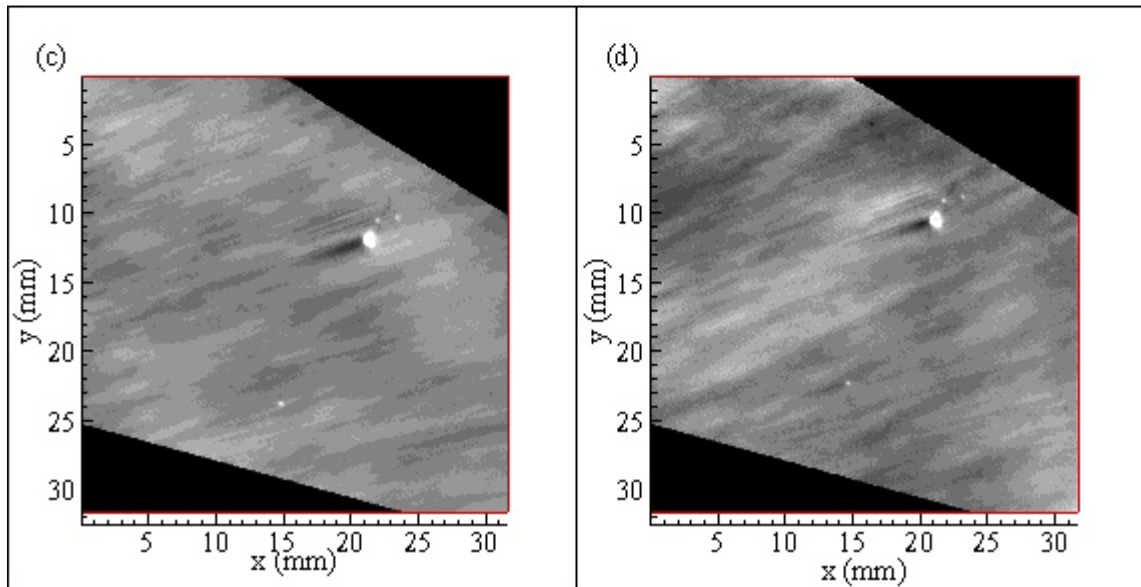
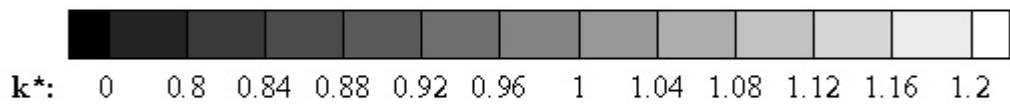
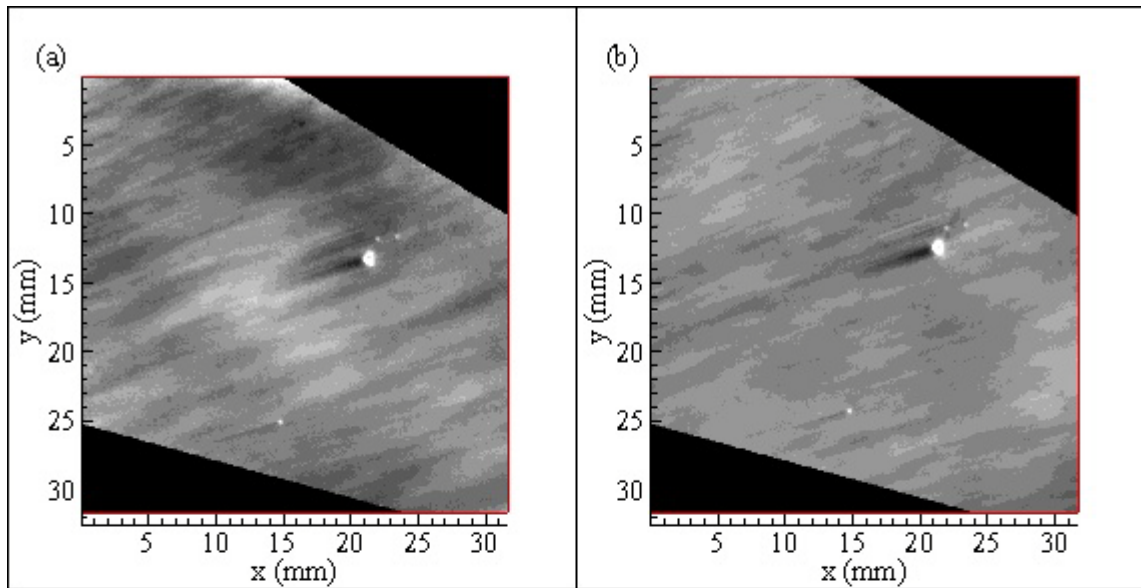


Figure C.43. Grayscale plots of normalized dimensionless mass transfer coefficient values at 58% relative humidity: (a) R58B\_84; 21 min.: 20 sec., (b) R58B\_87; 21 min.: 51 sec., (c) R58B\_88; 22 min.: 20 sec., (d) R58B\_94; 23 min.: 10 sec.

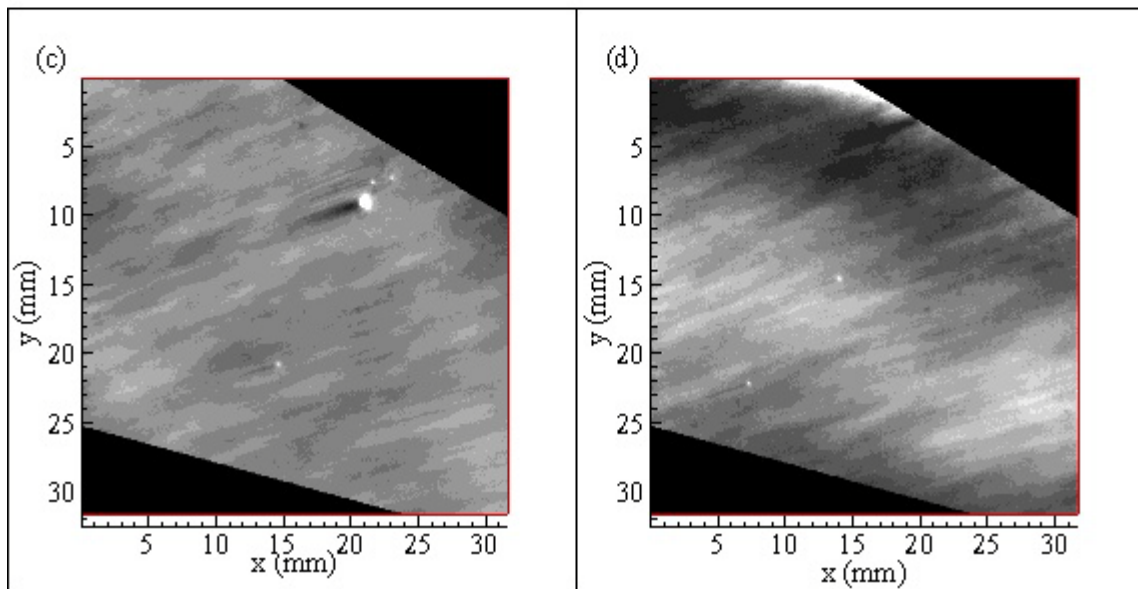
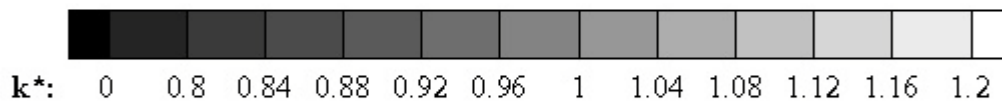
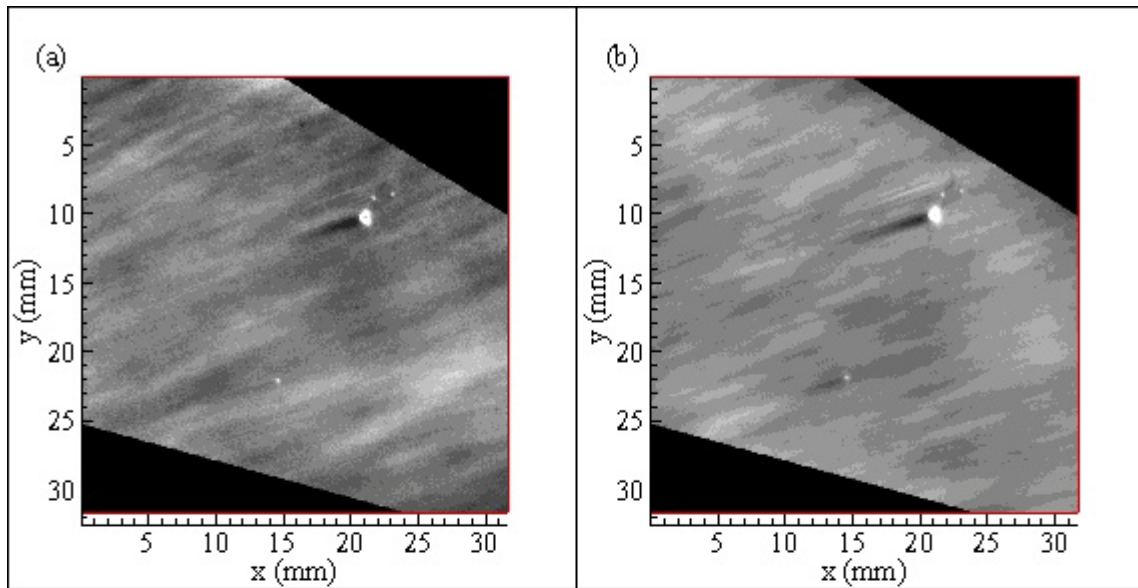


Figure C.44. Grayscale plots of normalized dimensionless mass transfer coefficient values at 58% relative humidity: (a) R58B\_95; 21 min.: 20 sec., (b) R58B\_96; 21 min.: 50 sec., (c) R58B\_98; 22 min.: 20 sec., (d) R58C\_1; 23 min.: 10 sec.

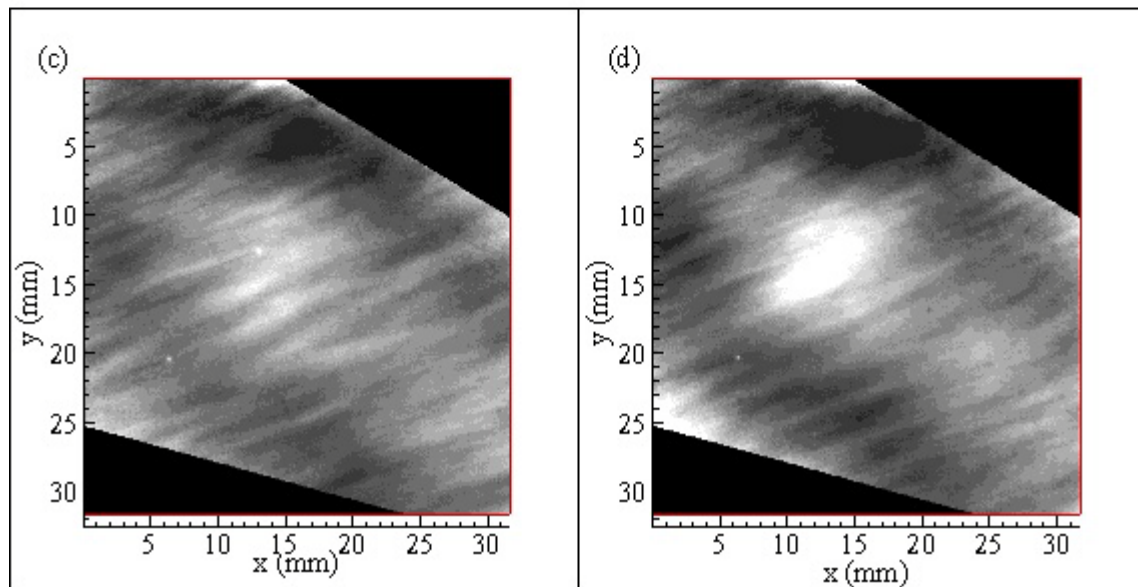
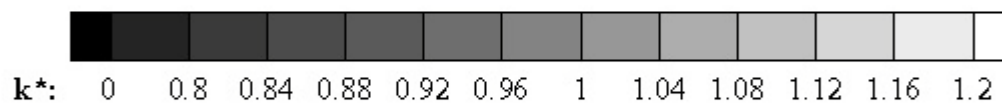
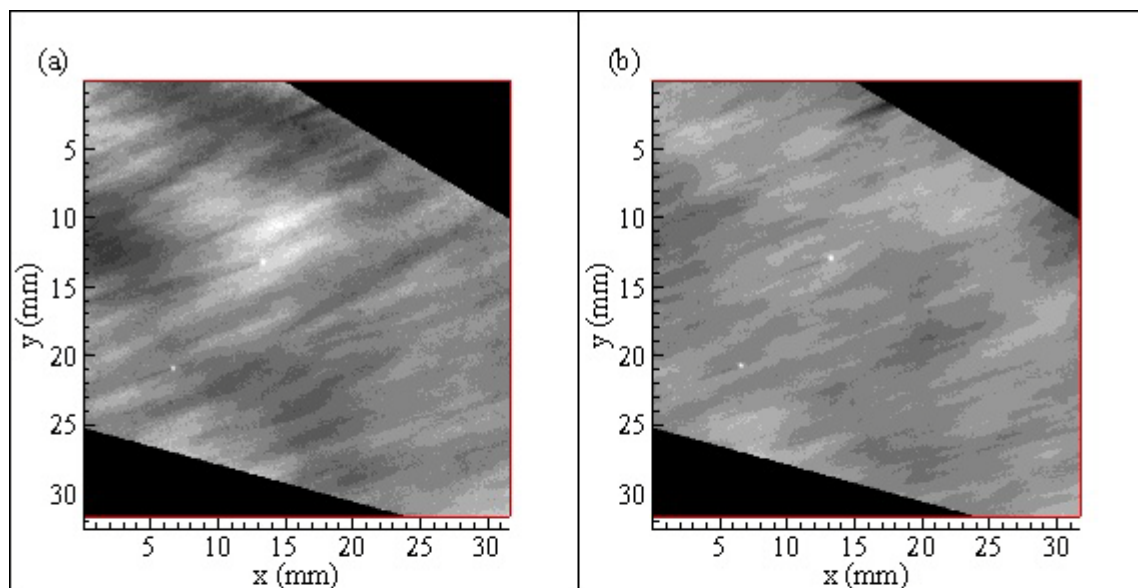


Figure C.45. Grayscale plots of normalized dimensionless mass transfer coefficient values at 58% relative humidity: (a) R58C\_8; 28 min.: 30 sec., (b) R58C\_9; 28 min.: 40 sec., (c) R58C\_10; 29 min.: 20 sec., (d) R58C\_11; 29 min.: 50 sec.

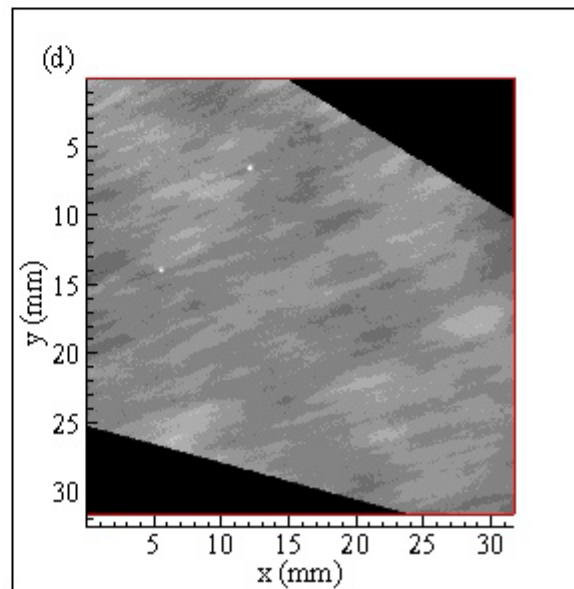
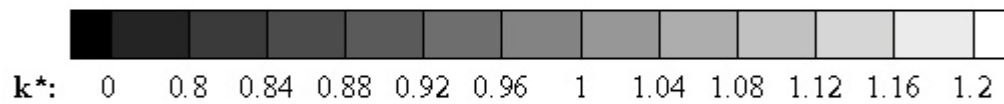
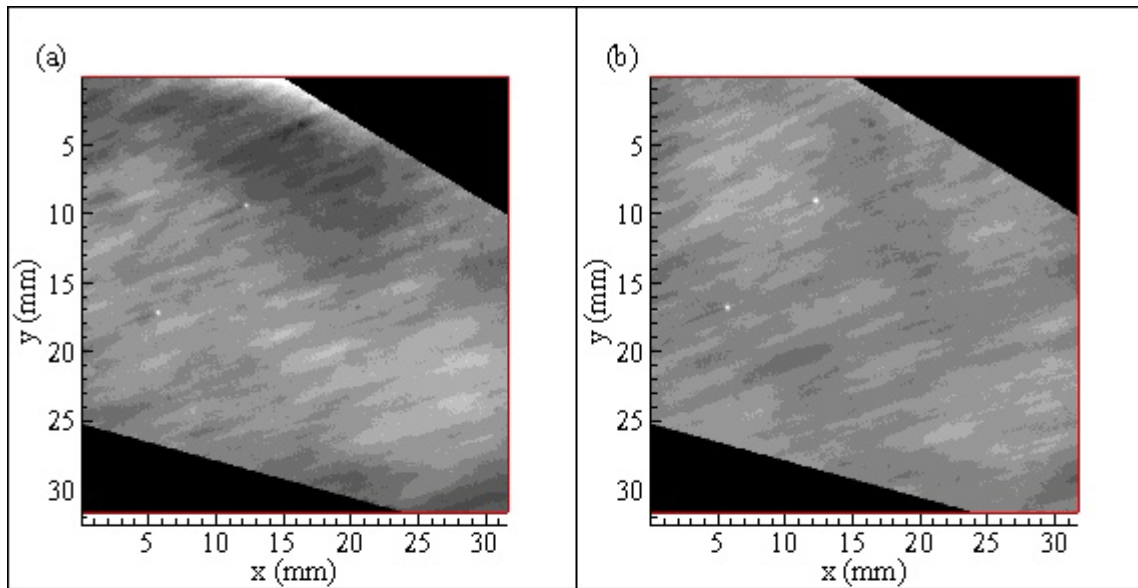


Figure C.46. Grayscale plots of normalized dimensionless mass transfer coefficient values at 58% relative humidity (a) R58C\_8; 28 min.: 30 sec.,  
 (b) R58C\_9; 28 min.: 35 sec.,  
 (d) R58C\_11; 29 min.: 50 sec.

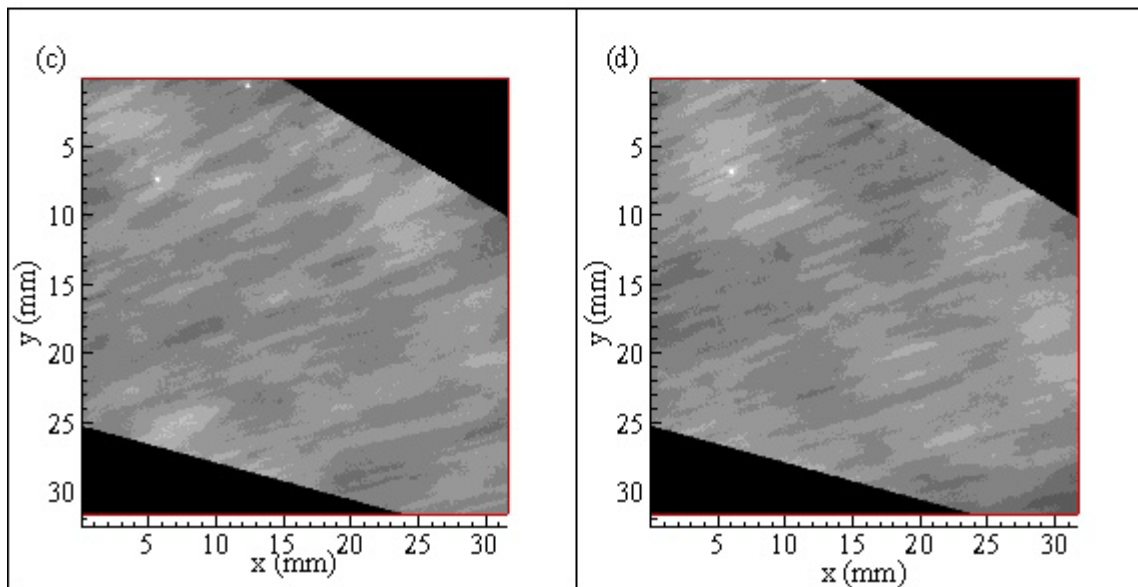
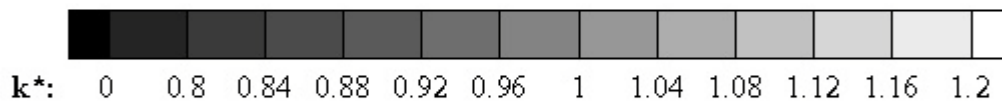
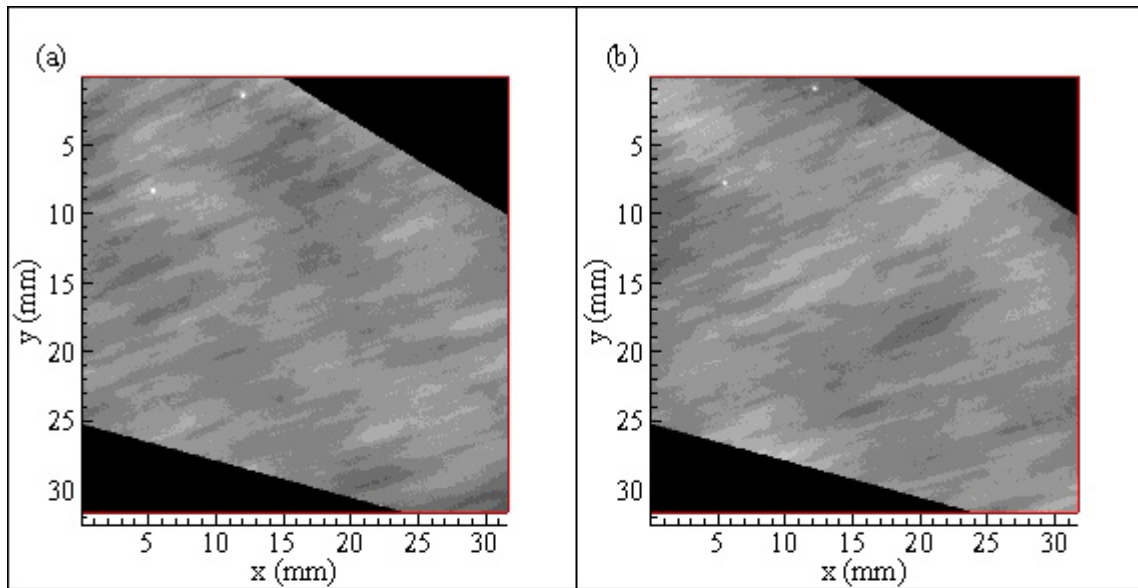


Figure C.47. Grayscale plots of normalized dimensionless mass transfer coefficient values at 58% relative humidity: (a) R58C\_13; 30 min.: 40 sec., (b) R58C\_14; 31 min.: 10 sec., (c) R58C\_15; 31 min.: 30 sec., (d) R58C\_16; 32 min.: 00 sec.

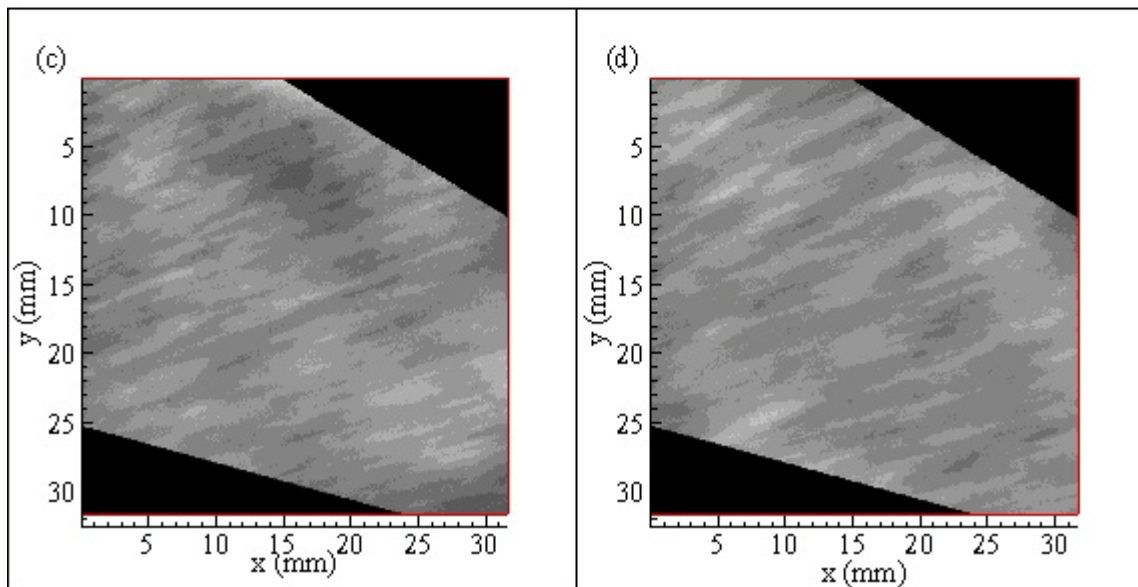
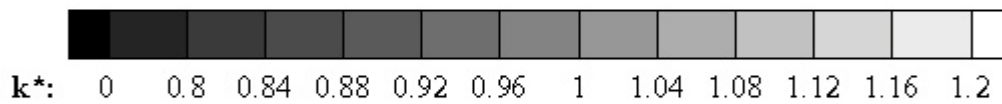
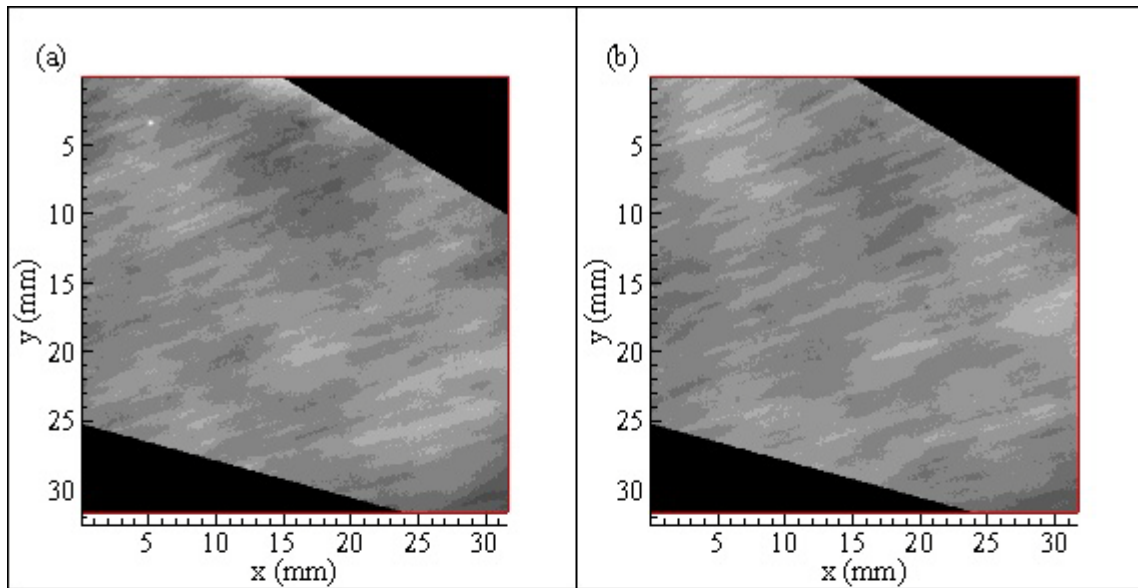
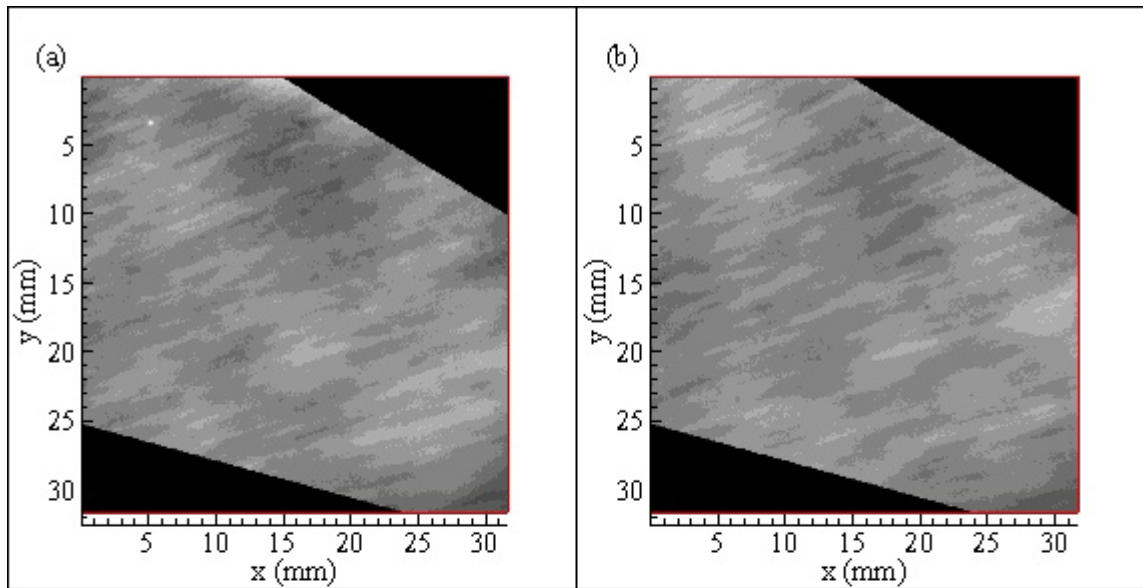


Figure C.48. Grayscale plots of normalized dimensionless mass transfer coefficient values at 58% relative humidity: (a) R58C\_17; 32 min.: 30 min., (b) R58C\_19; 33 min.: 20 sec., (c) R58C\_20; 33 min.: 50 sec., (d) R58C\_21; 34 min.: 10 sec.



$k^*$ : 0 0.8 0.84 0.88 0.92 0.96 1 1.04 1.08 1.12 1.16 1.2

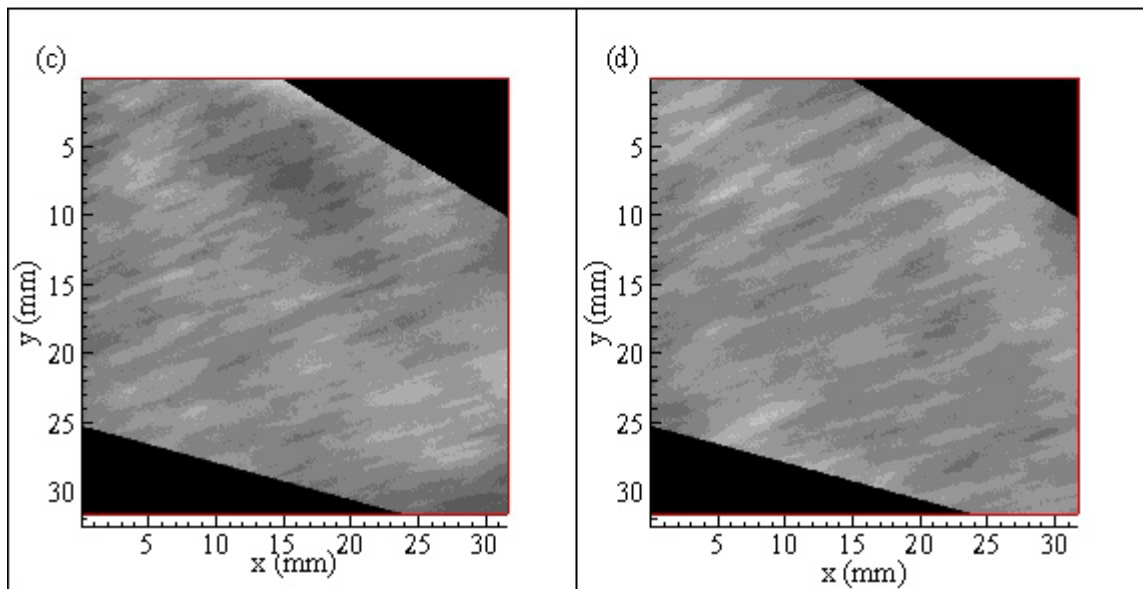
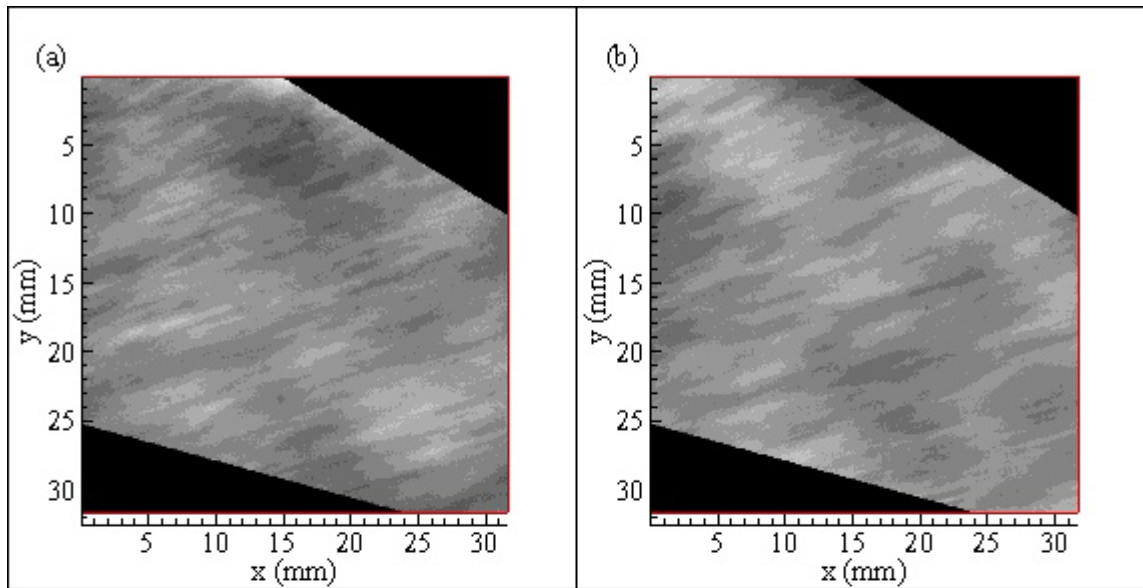


Figure C.49. Grayscale plots of normalized dimensionless mass transfer coefficient values at 58% relative humidity: (a) R58C\_22; 34 min.: 40 sec., (b) R58C\_28; 37 min.: 20 sec., (c) R58C\_29; 37 min.: 50 sec., (d) R58C\_30; 38 min.: 10 sec.



$k^*$ : 0 0.8 0.84 0.88 0.92 0.96 1 1.04 1.08 1.12 1.16 1.2

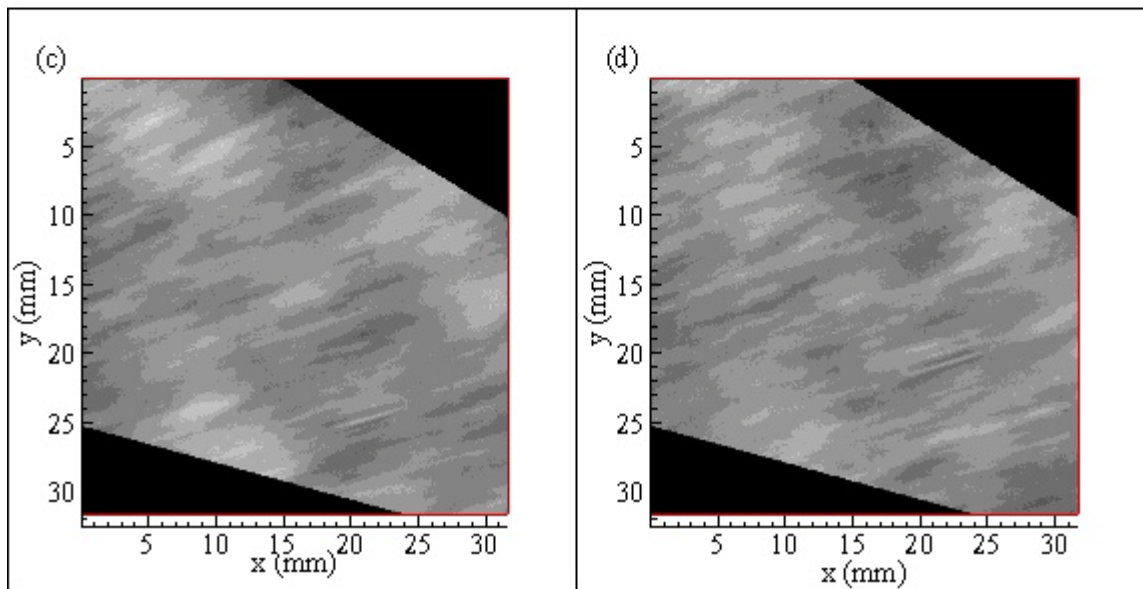
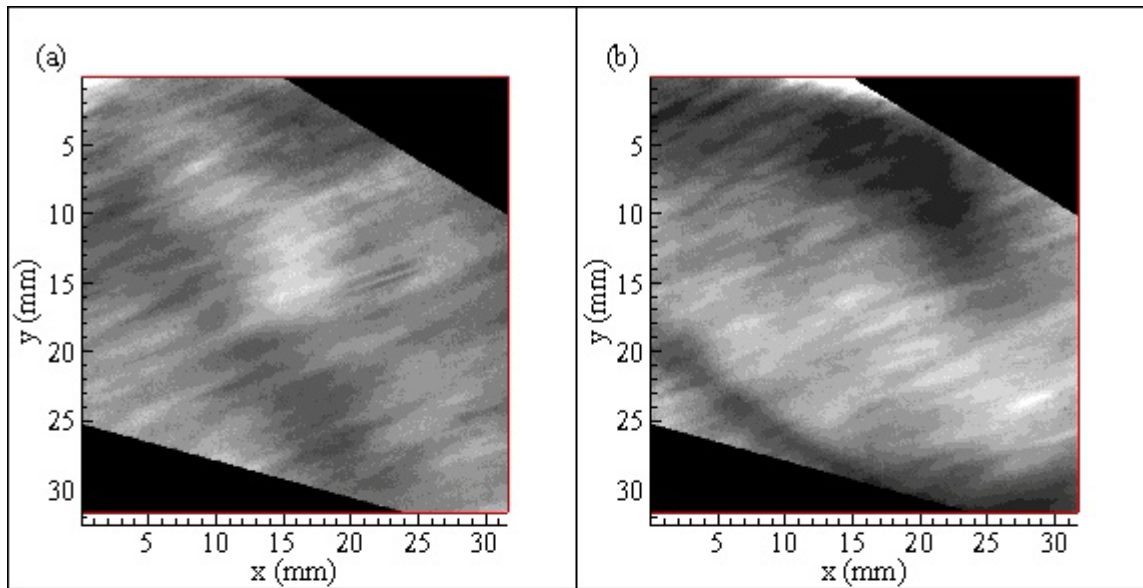


Figure C.50 . Grayscale plots of normalized dimensionless mass transfer coefficient values at 58% relative humidity: (a) R58C\_32; 39 min.: 10 sec., (b) R58C\_33; 39 min.: 30 sec., (c) R58C\_35; 40 min.: 50 sec., (d) R58C\_36; 41 min.: 00 sec.



$k^*$ : 0 0.8 0.84 0.88 0.92 0.96 1 1.04 1.08 1.12 1.16 1.2

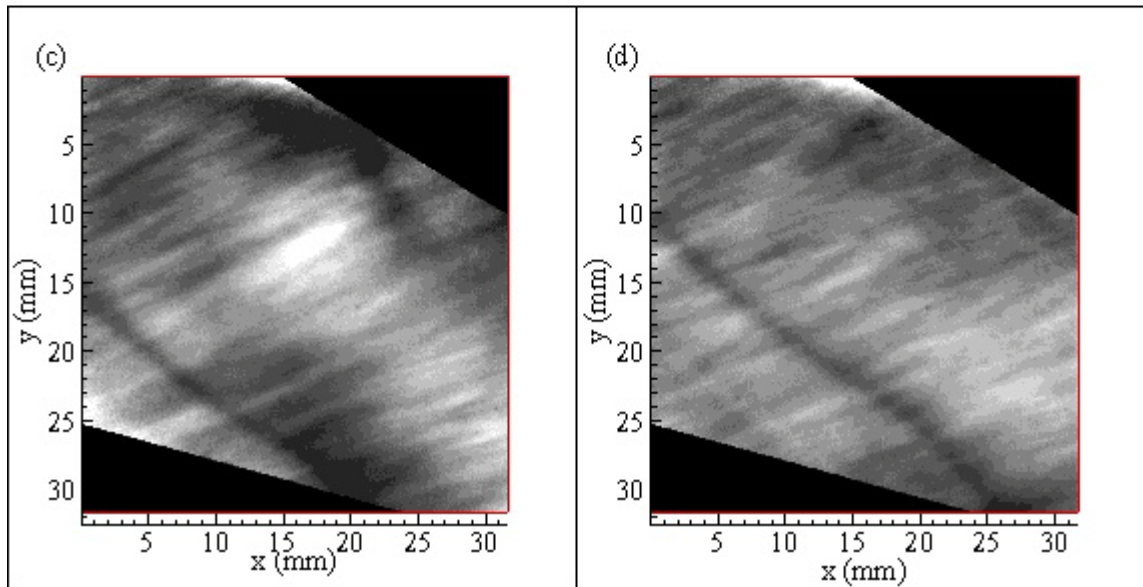
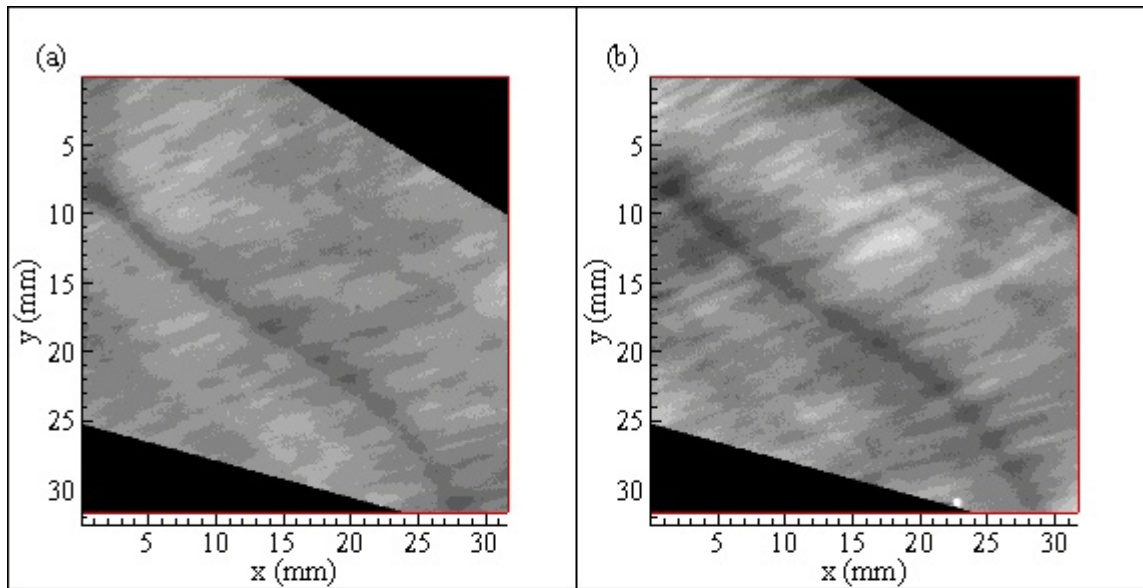


Figure C.51. Grayscale plots of normalized dimensionless mass transfer coefficient values at 58% relative humidity: (a) R58C\_42; 41 min.: 20 sec., (b) R58C\_48; 41 min.: 50 sec., (c) R58C\_51; 42 min.: 10 sec., (d) R58C\_67; 42 min.: 40 sec.



$k^*$ : 0 0.8 0.84 0.88 0.92 0.96 1 1.04 1.08 1.12 1.16 1.2

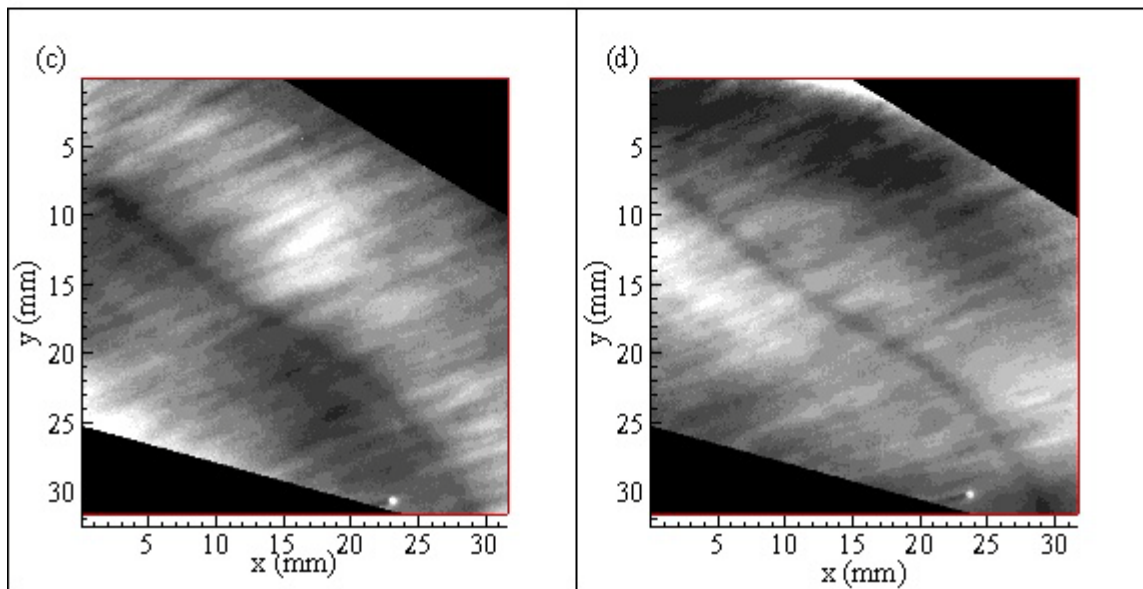
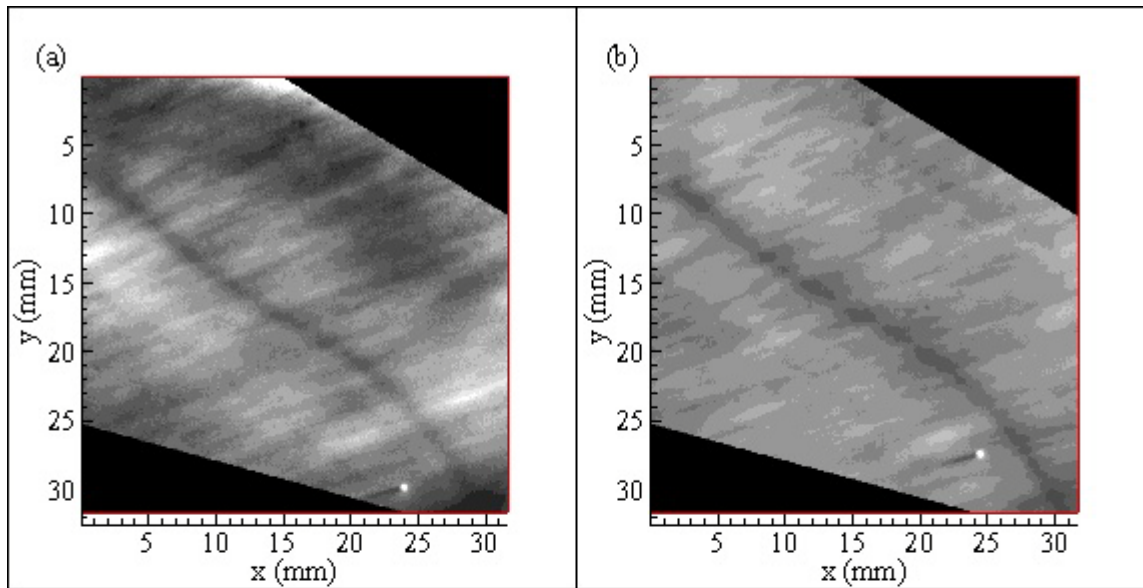


Figure C.52. Grayscale plots of normalized dimensionless mass transfer coefficient values at 58% relative humidity: (a) R58C\_81; 50 min.: 40 sec., (b) R58C\_83; 51 min.: 30 sec., (c) R58C\_84; 51 min.: 50 sec., (d) R58C\_86; 52 min.: 20 sec.



$k^*$ : 0 0.8 0.84 0.88 0.92 0.96 1 1.04 1.08 1.12 1.16 1.2

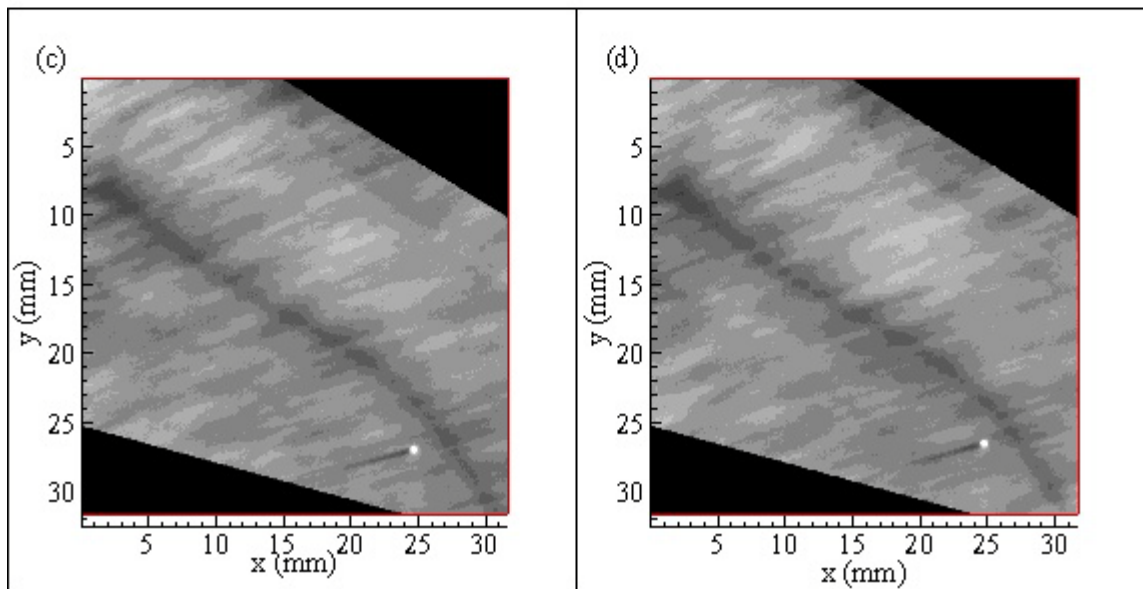
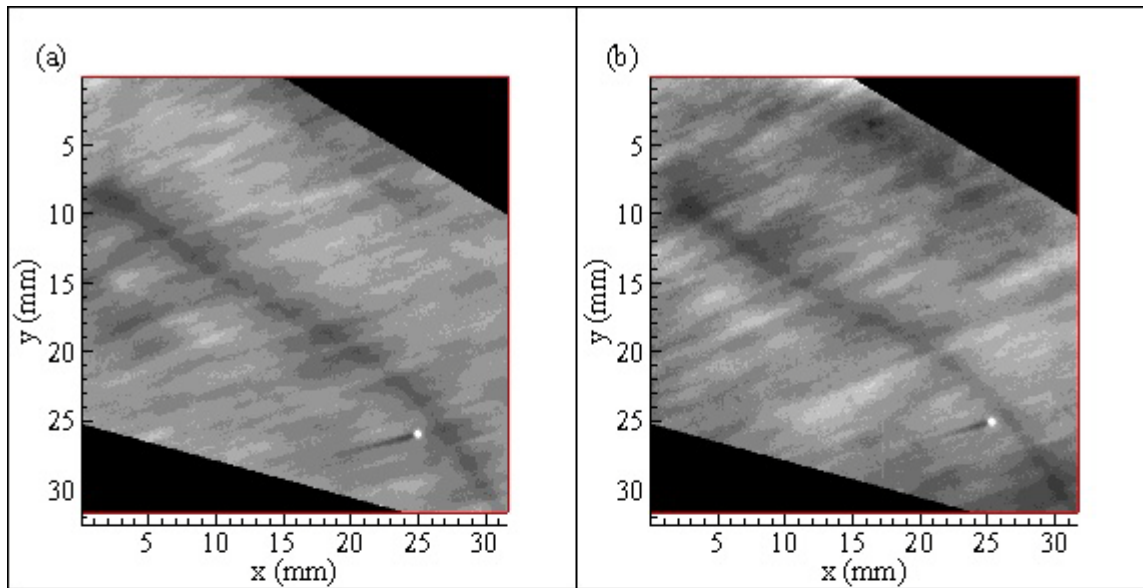


Figure C.53. Grayscale plots of normalized dimensionless mass transfer coefficient values at 58% relative humidity: (a) R58C\_87; 52 min.: 50 sec., (b) R58C\_93; 53 min.: 10 sec., (c) R58C\_94; 53 min.: 40 sec., (d) R58C\_95; 54 min.: 10 sec.



$k^*$ : 0 0.8 0.84 0.88 0.92 0.96 1 1.04 1.08 1.12 1.16 1.2

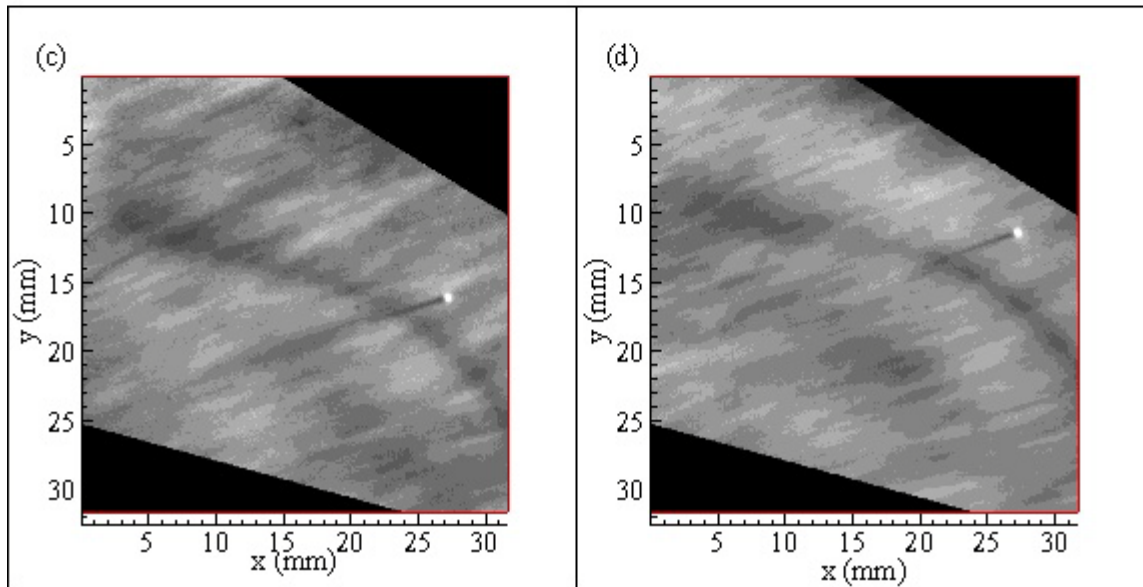
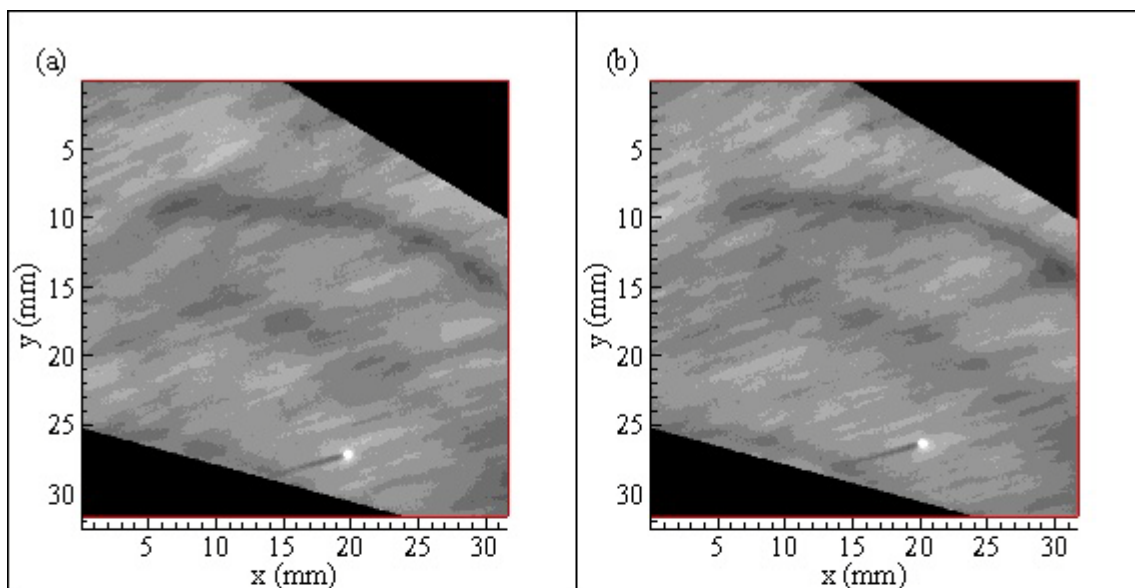


Figure C.54. grayscale plots of normalized dimensionless mass transfer coefficient values at 58% relative humidity: (a) R58D\_25; 58 min.: 20 sec., (b) R58D\_43; 59 min.: 10 sec., (c) R58D\_45; 59 min.: 30 sec., (d) R58D\_48; 59 min.: 50, sec.



$k^*$ : 0 0.8 0.84 0.88 0.92 0.96 1 1.04 1.08 1.12 1.16 1.2

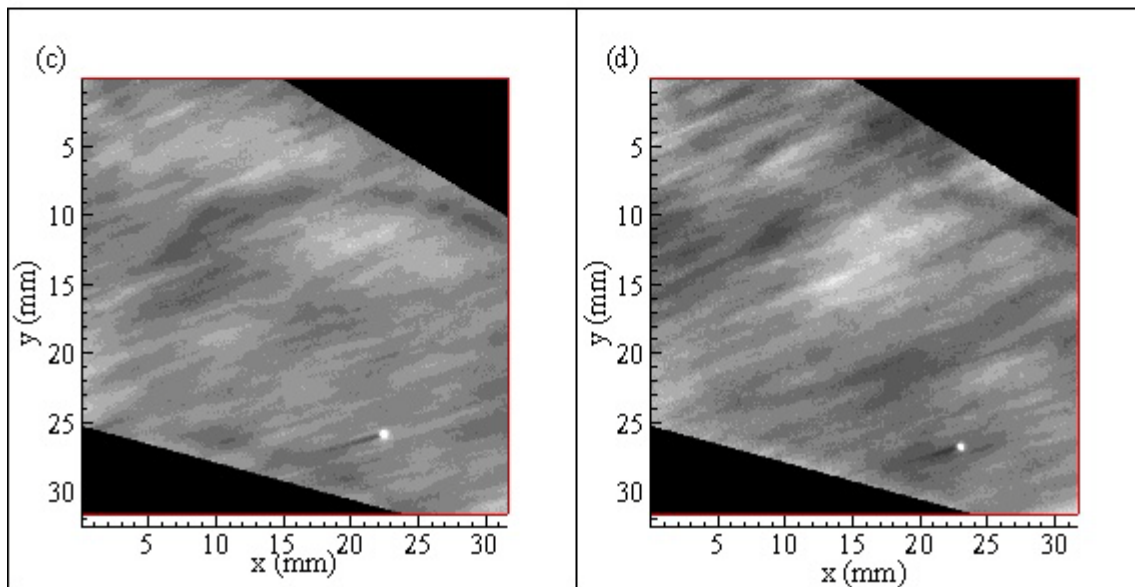
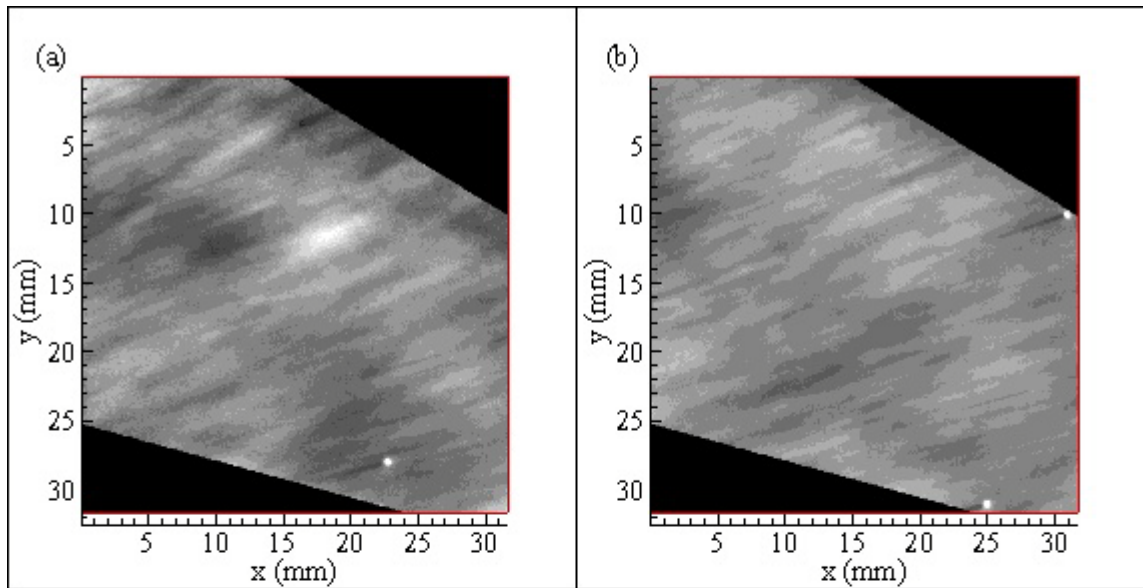


Figure C.55. Grayscale plots of normalized dimensionless mass transfer coefficient values at 58% relative humidity: (a) R58D\_49; 60 min.: 10 sec., (b) R58D\_54; 60 min.: 20 sec., (c) R58E\_27; 60 min.: 50 sec., (d) R58E\_35; 61 min.: 10 sec.



$k^*$ : 0 0.8 0.84 0.88 0.92 0.96 1 1.04 1.08 1.12 1.16 1.2

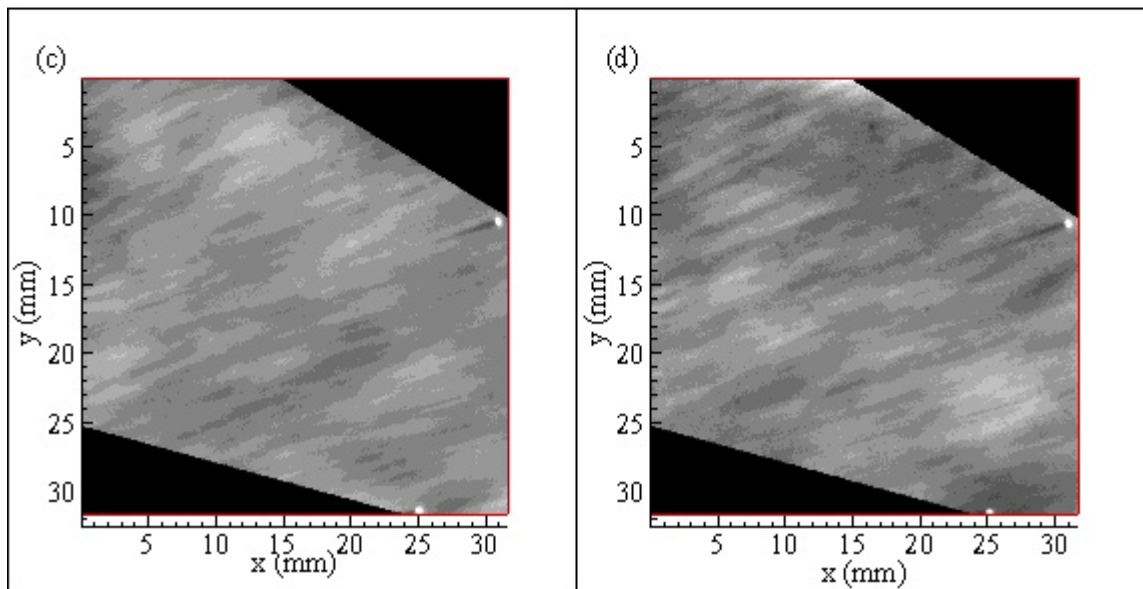
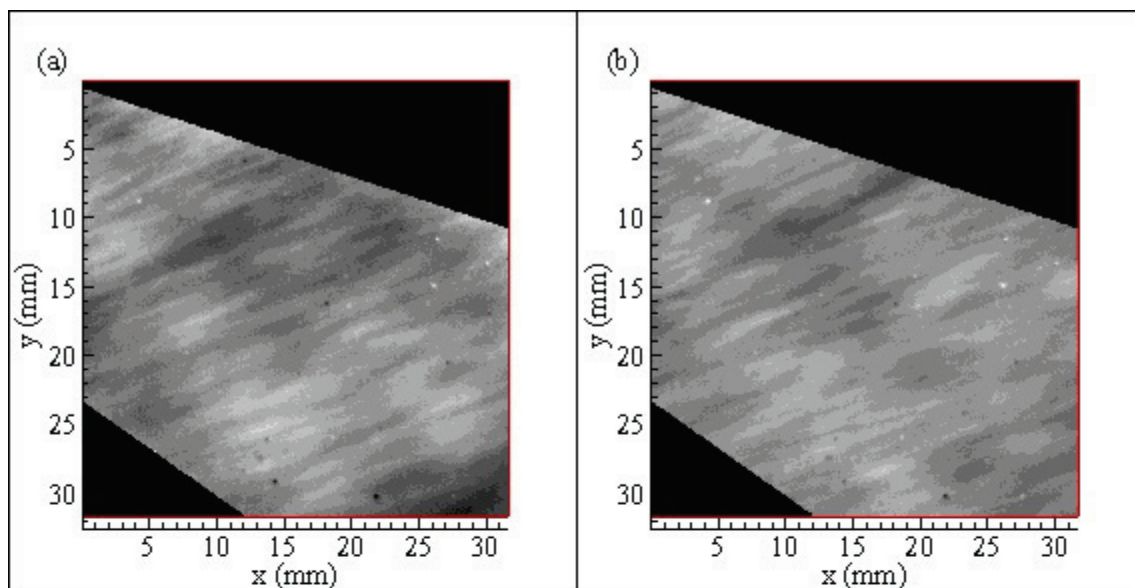


Figure C.56. Grayscale plots of normalized dimensionless mass transfer coefficient values at 58% relative humidity: (a) R58E\_51; 61 min.: 30 sec., (b) R58E\_3; 61 min.: 50 sec., (c) R58E\_7; 62 min.: 10 sec., (d) R58E\_9; 62 min.: 40 sec.



$k^*$ : 0 0.8 0.84 0.88 0.92 0.96 1 1.04 1.08 1.12 1.16 1.2

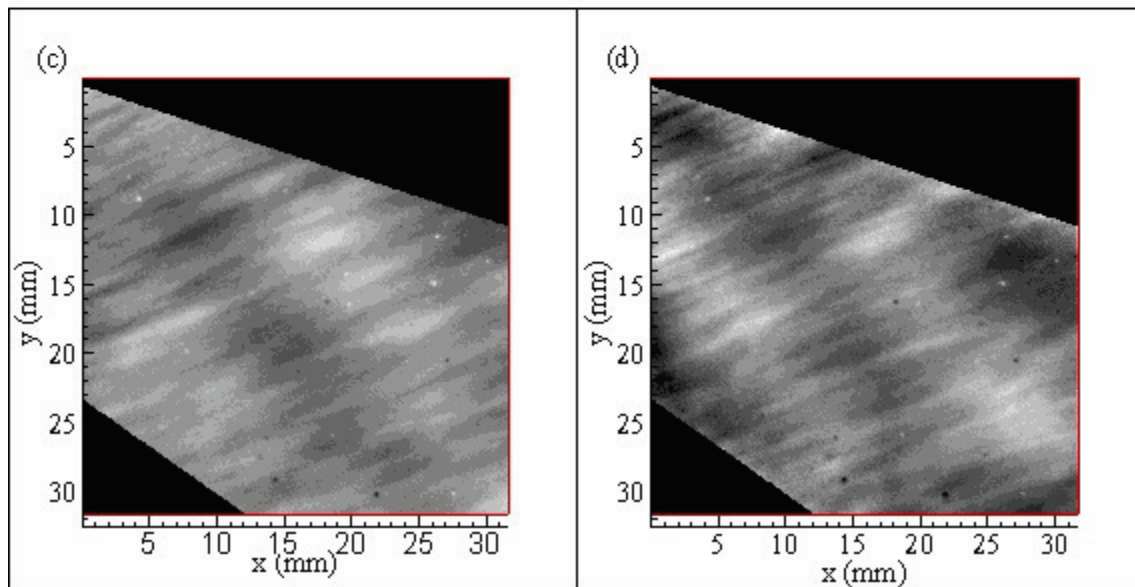
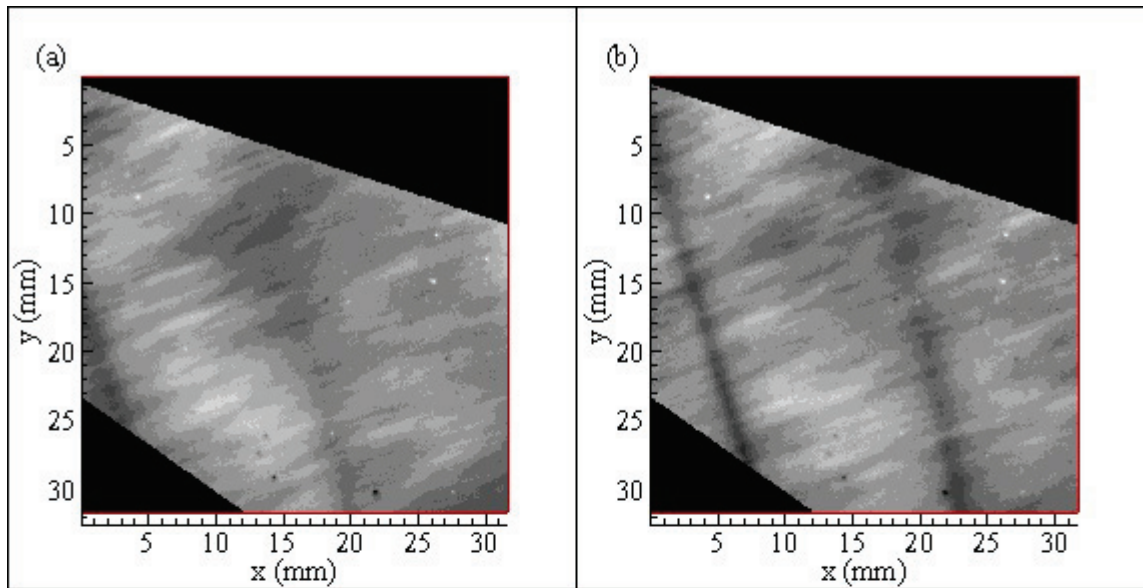


Figure C.57. Grayscale plots of normalized dimensionless mass transfer coefficient values at 63% relative humidity: (a) R63C\_5; 5 min.: 10 sec., (b) R63C\_10; 5 min.: 40 sec., (c) R63C\_12; 6 min.: 00 sec., (d) R63C\_18; 6 min.: 20 sec.



$k^*$ : 0 0.8 0.84 0.88 0.92 0.96 1 1.04 1.08 1.12 1.16 1.2

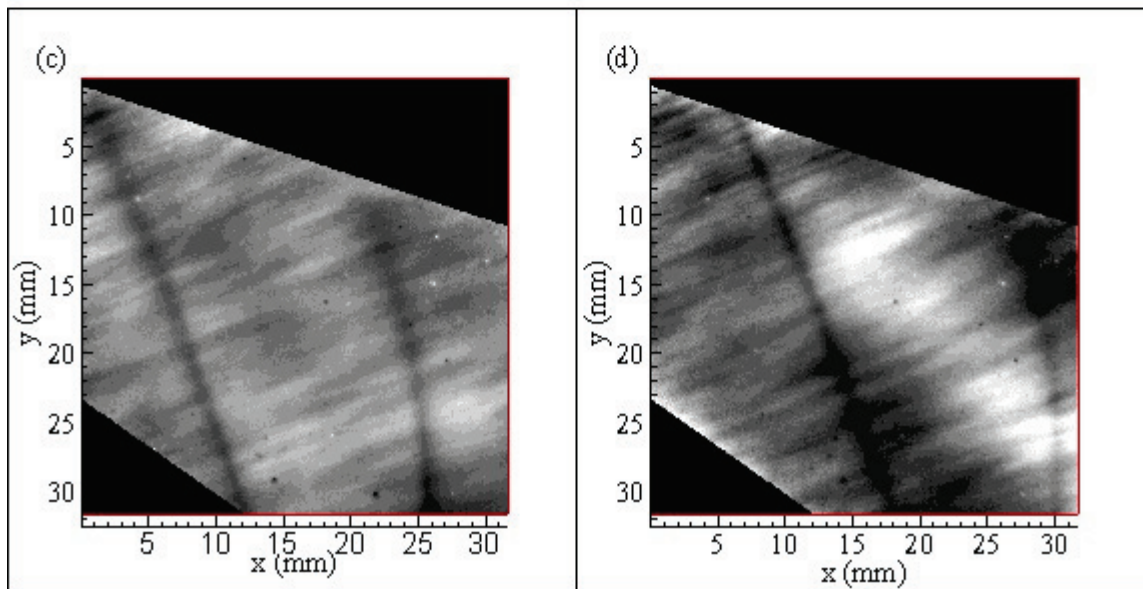
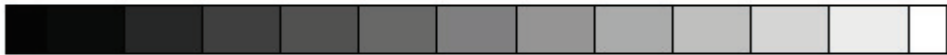
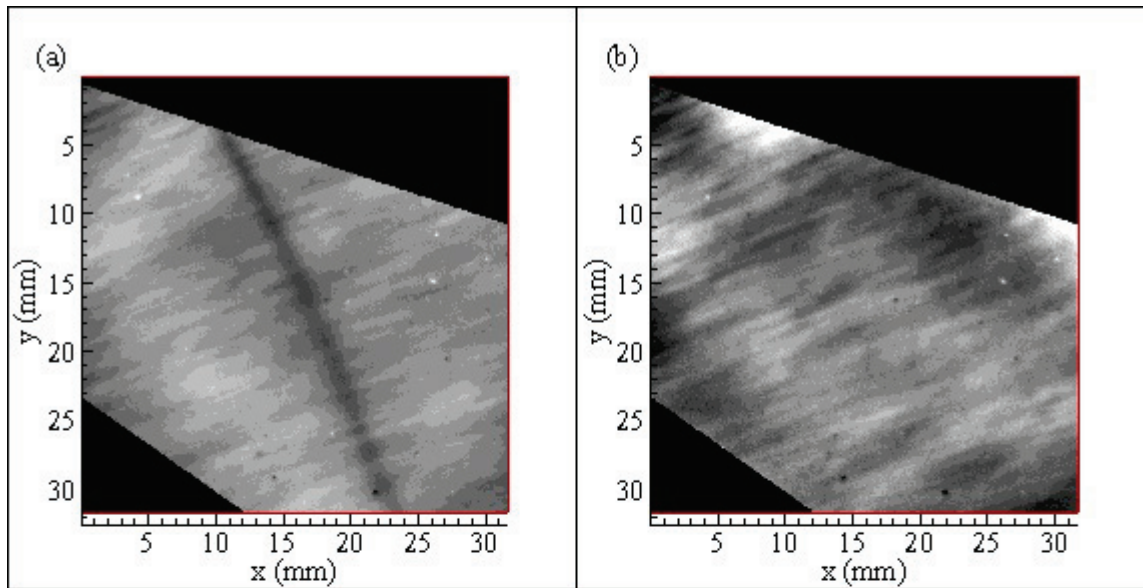


Figure C.58. Grayscale plots of normalized dimensionless mass transfer coefficient values at 63% relative humidity: (a) R63C\_24; 6 min.: 40 sec., (b) R63C\_32; 6 min.: 50 sec., (c) R63C\_34; 7 min.: 00 sec., (d) R63C\_13; 7 min.: 30 sec.



$k^*$ : 0 0.8 0.84 0.88 0.92 0.96 1 1.04 1.08 1.12 1.16 1.2

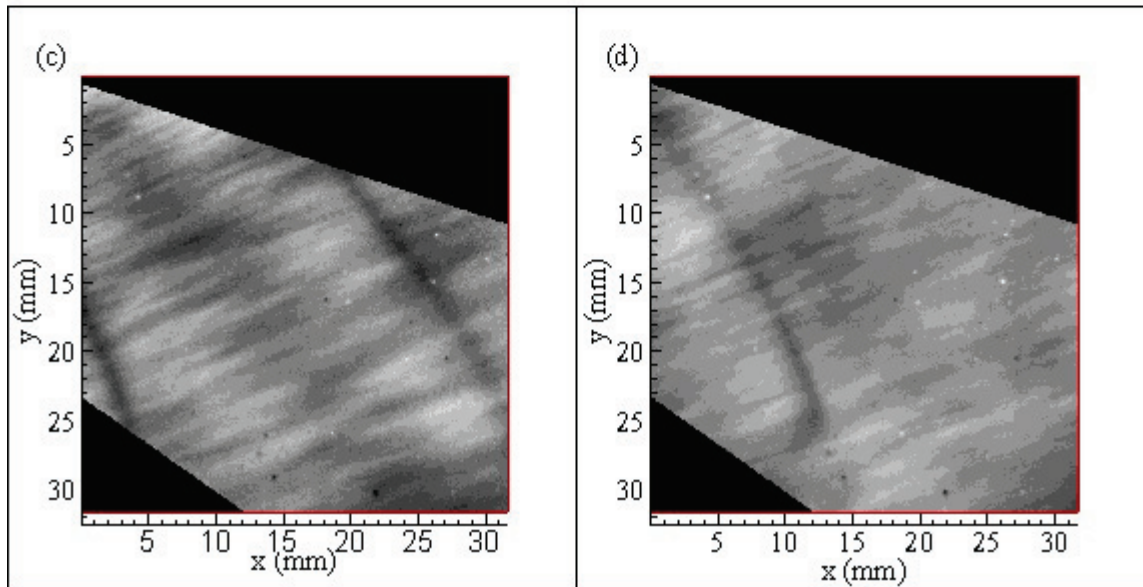
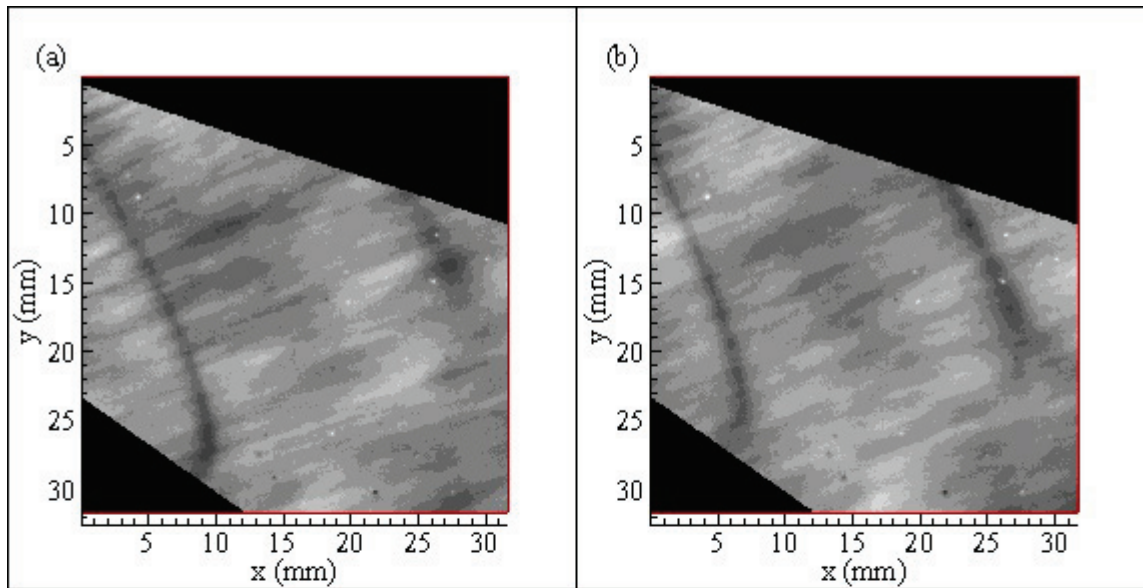


Figure C.59. Grayscale plots of normalized dimensionless mass transfer coefficient values at 63% relative humidity: (a) R63C\_54; 9 min.: 40 sec., (b) R63C\_63; 11 min.: 20 sec., (c) R63C\_77; 13 min.: 10 sec., (d) R63C\_88; 14 min.: 30 sec.



$k^*$ : 0 0.8 0.84 0.88 0.92 0.96 1 1.04 1.08 1.12 1.16 1.2

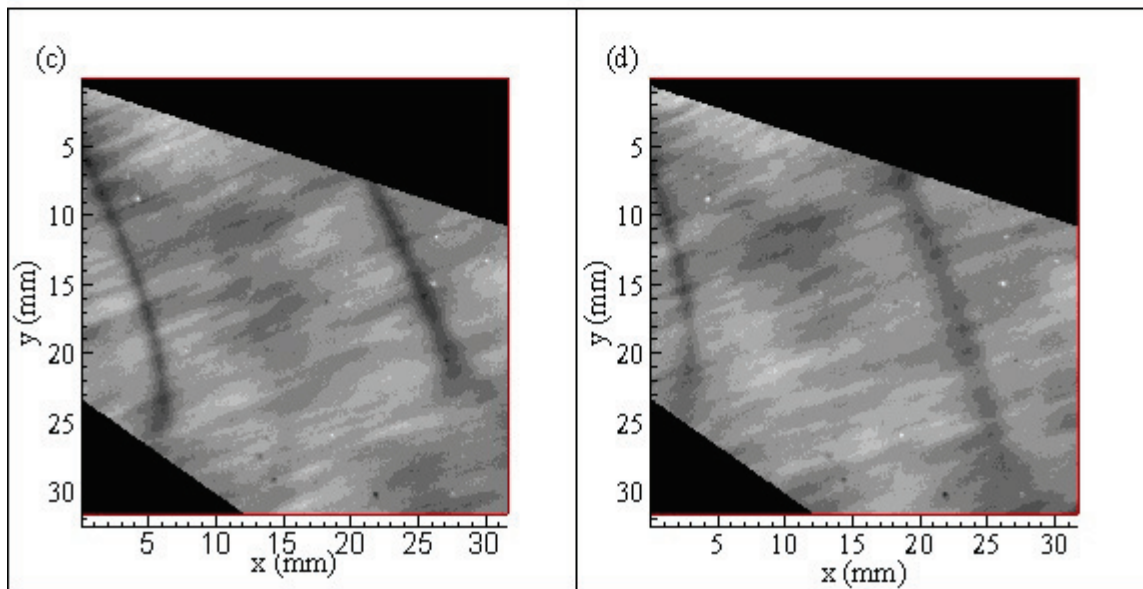
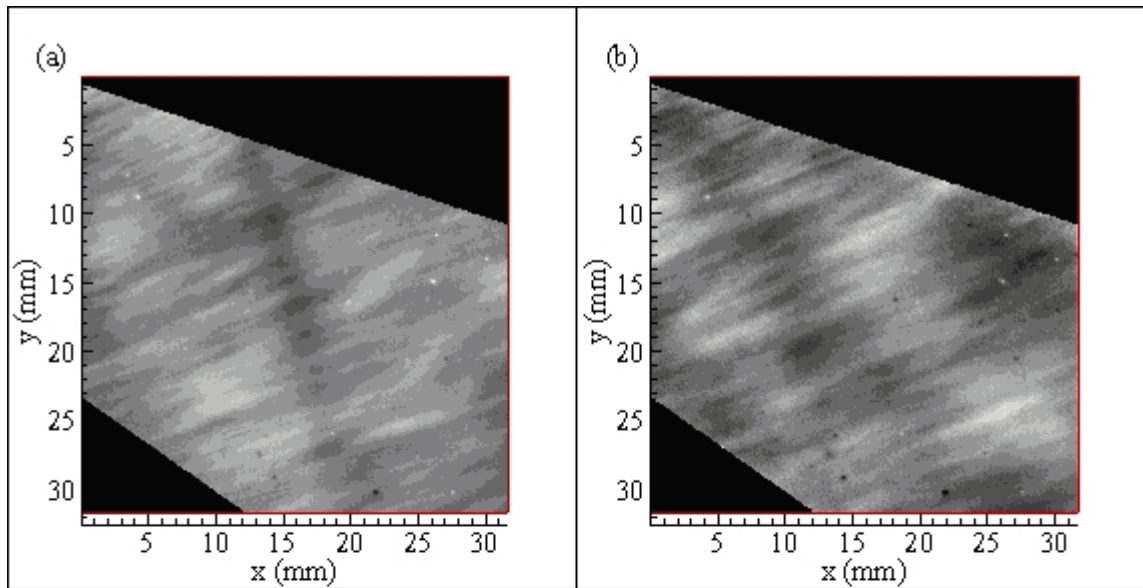


Figure C.60. Grayscale plots of normalized dimensionless mass transfer coefficient values at 63% relative humidity: (a) R63C\_91; 14 min.: 40 sec., (b) R63C\_94; 15 min.: 10 sec., (c) R63C\_95; 15 min.: 20 sec., (d) R63C\_97; 15 min.: 50 sec.



$k^*$ : 0 0.8 0.84 0.88 0.92 0.96 1 1.04 1.08 1.12 1.16 1.2

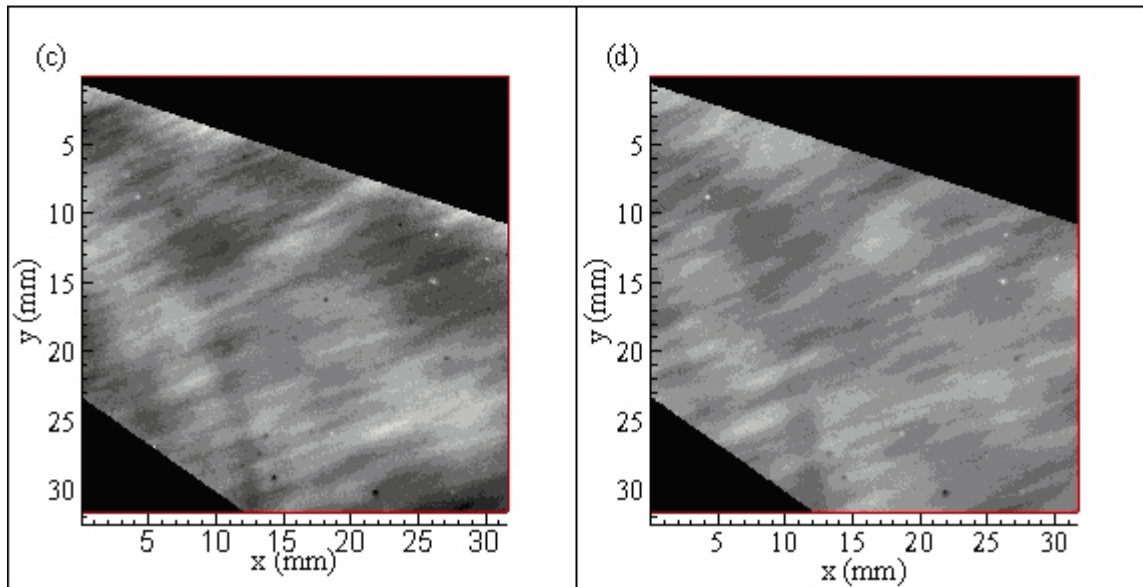
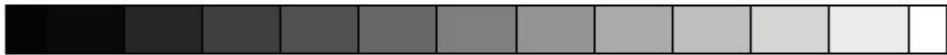
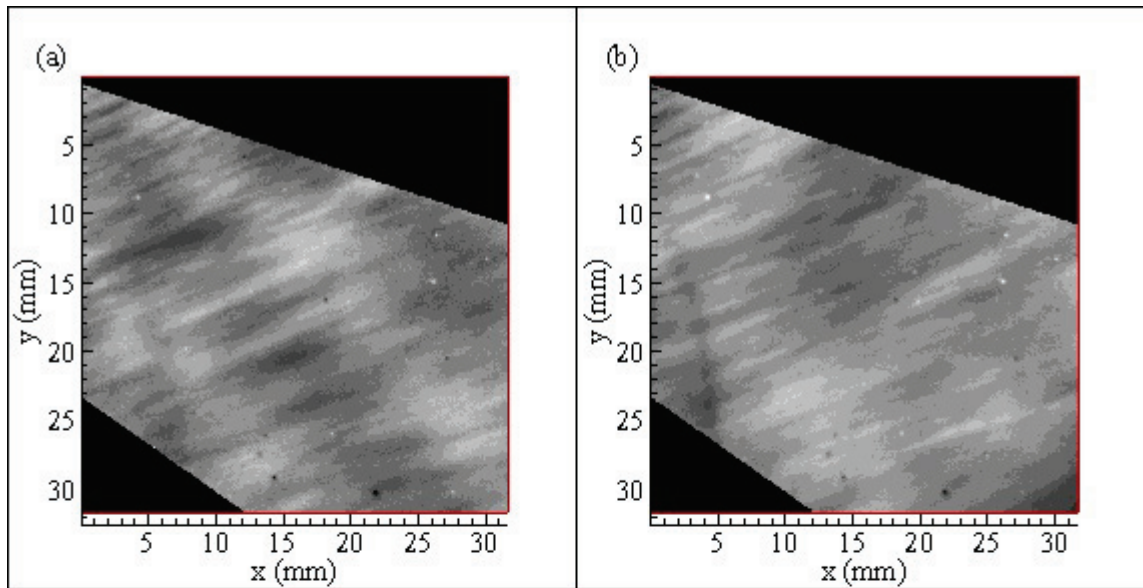


Figure C.61. Grayscale plots of normalized dimensionless mass transfer coefficient values at 63% relative humidity: (a) R63D\_3; 16 min.: 20 sec., (b) R63D\_8; 16 min.: 40 sec., (c) R63D\_16; 17 min.: 00 sec., (d) R63D\_17; 17 min.: 10 sec.



$k^*$ : 0 0.8 0.84 0.88 0.92 0.96 1 1.04 1.08 1.12 1.16 1.2

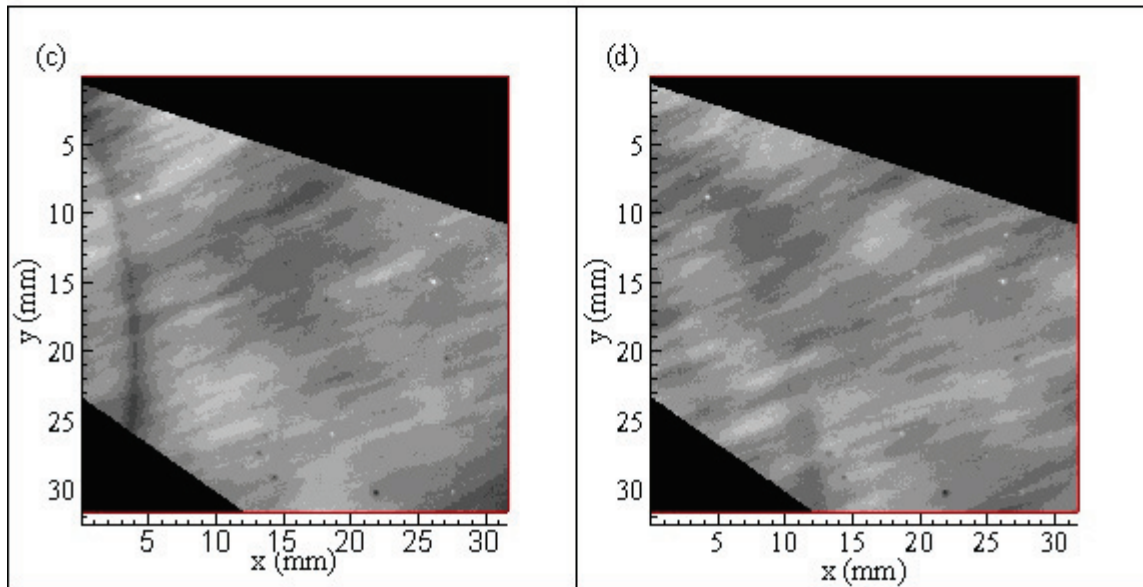
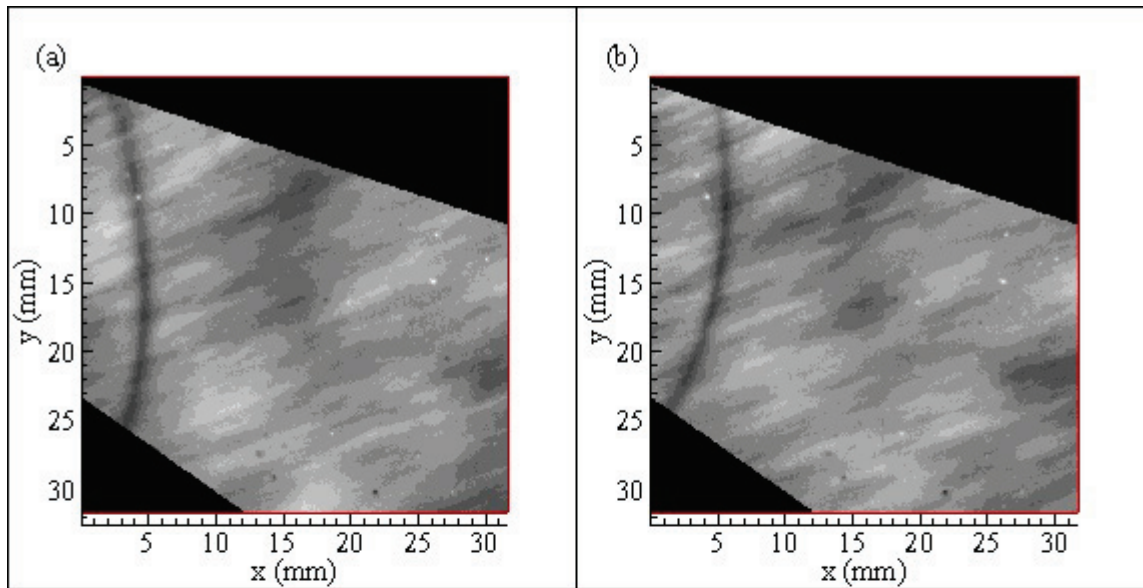


Figure C.62. Grayscale plots of normalized dimensionless mass transfer coefficient values at 63% relative humidity: (a) R63D\_18; 17 min.: 20 sec., (b) R63D\_26; 17 min.: 50 sec., (c) R63D\_28; 18 min.: 10 sec., (d) R63D\_30; 18 min.: 40 sec.



$k^*$ : 0 0.8 0.84 0.88 0.92 0.96 1 1.04 1.08 1.12 1.16 1.2

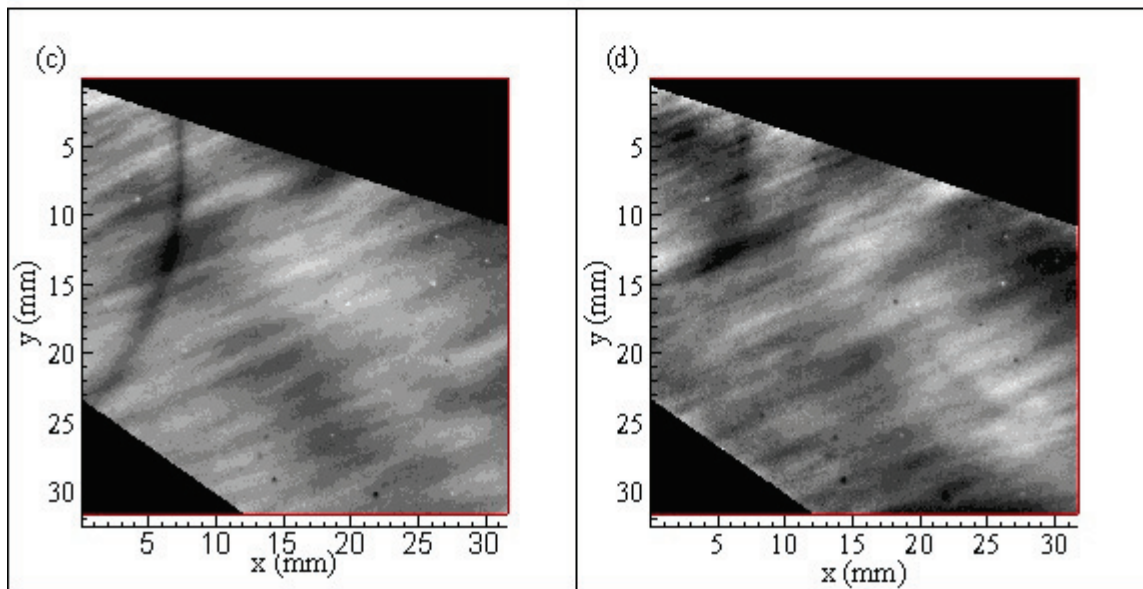
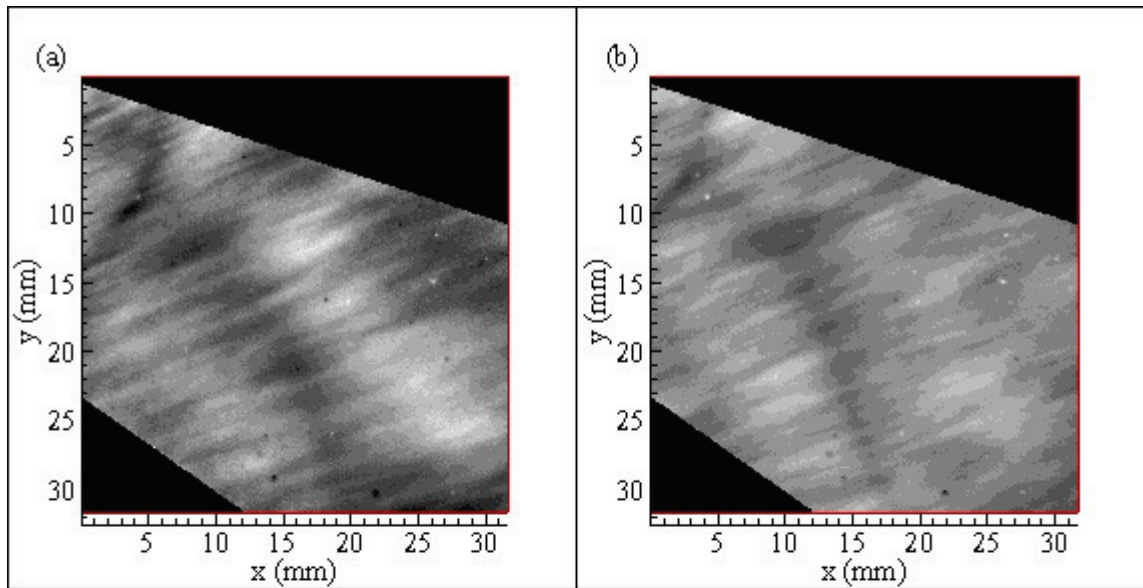


Figure C.63. Grayscale plots of normalized dimensionless mass transfer coefficient values at 63% relative humidity: (a) R63D\_34; 19 min.: 40 sec., (b) R63D\_35; 19 min.: 50 sec., (c) R63D\_36; 20 min.: 00 sec., (d) R63D\_40; 20 min.: 50 sec.



$k^*$ : 0 0.8 0.84 0.88 0.92 0.96 1 1.04 1.08 1.12 1.16 1.2

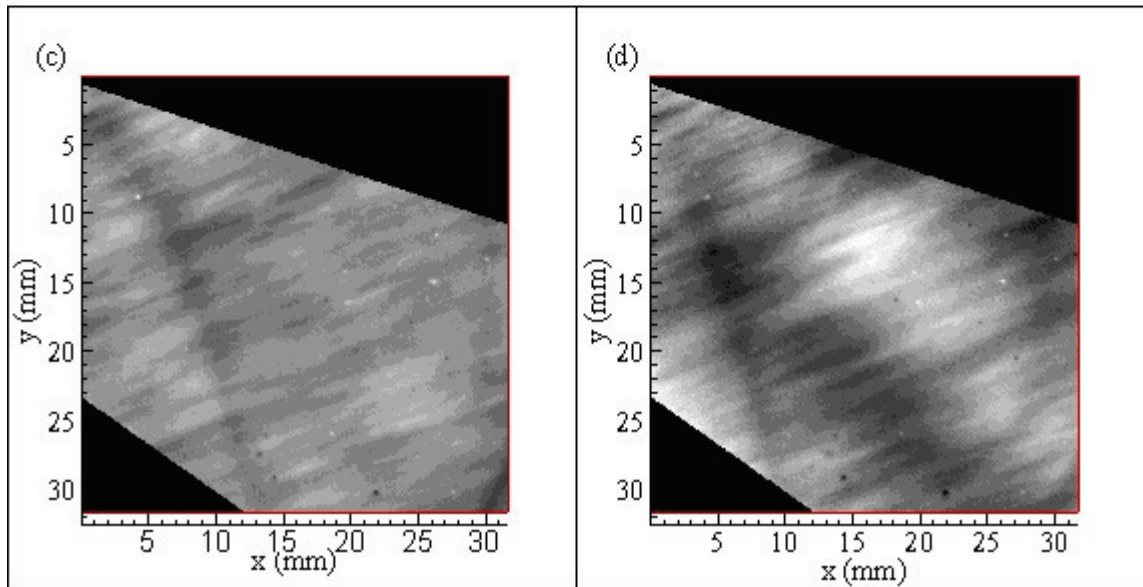
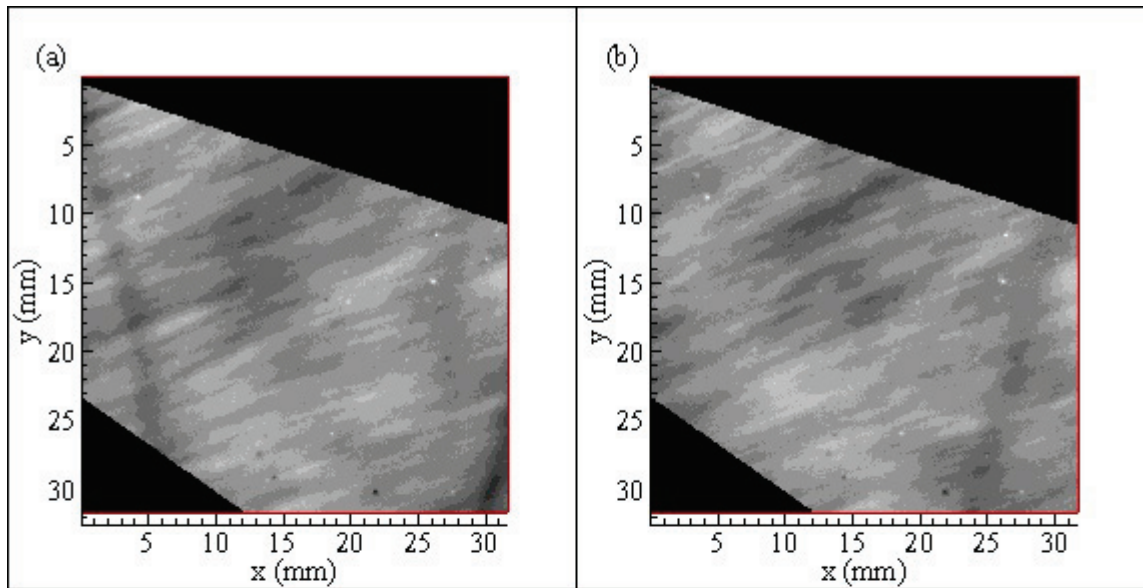


Figure C.64. Grayscale plots of normalized dimensionless mass transfer coefficient values at 63% relative humidity: (a) R63D\_53; 22 min.: 10 sec., (b) R63D\_57; 22 min.: 50 sec., (c) R63D\_59; 23 min.: 10 sec., (d) R63D\_61; 23 min.: 30 sec.



$k^*$ : 0 0.8 0.84 0.88 0.92 0.96 1 1.04 1.08 1.12 1.16 1.2

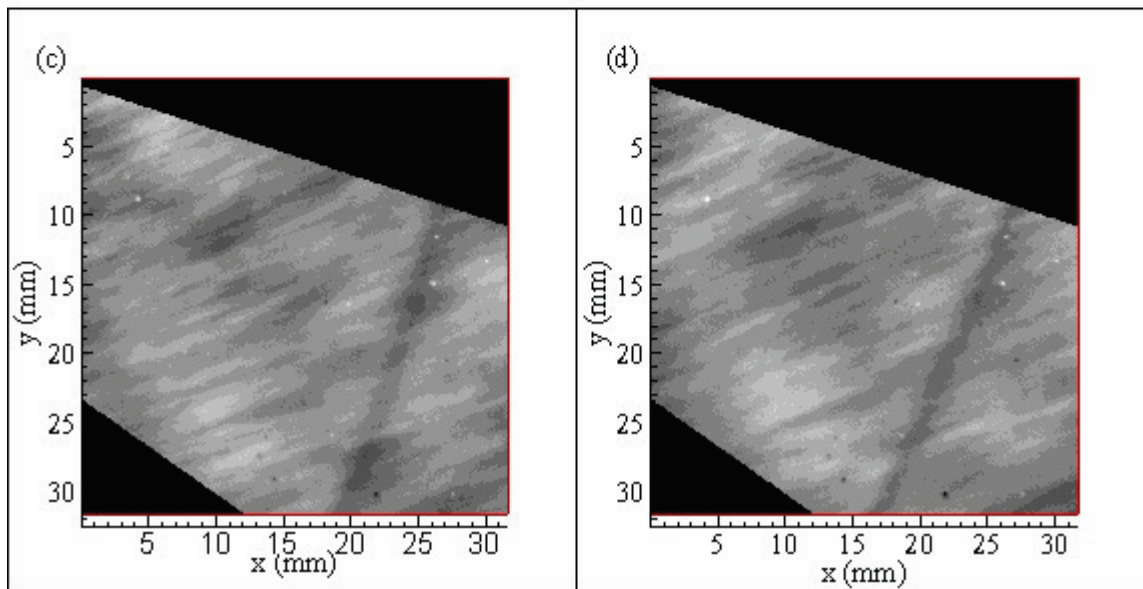
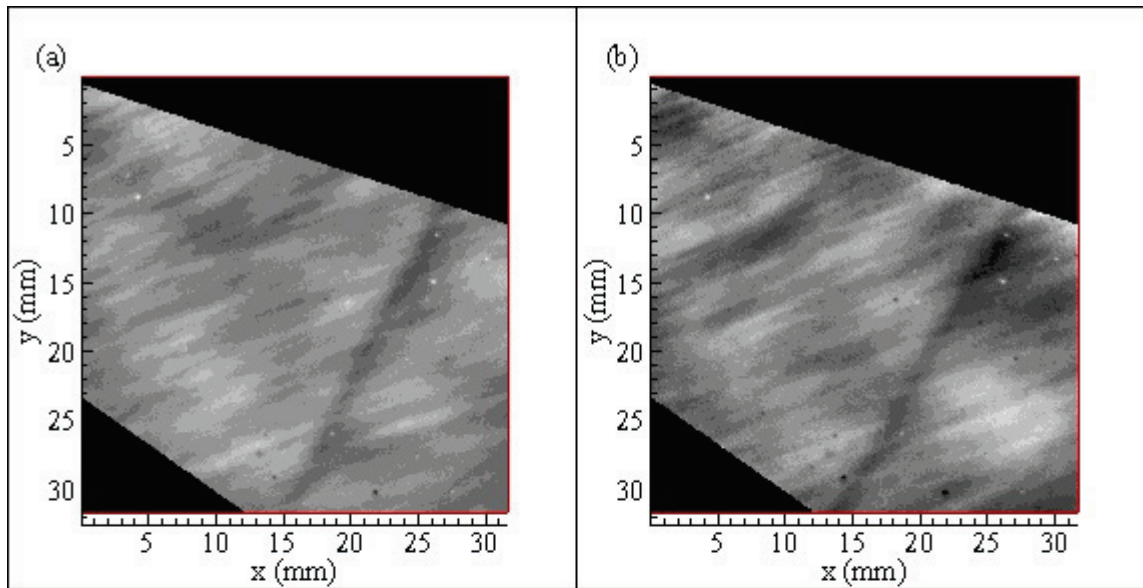


Figure C.65. Grayscale plots of normalized dimensionless mass transfer coefficient values at 63% relative humidity: (a) R63D\_63; 23 min.: 50 sec., (b) R63D\_66; 24 min.: 20 sec., (c) R63D\_70; 25 min.: 00 sec., (d) R63D\_61; 25 min.: 20 sec.



$k^*$ : 0 0.8 0.84 0.88 0.92 0.96 1 1.04 1.08 1.12 1.16 1.2

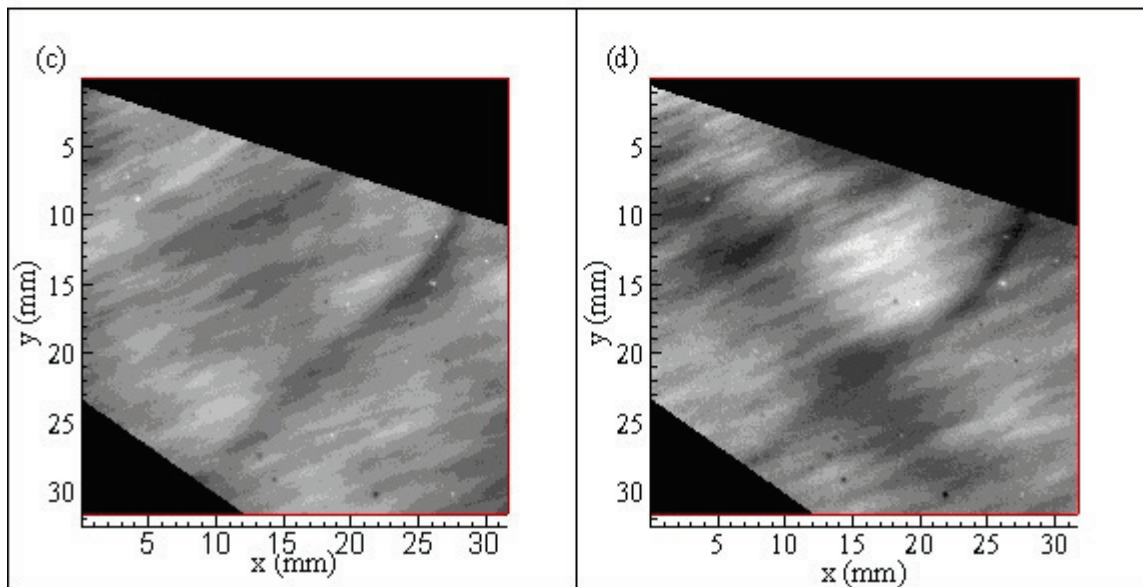
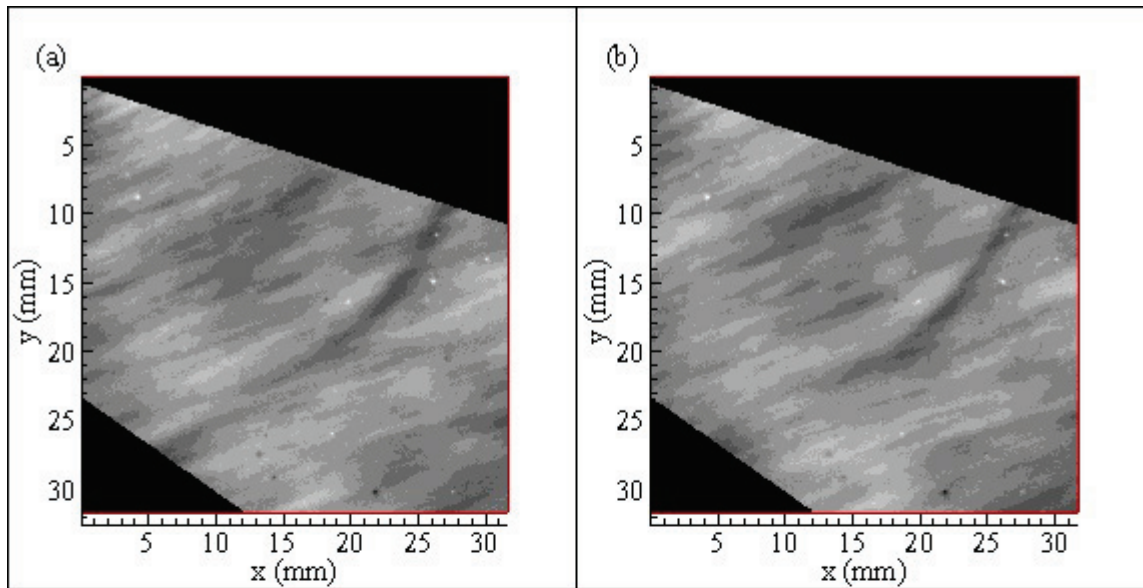


Figure C.66. Grayscale plots of normalized dimensionless mass transfer coefficient values at 63% relative humidity: (a) R63D\_79; 26 min.: 50 sec., (b) R63D\_80; 27 min.: 00 sec., (c) R63D\_85; 27 min.: 50 sec., (d) R63D\_87; 28 min.: 10 sec.



$k^*$ : 0 0.8 0.84 0.88 0.92 0.96 1 1.04 1.08 1.12 1.16 1.2

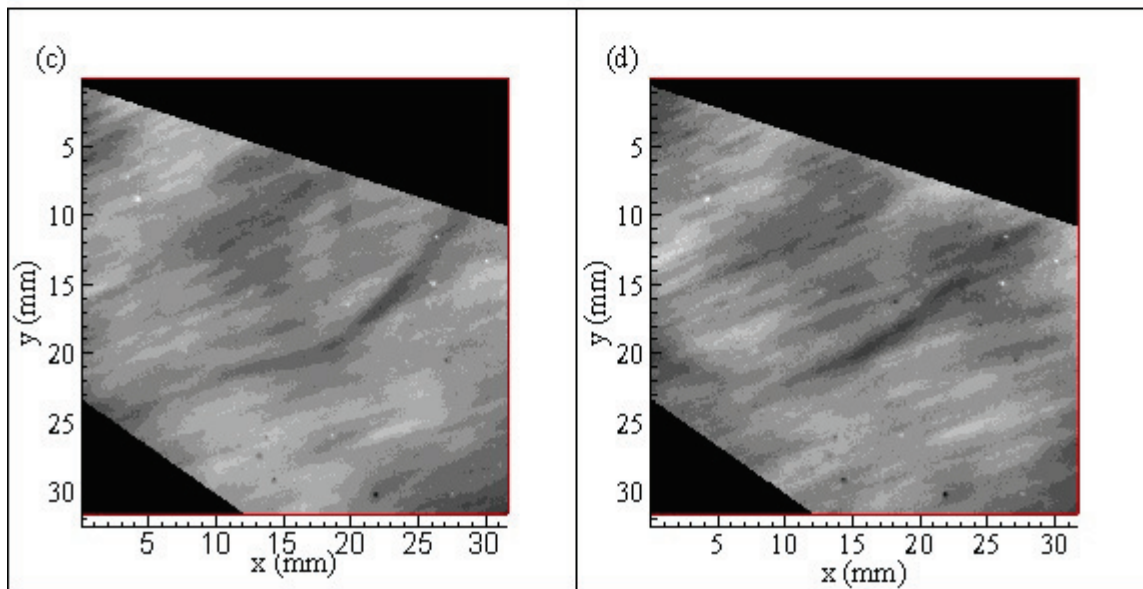
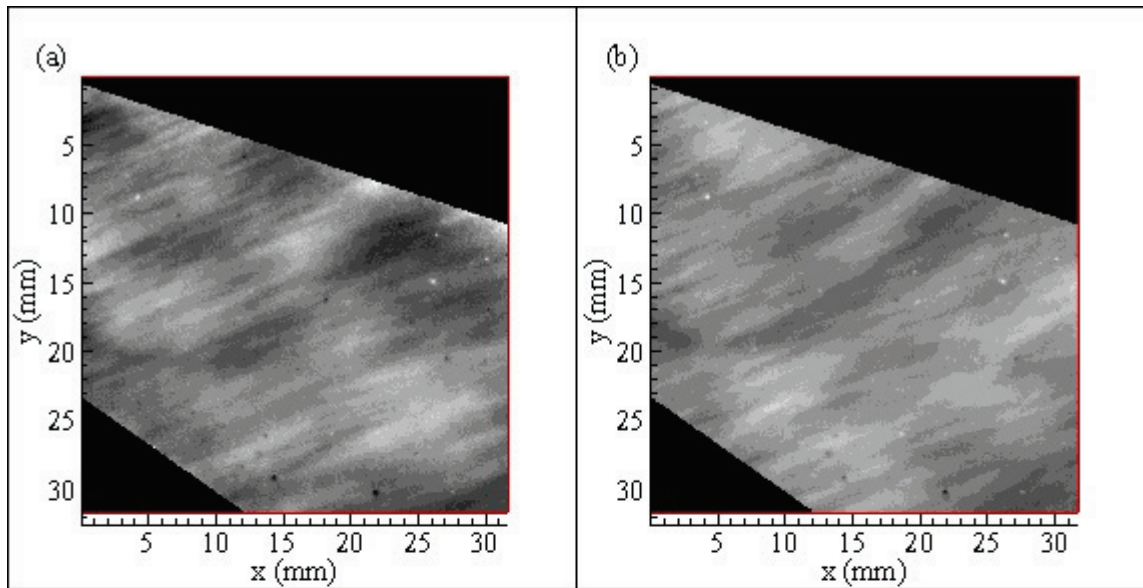


Figure C.67. Grayscale plots of normalized dimensionless mass transfer coefficient values at 63% relative humidity: (a) R63D\_94; 29 min.: 00 sec., (b) R63D\_96; 29 min.: 20 sec., (c) R63E\_1; 29 min.: 50 sec., (d) R63E\_5; 30 min.: 10 sec.



$k^*$ : 0 0.8 0.84 0.88 0.92 0.96 1 1.04 1.08 1.12 1.16 1.2

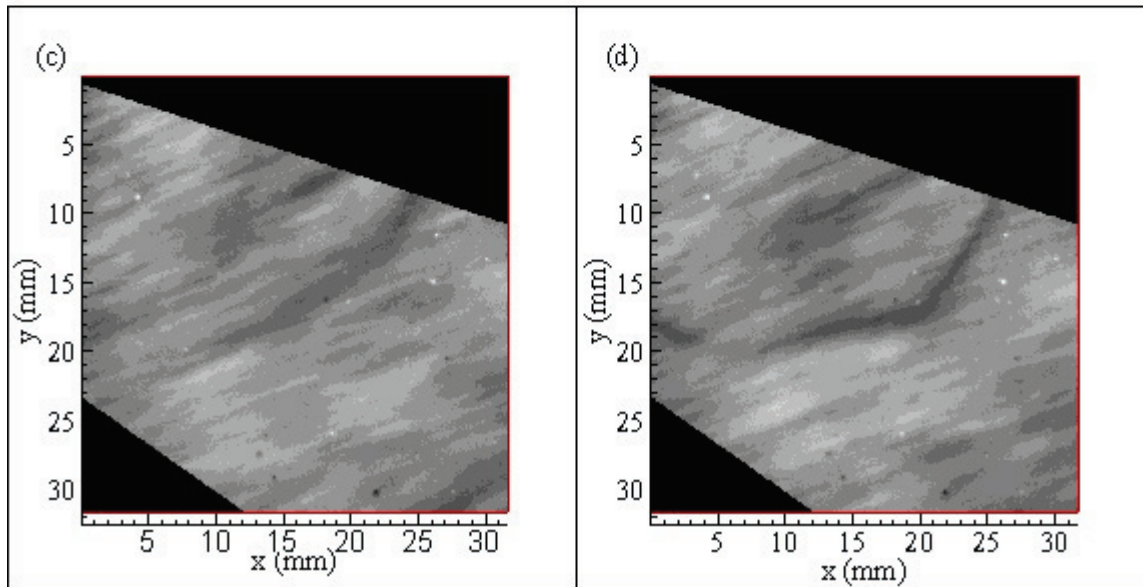
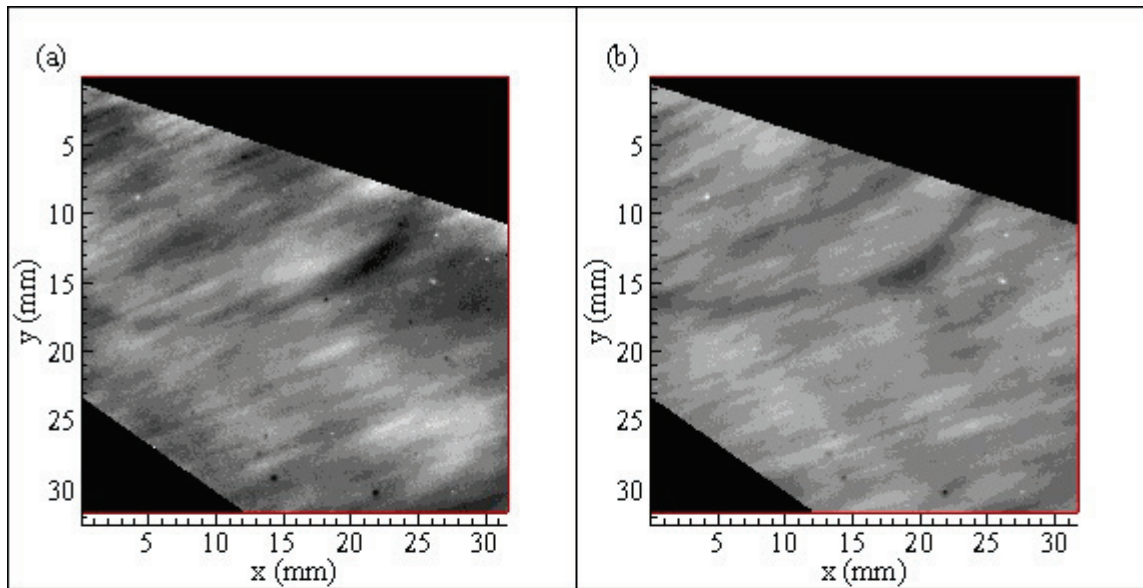


Figure C.68. Grayscale plots of normalized dimensionless mass transfer coefficient values at 63% relative humidity: (a) R63E\_9; 30 min.: 50 sec., (b) R63E\_17; 32 min.: 20 sec., (c) R63E\_18; 32 min.: 30 sec., (d) R63E\_23; 33 min.: 10 sec.



$k^*$ : 0 0.8 0.84 0.88 0.92 0.96 1 1.04 1.08 1.12 1.16 1.2

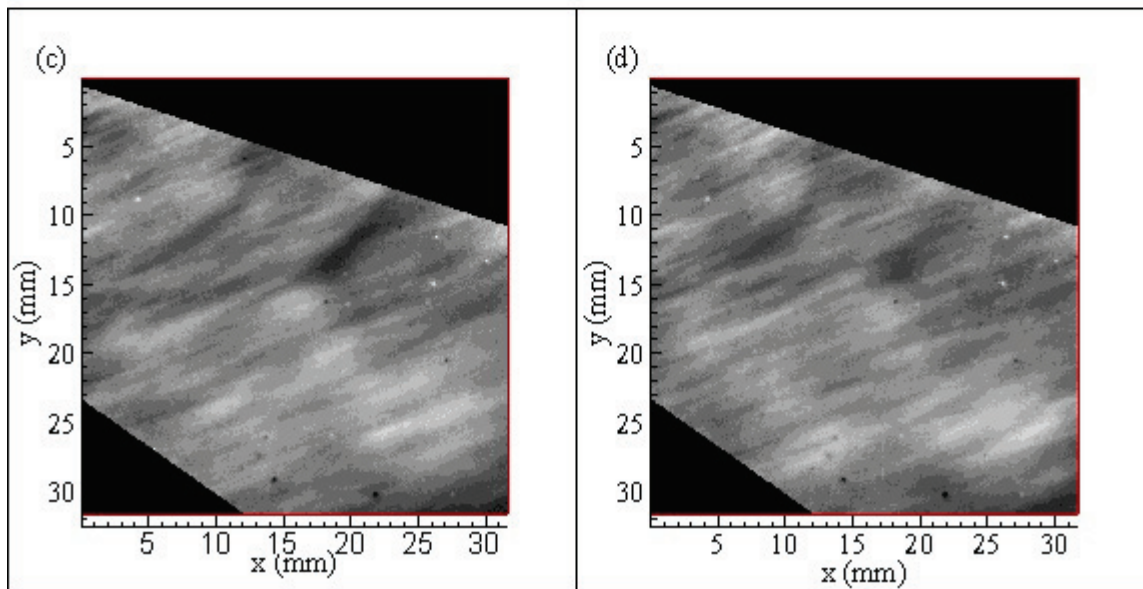
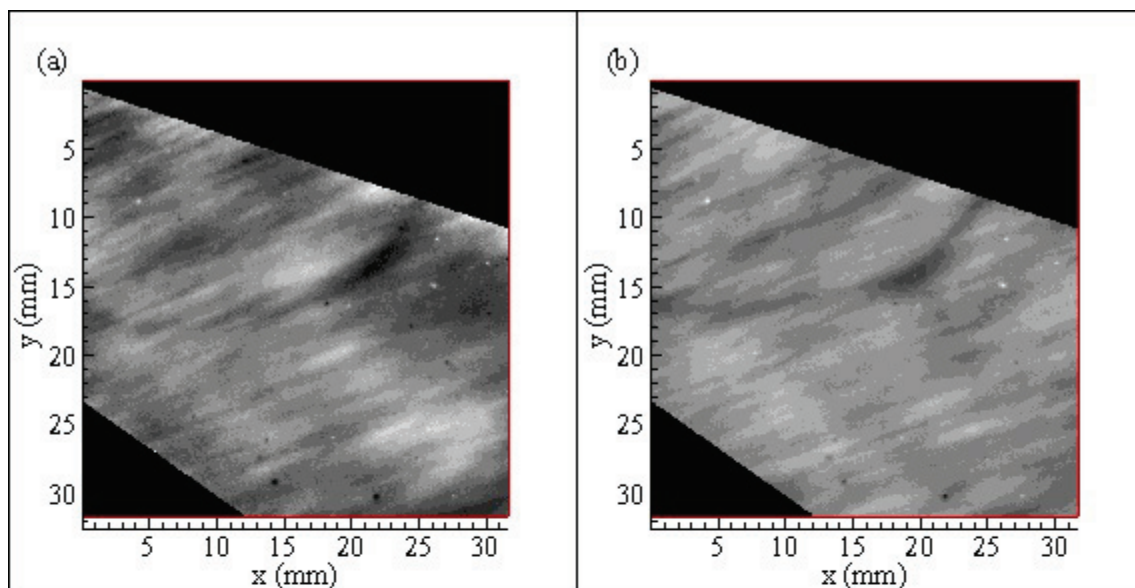


Figure C.69. Grayscale plots of normalized dimensionless mass transfer coefficient values at 63% relative humidity: (a) R63E\_24 32 min.: 40 sec., (b) R63E\_17; 32 min.: 20 sec., (c) R63E\_18; 32 min.: 30 sec., (d) R63E\_23; 33 min.: 10 sec.



$k^*$ : 0 0.8 0.84 0.88 0.92 0.96 1 1.04 1.08 1.12 1.16 1.2

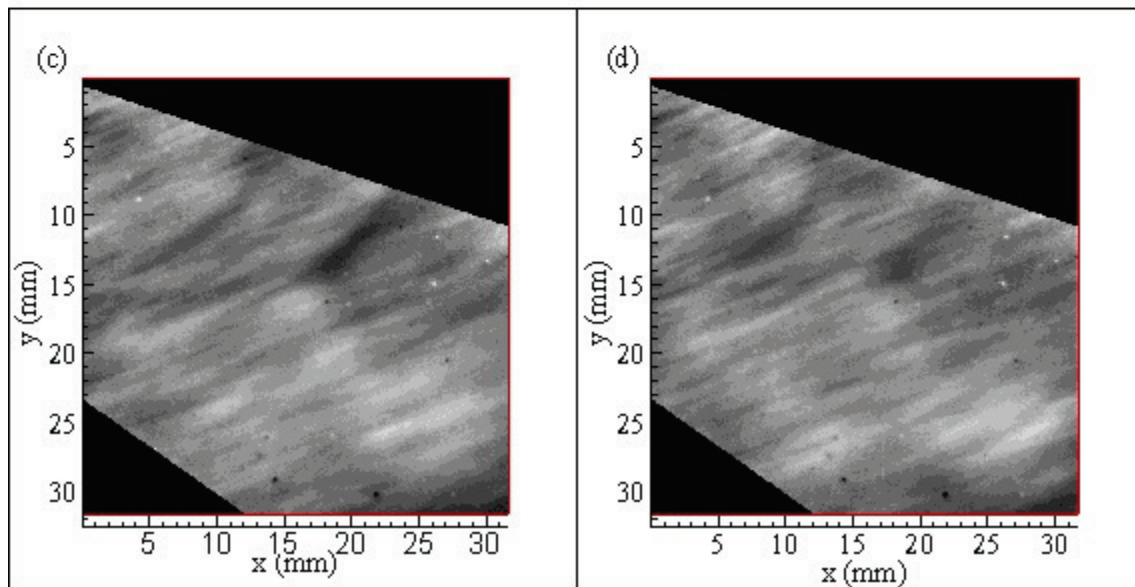


Figure C.70. Grayscale plots of normalized dimensionless mass transfer coefficient values at 63% relative humidity: (a) R63E\_24; 32 min.: 40 sec., (b) R63E\_26; 33 min.: 00 sec., (c) R63E\_29; 33 min.: 40 sec., (d) R63E\_33; 34 min.: 20 sec.

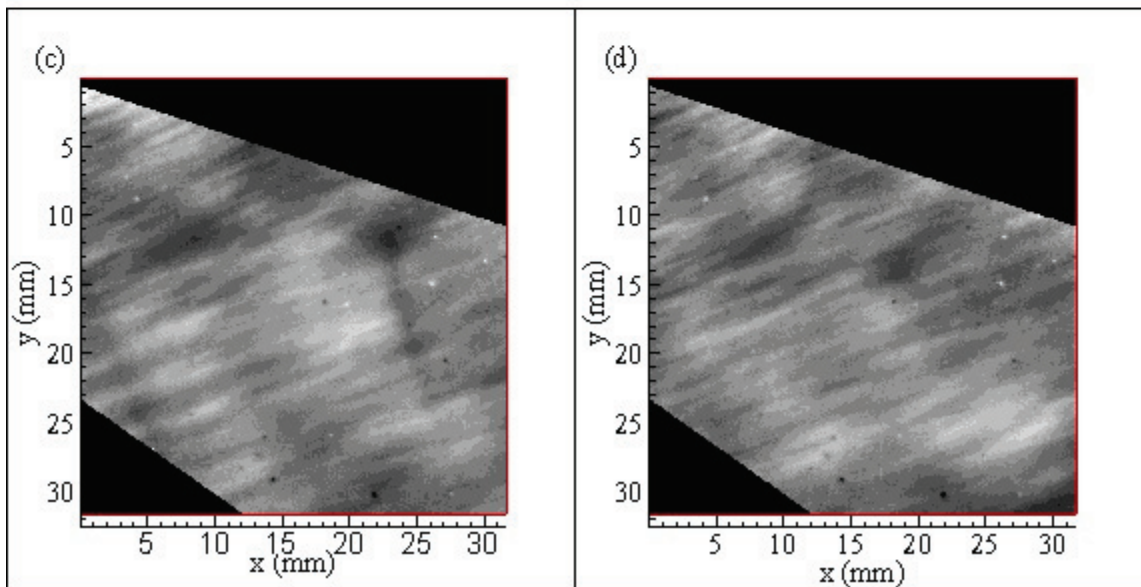
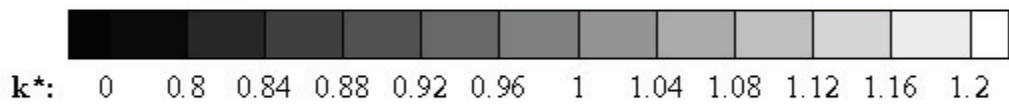
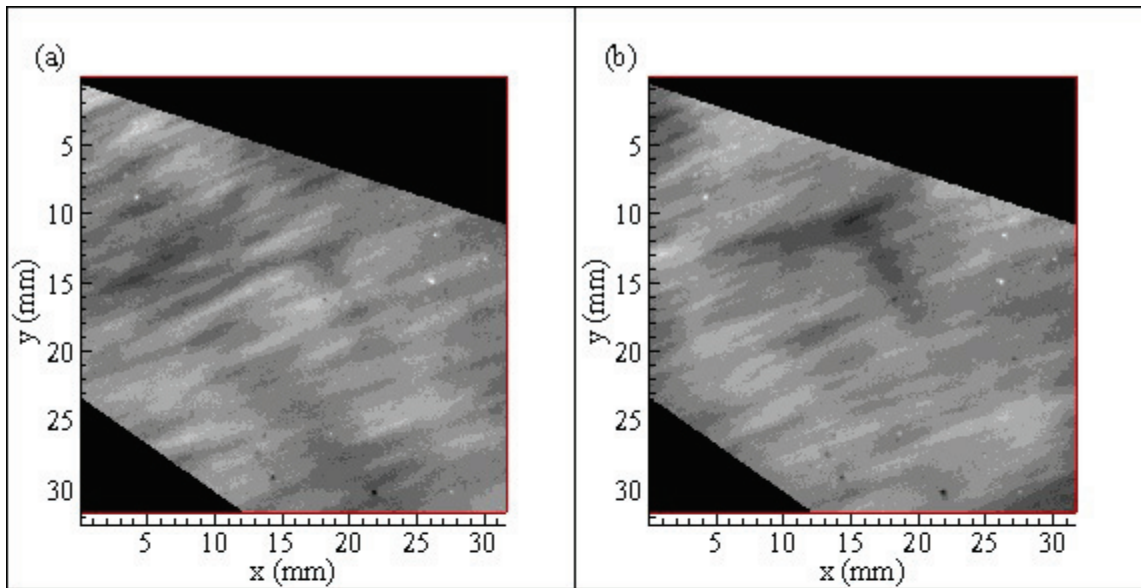


Figure C.71. Grayscale plots of normalized dimensionless mass transfer coefficient values at 63% relative humidity: (a) R63E\_34; 34 min.: 30 sec., (b) R63E\_38; 35 min.: 20 sec., (c) R63E\_40; 36 min.: 00 sec., (d) R63E\_69; 37 min.: 30 sec.

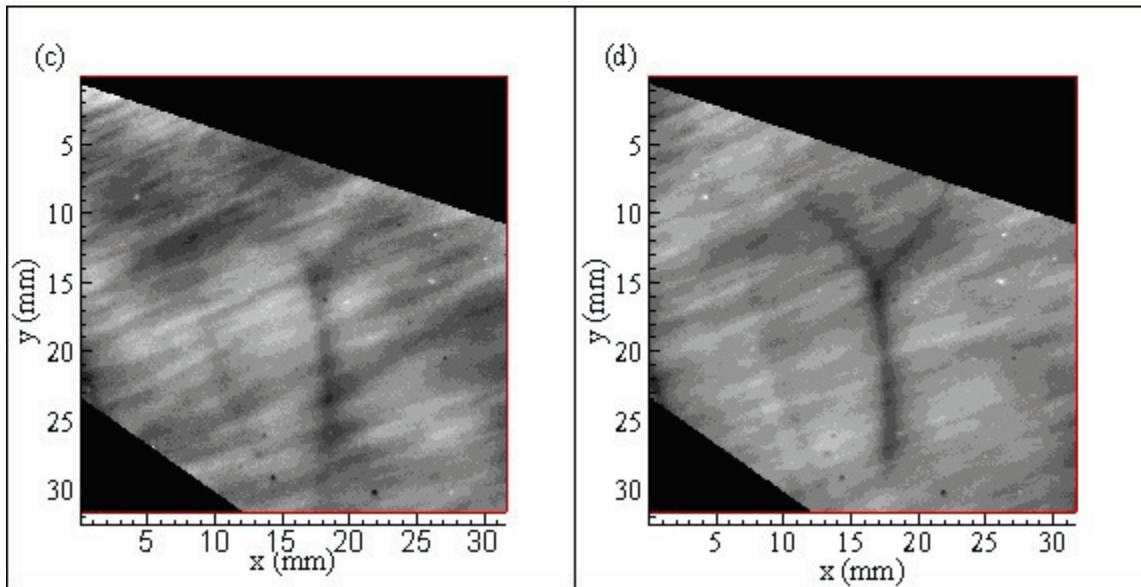
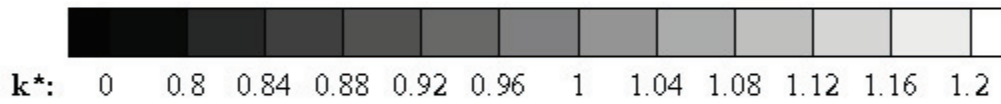
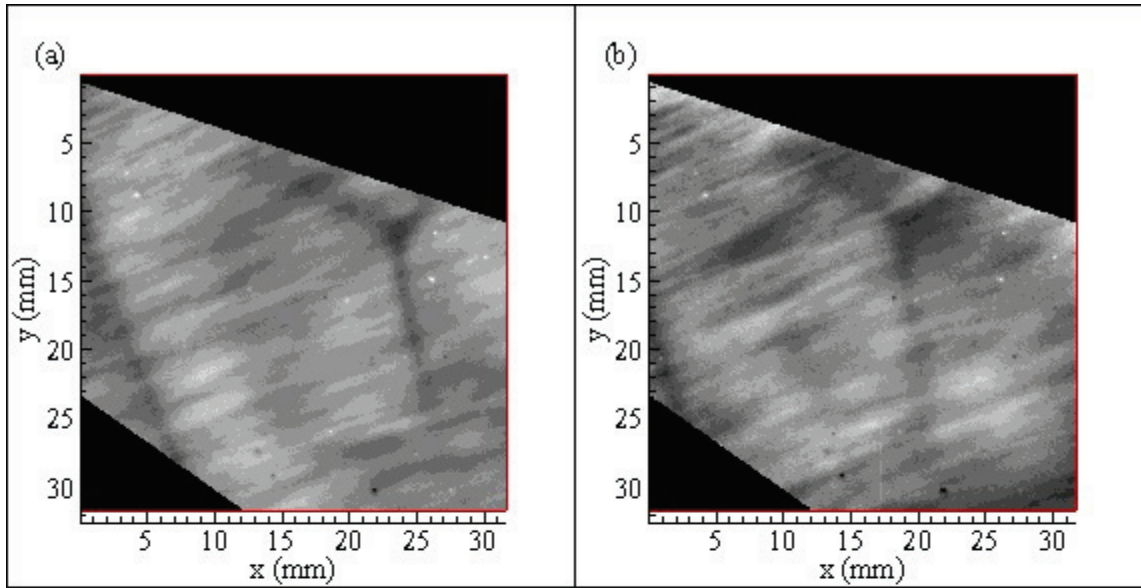


Figure C.72. Grayscale plots of normalized dimensionless mass transfer coefficient values at 63% relative humidity: (a) R63E\_72; 38 min.: 20 sec., (b) R63E\_80; 39 min.: 10 sec., (c) R63E\_85; 40 min.: 00 sec., (d) R63E\_92; 40 min.: 30 sec.

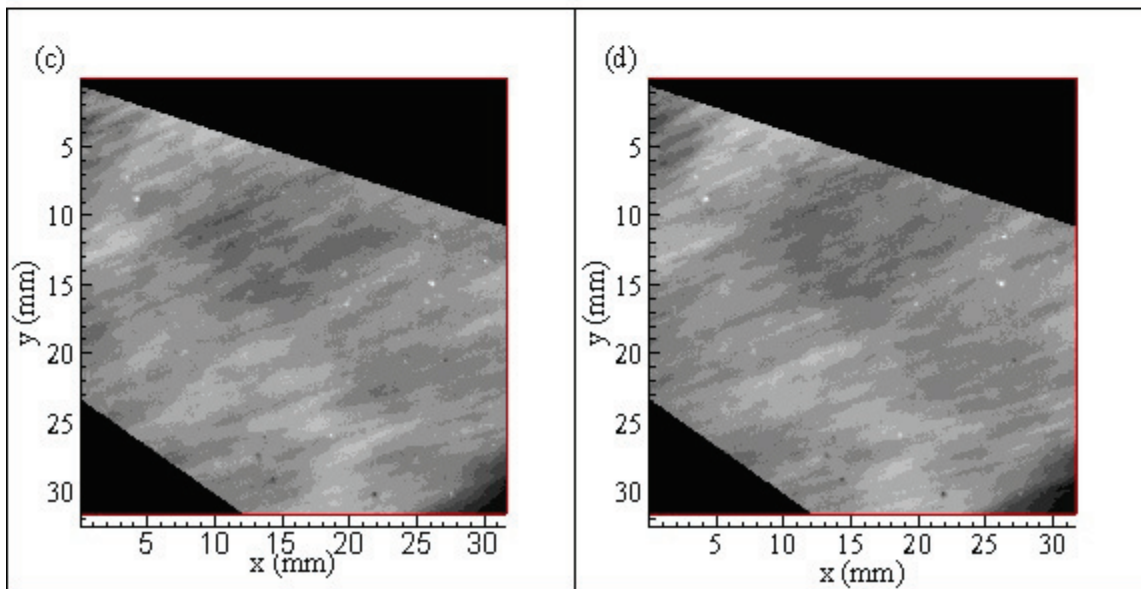
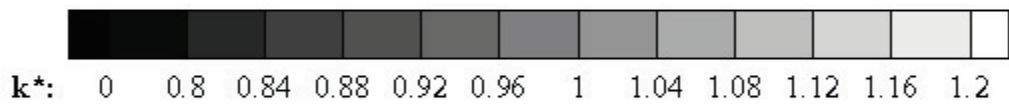
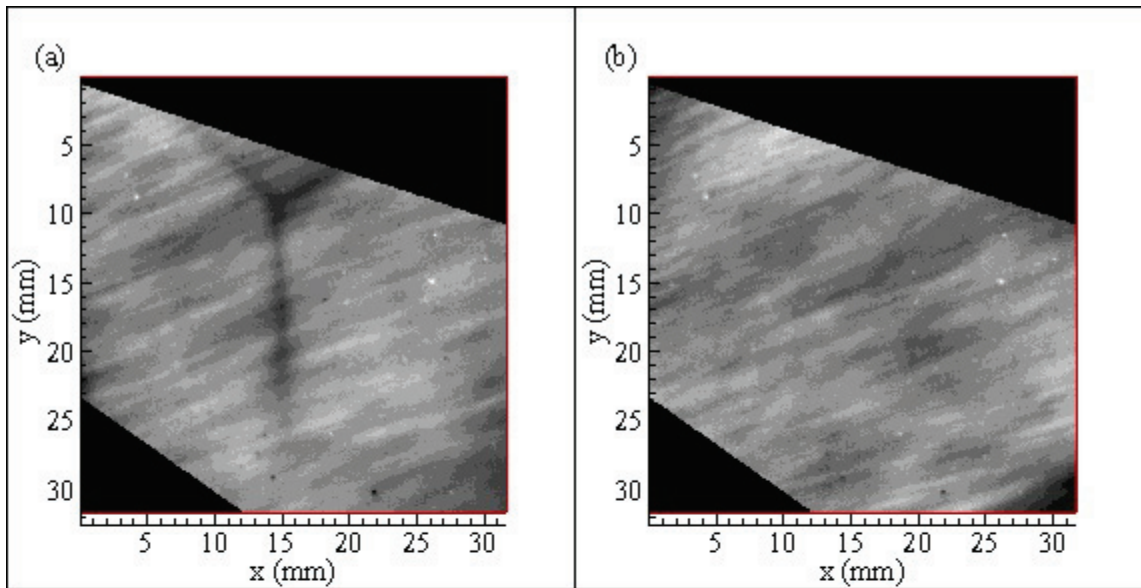


Figure C.73. Grayscale plots of normalized dimensionless mass transfer coefficient values at 63% relative humidity: (a) R63E\_98; 41 min.: 10 sec., (b) R63F\_1; 43 min.: 00 sec., (c) R63F\_3; 43 min.: 30 sec., (d) R63F\_4; 43 min.: 40 sec.

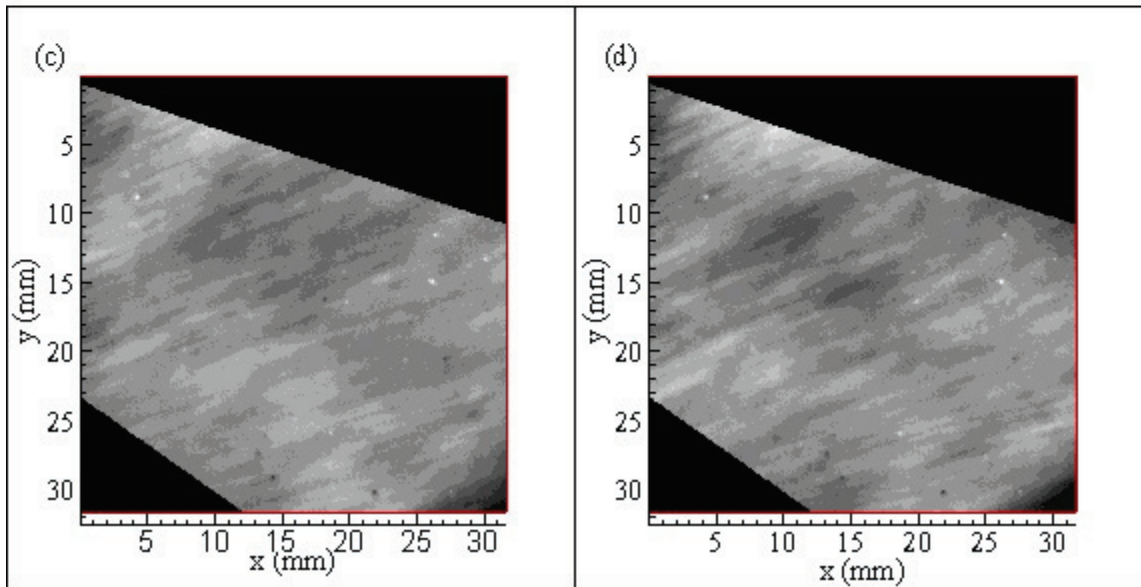
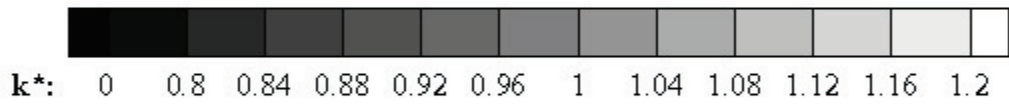
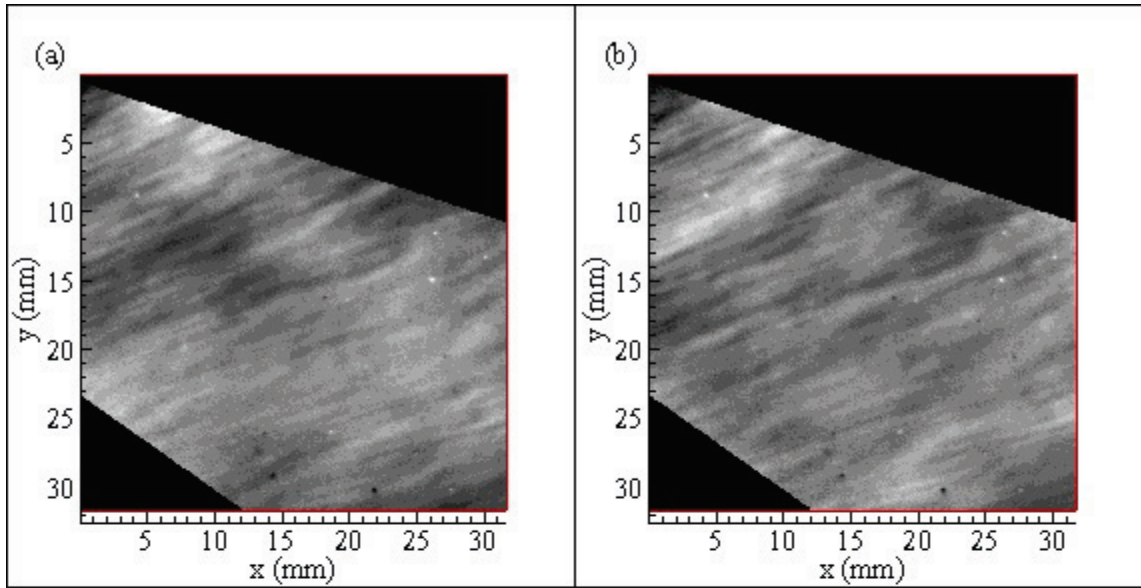


Figure C.74. Grayscale plots of normalized dimensionless mass transfer coefficient values at 63% relative humidity: (a) R63F\_8; 44 min.: 20 sec., (b) R63F\_9; 44 min.: 40 sec., (c) R63F\_18; 45 min.: 00 sec., (d) R63F\_13; 45 min.: 20 sec.

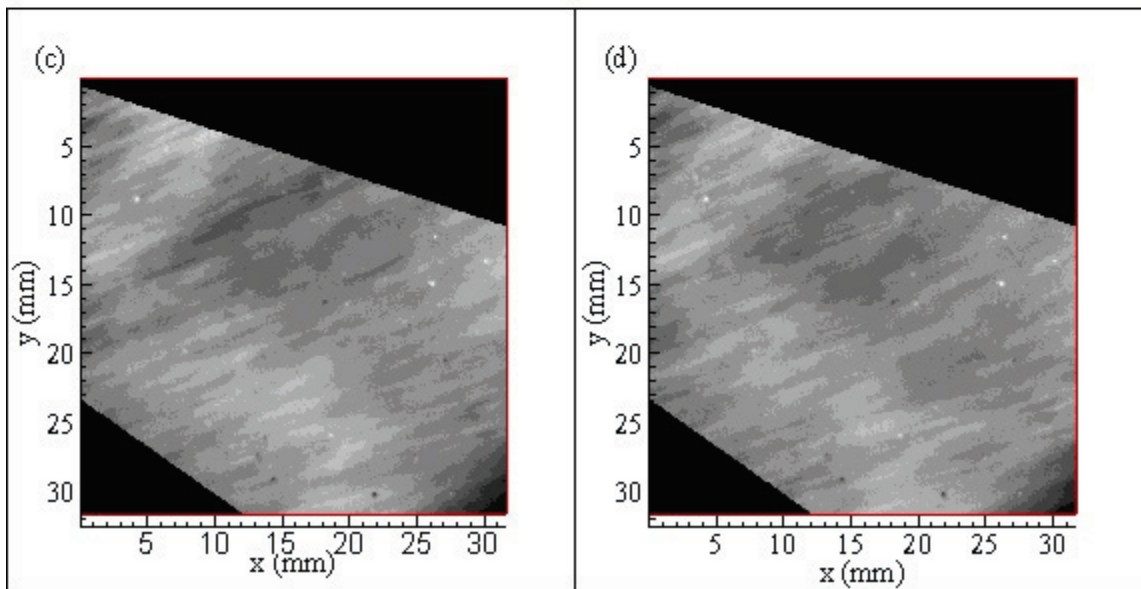
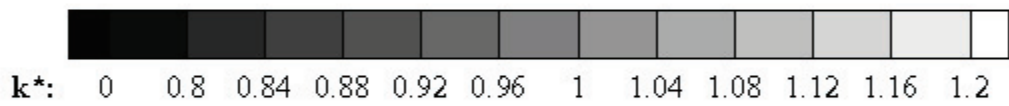
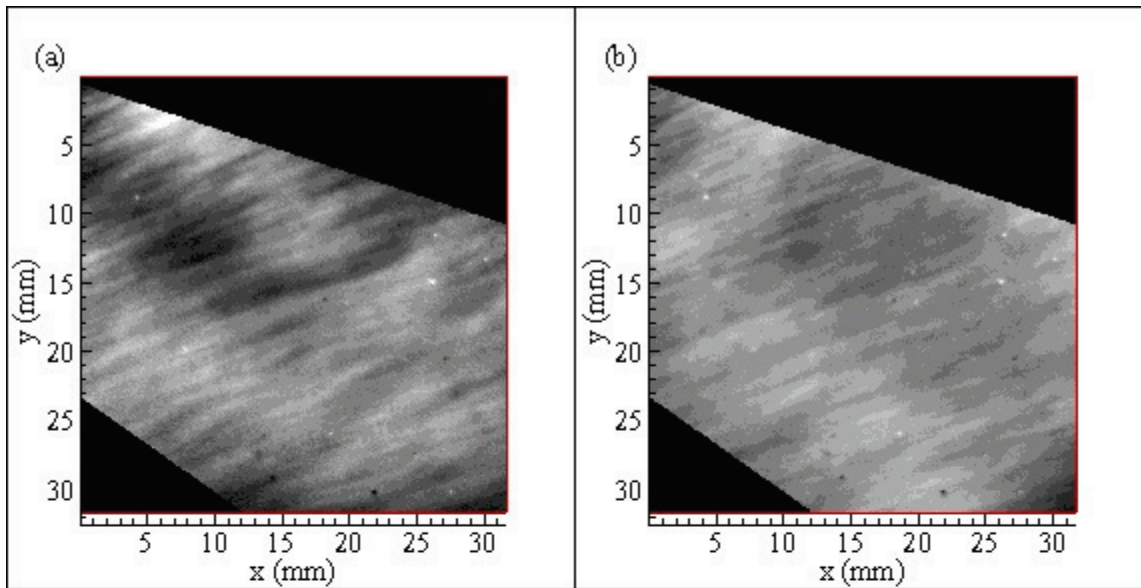
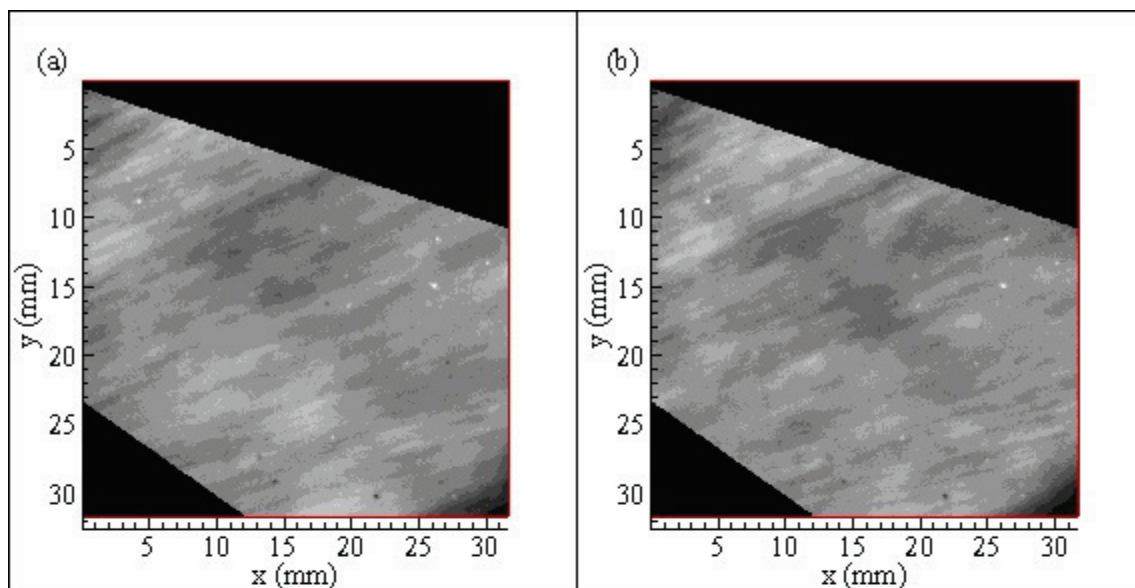


Figure C.75. Grayscale plots of normalized dimensionless mass transfer coefficient values at 63% relative humidity: (a) R63F\_14; 45 min.: 30 sec., (b) R63F\_15; 45 min.: 40 sec., (c) R63F\_20; 46 min.: 20 sec., (d) R63F\_27; 47 min.: 10 sec.



$k^*$ : 0 0.8 0.84 0.88 0.92 0.96 1 1.04 1.08 1.12 1.16 1.2

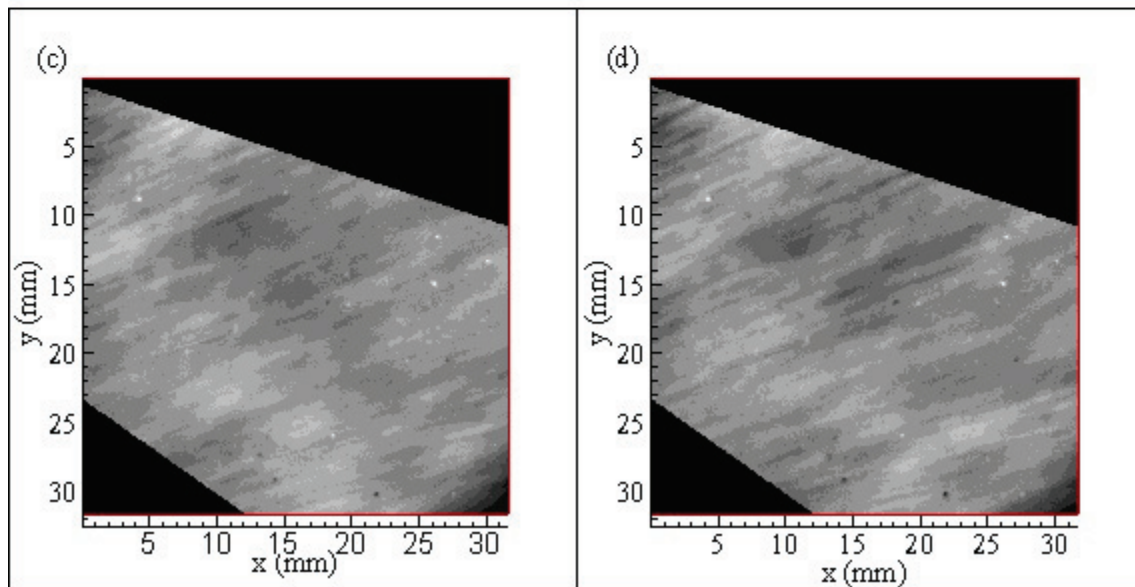


Figure C.76. Grayscale plots of normalized dimensionless mass transfer coefficient values at 63% relative humidity: (a) R63F\_28; 47 min.: 20 sec., (b) R63F\_30; 48 min.: 20 sec., (c) R63F\_42; 49 min.: 00 sec., (d) R63F\_50; 50 min.: 10 sec.

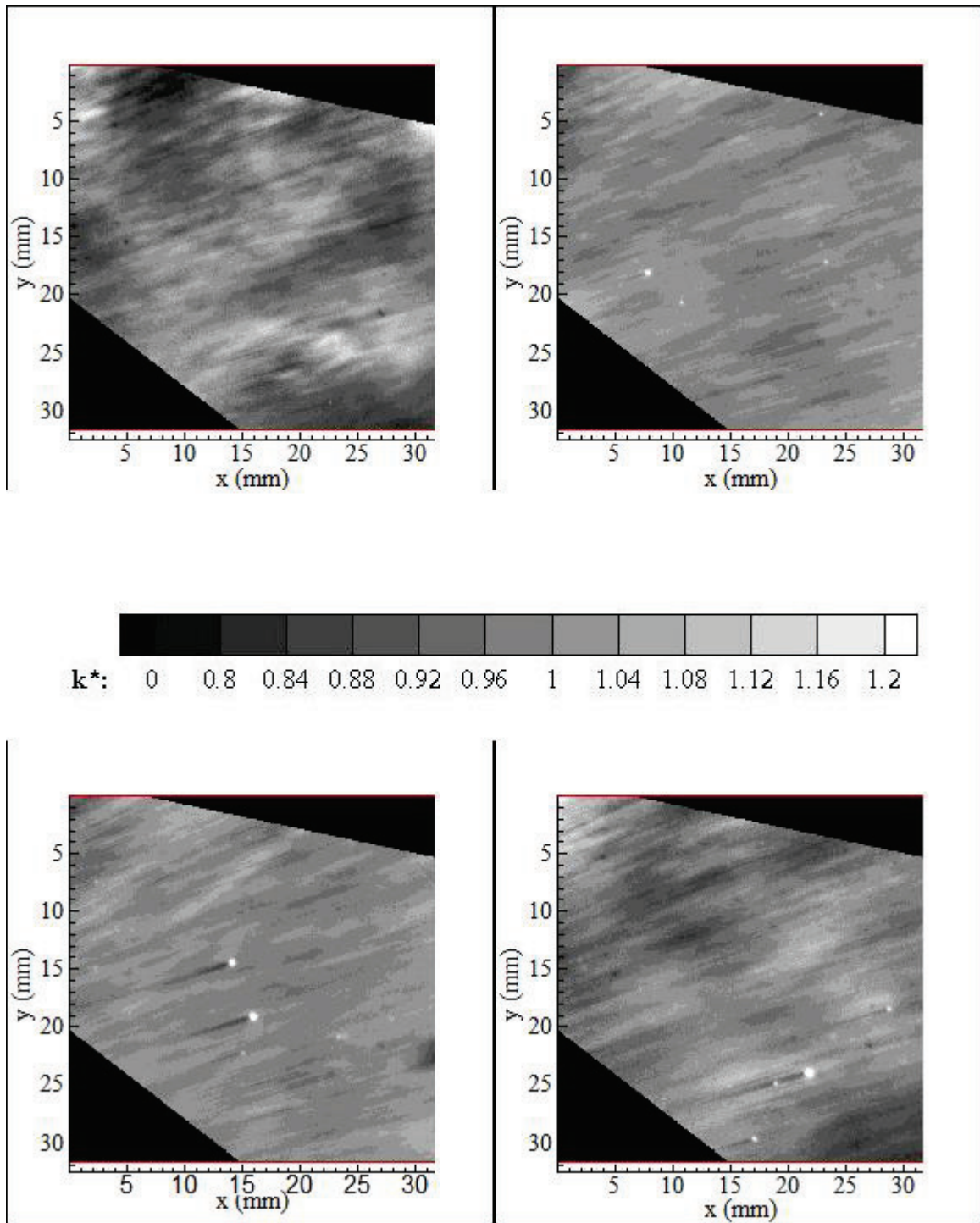


Figure C.77. Grayscale plots of normalized dimensionless mass transfer coefficient values at 91% relative humidity: (a) R91A\_1; 2 min.: 30 sec., (b) R91A\_10; 4 min.: 40 sec., (c) R91A\_19; 5 min.: 20 sec., (d) R91A\_30; 7 min.: 40 sec.

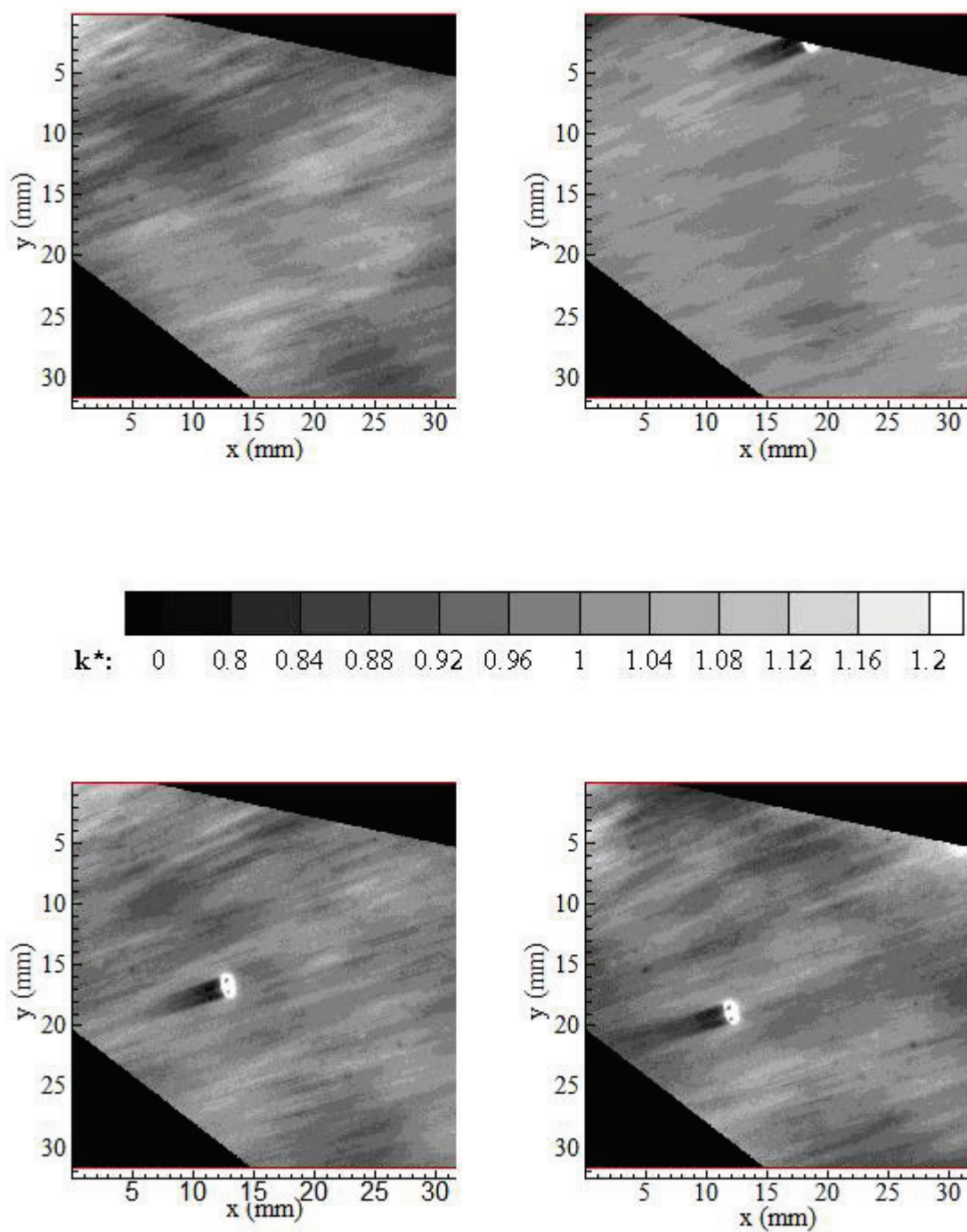


Figure C.78. Grayscale plots of normalized dimensionless mass transfer coefficient values at 91% relative humidity: (a) R91A\_45; 10 min.: 50 sec., (b) R91A\_46; 11 min.: 10 sec., (c) R91A\_48; 11 min.: 30 sec., (d) R91A\_49; 11 min.: 40 sec.

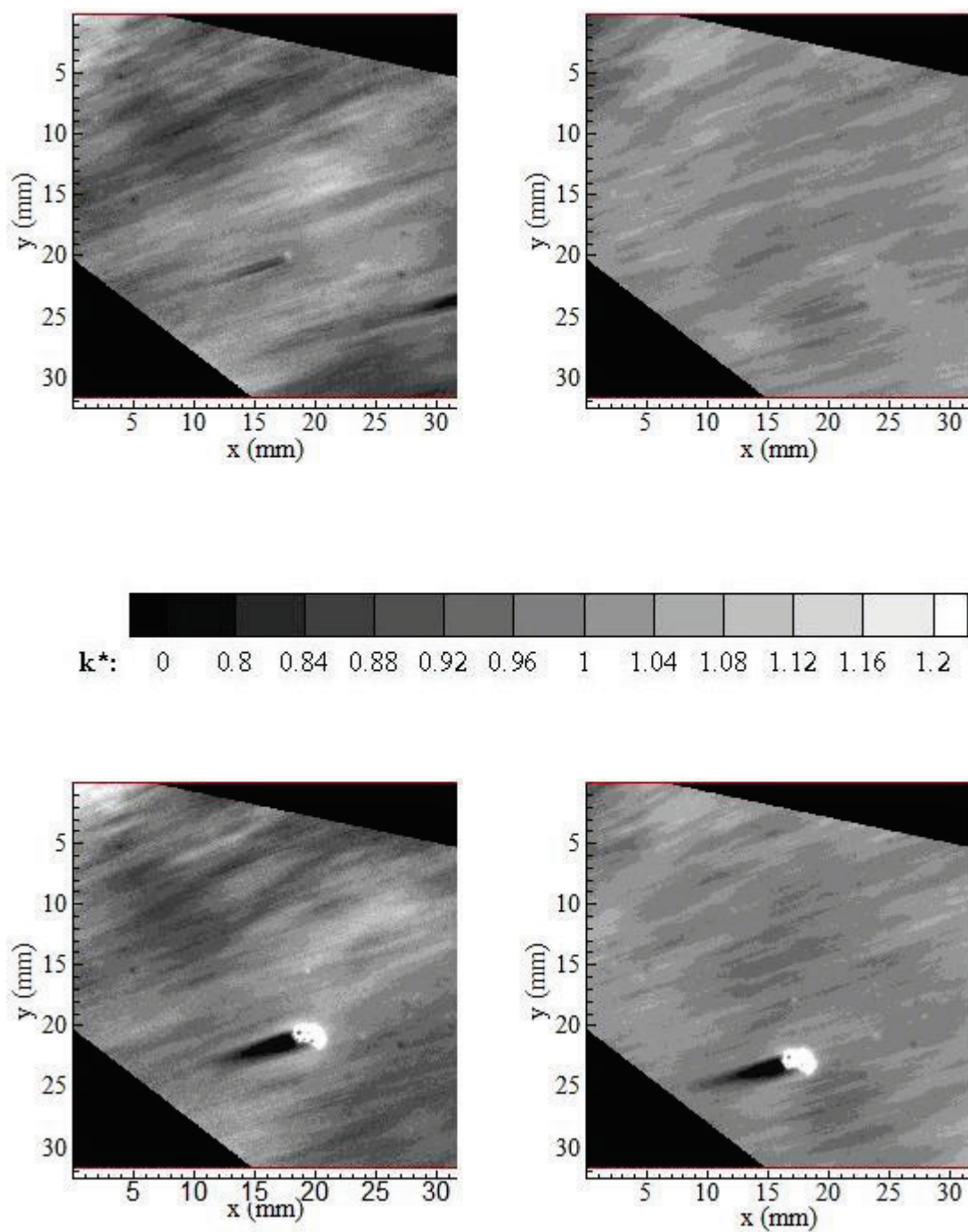


Figure C.79. Grayscale plots of normalized dimensionless mass transfer coefficient values at 91% relative humidity: (a) R91A\_64; 14 min.: 10 sec., (b) R91A\_65; 14 min.: 20 sec., (c) R91A\_69; 15 min.: 10 sec., (d) R91A\_70; 15 min.: 20 sec.

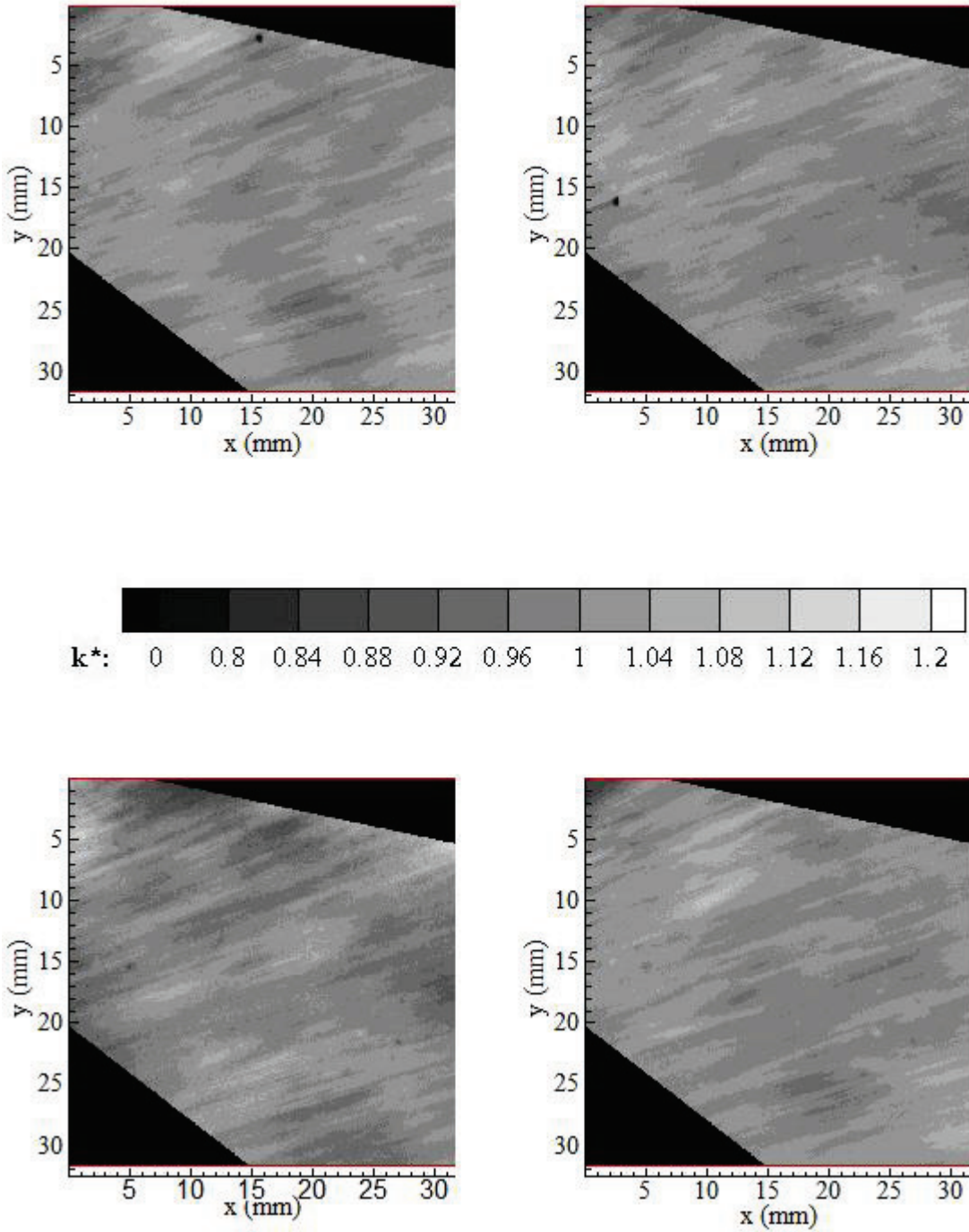


Figure C.80. Grayscale plots of normalized dimensionless mass transfer coefficient values at 91% relative humidity: (a) R91B\_7; 20 min.: 40 sec., (b) R91A\_8; 20 min.: 50 sec., (c) R91B\_10; 21 min.: 10 sec., (d) R91B\_15; 22 min.: 00 sec.

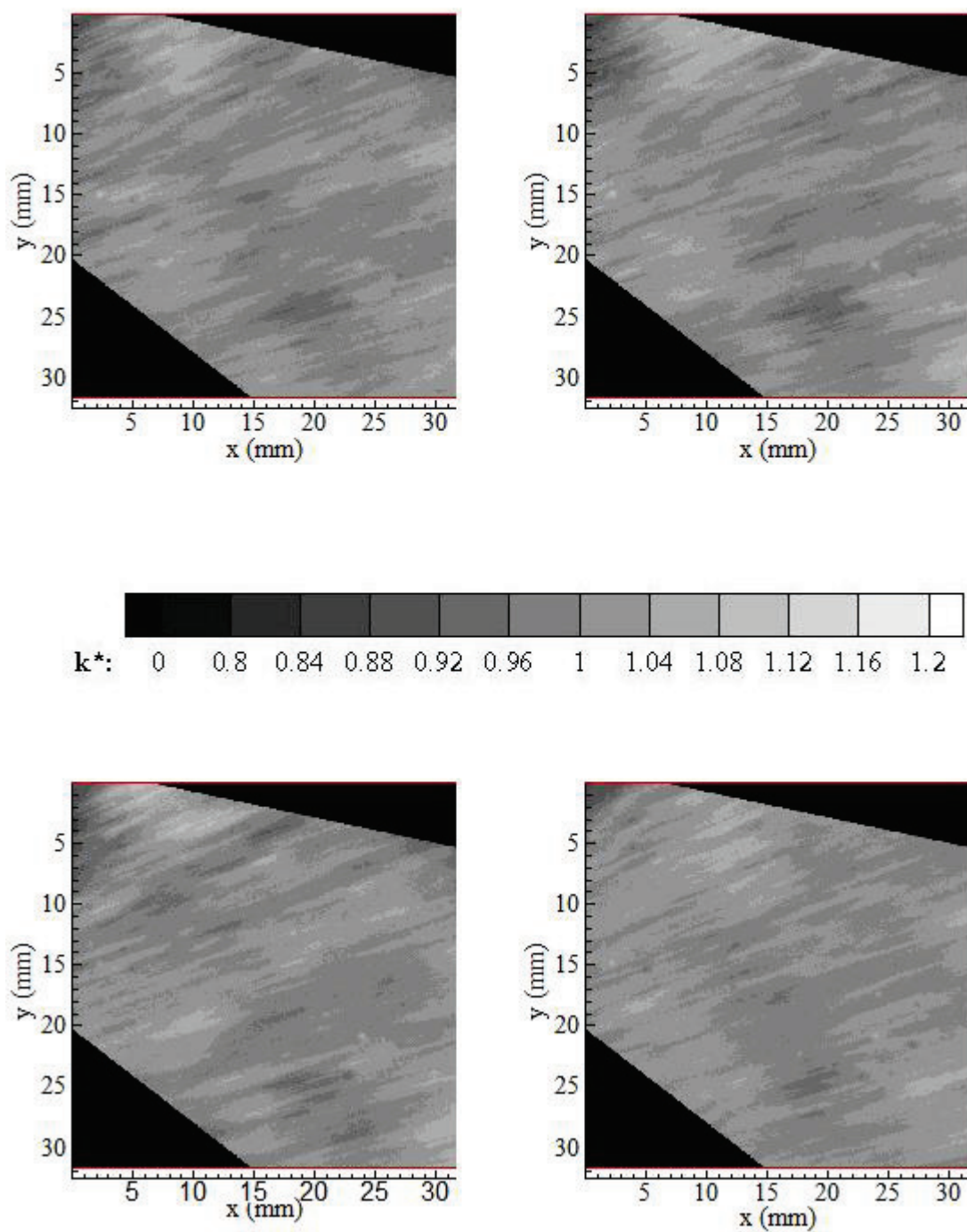


Figure C.81. Grayscale plots of normalized dimensionless mass transfer coefficient values at 91% relative humidity: (a) R91B\_40; 27 min.: 50 sec., (b) R91B\_41; 28 min.: 10 sec., (c) R91B\_43; 28 min.: 20 sec., (d) R91B\_45; 28 min.: 40 sec.

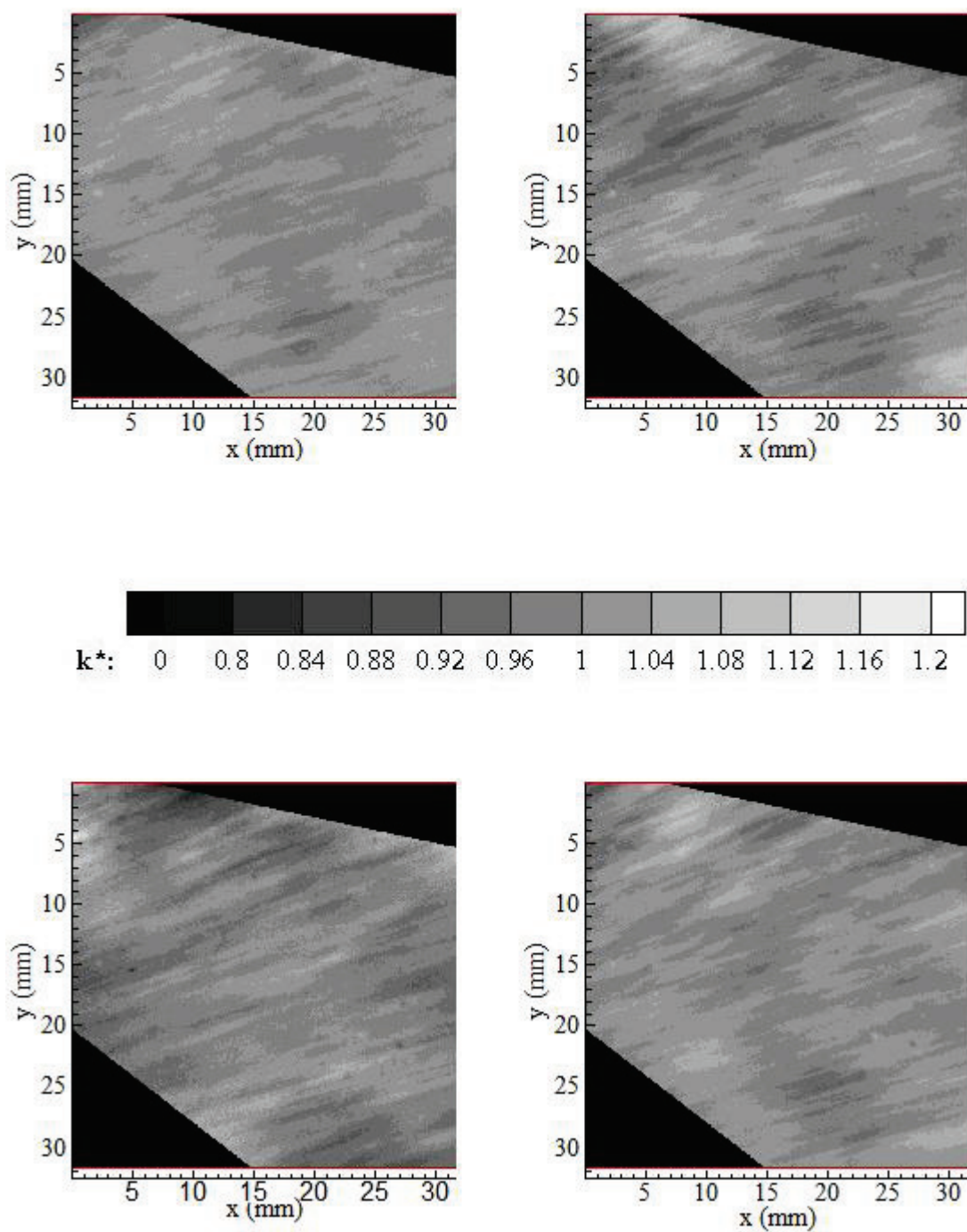


Figure C.82. Grayscale plots of normalized dimensionless mass transfer coefficient values at 91% relative humidity: (a) R91B\_69; 33 min.: 20 sec., (b) R91B\_73; 34 min.: 00 sec., (c) R91B\_79; 35 min.: 10 sec., (d) R91B\_86; 36 min.: 20 sec.

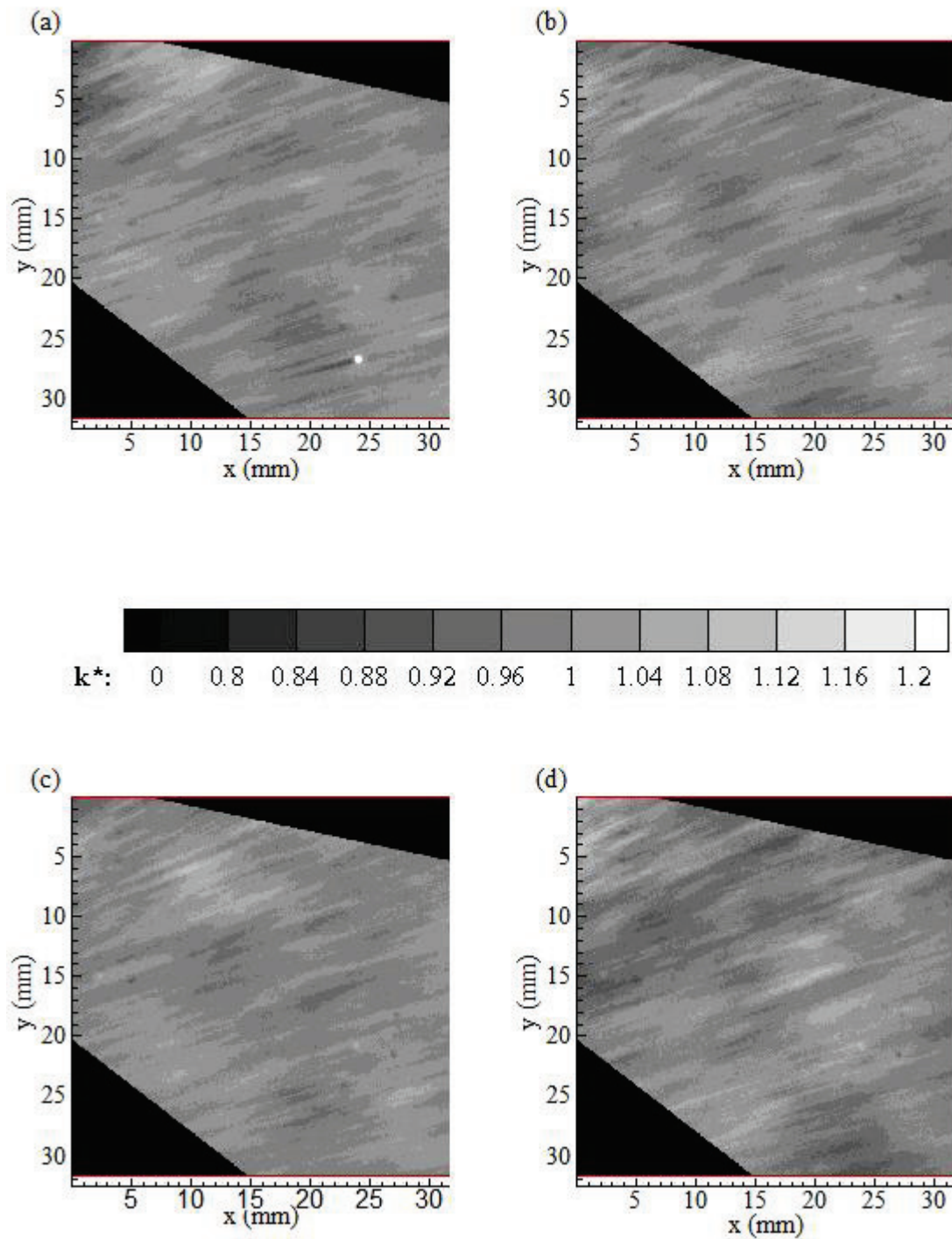


Figure C.83. Grayscale plots of normalized dimensionless mass transfer coefficient values at 91% relative humidity: (a) R91C\_6; 39 min.: 00 sec., (b) R91C\_10; 39 min.: 40 sec., (c) R91C\_22; 42 min.: 00 sec., (d) R91C\_31; 22 min.: 40 sec.

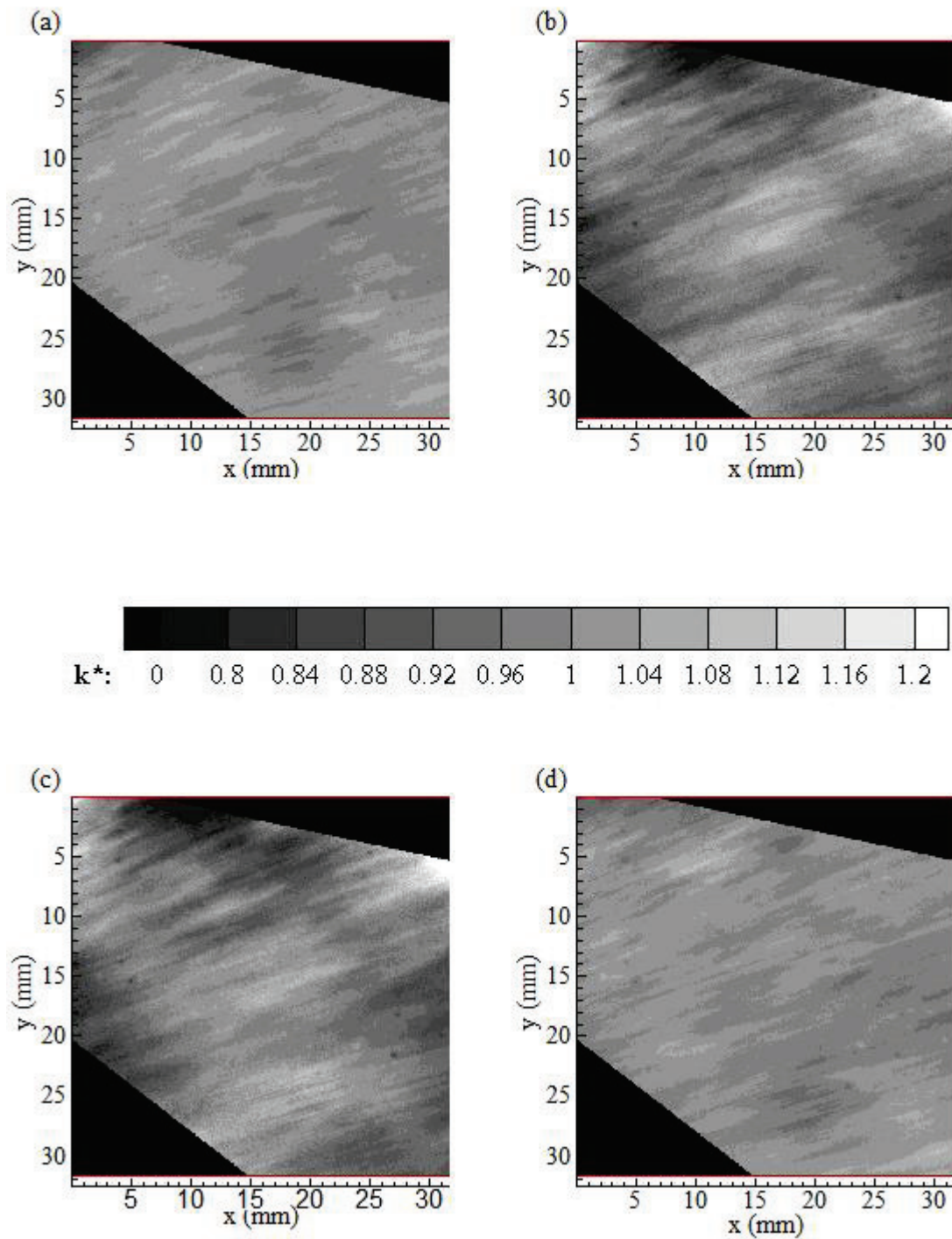


Figure C.84. Grayscale plots of normalized dimensionless mass transfer coefficient values at 91% relative humidity: (a) R91C\_45; 46 min.: 20 sec., (b) R91C\_46; 46 min.: 40 sec., (c) R91C\_47; 46 min.: 50 sec., (d) R91C\_48; 47 min.: 00 sec.

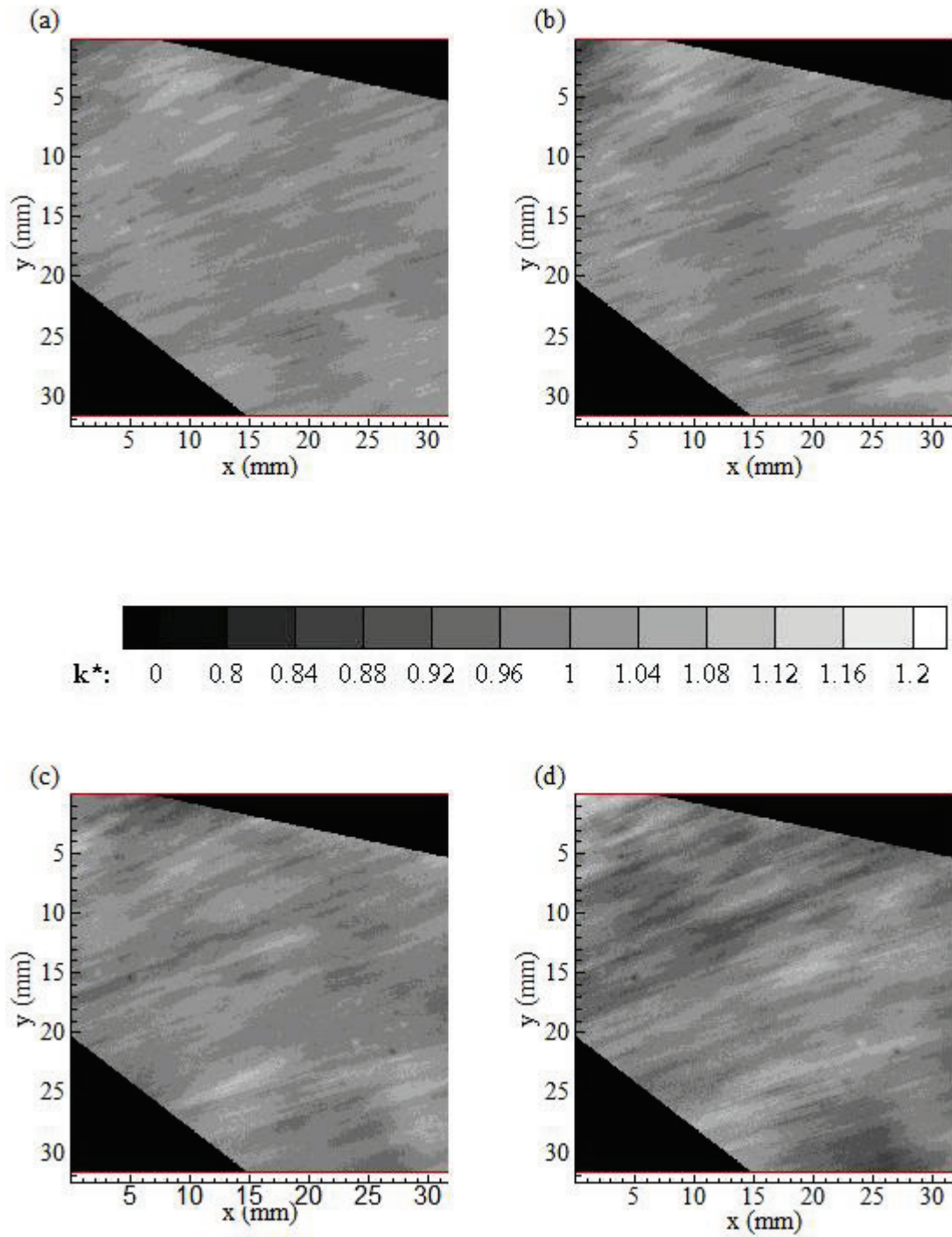


Figure C.85. Grayscale plots of normalized dimensionless mass transfer coefficient values at 91% relative humidity: (a) R91C\_56; 48 min.: 40 sec., (b) R91C\_62; 49 min.: 50 sec., (c) R91C\_72; 51 min.: 50 sec., (d) R91C\_76; 52 min.: 20 sec.

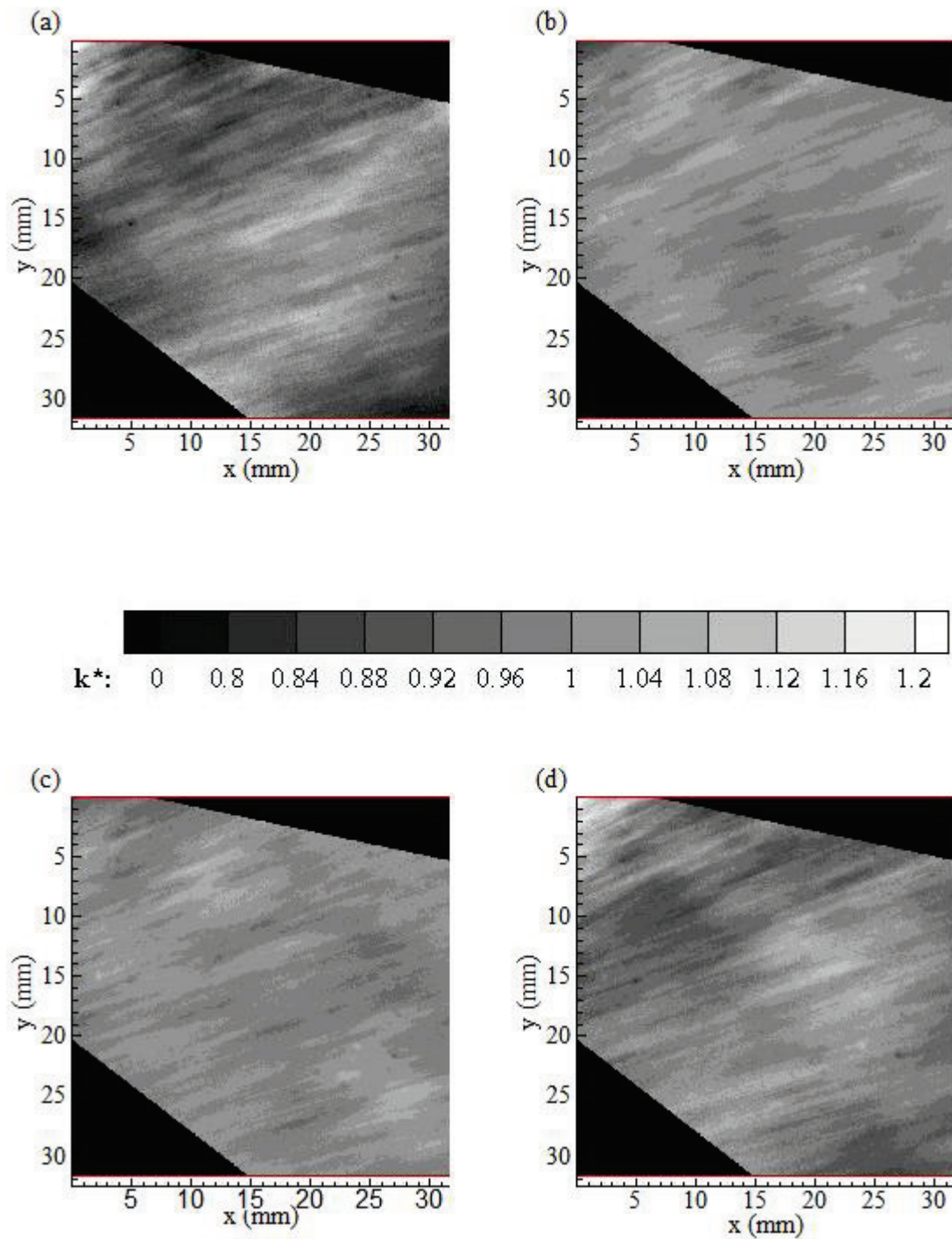


Figure C.86. Grayscale plots of normalized dimensionless mass transfer coefficient values at 91% relative humidity: (a) R91C\_90; 55 min.: 20 sec., (b) R91C\_92; 55 min.: 40 sec., (c) R91C\_95; 57 min.: 10 sec., (d) R91D\_1; 57 min.: 20 sec.

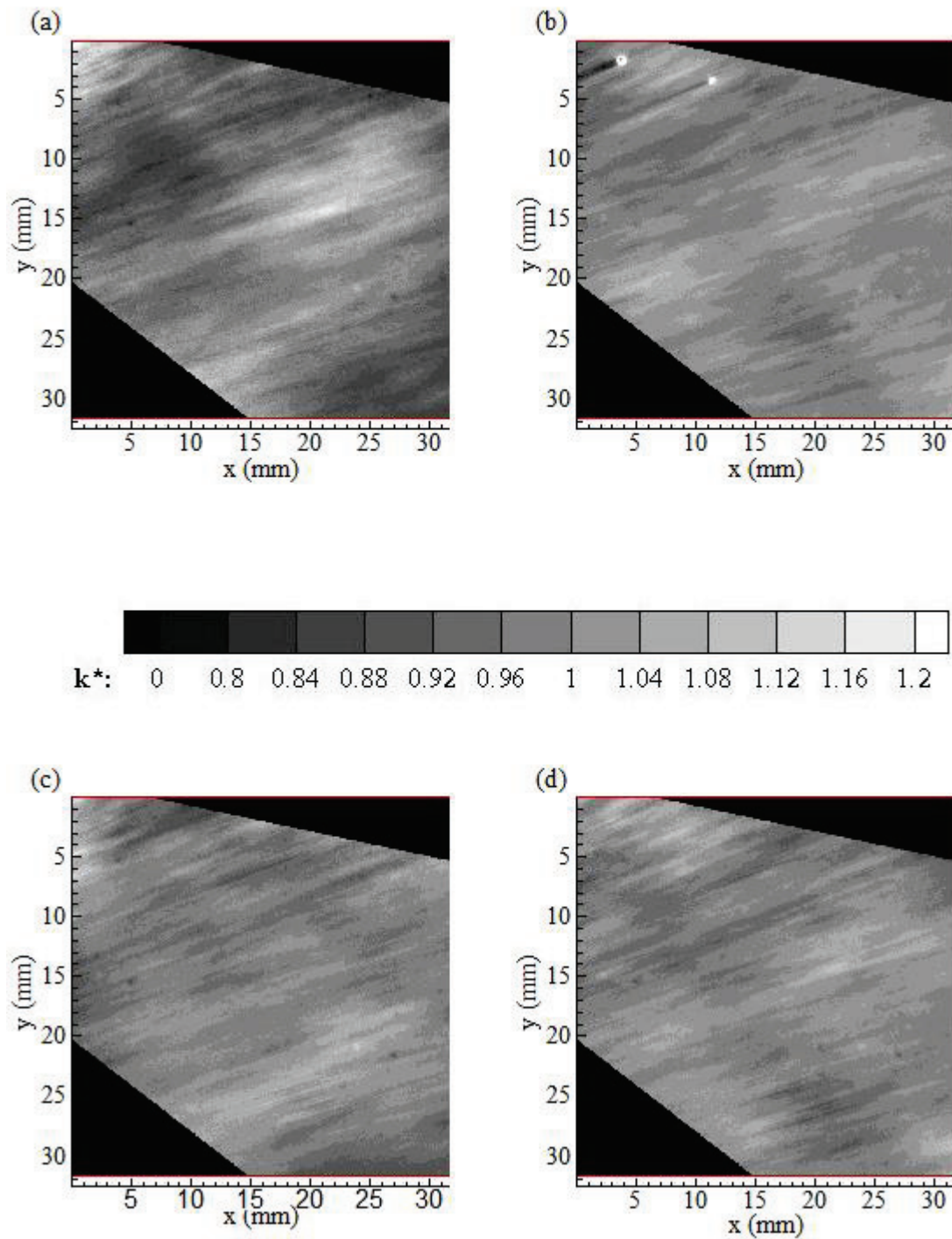


Figure C.87. Grayscale plots of normalized dimensionless mass transfer coefficient values at 91% relative humidity: (a) R91D\_4; 58 min.: 10 sec., (b) R91D\_10; 59 min.: 20 sec., (c) R91D\_19; 61 min.: 00 sec., (d) R63D\_20; 61 min.: 20 sec.

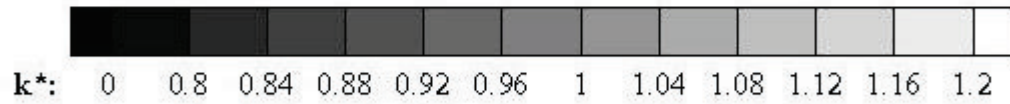
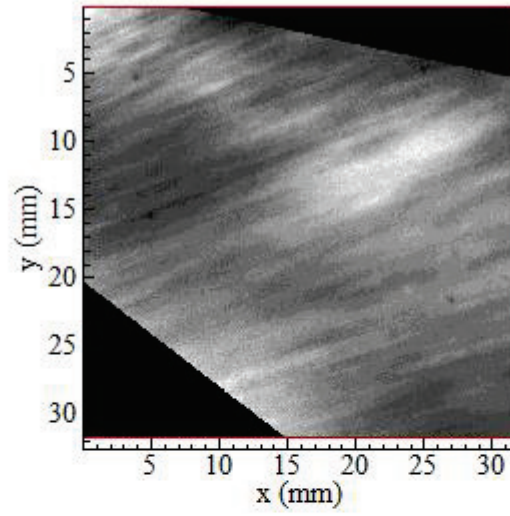


Figure C.88. Grayscale plots of normalized dimensionless mass transfer coefficient values at 91% relative humidity: R91D\_22; 61 min.: 40 sec.

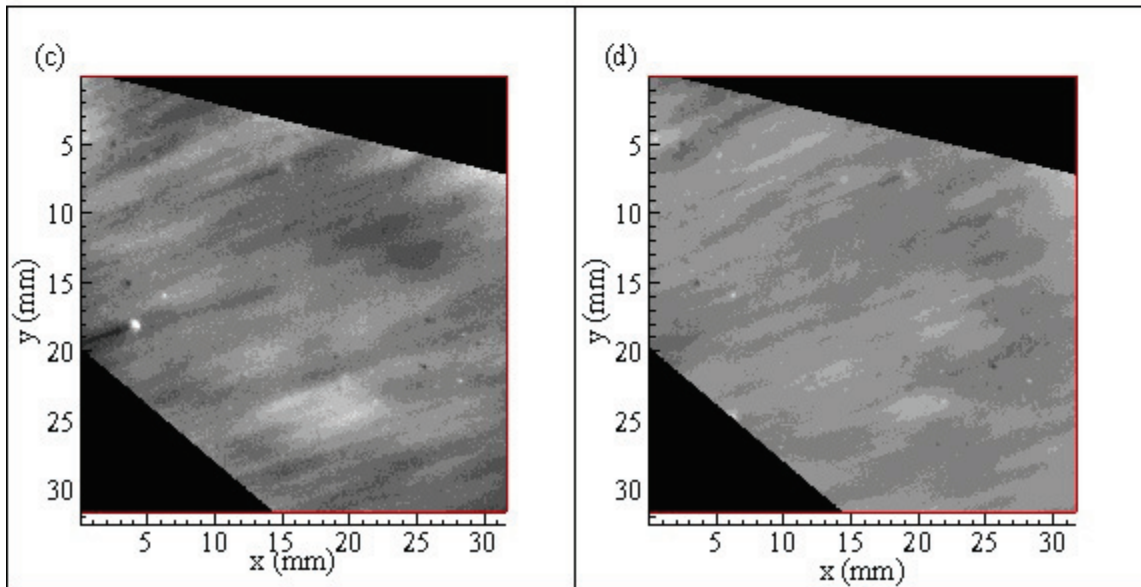
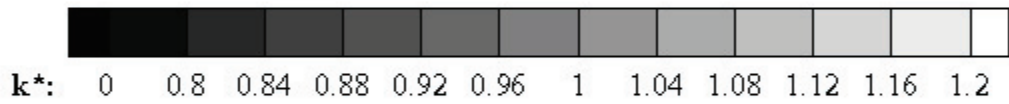
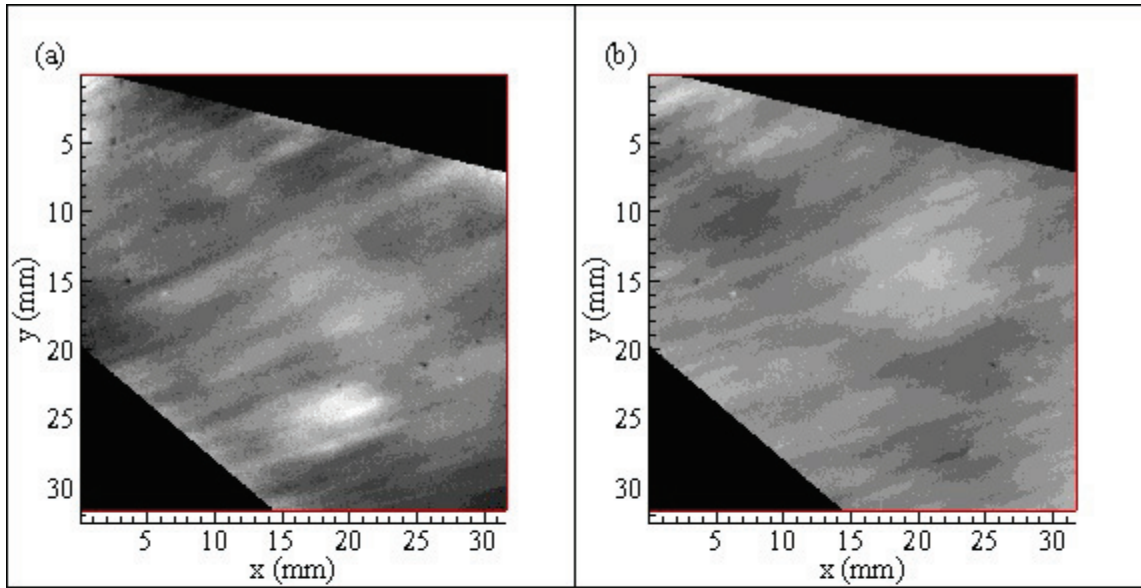


Figure C.89. Grayscale plots of normalized dimensionless mass transfer coefficient values at 96% relative humidity: (a) R96A\_3; 3 min.: 20 sec., (b) R96A\_4; 3 min.: 30 sec., (c) R96A\_28; 4 min.: 20 sec., (d) R96A\_30; 4 min.: 40 sec.

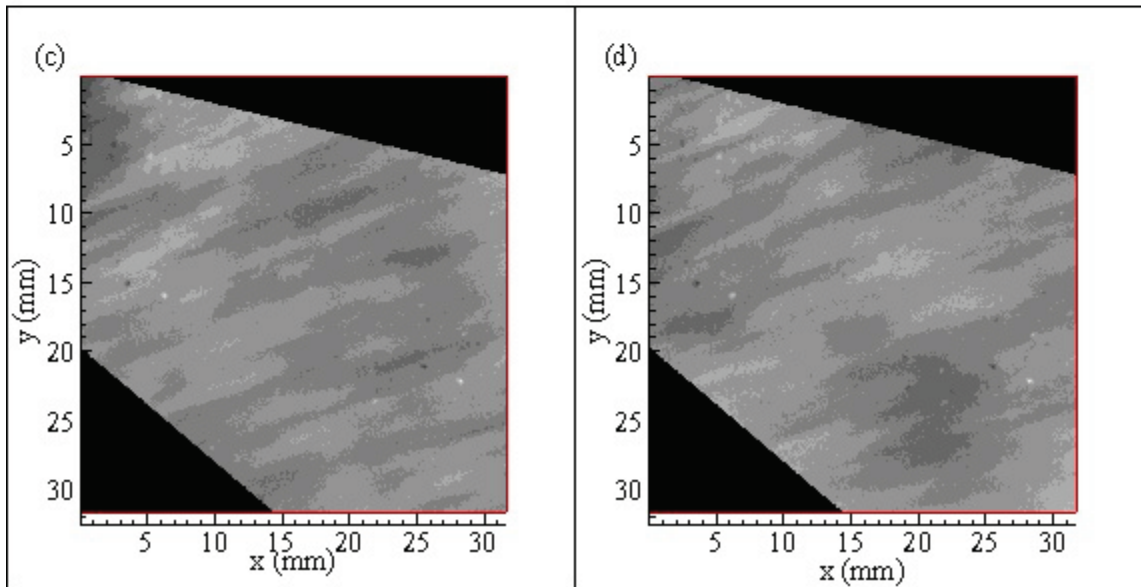
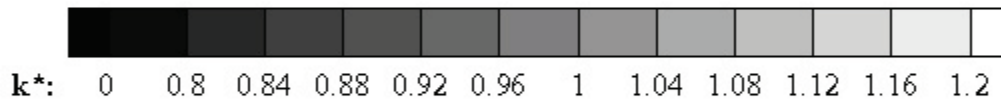
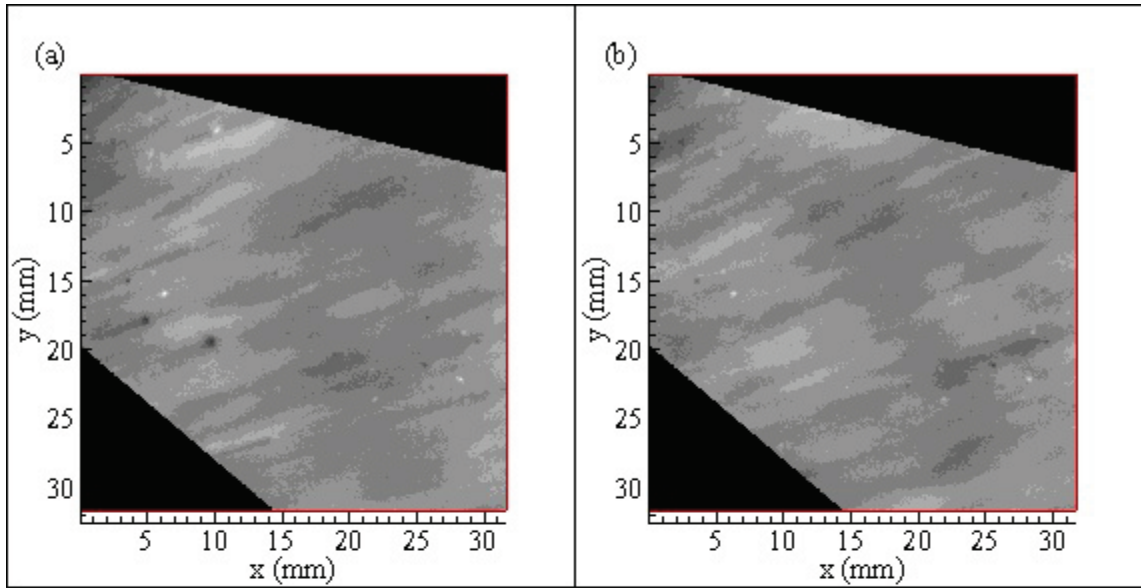


Figure C.90. Grayscale plots of normalized dimensionless mass transfer coefficient values at 96% relative humidity: (a) R96A\_55; 6 min.: 10 sec., (b) R96A\_57; 6 min.: 30 sec., (c) R96A\_59; 6 min.: 50 sec., (d) R96A\_87; 7 min.: 40 sec.

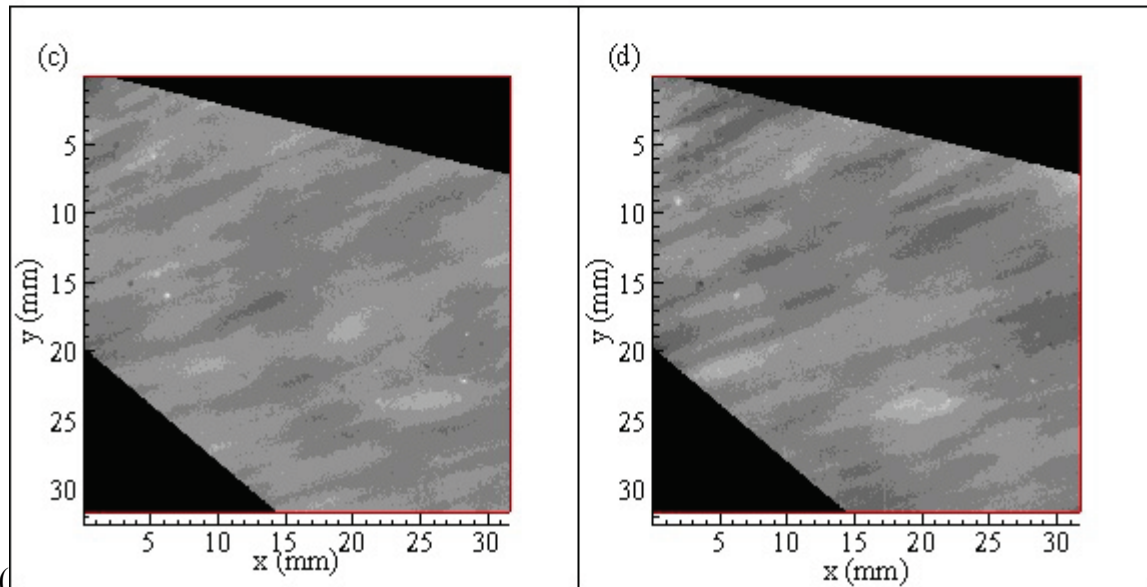
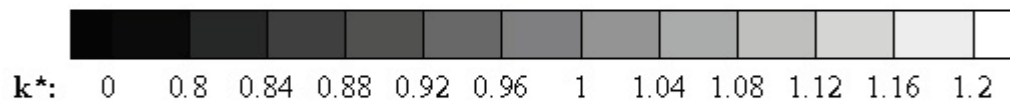
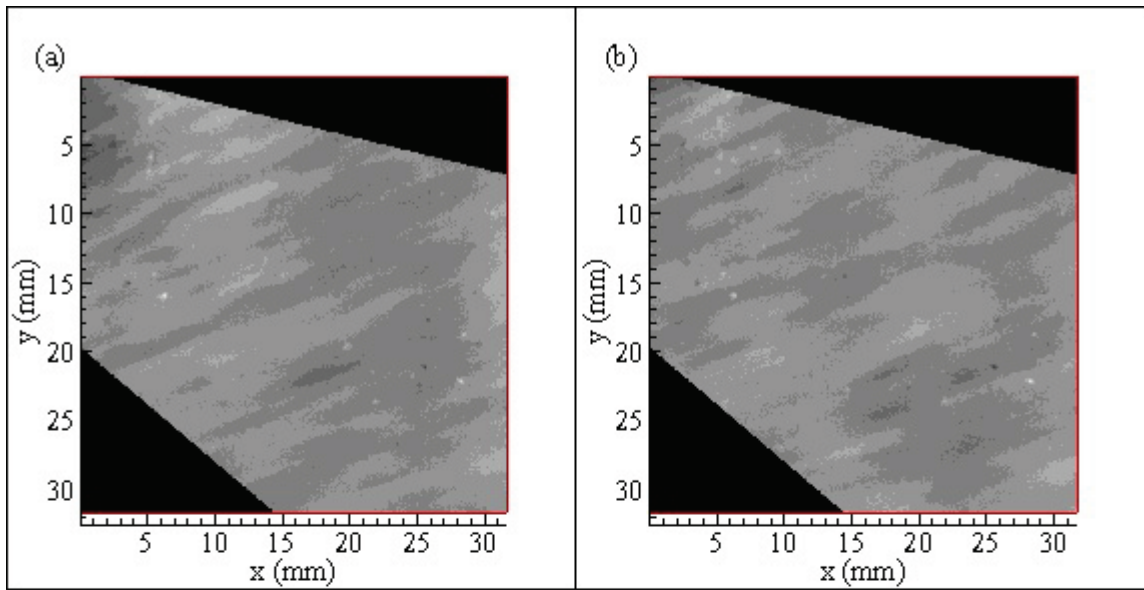


Figure C.91. Grayscale plots of normalized dimensionless mass transfer coefficient values at 96% relative humidity: (a) R96B\_9; 8 min.: 20 sec., (b) R96B\_14; 8 min.: 50 sec., (c) R96B\_20; 9 min.: 20 sec., (d) R96B\_40; 9 min.: 50 sec.

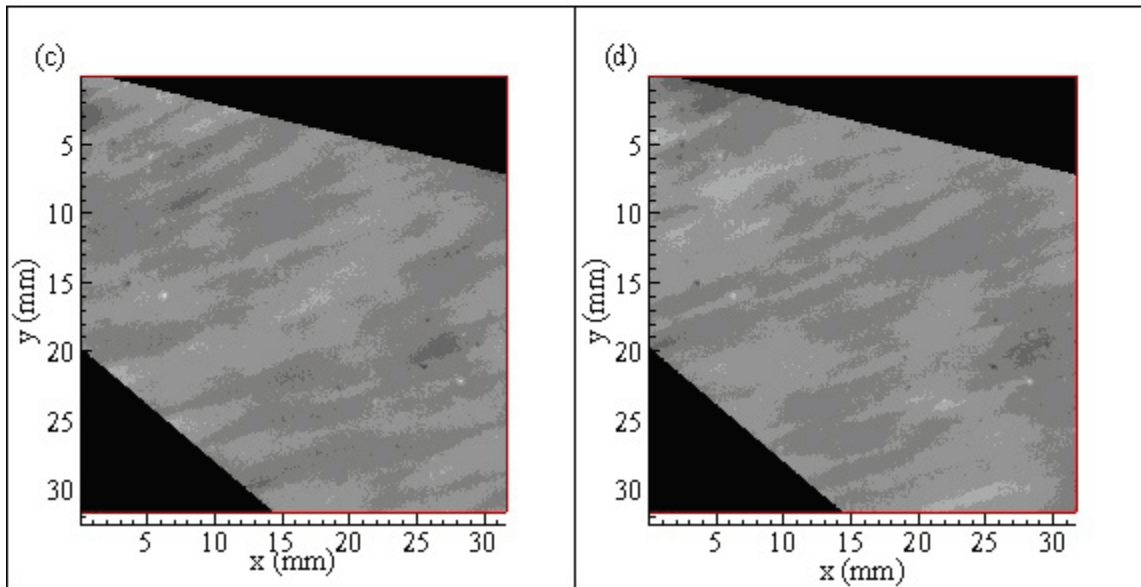
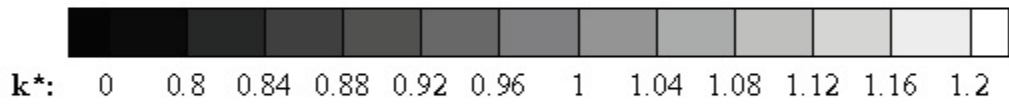
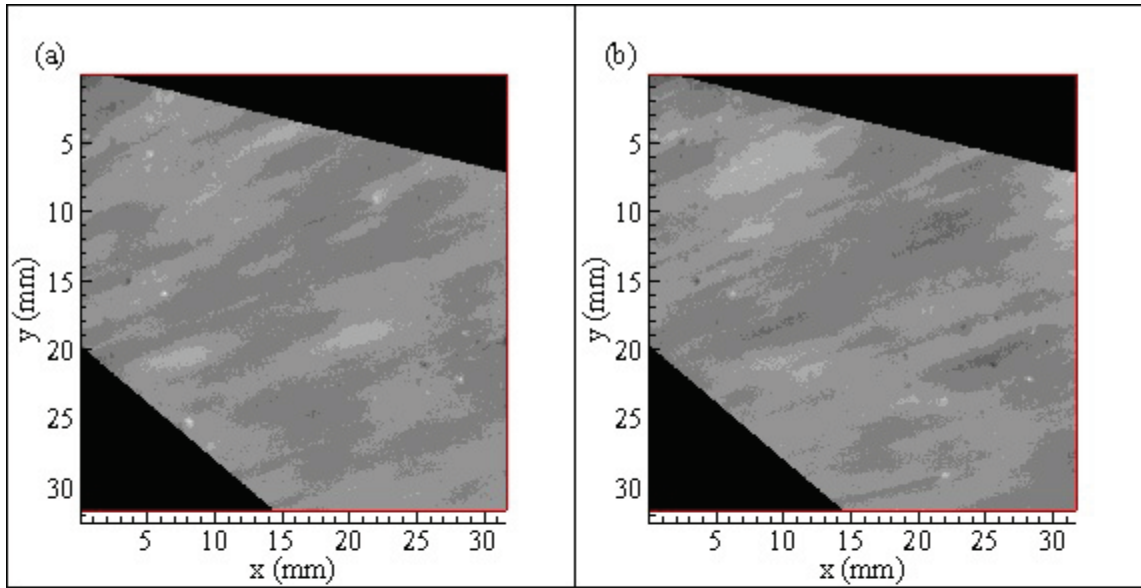


Figure C.92. Grayscale plots of normalized dimensionless mass transfer coefficient values at 96% relative humidity: (a) R96B\_59; 11 min.: 10 sec., (b) R96B\_61; 11 min.: 20 sec., (c) R96B\_63; 11 min.: 40 sec., (d) R96B\_75; 12 min.: 30 sec.

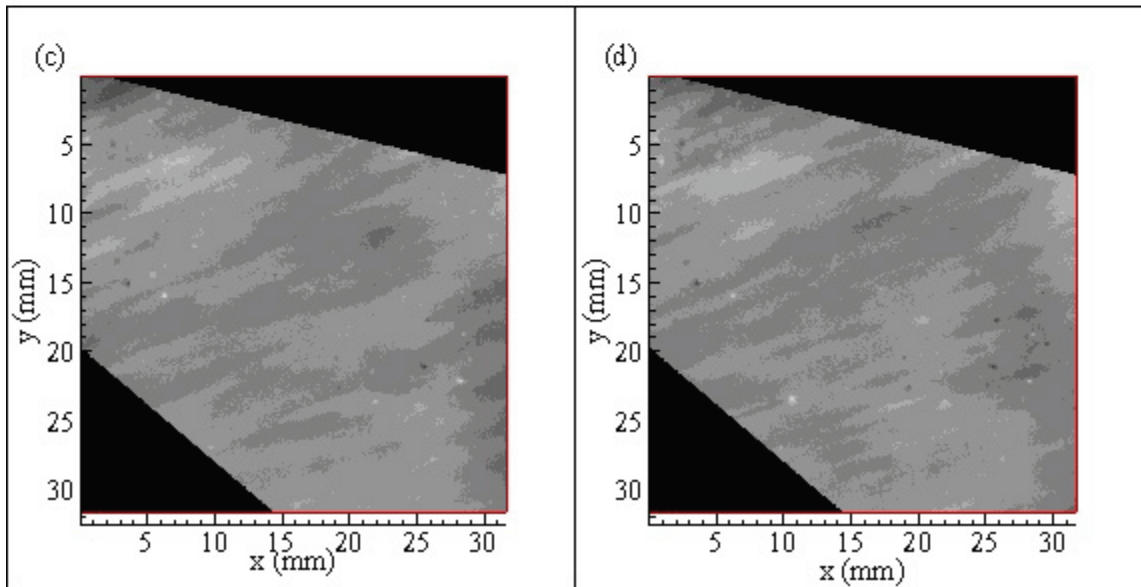
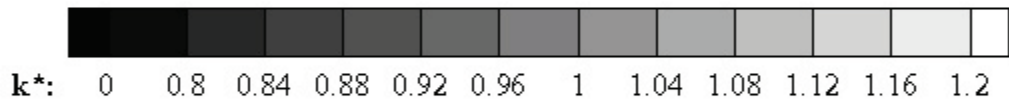
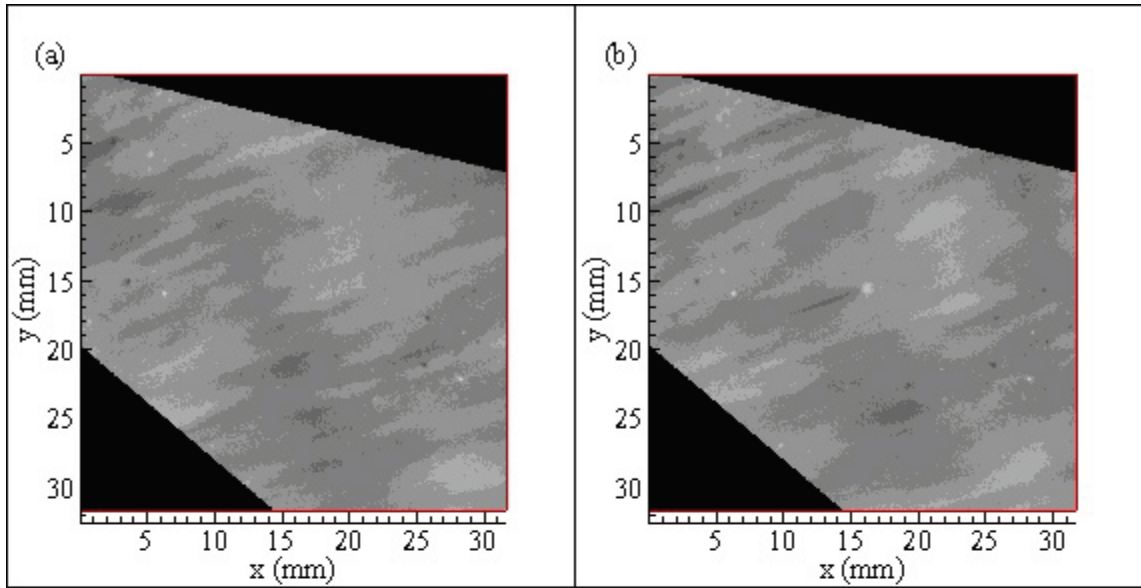


Figure C.93. Grayscale plots of normalized dimensionless mass transfer coefficient values at 96% relative humidity: (a) R96B\_78; 13 min.: 00 sec., (b) R96B\_80; 13 min.: 20 sec., (c) R96B\_84; 13 min.: 40 sec., (d) R96B\_96; 14 min.: 10 sec.

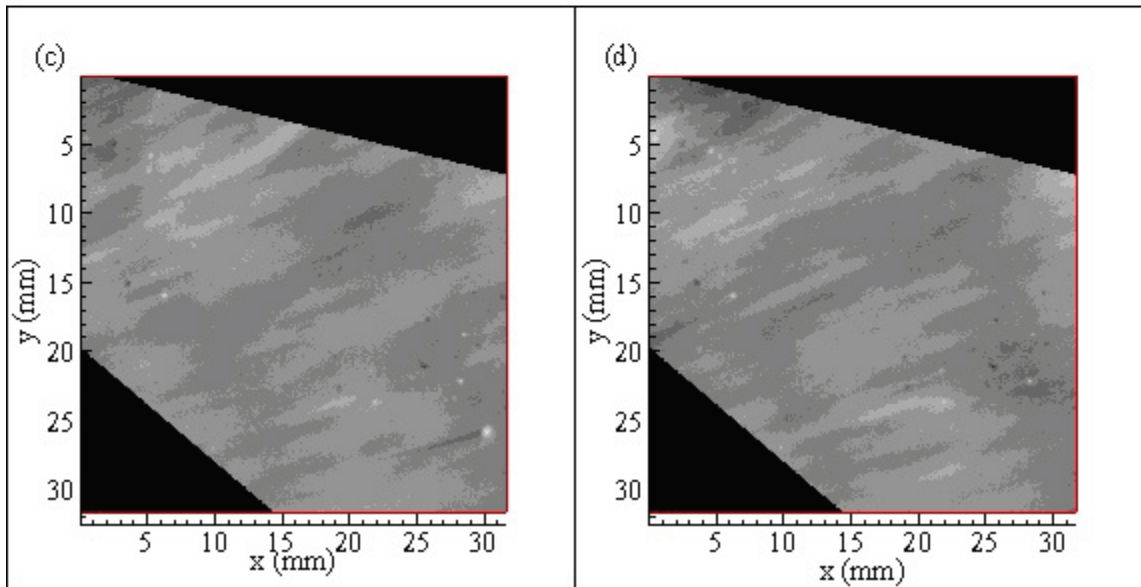
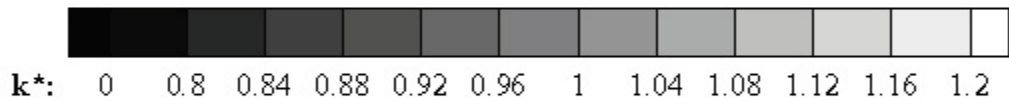
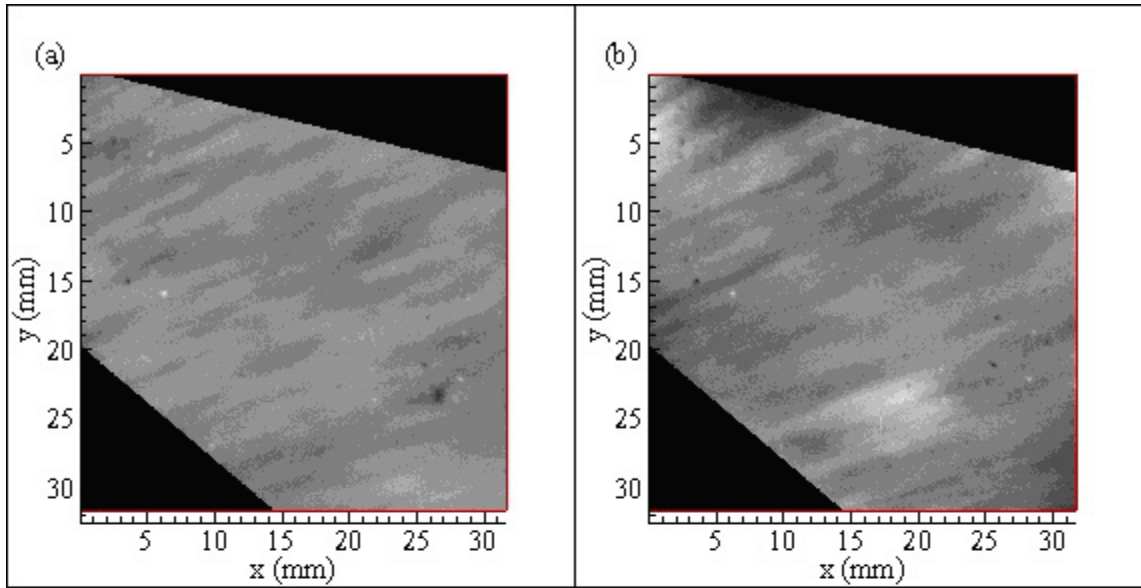


Figure C.94. Grayscale plots of normalized dimensionless mass transfer coefficient values at 96% relative humidity: (a) R96C\_6; 14 min.: 30 sec., (b) R96C\_17; 14 min.: 50 sec., (c) R96C\_22; 15 min.: 10 sec., (d) R96C\_23; 15 min.: 30 sec.

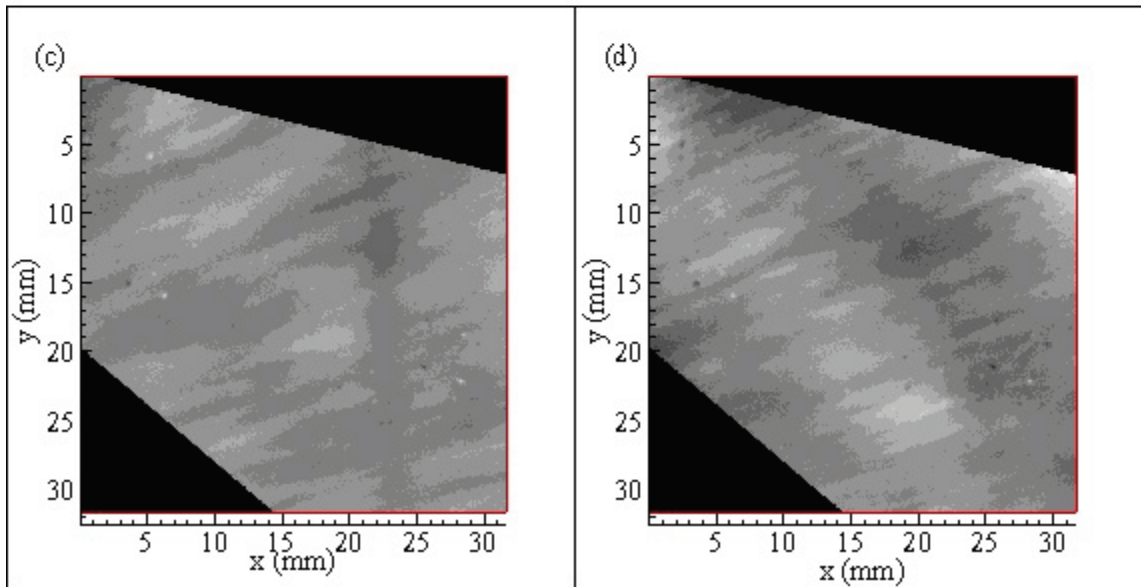
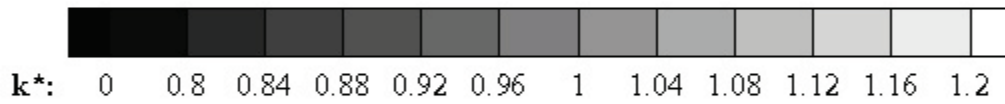
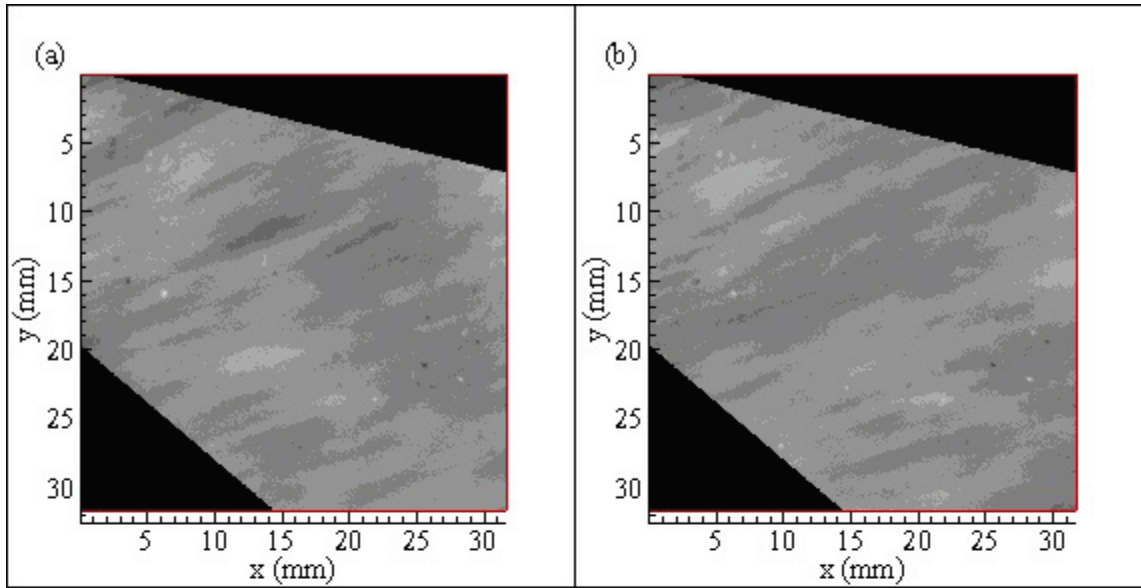
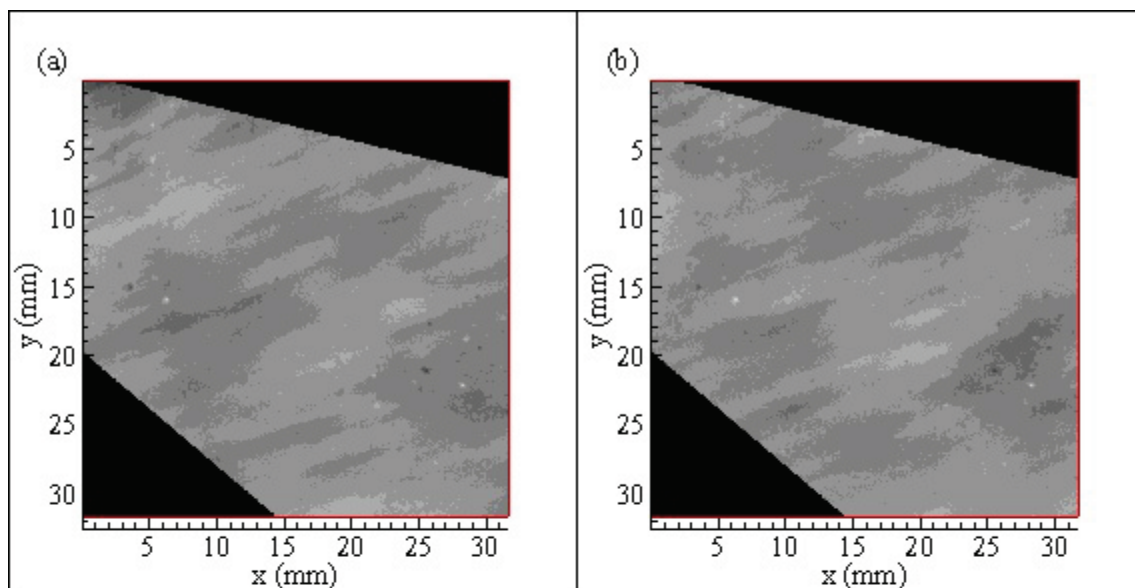


Figure C.95. Grayscale plots of normalized dimensionless mass transfer coefficient values at 96% relative humidity: (a) R96A\_26; 16 min.: 30 sec., (b) R96C\_29; 17 min.: 20 sec., (c) R96C\_30; 19 min.: 30 sec., (d) R96C\_36; 21 min.: 20 sec.



$k^*$ : 0 0.8 0.84 0.88 0.92 0.96 1 1.04 1.08 1.12 1.16 1.2

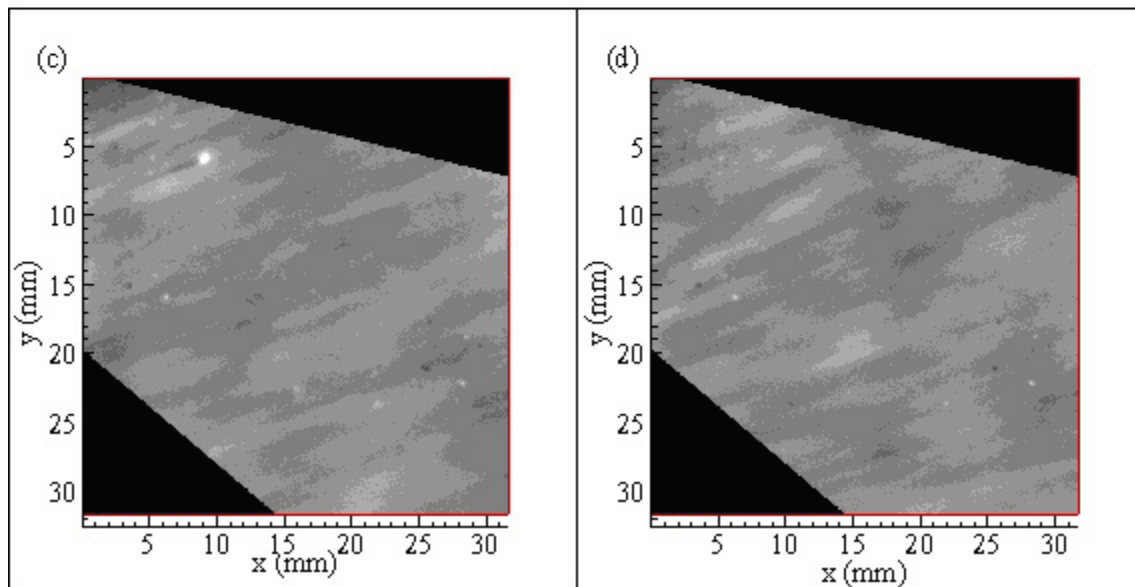


Figure C.96. Grayscale plots of normalized dimensionless mass transfer coefficient values at 96% relative humidity: (a) R96C\_38; 24 min.: 30 sec., (b) R96A\_45; 26 min.: 10 sec., (c) R96C\_47; 28 min.: 40 sec., (d) R96C\_50; 30 min.: 0 sec.

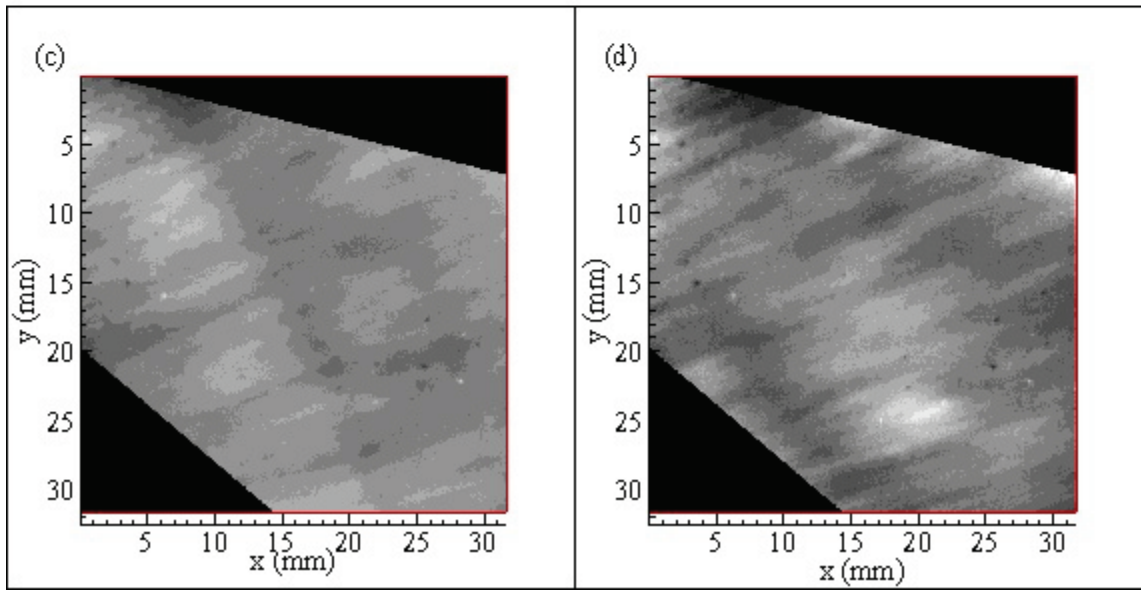
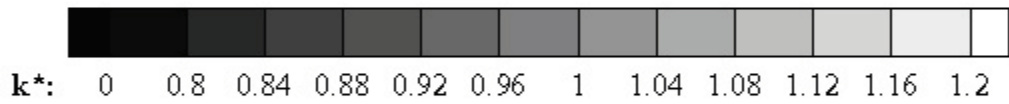
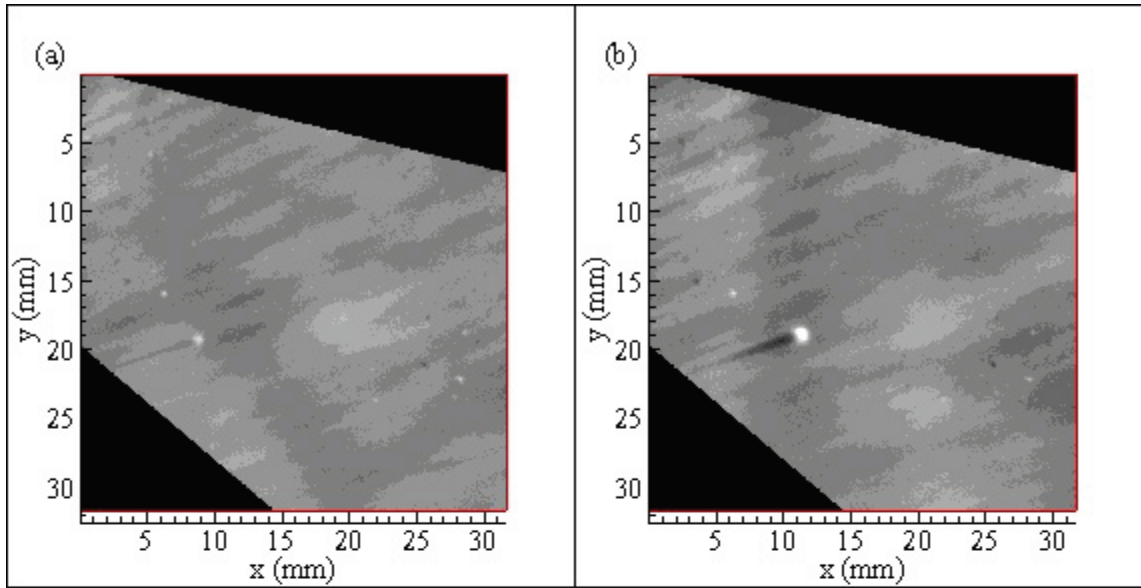


Figure C.97. Grayscale plots of normalized dimensionless mass transfer coefficient values at 96% relative humidity: (a) R96C\_61; 30 min.: 20 sec., (b) R96C\_63; 32 min.: 0 sec., (c) R96C\_66; 35 min.: 00 sec., (d) R96C\_89; 38 min.: 0 sec.

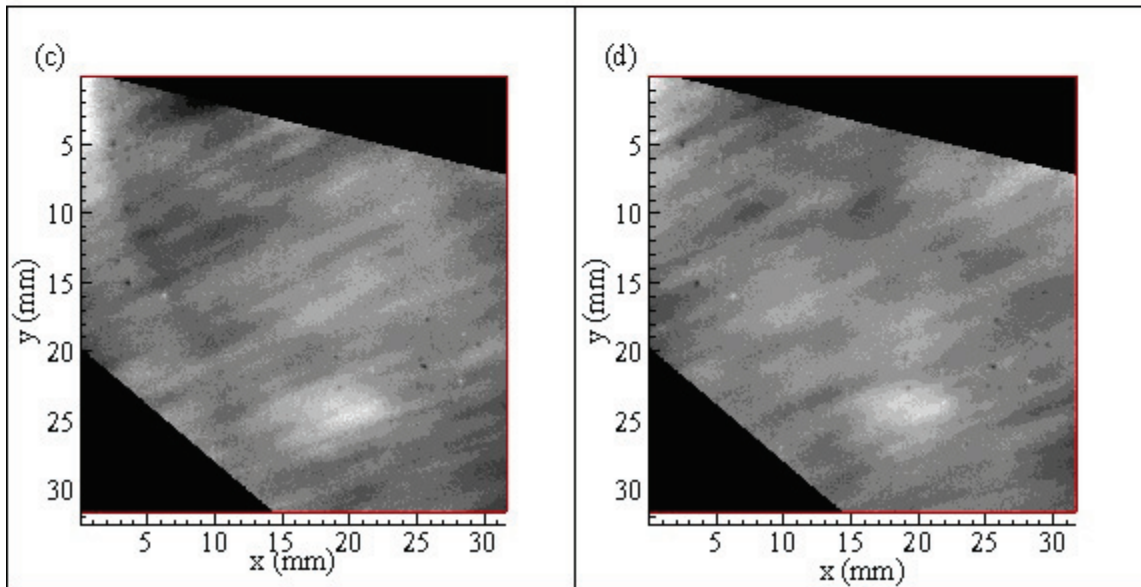
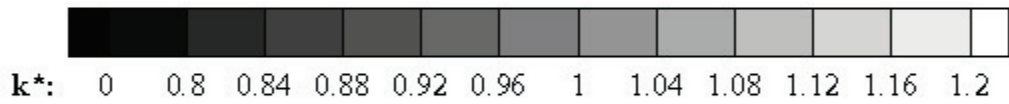
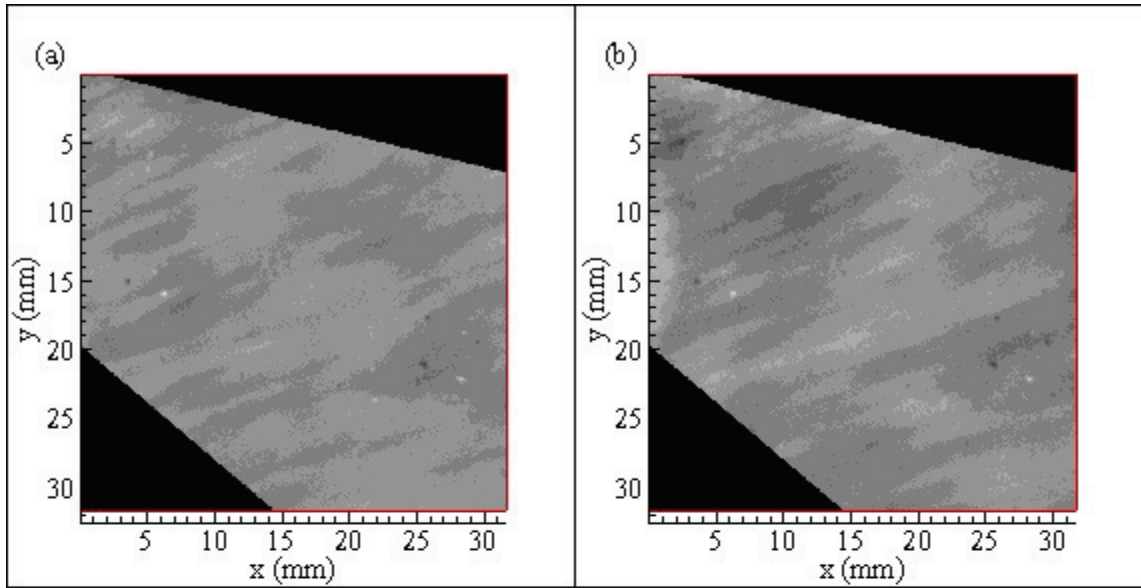
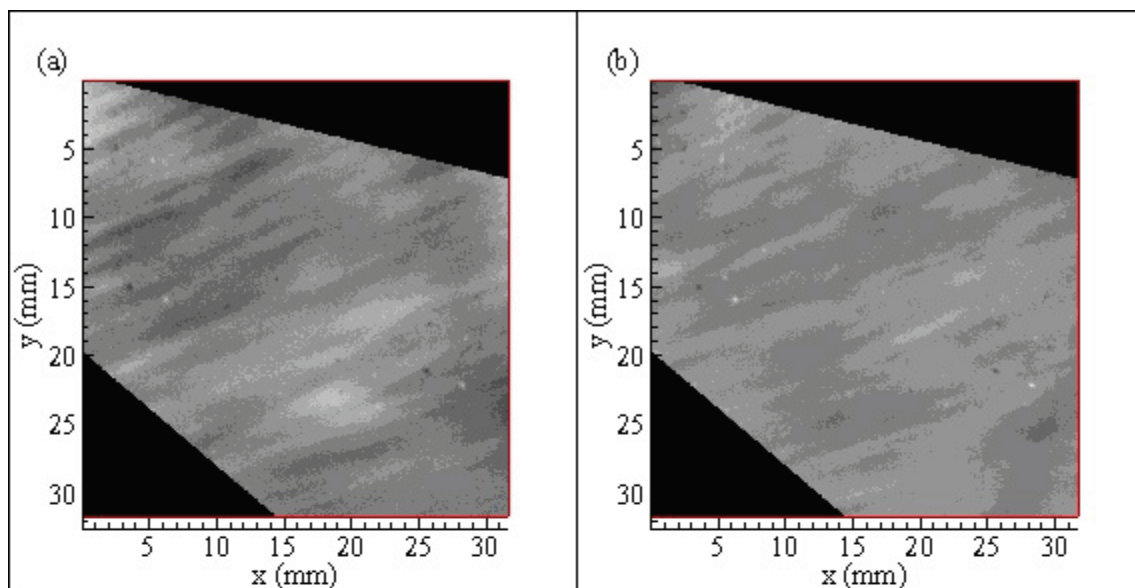


Figure C.98. Grayscale plots of normalized dimensionless mass transfer coefficient values at 96% relative humidity: (a) R96C\_94; 41 min.: 00 sec., (b) R96C\_95; 42 min.: 0 sec., (c) R96C\_98; 43 min.: 00 sec., (d) R96D\_7; 45 min.: 0 sec.



$k^*$ : 0 0.8 0.84 0.88 0.92 0.96 1 1.04 1.08 1.12 1.16 1.2

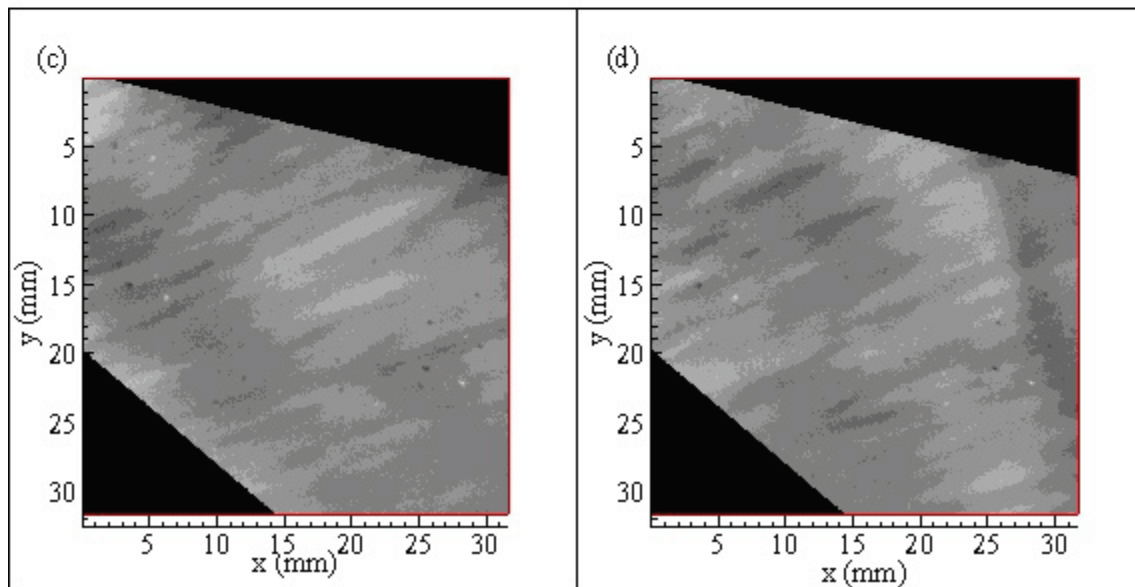
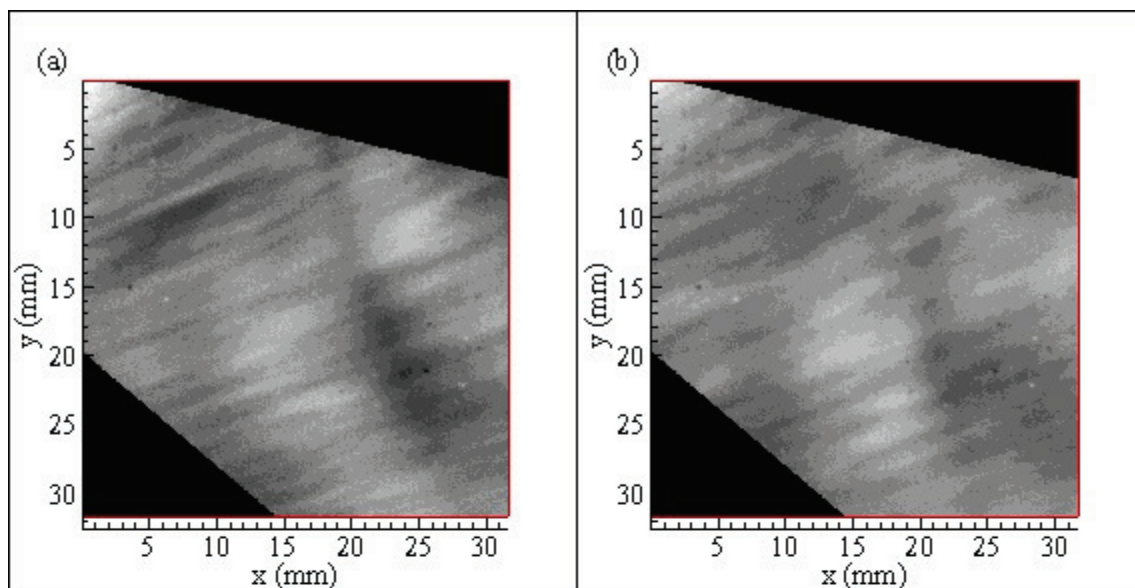


Figure C.99. Grayscale plots of normalized dimensionless mass transfer coefficient values at 96% relative humidity: (a) R96A\_6; 47 min.: 00 sec., (b) R96D\_18; 49 min.: 0 sec., (c) R96D\_19; 50 min.: 00 sec., (d) R96D\_37; 42 min.: 0 sec.



$k^*$ : 0 0.8 0.84 0.88 0.92 0.96 1 1.04 1.08 1.12 1.16 1.2

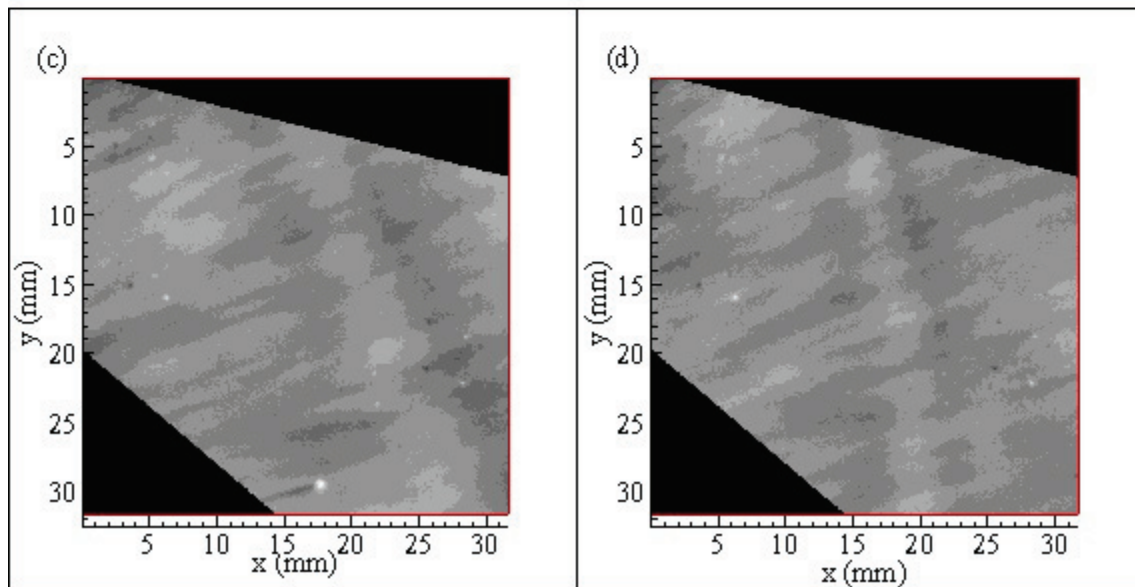


Figure C.100. Grayscale plots of normalized dimensionless mass transfer coefficient values at 96% relative humidity: (a) R96D\_45; 48 min.: 00 sec., (b) R96A\_D53; 51 min.: 20 sec., (c) R96D\_54; 52 min.: 00 sec., (d) R96D\_60; 55 min.: 0 sec.

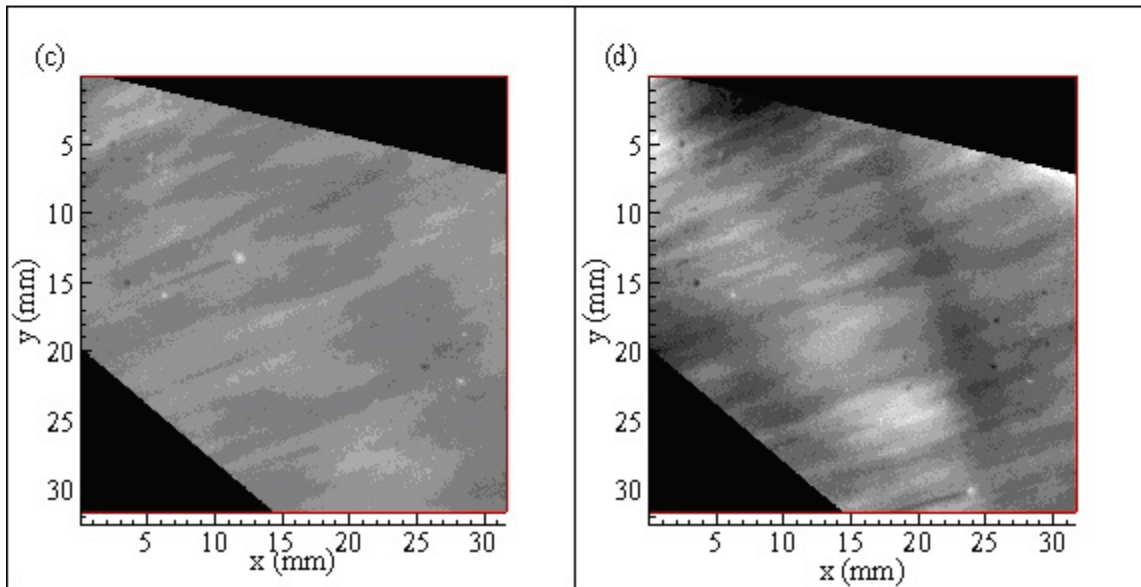
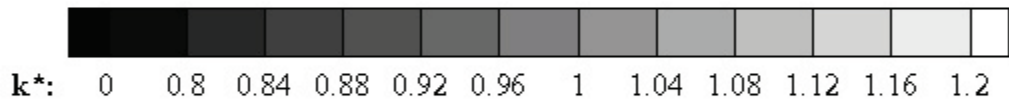
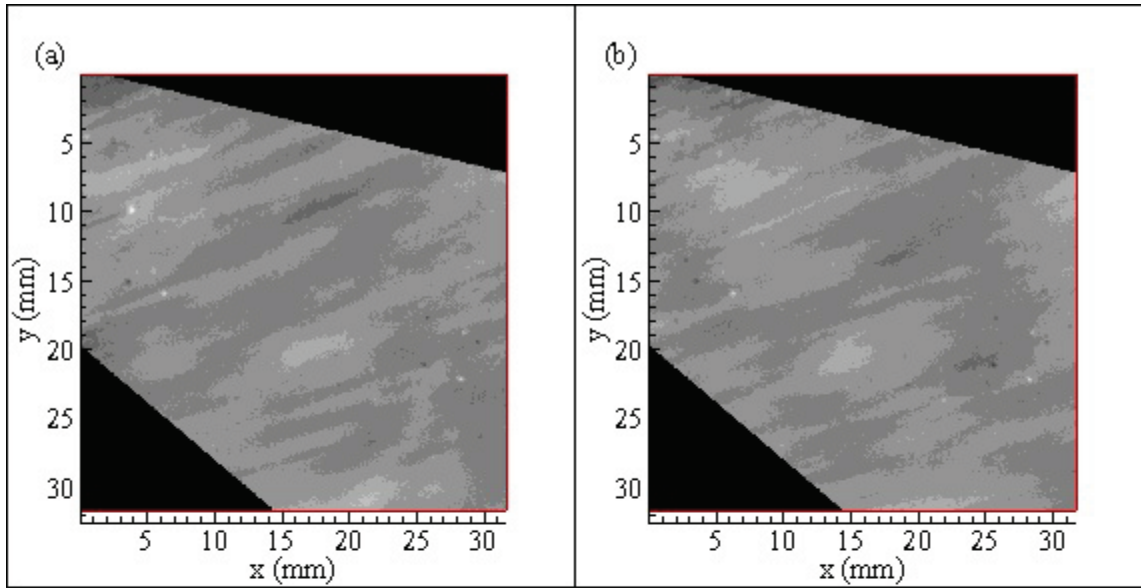


Figure C.101. Grayscale plots of normalized dimensionless mass transfer coefficient values at 96% relative humidity: (a) R96A\_6; 57 min.: 00 sec., (b) R96A\_10; 58 min.: 0 sec., (c) R96E\_10; 59 min.: 00 sec., (d) R96E\_21; 61 min.: 10 sec.

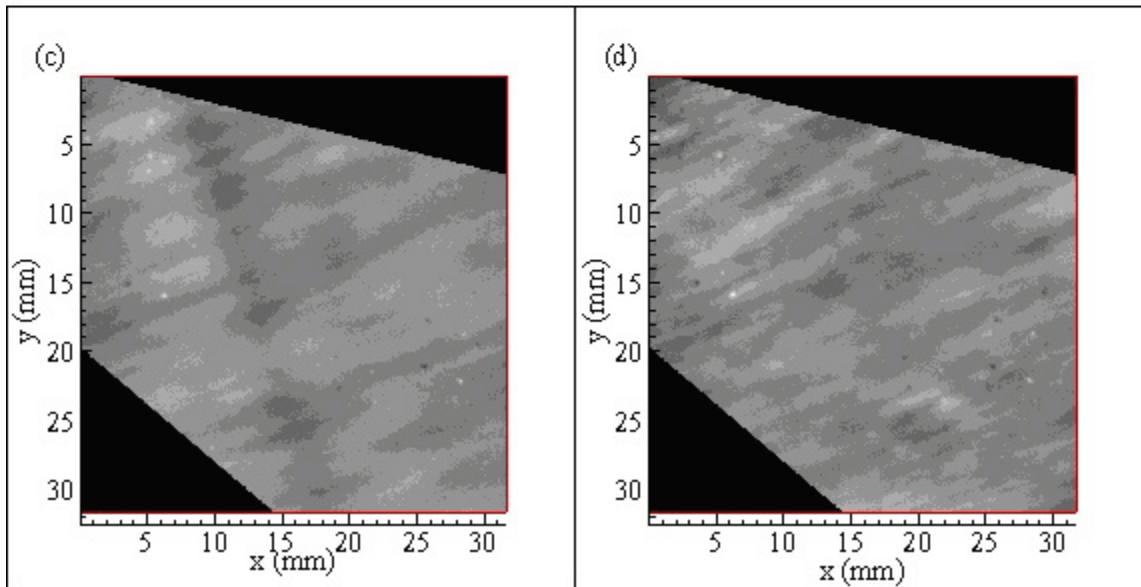
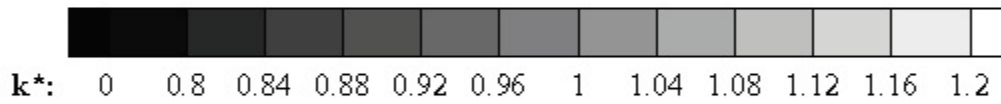
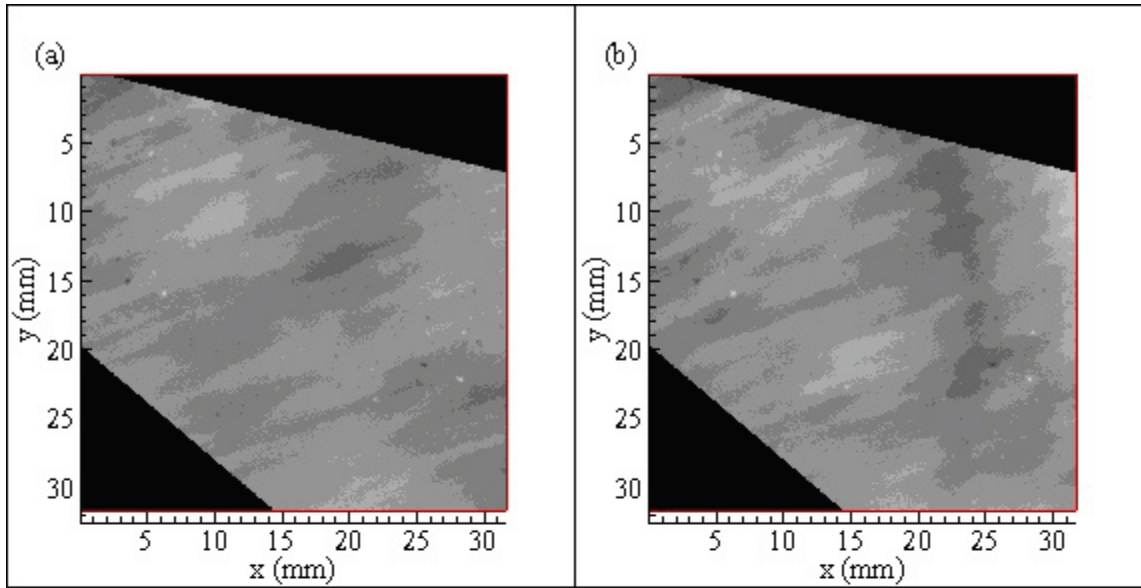


Figure C.102. Grayscale plots of normalized dimensionless mass transfer coefficient values at 96% relative humidity: (a) R96E\_36; 62 min.: 50 sec., (b) R96E\_54; 65 min.: 20 sec., (c) R96E\_63; 67 min.: 40 sec., (d) R96F\_6; 72 min.: 00 sec.

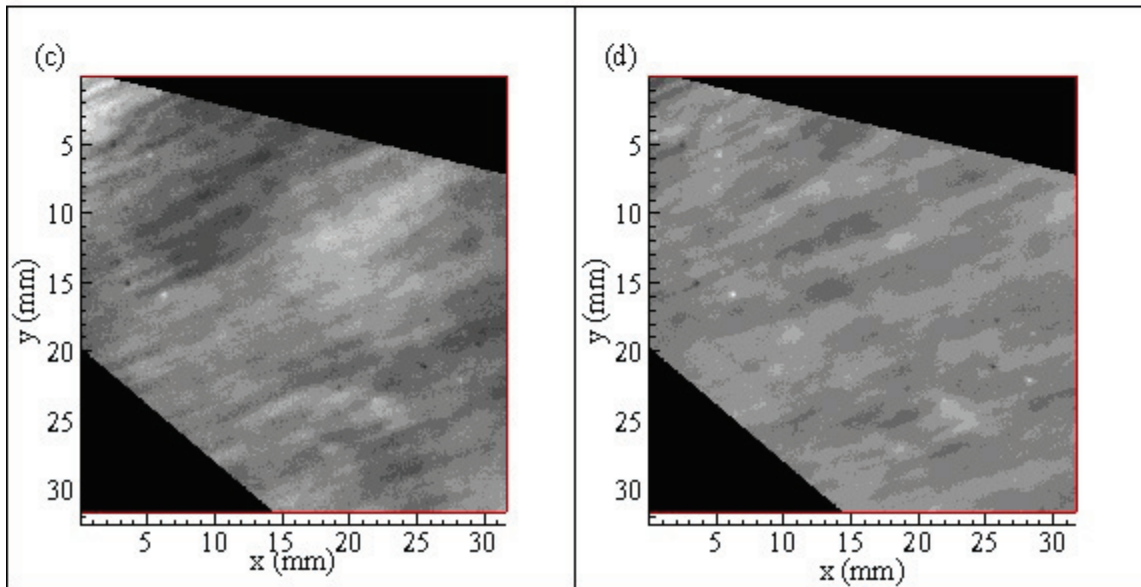
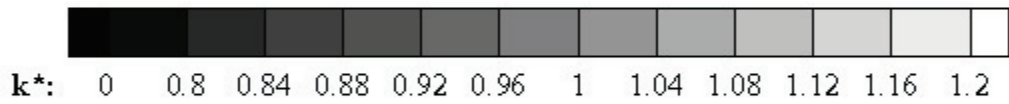
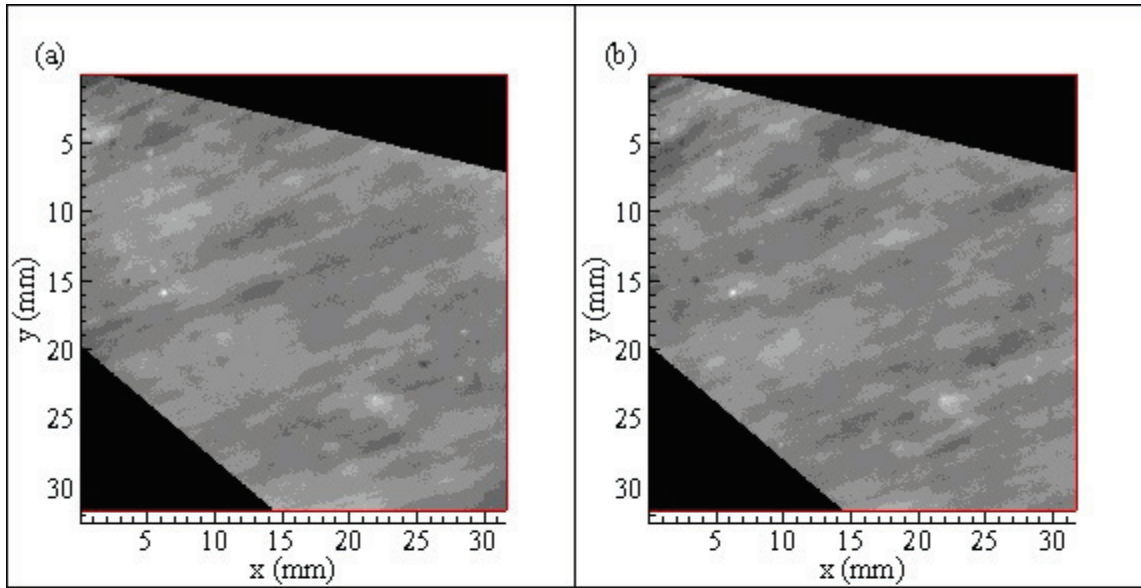


Figure C.103. Grayscale plots of normalized dimensionless mass transfer coefficient values at 96% relative humidity: (a) R96F\_8; 80 min.: 20 sec., (b) R96F\_12; 83 min.: 24 sec., (c) R96F\_17; 86 min.: 53 sec., (d) R96F\_23; 87 min.: 23 sec.

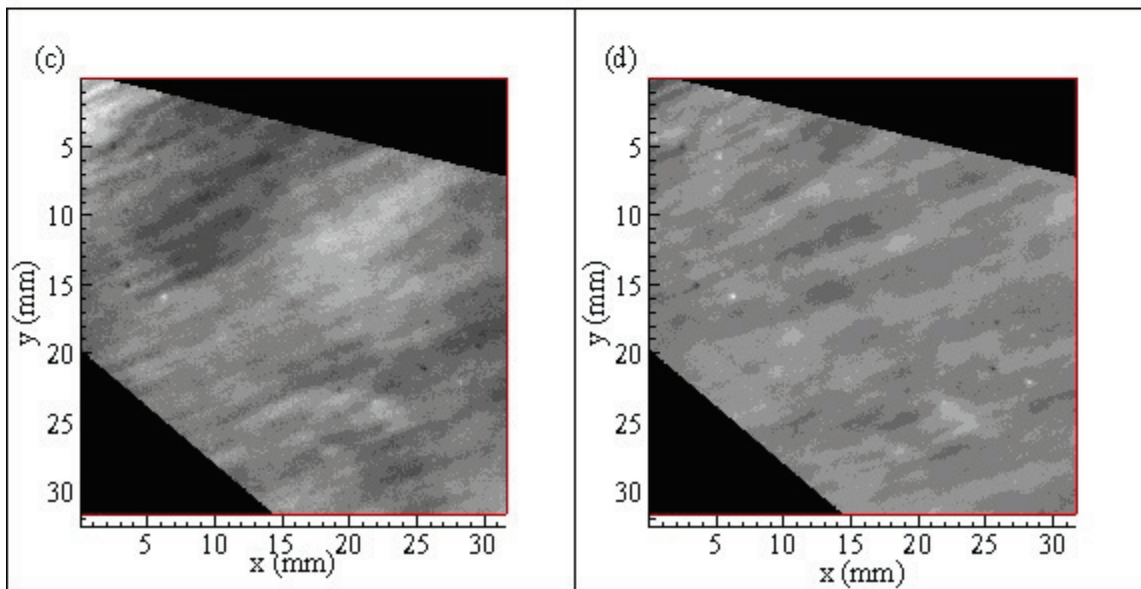
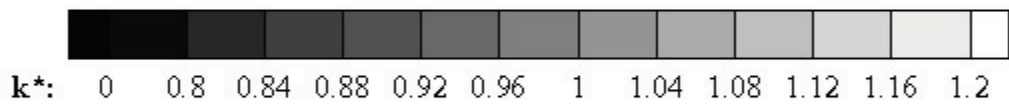
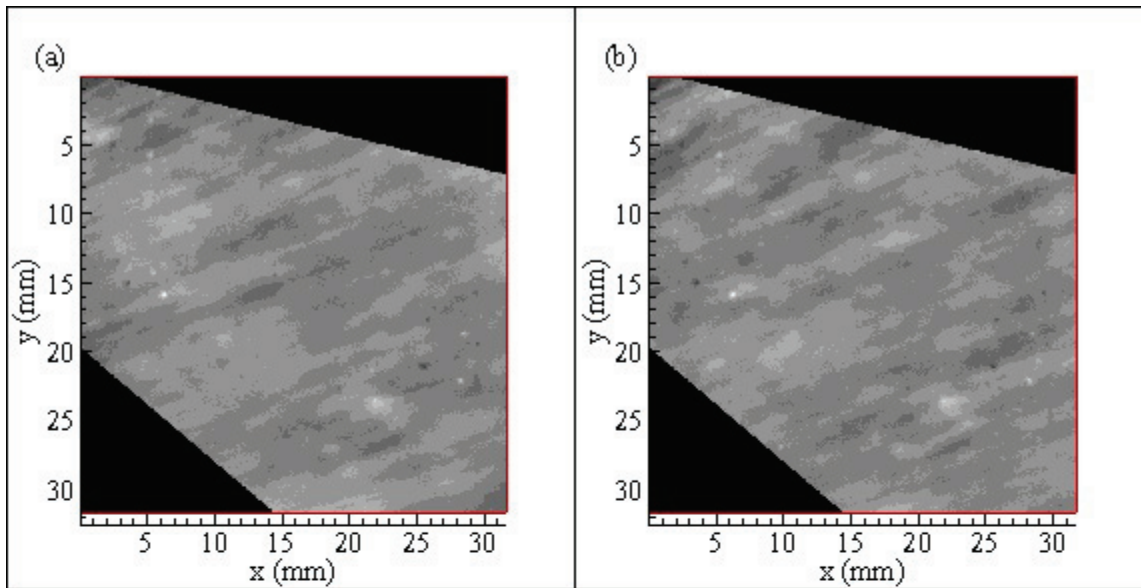


Figure C.104. Grayscale plots of normalized dimensionless mass transfer coefficient values at 96% relative humidity: (a) R96F\_37; 89 min.: 10 sec., (b) R96F\_38; 89 min.: 30 sec., (c) R96F\_39; 89 min.: 40 sec., (d) R96F\_47; 92 min.: 50 sec.

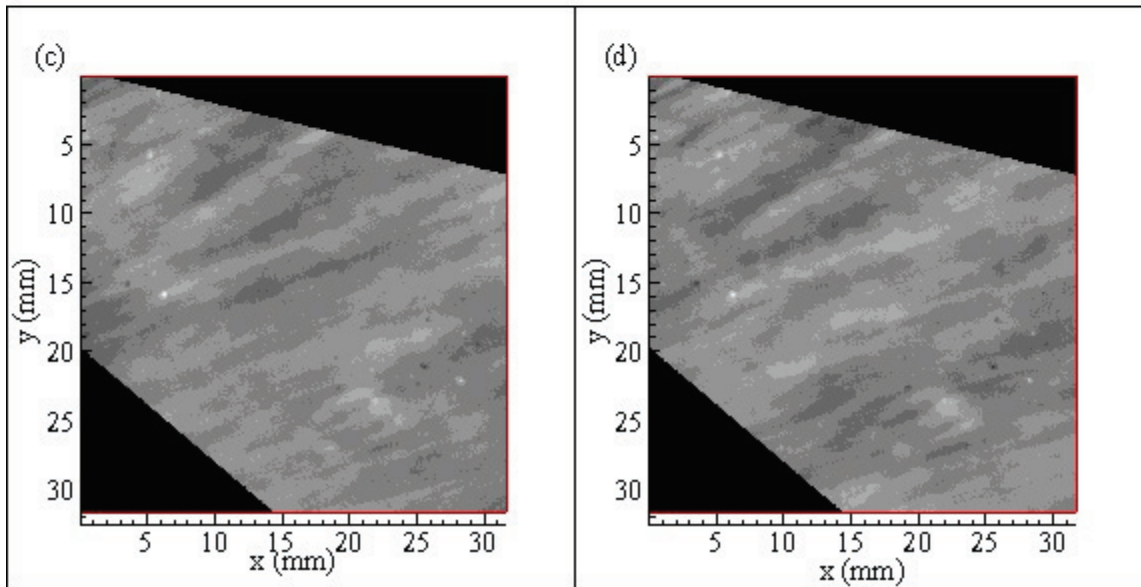
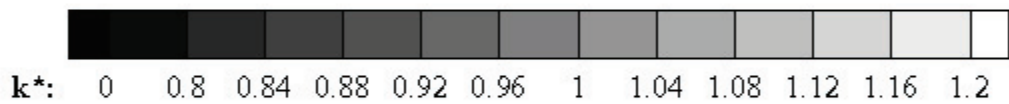
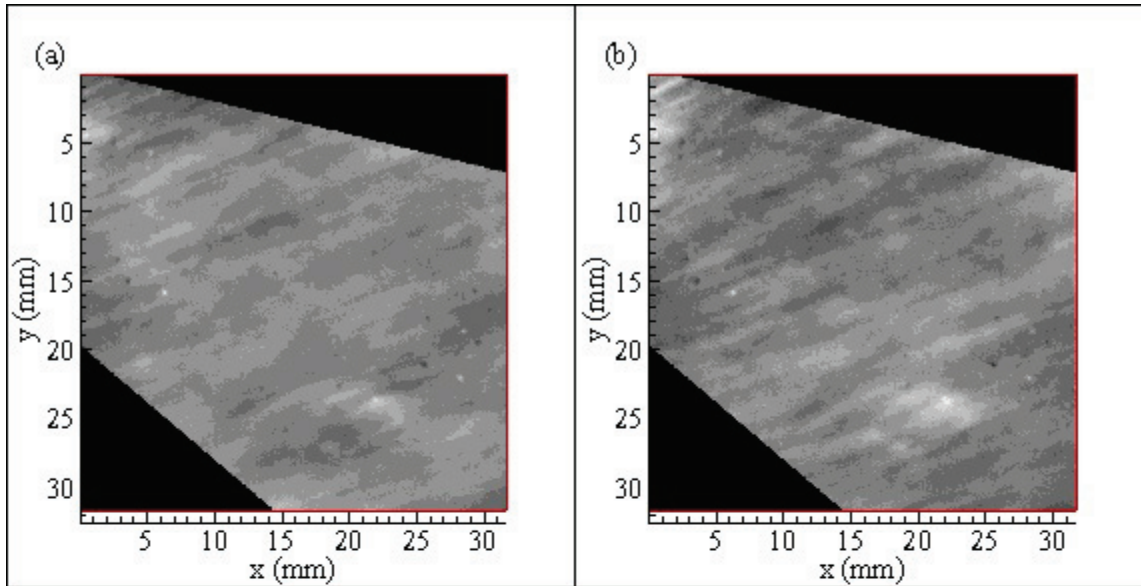
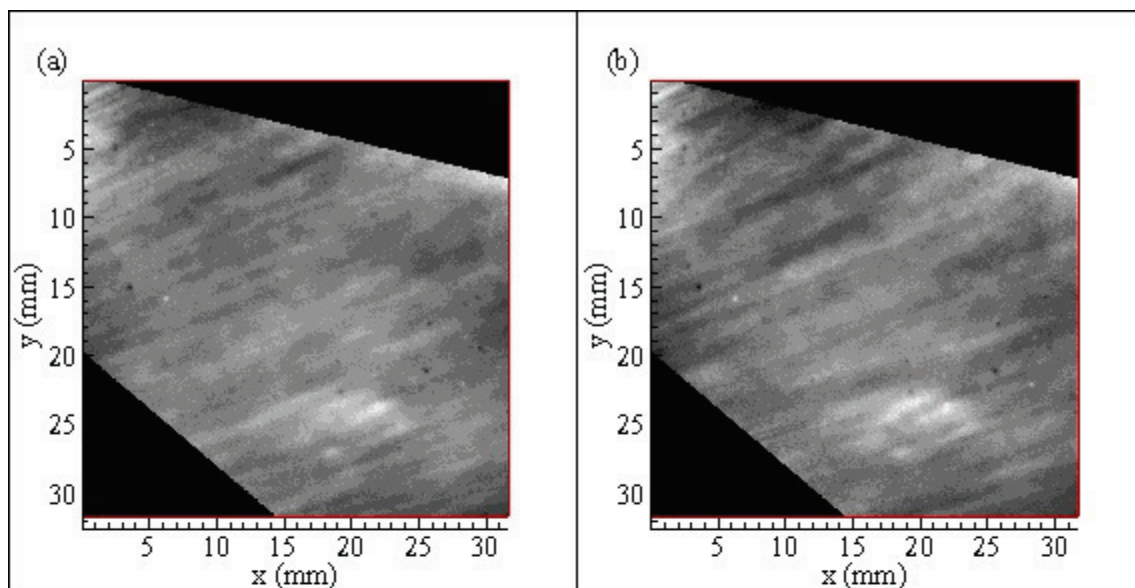


Figure C.105. Grayscale plots of normalized dimensionless mass transfer coefficient values at 96% relative humidity: (a) R96F\_6; 106 min.: 50 sec., (b) R96F\_81; 109 min.: 50 sec., (c) R96F\_94; 110 min.: 40 sec., (d) R96F\_98; 111 min.: 23 sec.



$k^*$ : 0 0.8 0.84 0.88 0.92 0.96 1 1.04 1.08 1.12 1.16 1.2

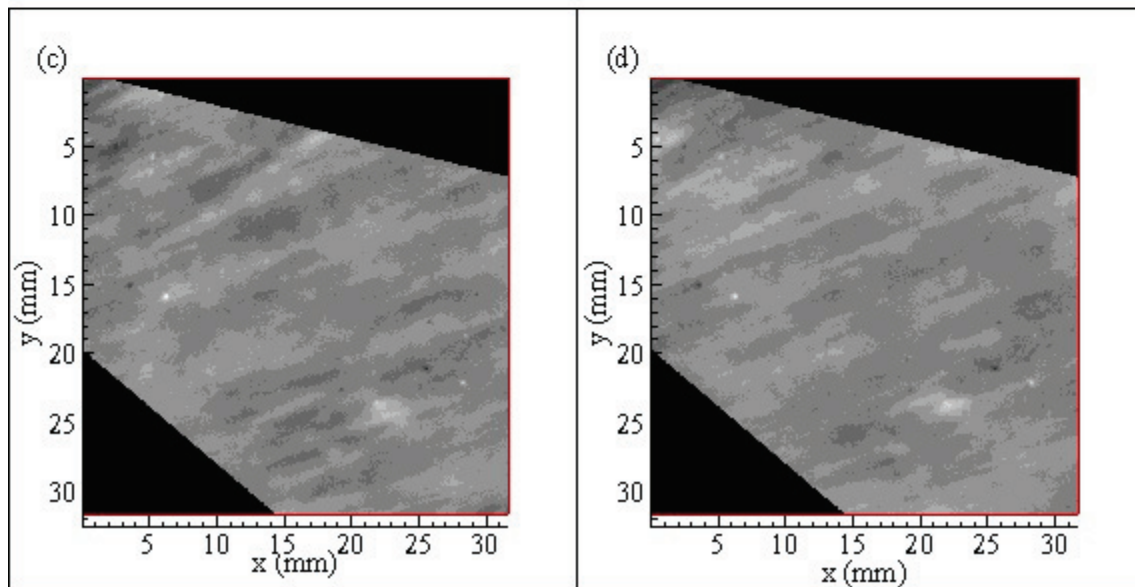


Figure C.106. Grayscale plots of normalized dimensionless mass transfer coefficient values at 96% relative humidity: (a) R96G\_7; 112 min.: 50 sec., (b) R96G\_20; 113 min.: 50 sec., (c) R96G\_37; 115 min.: 50 sec., (d) R96G\_56; 118 min.: 50 sec.

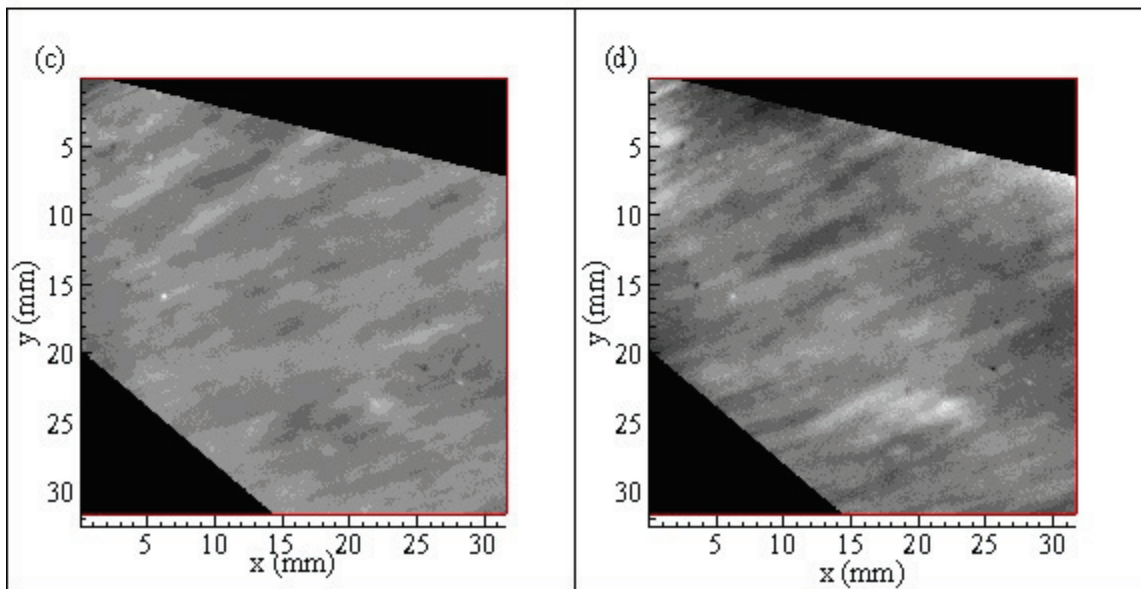
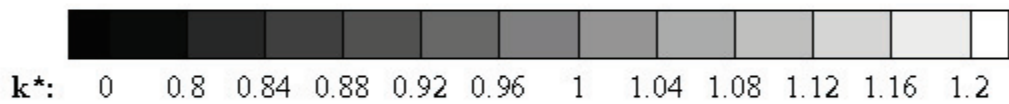
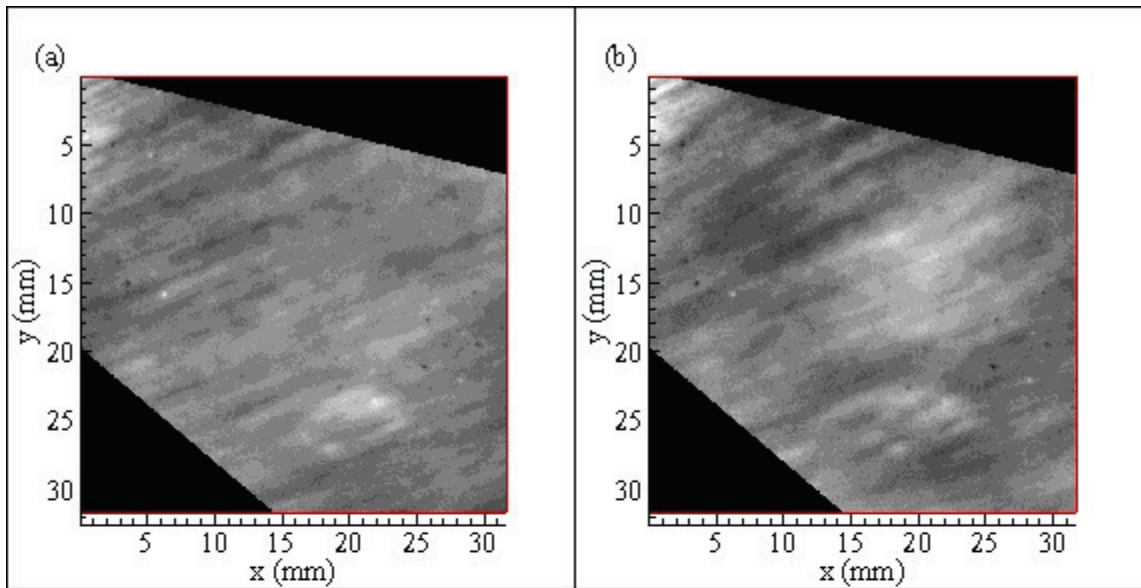
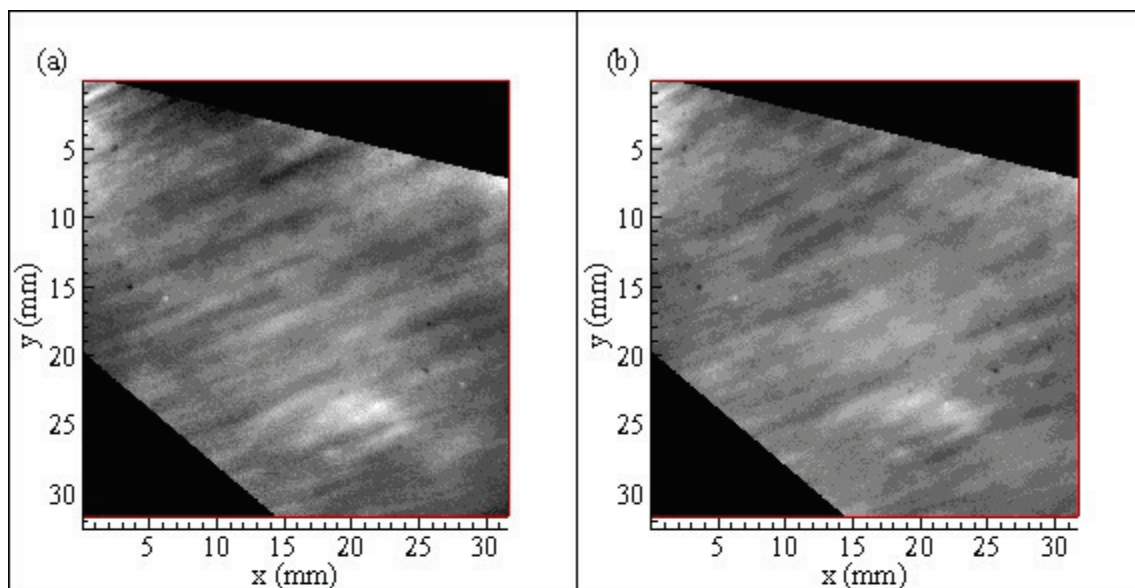


Figure C.107. Grayscale plots of normalized dimensionless mass transfer coefficient values at 96% relative humidity: (a) R96G\_60; 117 min.: 40 sec., (b) R96G\_74; 118 min.: 50 sec., (c) R96G\_91; 120 min.: 20 sec., (d) R96G\_97; 120 min.: 40 sec.



$k^*$ : 0 0.8 0.84 0.88 0.92 0.96 1 1.04 1.08 1.12 1.16 1.2

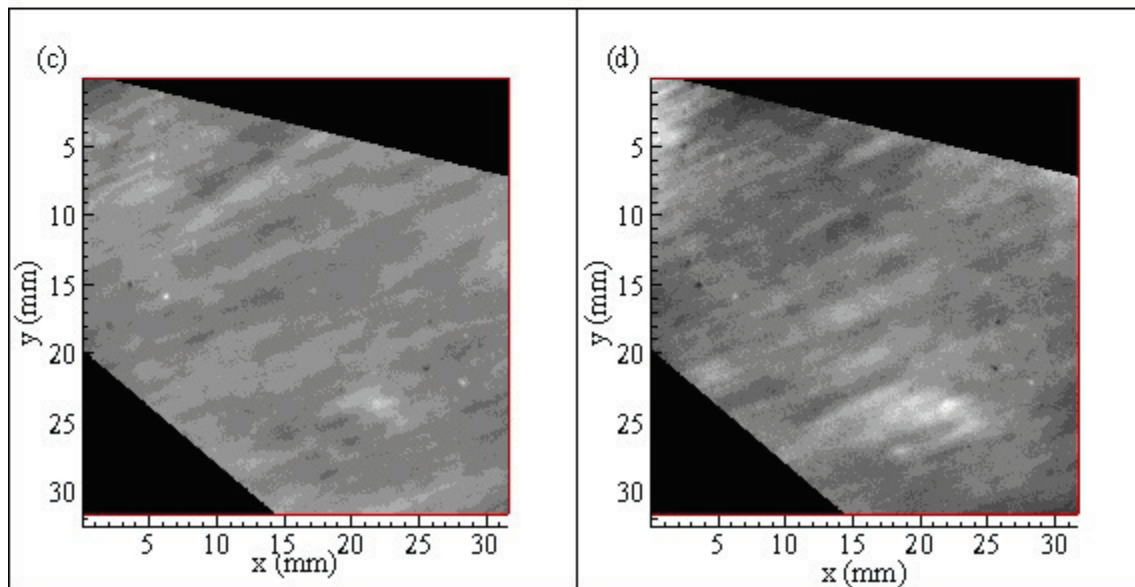


Figure C.108. Grayscale plots of normalized dimensionless mass transfer coefficient values at 96% relative humidity: (a) R96H\_15; 122 min.: 30 sec., (b) R96H\_21; 122 min.: 60 sec., (c) R96H\_55; 127 min.: 20 sec., (d) R96H\_63; 127 min.: 53 sec.

## APPENDIX D: IMAGE LABEL ROSETTA

Presentation labels presented in Chapters 7 and 8 were created for publication. The data images utilize a laboratory image labeling system based on the type of image, the month and year of the image being acquired, and the image's location within the imaging sequence. For example the image F035K\_31 is a fluorescence image (F) that was generated in March 2005 (035). The K\_31 indicates that the image is the 31<sup>st</sup> image in the 11<sup>th</sup> image set of that month. The image number is limited to a maximum value of 99 by the camera software V for windows which only allows an eight bit label. This led to substituting other first letters such as R and C are used to represent fluorescence images, originally only using the letter F. I have included a translation page for future reference.

Data Set	Image Set	Data Set	Image Set	Number range of images #	Temp °C	Pressure inHg	Humidity Relative	Image width mm	Ox' mg/L
D21A	A_[n]	F013	B_[n]	0-63	25	30.30	21%	17.2	8.45
D21A	B_[n]	F103	C-[n]	0-99	25	30.30	21%	17.2	8.45
D21B	A_[n]	F023	C_[n]	0-24	25	30.36	21%	17.2	8.74
D21B	B_[n]	F203	J_[n]	0-78	25	30.36	21%	17.2	8.74
D21B	C_[n]	F203	K_[n]	0-99	25	30.36	21%	17.2	8.74
D32A	A_[n]	F203	L_[n]	0-95	23	30.27	32%	17.2	8.64
D32A	B_[n]	F203	M_[n]	0-35	23	30.27	32%	17.2	8.64
D32A	C_[n]	F023	P_[n]	0-87	23	30.27	32%	17.2	8.64
D36A	A_[n]	Fo23	Q_[n]	0-77	24.5	30.21	36%	17.2	8.48
D29A	A_[n]	F033	A_[n]	31-42	24	30.39	29%	28.4	8.61
D29AB	B_[n]	F033	B_[n]	0-36	24	30.39	29%	28.4	8.61
D29AC	C_[n]	F033	C_[n]	0-99	24	30.39	29%	28.4	8.61
D29AD	D_[n]	F033	E_[n]	0-99	24	30.39	29%	28.4	8.61
D46AA	A_[n]	F033	F_[n]	0-64	22.5	29.83	46%	17.2	8.69
D46AB	B_[n]	F033	G-[n]	2-99	22.5	29.83	46%	17.2	8.69
D46AC	C_[n]	F033	I_[n]	1-99	22.5	29.83	46%	17.2	8.69
D46AD	D_[n]	F033	J_[n]	0-39	22.5	29.83	46%	17.2	8.69
D46AE	E_[n]	F033	K_[n]	0-32	22.5	29.83	46%	17.2	8.69
D46AF	F_[n]	F033	L-[n]	0-91	22	29.83	46%	28.4	8.69
D46AG	G_[n]	F0303	N_[n]	1-9	22	29.83	46%	28.4	8.69
D46AH	H_[n]	F0303	O_[n]	0-9	22	29.83	46%	28.4	8.69
D46AI	I_[n]	F030	3P_[n]	0-9	22	29.83	46%	28.4	8.69
D46AJ	J_[n]	F0303	Q_[n]	0-9	22	29.83	46%	28.4	8.69
D46AK	K_[n]	F0303	R_[n]	1-9	22	29.83	46%	28.4	8.69
DBA	1_[n]	R023	6_[n]	0-46	N/A	N/A	N/A	28.4	N/A
DBA	2_[n]	R0103	D[n]	0-10	N/A	N/A	N/A	28.4	N/A
DBA	3_[n]	R0103	B[n]	0-22	N/A	N/A	N/A	28.4	N/A
DBA	4_[n]	R0103	C[n]	0-5	N/A	N/A	N/A	28.4	N/A
D36B	A_[n]	F043	B_[n]	0-99	22	30.39	36%	17.2	8.95
D36B	B_[n]	F043	C_[n]	0-98	22	30.39	36%	17.2	8.95
D42AA	A_[n]	F043	D_[n]	0-98	21	30.33	42%	17.2	9.09
D42AB	B_[n]	F043	E_[n]	0-96	21	30.33	42%	17.2	9.09

Table D.1. Conversion table for development images to transfer from labels used in text to those generated by V for Windows software.

Data Set	Image Set	Data Set	Image set	Number range of images #	Temp °C	Pressure inHg	Humidity Relative	Image size Mm	Ox' mg/L
R27	A_[n]	F035	B_[n]	0-98	22	29.96	27%	31.75	8.45
R27	B_[n]	F035	C-[n]	0-22	22	29.96	27%	31.75	8.45
R27	C_[n]	F035	D_[n]	0-94	22	29.96	27%	31.75	8.45
R27	D_[n]	F035	E_[n]	0-27	22	29.96	27%	31.75	8.45
R27	E_[n]	F035	F_[n]	0-99	22	29.96	27%	31.75	8.74
R27	F_[n]	F035	G_[n]	0-99	22	29.96	27%	31.75	8.74
R27	G_[n]	F035	H_[n]	0-60	22	29.96	27%	31.75	8.74
R27	H_[n]	F035	I_[n]	0-40	22	39.96	27%	31.75	8.64
R27	I_[n]	F035	J_[n]	0-99	22	39.96	27%	31.75	8.64
R29	A_[n]	F035	K_[n]	31-42	24	30.39	29%	31.75	8.61
R46	A_[n]	F055	C_[n]	7-92	21.0	29.70	46%	31.75	8.91
R46	B_[n]	F055	D_[n]	4-92	21.0	29.70	46%	31.75	8.91
R46	C_[n]	F055	E_[n]	0-100	21.0	29.70	46%	31.75	8.91
R46	D_[n]	F055	F_[n]	1-99	21.0	29.70	46%	31.75	8.91
R58	A_[n]	F045	L_[n]	0-99	22.0	29.71	58%	31.75	8.74
R58	B_[n]	F045	M_[n]	0-99	22.0	29.71	58%	31.75	8.74
R58	C_[n]	F045	N_[n]	0-99	22.0	29.71	58%	31.75	8.74
R58	D_[n]	F045	O_[n]	0-99	22.0	29.71	58%	31.75	8.74
R58	E_[n]	F045	OB_[n]	0-99	22.0	29.71	58%	31.75	8.74
R61	A_[n]	R045	A_[n]	0-25	21.5	29.71	61%	31.75	8.82
R63	A_[n]	R045	Q_[n]	0-99	21.5	29.71	63%	31.75	8.82
R63	B_[n]	R045	S_[n]	0-99	21.5	29.71	63%	31.75	8.82
R63	C_[n]	R045	T_[n]	0-99	21.5	29.71	63%	31.75	8.82
R63	D_[n]	R045	U_[n]	0-99	21.5	29.71	63%	31.75	8.82
R63	E_[n]	R045	V_[n]	0-99	21.5	29.71	63%	31.75	8.82
R63	F_[n]	R045	VB_[n]	0-68	21.5	29.71	63%	31.75	8.82
R91	A_[n]	C045	L_[n]	1-81	23.0	29.72	91%	31.75	8.58
R91	B_[n]	C045	M_[n]	0-99	23.0	29.72	91%	31.75	8.58
R91	C_[n]	C045	N_[n]	0-97	23.0	29.72	91%	31.75	8.58
R91	D_[n]	C045	O_[n]	0-22	23.0	29.72	91%	31.75	8.58
R96	A_[n]	C045	D_[n]	0-95	23.0	29.72	96%	31.75	8.58
R96	B_[n]	C045	E_[n]	4-103	23.0	29.72	96%	31.75	8.58
R96	C_[n]	C045	F_[n]	6-98	23.0	29.72	96%	31.75	8.58
R96	D_[n]	C045	G_[n]	7-100	23.0	29.72	96%	31.75	8.58
R96	E_[n]	C045	H_[n]	5-63	23.0	29.72	96%	31.75	8.58
R96	F_[n]	C045	HA_[n]	2-36	23.0	29.72	96%	31.75	8.58

Table D.2. Conversion table for relative humidity study to convert labels used in text to those generated by V for Windows.